Development of an advanced geostatistical model for shear wave velocity profiles to manage uncertainties and variabilities in Ground Response Analyses

Doctoral Dissertation
Doctoral Program in Civil and Environmental Engineering (31st Cycle)

Development of an advanced geostatistical model for shear wave velocity profiles to manage uncertainties and variabilities in Ground Response Analyses

Federico Passeri

* * * * * *

Supervisors
Prof. Sebastiano Foti
Prof. Adrian Rodriguez-Marek

Doctoral Examination Committee:
Prof. Ellen Rathje, Referee, The University of Texas at Austin (US)
Prof. Scott J. Brandenberg, Referee, University of California Los Angeles (US)
Prof. Laura Valentina Socco, Referee, Politecnico di Torino (Italy)
Prof. Carlo Giovanni Lai, Referee, Università di Pavia (Italy)
Dr. Angeliki Lessi Cheimariou, Referee, Jacobs Engineering, London (UK)

Politecnico di Torino
15/3/2019

I hereby declare that, the contents and organisation of this dissertation constitute my own original work and does not compromise in any way the rights of third parties, including those relating to the security of personal data.

…….....

Federico Passeri

Torino, 15/3/2019

Summary

This dissertation primarily deals with the development of a new geostatistical model for the independent management of Epistemic Uncertainties (EUs) and Aleatory Variabilities (AVs) in shear wave velocity profiles (V_S) obtained with surface wave methods. This topic has gained much interest in light of the recent probabilistic advancements in of ground motion predictions, particularly in case of only deterministic available solutions.

An overview of the methods that address for the influence of epistemic uncertainties and aleatory variabilities in probabilistic hazard studies is initially presented. The essential role of the process for the Identification, Quantification, and Management (IQM) of uncertainties and variabilities is widely discussed along with the included practical criticisms.

The dissertation focuses on the role played by site effects in hazard studies. The research is primarily devoted to the study of these effects by means of 1D Ground Response Analyses (GRAs). In this regard, the dissertation presents an extensive analysis of the most critical sources of EUs and AVs included in this type of numerical simulations. Also, the effects of these sources on the results are explicitly investigated and summarized.

In particular, the dissertation highlights the primary importance of shear wave velocity profiles in GRAs. In this regard, substantial consideration is given to different seismic (i.e., geophysical) tests that experimentally estimate this parameter. An extensive and precise analysis of the sources of EUs and AVs in each geophysical tests is presented and summarized along with the issues for their identification and quantification. Also, the usually adopted methods for the management of uncertainties and variabilities are described and discussed in details.

The development of the new geostatistical model is strictly connected to the compilation of the Polito Shear Wave velocity Database (PSWD). This collection of high-quality surface waves experimental data represents the main ingredient for the analysis of the random variables involved in the problem and for the rigorous calibration of the model. Moreover, the availability of a large amount of data and the study of the geostatistical model allowed examining in depth three main side products of the dissertation. The first regards the accurate study of the uncertainties and variabilities included in the processing of surface wave tests and the experimental dispersion curve. The second concerns the development of a robust

transformation law between the wavelength of the Rayleigh waves and the depth of the harmonic average V_S profile. The third main side product of the research is the implementation of a method for inversions with a variable number of layers.

The primary characteristics of the proposed geostatistical model are the experimentally-based calibration, the separation of the random variables space and time, the site- and test-specific features, the user-friendliness, and the flexibility. The flexibility of the model is demonstrated by a prototype application to Down-Hole tests, which represents its natural future development.

The proposed geostatistical model is validated by means of a real case study for the site of Mirandola (Italy). Both the linear viscoelastic and the nonlinear responses of the deposit are modeled. The results show a significant improvement in the management of EUs and AVs in GRAs, compared to the methods usually adopted for scientific and technical applications. The geostatistical model allows a rigorous control of the level of uncertainties and variabilities introduced in the hazard study. However, further research should be devoted to additional validations of the randomization model in light of the possible separation of EUs and AVs in the final result. Indeed, the model is capable to manage indistinctly the uncertainties that are the results of the identification and quantification steps. Also, the extension of the model architecture to other geophysical tests (e.g., Down-Hole tests) can be easily implemented and represents a further research's goal. In this regard, a preliminary validation of the extended model is finally proposed and applied to a real Down-Hole test performed in Mirandola.

A Cecilia e Valentina

"Leave this world a little better than you found it."

Robert Stephenson Smyth Baden-Powell; Last message.

Contents

List of Tables

List of Figures

Chapter 1
Introduction

1.1 Motivation

The estimation of the seismic risk is of primary interest in a comprehensive framework, ranging from Earthquake Engineering to Civil Protection purposes. Massive efforts are made to provide an accurate prediction of the seismic hazard at a site by means of numerical simulations and/or analysis of recorded data. In this context, the performance of hazard-consistent site response analyses represents one of the most challenging aspects.

In particular, the seismic hazard is strongly dependent on the near-surface characteristics of the soil deposit that are usually modeled by one-dimensional site response analyses (termed Ground Response Analyses, GRAs). In this regard, both Epistemic Uncertainties (EUs) and Aleatory Variabilities (AVs) have to be Identified, Quantified and Managed (i.e., IQM method) along the GRA process. This operation is essential for a rigorous agreement with the hazard results obtained with Probabilistic Seismic Hazard Analyses. However, various criticisms arise moving from the theoretical to the practical point of view, particularly for the identification and quantification steps.

The epistemic uncertainties result from incomplete knowledge of the physics of the process and/or from insufficient and/or inadequate experimental data and adopted models. They can, in principle, be reduced by the collection of additional and higher quality information and can be managed with advanced models. The aleatory variability refers to the intrinsic randomness of natural systems. It can be quantified, but it cannot be reduced using multiple experimental measurements.

Epistemic uncertainties and aleatory variabilities in GRAs can be grouped in four main classes of parameters (Idriss 2004). These are included in the shear wave velocity profile, the modulus reduction and damping curves, the input motion selection process, and the numerical model adopted for the simulations (Rathje et al. 2010). The shear strength and the small-strain damping can be considered as two further sources of uncertainties and variabilities.

The shear wave velocity (V_S) profile is the parameter that controls the elastic behavior of the soil deposit as a small-strain "site signature". The V_S profiles are estimated by seismic (i.e., geophysical) tests that are often divided into two broad categories: invasive or non-invasive methods (Foti 2000). The invasive methods still represent a solid reference, even if they can be affected by large biases (resulting from both EUs and AVs). On the contrary, the non-invasive tests are increasingly spreading in standard practice because of their time and cost-effectiveness.

The *identification* of EUs and AVs in shear wave velocity profiles should be performed by expert analysts, explicitly accounting for the geophysical background theory. In particular, each seismic test shows specific sources of uncertainties and variabilities. This step is then dramatically delicate for the application of the theoretical definitions of EUs and AVs.

The *quantification* of EUs and AVs for shear wave velocity profiles should evaluate the global engineering perspective of the case study and the spatial scale of the specific problem. Different geophysical methods are associated with a specific amount of EUs and AVs that strongly depends on the characteristics of the investigated volume (e.g., geological environment). In addition, for most cases, an accurate separation of these contributes appears not feasible from a practical point of view.

The *management* of epistemic uncertainties and aleatory variabilities in shear wave velocity profiles still represents an open issue (Stewart et al. 2014a), particularly in case of a limited deterministic framework. For these purposes, two methods are presented in the Electric Power Research Institute (EPRI) guidelines and are usually adopted for scientific and technical applications. The first is referred to as alternative (upper-range and lower-range) method and is suggested for the management of epistemic uncertainties. The second is described in Toro (1995) as a geostatistical randomization model for the management of aleatory variabilities. Many authors demonstrated various limits of these methods in reproducing a consistent "picture" of uncertainties and variabilities. In particular, the upper-lower range profiles lead to a distorted response of the soil profile, mainly due to the scaling procedure. Similarly, the Toro model generates shear wave velocity models that are incompatible with the experimental evidence (i.e., site signatures). This is mainly due to the inadequate randomization approach. In addition, the separate management of EUs and AVs can be difficult in light of the various issues in the identification and quantification steps. However, the proposed model is independent of the type of uncertainty that is identified and quantified in the first steps of the IQM method. For example, the model calibration performed for the surface wave testing methods is based on the joint management of EUs and AVs, as a distinction is practically unfeasible for these tests.

1.2 Research Objectives and Achievements

The primary goal of the dissertation is the development of a new geostatistical model for the independent management of EUs and AVs in shear wave velocity profiles obtained with surface wave tests. The model has to be able to overcome the limitations of the usual methods adopted for scientific and technical applications indistinctly for EUs and AVs. On the same hand, the model should solve the limitations of the deterministic solutions usually available after the characterization of a site.

The geostatistical model has to be calibrated with a high-quality database of surface wave experimental measurements. The proposed model is based on the specifically compiled Polito Shear Wave velocity Database (PSWD) that ensures

high-quality standards. A systematic inversion conducted for each site guarantees the quality of the obtained solutions. The PSWD represents the fundamental ingredient for the development of the geostatistical model and the additional side-products presented in the dissertation.

The Toro model randomizes the interval velocities based on a stack of a finite number of horizontal layers with constant velocity. The inadequacies of the interval velocity scheme are extensively demonstrated in the dissertation, as they are only an engineering scheme adopted in GRA models. The new geostatistical model assumes a neat separation between the fundamental physical quantities of space and time, avoiding parasite (i.e., multiple) uncertainties. The double-counting of uncertainties is indeed typical if the model randomizes separately the interval velocity and the depth of interfaces (i.e., layer thicknesses), as proposed in Toro (1995).

The new geostatistical model has to be site- and test-specific. This allows reproducing realistic (i.e., experimentally-based) characteristics of the test regarding both EUs and AVs.

Finally, the new geostatistical model has to be flexible for further improvements (e.g., an extension of applicability to other geophysical tests). The "core" of the model remains fixed, whereas additional dedicated parts can be introduced to specify the problem. In this regard, the dissertation presents a prototype evolution of the model applied to Down-Hole tests that represents the natural extension of the model.

The dissertation also includes three side products. The first is the regression of a function for the experimental quantification of EUs and AVs in the dispersion curve. The proposed formulation could be used in case of deterministic processing of the seismic data. Then, a further achievement regards the development of a robust transformation law between the wavelength of the Rayleigh waves and the depth of the harmonic average V_S profile. This approach presented in Socco et al. (2017) is very appealing for the possible development of an "inversion-free" analysis of surface waves. The third main side product of the research is the implementation of a rigorous method for the inversion of the experimental dispersion curve with a variable number of layers. This methodology considerably enlarges the space of the solutions of the inverse process. These three results demonstrate the benefits of the PSWD that offers an excellent resource also for future research.

1.3 Dissertation Outline

The dissertation is organized in two different blocks. The first part is methodological: it gives an insight into the characteristics of modern approaches for hazard-consistent GRAs for ground motion predictions. The remaining part presents the new geostatistical model and its applications (both to surface wave methods and Down-Hole tests), the side products, and the conclusions.

More in detail, in Chapter 2, the global framework is presented, and the various contributes to the seismic risk are briefly analyzed. The discussion focuses on the more generic to the specific problem of site effects along with a list of examples of

hazard assessment studies. Then, the dissertation addresses the distinction between epistemic uncertainties and aleatory variabilities for IQM purposes in a non-ergodic perspective. The Chapter focuses on the practical issues included in the methodology.

Chapter 3 is entirely devoted to the specific problem of the site effects. The primary methods for evaluating the influence of the site effects are discussed (i.e., numerical simulations and/or analysis of recorded data). Then, the dissertation focuses on the primary sources of EUs and AVs in GRAs (i.e., 1D numerical simulations) that are summarized in a dedicated section. Also, the effects of these sources are presented by means of an extensive literature overview, always highlighting the delicate processes of identification and quantification.

Chapter 4 is dedicated to the V_S profiles and includes a brief introduction on seismic waves in elastic solids and associated geotechnical parameters. An overview of the methods currently used in practice and newly proposed for soil characterization is also presented. The Chapter includes a useful summary regarding the crucial identification and quantification of EUs and AVs for each seismic test. A specific section is devoted to the management process with a broad literature overview of the most adopted methods and their applications.

Chapter 5 describes the characteristics of the Polito Shear Wave velocity Database (PSWD) that has been specifically compiled for the present study. Particular attention is paid to the quantification of EUs and AVs in the experimental dispersion curve and their often unfeasible practical separation.

Chapter 6 presents the operations conducted on the PSWD in addition to the step-by-step development and calibration of the geostatistical model for surface wave methods. A systematic inversion with variable layers number was performed for each site in the database. This was conducted to study the optimal mathematical architecture for the model and the distribution of the considered random variables. Indeed, the results of the inversions allowed a rigorous evaluation of the essential characteristics of the experimental evidence that should be reproduced by the randomization model. The development and calibration of the geostatistical model are step-by-step presented in details, along with a final example of an application for a site in the PSWD. Chapter 6 also includes the extension of the geostatistical model to Down-Hole tests. This application represents a step-forward and demonstrates the flexibility of the proposed model. However, the lack of a dedicated database prevents the calibration of the geostatistical model also for these types of invasive tests. As for the application to surface wave methods, also in this case the model can manage indistinctly EUs or AVs.

A systematic application of the developed geostatistical model for surface wave tests is proposed in Chapter 7. In this case, however, the site was not part of the PSWD, in order to rigorously validate the results of the model. The site of Mirandola is chosen for a large amount of available information, as collected during the InterPACIFIC project. The Chapter can be seen as an extension of the work presented in Passeri et al. (2019) and concludes the topic with a broad comparison of the different methods for the management of EUs and AVs in V_S profiles. This Chapter presents also a further application of the geostatistical model to a Down-

Hole test performed in Mirandola. As already discussed, the capabilities of the model allow for an extension to invasive tests, although a test-specific set of model parameters would be required.

Finally, Chapter 8 summarizes some comments and conclusions, together with the indication of some specific topics for further development and research.

Appendix A reports details about the PSWD and the results of the inversions that were used as the main ingredient of the proposed geostatistical model.

Chapter 2
Probabilistic Seismic Hazard Analysis: Epistemic Uncertainty, Aleatory Variability, and Ergodicity

The present Chapter gives a global perspective of introductory definitions regarding the probabilistic hazard-consistent prediction of earthquake-induced ground motions. The discussion starts from the usual methods and procedures for the evaluation of the seismic hazard at a specific site. Particular attention is paid to the inclusion of site effects within the hazard estimations, as broadly discussed in Stewart et al. (2014). The importance of uncertainties and variabilities is discussed in Section 2.2, where a detailed discussion regarding the Identification, Quantification, and Management (IQM) of Epistemic Uncertainties (EUs) and Aleatory Variabilities (AVs) is presented. The discussion highlights the major challenges included in the three steps, particularly in terms of separation of the two main contributes to the identification and quantification steps.

2.1 Seismic Hazard

The study of seismic events has always been a crucial topic in earthquake engineering. The prediction and assessment of the effects of a seismic event is a multidisciplinary process that involves seismologists, geotechnical and structural engineers, risk management experts and politicians. In particular, the analysis of the seismic risk can be broken into three separate components (Figure 2.1) as suggested in the Performance-Based Earthquake Engineering (PEER, Pacific Earthquake Engineering Research center) methodology (Moehle 2003):

- Seismic hazard assessment (Hazard);
- Structural response and damage to components (Vulnerability);
- Repair costs and loss analysis (Exposure).

The first component (i.e., hazard) regards the prediction of a suitable set of ground motion *intensity measures* (i.e., simple parametrizations of the seismic ground motion). A vector of intensity measures (or a single parameter) is predicted as a function of site/seismic parameters adopting full probability distribution functions. The evaluation of the vulnerability requires *engineering demand parameters* to quantify the structural response. These parameters are predictable as a function of the prescribed intensity measures adopting full probability distribution

functions. The exposure is quantified by *decision variables* and provides tools for decision makers (e.g., owners, public policy officials) regarding the possible losses and the total cost.

Each of these components is affected by uncertainties and variabilities that propagate to the final result (i.e., global loss estimate) (Baker & Cornell 2008). In this dissertation, only the hazard contribution to the total risk is addressed. Indeed, the objective is to obtain design ground motions (i.e., described by appropriate intensity measures) expected at a site as a result of future earthquakes (i.e., for different return periods in a probabilistic framework.

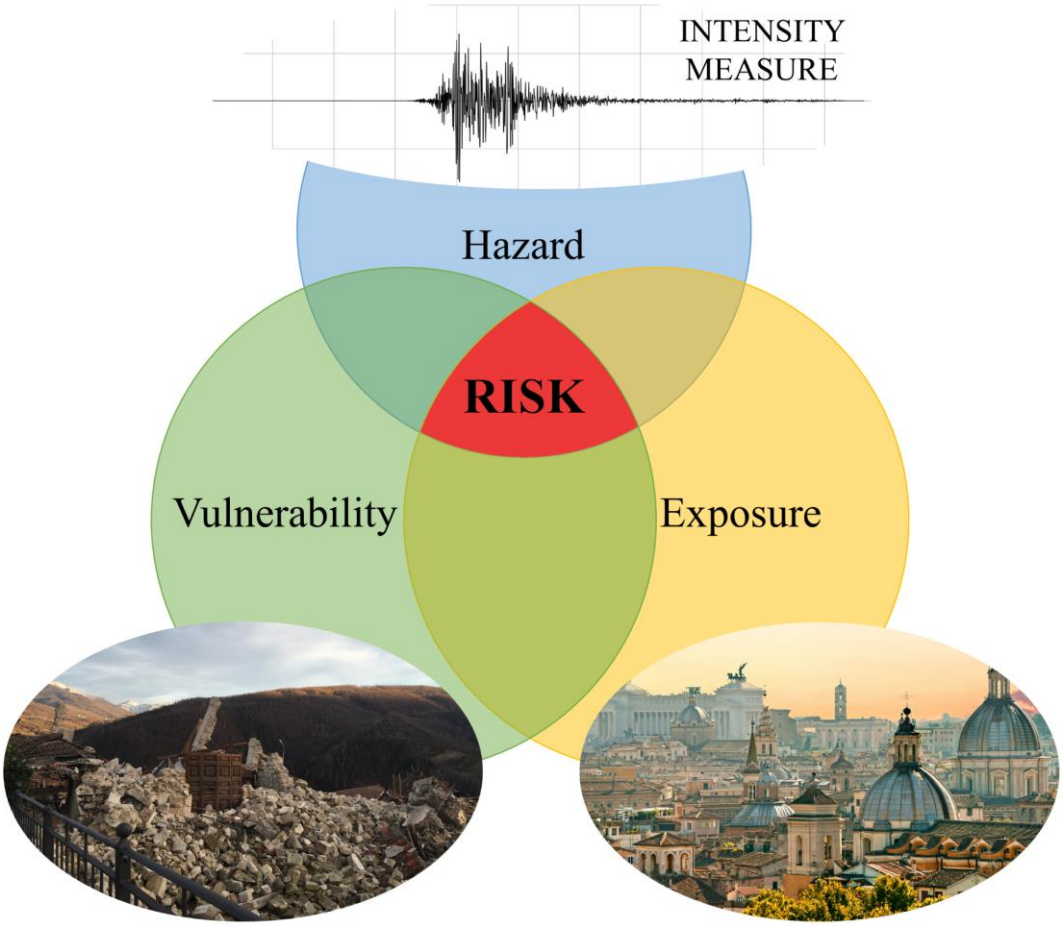

Figure 2.1. Schematic illustration of the three contributions to the final seismic risk.

A seismic hazard study accounts for all the complex factors that control the ground motion at a site. These are generally grouped into the source, path, and site effects (see Figure 2.3). In this work, the attention will be paid to the modeling of the site response (i.e., site effects). Indeed, examples in the literature showed that the site contribution is one of the most important (e.g., Bazzurro and Cornell 2004a), although some other studies contest this assertion (e.g., Lee & Anderson (2000)). Only in this Chapter, the following introductory definitions apply to the source, path, and site contributions in the global perspective of the seismic hazard assessment.

The most popular method adopted for seismic hazard assessments is the Probabilistic Seismic Hazard Analysis (PSHA) method, described by Allin Cornell in 1968. The PSHA method replaced the more straightforward Deterministic Seismic Hazard Analysis (DSHA). Figure 2.2 presents a schematic comparison of the two methods; further details can be found in Kramer (1996).

Specifically, a PSHA is a methodology that estimates the likelihood that various levels of earthquake-induced ground motion will be exceeded at a given location in a given future time period (Budnitz et al. 1997). A PSHA integrates (see Equation 2.1) over all possible ground motions at a site to produce a composite representation of the hazard at the site (Cornell 1968). The PSHA has a firm basis in earth sciences and earthquake engineering and allows decisions on seismic design levels for a facility to be made in the context of the earthquake magnitudes, locations, and ground motions that may occur (McGuire 2008). The "hazard integral" can generally be written as

$$P[Y > y^*] = P[Y > y^*|\boldsymbol{X}]P[\boldsymbol{X}] = \int P[Y > y^*|\boldsymbol{X}]\, f_x(\boldsymbol{X})dx \qquad \text{(Eq. 2.1)}$$

where $\boldsymbol{X}$ is a vector of random variables that influences Y. For simplicity, we can assume that the quantities in $\boldsymbol{X}$ are limited to the magnitude M, and the distance R. The result of a PSHA is usually associated with a reference condition (e.g., stiff and flat outcrop). The hazard at the reference condition is given as a mean (or median) hazard curve for a single intensity measure (e.g., spectral acceleration at a given oscillator period) and its associated uncertainties, represented by different fractiles for different confidence levels to be adopted in the design (Abrahamson & Bommer 2005) (Figure 2.3). The hazard curve plots the mean annual rate of exceedance of the intensity measure as a function of the amplitude of the intensity measure. For a given mean annual rate of exceedance, the hazard at a reference condition can also be given in term so the Uniform Hazard Spectrum, UHS (either mean, median, or at a given fractile level).

The analyst of a PSHA study accounts for the contributions of the uncertainties of the engineering approach and the inherent randomness of the seismic phenomenon. The Identification, Quantification, and Management (IQM) of the involved uncertainties always represented a critical issue (Budnitz et al. 1997, Bommer & Abrahamson 2006) in PSHA studies. Modern PSHA studies should consider the variability of the earthquake magnitude, distance, and intensity. Also, for very critical facilities, more complete methodologies are adopted to investigate also model uncertainties and different alternative modeling choices (Abrahamson & Bommer 2005).

In the early 2000s, the probabilistic approach was opposed by some practitioners and scientists who supported the more "transparent" deterministic approach (Krinitzsky 1995, Bommer 2003). In DSHA, a single, deterministic design earthquake resulted from the analysis, instead of an integrated description of the seismic hazard representing all events. This "design earthquake" was often desired wherein the earthquake threat was characterized by a single value of

magnitude, distance, and other relevant parameters (McGuire 1995). With the advent of PSHA and the inclusion of uncertainties in the seismic hazard assessment study, the design earthquake disappears, and this raised criticism and doubts in the scientific and professional community. One implication of the absence of a precise design earthquake is that it is no longer clear how to select realistic accelerograms when engineering design is required. The authors recognized the importance of the PSHA but affirmed that the adoption of recorded accelerograms in the reproduction of the hazard is strongly dependent on the analysis results. Sometimes, indeed, the PSHA integration operation leads to spectra (e.g., the UHS) that are not realistic for design purposes. Nowadays, however, the adoption of a consistent and complete probabilistic approach to evaluate the seismic hazard is globally recognized, and PHSA studies are conducted all around the world ranging from ordinary buildings to critical facilities (McGuire 2008, Rathje et al. 2015).

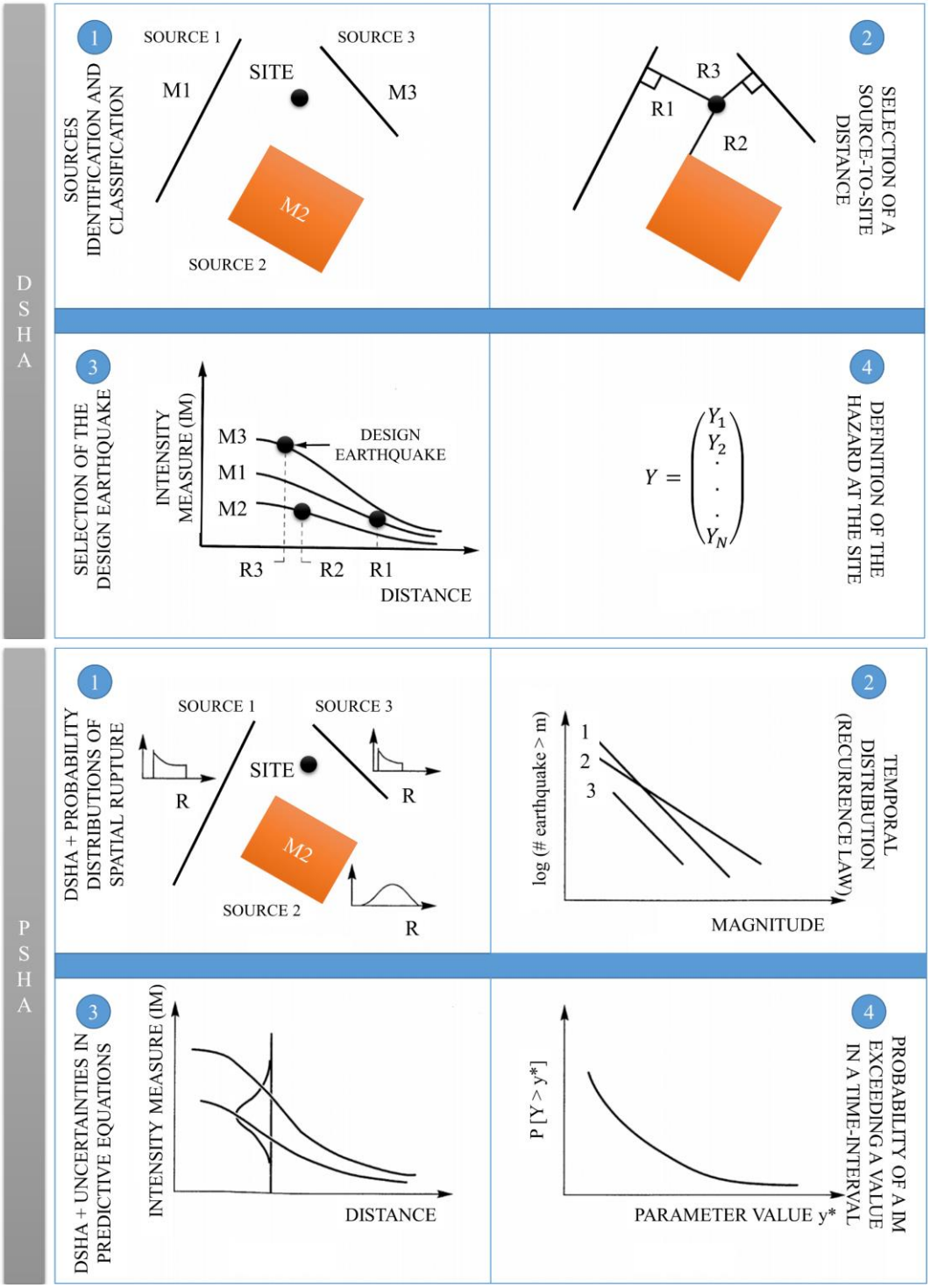

Figure 2.2. DSHA and PSHA method (modified from Kramer (1996)).

2.1.1 Site Effects

The site response (i.e., site effect) describes the effects of local site conditions on earthquake ground motions. Site effects are quantified by the difference between the ground motion for a given site condition (i.e., specific) and what would have occurred at a reference condition. Typically, the ground motion at the reference condition is prescribed by the PSHA study. Beyond the source and path, the site response should be addressed to evaluate a seismic hazard that includes the site

characteristics (see Figure 2.3). The UHS (or, equivalently, the hazard curve) is therefore used as input into the evaluation of the surface ground motion.

In recent years, considerable progress has been made in the evaluation of the site response. In 2004, Boore shared his skepticism regarding an accurate and precise evaluation of the surface motion with empirical or theoretical approaches. He showed that there was a significant amount of variability in ground motions, both site-to-site (i.e., for a given earthquake) and earthquake-to-earthquake (i.e., for a given site). For these reasons, he suggested the use of mean site responses for a broad class of sites.

Nowadays, an hazard-consistent ground motion prediction should include a specific site term (Baturay & Stewart 2003, Goulet et al. 2007, Papaspiliou et al. 2012a, Kaklamanos et al. 2013b, Pehlivan et al. 2016). The specific site term can be evaluated using analysis of recorded ground motions (i.e., data-based) and/or 1D numerical simulations (termed simulation-based Ground Response Analyses, GRAs,) reproducing the mean and standard deviation of the site response (Olsen 2000, Bazzurro & Cornell 2004a).

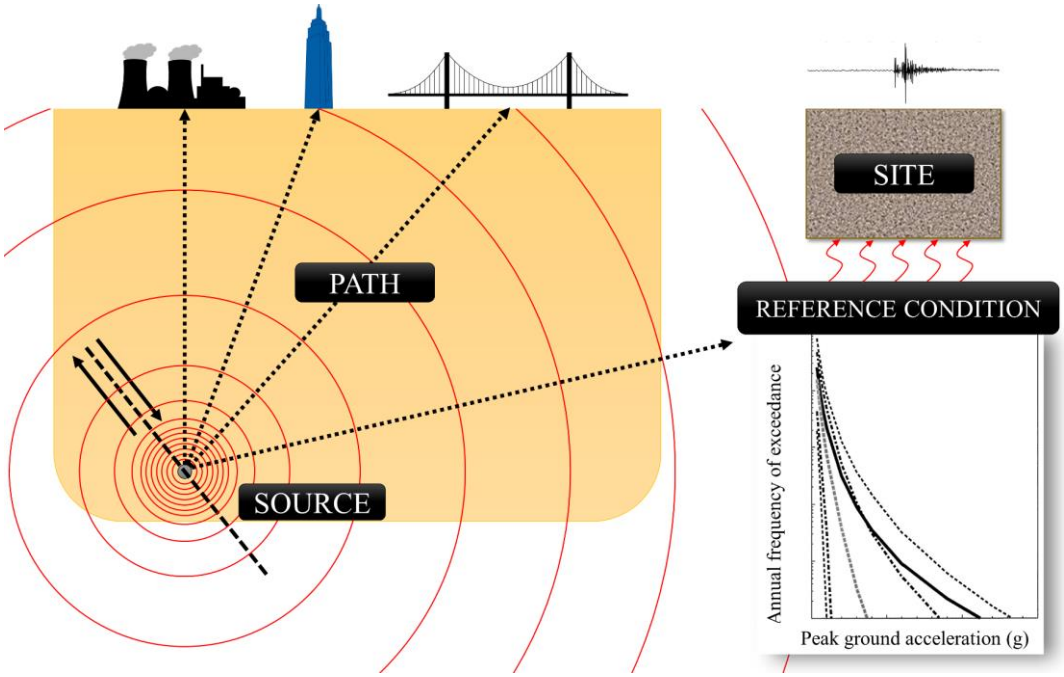

Figure 2.3. Surface hazard terms: source, path, and site along with an example of obtained hazard curve for a reference condition.

The site response (i.e., site effect) is represented in engineering seismology and geotechnical earthquake engineering in the frequency (or oscillator period) domain. The Spectral Acceleration (SA) at an oscillator period T_0, $SA(T_0)$, is the maximum acceleration of a Single Degree Of Freedom (SDOF) system with a period $T = T_0$, subjected to an input motion:

$$SA(T_0) = \max[a(t)]\}|_{T=T_0} \qquad \text{(Eq. 2.2)}$$

The curve obtained by discretely changing the period T of different SDOFs subjected to the same excitation is hereafter called Response Spectrum (RS). The spectral acceleration obtained for $T_0 = 0\ s$ (i.e., infinitely stiff system) is equal to the peak acceleration in the ground (i.e., the Peak Ground Acceleration, PGA). The mean Amplification Function (AF) is calculated as the ratio of spectral accelerations of the surface and of the input motion as:

$$\overline{AF(T)} = \frac{SA(T)_{surface}}{SA(T)_{input}} \qquad \text{(Eq. 2.3)}$$

As both functions are lognormally distributed, is preferable to quantify their standard deviations in natural log units (i.e., $\sigma_{\ln(\mathrm{SA})}(T)$, and $\sigma_{\ln(\mathrm{AF})}(T)$). Similarly, Eq. 2.3 can be rewritten as:

$$\ln\big(\mathrm{AF(T)}\big) = \big[\ln(\,\mathrm{SA(T)_{surface}}) - \ln\big(\mathrm{SA(T)_{input}}\big)\big] \qquad \text{(Eq. 2.4)}$$

It is essential to include $\overline{AF(T)}$ in PSHA studies to obtain a more rigorous and specific (not necessarily lower) (Papaspiliou et al. 2012a, Pehlivan et al. 2016) evaluation of the hazard at the site, including nonlinear effects (i.e., PSHA-NL) (Park & Hashash 2005b). Indeed, the shape and the mathematical model describing the amplification function of the site should be carefully evaluated (Bazzurro & Cornell 2004b, Goulet et al. 2007, Seyhan & Stewart 2014, Stewart et al. 2014a) to reproduce the nonlinear soil response (Afshari & Stewart 2015a).

The mean amplification function should be calculated along with its standard deviation $\sigma_{\ln(\mathrm{AF})}(T)$ (Olsen 2000, Bazzurro & Cornell 2004b, Papaspiliou et al. 2012b, Pehlivan et al. 2016, Aristizabal et al. 2018). The inclusion of $\sigma_{\ln(\mathrm{AF})}(T)$ along with the mean amplification function within a rigorous probabilistic approach to account for site effects allows for a consistent probabilistic evaluation of the hazard at the specific site. This does not occur when the reference condition of the PSHA (i.e., source and path) is modified simply by deterministic amplification function (Cramer 2003, Bazzurro & Cornell 2004b, Goulet et al. 2007, Papaspiliou et al. 2012a, Pehlivan et al. 2016).

The nonlinear response of the site deserves further observations, and several researchers have studied this phenomenon in the last few years (e.g., Bazzurro and Cornell 2004b, Park and Hashash 2005, Assimaki and Li 2012, Kaklamanos et al. 2013). The nonlinear response of natural materials was examined since the ’60s along with the experimental observation of earthquakes consequences (Hashash et al. 2010). It is nowadays recognized that natural materials exhibit nonlinearity (i.e., deviation from a simple linear constitutive model) and hysteresis (i.e., energy dissipation due to cyclic loads) even at small strains. Then, the site response study, by using both abovementioned approaches (data-based and/or simulation-based), should account for the nonlinearity of the soil response that can alter the hazard both for frequency content and amplifications (means and standard deviations). Figure 2.4 shows an example of a mean Amplification Function for PGA and a

specific period T_0.Figure 2.4. Example of amplification function for PGA (T=0 s) and generic $T=T_0$ (modified from Pehlivan et al. (2016)).

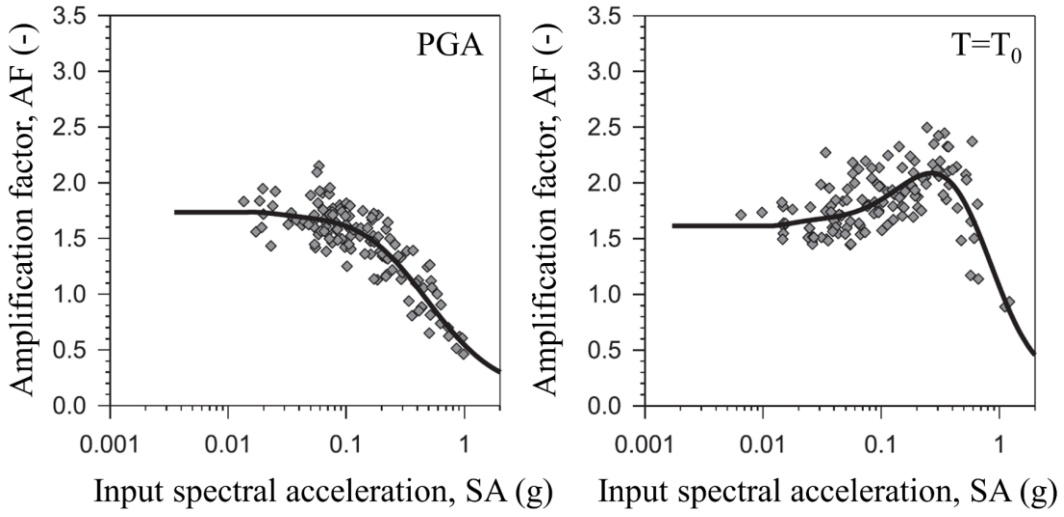

Figure 2.4. Example of amplification function for PGA (T=0 s) and generic $T=T_0$ (modified from Pehlivan et al. (2016)).

Once the mean and standard deviation of the amplification function have been estimated, the site term should be included in the PSHA results obtained for the reference condition. Many methods are proposed in the literature for merging the PSHA for the reference condition and the site-specific term. Uncertainty and variability in the site amplification should be incorporated in the PSHA, producing ground motions defined for specified hazard levels. If the analysis does not account for uncertainties in site response, the resulting surface motion would be associated with an unknown hazard level, and a non-rigorous result is obtained. However, not all the approaches respect the probabilistic framework. The following list starts from the most generic, to the most rigorous method for merging the site term into the PSHA:

- *Amplification factors* (e.g., simplified method prescribed by National and International regulations: EC8, NEHRP, and NTC[1]). This is a simplified approach to be used only for standard design projects (Bazzurro & Cornell 2004b, Papaspiliou et al. 2012a). This approach is a mixture of probabilistic and deterministic approaches (Goulet & Stewart 2009). In this case, both the mean and the standard deviation of the site response are not explicitly addressed (Papaspiliou et al. 2012a).
- *Hybrid method* (Cramer 2003). "Hybrid" because a probabilistic result at the bedrock is multiplied by a deterministic evidence from the site response study. The result is not still probabilistic (Goulet & Stewart 2009), as the method assumes the same uncertainties and variabilities at the bedrock and the surface. Moreover, it does not account for the different responses

[1] EC8, EuroCode 8;
NEHRP, National Earthquake Hazard Reduction Program;
NTC, Norme Tecniche per le Costruzioni (Italian Regulation).

between a rock material and soft material with respect to the characteristics of the input motion (e.g., magnitude and distance first). This approach is inadequate for high intensities (low probability of exceedance, critical facilities) and soft materials (Papaspiliou et al. 2012a) and can lead to non-uniform, inconsistent, and unconservative results, with no estimation of the event's probability of exceedance (Bazzurro & Cornell 2004b, Papaspiliou et al. 2012b, Pehlivan et al. 2016).

- *Modified hybrid* (Goulet & Stewart 2009). This method is a step forward compared to the previous ones. It first accounts for the influence of M and R as controlling parameters of the hazard at the site.
- *Convolution* (Bazzurro & Cornell 2004b) (Figure 2.5). Bazzurro & Cornell (2004b) were the first to recognize the importance of the uncertainties and variabilities inclusion in the site-specific seismic hazard studies and the study of the most influent variables on site amplification (Bazzurro & Cornell 2004a, Papaspiliou et al. 2012b, Papaspiliou et al. 2012a, Rathje et al. 2015, Pehlivan et al. 2016). Bazzurro and Cornell 2004a also showed results of the convolution method in agreement with the fully probabilistic method using a limited number of inputs. Moreover, Papaspiliou et al. (2012a) showed good results of a sensitivity analysis adopting this approach after driving through the model a limited number of inputs. A fascinating application of the convolution method and a clear picture of the deterministic and the probabilistic approach is given in Pehlivan et al. (2016). They studied the factors that influence soil surface seismic hazard curves. They encouraged, for modern applications, to avoid the deterministic approach (Cramer 2003), in favor of the more flexible convolution. Another application of the convolution approach is presented by Aristizabal et al. (2018) for a case study at the Euroseistest in Greece. In this case, satisfactory results were obtained, also comparing them to a fully probabilistic stochastic method. The results showed that the uncertainty in the adopted method for merging reference PSHA and site amplification has a second-order effect compared to other sources of uncertainties. However, it must be acknowledged that the choice of the regression formulation for the amplification term represents a source of uncertainty in the method (Afshari & Stewart 2015a).

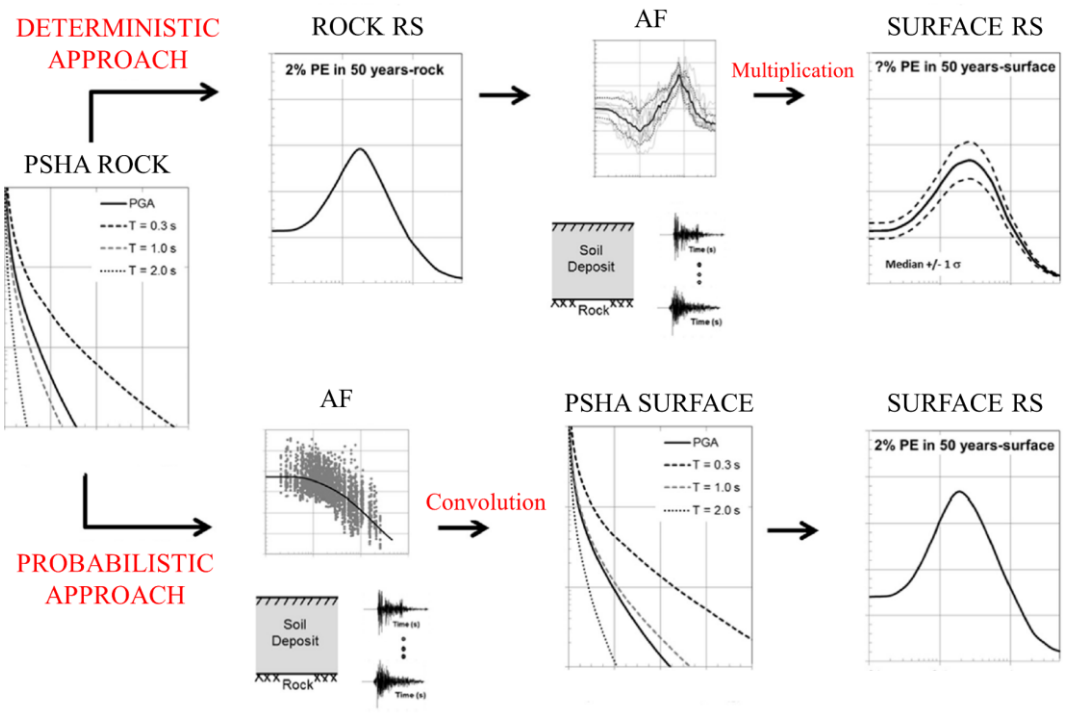

Figure 2.5. Differences between deterministic and probabilistic convolution method (modified from Pehlivan et al. (2016)).

- *Fully probabilistic calculation of the hazard integral* (Cornell 1968). This methodology is by far the most precise and rigorous (Papaspiliou et al. 2012a). An example is shown by Goulet et al. (2007) that found a considerable improvement in the hazard estimates especially for soft deposits. In this case, the PSHA is conducted for the specific site, recalculating the hazard in the most rigorous way. Another application is presented in Aristizabal et al. (2018), who satisfactorily compared the results from the convolution approach.

2.1.2 Examples of seismic hazard assessment studies

One of the first pioneering application of the PSHA method discussed above is presented in Algermissen & Perkins (1976) and Algermissen et al. (1982). They first applied the Cornell approach at a large scale for the US hazard maps. In particular, in 1982, the maximum horizontal accelerations and velocities were mapped for exposure periods of 10, 50 and 250 years at the 90% probability level of nonexceedance. The US hazard maps are then updated by Frankel (1995) preparing a new version for the 1997 edition of the NEHRP (National Earthquakes Hazard Reduction Program) building provisions. Frankel et al. (2002) were designated for the incremental production of new hazard curves in the US. In this updated version, besides the improvements of the previous work (i.e., spatially-smoothed seismicity), more modern approaches were adopted especially for uncertainties management.

After the Friuli 1976 earthquake, Faccioli (1979) applied the PSHA method for the north-east Italian area. Although simplified, this example of PSHA application first showed the advantage and potentials of the probabilistic method.

Another application of a wide-scale PSHA is presented in Cramer et al. (2004) and Cramer (2006). The authors extended the work by Toro et al. (1992) and studied the Memphis area, the Upper Mississippi Embayment, and adjacent areas, systematically accounting for the associated uncertainties. In this case, the presence of a thick (around 1 km) deposit of sediments was expected to have substantial effects on the computed seismic hazard regarding hazard maps. A fully probabilistic procedure, combined with the national seismic hazard study was performed improving the models for reproducing the nonlinear response of the sediments (Park & Hashash 2005b). An example of the final obtained hazard maps is provided in Figure 2.6.

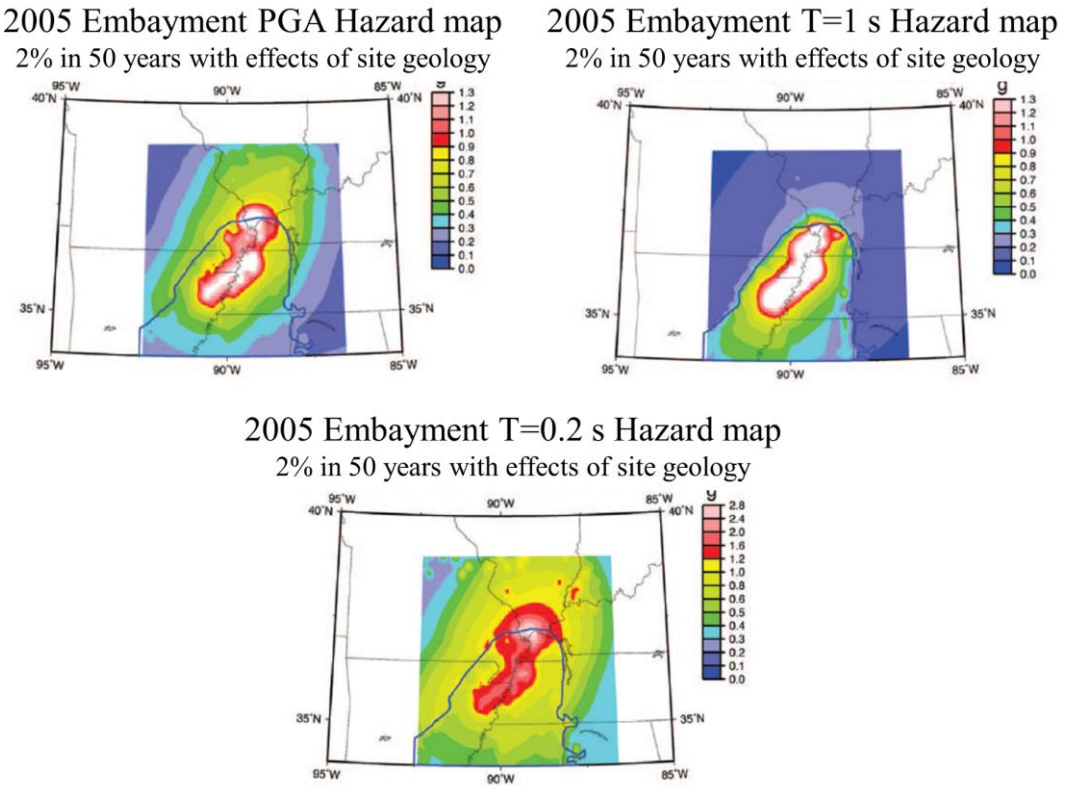

Figure 2.6. Mississippi embayment hazard maps for PGA, T=0.2 s, and T=1 s (modified from Cramer (2006)).

More recently, Grünthal et al. (2018) updated the German hazard assessment, considering the range of different types of uncertainties. This work is part of the national design regulations that are evaluating the seismic loads. Grünthal et al. (2018) performed a transparent and comprehensive analysis, systematically identifying, quantifying, and managing the uncertainties. The results are considered given both in terms of hazard maps (PGAs and macroseismic intensities) and response spectra, for three hazard levels (Figure 2.7).

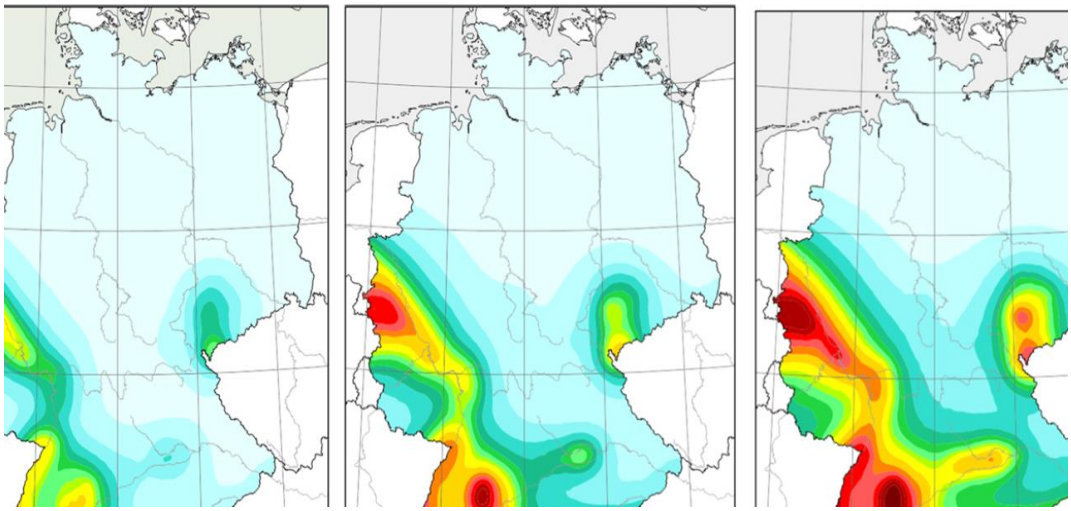

Figure 2.7. Hazard maps for T=0.1 s and 16th, 50th, and 84th percentile (from left to right) and return period of 475 years in Germany (after Grünthal et al. (2018)).

One of the most recent examples of a rigorous application of a modern PSHA is presented for a potential nuclear power plant in South Africa (Thyspunt) by Bommer et al. (2015) and Rodriguez-Marek et al. (2014). In this case study, the low-to-moderate seismicity of the area and the lack of records represented the most challenging aspects. The hazard study was conducted as an SSHAC (Senior Seismic Hazard Analysis Committee) Level 3 process. A site-specific evaluation of the hazard was obtained by correcting the adopted GMPEs (Ground Motion Prediction Equations) for high-frequencies damping kappa values and accounting for shear wave velocity profiles experimentally measured. In particular, the PSHA at Thyspunt confirmed the value of additional data collection activities (i.e., geological and geophysical surveys, historical research), in reducing uncertainties. With this respect, the amount of uncertainties in the process was handled, and rigorous hazard maps were produced as a total hazard and for each seismic source. An example of the mean hazard curves for spectral accelerations at 0.01 s is given in Figure 2.8.

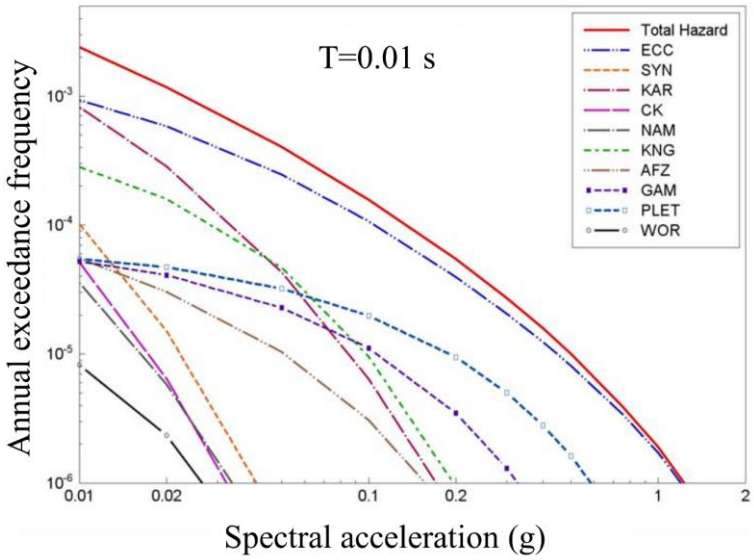

Figure 2.8. Mean hazard curves at the bedrock for spectral accelerations at 0.01 s and contributions to the mean hazard from the ten seismic sources at the Thyspunt site (after Bommer et al. (2015)).

2.2 Epistemic uncertainty and aleatory variability

The previous section also focused on the importance of uncertainties inclusion in seismic hazard assessment studies (Bommer 2003). This operation is essential a site-specific evaluation of the seismic hazard. For this purpose, the uncertainties have to be first identified (i.e., first step of the IQM method) distinguishing between two main contributions for engineering applications (e.g., reliability assessments, risk-based decision making, other than seismic hazard analyses). These contributions are termed Epistemic Uncertainty (i.e., EU) and Aleatory Variability (i.e., AV). Note that, although theoretically precise, the practical use of the following definitions is still challenging for identification and quantification purposes.

Epistemic is a transliteration of the Greek term meaning "scientific knowledge", which Plato opposed to *dòxa*, "opinion". In contemporary philosophy, it is the set of positive knowledge and scientific theories. On the other hand, aleatory derives from the Latin word *alea,* "dice", and it represents a total uncontrollable and random process, as in gambling.

Beyond the semantics, nowadays the epistemic and aleatory concepts have been used in different scientific areas. One of the first comprehensive discussions of the topic is presented in Budnitz et al. (1997). They defined two different classes of uncertainties for the SSHAC Guidelines. In particular, the epistemic portions are *"due to the lack of knowledge, the uncertainties arising because our scientific understanding is imperfect for the present, but are of a character that in principle are reducible through further research and gathering of more and better earthquake data".* The aleatory portion is *"uncertainties that for all practical purposes cannot be known in detail or cannot be reduced (although they are susceptible to analysis concerning their origin, their magnitude, and their role".*

Budnitz et al. (1997) also admitted that the division between the two different types of uncertainty is somewhat arbitrary. This is because, conceptually, some of the processes and parameters whose uncertainties are classified here as aleatory may be partially reducible through more elaborate models and/or further study.

Another pioneering distinction between epistemic and aleatory came from Toro et al. (1997) and termed as epistemic uncertainties (or just uncertainties) and aleatory uncertainties (or randomness). It interesting to see how modern concepts are tracing these initial definitions:

- *"Uncertainty that is due to incomplete knowledge and data about the physics of the earthquake process. In principle, epistemic uncertainty can be reduced by the collection of additional information."*
- *"Uncertainty that is inherent to the unpredictable nature of future events. It represents unique details of the source, path, and site response that cannot be quantified before the earthquake occurs. Collection of additional information can not reduce aleatory uncertainty. One may be able, however, to obtain better estimates of the aleatory uncertainty by using additional data."*

Toro et al. (1997) already distinguished the reducible and non-reducible characteristics of the two contributions. Then, the word "randomness" suggests the adoption of randomization methods for reproducing this type of variability. An interesting example is also discussed in Toro et al. (1997) about the generation process of a new GMPE. The standard practice defines a mean value for the ground motion intensity measure μ and a standard deviation related to aleatory variabilities σ. However, it is possible to estimate σ_μ and σ_σ that are the epistemic components due to epistemic uncertainties in the GMPEs generation (e.g., a limited number of data, adopted model).

A further contribution to the clarification of the EU and AV concepts is given by Bommer (2003). In his opinion paper titled *"Uncertainty about the uncertainty in seismic hazard analysis",* the author introduced the terms epistemic and aleatory in the *"probabilistic's arsenal".* At that time, indeed, many analysts and scientist were still supporting the use of deterministic approaches, and precise identification of the sources of uncertainty was not common yet. Bommer (2003) defended the adoption of a common and an unambiguous terminology for uncertainties identification concluding that *"uncertainties in seismic hazard assessment will clearly not in itself make things more certain, but it will certainly make things clearer".*

Later, a rigorous treatment of the distinction between epistemic uncertainty and aleatory variability is given by Abrahamson & Bommer (2005). They refer to epistemic uncertainty (i.e., uncertainty) as the scientific uncertainty in the models of earthquake occurrence and ground motion, whereas aleatory variability (i.e., randomness) as inherent variability. However, the semantics of the problem is not essential as the need for a specific treatment of these two main contributions.

In 2006, Bommer & Abrahamson (2006) reported many cases for which the PSHA study ignored (or, at least, mistreated) the GMPE aleatory variability. They strongly condemn some applications of the PSHA, even for critical facilities, that led to unconservative hazard estimates, because of the underestimation of the σ.

A general discussion of EUs and AVs is subsequently proposed in Der Kiureghian & Ditlevsen (2009). The paper titled *"aleatory or epistemic? Does it matter?"* is a manifesto of the crucial topic regarding the identification and classification of uncertainties. The authors mostly discussed sources and characters of uncertainties in engineering modeling for risk and reliability analyses. Their primary distinction criterion is based on the possibility of reducing these sources. In particular, an epistemic uncertainty can be reduced by gathering more data or by refining models. Contrarily, for an aleatory uncertainty, there is no chance to be reduced in an acceptable time interval (sophistically, each uncertainty could be reduced thanks to the scientific advancements). The distinction is also important from the viewpoint of transparency in decision-making since it then becomes clear as to which reducible uncertainties have been left unreduced by our decisions.

Nowadays, for seismic hazard assessment studies, modern concepts of EU and AV are discussed in the literature. Epistemic uncertainties result from incomplete knowledge of the physics of the process and/or from insufficient and/or inadequate experimental data and adopted models. They can, in principle, be reduced by the collection of additional and better quality information and can, in some senses, be managed utilizing more advanced models (Rodriguez-Marek et al. 2014, Stewart et al. 2014a). Aleatory variability refers to the intrinsic randomness of natural systems. It can be quantified, but it cannot be reduced using multiple experimental measurements. However, while the differences between EUs and AVs in hazard assessment studies appear to be theoretically clear, for most applications a proper identification is often not feasible (Passeri et al. 2019).

After the *identification* process, the following step for a rigorous treatment of EUs and AVs in seismic hazard assessment studies regards the *quantification*. A critical aspect for EU and AV is their balancing (i.e., the amount of each component in the global problem). It must be clear that a typical amount of the two contributions is involved in every engineering application. The amount of EU and AV should be carefully evaluated, moving from the global scale of the problem to the smaller scale. Each source of uncertainty should be rigorously classified before any further application is performed. Particularly for seismic hazard assessment studies, the spatial scale of the problem (i.e., source, path, and site) represents an essential contribution. Note that the previous observations regarding the identification and quantification steps still represent a crucial and "open" topic.

Once the identification and quantification process is completed, the *management* step should be considered (Budnitz et al. 1997). In particular, Abrahamson & Bommer (2005) assumed that the epistemic uncertainties should lead to alternative hazard curves, whereas the aleatory variabilities have to modify the shape of the single curve. Epistemic uncertainties should be handled establishing a rigorous logic tree approach with weights assumed by engineering judgment of experts. For the German seismic assessment, for example, a logic tree

of 4040 end branches was designed (Grünthal et al. 2018). A more limited, but complete, logic tree approach was used by de Almeida et al. (2018) to account for a significant amount of epistemic uncertainties in a PSHA in Brazil. Another example of a logic tree approach was performed for the Italian PSHA (Sismica 2004), and it is shown in Figure 2.9. In this case, the epistemic uncertainties regarded the database completeness, the method for calculating the maximum magnitude, the adopted GMPE, the type of magnitude. The last column of the logic flow shows the adopted weights.

Hence, the result of the logic tree approach for the PSHA applications leads to a different picture of the confidence level (i.e., fractiles) that can be assumed in the design. These different scenarios cannot be obtained with a single logic path. Generally, for wide-scale hazard studies, the 16th, 50th (median), and 84th fractiles are computed. For example, for critical facilities, Abrahamson & Bommer (2005) suggest using the 84th fractiles of the results.

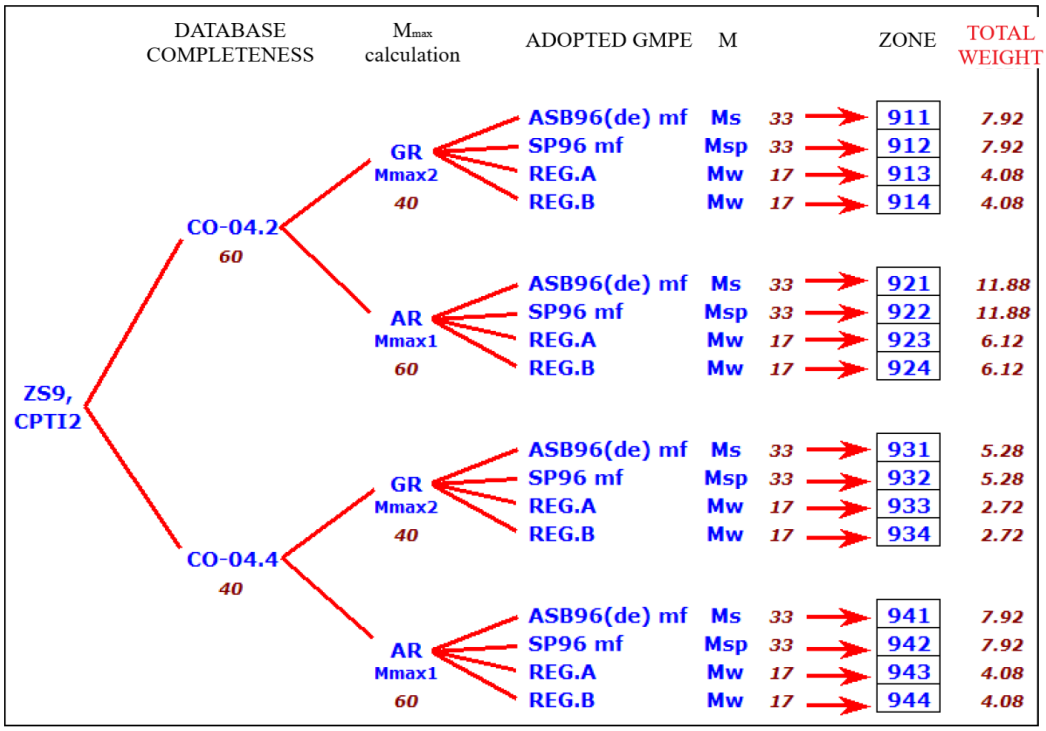

Figure 2.9. Logic tree adopted for the Italian PSHA. Weights are given in percent.

The aleatory variabilities have to enter the hazard integral. Indeed, the old definition of Probabilistic Seismic Hazard Analysis by Cornell (1968) should be respected:

"It is a process that integrates (aggregation) over aleatory uncertainties (e.g., future earthquake locations, future earthquake magnitudes) to calculate the likelihood of occurrence (or the probability of exceedance) of an earthquake characteristic, Y, at a site during a given period of time."

For example, Abrahamson & Bommer (2005) affirmed that a PSHA result for which the GMPE aleatory variability was not addressed in the hazard integral could not be considered a genuine hazard study.

At this point, should be clear to the reader that these two methods for the separate management of EUs and AVs appear theoretically precise, but difficult to implement in a practical application. There are engineering problems that prevent a rigorous identification and quantification of the uncertainties, leading to a more complex independent management step. One example regards the EUs and AVs in shear wave velocity profiles discussed in Chapter 4. In that case, each seismic test will be discussed and the main sources of EUs and AVs identified. In case of surface wave testing methods, a distinction within the experimental dispersion curve is practically unfeasible. For this reason, the model calibration of the geostatistical model performed for these types of tests leads to a joint management of the two contributes.

Ergodicity

Generally, for standard PSHA studies, the relationship between one intensity measure and other variables (e.g., magnitude, distance, site term) is given by a GMPE (Lee & Anderson 2000, Baturay & Stewart 2003, Stewart et al. 2014a, Thompson & Wald 2016). This equation provides an estimation of the motion at a site (as mean value and an associated aleatory variability for an intensity measure) obtained by collecting a significant amount of data in different regions (i.e., spatial variability) (Toro et al. 1997, Al Atik et al. 2010). However, the use of GMPEs with a site term can be seen as the typical example of an ergodic process (Stewart & Baturay 2001, Goulet et al. 2007, Asimaki & Li 2012) in the PSHA.

The ergodic process is a definition usually adopted in signal analysis. It is a random process in which the distribution of a random variable in space is the same as the distribution of that same random variable at a single point when sampled as a function of time (Anderson & Brune 1999). The ergodicity represents the underlying assumption for which the variability in space is assumed to be equal to the variability in time. Then, ergodicity for site-specific seismic hazard assessments means to deliberately "confuse" variability in space with variability over time. It means accepting that the average of the events measured at different sites, and different regions, represents the average over time, at a specific site (where it is impossible to obtain a reasonable statistical sample over time) (Anderson & Brune 1999). The problem is that, generally, the variability in time (for a site) is lower than the variability in the space, (for different sites), then a reduction criterion should be applied (Luzi et al. 2014, Rodriguez-Marek et al. 2014).

In light of the previous concepts, it should be clear that the adopted model in the GMPE (e.g., based on average shear wave velocities, bedrock depth…) cannot account for the multitude of complex physics phenomena that govern the site-specific response (Bazzurro & Cornell 2004b), even if it comes from a very robust regression and an extensive database (Atkinson 2006, Thompson & Wald 2016). The general adoption of a global database to estimate the hazard at the site inevitably produces an inaccurate result along with a large dispersion of the predicted ground motion (Baturay & Stewart 2003, Stewart et al. 2014a, Faccioli et al. 2015). The ergodic process usually fails also for weak input motions (i.e.,

approximately linear response) overestimating the associated aleatory variability (Kaklamanos et al. 2013b). The adoption of a generic model that attempts to reproduce the site response represents a typical example of epistemic uncertainty source (Thompson & Wald 2016). Although modern GMPEs try to refine the adopted model, incorporating a nonlinear term and a dependency of the uncertainty and variability on the site characteristics (usually more substantial for softer materials). However, great care should still be used (Goulet & Stewart 2009) when the study relies on these completely ergodic processes, especially in case of nonlinear responses (Asimaki & Li 2012, Kaklamanos et al. 2013b).

The single station method (Atkinson 2006) is an excellent example of IQM of uncertainties and variabilities in the study of the site component of a GMPE (Luzi et al. 2014, Rodriguez-Marek et al. 2014). It addresses uncertainties and variabilities, reducing the level of ergodicity in PSHA studies (Rodriguez-Marek et al. 2011, Faccioli et al. 2015). However, the price that must be paid is a higher level of detail on the site characterization (i.e., the price of implementation) and a large number of recorded motions across a wide intensities range (i.e., the price of adequately quantifying non-ergodic standard deviations) (Lin et al. 2011). The single station approach identifies what component of ground motions are repeatable and which are truly random. Then we assume that the repeatable component is "knowable", thus its uncertainty is epistemic. If the analyst can distinguish, within the site term, between site-to-site and single-station contributions, he can remove the site-to-site epistemic uncertainty, leading to less aleatory variabilities that enter in the hazard integral. Hence, the analyst is removing from the GMPE prediction the repeatable component from the aleatory variability of the site response that he can experimentally estimate at the site. However, the removed site-to-site epistemic uncertainty will be addressed incorporating a logic tree approach in the hazard study (Rodriguez-Marek et al. 2014). For these reasons, the separation will not necessarily produce a lower hazard at the site, but a more reliable estimate. Indeed, this application generates more consistent and non-ergodic evaluations, especially for low probabilities of exceedance (e.g., for critical facilities) (Rodriguez-Marek et al. 2014), because of the considerable overestimation of aleatory variability in GMPEs for strong motions. The results in Atkinson (2006) shows a reduction of 10% of the aleatory variability by adopting the single-station approach. In Italy, Luzi et al. (2014) showed a 15% decreased value adopting the single station approach. Moreover, this approach produces very stable values of standard deviation (Lin et al. 2011) equal to approximately 0.4 to 0.5 (in natural logarithmic units) (Stewart et al. 2014a) within specific areas as Japan (Rodriguez-Marek et al. 2011), Italy (Luzi et al. 2014), and the Po plain (Faccioli et al. 2015), or across various tectonic regions (Rodriguez-Marek et al. 2013).

A further approach is also proposed by Atkinson (2006), and it specifies the topic to a single-path condition. In this case, evidence showed a reduction of the aleatory variability, compared to the total in the GMPE, equal to 40%. However, this approach deserves a broader set of recorded motions, to own a sufficiently large database for each seismic source. Despite the difficulties, this approach can be seen

as a further removal of the ergodicity from the initial assumptions in the GMPE model (Lin et al. 2011).

Chapter 3
Uncertainties and variabilities in site response studies

The present Chapter focuses on site response studies for the estimation of the site effects. Site response studies can be performed using seismic event recordings (data-based) or numerical simulations (simulation-based, mainly 1D) (Stewart et al. 2014). The Identification, Quantification, and Management (IQM) of the Epistemic Uncertainties (EUs) and Aleatory Variabilities (AVs) for site response studies will be discussed through an extensive literature review.

As anticipated in Section 2.1, site response is the process for which considerable modifications of the seismic waves are produced by variations of the material properties and/or surface topography near the Earth's surface (Aki 1993, Kramer 1996, Boore 2004). Site response analysis considers the differences in the expected motion for amplitude, frequency content, and duration between a reference condition (e.g., consistent with the results of the PSHA studies) and a given site condition (Figure 3.1). It is important to remark that often in site response, the outcrop (i.e., reference) motion is assumed to be deterministically related to the bedrock condition. However, outcrop motions are known to be more variable than soft soil motions, and the treatment of the "rock motion" as an immutable constant in site response analysis is highly questionable. A recent discussion regarding this topic is presented in Passeri et al. (2018a).

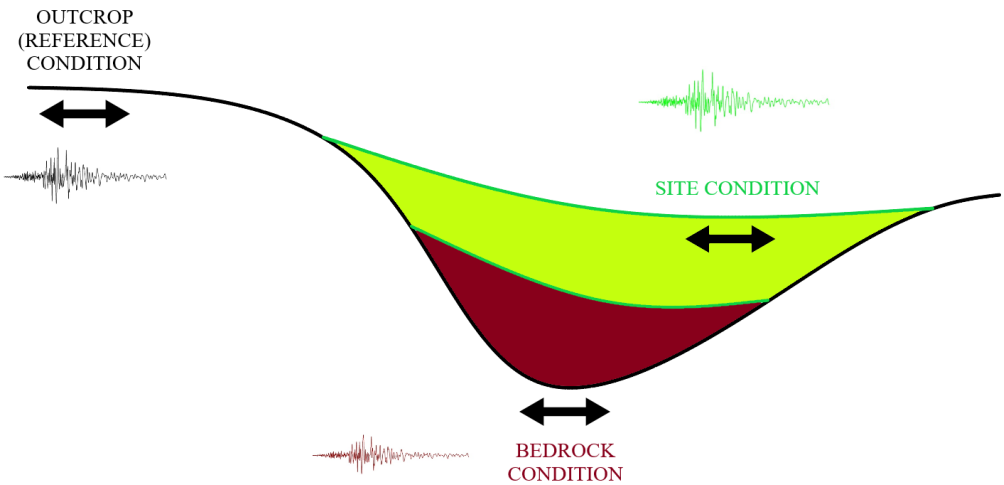

Figure 3.1. Site response scheme.

Site response (i.e., site effect) is usually evaluated in the frequency domain using Transfer Functions (TFs) defined as the ratio of Fourier spectra. Generally,

the Fourier spectra of the accelerations are computed at the surface and the input (Baise et al. 2011) as

$$TF(f) = \frac{U_{surface}(f)}{U_{input}(f)} \qquad \text{(Eq. 3.1)}$$

where $U_{surface}(f)$ is the accelerations Fourier spectrum of the ground motion at the surface obtained by surface recording instruments, $U_{surface-recorded}(f)$, or by numerical simulations, $U_{surface-simulated}(f)$. $U_{input}(f)$ is the acceleration Fourier spectrum of a type of input (real or stochastic), $U_{input-selected}(f)$, or the input motion obtained by an in-hole instrument (in case of DH-array), $U_{downhole-recorded}(f)$.

Therefore, it is useful to distinguish the empirical (i.e., experimentally measured) transfer function:

$$ETF(f) = \frac{U_{surface-recorded}(f)}{U_{downhole-recorded}(f)} \qquad \text{(Eq. 3.2)}$$

and the theoretical (i.e., simulated, Figure 3.2) transfer function:

$$TTF(f) = \frac{U_{surface-simulated}(f)}{U_{input-selected}(f)} \qquad \text{(Eq. 3.3)}$$

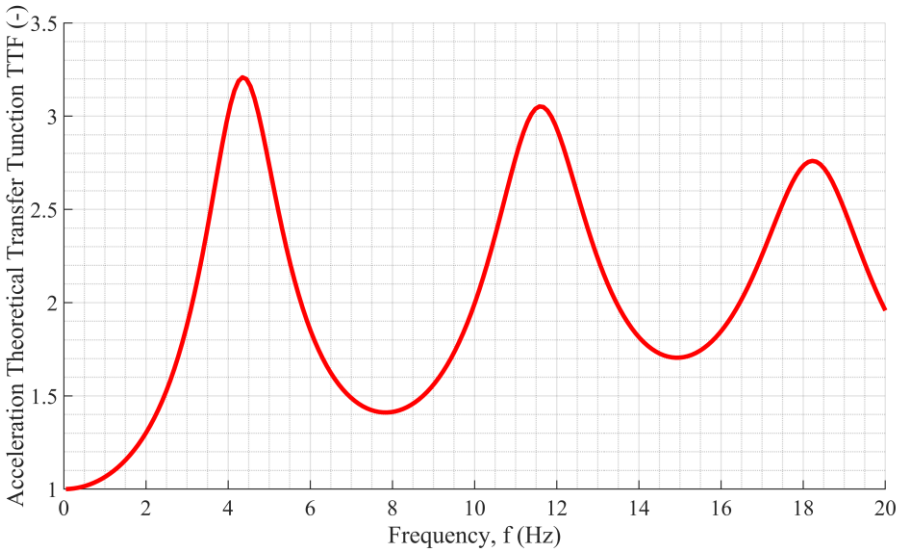

Figure 3.2. Example of Theoretical Transfer Function (TTF).

As discussed in 2.2 for global hazard studies, the "relaxation" of the ergodic assumption in site response studies can be performed with recorded data (an example is the single station reported in Section 2.2) and/or with 1D numerical simulations (termed Ground Response Analyses, GRAs). Both approaches allow for a specific evaluation of the mean hazard at the site and the estimation of the EUs

and AVs at stake (Stewart et al. 2014a). In particular, these two approaches provide an estimate of the mean (i.e., $\overline{AF}$) and the logarithmic standard deviation (i.e., $\sigma_{\ln(\mathrm{AF})}$) of the site amplification function. In addition, various contributions to the final uncertainty can be identified within the $\sigma_{\ln(\mathrm{AF})}$ term (Li & Asimaki 2010, Rodriguez-Marek et al. 2014).

The data-based methods estimate $\overline{AF}$ and $\sigma_{\ln(\mathrm{AF})}$ by collecting a large amount of high quality records (if available), whereas for GRAs a great number of simulations should be performed in a probabilistic (i.e., stochastic) framework, often leading to high computational demand. An important contribution to this topic is given in Hollender et al. (2018). They illustrate the summary of the CASHIMA project for the hazard assessment in low-to-moderate seismicity areas. In their opinion, both data-based and simulation-based methods are mandatory and complementary. The first is used to validate the results of the GRAs (in the small-strain behavior), then numerical simulations are fundamental to extend the observed ground motion to different hazard scenarios (i.e., high intensities and nonlinear responses).

If the data-based approach is adopted, the first and most important step in each study is the compilation (or query) of a high-quality database, according to specific characteristics (e.g., magnitudes, distances, period, hypocentral depth, the presence of aftershocks, filtering). The records can be collected only at the surface, or also exploiting the vast capabilities of in-hole recording arrays (Rodriguez-Marek et al. 2011, Kaklamanos et al. 2013b). Then, the data processing continues with the clustered parameters regression on most influent variables and the analysis of model residuals, along with standard errors. Comparisons with other studies are usually made to validate and/or extend the results applicability (Al Atik et al. 2010, Lin et al. 2011, Kaklamanos et al. 2013b, Rodriguez-Marek et al. 2013, Luzi et al. 2014, Faccioli et al. 2015). Results from the literature showed a stable value of the logarithmic standard deviation of the measured amplification function $\sigma_{\ln(\mathrm{AF})}(T) \approx 0.4$ to 0.5 over a wide range of periods (Rodriguez-Marek et al. 2013, Luzi et al. 2014, Faccioli et al. 2015). Many studies also showed a systematic and clear identification of the different sources as EU or AV.

If the 1D simulation-based approach is adopted, the analyst simulates the wave propagation phenomenon through the site taking advantages from the results of a single and/or multiple reference seismic hazard scenarios (Rodriguez-Marek et al. 2014). Note that also 2- or 3D models (termed Site Response Analyses, 2D or 3D SRAs) could be used for the estimation of the site-specific response. However, these methods still have a large amount of model (i.e., epistemic) uncertainties that would enter in the already complex process of hazard estimation.

In early literature of this topic, for example, Stewart and Baturay (2001) showed that, for low periods, non-ergodic numerical simulations always resulted in better prediction than GMPEs. Moreover, Baturay and Stewart (2003) showed a better result regarding both bias and variability and agreement with the spectral shape, compared to the ergodic processes. However, it should be acknowledged that mixed and controversial results have been obtained using GRAs in the literature predicting

the mean site response (Stewart & Baturay 2001, Baturay & Stewart 2003, Andrade & Borja 2006, Asimaki et al. 2008, Kwok et al. 2008, Stewart 2008, Li & Asimaki 2010, Baise et al. 2011, Asimaki & Li 2012, Thompson et al. 2012, Kaklamanos et al. 2013a, Kaklamanos et al. 2013b, Afshari & Stewart 2015b, Kaklamanos et al. 2015, Régnier et al. 2016a, Shi & Asimaki 2017, Aristizabal et al. 2018, Hollender et al. 2018, Régnier et al. 2018). These results prove that the user should possess the specific expertise and particular knowledge of the global procedures and phenomena. This is particularly true in case of the strong nonlinear response of the site (Park & Hashash 2005b, Hashash et al. 2010, Stewart et al. 2014a, Kim et al. 2016, Régnier et al. 2016b, Régnier et al. 2018) or for complex geological environments (Faccioli et al. 2002b, Thompson et al. 2012). An initial assessment of the applicability of GRAs should always be performed by a taxonomic procedure (Baise et al. 2011, Thompson et al. 2012, Kaklamanos et al. 2013b, Kaklamanos et al. 2015). The taxonomy is the practice and science of classification of things or concepts, including the principles that underlie such classification. In this case, the authors suggest a clear initial classification of a case study, based on the site complexity.

Nevertheless, the 1D numerical simulation of specific site characteristics always represents a step forward, compared to the total ergodic process (Stewart & Baturay 2001, Hashash et al. 2010, Papaspiliou et al. 2012b, Kaklamanos et al. 2013b). They also represent the only chance, in case no records are available at the specific site (also empirical, $V_{S,30}$-based factors can be used, but are not a standard procedure) (Olsen 2000, Rodriguez-Marek et al. 2014, Bommer et al. 2015, Faccioli et al. 2015).

Besides the mean amplification function estimation, an important step regards the evaluation of $\sigma_{\ln(\mathrm{AF})}(T)$ and the identification/quantification of different contributions of EU and AV. There are examples for which the resulted uncertainties and variabilities can be biased (Goulet et al. 2007, Stewart et al. 2014a). Generally, uncertainties and variabilities are overestimated for low periods and underestimated for long periods (Rodriguez-Marek et al. 2014, Afshari & Stewart 2015a, Pehlivan et al. 2016), compared to the constant results obtained with the data-based approach. However, other examples showed consistency with the variability obtained from recorded data (Papaspiliou et al. 2012a, Papaspiliou et al. 2012b, Kaklamanos et al. 2013b, Aristizabal et al. 2018).

These inaccuracies obtained by the GRAs can be due to an inadequate quantification step in the IQM process. The amount of epistemic uncertainties is dramatically dependent on the specific engineering application. For each problem, an ad-hoc evaluation of the relevant EUs should be performed. In site response studies, the analyst should precisely account for every single source of EU in the process, starting from the experimental tests and the adopted models used to reproduce the natural phenomenon. Specific expertise and a deep understanding of the physics of the problem is fundamental in the quantification of the EUs.

Similarly, the amount of aleatory variability in the site responses should be explicitly quantified depending on the size of the studied area and its geological complexity. This is inherent in the definition of spatial variability (i.e., AV). For

example, if the analyst considers a single building/facility, in a restricted and spatially homogeneous area, the most critical contribution to uncertainty in site response comes from the epistemic uncertainties. Of course, when enlarging the studied area to geologically complex environments (e.g., road projects or microzonation of heterogeneous regions), the contribution of the aleatory (i.e., spatial) variability increases and can be much more influent than epistemic uncertainties.

Contrarily, for global seismic hazard studies, also the contributions of source and path are essential for the aleatory variability estimation. The AV that is usually accounted for at the global scale is almost independent of the size of the area under analysis (earthquakes come from far away and cover vast distances). Contrarily, the AVs at the site scale (i.e., for site response studies) are strongly dependent on the extent of the studied area.

Even though the dissertation will focus on the uncertainties and variabilities estimates from GRAs, a reference list is given for examples using recorded data for the IQM of EUs and AVs (Chen & Tsai 2002, Atkinson 2006, Chiou et al. 2008, Morikawa et al. 2008, Al Atik et al. 2010, Lin et al. 2011, Rodriguez-Marek et al. 2011, Rodriguez-Marek et al. 2013, Luzi et al. 2014). On the other hand, more examples will be discussed for the EUs and AVs in GRAs (listed in Table 2). A hybrid-intermediate set of studies that investigate the propagation of EUs and AVs in site response studies by adopting both approaches (Thompson et al. 2012, Kaklamanos et al. 2013b, Seyhan & Stewart 2014, Afshari & Stewart 2015a, Faccioli et al. 2015, Kaklamanos et al. 2015).

3.1 Numerical simulations

As anticipated, numerical simulations can estimate the mean amplification function for a site and identify, quantify, and manage relative EUs and AVs as standard deviations. In this dissertation, the attention will focus on 1D site response simulations (GRAs), even if a brief introduction to 2D and 3D site response simulations (2D or 3D SRAs) will be provided.

The most critical point in this framework regards the study of the applicability of simplified GRAs. The analysis of the advantages and disadvantages of each method should always be carried out, accounting for all the characteristics of the specific problem from a global perspective.

One of the first contributions to the study of the applicability of GRAs is given by Faccioli et al. (2002a). The authors studied the complex site effects in predicting ground motions, including the topography. They found that, even for complex 2D-3D geological environments, the predominant resonance frequencies are controlled by the 1D simple formulations. However, 1D wave propagation models cannot account for the magnitude of the amplification, and the width of the relevant frequency band observed in weak motion records. For this purposes, a 2D (or, for some cases, even 3D) modeling of the problem could be required.

A further study was presented by Baise et al. (2011) and Thompson et al. (2012) who classified the investigated sites as “simple” or “complex”, depending on the

accuracy obtained by 1D GRAs. In this framework, the analyst can select the most suitable type of analysis (GRA or 2D/3D SRA) depending on the site complexity (Thompson et al. 2012, Afshari & Stewart 2015b), always accounting for the nonlinear response of the site (Zalachoris & Rathje 2015, Kim et al. 2016). In fact, preliminary results from GRAs found a general underprediction of the motion, for low periods (i.e., lower than the model period), possibly due to the difficulty in catching different phenomena (Kwok et al. 2008, Stewart & Kwok 2008, Li & Asimaki 2010) independent from the 1D model parameters (Baise et al. 2011). In some particular circumstances, 1D models show a "base-isolation effect" due to high shear strains (i.e., small stiffness) focused in a specific layer. This phenomenon is prevented in case of 2D and 3D processes, thanks to the lateral heterogeneity that allows a more realistic spatial spreading of stresses (Makra & Chávez-García 2016). However, there is a multitude of other alternative or additional reasons that could explain these experimental differences within the GRAs (e.g., nonlinear adopted approaches, Zalachoris & Rathje (2015)). For example, recent studies as Shi & Asimaki (2017) showed that a considerable improvement of the motion prediction obtained by GRAs could be achieved. In their work, the authors confirmed that a portion of the previous inaccuracies and bias obtained by 1D simulations could be due to inappropriate nonlinear constitutive models, as also confirmed by Régnier et al. (2018).

A recurring question regards accuracies (bias), and variabilities (precisions) (Kaklamanos et al. 2013b) obtained using these 1D procedures compared to independent DH-arrays in the linear and nonlinear behavior (Shi & Asimaki 2017).

The empirical transfer function represents a fundamental advancement offered by DH-arrays. Baise et al. (2011) and Thompson et al. (2012) first identified the transfer function as a useful tool in the validation of GRA by comparison with the DH-arrays. So, first, a helpful definition of site response from DH-arrays (Baise et al. 2011) is reported:

"Site response is a relative quantity and thus requires a pair of ground motions, one of which contains the effects of the near-surface soils and one that does not. The record without the effects of the soil is termed the "input" time series, and the receiver is either located at some depth below the free surface (i.e., a "downhole" receiver), or on outcropping bedrock. The "output" motion includes the effects of soil, so it is located either above a downhole input motion, or on soil near the outcrop motion. Site response is often represented as an input/output transfer function, and we refer to estimates of the site response transfer function derived from recordings of ground motions as the empirical transfer function (ETF). The ETF can be compared to theoretical predictions of the transfer function (TTF) based on in situ estimates of the seismic properties of the soil and a physical/mechanical model for wave propagation between the two points. The transfer function (empirical or theoretical) shows how the soil amplifies and attenuates seismic waves as a function of the frequency of the loading, f"

The TTF-ETF comparison from vertical arrays represents a handy tool to evaluate the goodness of a GRA result, especially in case of strong nonlinear responses for different spectral periods. Examples of this comparison can be found

in Andrade & Borja (2006), Asimaki et al. (2008), Kwok et al. (2008), Stewart (2008), Stewart & Kwok (2008), Hashash et al. (2010), Li & Asimaki (2010), Kaklamanos et al. (2013a), Kaklamanos et al. (2013b), Kim & Hashash (2013), Yee et al. (2013), Afshari & Stewart (2015b), Kaklamanos et al. (2015), Zalachoris & Rathje (2015), Régnier et al. (2016b), Shi & Asimaki (2017), Aristizabal et al. (2018), Régnier et al. (2018). This approach is highly recommended in Hollender et al. (2018) as data-based and simulation-based methods are complementary in the seismic hazard assessment. Studies in the early literature showed a general underprediction (i.e., overdamping) of the motion for short periods, comparing the GRA results with experimental evidence from DH-arrays. These differences are partially due to the influence of 2D and 3D phenomena (Stewart et al. 2014a) in the wave propagation process (e.g., base-isolation effect) and/or EU and AV of the adopted GRA model. An excellent analysis of the reasons for the possible inaccuracy obtained with GRAs is presented in Zalachoris & Rathje (2015). They state that in cases where significant topographic and basin effects are minimal, GRAs are adequate to represent the wave propagation conditions. However, considerable care is necessary to assign the correct boundary conditions at the base of the model (Bonilla et al. 2002, Asimaki & Steidl 2007, Stewart & Kwok 2008, Thompson et al. 2009, Régnier et al. 2016a) and to model the nonlinearity of the response (Régnier et al. 2018). In this respect, Shi & Asimaki (2017) proposed their Hybrid Hyperbolic (HH) nonlinear soil model that gave excellent outcomes, comparing the results with nine Kik-net down-hole arrays and 2743 input motions. Their results showed the most satisfactory performance across all ground-motion intensities (PGA up to 0.9g, strain up to 3.67%) and for both broadband and high frequencies. In light of these recent studies, it can be stated that a sophisticated and modern GRA that includes advanced constitutive models can give excellent results.

So the question is *"Does one-dimensional site response work?"*. Baise et al. (2011) attempted to answer this question. They collected evidence from other studies (some of them later published) (Thompson et al. 2009, Kaklamanos et al. 2011, Thompson et al. 2012, Kaklamanos et al. 2015) and exploited DH-arrays to distinguish "simple" and "complex" sites (i.e., taxonomic procedure). The approach is systematic, as they begin the study at the most straightforward scale, investigating first the linear response of the deposit. They evaluate the goodness of the 1D hypothesis through linear GRAs and weak input motions. In this step, they compared the ETF measured for weak motions and the TTF calculated using the Haskell-Thomson matrix method (Thomson 1950, Haskell 1953) and a rigid bottom halfspace (Figure 3.3). Once the elastic response and the 1D assumption is verified, they suggest the step-forward, adopting nonlinear GRAs approaches, as proposed in Kaklamanos et al. (2015) and Hollender et al. (2018).

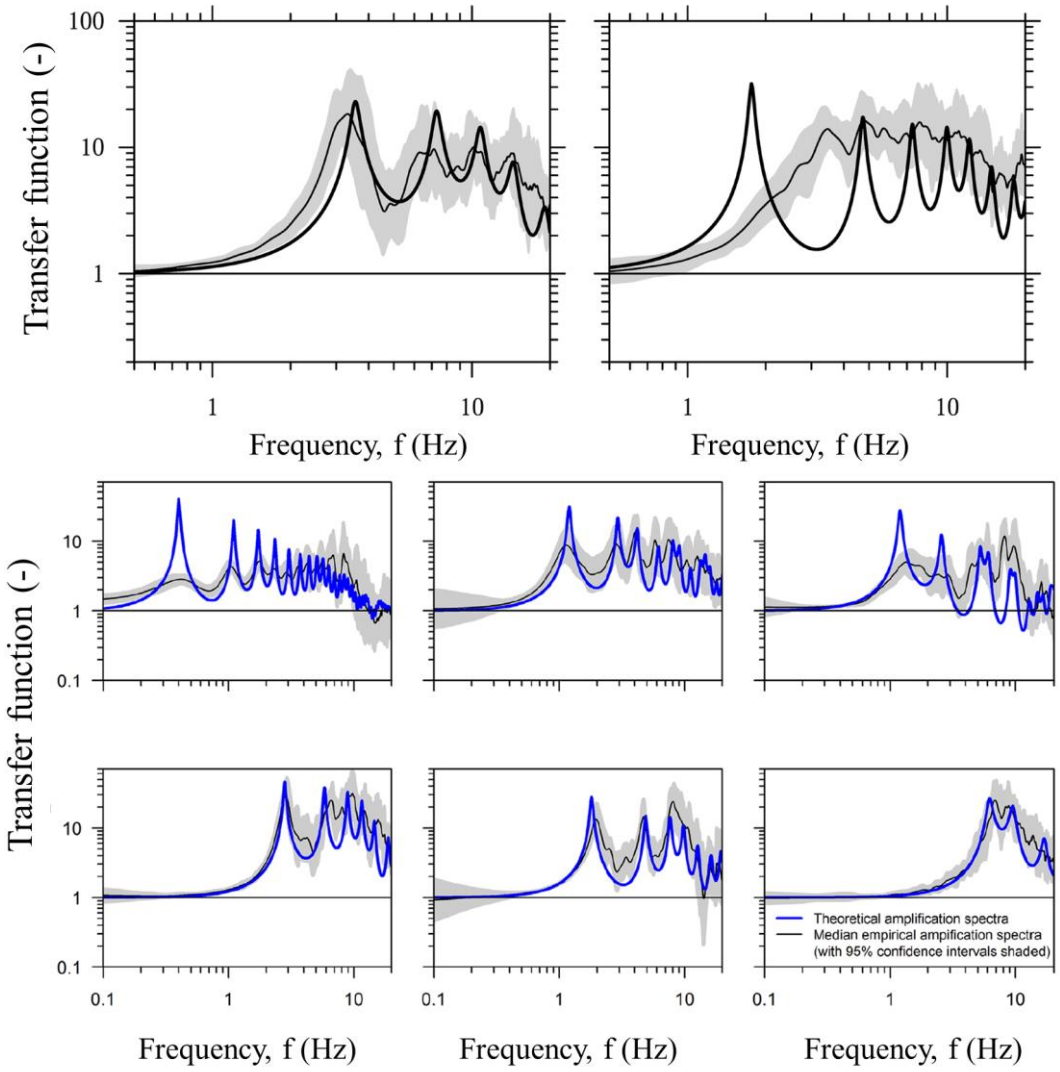

Figure 3.3. Examples of comparison of Theoretical Transfer Functions and Empirical Transfer Function (after Baise et al. (2011) and Kaklamanos et al. (2015)).

Similarly, Afshari & Stewart (2015b), performed the same initial validation between TTF-ETF. They found a better agreement compared to the Japanese sites for ten sites in California, also for the event-to-event consistency. Later, Shi & Asimaki (2017) showed excellent results for nine Japanese sites, sign that advanced 1D simulations are giving increasingly better results if appropriate nonlinear models are used (Figure 3.4).

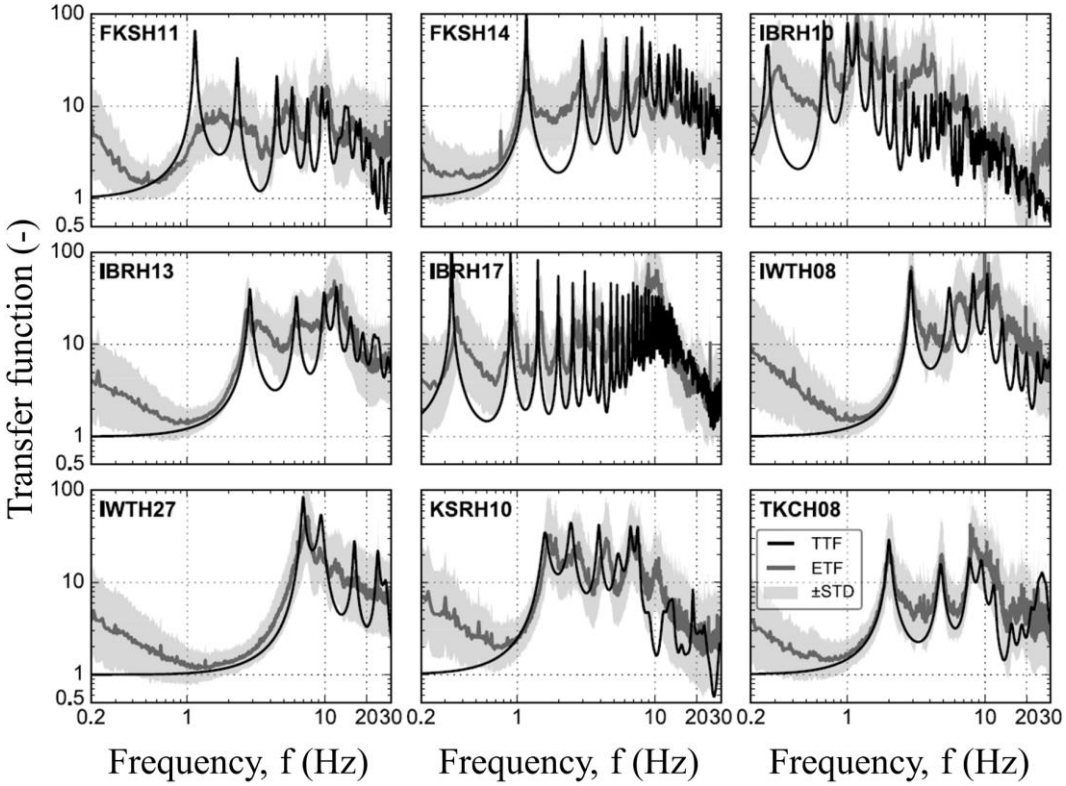

Figure 3.4. TTF-ETF comparison adopting the advanced HH model (after Shi & Asimaki (2017).

The TTF-ETF validation step was also conducted by Régnier et al. (2018) for two sites in Japan (Figure 3.5). In this work, the authors focused their attention also on the quality of GRA input data, besides the limitations of the 1D approach. They showed that the bias and inaccuracies of GRAs mainly depend on the EU and AV of the shear wave velocity profile for the small-strain response. Based on this assumption in the viscoelastic behavior, they proposed a benchmark for the assessment of the NL code-to-code variability.

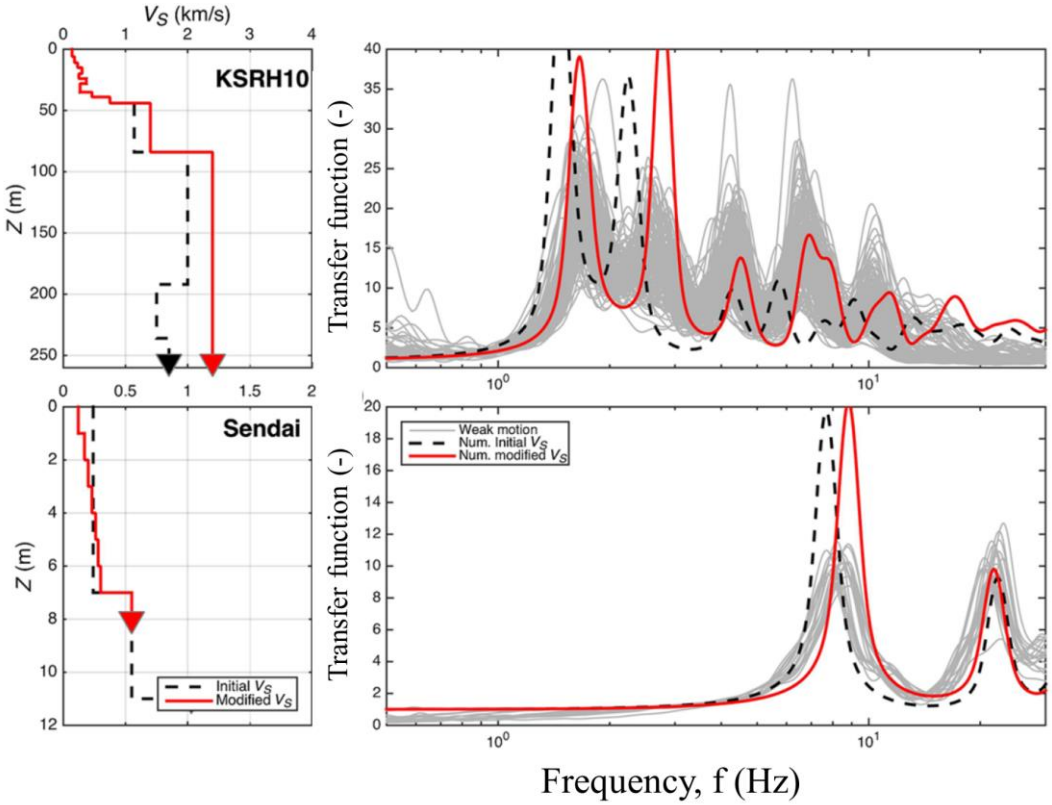

Figure 3.5. TTF-ETF comparison and correction of the shear wave velocity profiles (after Régnier et al. (2018)).

Figures 3.3, 3.4, and 3.5 showed that the availability of an experimental transfer function allows validating the numerical model in the visco-elastic behavior. This procedure is essential before moving forward with the numerical simulations that account for the nonlinearity of the response.

Summarizing the observations in the papers reviewed above, we can conclude that there are five main causes for the ETF-TTF disagreement during the validation stage:

1. Epistemic uncertainties in the soil property measurements and adopted numerical models;
2. Aleatory variability (i.e., soil heterogeneity) of the soil properties;
3. Non-vertical incidence of the waves;
4. Surface waves and basin effects;
5. Topographic effects.

Therefore, it is clear that, if GRAs are performed, the influence of the non-vertical incidence of the waves, surface waves, basin effects, and topographic effects cannot be studied (Olsen 2000). These additional sources of uncertainty could be handled using SRAs with an appropriate degree of 2D and/or 3D site characterization. The use of SRAs includes a more significant number of parameters, critically complicating the discussion and the analysis of EUs and AVs propagation on the results, particularly for nonlinear simulations. For SRAs, the

distinction of each singular contribution to the final uncertainty appears still very challenging (Taborda et al. 2010, Pagliaroli et al. 2015, Amorosi et al. 2016, Falcone et al. 2018, Hollender et al. 2018). Moreover, recent studies demonstrated that the inaccuracies and bias in GRAs are likely due to the nonlinear constitutive models, along with EUs and AVs of the input parameters (points 1-2) (Shi & Asimaki 2017, Régnier et al. 2018). For some cases, other potential errors (2D or 3D topography, basin effects) may be the primary culprits in other cases.

For these reasons, GRAs are still primarily used for the non-ergodic assessment of the site response and, particularly, for the IQM of EUs and AVs.

3.1.1 Site Response Analysis (SRA, 2- or 3D)

The main advantage of SRAs regards the simulation of the complete wavefield within the numerical model. Then, also surface waves (e.g., Rayleigh and Love), compressional waves (i.e., P) and vertically polarized shear waves (i.e., S_V) can propagate into the model. Moreover, the multidimensional simulations allow evaluating the effects of local topography, showing results in a 2D space (an example is given in Figure 3.6). However, the more complex formulation of the physical problem requires careful evaluation of other aspects as:

- Lateral boundary conditions assignment;
- Input motion applications;
- Mesh discretization and dimension (geometrical schemes);
- Damping formulations;
- Integration schemes (e.g., finite differences or finite elements);
- 2D and 3D constitutive models (especially in the nonlinear domain) and parameters calibrations;
- Computation demand.

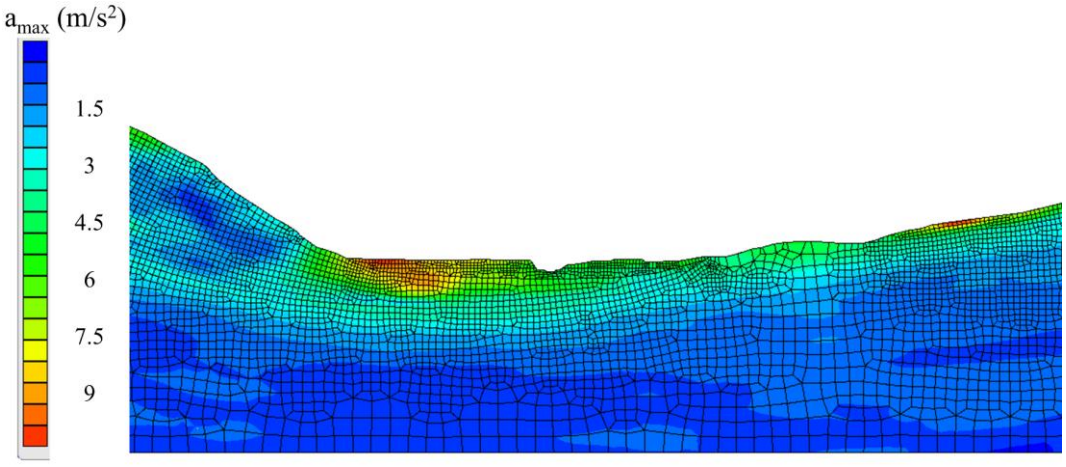

Figure 3.6. Results of a 2D Site Response Analysis (SRA) using LSR2D (Local Seismic Response 2D).

One of the first examples in the literature that studied the entire wave propagation phenomenon for irregular interfaces, in case of plane incident waves

from below, is given by Aki & Larner (1970). They provided a simple but efficient method to calculate an elastic wavefield propagation in a single layer over a bedrock. The importance of a 2D and 3D approach is also shown in Bard & Bouchon (1980a) and Bard & Bouchon (1980b), where the Aki-Larner method was extended to time-domain analyses separately for SH waves and P-SV wave propagation. They showed that the influence of generated Love and Rayleigh waves could be very strong in the case of valley formations and suggested the use of SRA for very complex site conditions.

An intermediate example of 3D modeling of ground motion is given by Olsen (2000) who studied the sedimentary Los Angeles valley. The author compared theoretical finite-difference, finite-fault simulation results with regional 1D crustal models. In this particularly complex environment, the use of 3D approaches showed quite large differences with the more straightforward one-dimensional method. However, the author admits that large uncertainties are involved in the definition of the 3D numerical model, and its results should be taken as a guide.

A similar analysis is conducted by Makra & Chávez-García (2016) for a site of the Euroseistest project. They showed an essential difference between 2D-3D and 1D models for this complex geological and topographical environment. In this particular case, however, only an inter-method comparison was performed with a single input motion on an idealized case. Also in this case study, despite the expected better performance of multidimensional models (otherwise, the adjective "simplified 1D" would be meaningless), a limited application is proposed. This limitation is mainly due to computational demand and the need for sufficient information at the site, which prevents a systematic evaluation of the EUs and AVs at stake.

Significant progress was made in the scientific literature, thanks to the development of high-performance computers, stable numerical codes and sophisticated constitutive models. One of the most recent applications of a multi-dimensional and non-linear site response analysis is given by Falcone et al. (2018). They examined the accuracy and bias of 2D and 3D numerical simulations performed by PLAXIS code for an ideal and real (i.e., urban environment) case. The ideal case study is fundamental for the validation of the model with independent analytical known solutions. Then, the real case is carefully studied accounting for the nonlinearity of the soil response. In the paper, the authors attempted to recognize the primary sources of uncertainties as geometrical schemes, non-linear soil response, and shear wave velocity profiles. However, the initial complexity of the numerical models prevents a systematic analysis of the propagation of those uncertainties on the results, as discussed above.

Another recent example is given in Volpini & Douglas (2018). This study aimed at giving suggestions on the behavior of quasi-horizontal layered deposits. In particular, the authors questioned how far the one-dimensional approach can be used, without significant mistakes and when, on the contrary, the analyst is forced to approach this kind of geometry with a two/three-dimensional approach. The chosen methodology considers the construction of a chart, with reliable and straightforward variables, such as the slope of the critical interface and impedance

contrast at this interface. A power law gives the limit between one-dimensional and two-dimensional methods. The generation of this power followed a parametrical study on a simple geometry, consisting of two layers. The aspects studied are:

- The influence of the dipping layer and the angle of the slope;
- The influence of the impedance contrasts;
- The influence of location within the model.

3.1.2 Ground Response Analysis (GRA, 1D)

Differently from SRAs, ground response analyses are based on the assumption that all boundaries are horizontal and extend infinitely, whereas the response is dominated by vertically propagating and horizontally polarized shear (S_H) waves. These formulations involve the propagation of S_H waves from the base rock to the ground surface through a model of the soil layers that can be modeled as lumped mass or distributed mass (Figure 3.7). However, the difference between a lumped mass system and a distributed mass model is purely semantic. In the distributed mass model, the masses are lumped at the nodes; therefore, the two approaches are actually the same. Analytical solutions are able to account for spatially distributed mass, but numerical solutions always lump the masses to set up a mass and stiffness matrix.

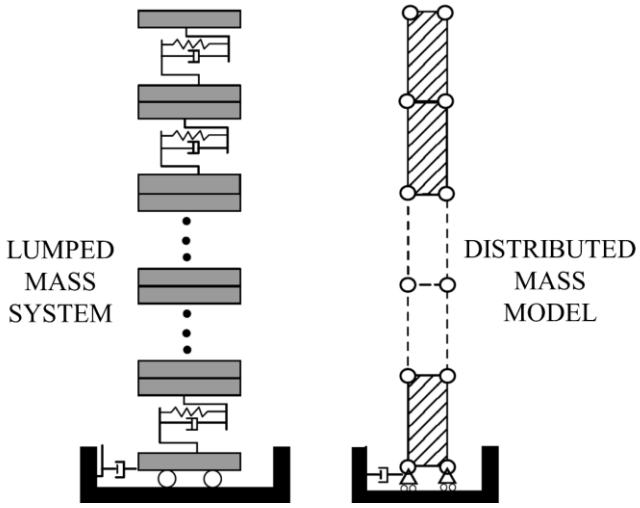

Figure 3.7. Mass discretization models for a Ground Response Analysis (GRA) (after Kwok et al. (2007))

It is mostly recognized that GRAs are a useful tool to investigate the role of EU and AV in the site-specific hazard assessment (Field & Jacob 1993). In this dissertation, six main inputs and models are identified as sources of uncertainties on the results, in agreement with Idriss (2004) and Rathje et al. (2010):

- Shear wave velocity (V_S) profile;
- Modulus reduction and damping (MRD) curves;
- Input motions selection;
- Nonlinear approach;

- Shear strength;
- Small strain damping (D_{min}).

In Idriss (2004) and Rathje et al. (2010), the shear strength and the small strain damping ratio contributions were not explicitly identified as crucial parameters. In this dissertation, also these further sources of uncertainties and variabilities are briefly presented, even if they are likely second-order importance (at least for shallow profiles, as discussed in Cabas & Rodriguez-Marek (2018)) compared to the four main ingredients discussed in the previous literature (Figure 3.8). In fact, for these two sources, there is not a large number of studies in the literature where only their influence on the results was explicitly assessed. However, D_{min} and the shear strength, respectively, could strongly influence the small strain and the large strain response. Also, the shear wave velocity profile will be separately addressed in the dedicated Chapter 4 (i.e., only a brief presentation is given in Section 3.1.2.1 for completeness).

In the following sections, the dissertation will first address the main intrinsic causes of EU and AV within each contribution. A comprehensive summary is then provided in Table 3.1 (see Section 3.1.2.7) to guide in the IQM of EUs and AVs in GRAs. Then, the influence of each parameter on the results of GRAs will be presented through an extensive literature review in Section 3.2.

Note that also in this case, the theoretical separation between EUs and AVs for each source is elegant and precise. However, this separation still appears very challenging from the practical point of view and strongly influences the management step of the IQM methodology. For these reasons, the geostatistical model that manages the uncertainties should be independent of their type and size. However, a calibration of the model's parameters can be performed based on a rigorous analysis of a database, as discussed in the following for surface wave testing methods. In that case, however, the distinction within the experimental data in practically unfeasible. For this reason, the set of parameters provided will represent simultaneously the EUs and AVs.

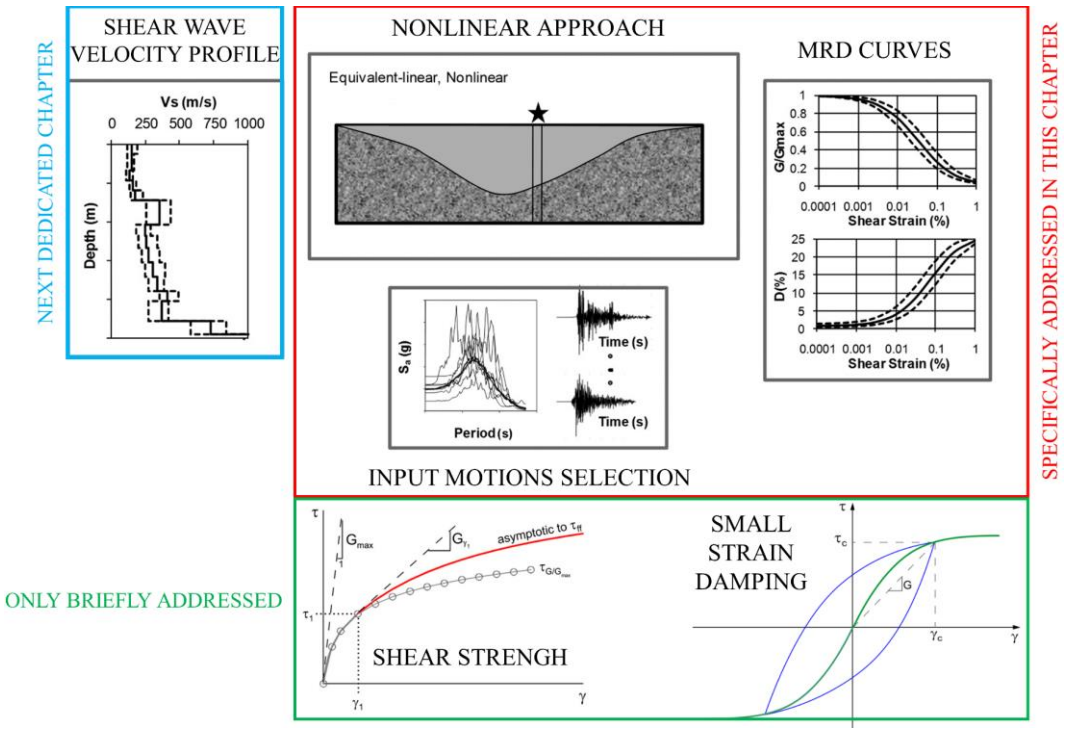

Figure 3.8. Primary sources of epistemic uncertainties and aleatory variabilities in GRAs (modified from Rathje et al. (2010)).

3.1.2.1 V_S profile

The shear wave velocity profile is the input parameter that governs the waves propagation in the elastic medium. It defines resonance frequencies and amplification ratios, especially for shallow depths (Kwok et al. 2008). The V_S profile controls the mechanical amplification/deamplification of the motion at the interfaces. The adopted V_S profile for a GRA must be based on in situ geophysical measurements (Stewart et al. 2014a). Each type of test shows a different amount and proportion of EUs and AVs (Passeri et al. 2019), also depending on the site complexity (Baise et al. 2011, Thompson et al. 2012) (e.g., deposition environment Rathje et al. (2010)). Note that an in-depth discussion regarding this parameter is given in Chapter 4.

3.1.2.2 Modulus reduction and damping (MRD) curves

The modulus reduction and damping curves are the input parameter that characterizes the nonlinear response of the soil material. MRD curves are necessary to describe the shape of the backbone curve (MR) and the relationship between hysteretic damping (D) and shear strain. Various laboratory tests can evaluate MRD curves (e.g., resonant column, cyclic triaxial test, cyclic torsional or simple shear test), however they are often chosen from the large number of empirical models (Hardin & Drnevich 1972a, Hardin & Drnevich 1972b, Iwasaki et al. 1978, Seed et al. 1986, Sun et al. 1988, Vucetic & Dobry 1991, Ishibashi & Zhang 1993, Lanzo et al. 1997, Rollins et al. 1998, Darendeli 2001, Andrus et al. 2003, Menq 2003, Roblee & Chiou 2004, Stokoe et al. 2004a, Zhang et al. 2005, Amir-Faryar et al.

2017). Each empirical model considers a different number of variables (e.g., IP, mean confining effective stress, OCR, K_o, frequency). Cross-validation between laboratory and empirical curves is always encouraged, before starting large-strain numerical simulations (Régnier et al. 2018).

Along with the mean values, for each shear strain level, some empirical formulations also give the EU as standard deviations. This uncertainty represents measuring error and can be used for a stochastic study of the parameter sensitivity (Darendeli 2001, Zhang et al. 2008). However, a further EU is related to the adoption of the empirical correlation itself (Papaspiliou et al. 2012b, Kaklamanos et al. 2013a, Faccioli et al. 2015, Kaklamanos et al. 2015) and great care should be taken respecting the model assumptions (e.g., strain range applicability) (Baturay & Stewart 2003, Stewart et al. 2014a). In case of laboratory results, usual experimental limitations (state of stress, boundary conditions, and sample disturbance) should be evaluated as EU, particularly in case of high confining pressures (i.e., deep deposits) (Park & Hashash 2005a).

The AV in the MRD curves can be seen as the natural randomness of these properties at the site scale, always analyzing a realistic amount of variability, depending on the geological complexity and the size of the study (Park & Hashash 2005a).

3.1.2.3 Input motion selection

The input motions in a GRA should correspond to a seismic demand consistent with the hazard at the reference condition (i.e., consistent with a hazard scenario at the reference condition). It is the only source of EU and AV that can be almost entirely removed, in the case of in-hole measurements and for the trivial case of predicting something that is already measured. The primary goal is to select input motions in agreement with a motion that is expected at the PSHA reference condition (as a mean and standard deviation) when the site response is ideally removed (see Figure 3.1). There are two main types of inputs for a GRA: recorded time histories and stochastic/physics-based motions (Silva et al. 1997, Boore 2003b, Asimaki & Li 2012, Aristizabal et al. 2018).

Generally, recorded time histories that reproduce multiple hazard levels at the reference site conditions are used for GRA to better constrain the evaluation of the amplification function. The goodness of fit can be evaluated following the approach by Kottke & Rathje (2008) which accounts for the fit with both the mean and standard deviation of the target spectrum. Moreover, the input motion suite has to produce stable results (Baturay & Stewart 2003, Bazzurro & Cornell 2004a, Rathje et al. 2010). However, there are cases where just one seismic source does not control the hazard at a site, and then it is difficult to define a single input that is compatible with the results of PSHA (Bommer et al. 2000).

An alternative to physical records is the use of stochastic/physics-based motions. The use of stochastic/physics-based motion generation can be very appealing when there is a small number of real records to choose from, and when a large number of analyses are required (Li & Asimaki 2010, Asimaki & Li 2012,

Rodriguez-Marek et al. 2014, Pehlivan et al. 2016, Aristizabal et al. 2018). However, care has to be taken for the correct simulation of the wave propagation from the source to the near-surface (Asimaki & Li 2012).

The EU in the selection process is due to the choice of the hazard level, the type of reference spectrum (Uniform Hazard Spectrum or Conditional Mean Spectrum (Baker & Allin Cornell 2006)), and the matching approach adopted (scaled or modified) (Faccioli et al. 2015). Then the type and number of inputs (Rathje et al. 2010), the searching method, and the consistency with the reference condition (Passeri et al. 2018a), also accounting for near-field and far-field effects (Stewart et al. 2014a).

In this case, the AV should be due to the source and path spatial variabilities that control the hazard at the reference condition. These AVs can be obtained from the PSHA results in terms of spectral standard deviations.

3.1.2.4 Nonlinear approach

Several approaches may be used to simulate the nonlinear response of the natural material (Joyner & Chen 1975). A GRA is typically implemented in numerical codes adopting one of the following methods to account for the nonlinear response of the medium: frequency-domain EQuivalent Linear (EQL) and time-domain NonLinear (NL) (Figure 3.9).

However, also visco-ELastic (EL) analyses are useful for the initial validation of the model (TTF-ETF comparison). Frequency-dependent analyses are not addressed as they are not often used (Kausel & Asimaki 2002, Huang et al. 2018)). Let's use an excellent definition by Kim et al. (2013a):

"An equivalent-linear (EQL) site response analysis approximates the nonlinear response of soil using strain-compatible time-invariant soil properties, and provides reasonable estimation of ground response for many situations. Time domain nonlinear (NL) site response computes the dynamic response of the soil at each time step. This more rigorous approach can better capture soil behavior under large strains such as for soft soil sites subject to strong ground motions, but it is computationally expensive and requires the use of input parameters (such as Rayleigh damping) that are relatively unfamiliar for most engineers. Due to the advantages and disadvantages of these two approaches, the conditions under which the two methods produce consistent and divergent estimates of site amplification are of practical interest."

An equivalent-linear (EL) one-dimensional (1-D) site response analysis simulates the nonlinear response of soil using strain-compatible invariant soil properties. The EL soil property estimates are set for an averaged strain computed as a percentage of the peak strain and provide a response that is likely in error for lower and higher strains than the average strain. Time domain nonlinear (NL) site response analyses incorporate changes in the soil properties at each time step. This more rigorous approach can better capture soil behavior under large strains such as for soft soil sites subject to strong ground motions. NL analyses require greater care in the development of required input parameters such as model parameters, viscous

damping and profile discretization, and are generally more computationally demanding than EL analyses.

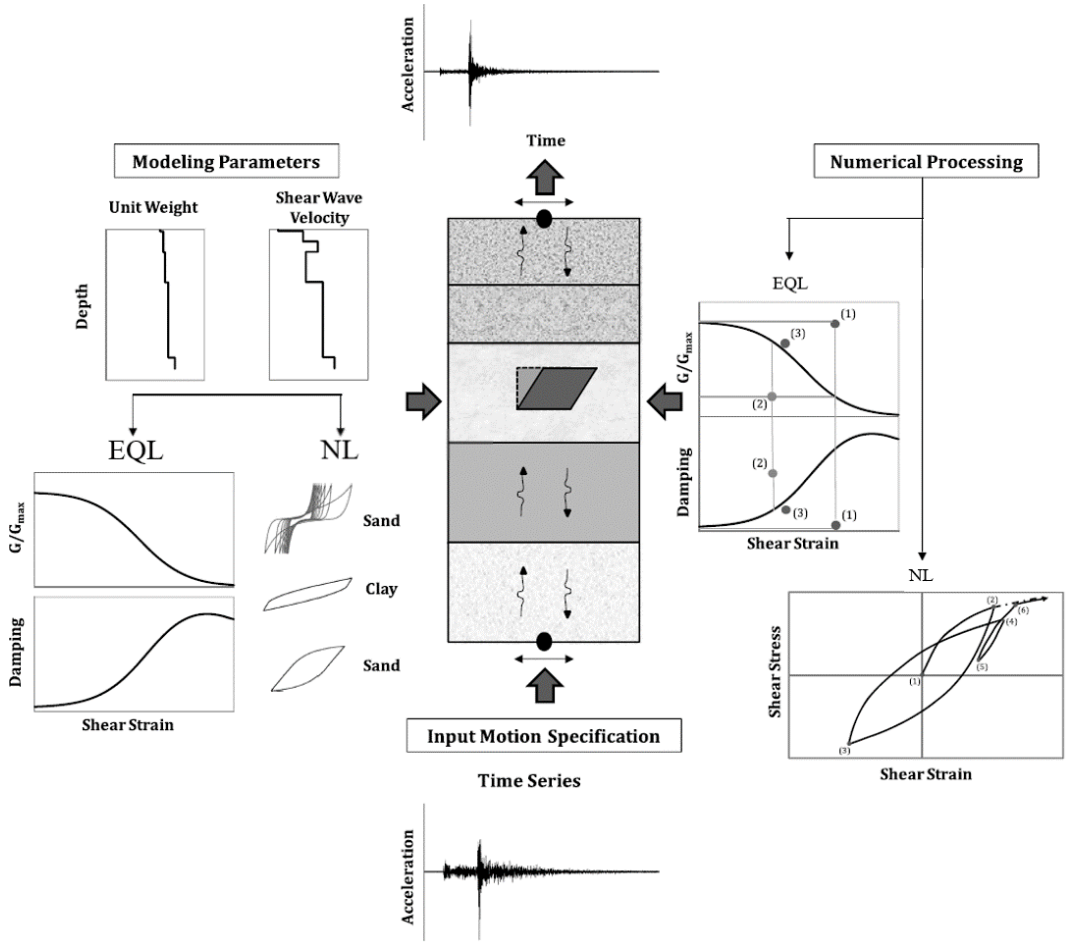

Figure 3.9. Schematic illustration of the main two nonlinear approaches (i.e., EQL and NL) (after Zalachoris & Rathje (2015)).

Depending on the expected strains level induced in the medium and/or the possible development of excess pore pressure (i.e., total or effective stress analysis), the choice should be made between EQL-NL approaches (Kramer & Paulsen 2004, Stewart et al. 2014a, Kim et al. 2016). In particular, the EQL method is a simplified and usually more stable procedure, however, NL analyses are catching on in the usual practice showing more consistent results (Andrade & Borja 2006, Hashash et al. 2010, Asimaki & Li 2012, Papaspiliou et al. 2012b, Régnier et al. 2016a, Régnier et al. 2018), even if they are still more computationally demanding (Kim et al. 2016). Many shear strain applicability boundaries are suggested in the literature for the use of the EQL or the NL approach. However, a single value cannot be proposed, as the effectiveness of each method is depending on the specific characteristics of the model (Aristizabal et al. 2018).

Equivalent linear analyses should be avoided in case of strong nonlinear response and large induced shear strains (i.e., soft, sandy soils subjected to strong high-frequency motions) (Baturay & Stewart 2003, Hartzell et al. 2004, Asimaki et al. 2008, Asimaki & Li 2012, Kaklamanos et al. 2013b, Kim et al. 2013a, Kaklamanos et al. 2015, Kim et al. 2016) and in case of no convergence of the

iterative process (Papaspiliou et al. 2012b, Papaspiliou et al. 2012a). A source of uncertainty in the EQL analysis is related to the time-independent assumption of the converged stiffness and damping parameters (Kaklamanos et al. 2013b, Kaklamanos et al. 2015, Zalachoris & Rathje 2015, Kim et al. 2016). In particular, a Shear Strain Ratio (SSR) is adopted in the EQL analyses to scale the shear strain time history by a factor less than one (usually 0.65). This scaling should account for the time-invariant choice of the operative mechanical parameters. However, there are no specific studies that prescribe a consistent value, depending on other simulation parameters (Kim et al. 2016).

On the other hand, the results of nonlinear approaches should be initially verified against more straightforward methods (EL or EQL) and experimental evidence (e.g., from DH arrays) as the user expertise plays a fundamental role in this framework (Kwok et al. 2007, Stewart 2008, Stewart & Kwok 2008, Hashash et al. 2010, Kaklamanos et al. 2015, Kim et al. 2016, Hollender et al. 2018, Régnier et al. 2018).

Many specific sources of EU can be identified in the NL methods, and are discussed in Hashash et al. (2010), Régnier et al. (2016a), and Régnier et al. (2018). In particular, the PRENOLIN (PREdiction of NOn-LINear soil behavior) project investigated the primary sources of EU in GRAs due to differences in NL codes with various constitutive models. The project was organized in two steps: the verification phase (i.e., the comparison between numerical codes on simple idealistic cases) and the validation phase (i.e., predictions of numerical estimations with actual strong-motion recordings obtained at well-known sites). Twenty-three different computational codes were used in this international benchmark. The results of these studies demonstrated that the most critical aspects for an NL GRA are numerical integration schemes, damping formulations, constitutive models and parameters calibration (curve fitting), especially in the case of pore water pressure generation models. The boundary conditions (mainly for the input motion boundary) and layers thickness should also be checked to guarantee a consistent wave propagation within the model. Other references on this topic can be found in Kwok et al. (2008), Stewart (2008), Stewart & Kwok (2008), Papaspiliou et al. (2012b), Kaklamanos et al. (2015), Zalachoris & Rathje (2015), Kim et al. (2016). In addition, a novel method for matching the MRD curves in nonlinear methods is proposed in Yniesta et al. (2017). This method should solve the typical overcoming of the delicate calibration step.

Hence the model adopted for nonlinear GRAs (EQL or one from the vast multitude of NL approaches) is mainly a source of EU and should be carefully treated (Papaspiliou et al. 2012b). However, a very promising formulation of a new constitutive model termed Hybrid Hyperbolic was proposed by Shi & Asimaki (2017). This model, although not many applications are proposed in the literature so far, seems to provide a consistent step forward for GRAs, for both EQL and NL analyses.

3.1.2.5 Shear strength

The shear strength is the input parameter that should be used in GRAs when a large shear strain is mobilized, aiming at assuring consistency between the small strain behavior characterized by the adopted MRD curves and the large strain behavior of the material (Baturay & Stewart 2003, Stewart & Kwok 2008, Hashash et al. 2010, Yee et al. 2013, Zalachoris & Rathje 2015, Kim et al. 2016, Shi & Asimaki 2017, Régnier et al. 2018). The importance of the inclusion of this consistency in GRAs is remarked in Aaqib et al. (2018) for both deep-soft sites in high seismicity regions and shallow sites at moderate-to-low seismicity regions. The differences are period-dependent, as expected.

The associated EU has to be evaluated depending on the type of laboratory test adopted for the evaluation of the shear strength (Jones et al. 2002). A further source of EU is the model adopted for "merging" the small-strain and large-strain (i.e., at failure) behavior (Li & Asimaki 2010). An example adopting the Yee et al. (2013) is presented in Zalachoris & Rathje (2015) (Figure 3.10). However, a new perspective for consistent modeling from stiffness to strength is given in Shi & Asimaki (2017). The authors showed that the proposed HH model could reproduce both the small-strain behavior from a resonant column test and a moderate-to-large strain behavior from the direct shear test. Also, the empirical correlations they propose between the shear wave velocity and the model parameters are appealing for the initial calibration process and can capture the material strength. Moreover, a new method is presented in Aaqib et al. (2018) as a quadratic/hyperbolic model. As for the MRD curves, the contribution of AV depends on the geological complexity of the project area under analysis.

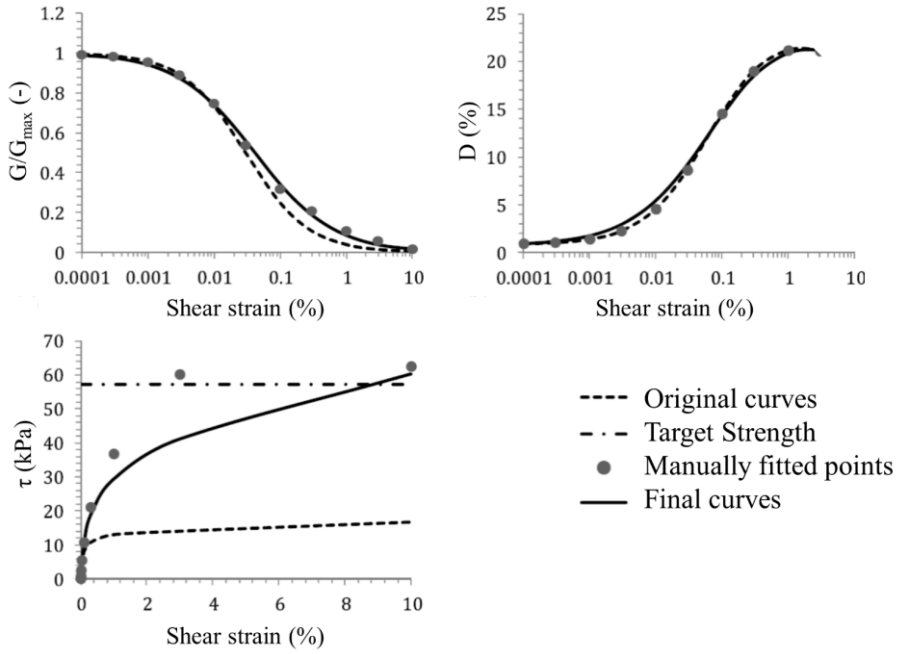

Figure 3.10. Matching process between small strain and shear strength (after Zalachoris & Rathje (2015)).

3.1.2.6 Small strain damping D_{min}

Laboratory measurements of damping at low strains (D_{min}) are generally at odds with experimental evidence from downhole arrays. The small strain damping is the input parameter that should be added to laboratory evidence in the GRA model to fit the experimental evidence. In fact, at the site scale, larger values of energy loss are observed from very low strain levels (Régnier et al. 2018), likely due to complex wave propagation interaction (Stewart et al. 2014a). One of the controlling phenomena is the wave scattering, which produces a variable energy loss in the model, depending on the mechanical conditions. This phenomenon is more evident in the case of strong impedance contrasts (Zalachoris & Rathje 2015). The central problem of this parameter regards the amount of damping at various depths (even five times the one from laboratory tests). This D_{min} profile can be evaluated, for example, using weak motions recordings and back-calculation procedures (Park & Hashash 2005a). Then a complex mix of EU and AV strongly influences this parameter, as it represents the portion of geometrical damping that controls the global spatial wave propagation.

Moreover, for NL analyses, further EUs are mainly due to the numerical approach that is implemented for the addition of the viscous damping to the hysteretic damping (Hashash & Park 2002, Park & Hashash 2004, Kwok et al. 2007, Stewart & Kwok 2008, Phillips & Hashash 2009, Papaspiliou et al. 2012b, Kaklamanos et al. 2015, Rayleigh 2015, Zalachoris & Rathje 2015).

3.1.2.7 Summary

The next Table 3.1 summarizes the most common sources of EUs and AVs involved in each parameter of a GRA and discussed in previous sections from a purely theoretically point of view.

Table 3.1. Summary of the most critical sources of epistemic uncertainties and aleatory variabilities in Ground Response Analyses.

	EPISTEMIC UNCERTAINTIES	ALEATORY VARIABILITIES
V_S profile	Epistemic uncertainties are associated with measurement errors; AVs are associated with spatial variability. Different tests used to measure V_S in the field have different amounts of EUs, and capture spatial variability (AV) in different ways, depending on the site complexity.	
MRD curves	Regression residuals and specific characteristics of the adopted model (in the case of empirical curves). Experimental measurements limitations (in the case of laboratory tests). Cross-validation between laboratory and empirical curves is always encouraged.	Variation of these properties at the site scale depending on the geological complexity and the size of the study.
Input motion selection	• Choice of the hazard level • Type of reference spectrum and goodness of fit evaluation • Matching approach • Number and type of inputs • Searching method • Consistency with the reference condition • Near-field and far-field effects	Variability included in the reference hazard result that is obtained by the PSHA.
Nonlinear approach	**EQL** • Time-independent parameters • High nonlinear responses (i.e., soft, sandy soils subjected to strong high-frequency motions) • Convergence • Shear Strain Ratio (SSR) assumption • Total stress analysis (possible development of excess pore pressures) **NL** • Integration schemes (e.g., implicit or explicit) • Damping formulations • Constitutive models and parameters calibration (curve fitting), especially in the case of pore water pressure generation models • Boundary conditions (especially at the halfspace) and layers thickness • Requirement of a specific expertise	No aleatory variability.
Shear strength	Dependent on the laboratory test used for the shear strength evaluation and in situ stress conditions. Then, the merging law (i.e., between small strains and large strains) or the constitutive model adopted.	Variation of these properties at the site scale depending on the geological complexity and the size of the study.
Small strain damping	Lack of a rigorous knowledge of the amount of dissipation phenomena at the site scale, especially for high frequencies. Adopted model in NL analyses for the additional viscous damping, particularly for low periods.	A portion of geometrical damping that is controlled by the global spatial wave propagation.

3.2 Effects of uncertainties and variabilities on GRA results

This section refers to Idriss (2004) and Rathje et al. (2010) who discussed the influence of the primary four sources of EUs and AVs on GRA results. As previously anticipated, the shear wave velocity profiles will be separately discussed in Chapter 4. However, Table 3.1 and Section 3.2.1 list references that accounted for EUs and AVs in V_S profiles. The next paragraphs summarize the primary examples of IQM of EUs and AVs proposed in the literature also for the shear strength and the small strain damping ratio. A final summary is given in 3.2.5 and Table 3.2.

Generally, input parameters randomization methods have been used in the literature by adopting Monte Carlo (MC) algorithms (Field & Jacob 1993, Roblee et al. 1996, Bazzurro & Cornell 2004a). This choice was critically discussed in Andrade & Borja (2006) and Li & Asimaki (2010) who focused their attention on the result of the sensitivity analysis, mainly looking at the number of realizations at convergence. Monte Carlo randomizations are more time-consuming than other approaches, but they are a robust method independent of the problem complexity (i.e., nonlinearity) (Li & Asimaki 2010). For these reasons, in recent studies, the adoption of MC methods is mostly accepted and corroborated for the evaluation of the probabilistic distributions of GRA results (Rathje et al. 2010, Rodriguez-Marek et al. 2014, Bahrampouri et al. 2018). However, Rathje et al. (2010) encourage the use of logic trees and the engineering judgment to better model some uncertainties contributions.

Another method to evaluate the final dispersion of the results is the FOSM method (Kwok et al. 2008, Stewart & Kwok 2008, Melchers & Beck 2018) which requires a reduced number of parameter realizations.

Historically, Field & Jacob (1993) were the pioneers who investigated the effects of EUs and AVs on the GRAs results. Their work was part of the first step (i.e., weak motion) benchmark that blindly studied the Turkey Flat array (Kwok et al. 2008). In the first step of the work, the results showed good consistency between different theoretical techniques in estimating the site response. Then Field & Jacob (1993) also investigated the influence of the parameters on the theoretical predictions using MC analyses. In this framework, the authors first recognized the high degree of variability introduced in the predictions. In particular, they found the V_S profile to have an important role, especially for a low constraint of the shallow, thin, layers. They concluded their study highly recommending the analysis of uncertainties influence for GRAs.

An outside voice regarding the influence of EUs and AVs in the GRA can be found in one of the first studies on the topic by Bazzurro and Cornell (2004a). They studied the effects of soils parameters uncertainties on the results expressed as spectral accelerations, amplification functions and related logarithmic standard deviations (both parameters are assumed lognormally distributed). They also stated that parameters variability did not seem to produce significant effects on the results.

However, in light of modern studies, this observation is not still valid, as their pioneer attempt was based on a limited case study and simplified randomization models. They proposed a Monte Carlo randomization of seven parameters and calculated the site response adopting one input motion for each realization of the soil parameters, not detecting an increased variability on the results (Figure 3.11). Then, they increased the number of parameter realizations to 10, for each input motion, still not detecting an essential difference between the mean responses $\overline{AF(T)}$ and/or an increased variability $\sigma_{\ln(\mathrm{AF})}(T)$.

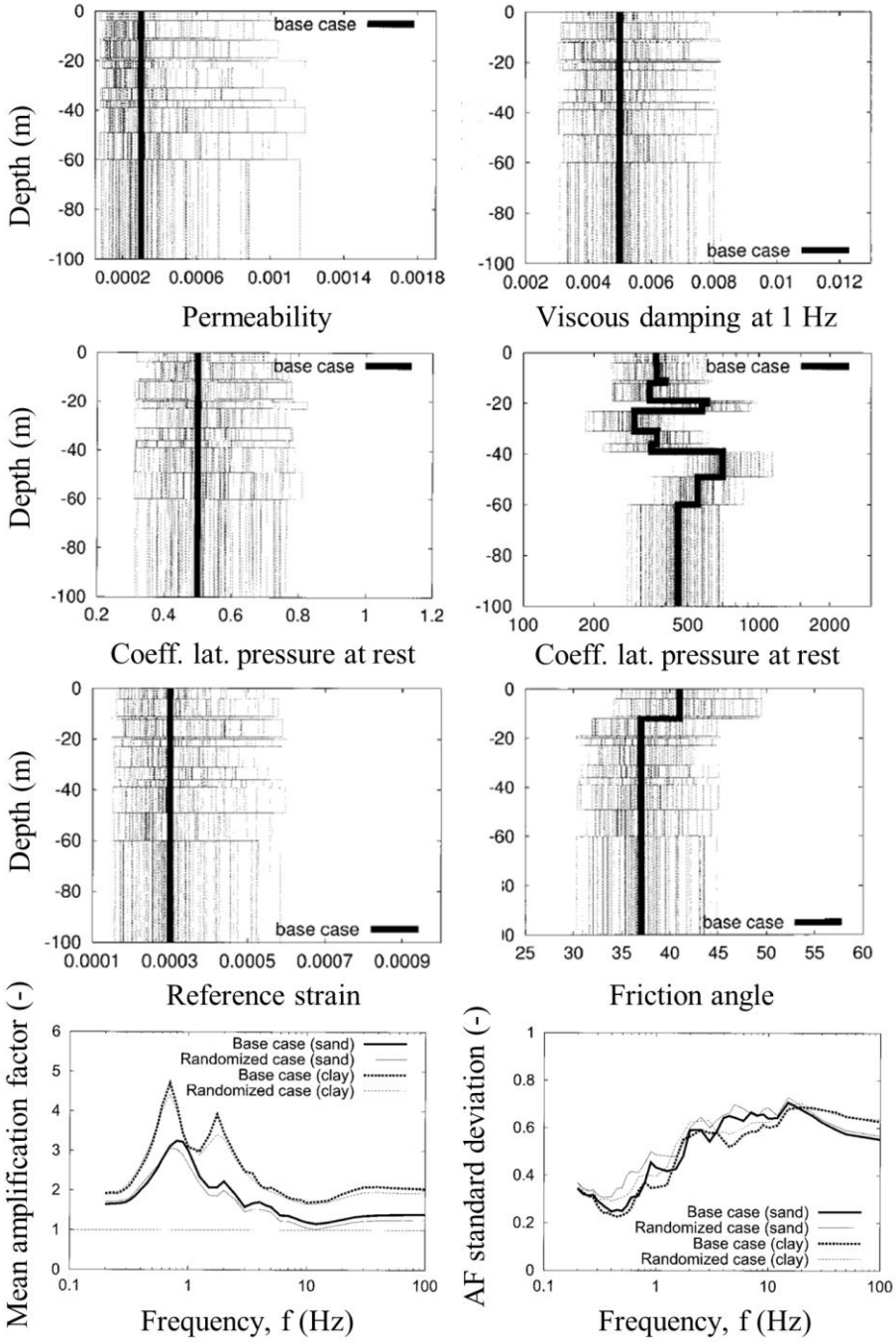

Figure 3.11. Randomization of the parameters and results illustrated as mean amplification function and logarithmic standard deviation (after Bazzurro and Cornell (2004a)).

More recent studies (e.g., Rathje et al. (2010)) demonstrated that the inclusion of the input parameters uncertainties and variabilities in GRA is of paramount importance. The authors proposed a systematic evaluation of the effect of randomized V_S profiles and MRD curves using the software STRATA (Kottke & Rathje 2009). STRATA represents the first example of a publically-available GRA software where also randomization analyses can be performed. Kottke & Rathje (2009) first implemented a series of models for the randomization of shear wave velocities and MRD curves that included correlations between the parameters. Differently from Bazzurro & Cornell (2004a), they showed a substantial impact of randomized soil properties on the results, regarding both amplification functions and their logarithmic standard deviations (Figure 3.12 and Figure 3.13).

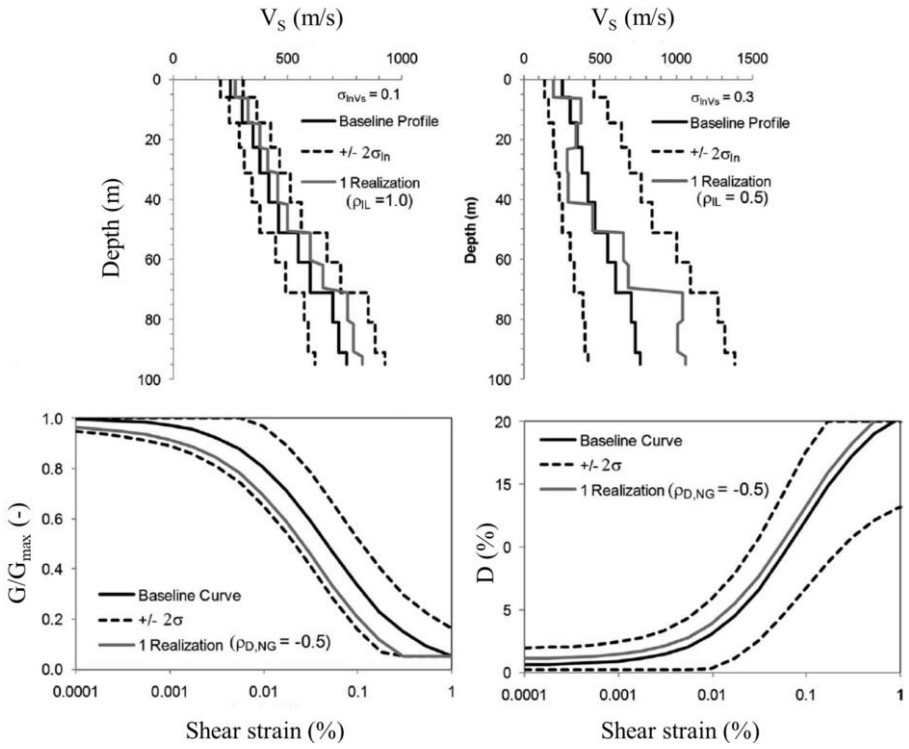

Figure 3.12. V_S profiles and MRD curves randomization proposed in Rathje et al. (2010) for the assessment of the parameter uncertainties and variabilities.

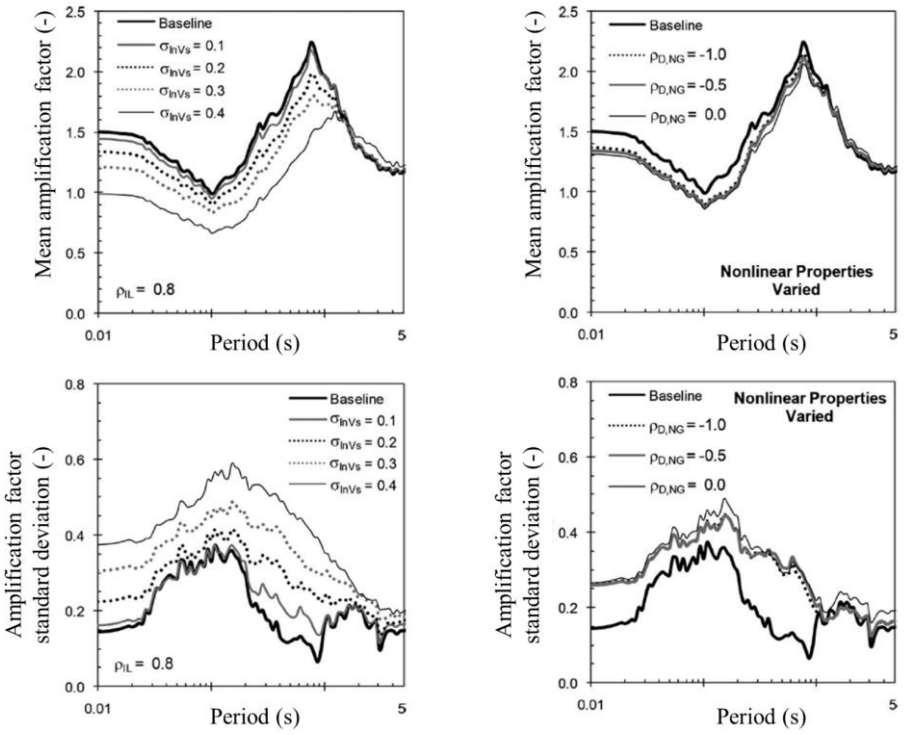

Figure 3.13. Results obtained in Rathje et al. (2010).

Li & Asimaki (2010) analyzed the number and type of input motions to be used in the simulations to reproduce a wide strain range of soil and rock responses (Papaspiliou et al. 2012a, Aristizabal et al. 2018). As briefly discussed in the previous Chapter, the nonlinearity of the response should always be precisely evaluated (Hashash et al. 2010, Asimaki & Li 2012). Li & Asimaki (2010), Papaspiliou et al. (2012b), Pehlivan et al. (2016), Bahrampouri et al. (2018), and Passeri et al. (2019) showed that the input motion intensity strongly influences the propagated EU and AV in GRA. In general, they showed increased results variability due to the nonlinear response of the soil deposit at large strains. In particular, Pehlivan et al. (2016) and Aristizabal et al. (2018) showed a strong influence of the soil nonlinearity on the calculated hazard curves, even more than other sources of EU and AV. Accordingly, Baise et al. (2011) suggested adding the nonlinearity to the analyses only when the linear response was carefully studied, regarding mean response and associated variabilities.

For this reason, Li & Asimaki (2010) used a broad set of synthetic motions coming from various ranges of magnitudes and distances for three instrumented and well-characterized sites in California. The results are shown as a function of the input motion intensity and frequency content as a logarithmic standard deviation of the surface response spectrum $\sigma_{\ln(SA)}(T)$ (Figure 3.14).

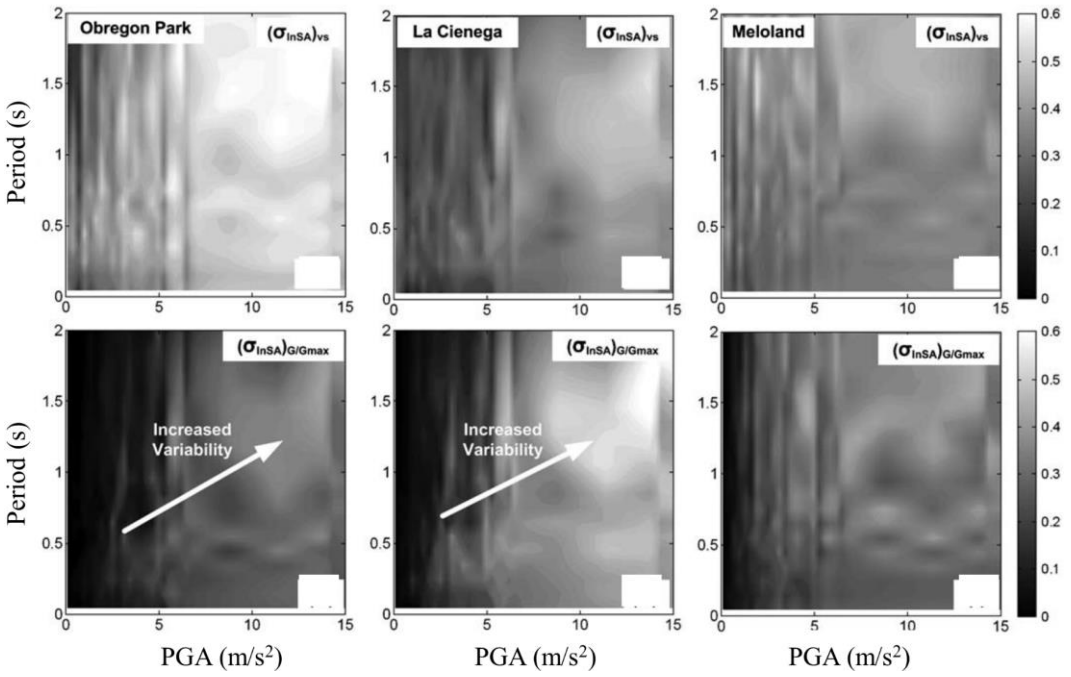

Figure 3.14. Epistemic uncertainties and aleatory variabilities of V_S profiles and MRD curves propagated on the surface response spectra (after Li & Asimaki (2010)).

Another example of site-specific (i.e., non-ergodic) assessment of the seismic hazard a site that also systematically accounted for EU and AV is proposed in Rodriguez-Marek et al. (2014). Their study also regards a few concepts discussed in the previous Chapter, condensing various observations in an application for a project in South Africa (Bommer et al. 2015). First, they evaluate the EU in the model for the reference hazard scenario; then they applied a mixture of logic tree and randomization approaches for the subsequent GRAs (Figure 3.15). This study represents a modern application of a specific operational flow to perform a hazard study for a critical facility, managing all sources and types of EUs and AVs in both the reference hazard GRAs.

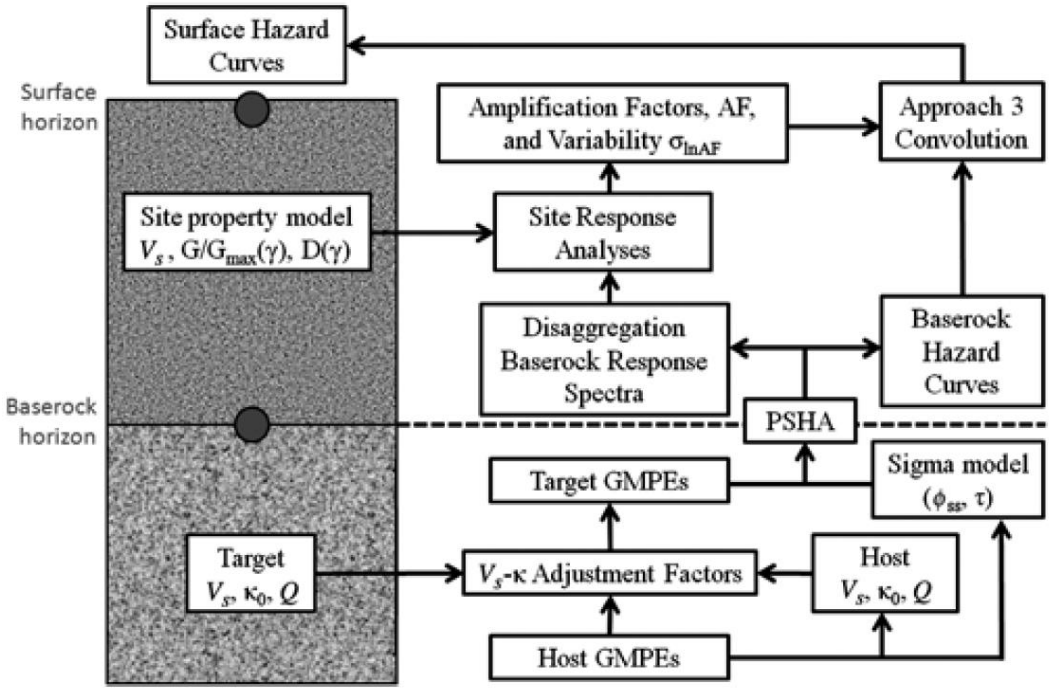

Figure 3.15. PSHA low designed by Rodriguez-Marek et al. (2014) for a project in South Africa.

A fascinating case study is presented in Pagliaroli et al. (2015) who studied the seismic response of Rome's downtown. Besides the results of the analyses (both 1D and 2D), this example shows an uncommon source of aleatory variability. The Roman subsoil presents large heterogeneities regarding geotechnical parameters. This spatial variability is mainly due to buried morphologic and anthropogenic coves that reach a thickness of 20 m in the Colosseum area (Figure 3.16). This layer is made by "dominant masonry" and "dominant infill" with a high level of uncertainties. These uncertainties do not regard a natural variability, but the effects of artificial understructures that should be accounted in the site response study. In particular, they investigated the effects of EU and AV in V_S and MRD curves.

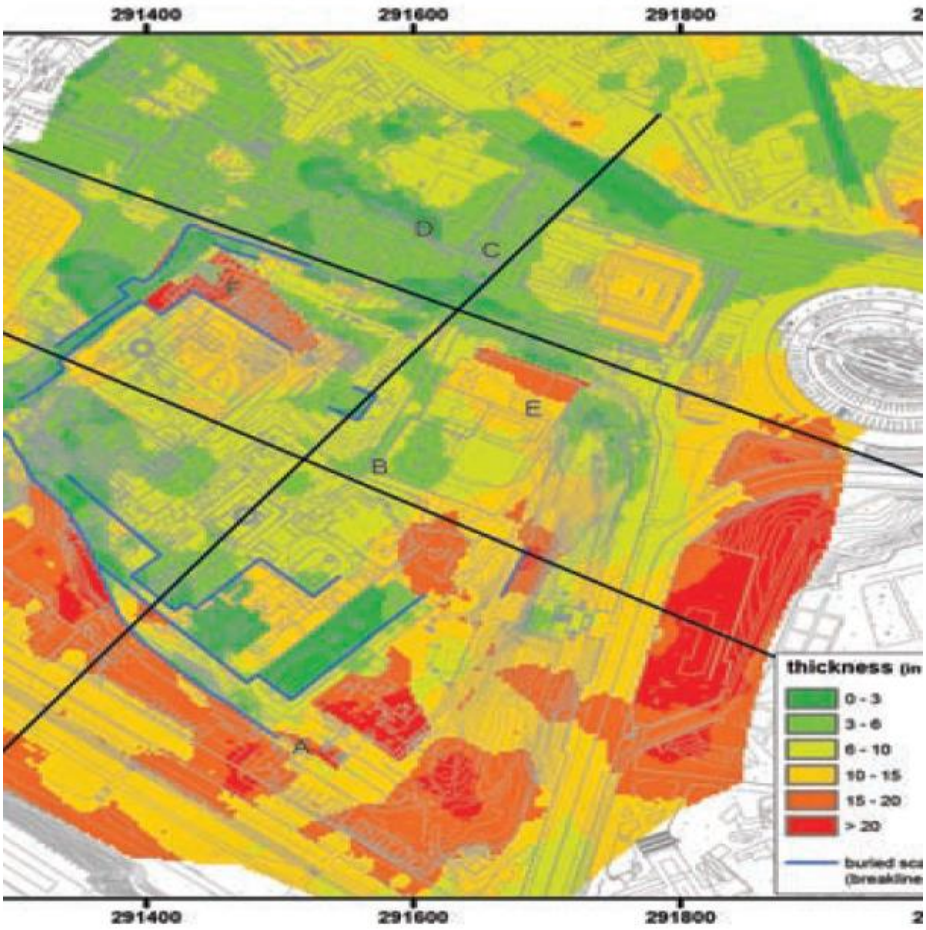

Figure 3.16. Map of the substantial spatial (i.e., aleatory) variability investigated in the Rome's downtown (after Pagliaroli et al. (2015)).

Bahrampouri et al. (2018) presented a study that investigated in depth the influence of EUs and AVs for the Groningen gas field hazard assessment. The authors systematically investigated the influence of V_S and MRD curves on the results of the GRAs, as $\overline{AF}$ and $\sigma_{\ln(AF)}$. However, the main results regarded the influence of the variability of the MRD curves. In particular, they classified the input motions in low-intensity and high-intensity and showed the results of MRD curves randomization as $\sigma_{\ln(AF)}\big|_{MRD}$ (Figure 3.17). For low-intensity motions, the contribution of MRD curves uncertainty is only significant (i.e., larger than about 0.15 in natural log units) for periods slightly higher than 0.1 s. As expected, the effects of MRD curves uncertainty increase for larger strains and strong nonlinear behavior and are highly site-dependent.

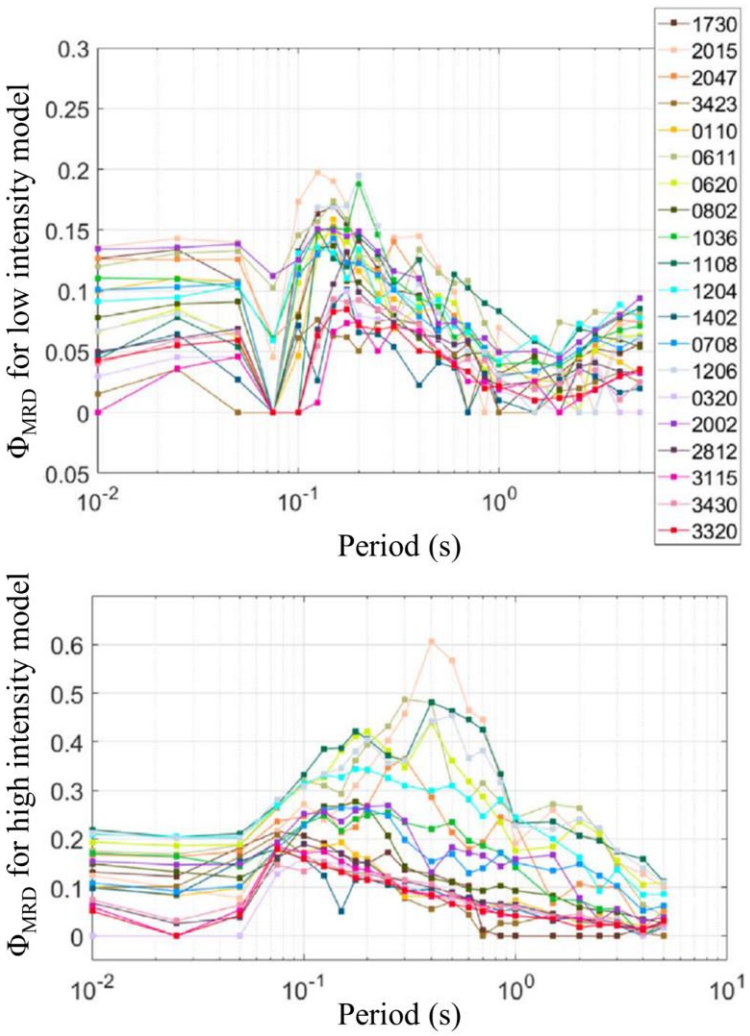

Figure 3.17. MRD curves influence resulted after the stochastic study conducted by Bahrampouri et al. (2018) at the Groningen gas field.

Rathje et al. (2010), Li & Asimaki (2010), Rodriguez-Marek et al. (2014), and Bahrampouri et al. (2018) provided multiple reasons to incorporate soil property variability in seismic ground response analyses rigorously identifying and managing EUs and AVs. In particular, all of them used statistical models for the randomization of the input parameters, including the Toro (1995) model for V_S and the Darendeli (2001) model for MRD curves.

Besides the EU and AV due to input parameters, a specific focus on the EU due to the nonlinear adopted approach is given in Régnier et al. (2016a) and Régnier et al. (2018). The increasing spread of nonlinear approaches led the authors to a systematic assessment of the most common GRA nonlinear codes performance. In Régnier et al. (2018), 19 teams utilizing 23 different codes took part in the international project PRENOLIN. They provided a rigorous estimation of code-to-code variability for two real sites in Japan (i.e., Sendai and KSRH10), where in-hole measurements were available (i.e., no influence of the input). The authors found a variability ranging from 0.05 to 0.25 in $\log_{10}$ units (an average of 0.1 is proposed). This indicates a quite considerable influence of the numerical methods

on site-effect assessment and more generally on the seismic hazard. The level of epistemic uncertainties was found to be also dependent on the site characteristics (i.e., shallow or deep deposits) and the quality of the experimental measurements, especially for V_S profiles and MRD curves (Figure 3.18).

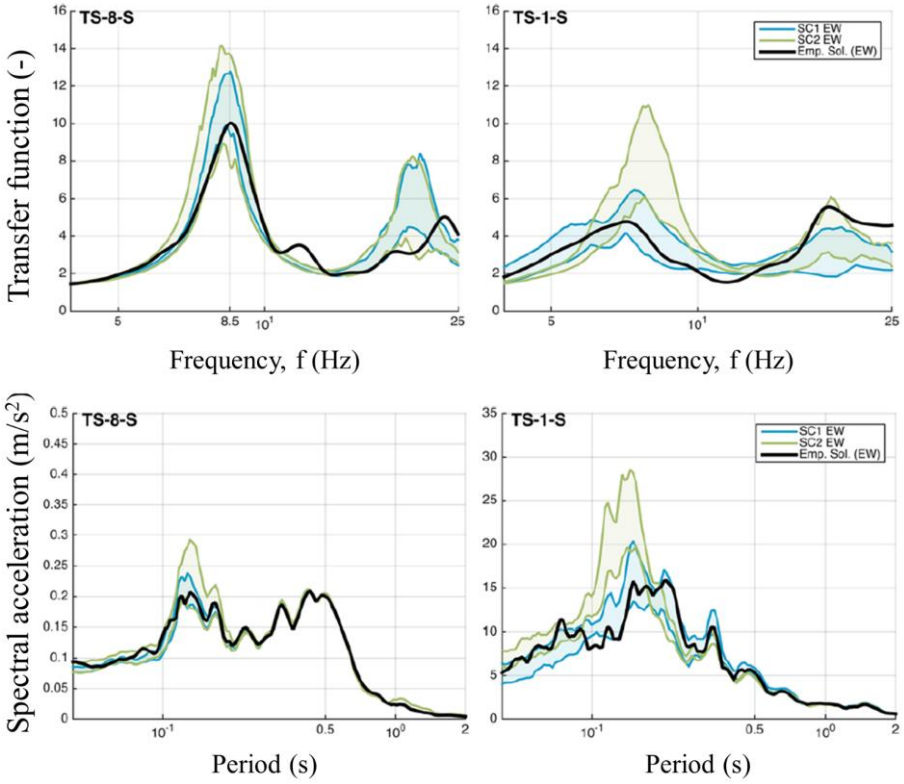

Figure 3.18. Comparisons of obtained results from the different NL codes at Sendai with the experimentally-measured solution (after Régnier et al. (2018)).

Due to the lack of a large number of specific studies, the assessment of the influence of uncertainties and variabilities in shear strength and small strain damping ratio are not widely discussed. However, particular attention should also be paid to these two sources of uncertainty when a GRA is performed. For this reason, few examples are reported in the next paragraphs.

In this context, Zalachoris & Rathje (2015) demonstrated that the inclusion of the material shear strength in GRAs leads to more accurate results, compared to DH-arrays records. They adopted the formulation by Hashash et al. (2010), Yee et al. (2013). In particular, both EQL and NL analyses better reproduced the measured motions, for all investigated periods. Later, Aaqib et al. (2018) showed the results of their quadratic/hyperbolic model for 15 sites, showing period-dependent differences regarding RS and induced shear strains.

The epistemic uncertainties in D_{min} lead to an underestimation of the motion and more considerable variability of the results. This is more evident for low periods (lower than the site elastic or inelastic period) and high-intensity inputs (Papaspiliou et al. 2012b, Papaspiliou et al. 2012a, Kaklamanos et al. 2015, Zalachoris & Rathje 2015) when the frequency-dependent Rayleigh formulation is implemented. For small strain responses, the small strain damping from laboratory

curves should be increased according to the wave scattering (i.e., energy loss) processes at the field scale (Zalachoris & Rathje 2015). Generally, the EU and AV of the small strain damping are likely responsible for the biases in the evaluation of the resulted uncertainties and variabilities (Pehlivan et al. 2016). An interesting calibration of D_{min} is presented in Zalachoris & Rathje (2015) for nine sites in Japan. They calibrated the small strain damping for the viscoelastic behavior and compared ETFs to TTFs (Figure 3.19), remarking the importance of this input parameter in the simulation of the physical phenomenon.

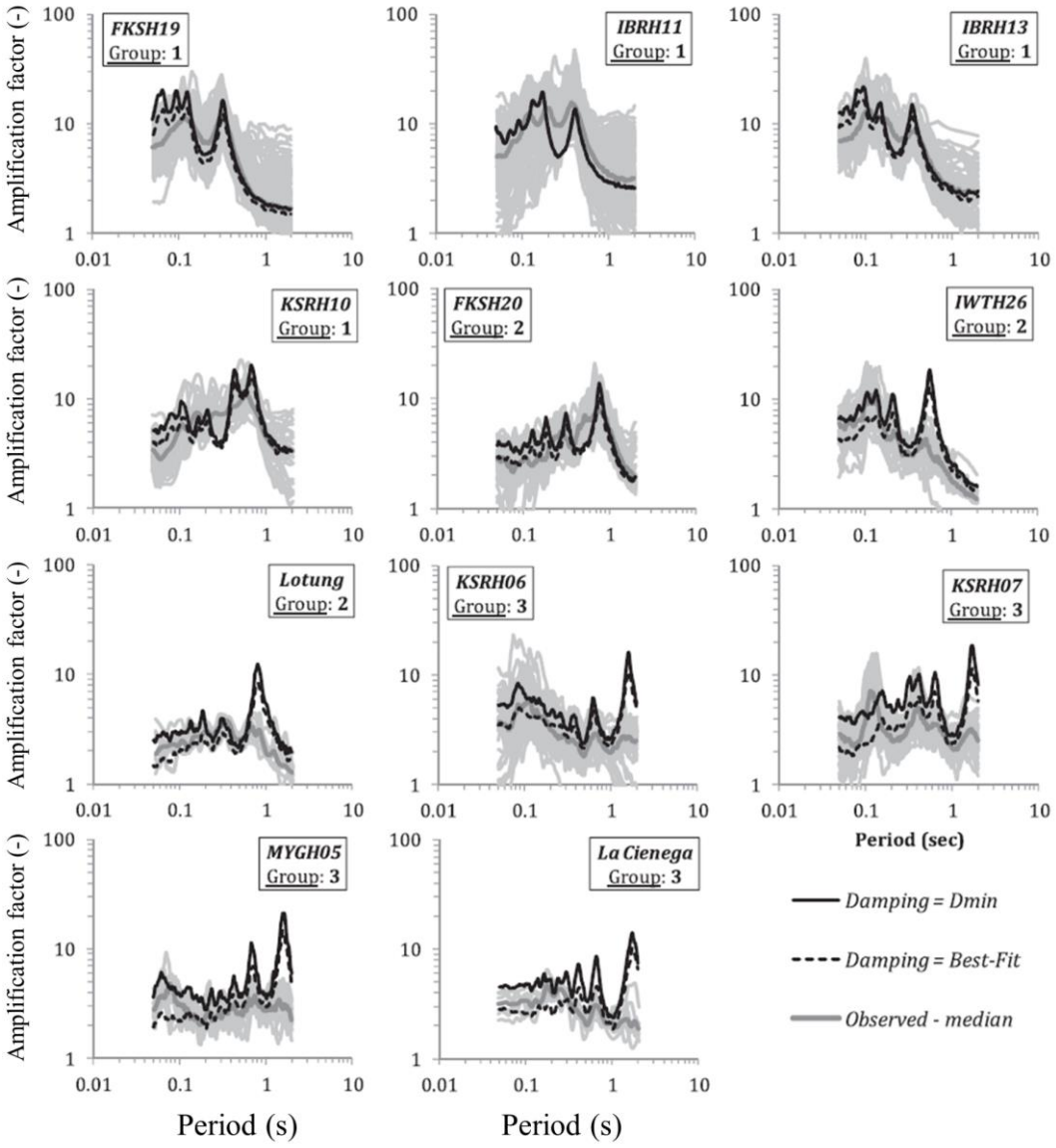

Figure 3.19. Small strain damping calibration and TTF-ETF comparison (after Zalachoris & Rathje (2015)).

In the following sections, a further literature review will be presented for each of the four main parameters/approaches (Rathje et al. 2010), then listed in Table 3.2. As already discussed, EUs and AVs propagated from V_S profiles will be only briefly discussed for completeness in Section 3.2.1, as an extensive analysis is provided in Chapter 4.

3.2.1 V_S profile

Kwok et al. (2008) demonstrated that the more substantial contribution to the total variability is due to the V_S profiles for low periods. They observed that the introduction of the V_S variability in the analyses produces responses in line with the experimental evidence by DH arrays.

Rathje et al. (2010) and Field & Jacob (1993) demonstrated that the V_S profile and the MRD curves are the most relevant input parameters. Rathje et al. (2010) studied two sites in California with 600 MC GRAs. They also focused their attention on randomized soft, shallow layers that are tremendously dangerous for the results of the analyses. In particular, an uncontrolled stiffness reduction of these layers can lead to unconservative results due to overdamping of the response. In this regards, consistent correlation coefficients should be used, along with a logic tree approach and an independent engineering judgment.

Li & Asimaki (2010) showed the high influence of the EUs and AVs in V_S for sites with strong impedance contrasts. However, they did not find a strong dependency on the result variabilities on the frequency content of the input motions.

Baise et al. (2011) proposed a class of their taxonomic approaches, where the GRA responses were due to inaccuracies in V_S profiles. They showed that the adoption of consistent V_S profiles provides an agreement between ETF and TTD for weak motions.

Pehlivan et al. (2016) investigated the influence of V_S profile aleatory variability randomizing a base case profile, looking at the effects on the surface hazard curve obtained by the Bazzurro & Cornell (2004b) convolution method. They performed different GRAs with increasing values of V_S variability. The increased variability on V_S produced a stronger prediction for low exceedance probabilities, which are typical for critical facilities. In general, the results showed a lower amplification, but an increased variability of the amplification function, which leads to higher predictions in general. In their study, they stated that the high level of V_S randomization is likely the primary cause of the overestimation of uncertainties and variabilities at low periods.

Note that the discussion about the influence of V_S profiles on the results of GRAs will be enlarged in the dedicated Chapter 4. This section condenses an initial literature overview of the problem that is the main topic of the entire dissertation. For this reason, the next Chapter will provide a more exhaustive picture of the topic.

3.2.2 Modulus reduction and damping (MRD) curves

Rathje et al. (2010) and Field & Jacob (1993) demonstrated that the MRD curves along with the V_S profile are the most relevant input parameters for GRAs. Li & Asimaki (2010) illustrated the considerable influence of the MRD curves, especially for very soft profiles. Papaspiliou et al. (2012b) showed that the influence of the empirical model adopted for the simulations dramatically increases for strong input motions.

Kaklamanos et al. (2013a) and Kaklamanos et al. (2015) found a low performance of the Darendeli formulation in reproducing the surface motion at six sites of the Kik-Net DH-array network. The Darendeli model showed an overestimation of the damping for large strains, then an underprediction of the motion, even if the analyses did not exceed the 0.3% (i.e., suggested an experimental limit for this model). A possible reason for this inaccurate performance of the Darendeli model can be its large number of model parameters. Similarly, the excellent performance obtained by the Zhang et al. (2005), Zhang et al. (2008) models can be due to the introduction of the parameter that accounts for the age of the deposit.

Faccioli et al. (2015) showed that, for the specific site of Mirandola (Italy), the most influent EU was due to different choices in the MRD curves. In their results, the influence of the choice of the MRD curves is even more significant than the nonlinear approach adopted (i.e., EL, EQL, or NL), especially for long return periods.

Pagliaroli et al. (2015) showed the second-order importance of the EU and AV in the MRD curves. They stated that, for low seismicity areas (i.e., Rome), the induced nonlinearity is not enough to show an apparent influence of the MRD curves randomization.

Régnier et al. (2016a) and Régnier et al. (2018) showed that the analyst should make an accurate choice of the literature formulations and compare them to the specific experimental results. The goodness of empirical or experimental data depends on the case study.

Bahrampouri et al. (2018) systematically show that the MRD curves randomization is strongly dependent on the site and the input motion intensity. The logarithmic standard deviation of the computed amplification function increases for soft soil and strong input motions.

3.2.3 Input motion selection

The significant finding of Bazzurro & Cornell (2004a) is the assessment of the main influencing parameters for the mean amplification function. They found that the most influencing parameter is the spectral acceleration of the input motion. Bazzurro & Cornell (2004a) also studied the effect of the number of input motions on the stability of the solution, suggesting ten input motions for estimation within 10% of the variability.

Also, Rathje et al. (2010) systematically investigated the influence of the number of input motions to obtain a sufficient fit with the mean reference spectrum and its standard deviation. They proposed a minimum number of 10 input motions that also assures a stable statistical response after analyzing the results of 15 classes and 175 input motions.

A different approach was proposed in Li & Asimaki (2010), where the authors used the stochastic method to generate a large sample of inputs with a broad range of characteristics (e.g., M and distances).

Faccioli et al. (2015) used an iterative procedure in the frequency domain to scale a set of carefully selected real records to the target UHS on exposed bedrock at Mirandola (Italy). They propose an efficient method for preserving the physical nature of the records and, at the same time, for avoiding double counting of aleatory variability. In particular, the authors first carefully selected real records approaching as closely as possible the target spectrum in a broadband periods range. Then, they suggested to iteratively scaling the amplitude of such records in the frequency range, with no phase change, to closely match the target spectrum.

Pehlivan et al. (2016) found no significant differences using recorded input motions or adopting the Random Vibration Theory (RVT). In their study, they investigated the motion-to-motion variability adopting 130 recorded inputs and 19 RVT inputs. It is important to remark that, in case of RVT, the obtained variability of the response cannot be introduced in the convolution (Bazzurro & Cornell 2004b), as they are not representing a real record-to-record variability.

In Aristizabal et al. (2018), the use of synthetic simulations calibrated with real data is highly recommended. They stated that synthetic simulations allow a better understanding and accounting for the variability of the physical phenomenon. In most cases, this achievement is presently not possible with real data because of their scarcity at high acceleration levels.

3.2.4 Nonlinear approach

Hartzell et al. (2004) proposed one of the first studies for the investigation of EU due to the nonlinear approach adopted. They used EQL, EQL-FD, and NL (both for total and effective stresses) models for five synthetic profiles from the NEHRP provisions and wide ranges of PGAs. As expected by the authors, for stiffer conditions no significant differences existed between the models. Then, as the average stiffness of the deposit decrease, the EQL models start to deviate from the NL predictions. They recommended the use of NL models for soft deposits and strong input motions.

Andrade and Borja (2006) adopted a simple, but efficient, approach imposing the same parameters variability to an EQL and an NL code and analyzing the dispersion of the results regarding Arias intensity. They proposed an MC randomization for V_S and the MRD curves of 500 or 300 samples and plotted the obtained variabilities regarding experimental probability functions. Their results illustrate that the resulted variability from EQL and NL GRAs is similar.

Stewart and Kwok (2008) and Kwok et al. (2008) proposed rigorous protocols for the NL codes usage and verification against DH-arrays records. They found that EQL methods tend to over-damp the small periods range (i.e., lower than the natural period) more than NL approaches, that also show this limitation. Particularly in Kwok et al. (2008) substantial differences of the goodness of prediction depending on the model fundamental period are shown. For higher nonlinear responses, however, the fundamental shifted period should be addressed as an index. Moreover, Stewart and Kwok (2008) and Kwok et al. (2008) also found a more considerable variability of the results close to the site period, especially for EQL

analyses and sites with strong impedance contrasts. Then, the variability usually drops at higher periods, together with increased global accuracy of the GRA.

A systematic and rigorous treatment of the topic is discussed in Asimaki et al. (2008) and Asimaki & Li (2012). They showed parameters that a-priori suggest a strong nonlinearity response by the soil deposit. In particular, they found two controlling parameters of the site and two parameters of the input. The site parameters that mostly control the nonlinear response of the deposit are $V_{S,30}$ and the amplification at the first resonant peak (Amp). The input parameters that mostly control the nonlinear response of the deposit are the PGA of the input motion at the bedrock and the Frequency Index (FI) (Figure 3.20). Following the controlling parameters, they showed that an increasing computational effort in the GRAs is needed moving from EL to EQL and NL approaches that always provide the better estimation of the response (Asimaki et al. 2008). This increasing complexity reduces the amount of EU introduced into the solution by different nonlinear approaches.

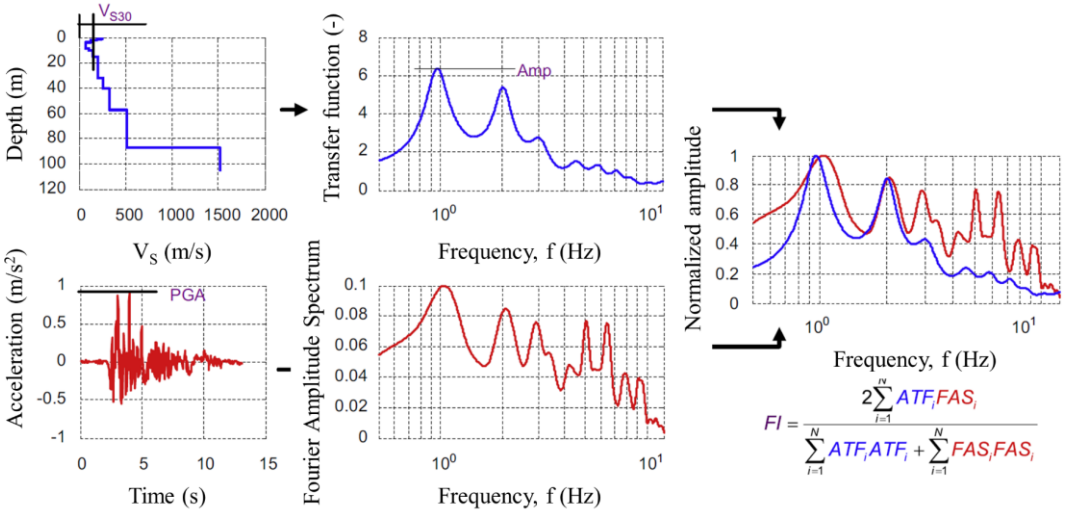

Figure 3.20. Illustration of the Frequency Index proposed by Asimaki & Li (2012).

The same dependency of the result variabilities on the period was identified by Li & Asimaki (2010). They also associated the drop at high periods with a dominant influence of the source and path EU and AV in the results. This is consistent also with the propagated wavelengths, which are longer than the site scale for very high periods.

Rathje & Kottke (2011) identified epistemic differences between EQL and NL results for two case studies. The authors showed disagreements for frequencies higher than 25 Hz, between 5 Hz and 25 Hz, and at the resonance frequency of the deposit. For high frequencies, less amplification is produced by NL models due to the incoherence of the phase in the ground motions introduced by the nonlinear response. For intermediate frequencies, the opposite is observed, likely due to an over-damped EQL response. At resonance conditions, the NL models showed a reduced amplification mainly due to the continuous change of soil stiffness in the NL response.

Baise et al. (2011) showed that nonlinear approaches are necessary for high strains and low periods, especially for soft deposits, where EL analyses show a consistent overestimation of the motion.

Another example of an analysis of the influence of the adopted nonlinear approach on GRA results in given in Thompson et al. (2012) and Kaklamanos et al. (2013b). The authors systematically investigated the critical parameters affecting bias and variability using 100 Kik-Net DH-array data, thanks to the availability of a large number of high-quality surface/downhole records. They demonstrated that the most influencing parameters on the result are the maximum induced shear strain γ_{max}, the input motion Peak Ground Acceleration (PGA), and the predominant input motion period. Depending on the characteristics of the analyses, an initial evaluation of the uncertainties in the results can be obtained by using the following charts in Figure 3.21.

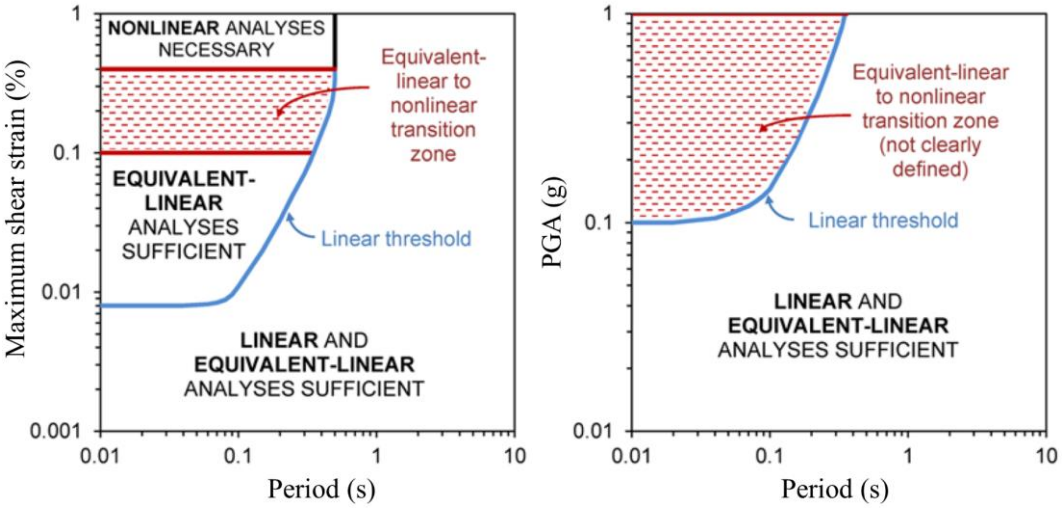

Figure 3.21. Guidance thresholds for the nonlinear approaches applicability (after Kaklamanos et al. (2013b)).

Moreover, Thompson et al. (2012) and Kaklamanos et al. (2013b) observed a systematic underestimation of the motion for low periods (i.e., short wavelengths) by both EL and EQL analyses. In their opinion, this result is due to the time-invariant assumptions of G and D at convergence during the entire analysis. In particular, the converged values are associated with the low frequencies, and they are usually overestimated for high frequencies, showing a typical flatness in the response spectrum.

Kaklamanos et al. (2013a) and Kaklamanos et al. (2015) used 6 of the 100 sites in the previous study that showed clear 1D responses (Baise et al. 2011), also performing NL analyses using DEEPSOIL (Hashash et al. 2015) and ABAQUS (Hibbett et al. 1998). They still found an overprediction of the motion obtained by the EL analyses for $\gamma > 0.01\%$ and low periods. An underestimation of the motion is showed for low periods, for both EQL and NL analyses, even though the ABAQUS model performed better. For periods around the system period, they found a great advancement of EQL and NL analyses over EL, even if still larger biases are detected at resonance, which disappear for long periods. These periods

are, in fact, associated with a long wavelength that does not detect the thin surface layers, mainly responsible for the site nonlinear amplification. Contrarily, for small periods and limited wavelengths, the influence of thin layers with strong impedance contrasts and the wave scattering phenomenon control the site response.

An extension of the work by Asimaki et al. (2008) and Asimaki & Li (2012) can be found in Kim et al. (2013a). The goal is the analysis of the applicability boundaries between EQL and NL analyses, estimating the EU introduced in the results. As discussed in Asimaki et al. (2008) and Asimaki & Li (2012) they want to suggest a priori criteria for avoiding large EUs by EQL analyses. Differently from Kaklamanos et al. (2013b), they want to predict the introduced uncertainty before performing the analyses (i.e., a criterion not based on strain ranges). They found the usual inaccuracy depending on both the site and input characteristics, in parallel. In particular, a new parameter is suggested and calculated as:

$$\gamma_{est} = \frac{PGV_{input}}{V_{S,30}} \qquad \text{(Eq. 3.4)}$$

Accordingly with the performed analyses, they proposed a new chart (Figure 3.22) to a-priori guide the choice of the nonlinear approach and to eventually limit the introduced uncertainties. This chart is defined assuming a 10, 20, and 30% of differences between EQL and NL analyses.

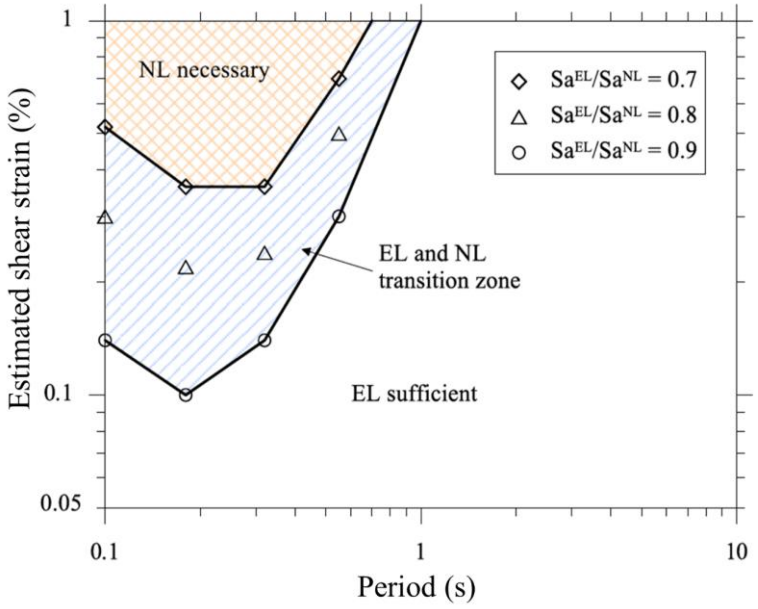

Figure 3.22. Guidance thresholds for the nonlinear approaches applicability (after Kim et al. (2013a)).

Zalachoris & Rathje (2015) intensely studied the epistemic uncertainties in the results of a GRA evaluating EQL, EQL-FD, and NL simulations. They initially showed good consistency in the results for small values of PGAs. Then, when the PGA increases, a different frequency-dependent response is observed by the three approaches. However, one input motion measure (i.e., PGA) is not enough to predict the nonlinear response of a deposit, which depends necessarily on material

characteristics. They adopted the maximum shear strain as an index, illustrating a different response for $\gamma > 0.1\%$ at low periods. In particular, both EQL and NL analyses showed an underestimation of the motion for high frequencies. This is due to high-converged damping values (EQL) and viscous damping formulations (NL). The results obtained using EQL-FD become inaccurate for smaller strain levels ad across a wider range of periods. As the EUs on the results are largely dependent on induced strains and frequencies, they also proposed contour plots, as presented in Kaklamanos et al. (2013b) and Kim et al. (2013a) (Figure 3.23).

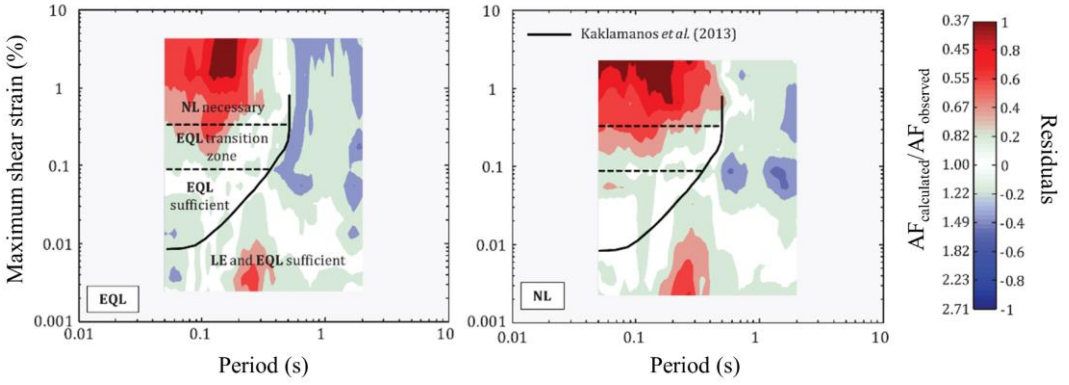

Figure 3.23. Guidance thresholds for the nonlinear approaches applicability (after Zalachoris & Rathje (2015)).

Kim et al. (2016) published likely the last and most comprehensive study on the topic. Their primary goal was to expand the 2013 study, showing new and the last results of their research on the relative differences between NL and EQL GRAs. They proposed this study to investigate the conditions under which the two methods produce consistent and divergent estimates of the site amplification. Differently from 2013, they used recorded input motions representative of two central US regions. Then, they introduced the influence of the shear strength in the simulations and proposed their regressions based on Fourier spectra, instead of RS. The central question is still the same as in 2013: *"can we a priori predict the effectiveness and goodness of EQL, compared to NL approaches?"*. For this purpose, they selected 145+176 input motions for 24+18 sites and 13296 GRAs. In the paper, they were looking for the most influent parameter that could predict the divergence between the EQL and NL results. In particular, they investigated five main parameters, some of the input motions, some of the site. At the end of the study, they found a strong relationship with:

$$\gamma_{est} = \frac{PGV_{input}}{V_{S,30}} \qquad \text{(Eq. 3.5)}$$

that is a potentially very useful parameter, as it can be a priori computed.

This parameter, however, should be studied in combination with the frequency. As primarily discussed, in fact, the EQL analyses often showed biases for high frequencies, whereas for low frequencies the 1D approach could be not very efficient. They proposed the following relation for a 20% relative difference between EQL and NL (Figure 3.24):

$$\gamma_{est} = 0.09 f^{-0.08} \qquad \text{(Eq. 3.6)}$$

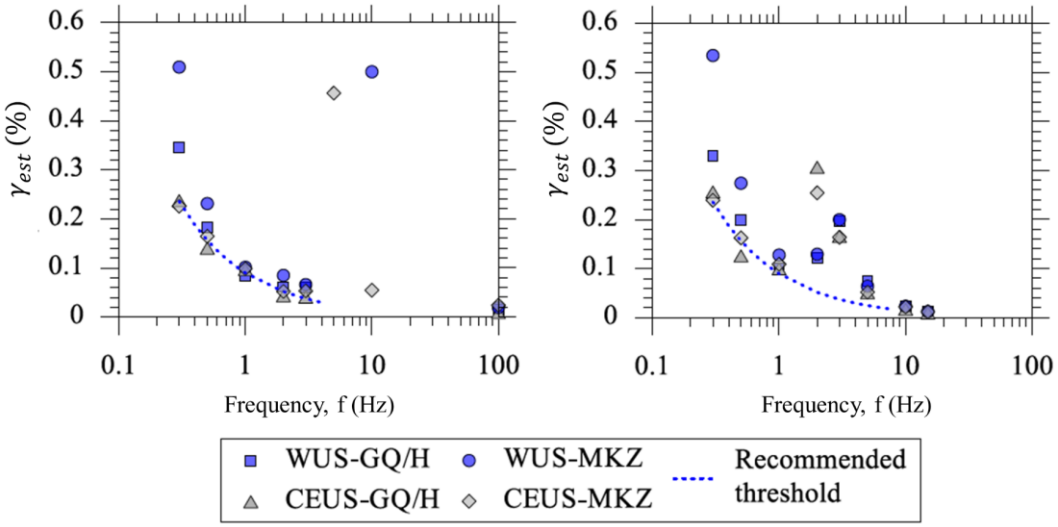

Figure 3.24. Estimated shear strains interpolation illustrated in Kim et al. (2016).

If the user is interested in relative differences of also 10-30%, the authors proposed a final comparison with the other studies about the same topic (Figure 3.25).

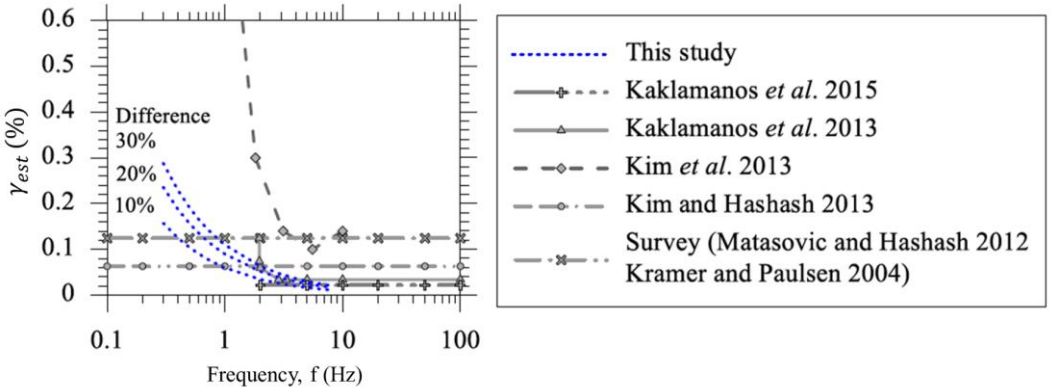

Figure 3.25. Final comparison of suggested applicability thresholds in various studies (after Kim et al. (2016)).

The leading causes of high, frequency-dependent, relative differences between EQL and NL can be due to time-invariant parameters (because of the SSR assumption) and/or overdamping of the EQL analyses. However, their last comparison showed that the γ_{est} can be a very useful a-priori index for an initial engineering judgment.

Another study that investigated the EUs introduced by the nonlinear model chosen is given by Aristizabal et al. (2018). The authors investigated the case of the Euroseistest site in Greece, comparing the results from 21806 synthetic rock motions regarding surface hazard curves computed with two different methods. The site shows a very soft behavior, and then a strong nonlinear response was expected

by the simulations. Besides the differences between the hazard assessment method, the epistemic uncertainties introduced by the adoption of an EQL or an NL approach were predominant, even for PGAs less than 0.1 g. For these intensities, also a good comparison with recorded motion is obtained by using both approaches (Figure 3.26).

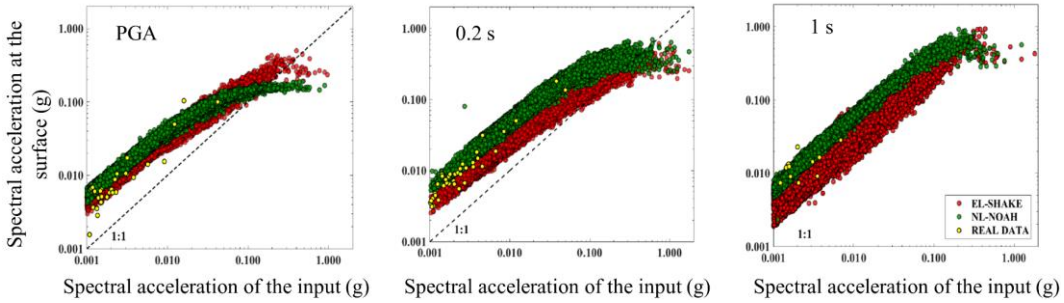

Figure 3.26. Analysis of the GRAs accuracies obtained by different NL approaches (after Aristizabal et al. (2018)).

A systematic assessment of the code-to-code uncertainties introduced in NL GRAs is proposed in Régnier et al. (2018). They firstly computed the logarithmic standard deviation due to this contribution of EUs. The average, almost period-independent, proposed value is 0.1 for the logarithmic standard deviation.

3.2.5 Summary

Table 3.2 presents the primary studies that are summarized in this dissertation and that evaluated the influence of EUs and AVs in GRAs. In particular, the references are given along with the NL approach adopted in the analyses, the number of investigated sites and the availability of in-hole records (no influence of the input motion selection). Moreover, the same studies are listed concerning the type of EU and AV studied in GRAs (cells filled in black). Note (once more) that a precise distinction between EUs and AVs is not always presented, as it appears often not feasible from a practical point of view. Most of the proposed literature examples only studied the effects of the single source of generic uncertainty on the final result, without separating the two major contributes (i.e., EU and AV).

Table 3.2. List of most studies regarding the evaluation of the influence of epistemic uncertainties and aleatory variabilities in Ground Response Analyses.

Reference	Nonlinear approach	# sites	Available records	V_S profiles	MRD curves	Nonlinear approach	Input motions selection
Field & Jacob (1993)	LE	1	Bottom-Surface	■			
Bazzurro & Cornell (2004a)	NL (SUMDES)	2	-	■	■		■
Hartzell et al. (2004)	EQL, EQL (FD), and NL (NOAHW and NOAHB)	5	-			■	■
Andrade & Borja (2006)	EQL and NL (SPECTRA)	3	Bottom-Surface	■	■	■	
Stewart & Kwok (2008)	EQL and NL (D_MOD_2, DEEPSOIL, OpenSees, SUMDES, TESS)	4	Bottom-Surface	■	■	■	
Kwok et al. (2008)	EQL and NL (D_MOD_2, DEEPSOIL, OpenSees, SUMDES, TESS)	1	Bottom-Surface	■	■	■	
Rathje et al. (2010)	EQL	1	-	■	■		■
Li & Asimaki (2010)	NL	3	Bottom-Surface	■	■		■
Rathje & Kottke (2011)	EQL and NL (DEEPSOIL)	2	-			■	■
Baise et al. (2011)	EQL and NL (DEEPSOIL)	74	Bottom-Surface	■	■	■	
Papaspiliou et al. (2012b), Papaspiliou et al. (2012a)	EQL and NL (DMOD2000 and DEEPSOIL)	2	-		■	■	■
Asimaki et al. (2008) and Asimaki & Li (2012)	LE, EQL, and NL	24	Bottom-Surface			■	■
Thompson et al. (2012) and Kaklamanos et al. (2013b)	LE, EQL	100	Bottom-Surface			■	
Kaklamanos et al. (2013a) and Kaklamanos et al. (2015)	LE, EQL, and NL (DEEPSOIL and ABAQUS)	6	Bottom-Surface		■	■	
Kim et al. (2013a)	EQL and NL	24	-			■	■
Rodriguez-Marek et al. (2014)	EQL	1	-	■	■		■
Zalachoris & Rathje (2015)	EQL, EQL (FD), and NL (DEEPSOIL)	9	Bottom-Surface			■	
Faccioli et al. (2015)	LE, EQL, and NL (DEEPSOIL)	1	-	■	■	■	■
Pehlivan et al. (2016)	EQL	1	-	■			■
Kim et al. (2016)	EQL and NL (DEEPSOIL)	42	-			■	■
Bahrampouri et al. (2018)	EQL	1	-	■	■		■
Aristizabal et al. (2018)	EQL and NL (NL-NOAH)	1	Bottom-Surface			■	■
Makra & Raptakis (2016)	LE	1	-	■			
Pagliaroli et al. (2015)	EQL	1	-	■	■		■
Park & Hashash (2005b)	EQL and NL (DEEPSOIL)	6	-	■	■	■	■
Régnier et al. (2016a) and Régnier et al. (2018)	NL (23 different codes)	2	Bottom-Surface		■	■	

Chapter 4
Shear wave velocity models

This Chapter is devoted to epistemic uncertainties and aleatory variabilities in shear wave velocity models and their influence on the ground response. After the introduction of seismic site investigation objectives and seismic waves, a part of the Chapter will discuss invasive and non-invasive in situ tests. The discussion will account for the identification and quantification of Epistemic Uncertainties (EUs) and Aleatory Variabilities (AVs) from a purely theoretical point of view. Then, the effects of these sources of EU and AV on Ground Response Analysis (GRA) results will be discussed through an extensive literature review. Particular attention will be paid to conventional methods for managing EUs and AVs in V_S profiles as proposed in the literature and technical provisions/guidelines. These methods will be presented along with the typical challenges regarding the separation of the two main contributions to global uncertainty.

4.1 Topic overview

Seismic site investigation methods are a multidisciplinary topic across geotechnical earthquake engineering and geophysics. However, in general, geotechnical engineers are interested in the near-surface characterization of the subsoil, differently from the most common exploration geophysics applications (Foti et al. 2014). Nowadays, near-surface characterization represents a fundamental step for civil engineering projects (Jamiolkowski 2012, Foti & Passeri 2018). The major challenge of this type of investigations regards the lack of an a-priori conservative assumption for soil dynamics applications. Soil dynamics analyses are dependent on a wide range of parameters that are complexly interconnected. Indeed, the analyst cannot assume a "safer" choice in the parameters.

The primary objectives of a seismic site investigation surveys are:

- Determination of subsurface (near-surface) stratigraphy;
- Identification of the groundwater table;
- Development of shear (S) wave interval velocity (V_S) profile and/or compressional (P) wave interval velocity (V_P) profile.

The first point regards the determination of the geometrical characteristics of the subsurface mainly including the thicknesses of the soil layers and the depth to bedrock. However, the conceptual differences between soil and rock materials (i.e., bedrock) are not entirely defined and still represent a critical issue in GRA applications (Table 4.1, Foti et al. (2018)). The seismic bedrock is usually defined by a measured V_S higher than 800 m/s. This value also defines the 'stiff soil class'

($V_{S,30}$ > 800 m/s) in many national and international regulations as NTC (2018) and EC8 (2005). However, the definition of "stiff" is inherently relative. For example, US NEHRP provisions introduced a further classification for materials that show V_S higher than 1500 m/s. There are situations in seismic site characterization where it is impossible to identify a stiff material. In these cases of deep bedrock and/or insufficient resolution of the seismic test, the V_S interval profile ends with a soil-halfspace, instead of bedrock, if a GRA is to be performed (Foti et al. 2009).

Besides the mechanical classification, the bedrock represents the conjunction between the seismic assessment for the reference condition and the site response. Then sources and path effects are usually investigated by seismologists, whereas the site response by geotechnical engineers. For these reasons, the consistency with the reference stiffness condition prescribed in the PSHA should be guaranteed (Passeri et al. 2018a).

The second primary objective of a seismic site investigation is the identification of the water table. This information is fundamental to estimate the saturation degree of the soil and/or rock material in case of effective stress GRAs (or for others applications, e.g., liquefaction hazard assessment). Also, the water table depth indicates a physical boundary that controls the Poisson's ratio (ν) values with depth. In the next sections, the importance of the parameter ν will be illustrated in light of the wave propagation phenomenon.

The third main result of a geophysical survey is the development of interval V_S and V_P profiles. These interval profiles are essential in many geotechnical applications other than site response studies, such as liquefaction analyses (Andrus & Stokoe 2000), settlement calculations, and in-situ void ratio estimates (Foti et al. 2002, Foti & Passeri 2016). They are also directly linked to critical geotechnical properties discussed in the next sections.

However, the profiles of interval velocities are an engineering representation (i.e., schematization) of a more complex variation of the soil and rock properties with depth. The interval velocities are the results of the processing of the geophysical data that fit the need of a GRA. Numerical simulations are typically based on a stratified (i.e., stack of horizontal and parallel layers) subsurface model that, sometimes, should be seen from a different perspective (Comina et al. 2011). For this purpose, an interval velocity profile can be converted in a harmonic average profile defined as:

$$V_{k,z}(z) = \frac{z}{\sum_{i=1}^{n}\left(\frac{d_i}{V_{k,i}}\right)} \qquad \text{(Eq. 4.1)}$$

where k depends on the type of waves, z is the depth, n the number of layers of the interval velocity profile, d_i the thickness of the layer i, and $V_{k,i}$ is the velocity of the layer i. In fact, it is possible to define the shear wave harmonic average profile as

$$V_{S,z}(z) = \frac{z}{\sum_{i=1}^{n}\left(\frac{d_i}{V_{S,i}}\right)} \quad \text{(Eq. 4.2)}$$

moreover, the compressional wave harmonic average profile

$$V_{P,z}(z) = \frac{z}{\sum_{i=1}^{n}\left(\frac{d_i}{V_{P,i}}\right)} \quad \text{(Eq. 4.3)}$$

The harmonic average profile is closer to the real physics of the problem than the interval velocity profile as it is obtained by dividing a length (i.e., depth) by the cumulated travel time defined as

$$tt_{k,z}(z) = \sum_{i=1}^{n}\left(\frac{d_i}{V_{k,i}}\right) \quad \text{(Eq. 4.4)}$$

This last contribution is indeed the time that the wave spends to travel from the depth z to the surface. This approach was first proposed by Boore & Brown (1998) to compare shear wave velocity profiles from inversion of surface wave and down-hole measurements. The authors suggest to evaluate the differences in V_S profiles of six sites in the US by looking at the travel times, instead of the typical visual inspection of the interval velocities. The comparison of the travel times (or, equivalently, the $V_{S,Z}$ profiles) highlights the influence of the shallower layers that typically control the dynamic response of the site at small strains. Indeed, the resonant frequencies and dynamic amplifications (i.e., the transfer functions) of a soil deposit depend on the $V_{S,Z}$ profile. In soil dynamics, the fundamental resonant frequency of a soil deposit can be approximated by the equation (Kramer 1996)

$$f_0 = \frac{V_{S,Z}(z)}{4z} \quad \text{(Eq. 4.5)}$$

where $V_{S,Z}(z)$ is the harmonic average shear wave velocity profile down to the depth z. Further suggestions for the comparison of the results of different seismic tests are given in Brown et al. (2002). In this case, the authors proposed to drop the interval velocities and use the slowness profile (i.e., the inverse of the $V_{S,Z}$ profile) for the comparisons. In the next sections, more advantages of the harmonic average profile will be discussed, particularly for the similarities with the seismic test results.

One of the best-known applications of the harmonic average velocity is for the shear wave velocity profile down to 30 m (100 feet) (Borcherdt 1994, Borcherdt 2012), $V_{S,30}$. This parameter is widely used in national and international regulations for the definition of generic amplification factors for different soil classes (EC8 2005, NTC 2018). Some approaches allow estimating the soil class just from general considerations on the local geology. This procedure, like the ones that estimate $V_{S,30}$ from empirical correlations, is vehemently discouraged for the large approximation introduced in the seismic hazard study of the site (Foti et al. 2011b).

Figure 4.1a shows an example of V_S and V_P interval and harmonic average profiles for the site of Mirandola in the InterPACIFIC project (Garofalo et al. 2016a, Garofalo et al. 2016b, Griffiths et al. 2016a, Passeri et al. 2019). In Figure 4.1b, a zoom on the V_S profile is shown, with an example of $V_{S,30}$.

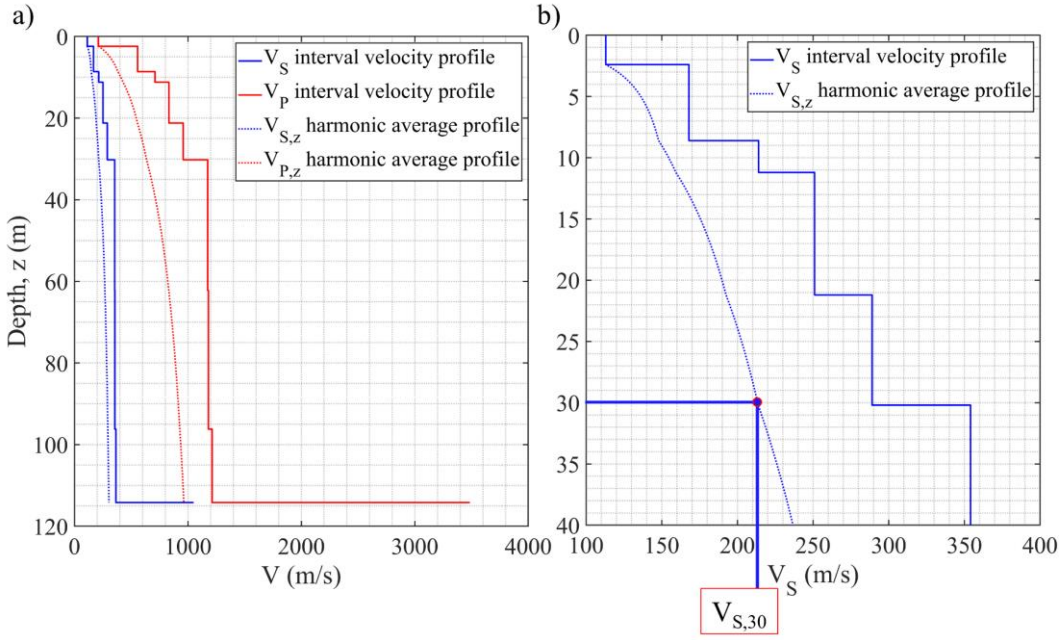

Figure 4.1. a) Example of P and S-wave interval and harmonic average profiles, and b) zoom on the S-wave interval and harmonic average velocity profiles with $V_{S,30}$ for Mirandola (data from Griffiths et al. (2016a)).

The choice to consider the first 30 m does not have a specific scientific reason but derives from an operative choice in the analysis of the amplification phenomena that occurred following the Loma Prieta earthquake in 1989 (Borcherdt 1991). This choice was then translated into a classification criterion adopted by American regulations (Borcherdt 1994, Dobry et al. 2000) and, subsequently, in the EC8 and the NTC 2018 with a modification of the subsoil classes.

However, a single parameter cannot be considered representative of the seismic response of the subsoil, typically characterized by very varied stratigraphic situations and strongly influenced by the characteristics of the seismic input (Boore 2004, Albarello & Gargani 2010). For example, a sensitivity study of the seismic response demonstrates the considerable variability of results with the same values of $V_{S,30}$ (Ciancimino et al. 2018). Other classification systems have been proposed, adopting alternative or additional parameters to $V_{S,30}$. However, these alternative classifications lead to a considerable dispersion of the amplification values within the same subsoil class (Pitilakis et al. 2013).

The non-linearity of soil behavior dramatically influences the local seismic response. Therefore, the use of the small strain stiffness can lead to erroneous predictions. Some regulations propose a variability of the amplification factors according to the intensity of the expected motion at the site. However, these procedures neglect entirely the evidence that the nonlinearity acts in very different ways for different types of soils.

All the target parameters of a seismic site investigation are subjected to a different amount of epistemic uncertainties and aleatory variabilities, mainly depending on both the adopted seismic method and the investigated site test (Foti & Passeri 2018). Therefore, a systematic Identification, Quantification, and Management (IQM) process of EU and AV should be performed in seismic applications. This engineering process should be then introduced in the assessment of the seismic hazard at a site, as discussed in previous Chapters.

Further analysis of the investigation results might distinguish between the reliability and accuracy of the measurements (Foti & Passeri 2018). In general, reliability (i.e., repeatability) is the possibility of obtaining the same result repeating the measure, whereas accuracy represents the ability of a measure to return the true value. The quantification of the latter is particularly complex as the true value is not known. Comparisons between results are inevitably affected by the different nature of the measurement techniques, and it is generally not possible to consider some of the results as the true value. For the geophysical inverse problems, accuracy is usually quantified by using numerical simulations in which the true value of the parameter is known as a priori established for the definition of the reference model. On the other hand, a statistical evaluation of the reliability of experimental data is typically prevented from the difficulty of obtaining a number of such measures to be considered a representative statistical sample.

The primary EUs and AVs associated with the experimental estimates depend on numerous factors, including the:

- Adequacy of the measurement system;
- Validity of the hypotheses used for interpretation;
- Expertise of the operator in the performance of the test and the interpretation of the results.

The last point may seem somewhat trivial, but it is undoubtedly the most difficult to control. Unfortunately, the state of the practice for seismic site investigation is in many cases far from what could be considered an acceptable level. Verification of results obtained in the seismic tests requires excellent attention and sufficient knowledge of the methods.

4.1.1 Seismic waves in elastic solids

Seismic tests allow the evaluation of geotechnical parameters by analyzing the propagation of the seismic waves in the soil. Seismic waves are classified as body waves or surface waves. Body waves travel through the body/interior of the earth, whereas surface waves travel at layer interfaces. Wave propagation theory distinguishes compressional (P) and shear (S) body waves. On the other hand, surface waves are Rayleigh (R), Love (L), Scholte, and Stonely waves. In this dissertation Love, Scholte, and Stonely waves are not considered since their minor relevance for site characterization.

Body waves

P-waves are also termed primary, (constrained) compression, longitudinal, or dilatational waves. They cause volume changes in the interested medium, with an induced particle motion parallel to the wave propagation direction (Figure 4.2a). Primary waves can travel through fluids and solids and take the name because they are faster than the shear waves (i.e., $V_S < V_P$).

On the other hand, S-waves are also called secondary, shear, transverse, or distortion waves. This type of body waves does not induce any volume change in the medium, but a shape (i.e., angular) change. The particle motion is perpendicular to wave propagation direction (Figure 4.2b), and they do not travel in fluids (material with no shear stiffness).

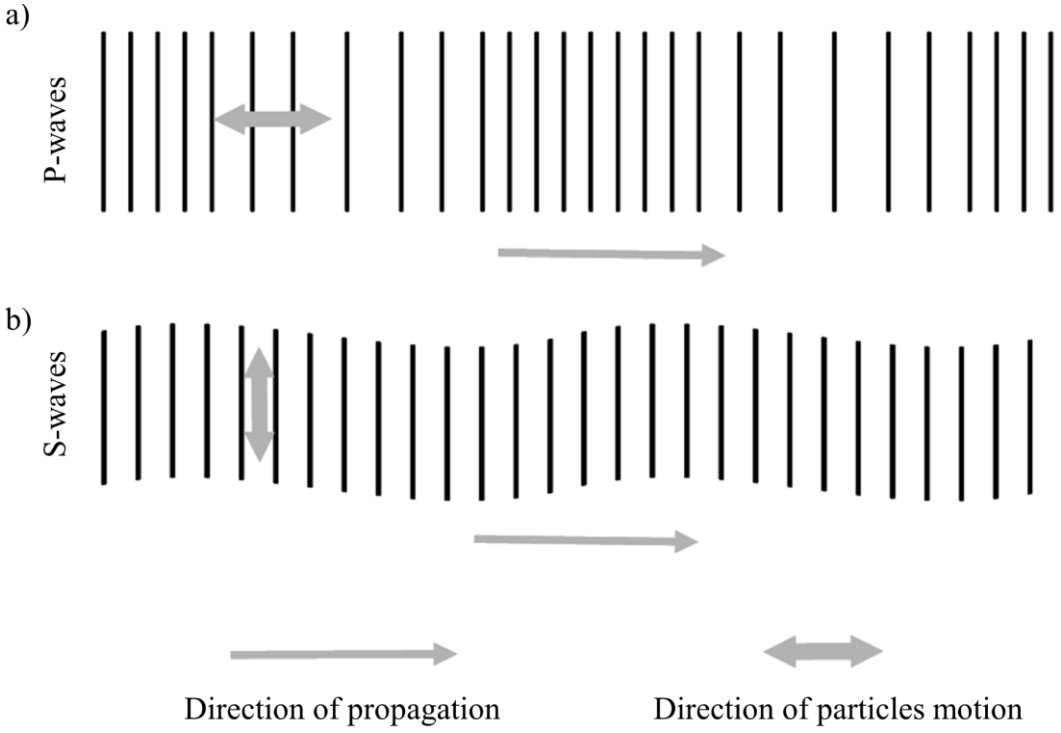

Figure 4.2. Representation of the a) P and b) S-wave propagation in a medium as the direction of propagation and direction of the induced particles motion (after Foti et al. (2014)).

Moreover, shear waves can be decomposed into S_V (i.e., shear on a vertical plane), or S_H (i.e., shear on a horizontal plane) depending on the polarization plane (Figure 4.3).

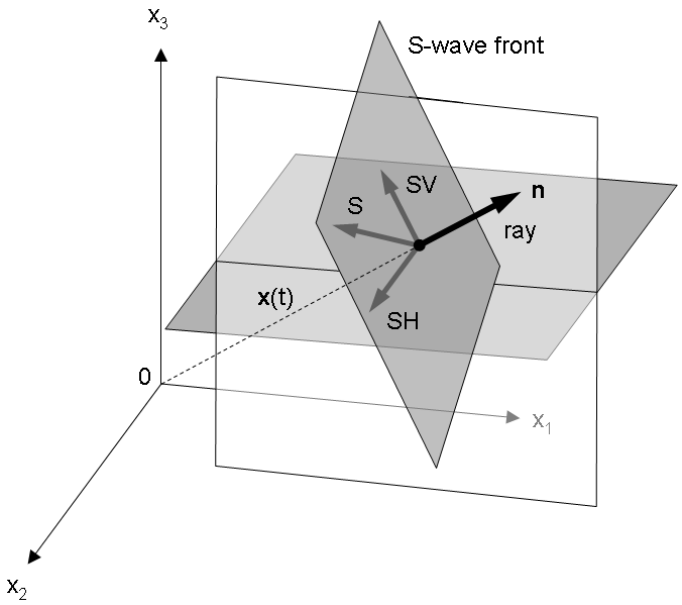

Figure 4.3. Polarization of S-waves in S_V (i.e., shear a vertical plane), and S_H (i.e., shear a horizontal plane) (after Foti et al. (2014)).

A fundamental law that governs the body waves propagation phenomenon was proposed by Snell (i.e., Snell's law also known as Snell–Descartes law or the law of refraction) (Sabra 1981). The Snell's law explains the refraction of waves traveling through different materials. The application of this law is fundamental for the interpretation of seismic tests, as it relates the wave velocity to the incidence angle

$$\frac{\sin a}{V_1} = \frac{\sin b}{V_2} \qquad \text{(Eq. 4.6)}$$

where a is the angle of the incident wave travelling in the medium one and b is the angle of the refracted wave in the medium 2 (Figure 4.4). If a downgoing wave with $V_1 < V_2$ touches the interface with the called "critical angle of incidence"

$$\gamma_{crit} = \sin^{-1}\left(\frac{V_1}{V_2}\right) \rightarrow b = 90° \qquad \text{(Eq. 4.7)}$$

a "critically refracted wave" is generated at the interface, which travels with the velocity V_2. This particular case is important for seismic test applications (e.g., seismic refraction and Cross-Hole tests).

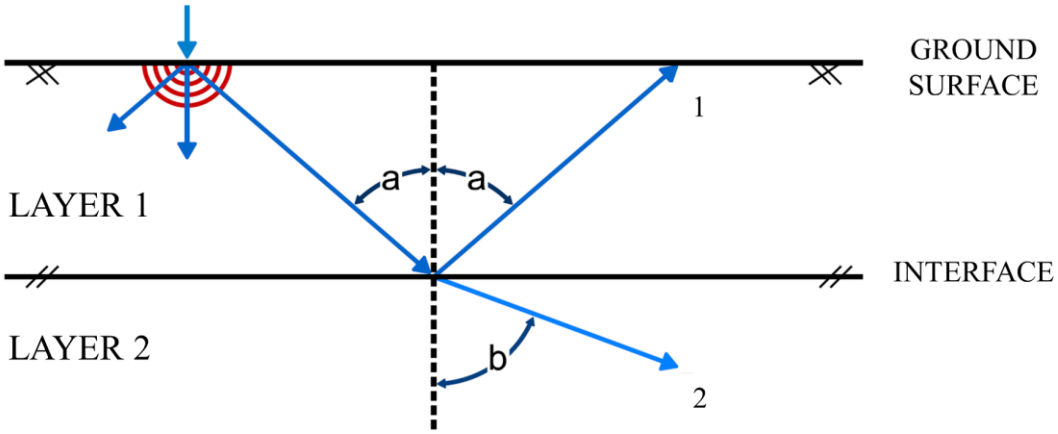

Figure 4.4. Schematization of the wave refraction phenomenon for a double-layers system and a single impinging wave.

Once Snell's law is applied, it is possible to evaluate the partitioning of body waves hitting an interface. As discussed above, primary waves travel faster than secondary waves; then Figure 4.5 shows three different cases of P, S_V, and S_H incident waves. In case of incident P-wave, it is converted in two reflected, and two refracted P and S_V waves (they quadruple every time they hit an interface). In the case of incident S_V-wave, it converts in two reflected, and two refracted S_V and P waves (they quadruple every time they hit an interface). If an S_H is incident, no splitting is observed, and only one reflected S_H and one refracted S_H waves are generated.

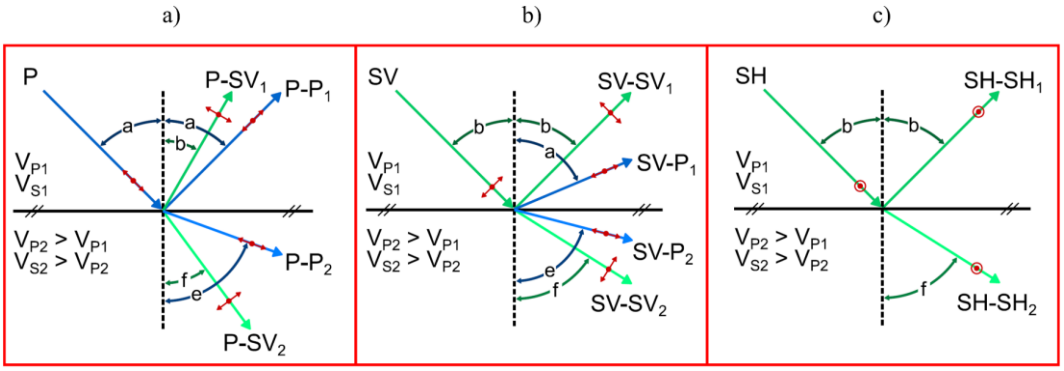

Figure 4.5. Partitioning of waves traveling from a less stiff to a stiffer material. a) Incident P-wave partitioned in a reflected P and an S_V and a refracted P and an S_V waves, b) incident S_V-wave partitioned in a reflected P and an S_V and a refracted P and an S_V waves, and c) incident S_H-wave partitioned in a reflected S_H and a refracted S_H waves (courtesy of Prof. Brady R. Cox).

The impedance ratio (i.e., IR) completes the description of the partitioning of body waves hitting an interface. In particular, one can define

$$IR = \frac{\rho_2 V_2}{\rho_1 V_1} \qquad \text{(Eq. 4.8)}$$

where ρ_2 is the mass density of the refracted wave material, and ρ_1 is the mass density of the incident wave material. The impedance ratio describes how much of the incident wave amplitude is reflected or refracted. If the interface shows high IR, it yields large reflections and small refractions/transmittal for downgoing waves. In this case, it is difficult to irradiate a downgoing wave energy into a stiff material. In case the of low IR, it yields small reflections and large refractions/transmittal; in fact, the amplitude of the refracted wave may be amplified relative to the incident wave. For upgoing waves, this means that the energy/amplitude of the waves coming out of rock into the soft soil can be greatly amplified (i.e., stratigraphic amplification phenomenon).

Surface waves

The surface waves produced at air/solid interface are Rayleigh and Love waves. Scholte and Stonely waves are created at water/solid or solid/solid interface and are not discussed in this dissertation, as their use in near-surface characterization is minimal (e.g., underwater surface wave analysis).

Rayleigh waves were predicted in 1885 by Lord Rayleigh, after whom they were named (Lai & Wilmanski 2007). They are increasingly used in an ample amount of scientific and engineering fields for their non-destructive investigation characteristics (Foti et al. 2014). They are produced by an interaction of P and S_V waves with the ground surface, and they induce an elliptical particle motion (retrograde or prograde depending on the depth) (Figure 4.6a-b).

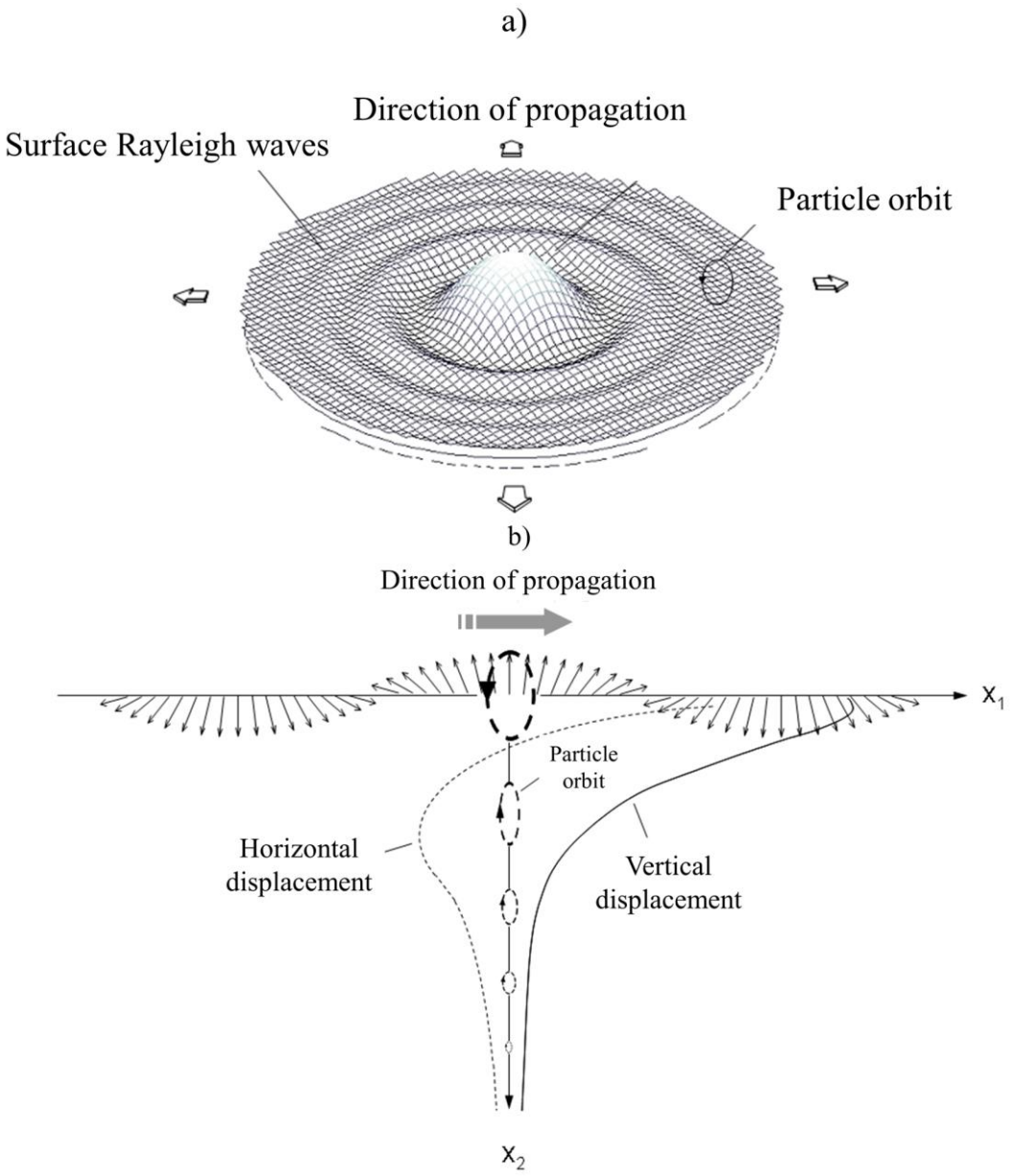

Figure 4.6. a) Rayleigh waves surface wavefield direction of propagation and induced displacement for a point source. b) Particle orbit with depth as a horizontal and vertical component of the displacements (after Foti et al. (2014)).

Love waves are produced by the interaction of S_H waves with the ground surface. They show a particle motion that is perpendicular to the wave propagation direction. Love waves do not exist in homogeneous media. Love wave velocity depends only on how V_S and mass density vary with depth. In this dissertation, the attention will be paid mostly to Rayleigh waves.

The main characteristic of the Rayleigh waves is that their velocity of propagation (V_R) in a vertically non-homogeneous, elastic, and isotropic medium is frequency-dependent. For this reason, Rayleigh waves are subjected to geometrical dispersion (different from the material dispersion that is introduced for visco-elastic models) (Foti 2000). This intrinsic characteristic is exploited for non-destructive surface wave investigations, from materials engineering to exploration

geophysics. The geometrical dispersion is inherently linked to the sampling depth obtained by surface wave methods. Indeed, if the relationship between the frequency f and the wavelength λ

$$V_R = f * \lambda \qquad \text{(Eq. 4.9)}$$

is used, high frequencies correspond to low wavelengths, whereas low frequencies correspond to long wavelengths. The amount of the vertical soil deposit that is sampled by the R waves is then related to the V_R wavelength (Figure 4.7). In vertically heterogeneous media with increasing velocity (both V_S and V_P) with depth, the velocity of propagation of surface waves decreases for increasing frequency (i.e., normally dispersive profiles).

Surface waves can be studied by solving the eigenvalue problem of the Rayleigh secular equation (Socco & Strobbia 2004, Socco et al. 2010). The surface waves propagation is also a multimodal phenomenon in a horizontally layered medium (Aki & Richards 1980). This means that at each frequency (higher than a well-defined cut-off frequency), different modes of vibration exist. Each mode is characterized by its propagation velocity, which always increases from the fundamental to the higher modes (i.e., overtones) (Foti et al. 2018). The existence of higher modes is due to constructive interference phenomena occurring among waves undergoing multiple reflections at the layer interfaces. Although their exact number and frequency cut-offs depend only on the solution of the free vibration problem, the different overtones carry different energy, making them not always detectable with seismic tests.

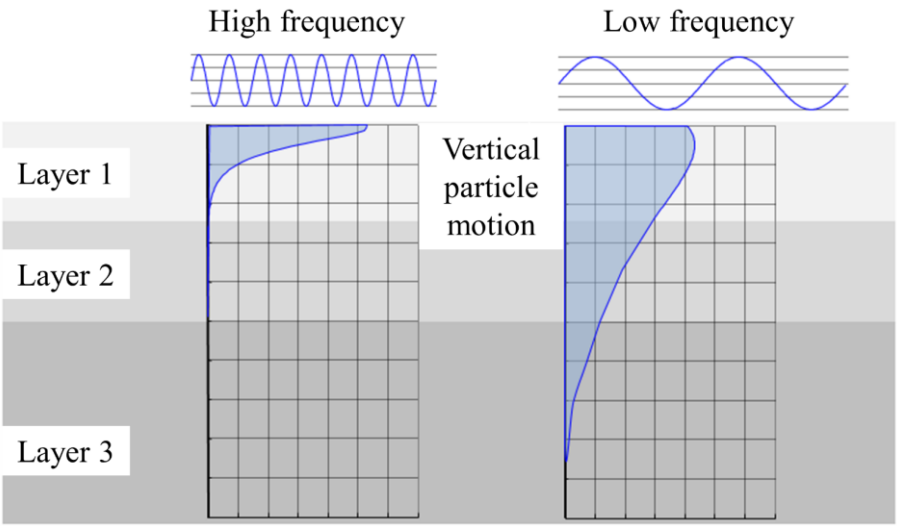

Figure 4.7. Sampled depths by Rayleigh waves with different frequencies for a three-layers system (after Foti et al. (2014)).

4.1.2 Geotechnical parameters associated with seismic waves

Seismic tests are a powerful tool to estimate geotechnical parameters (Foti & Passeri 2018). In principle, the velocity of propagation (V_P, V_S, or V_R) represents

the link between the geophysical and the geotechnical applications. Geotechnical engineers are, indeed, interested in the stress-deformation behavior of the material. In particular, natural materials show their failure for shear stresses, then for Isotropic, Linear-Elastic, and Homogeneous (ILEH) materials we can refer to Figure 4.8a. This Figure shows the physical meaning of the shear modulus G, the shear stress τ, and the shear strain γ. The ILEH model is then based on

$$M_{max} = \frac{1}{m_v} = \rho V_P^2 \qquad \text{(Eq. 4.10)}$$

and

$$G_{max} = \frac{\tau}{\gamma} = \rho V_S^2 \qquad \text{(Eq. 4.11)}$$

where M_{max} is the maximum compression/oedometer (i.e., constrained) modulus, m_v is the coefficient of volume change obtained in a oedometer condition (i.e., lateral strains prevented), and ρ is the mass density (i.e., the unit weight divided by the gravitational acceleration). An important observation regards the linear elastic assumption. For seismic tests performed in situ, the induced shear strains (usually $\gamma < 10^{-3}\%$) are compatible with a linear elastic response of the material (Figure 4.8b). For this reason, seismic tests estimate G_{max} that corresponds to G_{sec} at small strains. Then, G_{sec} decreases at larger strains. The range of strains for which the ratio $\frac{G_{sec}}{G_{max}} < 0.99$ is defined by the elastic threshold γ_{el}. This means that, for GRAs, the V_S interval profile is the parameter that controls the response of the deposit without accounting for the nonlinearity. Shear wave velocities lead the response of the material defining the initial (i.e., zero strains) behavior (Foti et al. 2009).

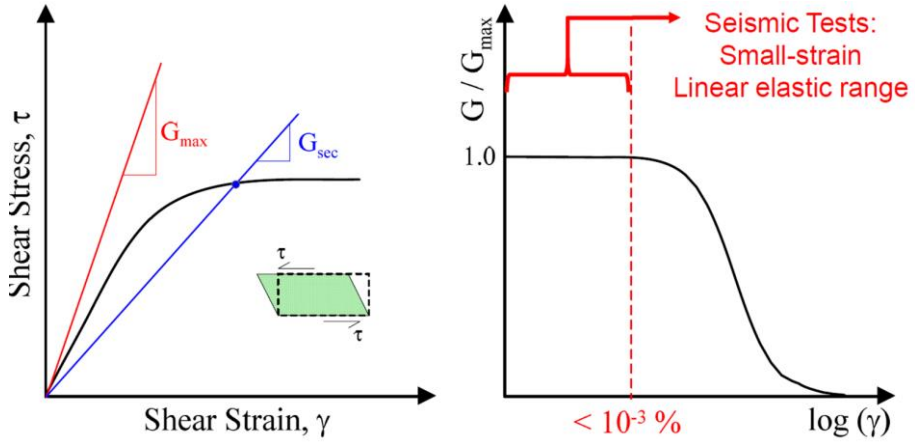

Figure 4.8. a) Maximum shear modulus and secant shear modulus and b) modulus reduction (MR) curve and small-strain linear elastic range investigated by the in situ seismic tests (courtesy of Prof. Brady R. Cox).

A second observation regards the difference between the constrained modulus M and the more common unconstrained (i.e., Young's) modulus E. In that case, the Hooke's law states that

$$E_{max} = \frac{\sigma}{\epsilon} = \rho V_C^2 \qquad \text{(Eq. 4.12)}$$

where σ is the compressive stress, ϵ is the compressive strain, and V_C is termed (unconstrained) compression wave velocity (or rod velocity). This last velocity is measurable in the case of free lateral strains, as in cylindrical specimens. It is possible to demonstrate that the following relations exist between the velocities and moduli

$$M > E > G \qquad \text{(Eq. 4.13)}$$

$$V_P > V_C > V_S \qquad \text{(Eq. 4.14)}$$

The mechanical theory for ILEH materials states that only two parameters are independent in the formulations. The forth other common elastic parameter is the Poisson's ratio. This parameter represents the ratio of the proportional change in a lateral measurement to the proportional change in length. Theoretically, this parameter ranges are

$$0 < \nu < 0.5$$

even if a few innovative materials show a negative value. In particular, a material with a small value of ν (e.g., cork) shows almost no lateral variations, if a load is applied longitudinally. Contrarily, a value close to 0.5 means an infinitely rigid response. For soils, typical values range between 0.25 and 0.33, whereas $\nu = 0.5$ is adopted for saturated/undrained conditions. The relationship between the three propagation velocities described above can be expressed in terms of ν (Richart et al. 1970) as and illustrated in Figure 4.9

$$\frac{V_P}{V_S} = \sqrt{\frac{2(1-\nu)}{1-2\nu}} \qquad \text{(Eq. 4.15)}$$

$$\frac{V_C}{V_S} = \sqrt{2(1+\nu)} \qquad \text{(Eq. 4.16)}$$

$$\frac{V_R}{V_S} = \frac{1.748 + 1.282\nu}{2+\nu} \approx 0.9 \qquad \text{(Eq. 4.17)}$$

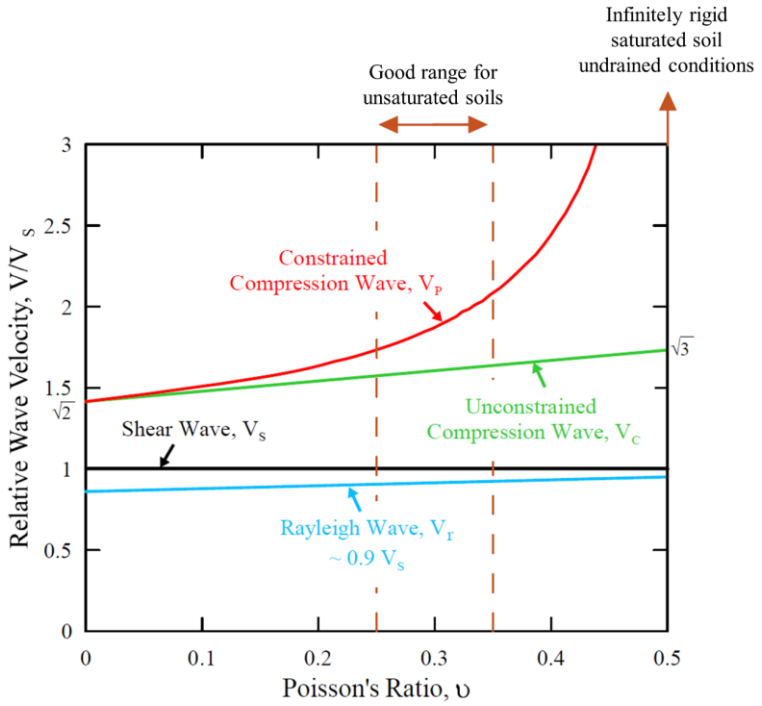

Figure 4.9. Relationships between velocities of propagations in an ILEH material (courtesy of Prof. Brady R. Cox).

From Figure 4.9 it is clear that V_P strongly depends on the degree of saturation (in soils). Indeed, seismic tests in saturated soils measure a velocity always higher than the velocity of propagation in water (i.e., $V_P > V_{P,water} \approx 1500$ m/s). A proof of the dependency of V_P on the degree of saturation is given by Valle-Molina (2006) (Figure 4.10). In this case, the Skempton B-value is used to confirm the extreme sensitivity of the P-wave velocity (measured with piezoelectric transducers) to even small deviations from the full saturation.

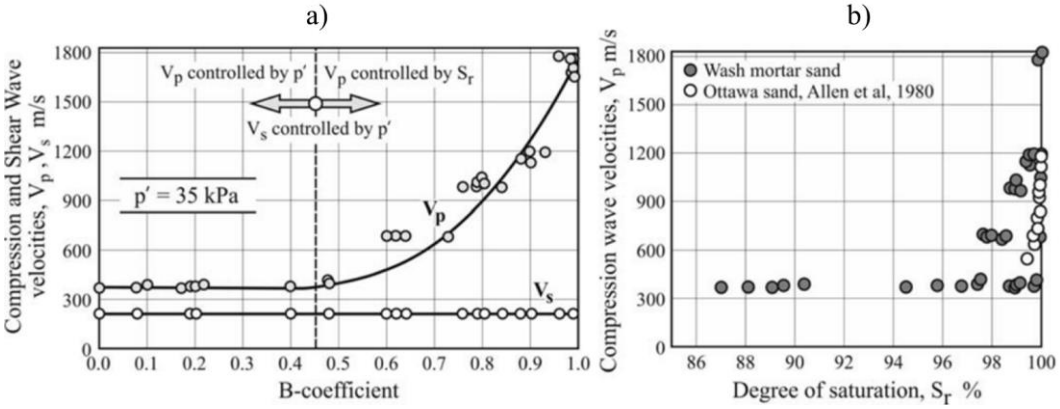

Figure 4.10. V_P dependence on the a) B-value of the material and b) the degree of saturation S_r (after Valle-Molina (2006)).

For example, Jamiolkowski et al. (2009) showed a portion of unsaturated soils detected by Cross-Hole tests in Venice (Figure 4.11). The V_P profile highlights the presence, below the sea bottom, of an unsaturated soil zone, 12 m thick, due to marsh gas.

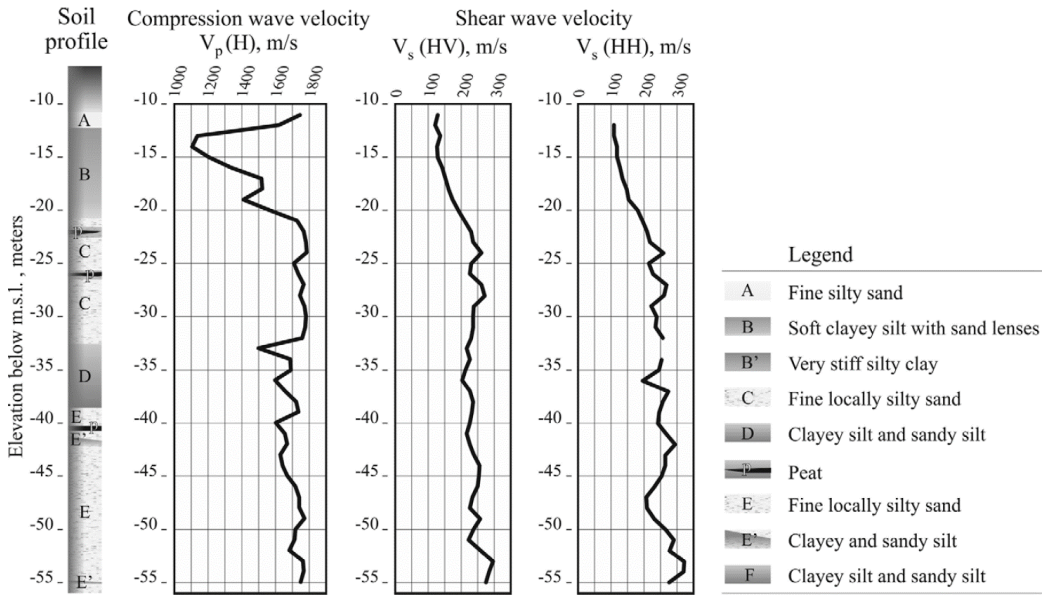

Figure 4.11. Seismic wave velocity profiles estimated in the Venice Lagoon with clear evidence of an unsaturated zone around 12 m (after Jamiolkowski et al. (2009)).

On the other hand, V_S is almost independent of saturation (i.e., ρ becomes ρ_{sat} for saturated conditions). It is mainly controlled by effective stress, density, age, and cementation of the natural material. The influence of the in situ state of stress, in particular, can be evaluated as

$$V_S = V_{S,1atm}\left(\frac{\sigma'_0}{P_a}\right)^n \qquad \text{(Eq. 4.18)}$$

where $V_{S,1atm}$ is the V_S corresponding to an effective mean stress equal to 1 atm, σ'_0 is the mean effective stress, P_a the atmospheric pressure, and n is typically assumed equal to 0.25 for sands.

The shear wave velocity is sometimes associated with SPT (Sykora & Koester 1988, Pitilakis et al. 1999, Brandenberg et al. 2010) and CPT (Mayne & Rix 1995, Hegazy & Mayne 2006, Andrus et al. 2007, Robertson 2009, Robertson 2012, McGann et al. 2015) correlations or with other empirical correlations (Dobry & Vucetic 1987, Wair et al. 2012, Wood et al. 2017). In some regulations, if no seismic tests are available, it is possible to infer a soil class by SPT and CPT results. Many studies showed similar SPT/CPT-V_S trends, but a specific blow count value or tip resistance cannot correspond to a specific V_S value (i.e., no one-to-one relation) (Cox et al. 2018). Also, the induced strains are entirely different. Shear wave velocities are a small-strain measurement, whereas SPT and CPT tests lead the material to failure (Wood et al. 2017). For these reasons, the V_S profile should always be obtained only by high-quality geophysical tests. Every use of empirical correlations is strongly discouraged and represents an uncontrollable source of epistemic uncertainty (EPRI 1993, Lopes et al. 2014, Stewart et al. 2014a, Passeri et al. 2019).

Typical values for V_S are proposed in the scientific literature (Foti et al. 2018) as a reference term of comparison for obtained results (Table 4.1).

Table 4.1. Typical V_S values for soils (after Foti et al. (2018)).

SOIL TYPE	V_S (m/s)
Soft Clay	80-200
Stiff Clay	200-600
Loose Sand	80-250
Dense Sand	200-500
Gravel	300-900
Weathered Rock	600-1000
Competent Rock	1200-2500

Figure 4.9 also shows that the velocity of Rayleigh waves is almost independent on the Poisson's ratio, and can be approximated to the V_S in an ILEH medium. This assumption will be very useful for surface wave testing.

4.2 Seismic tests

The near-surface characterization of soil deposits or rocks is generally performed by in situ seismic tests (Jamiolkowski 2012). The investigation of a large sample of the medium in its natural state is the essential advantage of in situ tests. However, also laboratory tests can be used to evaluate geotechnical parameters, accounting for various limitations (e.g., sampling disturbance and representativeness, scale problems, strain ranges). Moreover, the back-calculation from observed ground motions (e.g., from down-hole arrays) represents a useful tool for the validation of experimental results (EPRI 1993). Generally, the small-strain stiffness is deduced from seismic tests, whereas the nonlinear response of the material is obtained by laboratory tests (or literature models) and then normalized.

Seismic tests are generally classified as invasive and non-invasive. However, this classification can be misleading because, in reality, all geophysical methods investigate the medium in its undisturbed natural state, so they are all strictly non-invasive. Seismic tests can be alternatively classified as in-hole and surface methods, because the measurements are performed respectively positioning the instruments within the ground or on the surface. However, in-hole excludes the seismic cone (SCPT) (Campanella 1994), the seismic dilatometer (SDMT) (Marchetti et al. 2008), and the direct-push cross-hole (DPCH) (Cox et al. 2018) which are methodologically analogous to down-hole and cross-hole tests. The only difference is that the receivers are placed inside the rods used to insert the cone or dilatometer, rather than in a hole.

For critical sites, is it desirable to use a minimum of two different and independent measurement techniques so that they can serve as a cross-check on each other and the occurrence of gross errors (EPRI 1993).

In this dissertation, the invasive and non-invasive classification is adopted. Particular attention will be paid to surface wave testing (i.e., non-invasive methods). However, a general introduction of invasive methods is also proposed to identify and quantify epistemic uncertainties and aleatory variabilities included in all the V_S estimations. Examples of applications are given for each class of methods, drawing upon the Polito Shear Wave velocity Database (PSWD) presented in the next Chapter. Then, typical sources of epistemic uncertainties and aleatory variabilities are summarized in a dedicated concluding section (Table 4.3).

4.2.1 Invasive Methods

Invasive methods consider a source and receivers placed beneath the surface. Conventionally, they are lowered into appropriate boreholes. More recently, new methods are proposed for directly pushing the instruments into the ground. The substantial outcome of invasive methods is an evaluation of V_P and V_S in a restricted and localized area.

Typical invasive (i.e., borehole-based) methods are:

- Down-Hole seismic testing (DH);
- Cross-Hole seismic testing (CH);
- PS suspension logging (PS).

The other subclass (i.e., direct-push) is based on the same procedures:

- Seismic cone penetration testing (SCPT, DH equivalent);
- Seismic dilatometer testing (SDMT, DH equivalent);
- Direct-push Cross-Hole seismic testing (DPCH, CH equivalent);

In the next sections, DH, CH, and PS borehole-based tests and associated EUs and AVs are illustrated. At the same time, the direct-push methods are addressed, as they are a particular application of the same theoretical assumptions.

4.2.1.1 Down-Hole Seismic Testing

The Down-Hole seismic testing technique is outlined in ASTM Standard D7400-17. The source is located at the ground surface, and the receiver/s is/are advanced into the ground either by lowering them in a well-prepared cased and grouted borehole (i.e., borehole-based) or directly pushing them (i.e., direct-push). A cross section of the usual test arrangement of the borehole-based DH test is shown in Figure 4.12. The measured travel time is referred to slanted travel paths (L1 and L2) and can be influenced by potential refracted ray paths in the near-surface characterization. Generally, the borehole/cone deviation is not accounted for in the analysis as for Cross-Hole tests. Multiple interpretation methods can be used for the DH test processing and V_P-V_S interval profiles evaluation (e.g., pseudo- or true-interval, slope-based, raytracing inversion).

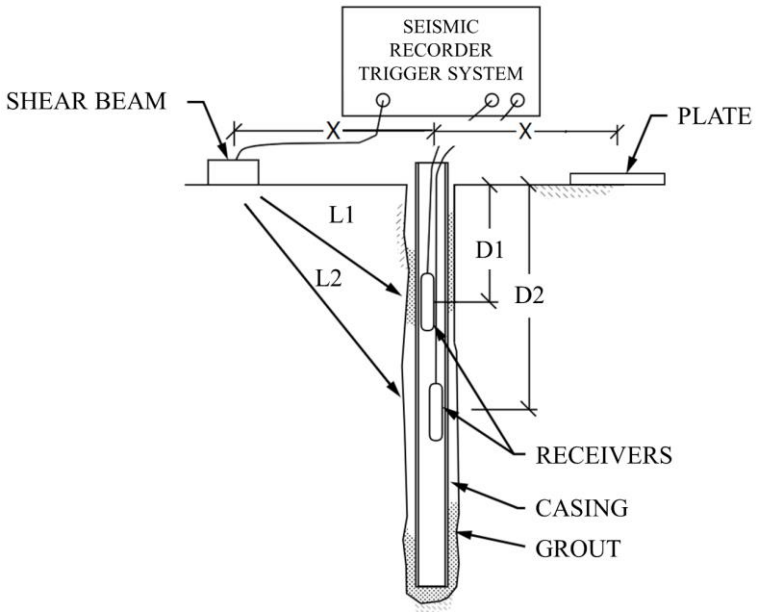

Figure 4.12. Down-Hole (borehole-based) test setup (modified from ASTM D7400-17).

The equipment for a high-quality DH test are sources, receivers, and data acquisition (DAQ) system.

Seismic waves are excited at the ground surface introducing in the medium vertically propagating, horizontally polarized shear waves (S_H) or compression (P) waves. The first are excited using a horizontal sledgehammer striking on shear/traction beam (Figure 4.13a), a mobile shaker, or a vibroseis truck (e.g., T-Rex NHERI@UTexas, Figure 4.13b). Compression waves are produced using a vertical sledgehammer striking on a metal plate, a mobile shaker, or a vibroseis truck.

In the case of borehole-based, the receiver/s is/are lowered into the borehole and clamped to provide coupling with the surrounding soil. The singular or plural formulation is due to different techniques that can also use a single receiver (i.e., pseudo-interval method), two (i.e., true-interval method), or a string of multiple sensors. The pseudo-interval method is highly discouraged by the significant uncertainties involved in the triggering system (i.e., timing errors), whereas the adoption of a 2-sensor array can lead to time-consuming acquisitions. An example of the 7 m (8 triaxial geophones) string used at the Politecnico di Torino is shown in Figure 4.13c.

In case of SCPT, receivers are pushed into the ground in a conical probe (i.e., in the CPT cone) or are located in the back part of the rod.

Both for borehole or direct-push methods, three-dimensional, adequately oriented transducers (e.g., geophones or accelerometers) are usually adopted to measure the seismic wavefield (both P and S_H).

The DAQ system (Figure 4.13d) is used to acquire, digitize, and store electric signals from the source and receiver/s. It is often connected to a laptop (Figure 4.13d) for first data visualization and storage. The triggering system (Figure 4.13d) always represents a critical part of the seismic test. The DAQ continuously monitors

and buffers input from the instrumentation. When triggered, the DAQ pulls data from the buffer to the storage system. The triggering is detected with an electrical contact, switch, or shock accelerometer installed on the source.

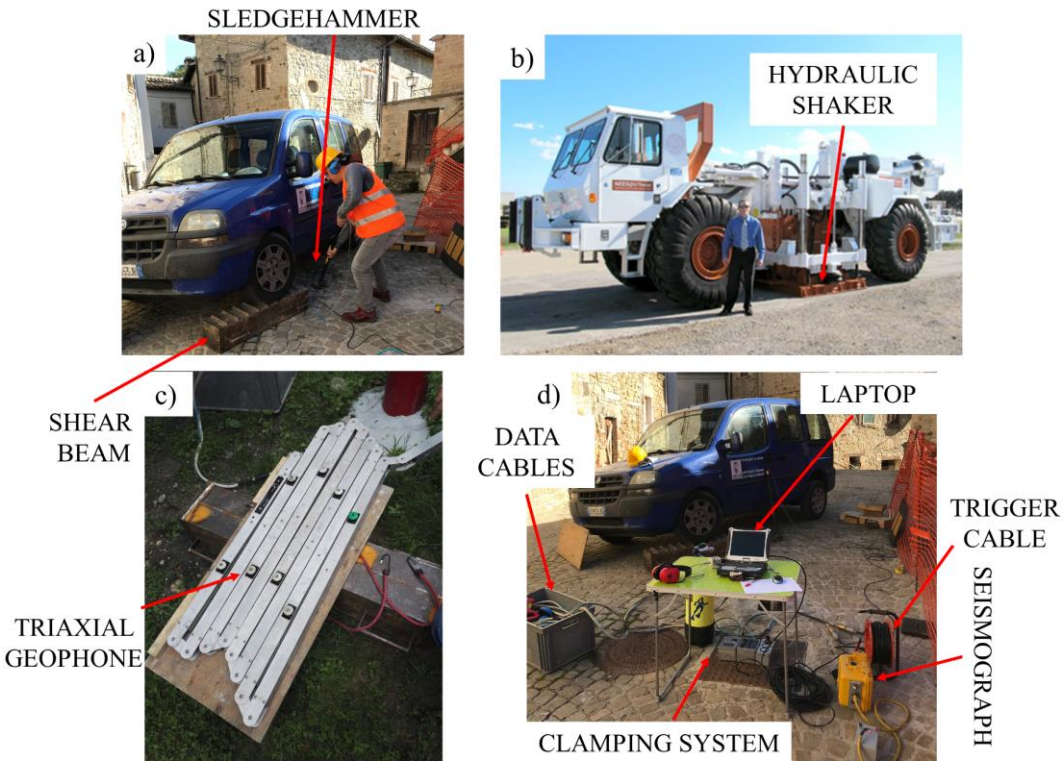

Figure 4.13. Picture of some equipment used for a Down-Hole test. a) Horizontally striking sledgehammer source on a shear beam, b) T-Rex Vibroseis truck (courtesy of Prof. Brady R. Cox), c) 8 triaxial geophones string (Politecnico di Torino), and d) DAQ system and general test setup (data cables, laptop, clamping system, and seismograph).

The seismic source is placed at a horizontal offset (i.e., X; from 1 to 4 m) from the cased borehole or cone push rod (Figure 4.12). The offset distance should be evaluated depending on the interpretation method used, the problems of disturbance and rod/tube waves, and the influence of near-surface refractions. Generally, for borehole-based DH, a dry borehole is preferred to avoid measuring tube waves traveling through the water. If a sledgehammer is used to generate S_H waves, the operator must strike one end of a well-coupled shear beam (usually a truck or a van is placed on the shear beam). It is common to strike each end multiple times (3 to 10 times) and stack (i.e., superimpose) the recorded waveform from each strike. The reverse shot allows correct identification of the shear wave (i.e., the one that have an opposite polarity in the seismogram, creating a butterflied waveform) and the stacking improves the Signal-to-Noise Ratio (SNR). The hits will generate vertically propagating, horizontally polarized shear waves at the ground surface. The waves propagate from the source at the surface to the receiver at depth along an assumed straight-line travel path. The S_H arrival time is manually picked from the seismic waveform recorded on adequately oriented transducers within the receiver.

Once the stacking is completed, both sides of the shear beam have been hit, and a first data quality check is carried out on the laptop. The operator advances the receiver/s to the next testing depth (typical testing intervals per ASTM are from 0.5 to 1.5 m) and the procedure described above is repeated. At the end of the test, a waterfall plot is developed from the stacked waveform at each testing depth, showing the typical butterflied aspect. An example of recorded traces for the site of Mirabello (a site from the PSWD) is given in Figure 4.14a (Passeri et al. 2018b).

In the case of evaluation of V_P with DH testing method, the testing methodology is similar to S-waves. The main difference is the seismic source. Compression waves are generated using vertical, downward sledgehammers that hit on a metal strike plate. The waves are best observed using vertically oriented transducers. It is generally more difficult to obtain reliable P-wave velocities with DH tests. These waves that travel into the borehole casing/fluid or the steel cone push rod are referred to "tube waves". An example of a waterfall plot for P-wave records is given in Figure 4.14b for Mirabello (Passeri et al. 2018b).

In Figure 4.14, also the picking is shown on the recorded traces. This operation is by far the most delicate in the interpretation of a DH test.

For the S-waves, the analyst can pick the First Arrivals (FA) (i.e., first departure from the noise floor, with correct polarity), the First Peak/Trough (PT) (can be semi-automated by searching for local min/max with correct polarities), or the First Crossover (CO) (requires butterflied waveform pairs and can be semi-automated by searching for local minimum differences in waveform amplitude) (Stolte & Cox 2019).

For the P-waves, usually, the analyst should pick the first departure from the noise floor, regardless of the polarity.

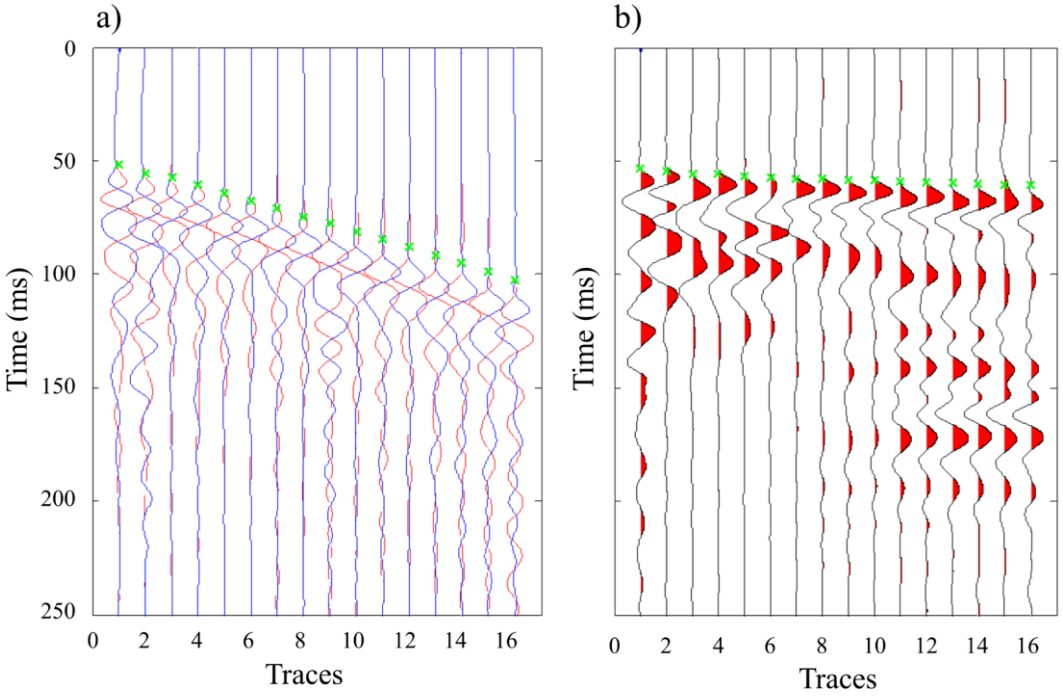

Figure 4.14. Example of the acquired waterfall a) S_H-waves and b) P-waves DH seismogram at the Mirabello site (Italy) for the first Italian blast test experiment and included in the PSWD (after Passeri et al. (2018b)).

Different methods for the DH velocity analysis are proposed in the literature and are permitted by the ASTM D7400-17. Commonly used DH velocity analysis methods include:

- Interval Methods (True- and Pseudo-Interval) (detailed in ASTM D7400-17);
- Corrected-vertical travel time, slope-based method (also called "direct methods") (Patel 1981, Kim et al. 2004, Redpath 2007, Stolte & Cox 2019);
- Raytracing Algorithms (Stokoe et al. 1989, Baziw 2002).

Interval methods assume a straight-line travel path from the source to the receiver, based on the testing geometry. They are commonly not reasonable for the near-surface characterization (i.e., less than 3 m). The true interval method uses pairs of seismic measurements that are simultaneously recorded at two depths (0.5 to 1 m apart) (Figure 4.15a for the site of Acquasanta Terme). The pseudo-interval method uses a pair of seismic measurements that are separately recorded at two depths using a single-sensor receiver. In this method, large triggering/timing errors may be introduced in the evaluation of the interval time.

Slope-based methods utilize the vertical travel time corrected using the testing geometry. The analyst plots the corrected vertical travel time versus depth and fits slopes to data points according to clear breaks in the data and/or layer boundaries identified using independent measures (e.g., CPT or boring logs). In this case, the V_S or V_P is evaluated as the slope of the fitting line, as can be seen for Acquasanta Terme (a site in the PSWD) in Figure 4.15b-c.

Raytracing algorithms evaluate refracted seismic wave travel paths through a layered velocity model, based on the Snell's law. The method is based on the solution of an inverse problem.

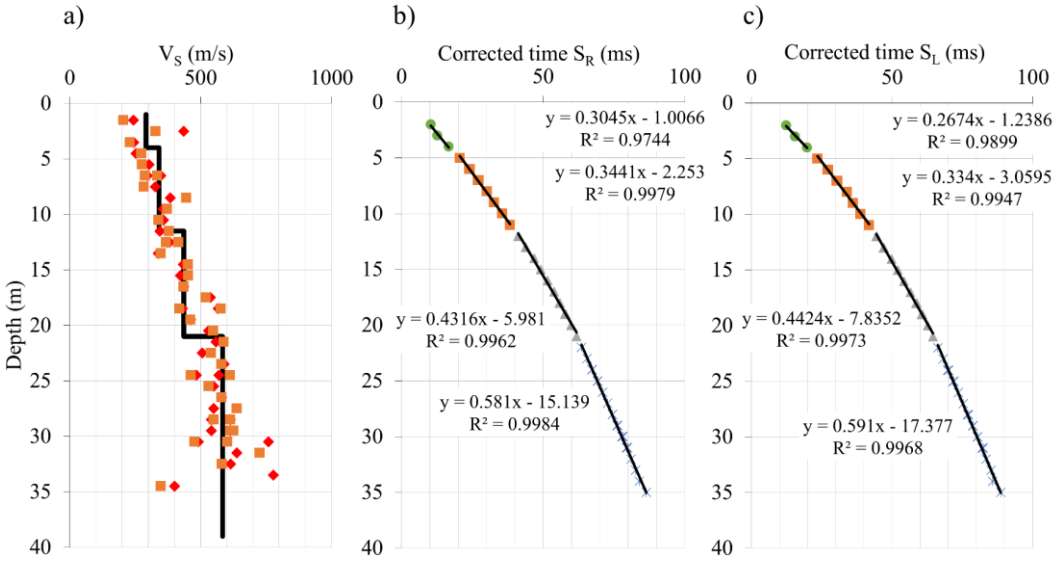

Figure 4.15. DH data processing adopting for the site of Acquasanta Terme (Italy) included in the PSWD a) the true-interval method and b), c) the slope-based method for the right (R) and left (L) strike.

The reliability of the down-hole tests was the subject of a comparative study conducted in Korea near the city of Pyeong-taek (Kim et al. 2013b, Passeri et al. 2019). The local litho-stratigraphical conditions are characterized by the presence of a relatively shallow bedrock (at about 15 m depth), covered by residual soil resulting from the alteration of the bedrock. Six different operators performed down-hole measurements within the same hole. The measurements were interpreted by each of the operators using both the linear interpolation and raytracing algorithms.

Interpretations based on the first of the two methods led to minor differences, confirming greater robustness. Results show local interval velocity differences. However, the average velocity remains unchanged since the profiles are equivalent to the experimental information available.

For the raytracing algorithms, the differences appear significantly greater. The uncertainties on the individual values of the first arrival times assume greater importance.

4.2.1.2 Cross-Hole Seismic Testing

The conventional, borehole-based application of the CH seismic testing is described in ASTM D4428/D4428M-14. For this class of tests, the source and the receivers are lowered down in well-prepared cased and grouted boreholes (two, S & R1, or three, S, R1, & R2). The boreholes spacing should range between 1.5 m and 5 m, whereas measurements should be performed at different depths every 0.5 to 3 m. Differently from DH tests, deviation surveys of boreholes are required to evaluate the distance between instrumentation at each testing depth. Moreover, the problems with the consistency of the wave travel path, SNR, and potential refractions should be addressed during the test. A cross section and a plan view of the usual test arrangement of the borehole-based CH test is shown in Figure 4.16.

A new direct-push CH testing method is outlined by Cox et al. (2018), and it is very appealing for analysis of ground improvements works. This method represents a step-forward with respect to a prototype presented in ’90 using CPT equipment. This method was born for P-wave velocity measurement to identify saturated soils in-situ (Cox 2006) and, nowadays, it is well-suited to testing near-surface, soft soils (Stokoe et al. 2014, Wotherspoon et al. 2015). The source and the receiver are directly advanced into the ground using conical probes (i.e., CPT-type equipment). The cone spacing ranges between 1.5 and 2.5 m, whereas depth intervals between 0.2 and 0.5 m. Cone deviation is tracked via tilt measurements and used to evaluate the distance between cones at each testing depth.

Generally, large borehole/cone-rod spacing result in longer direct travel paths, increasing the potential for the early arrival of refracted waves. Also, a lower SNR is detected.

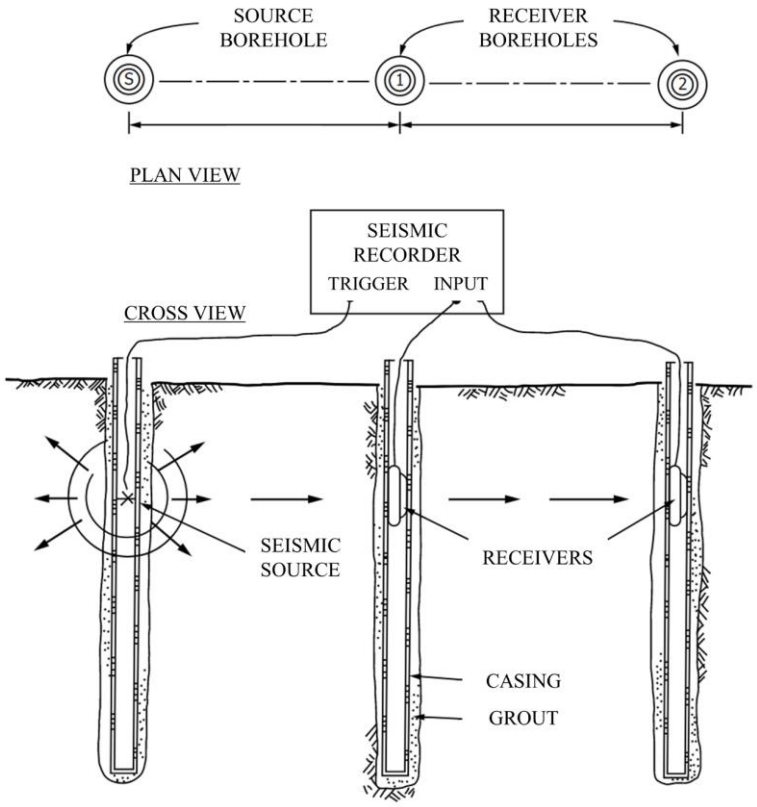

Figure 4.16. Cross-Hole (borehole-based) test setup (modified from ASTM D4428/D4428M-14).

Similarly to DH tests, CH tests are composed by a source, receiver/s, and a data acquisition system (DAQ) (Stokoe & Woods 1972).

The source for borehole-based CH tests is lowered into the borehole and wedged in place to provide coupling with the borehole casing. The CH source is engaged in generating P-, and S_V-waves using different mechanisms (e.g., sliding hammers, solenoids). For direct-push methods, the source is included in the penetrating cone with mechanisms to generate seismic waves.

The receiver/s for a CH method are similar to the DH test, both for the borehole-based and direct-push applications. Also in this case, each receiver contains a sensor package capable of measuring capable of measuring vibrations in three directions.

Also, the DAQ system is similar to the one used for the DH test. The triggering system still represents a crucial practical issue. A sensor in the source is used to start data acquisition when seismic energy is excited by the source and propagated into the soil/rock.

The first step of the testing methodology consists of propagating waves between the source and receiver by exciting the seismic source. As for DH tests, it is common to stack 3 to 10 source excitations to improve the SNR. Often, P-waves and S-waves are generated by different source excitation, and best observed on differently oriented transducers. If possible, the reverse polarity S-waves should be generated to aid in picking the arrivals. The operations are then repeated for each advance of the source and receiver/s. An example illustrated in Stokoe &

Santamarina (2000) is proposed in Figure 4.17 in the case of two- (a) or three-holes (b) test setup.

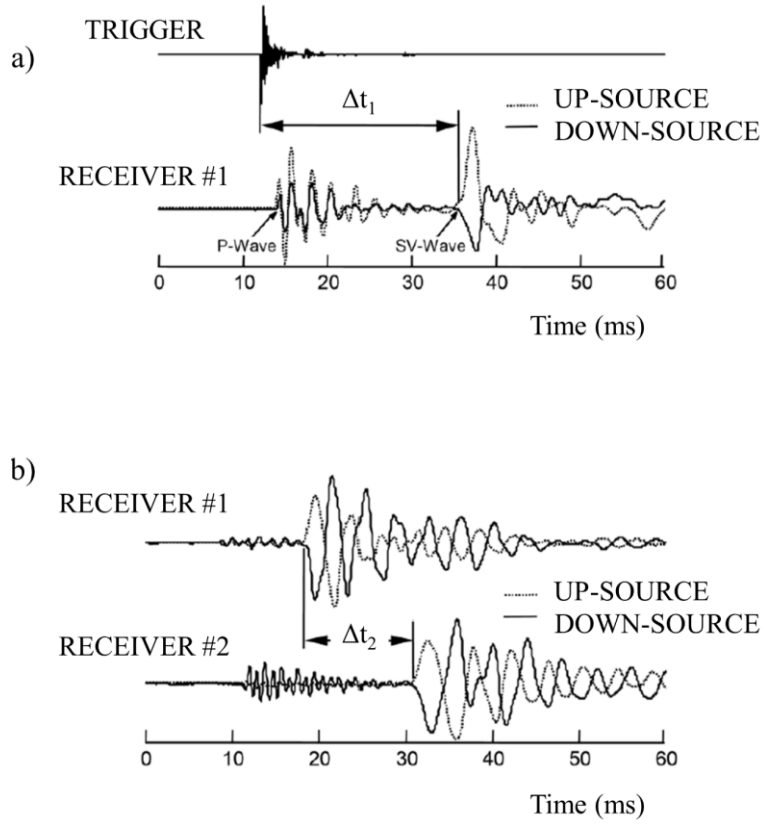

Figure 4.17. Cross-Hole (borehole-based) test setup (modified from ASTM D4428/D4428M-14).

The analysis of a CH test results leads to a velocity estimation obtained as the travel path distance divided by the direct travel time. The distance is obtained by borehole deviation surveys at each depth, aiming at assessing the correct source/receiver position. The travel time requires the process and plot of the waveform records, the picking of the trigger and direct arrivals, and the trigger calibration/correction. In case of soft, embedded layers, the generation of a faster head wave traveling at the interface can compromise the test results. For these reasons, the independent information coming from the borehole log should be exploited in the data processing.

An example of CH results is shown in Figure 4.18 for the Zelazny Most tailing dam (Prof. Jamiolkowski, personal communication) as part of the massive monitoring activity of the largest European tailing dam. The Figure shows the typical output for a CH test. In this case, also a statistical sample of repeated measurements was obtained to evaluate the experimental uncertainty on the velocities.

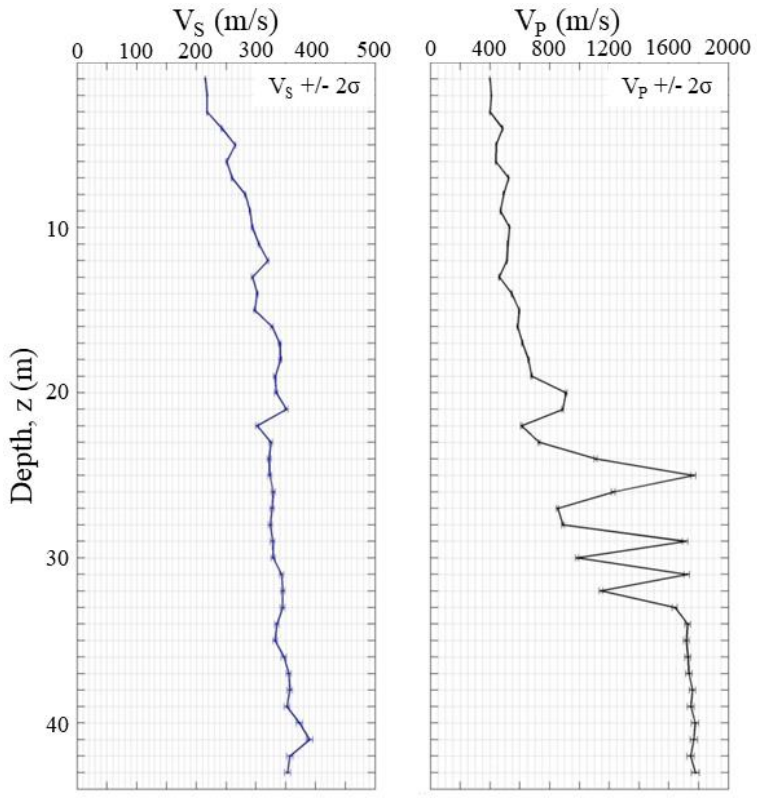

Figure 4.18. CH results for the Zelazny Most tailing dam (Prof. Jamiolkowski, personal communication).

A study on the reliability of the results obtained in the cross-hole tests is reported by Callerio et al. (2013). In particular, the authors repeated several times both the measurements of wave propagations and the deviation surveys to compute means and standard deviations. The results obtained show that the uncertainty associated with the deviation from the vertical grows with the depth. On the contrary, the uncertainty associated with the estimate of the time of the first arrival remains substantially stable with depth. Therefore, the reliability of the CH test appears very conditioned by the measurements of deviation from the verticality. The deviation surveys should be conducted with great care, especially when V_S and V_P are then used for the estimation of porosity (Foti & Passeri 2016).

In light of previous considerations, it can be stated that the reliability of a cross-hole test depends mainly on the quality of the instrumentation and the measurements performed, while the interpretation does not require particularly refined techniques.

4.2.1.3 PS suspension logging

The OYO Company developed the suspension logging method (PS) in Japan. This seismic method can be seen as a mixture of DH (i.e., single borehole) and the CH testing (i.e., lowered source). Indeed, the PS logging test setup consists of a rigid cable lowered in a cased or uncased single borehole. The measurements can be performed either in uncased or PVC cased boreholes (also in marine environments), although uncased mud-rotary boreholes show better results. The

cable sustains the instrument package primary composed of two geophones (i.e., an upper and a lower spaced of 1 m) and a source. The total length is approximately 8 m long. At the surface, a system of winches allows the safe advance of the instrument, whereas a logger/recorder acquire, digitize, and store the acquired seismograms. The schematic illustration of the test setup is shown in Figure 4.19a.

The source strikes in two horizontal directions, then in the vertical direction. For each energization, the lower and upper geophones record the generated wavefield, similarly to the true-interval method described for the DH test. As for the DH application, this approach leads to a significant influence of the picking strategies. Clear evidence of this influence is shown in Figure 4.19b, where the Mirandola's (Garofalo et al. 2016a, Passeri et al. 2019) results are reported. The epistemic uncertainty in the picking does not produce a stable result, as even small differences in the picked time are amplified in the calculation of the velocity. However, the 1-m resolution allows detecting localized V_S oscillations.

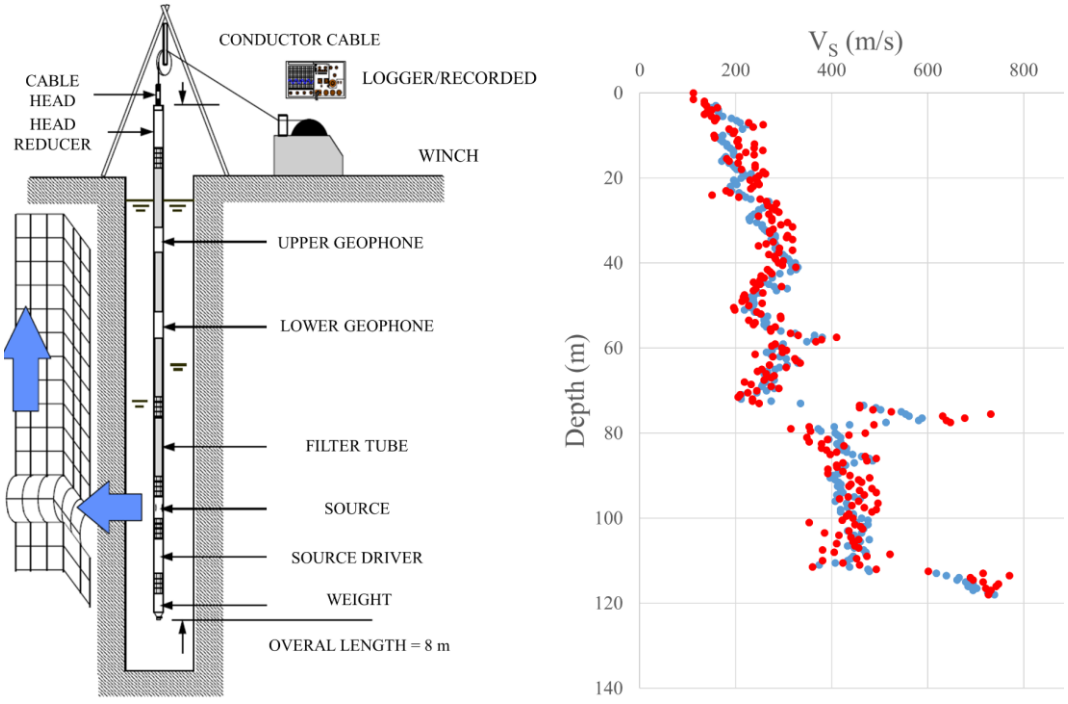

Figure 4.19. Scheme of the PS suspension logging test and an example of results at Mirandola (Garofalo et al. 2016a, Passeri et al. 2019).

The PS suspension logging is the only seismic test that gives both P and S_H wave velocities in a single hole at depths higher than 100 m. The close distance between the receivers provides an almost depth-independent high resolution.

This method shows limitations in case of fractured rocks above the water table (i.e., the risk of losing the probe). Other limitations are the possible detection of tube waves (particularly pronounced with heavy casing and thick grout), the poor signal quality at considerable depths, and the very restricted investigated volume.

4.2.2 Non-invasive Methods

Non-invasive seismic testing methods allow for characterizing sites without placing the source or the sensors within the ground. Typically, the interval velocity profiles obtained by these methods refer to a global response of the soil deposit, differently from the localized measurements of the invasive methods. This characteristic is crucial for the evaluation of the AVs involved in this class of seismic tests.

Common non-invasive methods are:

- Seismic reflection;
- Seismic refraction;
- Surface wave testing;
- Horizontal-to-vertical spectral ratio.

The seismic reflection is often used for exploration geophysics and not usually adopted for near-surface characterization (therefore, it is not discussed in this dissertation). In the next section, the seismic refraction will be briefly described along with the identification and quantification of EUs and AVs. Then, the surface wave class of tests, which includes a wide range of different applications that exploit the characteristics of surface waves propagation, is presented in Section 4.2.2.2.

4.2.2.1 Seismic refraction

A complete reference to this type of non-invasive method can be found in Redpath (1973). Many interpretation methods are illustrated in the literature for refraction tests, from the simplest time-intercept method to more complex full tomographic inversion algorithms. More details can be found in ASTM D5777 which provides a standard of execution and interpretation.

For near-surface characterization, a linear array of 24-48 geophones is used, with a spacing varying between 1 and 5 m. Both V_P and V_S velocity models can be estimated by refraction tests. P-wave refraction uses vertical geophones and is often performed in conjunction with Rayleigh waves active-source methods (i.e., they share the same test setup and instrumentation) (Foti et al. 2003). S_H-wave refraction is performed with horizontal geophones. It is less frequent than the P-wave refraction as it requires higher energies. Once the wavefield is produced from the ground, a manual picking method of the first arrivals is usually adopted, similarly to DH and CH based methods.

The primary applications of the seismic refraction testing method are (Foti et al. 2003):

- Locating and profiling irregular bedrocks;
- Determining bedrock rippability and locating the depth of saturation in soft soils (based on P-wave velocity and handy a-priori information for surface wave tests);

- Shear wave velocity profiles in case of normally dispersive (i.e., V_S increasing with depth) and simple models;
- Locating pipes, tunnels, voids, faults, fracture zones, buried structures (e.g., paleochannels);
- Identify strong lateral variations and inhomogeneity.

Similarly to invasive tests, the seismic refraction instruments are usually a source, a number of receivers, and a data acquisition system (DAQ). The most commonly used source is a sledgehammer that impacts vertically on a steel strike plate (P-waves) or horizontally on a traction beam (S_H waves). If a more in-depth profile is needed, also an accelerated weight drop can be used as a source. The most crucial part of the test regards the triggering system that should establish the zero time. The stacking of 10 traces is usually done also for these tests (as discussed for invasive tests) aiming at improving the SNR, especially in noisy environments.

The generated wavefield is measured by 4.5 to 14 Hz natural frequency geophones placed on the ground. These sensors are vertical or horizontal, depending on the source. The spacing can vary between 1 to 5 m, depending on the designed near-surface resolution and the maximum investigation depth (array length approximately 4-5 times the maximum desired depth).

The DAQ system is the same described for invasive tests (i.e., high-quality with 24-bit digitizer and anti-alias filter) with a system of seismic cables allowing the connection of the test equipment.

The test procedure is quite simple. The vertical/horizontal geophones should be placed on the soil/rock surface depending on the generated wavefield. The shot locations should be placed off each end of the array (typically at half the geophones spacing distance) to detect dipping layers. Then, also within-array shots are desirable. Hitting at the ¼ and ¾ inside the array is common. An example of a forward and a reverse shot of a P-wave refraction test is given in Figure 4.20.

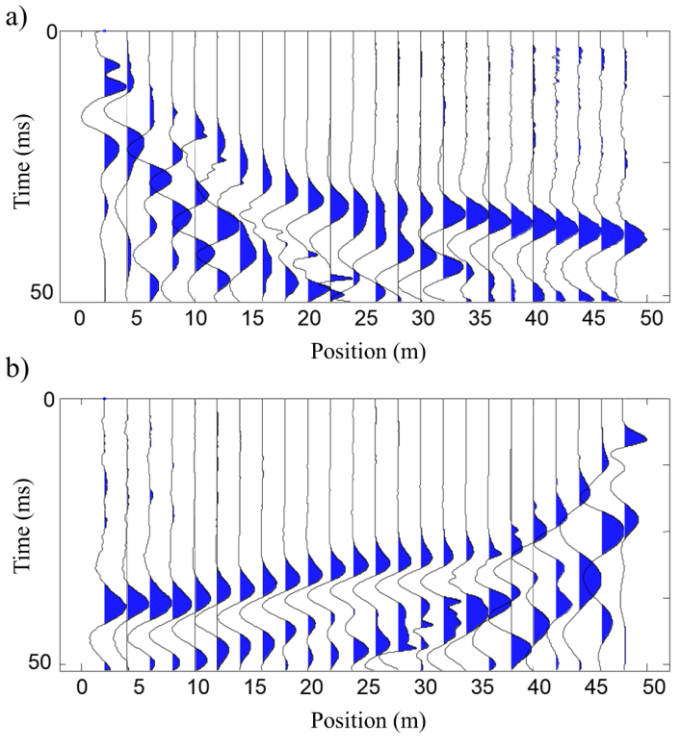

Figure 4.20. P-wave refraction: a) seismogram for a forward shot, and b) seismogram for a reverse shot (after Foti et al. (2014)).

A typical example of refraction data visualization is given as travel-time vs. distance plot. Figure 4.21 reports an example from Lippus (2007) that clearly explains the case of critical refraction of waves off of deeper, stiffer layer. When a refraction test is performed, one of the most delicate operations is the identification of the head wave. The distance at which the head waves overtakes the direct wave arrivals is known as the crossover distance (Kramer 1996) (X_C in Figure 4.21).

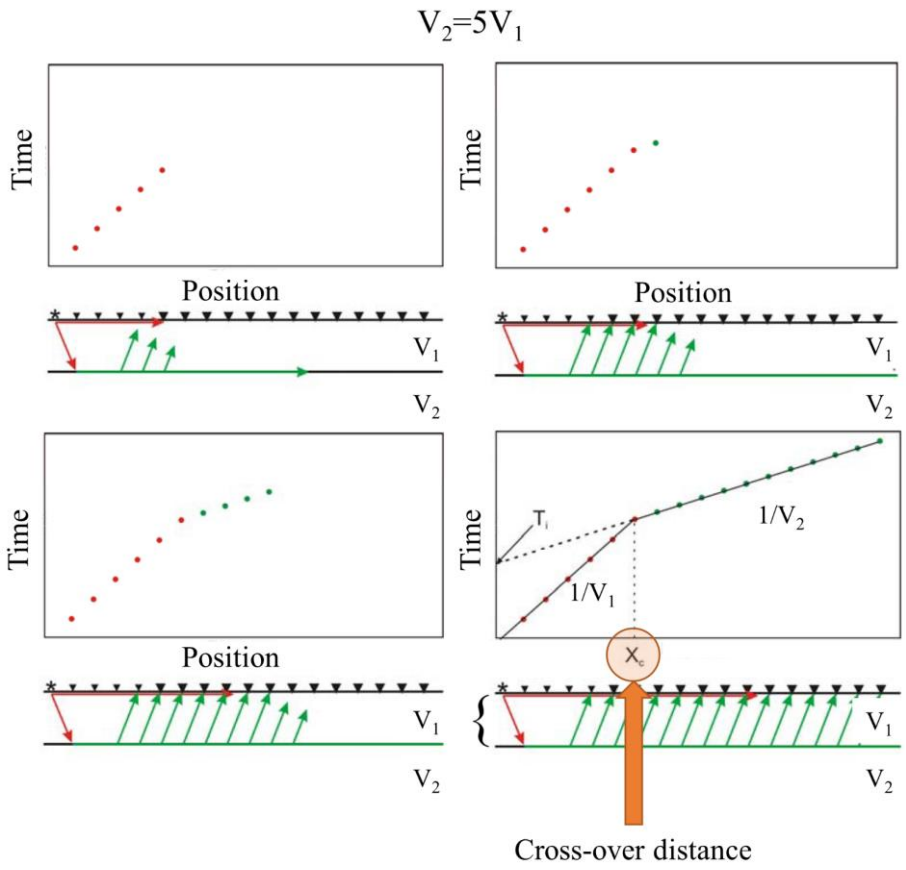

Figure 4.21. Travel-time vs. distance plot for an example single layer deposit and identification of the crossover distance (after Lippus (2007)).

Then, for more complex and multiple layers models, the interpretation of the test becomes more challenging (Reynolds 2011). In particular, it is important to reaffirm that the refraction test gives reliable results only in case of no velocity inversions in the model. The refraction testing will not detect a softer/slower layer beneath a stiffer/faster layer. Moreover, even if the velocity increases with depth, a "hidden layer" can be lost in the interpretation, due to its limited thickness. However, the seismic refraction can be combined with surface wave testing methods to constraint the final solution and provide a more realistic result (Foti et al. 2003). An example of undetectable layers resulted from equivalent seismic refraction models is given in Foti et al. (2014) and shown in Figure 4.22. In practice, the equivalence is due to multiple velocity profiles that can generate the same travel time curves. The example of Figure 4.22 shows how two different velocity profiles can generate the same travel time curves. Moreover, the presence of a softer layer beneath a stiffer layer (e.g., shallow crust) will lead to errors in the subsurface profile.

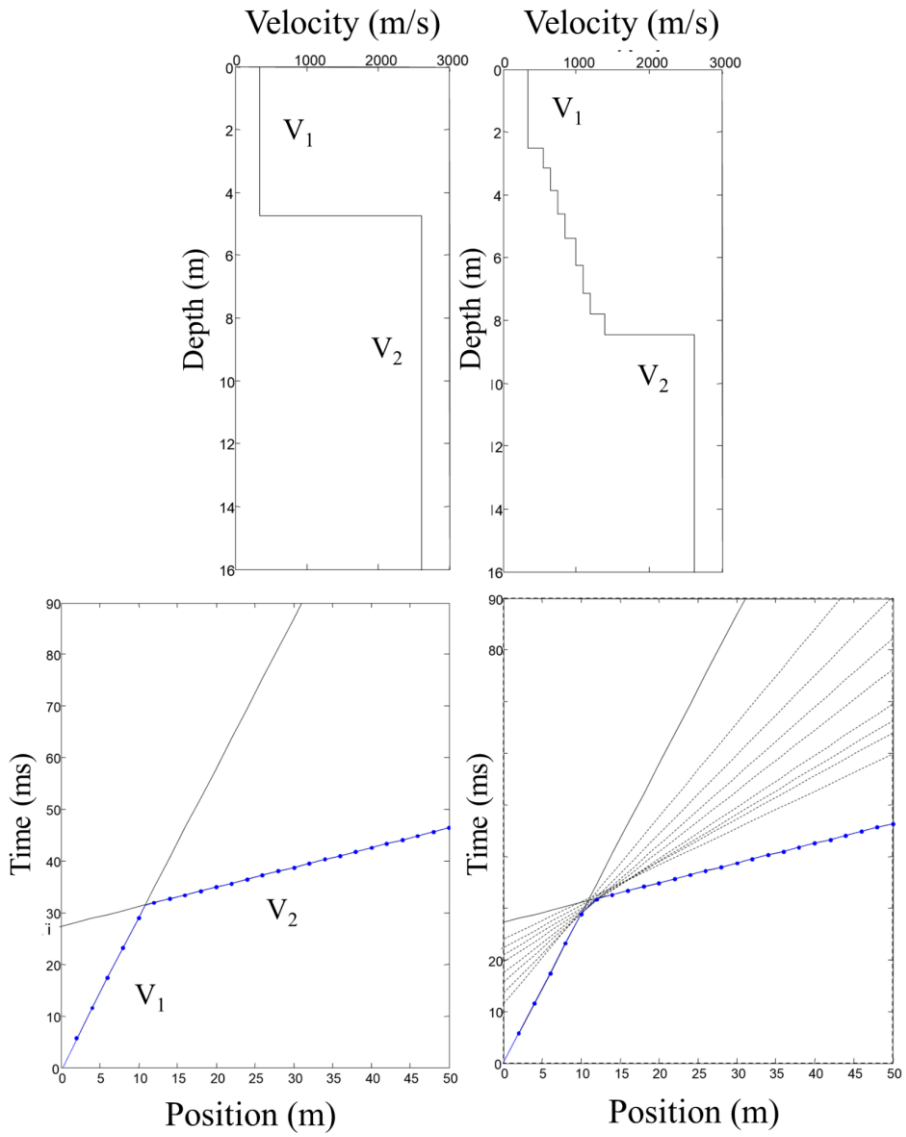

Figure 4.22. Equivalence of travel time curves for different profiles (after Foti et al. 2014)).

The 2D tomography is the most challenging (and fancy) method for the interpretation of refraction tests with multiple shot locations. The result is usually given as a 2D map of the soil/rock velocities obtained from the inversion of multiple shots (outside and within the array). An example of P-wave refraction results is given in Figure 4.23 for a site in the PSWD (Fonte del Campo, Passeri et al. (2018a)). In this case, the 2D information is balanced with an increasing epistemic uncertainty due to the ill-posedness of the inversion process. However, in Figure 4.23, the water saturation depth is identified around 10 m. It represents fundamental information in the geophysical survey to be used as a-priori constrain for the inversion of surface wave tests (next section).

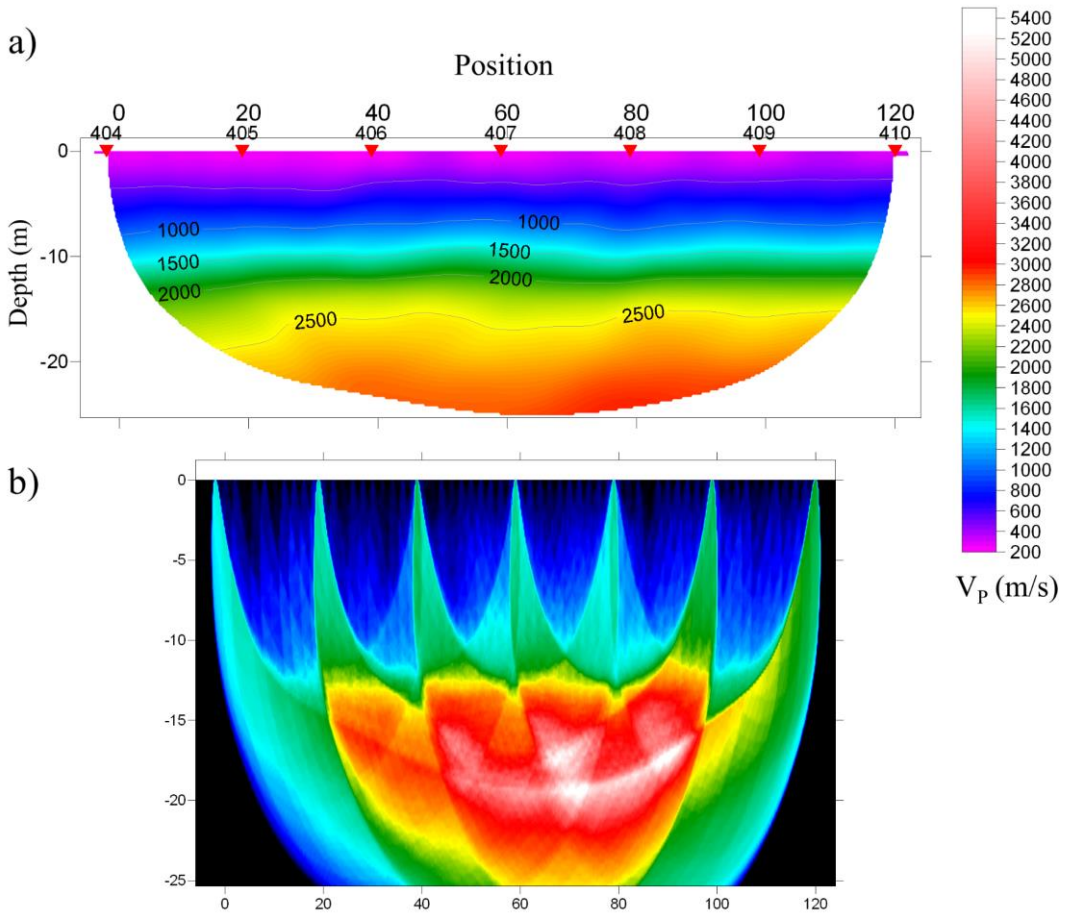

Figure 4.23. Example of 2D P-wave tomography at Fonte del Campo (PSWD), a) 2D map of the estimated V_P velocities with clear evidence of the saturated depth (i.e., V_P>1500 m/s), and b) seismic rays coverage (after Passeri et al. (2018a)).

4.2.2.2 Surface wave testing

Surface waves are appealing because they are ideal for the development of non-invasive techniques for material characterization for a wide range of investigation scales (Foti et al. 2014). The maximum investigated depth represents the most crucial issue. This depth mainly depends on the frequency content of the signal, the array layout, the characteristics of the sensors, and the velocity structure of the site.

The basic idea is inspired by the applications in the seismological field for the characterization of the layers of the earth's crust using recordings of seismic events (Romanowicz 2002). The first application in the geotechnical field dates back to the Steady State Rayleigh Method (Jones 1958) which was however abandoned due to the long and complicated test procedures. However, in the past, the presence of recorded surface waves in the acquired seismic traces was undesirable and considered a "ground roll" to be eliminated (Socco & Strobbia 2004, Socco et al. 2010).

The discussion regarding the essential features of this class of waves was given in previous Section 4.1.1. Here, surface wave tests based on Rayleigh (R) waves will be presented (i.e., Love waves are only briefly addressed). A particular focus

on the identification and quantification of EUs and AVs is also given and summarized along with the other discussed seismic tests in Table 4.3. The most recent reference for the good practice of surface wave analysis is given in Foti et al. (2018). These guidelines include a large number of examples and 11 appendices with more details and references on the topic.

Surface waves are adopted in the last two decades for earthquake engineering purposes mainly to evaluate 1D V_S interval velocity profiles (i.e., for GRAs) (Foti et al. 2009, Stewart et al. 2014a) and/or estimate $V_{S,30}$ (i.e., soil class determination) (Brown et al. 2000, Martin & Diehl 2004, Albarello & Gargani 2010, Bergamo et al. 2011, Comina et al. 2011). Studies in the literature proposed methods to estimate 2D and/or 3D V_S models from inversion of surface waves. However, a substantial increase in the lateral variability is the price to be paid for these multidimensional approaches (Socco et al. 2009, Bergamo et al. 2012, Piatti et al. 2013a). Further studies that estimate the dynamic attenuation characteristics of the site are presented in the literature, even if are not yet commonly adopted in current practice (Foti 2003, Socco et al. 2010, Foti et al. 2014).

Surface wave testing methods are a non-invasive (i.e., sources and receivers on the surface, as the seismic refraction), economical, and rapid type of tests (Foti et al. 2011b). Differently from other non-invasive techniques, they can detect inverse low-velocity layers (i.e., inversely dispersive deposits) and can tailor testing for shallow (less than 1 m) to deep (more than 1 km) analyses (Foti et al. 2003). However, the data processing is complex, and it is followed by an inverse problem for model parameter identification. This leads to an ill-posed problem due to the lack of information. These complexities could induce interpretation ambiguities in the estimated shear wave velocity model. For these reasons, the results of surface wave analyses can be considered reliable only when obtained by expert users. However, because of the cost and time effectiveness of surface wave methods and the availability of ‘‘black box’’ software, non-expert users are increasingly adopting surface wave methods. This often leads to strongly erroneous results that may induce a general lack of confidence in non-invasive methods in a part of the earthquake engineering community (Foti et al. 2018). However, many studies demonstrated that surface wave testing methods could provide comparable reliability and accuracy with respect to invasive tests (Comina et al. 2011, Garofalo et al. 2016b).

The surface wave testing procedure is divided into three main steps (Figure 4.24):

- Acquisition (i.e., measurement of stress waves at the ground surface) using active or passive methods;
- Processing (i.e., determination of the Experimental Dispersion Curve, EDC as the velocity of waves propagation vs. frequency);
- Inversion (i.e., evaluation of the shear wave interval velocity profile vs. depth).

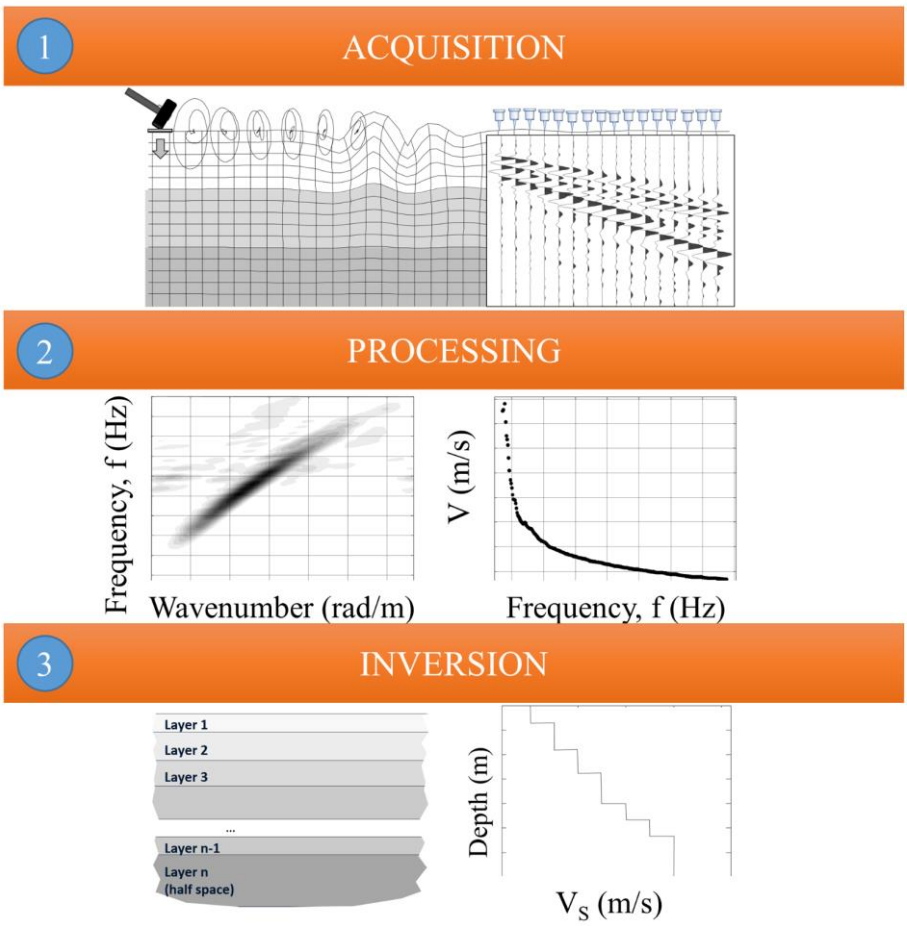

Figure 4.24. Three main steps in surface wave testing methods, 1) acquisition, 2) processing, and 3) inversion (modified from Foti et al. 2014)).

Surface wave testing methods are a broad class of seismic tests that includes many different methods. These methods can be performed with a vast variety of procedures. If correctly implemented and adequately applied, almost any of them could provide equivalent results regarding accuracy and reliability (Foti et al. 2018, Foti & Passeri 2018). The main differences within this class of methods can be in each stage of the measuring process (Figure 4.24). However, surface wave testing methods can initially be grouped for the type of source used in active-source or passive-source methods.

For active-source methods, the surface waves are artificially generated by a specific seismic source. The first engineering methodologies are described by Jones (1958) and Ballard (1964). In particular, Jones (1958) proposed the use of one harmonic source and a single receiver that was moved radially with respect to the source until the source and receiver were in phase. At this point, the analyst can determine, for all single frequencies, the corresponding wavelength and therefore the phase velocity. The complexity of the procedure strongly influenced the duration of the test.

A subsequent example of an active test was termed Spectral Analysis of Surface Waves (SASW) and was proposed by researchers of the University of Texas (Narazian & Stokoe 1983, Stokoe 1994). This type of test required the use of an

impulsive source and a pair of receivers. Light sources were used with receivers placed at a small distance to obtain information related to high frequencies. On the contrary, more massive sources and larger spacing between the receivers investigate lower frequencies. For each test configuration, the velocity of propagation for a given range of frequencies is obtained from the analysis of the phase of the mutual power spectrum for each pair of signals. Assembling the information obtained using different configurations is possible to obtain an estimate of the EDC for a sufficiently wide frequency range in relation to the subsequent inversion process. This test methodology was widely diffused in the geotechnical field. The main problems were related to the interpretation of the phase of the mutual power spectrum (Poggiagliolmi et al. 1982), which can lead to interpretative ambiguities.

The use of techniques based on the analysis of several signals related to an array of receivers aligned with the source (Nolet & Panza 1976, McMechan & Yedlin 1981, Gabriels et al. 1987), allows a faster and more stable estimate of the experimental dispersion curve (Foti 2002). This method nowadays represents the most popular test mode, and it is often referred to by the acronym MASW (Multistation/Multichannel Analysis of Surface Waves) (Park et al. 1999, Foti 2000).

Passive-source methods use low-frequency vibrations from large-scale natural phenomena (e.g., sea waves, wind, and micro-seismicity) and/or high-frequency vibrations from human activities (e.g., constructions, industries, called anthropogenic noise) that are not directly generated for the test purposes (Horike 1985, Tokimatsu 1997). The most common passive methods are termed ReMi^{TM} (Refraction Microtremors) (Louie 2001, Zywicki 2007, Strobbia & Cassiani 2011) and AVA (Ambient Vibration Array) (Tokimatsu et al. 1992a, Okada 2003). The main difference between these two methods is the linear (ReMi) or 2D (AVA) acquisition array. AVA tests are much preferred for passive measurements and far superior for developing robust results. Indeed, the direction of propagation cannot be determined using a linear array; then the exact phase velocity cannot be verified using ReMi arrays (Cox & Beekman 2010, Foti et al. 2018).

Modern approaches in near-surface characterization use MASW tests combined with AVA methods to extend the frequency of the EDC (Socco et al. 2010, Foti et al. 2018). The most common acquired waves are Rayleigh waves, even though the combined use or Rayleigh and Love waves is becoming more common. However, in the present work, from this point forward the attention will be paid only on surface wave tests (MASW and AVA) based on R-waves (Figure 4.25). Many of the same principles apply to the analysis of other kinds of surface waves, such as Love and Scholte waves, which however requires specific data acquisition procedures and forward modeling algorithms. For further details about the acquisition, processing, and inversion of other surface wave testing methods the reader can refer to textbooks such as Okada (2003), Foti et al. (2014). A vast scientific literature is also available on the topic (e.g., Socco & Strobbia (2004), Bard et al. (2010), Socco et al. (2010), Foti et al. (2011a), Schramm et al. (2012), Yong et al. (2013) Foti et al. (2018)).

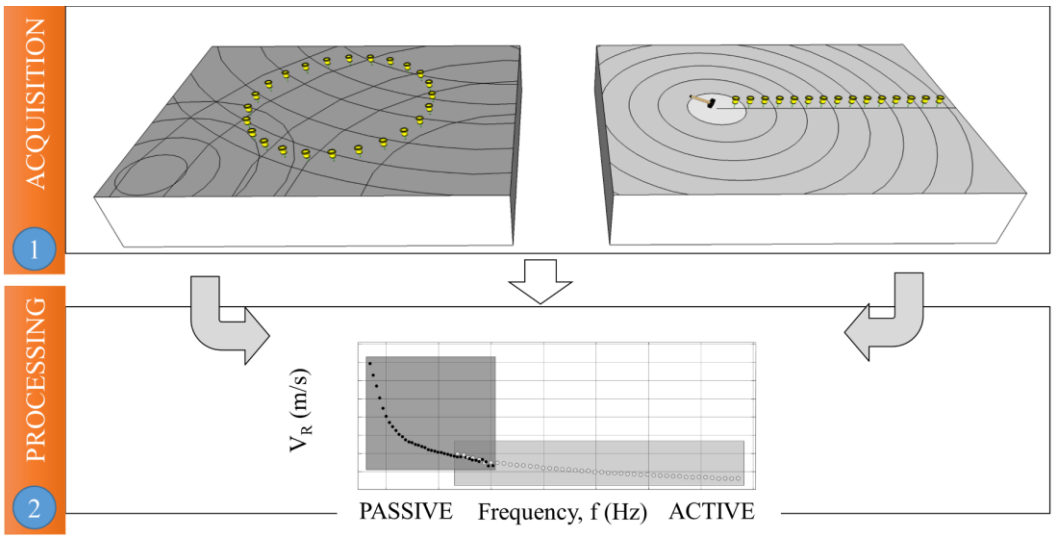

Figure 4.25. Combined acquisition of passive and active Rayleigh waves for the evaluation of a broadband experimental dispersion curve (modified from Foti et al. (2014)).

Acquisition

A MASW data acquisition setup (Figure 4.26) consists of a linear array of n vertical (usually 4.5 Hz) geophones in line with the seismic source and with a constant spacing Δx. The length of the array (L) is calculated as $L = \Delta x\,(n-1)$. The sources are usually placed at multiple locations off both ends of the array (at a distance L_S from the first receiver). For specific applications, also multiple shots within the line can be performed. Hence, the MASW equipment consists of a source (e.g., sledgehammers, drop weights, mobile shakers, bulldozer, vibroseis trucks, seismic guns or explosives), a number of geophones, a high-quality seismograph (DAQ), a trigger system, and data cables.

The frequency content of the propagating seismic signal depends on the type of seismic source and the specific characteristics of the site. In particular, active light sources (e.g., sledgehammers) generate energy concentrated between several hertz and several tens of Hertz. If a very large active source is used, lower frequency surface waves can be generated. The use of hydraulic shakers or trucks is an expensive but effective solution for the broadband of frequencies generated and the high level of energy produced. Seismic guns and explosives should be carefully managed for the involved risks and are less frequent for near-surface characterization.

The natural frequency of the geophones should be adequate to sample the expected frequency band of surface waves without distortions due to sensor response (i.e., nonlinear with some phase distortions that can be visible below the resonant frequency). Moreover, the sensors should be adequately coupled with the ground both using spikes (i.e., natural surface) or baseplates (e.g., pavements) and they should be protected from the eventual inclement weather.

When the trigger system is activated, the DAQ system acquires a sufficiently long window that should include the entire generated R waves wavefield. Usually,

5 to 10 shots are stacked to improve the SNR for each source location (Neducza 2007).

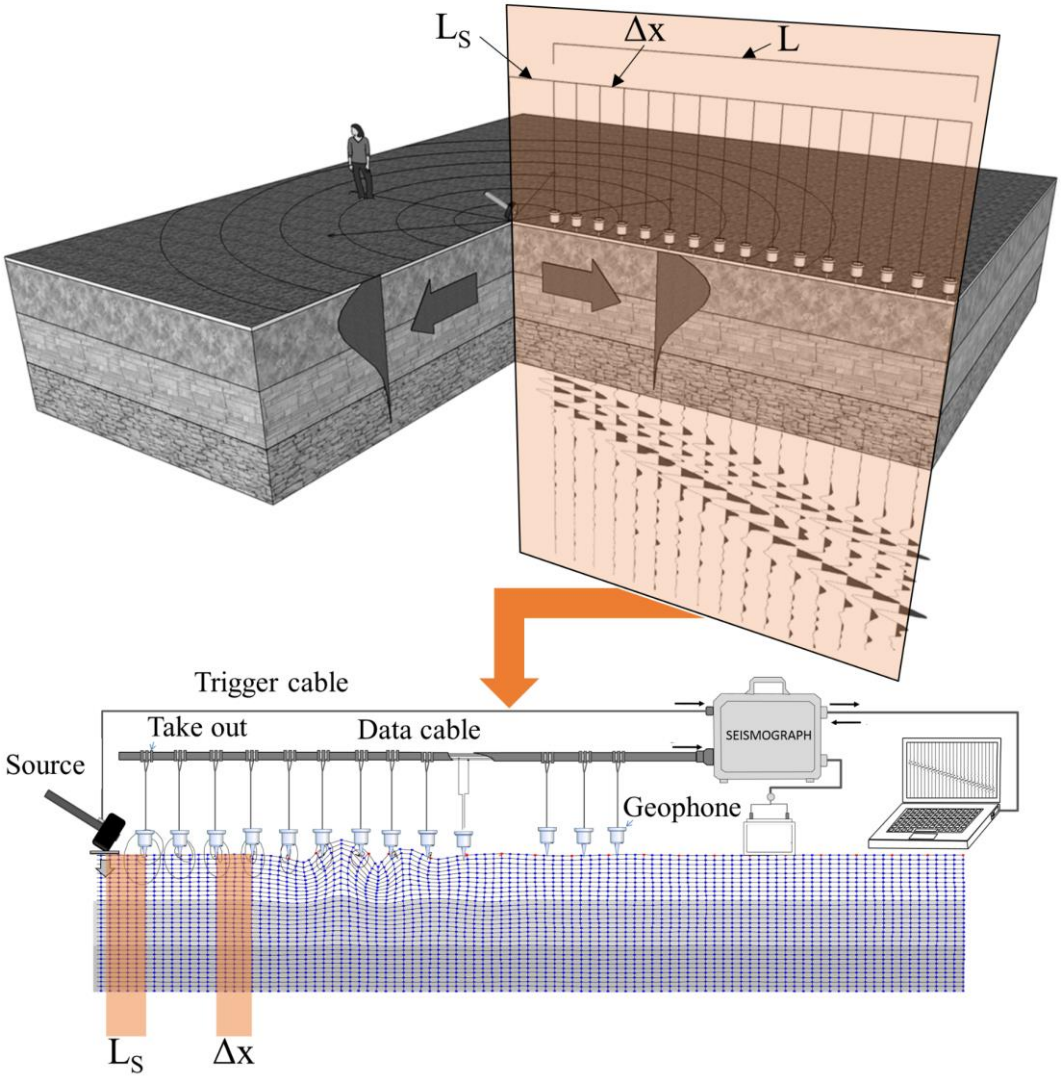

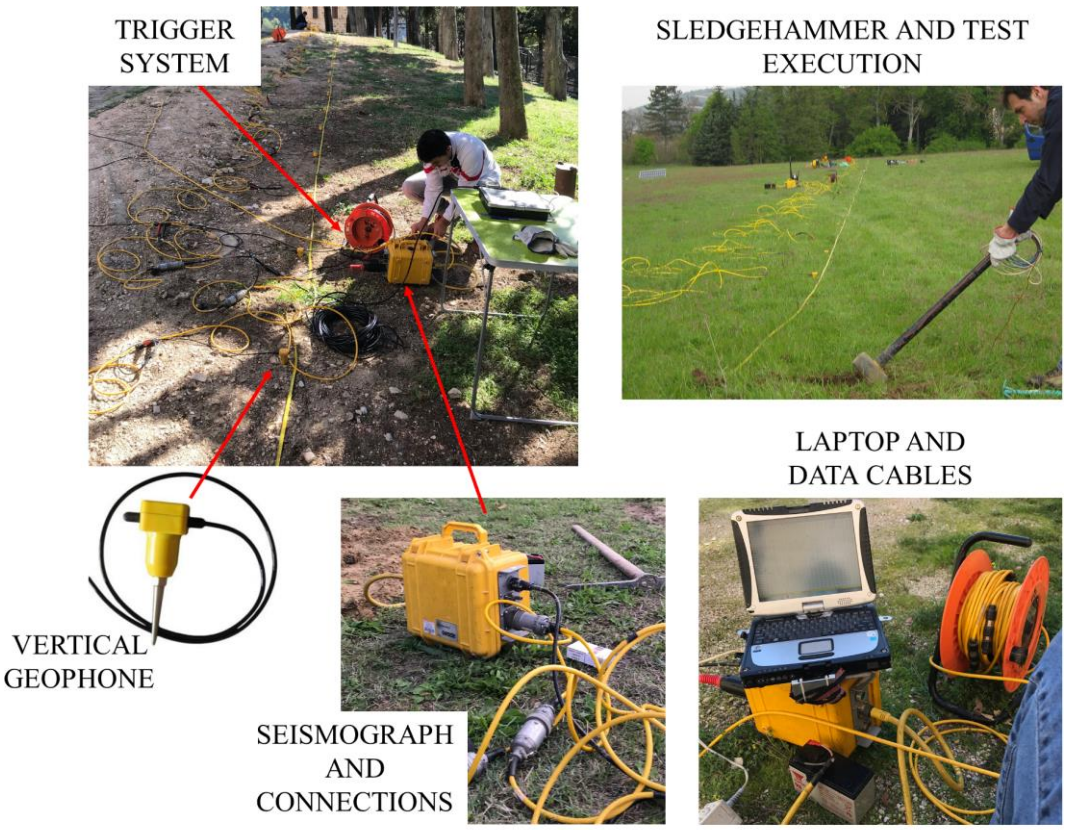

Figure 4.26. Typical setup of a MASW test and equipment including the trigger system, sledgehammer, vertical geophones, DAQ system with a seismograph and data cables and a laptop (modified from Foti et al. (2014)).

The geometric setup of the MASW array and the recording parameters have to be initially carefully designed for each particular application. The geometric characteristics are the array length L, the geophones spacing Δx, the geophones number n, and the source (i.e., shot) position about the first geophone L_S.

The first rule of thumb is that the array length (i.e., related to the maximum generated wavelength) needs to be at least two times the desired depth of profiling. Also, the maximum depth of profiling is mainly dependent on the type and location of the source and the velocity structure of the site. Indeed, the wavelength is a function of both frequency and phase velocity; then it is necessary to make a preliminary hypothesis about the expected velocity range to define the frequency band of the source. At a soft site, lower frequencies will be necessary to achieve the same investigation depth than at a stiff one. Furthermore, in the presence of a sharp velocity contrast at shallow depths, the amplitudes of low-frequency surface waves are sharply reduced and challenging to measure irrespective of the seismic source. Generally, if a profile down to 30 m is required, a 60-90 m array is necessary. However, long arrays are more susceptible to the influence of lateral variations in the subsoil.

The receivers spacing should be adequately chosen for the correct identification of the generated short wavelengths. In particular, the receivers spacing controls the resolution of the layers close to the surface. Signals with wavelengths less than $2^* \Delta x$ are spatially aliased, as demonstrated by the Shannon-Nyquist theorem.

The number of receivers can be obtained from L and Δx. Theoretically, in the absence of intrinsic material damping, the higher the number of receivers the cleaner the dispersion image of the signals processing.

A more significant source offset distance leads to more in-depth profiles, but a low-frequency and a high-energy source are necessary. On the other hand, test geometries with sources close to the array can generate a recorded wavefield contaminated by near-field effects. Then, the source offset should be selected as a compromise between the need to avoid near-field effects and the opportunity to preserve high-frequency components, which are heavily attenuated with distance (i.e., far-field effects) (Foti et al. 2018). The acquisition should be repeated placing the source at both the ends of the array (i.e., at least one forward and one reverse shot) to verify the 1D assumption by comparing the obtained EDCs.

Hence, the choice of the test geometry and recording parameters represents an essential part of the test. A summary is given in Table 4.2. Initial visual checks should always be performed by the analyst in the field and include that:

- All sensors are correctly recording and correctly coupled to the ground (similar waveforms on receivers close to each other);
- The time window contains the whole surface wave train, if possible with sufficient pretrigger;
- The overall signal-to-noise ratio is good (the typical cone pattern of surface waves is visible in all the shots with good repeatability).

Table 4.2. Suggested parameters for MASW surveys (after Foti et al. (2018)).

PARAMETER	Not.	Suggested values	Theoretical implications
Geophone spacing	Δx	1-4 m	Aliasing. Usual minimum measurable wavelength $\lambda_{min} \sim 2\Delta x$ Minimum near-surface layer thickness/resolved depth $\lambda_{min}/3$ to $\lambda_{min}/2$
Array length	L	23-96 m	Maximum wavelength $\lambda_{max} \sim L$ Expected maximum investigation depth $\lambda_{max}/3$ to $\lambda_{max}/2$
Number of geophones	n	24-48	Quality of the dispersion image
Offset between source and 1st geophone	L_S	5-20 m	Near field and far field effects Multiple shot locations strongly recommended
Sampling interval	Δt	0.5 ms	Nyquist/Shannon frequency: $f_{max} = \frac{1}{2\Delta t} = 1000\ Hz$
Sampling frequency	Δf	2000 Hz	

Post-trigger recording length (time window)	T_w	2 s	Record the whole surface wave train
Pre-trigger recording length		0.1-0.2 s	Mitigating leakage during processing

The test design for geometry and recording parameters of AVA tests is more complicated than for active acquisitions (Peterson 1993). A AVA test acquisition setup consists of a 2D array made by at least 8-10, 3-components broadband seismometers, and an acquisition system. In this case, ambient vibrations (erroneously sometimes called "seismic noise") are recorded with no need for an active source.

These ambient vibrations primarily contain surface waves since far away from the source they carry most of the energy. This further characteristic of surface waves is due to their cylindrical wavefront, whereas the wavefront of body waves is hemispherical (Socco et al. 2010). For this reason, surface wave amplitude decays much less with distance than that of body waves and dominate the far field recorded with passive methods.

Moreover, differently from actively generated signals, ambient vibrations have sufficient energy up to periods of tens of seconds. However, the ambient vibration level for passive methods is highly variable from one site to the other one, and a regular signal quality check is more difficult than for active methods.

The sensors should be carefully placed on the ground or, better, buried (Figure 4.27a-b) in order to limit the undesirable type of noise (e.g., due to weather, sensor instability, or lack of connections). The natural frequency of the sensors should be sufficiently low concerning the target depth of investigation.

The choice of a given test geometry is a compromise between the available number of sensors, the level of ambient vibration, and the operating time that could be afforded at the site. Generally, circular arrays are preferred even if spatial restrictions in urban areas can force the choice of other geometries (e.g., triangles, L-shaped) (Figure 4.27c). Indeed, the ambient vibration wavefield might propagate from any direction, as it is difficult to identify a predominant source. The array diameter (i.e., aperture) can range from 50 m to 120 m or up to 1000 m. These limitations of the array aperture depend on the desirable investigation depth (i.e., measured wavelength) and the adopted technical solution. First, a rule of thumb suggests a profile depth close to the maximum array aperture. Given the number of available sensors, arrays from small to large aperture are usually deployed successively in order to sample over a broad wavelength range. Second, standalone or wireless equipment are preferred for the ease of use with respect to cabled systems. A GPS can provide the time synchronization and the precise location of the sensors at the site.

The recording windows are extended up to 2 hours, and only the vertical component is then processed for Rayleigh wave dispersion. The horizontal components recorded with the 3-component seismometers can be used for the

Horizontal to Vertical Spectral Ratio (HVSR) method (briefly addressed in 4.2.2.3) and for Love wave analyses.

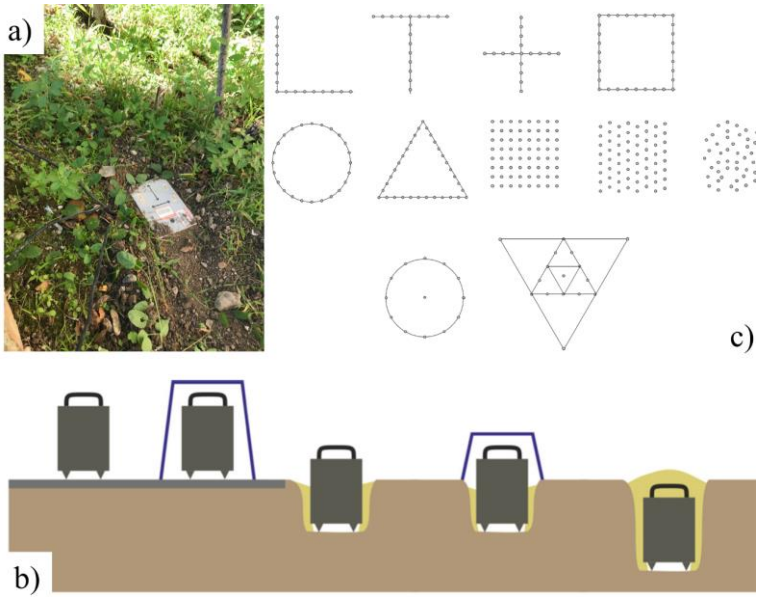

Figure 4.27. a) and b) three-component seismometer ground coupling for AVA tests, and c) typical AVA array geometries (after Foti et al. (2018)).

Further recommendations for the acquisition of both active and passive test regard the proximity of strong vibration sources and unideal surface conditions. The first can introduce an uncontrollable, frequency-dependent, transient noise mainly composed of body waves and non-planar surface waves. The presence of pavement is usually overcome by using specific metal plates for the sensor coupling. However, the presence of underground facilities and buried structures should be initially investigated and accounted in the design of the test.

Processing

A wave is dispersive if its velocity depends on the frequency (or wavelength). Surface waves are subjected to geometrical dispersion for vertically non-homogeneous deposits. In this case, the wave is dispersive because it samples different materials for each frequency. In the case of vertically homogeneous, linear elastic and isotropic materials, indeed, the Rayleigh waves velocity shows no dependence on the frequency (equal to about 0.9 V_S). From this point forward, the relationship between frequency f and wavelength λ (Eq. 4.9) will be frequently used. This means that high-frequencies components travel in (i.e., sample) the shallow portion of the deposit, whereas low-frequencies components travel in (i.e., sample) the deeper portion of the deposit (Figure 4.7).

The fundamental tool that 'condenses' the R-waves geometrical dispersion and that represents a "site signature" of the deposit is the experimental dispersion curve. The fundamental goal of the processing stage is to evaluate a robust and consistent EDC for the site. The experimental dispersion curve usually plots the R-waves velocity vs. the frequency, even if the dependence on the wavelength is often more practical (i.e., it is related to the depth). An example of an EDC obtained at

Mirandola (Garofalo et al. 2016b) by the University of Texas at Austin is given in Figure 4.28 in different domains (i.e., in this case, linear scale, even if a logarithmic plot can also be obtained) as: $V_R - f$ (a) and $V_R - \lambda$ (b-c) (Griffiths et al. 2016b). The dispersion curve was obtained including MASW and AVA arrays and it is given with the associated velocity uncertainty (i.e., +/- one standard deviation) (Lai et al. 2005).

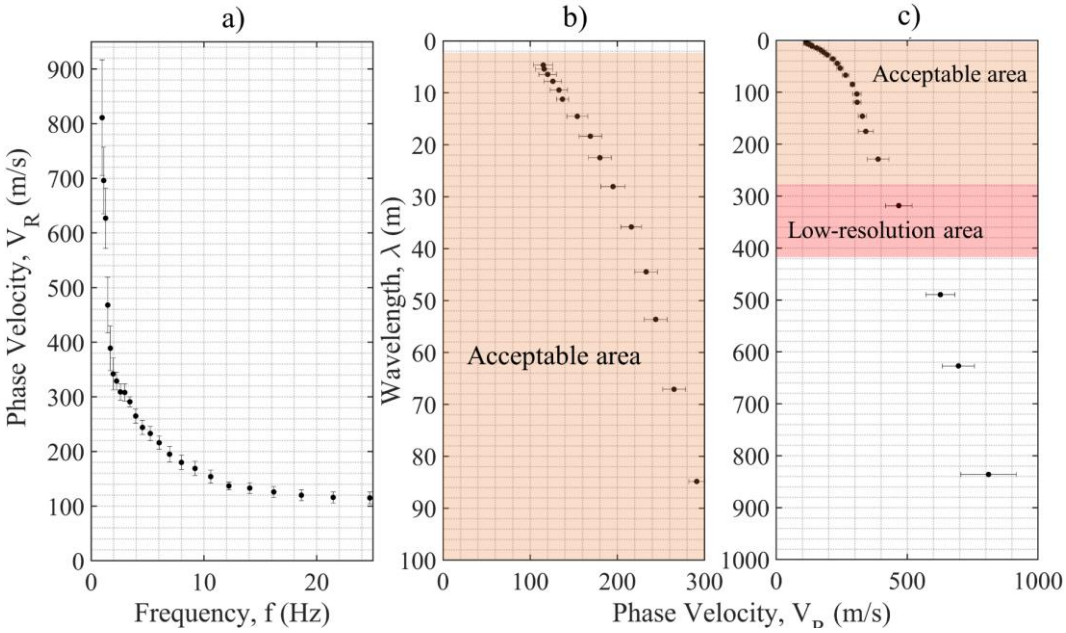

Figure 4.28. Experimental dispersion curve obtained by the University of Texas at Austin for the Mirandola site (Griffiths et al. 2016b). a) Typical velocity-frequency plot, b) wavelength-velocity plot, and c) same of b) but for larger depths and suggested resolvable depth limits.

The experimental dispersion curve provides necessary information about the investigated deposit also by simple visual inspection, especially if combined with a careful assessment of the local geology. First, by looking at the velocities, it is possible to infer an estimate of S-wave velocity versus depth. A rough estimate can be obtained by equating the depth to one-half of the wavelength. This depth is termed pseudo-depth:

$$D \cong \frac{1}{2 \div 3}\lambda \qquad \text{(Eq. 4.19)}$$

This method provides a good first approximation of the interval velocity V_S profile that can be introduced in the inversion process (next section). Moreover, a first simple calculation can give support in the verification of the inversion results, as shown in Figure 4.29 for three different V_S interval profiles.

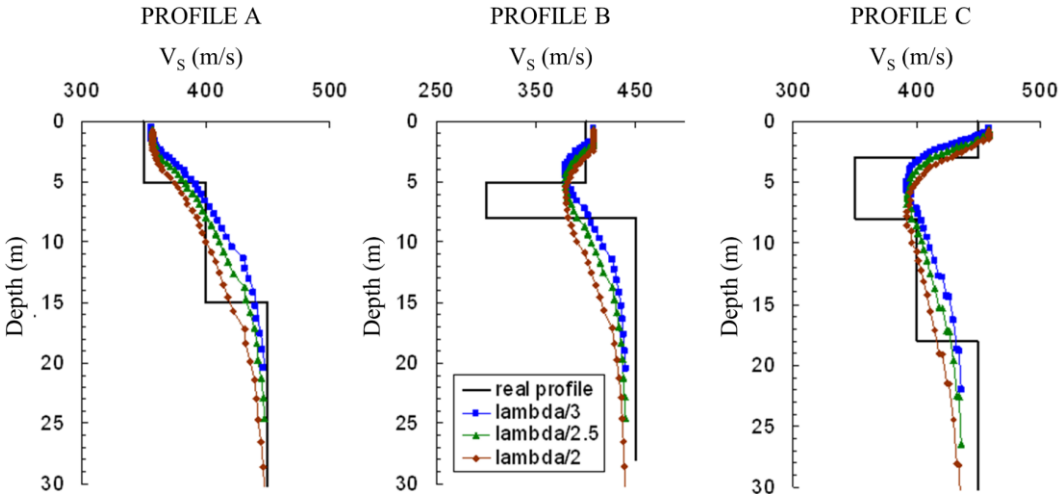

Figure 4.29. Example of the application of the pseudo-depth method for a first assessment of the Vs interval profile and/or a check of the obtained results after the inversion (after Foti (2000)).

The previous assumption on the pseudo-depth is based on the Rayleigh waves particle motion. Most R-wave vertical particle motion occurs over a depth approximately equal to one wavelength (Socco et al. 2010). Thus, the velocity of propagation is most influenced by the material within one wavelength of the surface, as demonstrated by Richart et al. (1970) and reported in Figure 4.30.

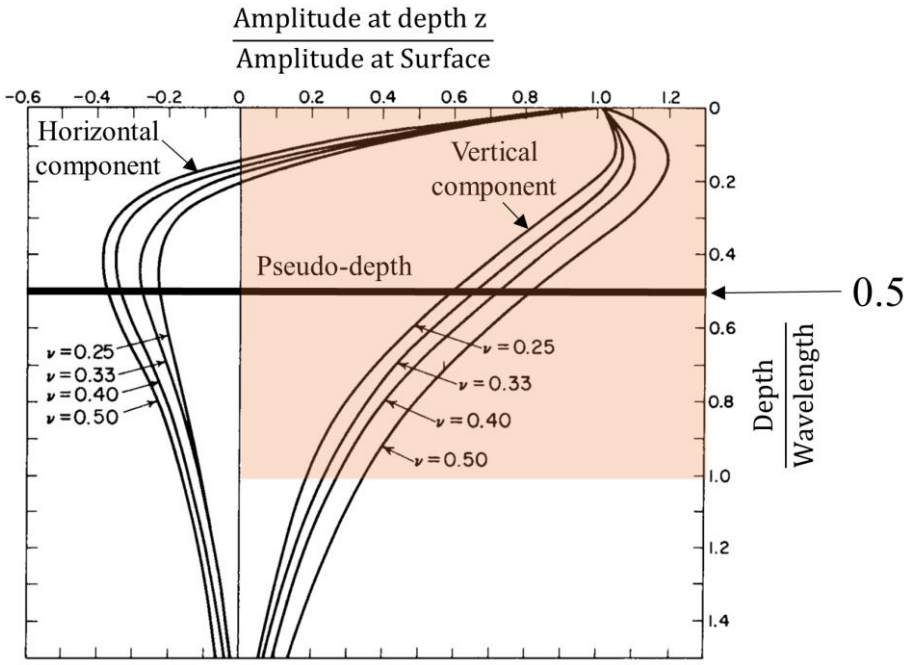

Figure 4.30. Rayleigh waves particle motion with depth and usually adopted pseudo-depth (i.e., equal to half the experimental wavelength) (modified from Richart et al. (1970)).

The experimental wavelength is also used to evaluate the resolvable minimum and maximum depth. A typical limitation provided in surface waves guidelines (Foti et al. 2018) and Table 4.2 is:

- $z_{min} > \lambda_{min}/2$
- $z_{max} < \lambda_{max}/2$ or $\lambda_{max}/3$

With the previous assumptions, it is possible to evaluate a first V_S interval profile trial for the inversion (or an area of possible solutions). At the same time, a critical inspection of the EDC can identify errors in the obtained/provided shear wave interval velocity profile. For example, from Figure 4.28, the analyst should immediately have an idea of the possible range of solutions. First, the minimum and maximum resolvable depths (with colored orange and red areas in Figure 4.28b-c) are

$$z_{min} = \frac{\lambda_{min}}{2} = \frac{1}{2} * \frac{115\frac{m}{s}}{\frac{24.7}{s}} = 2.3\ m$$

$$\frac{\lambda_{max}}{3} = \frac{1}{3} * \frac{811\frac{m}{s}}{\frac{0.97}{s}} = 279\ m \div z_{max} \div \frac{\lambda_{max}}{2} = \frac{1}{2} * \frac{811\frac{m}{s}}{\frac{0.97}{s}} = 418\ m$$

Then, the analyst can initially estimate an S-wave velocity for the shallower layer and the half-space (i.e., deeper resolvable layer)

$$V_{S,1} \cong 1.1 * 115\ \frac{m}{s} = 127\frac{m}{s}$$
$$V_{S,last} \cong 1.1 * 811\ \frac{m}{s} = 892\frac{m}{s}$$

Also, the shape of the EDC can provide further information and hints on the expected trends of the V_S velocity with depth. Dispersion curve with a smooth and continuous decrease of phase velocity for increasing frequency is typically associated with simple stratigraphic conditions (i.e., normally dispersive deposits). On the contrary, a definite kink or a flat zone (i.e., a region close to a local velocity minimum) usually suggests a velocity inversion at a specific depth (about the associated pseudo-depth). This is the result of two points with the same R-wave velocity, but different frequency/depth and a lower velocity in between.

Another preliminary analysis of the EDC can be conducted using the harmonic average shear wave velocity profile. The pseudo-depth, indeed, is an empirical relationship that allows estimating the interval shear wave velocity V_S at a specified depth (Figure 4.29). This assumption is based on the particle motion function with depth that roughly integrates a depth equal to one wavelength. Then, the measured velocity is associated with half of the pseudo-depth, for the interval velocity profile. However, the harmonic average shear wave velocity function with depth is, naturally, a parameter that integrates a velocity over a specified thickness. It represents the simplest, physical, description of a traveling wave since it is calculated as a distance (i.e., a thickness) over time (i.e., the travel time). If the analyst plots the Rayleigh wave velocity versus the wavelength and the $V_{S,Z}$ profile of the best solution (Figure 4.31a-b) a remarkable similarity can be observed, as

suggested in Socco et al. (2017) and proposed by Brown et al. (2000), Martin & Diehl (2004), and Albarello & Gargani (2010) for the estimation of the $V_{S,30}$. This is true also for velocity inversions (i.e., knees) that generates an inversion of the $V_{S,Z}$ curve. This topic will be further discussed later on. However, the reader should have clear in mind from this point the simple concept of harmonic average and the affinity with the EDC.

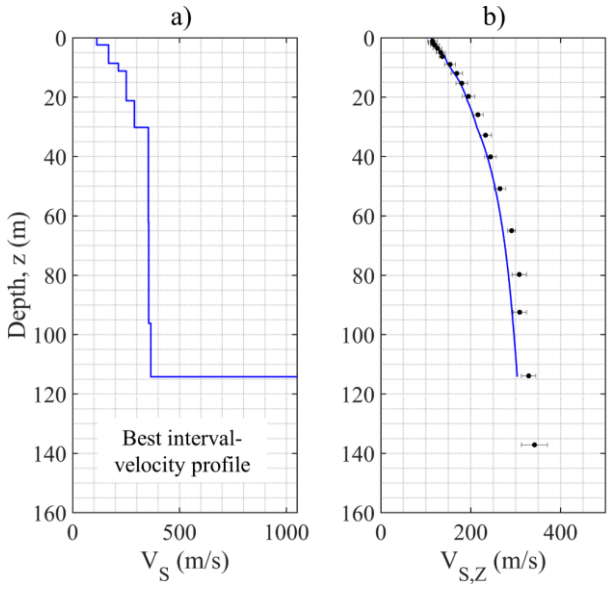

Figure 4.31. a) Best interval velocity profile, and b) comparison between the best solution $V_{S,Z}$ profile and the EDC at Mirandola (the University of Texas at Austin solution).

The experimental dispersion curve can be obtained through various dispersion processing techniques. Most of these techniques operate in the spectral domain, assuming a 1D medium below the array (i.e., horizontally stratified, velocity only varies with depth) and a plane wave propagation (i.e., the surface wave is fully developed) (Wielandt 1993).

For active-source tests (i.e., MASW tests), the most common method is the f-k transform that uses a double Fourier Transform to shift from the time (t) to the frequency (f) domain and from the space (x) to the wavenumber ($k=2\pi/\lambda$) domain. It is possible to demonstrate (Foti et al. 2014) that the velocity of Rayleigh waves is associated with a local maximum in the f-k spectrum for each propagation mode. Hence, the EDC can be extracted from the seismograms by picking the local maxima of the f-k spectrum. The searching area for each mode is selected after a visual inspection of the spectrum. It is essential to check the continuity for each branch (i.e., mode) of the EDC over a sufficiently broad frequency band. An example of an f-k spectrum obtained at the site of Accumoli (included in the PSWD) is given in Figure 4.32.

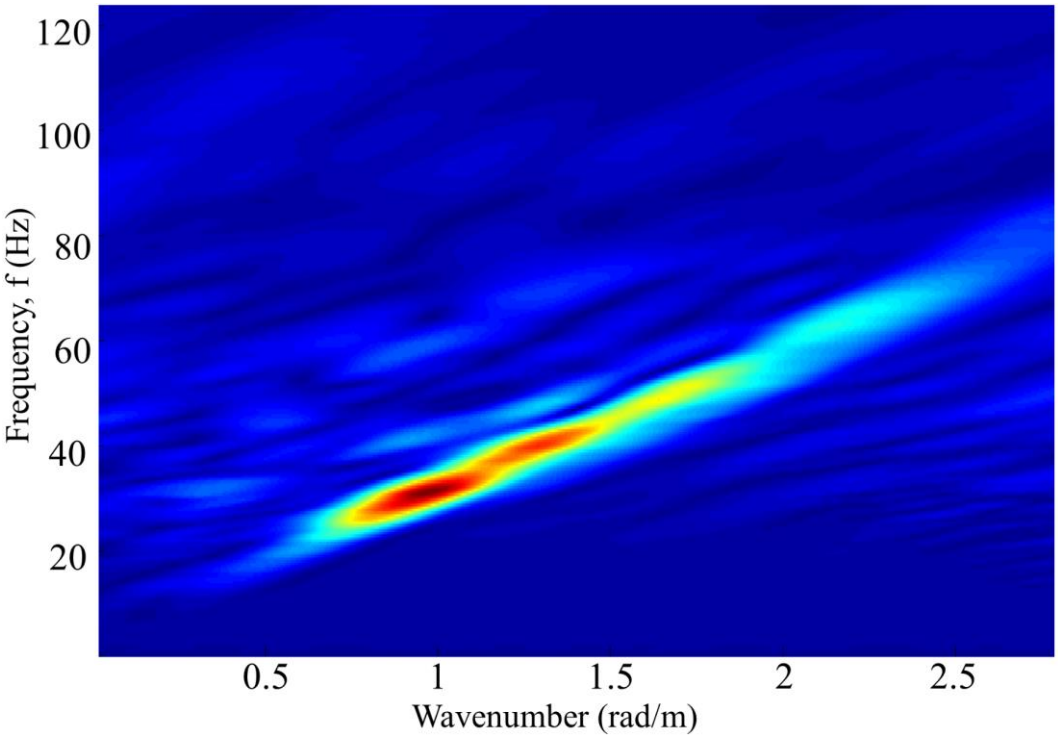

Figure 4.32. Example of an f-k spectrum obtained for one shot at the site of Accumoli, Italy.

Other approaches for the MASW data processing are:

- Frequency-domain beamformer (FDBF) (Lacoss et al. 1969);
- High-Resolution f-k approach (Capon 1969);
- Intercept-slowness Linear Radon transform (McMechan & Yedlin 1981);
- Phase-shift (Park et al. 1999);
- Frequency Decomposition and Slant Stack (Xia et al. 2007);
- High-Resolution Linear Radon Transform (Luo et al. 2008).

A collection of a statistical sample of EDCs is usually obtained by performing multiple shots at different locations and by using different sources for a single MASW test. This step of the analysis is mandatory, even if there is not yet any clear protocol internationally shared. When the statistical sample is available, it is also possible to quantify the data dispersion and identify associated EUs and AVs in V_R. It is recommended that the observed variability on the EDC always be reported with the results. This may be represented in the form of condensed statistical parameters, as seen in Figure 4.28. Data variability is a clear indicator of the reliability of the results and can be used for further assessments during the inversion. Moreover, the data quality control during the processing should be carried out. This consists of checking that the assumptions on which is based the applied method are valid, at least approximately (Foti et al. 2018).

In Foti et al. (2014), the typical errors for MASW tests were classified as coherent (i.e., deterministic) and incoherent (i.e., pseudorandom) noise (i.e., the part of the data that does not carry any useful information). For the authors, coherent noise is related to the experiment. It is deterministically reproducible and is

correlated to the signal. On the contrary, incoherent noise is often referred to in Foti et al. (2014) to as ambient noise, or random noise, even if it is statistically not random. Incoherent noise is not deterministically reproducible, it is not a source-generated effect, and it is not correlated with the signal.

In the present dissertation, most of the coherent and incoherent sources of noise are identified as epistemic uncertainty. However, the presence of lateral variations is included in the aleatory variabilities, as it can be quantified, but cannot be reduced by multiple test repetitions. In the following, the new classification of each source of uncertainty or variability is presented, along with the alternative distinction made in Foti et al. (2014).

One of the most influent sources of EUs for MASW tests is related to near-field effects (i.e., coherent noise). These effects are mainly due to body wave interference and/or cylindrical wavefront of Rayleigh waves near the source (or in case of nearby noise in passive acquisitions). Indeed, surface waves must propagate a certain distance relative to their wavelength before they fully develop and yield the correct phase velocity. Rayleigh waves can be regarded as plane waves only beyond a certain distance from the source (i.e., in the far-field) (Richart et al. 1970). Recording wavelengths that are not fully developed results in near-field effects, which usually result in an underestimation of the R-waves velocity. Using multiple source offsets helps to identify near-field effects and remove contaminated data.

Many studies in the literature attempted to provide practical guidelines to avoid the inclusion of near-field effects. (Zywicki 2007), Yoon & Rix (2009) found that for most soil profiles the error in phase velocity is less than 10% for

$$\lambda_{max} < \bar{x} \qquad \text{(Eq. 4.20)}$$

where $\bar{x}$ is the array center distance. Li & Rosenblad (2011) showed that for saturated soils (i.e., high Poisson's ratio) the maximum wavelength could be set to twice the array center distance. In reality, near-field effects are strongly site-dependent and difficult to predict and great care should be taken by the analyst not to include this contamination in the processing. In particular, the frequency-dependent nature (i.e., higher for low frequencies) of the near-field effects represents a further characteristic to be accounted for.

Body waves can show a significant influence also in the far-field and represent a further source of EU, identified as coherent noise in Foti et al. 2014. Body waves can propagate from the source to receivers with different paths. In shallow, small-scale tests, body wave amplitude is often much lower than the surface wave amplitude. They are superimposed onto each other in time-offset, but often they tend to map into different portions of the f-k spectrum. They can be easily identified and removed or ignored.

Along with the body waves, also the air blast detection can lead to undesired noise. It represents an EU, and it is identified as a coherent noise. In particular, the sound emitted by the hitting source sometimes couples with the ground, being detected by seismic receivers. The presence of a loud air blast is potentially troublesome in surface wave measurement because it may superimpose on the

Rayleigh wave signature. Indeed, the velocity of propagation in air may be very close to Rayleigh wave propagation. The air blast can be observed in time-offset, and it is identified in the f–k spectrum as a linear event, with constant velocity and very low attenuation, usually extending to high frequency.

Also, the incoherent noise can be identified as epistemic uncertainty. Incoherent noise can be the effect of the background vibrations at the site produced by natural and human sources: traffic, vibrating and moving machines, wind, and movements of surface or groundwater. It is often dominated by surface waves, which are, however, incoherent with respect to the experiment. They are generated by sources, the position and time of activation of which are unknown. On the contrary, these ambient vibrations represent the signal (i.e., the part of the data that carries useful information) for the AVA tests.

Increasing the SNR is a primary objective of the acquisition of a MASW test, and it can be achieved either by reducing the level of the noise or by increasing the level of the signal. Reducing the noise is sometimes possible. It can be done by acquiring data during quiet times (at night, the human noise is lower) or by using better equipment with a lower noise level. Careful execution of the field operations can reduce the incoherent noise. The meticulous deployment and ground coupling of the receivers including burying receivers, avoiding people and vehicle movements, and avoiding vibrations during the acquisition are essential practices for minimizing the incoherent noise. Increasing the signal level can be done by increasing the energy of the active-source. Possible strategies for increasing the signal level include using sources that are more powerful or combining different sources for different frequency ranges. An alternative approach is stacking more traces during the acquisition stage.

Once the typical epistemic uncertainties in the processing of a MASW test have been discussed, the identification and quantification of aleatory variability are presented in the following. According to the definitions in 2.2, the aleatory variability is a source of uncertainty that can be quantified but cannot be reduced. This definition applies to the presence of lateral variations in the soil deposit, which are classified as coherent noise by Foti et al. (2014). The acquired data are usually processed with the aim of extracting a 1D V_S model (i.e., no significant lateral variations of the seismic properties are expected and with the flat or mildly inclined surface), as discussed in the next sections about the inversion process. The propagation of Rayleigh waves is therefore assumed to be laterally homogeneous linear in time-offset and phase-offset. In this context, the effects of lateral variations can be considered as the primary source of aleatory/space variability.

This requirement should be considered when selecting the location of the test, avoiding known lithological boundaries but also trying to avoid the acquisition along the dip direction for expected dipping layers. For these reasons, the lateral variations influence on the obtained result cannot be reduced, because it is independent on the test. In general, it can be observed that the characteristics of the array are essential, as far as the risk of lateral variations is concerned. Indeed, different test setups (i.e., L, Δx, and the number of geophones, repeated shots at different positions using different sources) lead to different investigated volumes.

Then, the multiple setups allow investigating different portions of the deposit, and the different gathered EDCs are a good picture of the spatial/aleatory variability for the specific scale of the problem (Wood & Cox 2012, Stewart et al. 2014a). For example, the longer the array, the higher the chance of significant lateral variations. In addition to different processing techniques, a set of shorter arrays might be preferred for investigating sites where lateral variations are expected.

In Chapter 3, the quantification of aleatory variabilities in site response studies was related to the size of the investigated area (Stewart et al. 2014a). Also for surface wave testing, the scale of the problem predominantly controls the quantification of aleatory variability in the EDC that is mainly due to lateral variations. Then, in practice, the identification of lateral variations is an essential step of processing and can be done by comparison of information extracted from different portions of the array. In particular, shots at both the sides of the array are mandatory for assessing the 1D geometry (i.e., no lateral variations) of the investigated deposit.

A summary of the EUs and AVs that can be identified and quantified during the processing of MASW data is given in Figure 4.33.

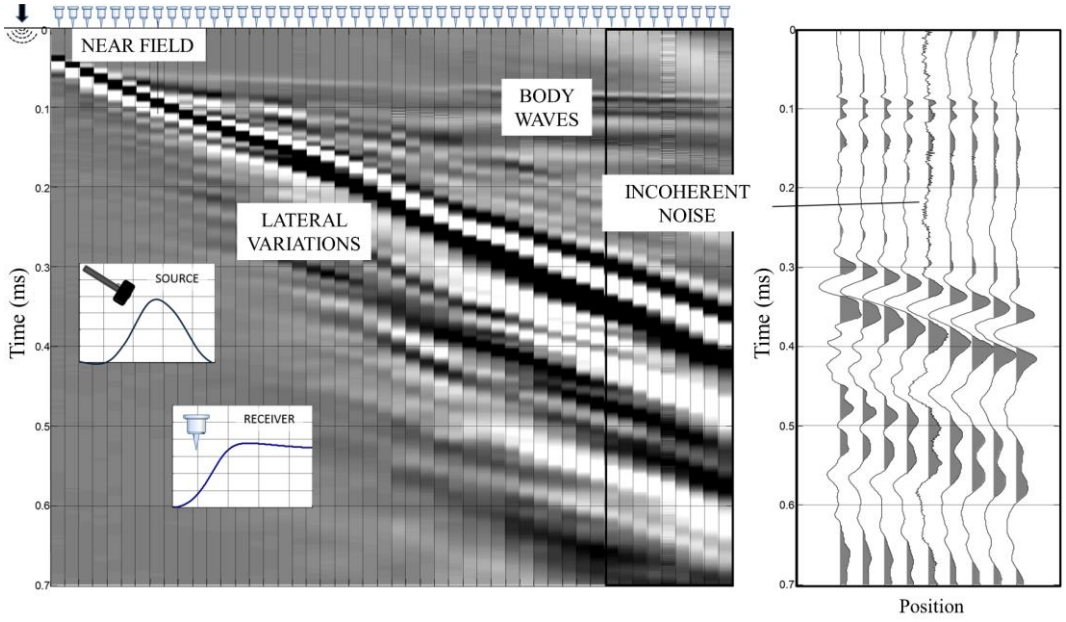

Figure 4.33. Primary sources of epistemic uncertainties and aleatory variabilities identifiable during the MASW processing stage (after Foti et al. (2014)).

For passive-source tests (i.e., AVA tests), data processing techniques usually derive the dispersion characteristics from statistics computed on a large number of small time windows extracted from the long duration recorded signals. The EDC can be obtained by frequency-wavenumber techniques (similarly to MASW tests) or spatial auto-correlation (SPAC) techniques. For f-k methods, high-resolution methods include the high-resolution f-k (HFK), the maximum entropy, and MUSIC. Spatial auto-correlation methods include ESAC, MSPAC, MMSPAC, krSPAC and other approaches (Bettig et al. 2001). For further details, the reader can refer to Okada (2009) and Foti et al. (2014). Generally, for f-k methods, any array shape

may be used. However, the array response should be considered. Indeed, the k_{min} and k_{max} at low frequencies are essential experimental parameters of the method, as computations are performed in the wavenumber domain. Frequency-wavenumber methods are best applied for highly directional energies and can separate modes by distinguishing multiple phase velocities at a single frequency (as discussed for active-source methods). On the contrary, SPAC methods strongly benefit from regular arrays (e.g., circles or triangles, Figure 4.27c). They are mostly applicable at locations where the impinging energy is well azimuthally distributed. As for f-k methods, they are limited at low frequencies by the array aperture, but are not as sensitive to the array response as f-k methods since the computations do not involve wavenumber domain. In this case, the multiple phase velocity at a single frequency are not allowed, and therefore the analyst can mix the modes together. In light of the previous discussion, it is recommended that both f-k and SPAC methods be performed contemporaneously to mitigate the weaknesses of each method.

An example of the application of the HFK method is given in Figure 4.34 for two different couples of frequencies and wavenumbers. The theoretical approach is similar to the f-k method applied for active tests. In this case, however, the evaluation of the predominant direction of the ambient vibration is fundamental, and then the R-wave velocity is obtained as

$$V_R = f\frac{2\pi}{k} \qquad \text{(Eq. 4.21)}$$

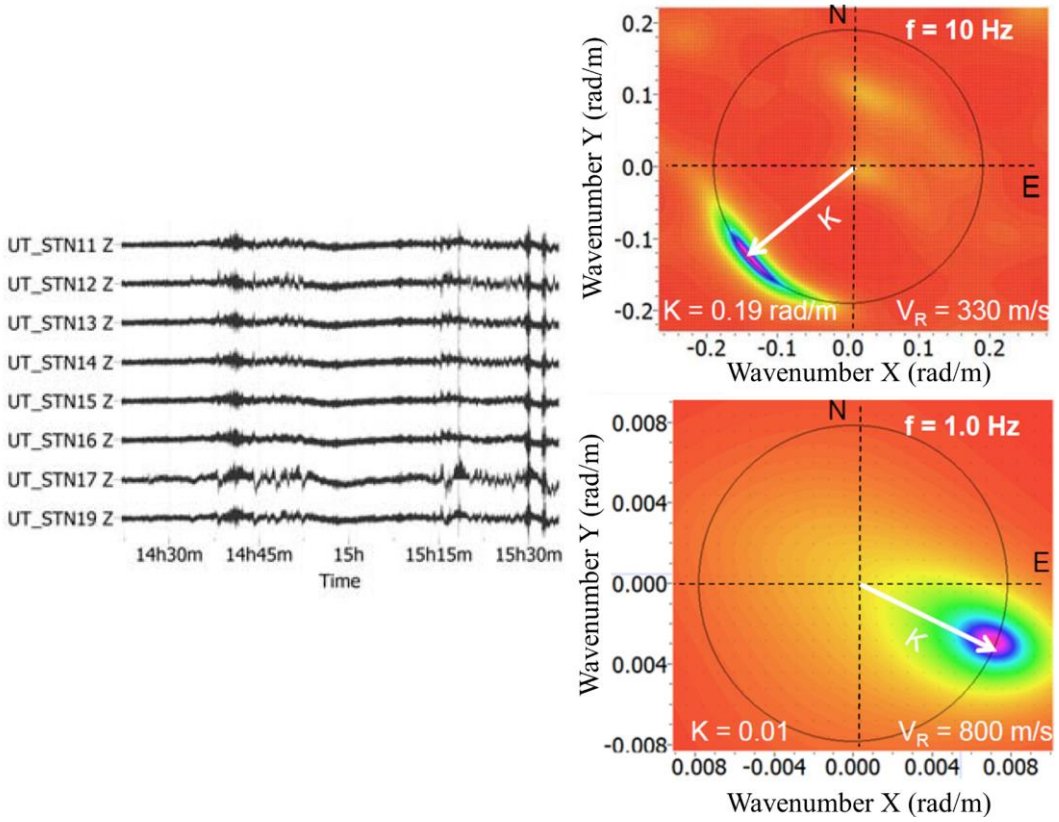

Figure 4.34. Example of acquired 8-sensor ambient vibrations and estimation of the R-wave velocity by HFK method (courtesy of Prof. Brady R. Cox).

The identification and quantification of EUs and AVs are mandatory also for passive tests. Differently from MASW tests, now the EDCs are most often obtained by averaging the dispersion estimates from the various time blocks. Such uncertainties are related to time variation of ambient vibration wavefield properties, in relation with the array capability to separate simultaneous propagating waves across the array, with the lateral variation of the subsurface, and with near-field effects (Foti et al. 2018).

An important source of EU for both MASW and AVA tests regards the presence of higher modes in the recorded data (i.e., coherent noise) (Figure 4.35). The Rayleigh wave propagation is a multimodal phenomenon. The energy can jump from the fundamental mode to higher modes (i.e., "mode kissing", Gao et al. (2016)), leading to an apparent dispersion curve (Bergamo et al. 2011). Indeed, the energy distribution is a frequency dependent phenomenon: a mode can be actively dominating within a specific frequency band, while negligible in other frequency bands. Many factors control the energy distribution: primarily the site-specific (3D) velocity and attenuation characteristics, in combination with the source type, location, and coupling with the ground.

For typical stratigraphic conditions, the propagation is dominated by the fundamental mode, as it typically happens in media characterized by a gradual increase of shear wave velocity with depth (i.e., normally dispersive).

In some cases, however, mainly where extreme velocity contrasts exist between layers at shallow depths (e.g., the contact between low-velocity sediments and bedrock, typical of class A and E deposits for EC8), or where a low-velocity layer exists between two high-velocity layers (i.e., inversely dispersive media), higher modes may be excited and need to be considered in the inversion analyses (Bergamo et al. 2011). Generally, the EDC shows a jump at low frequencies if the bedrock has a significant stiffness, whereas the jump is located at high frequencies if there is a stiff and shallow layer (e.g., pavement) (Maraschini et al. 2010).

Other reasons for an ''apparent'' mode superposition (i.e., modes are theoretically separated but cannot be distinguished by the operator) may be related to other factors related to the acquisition geometry (e.g., lack of spatial resolution). The energy may move from one mode to the other at particular frequencies where two continuous modes have similar velocities, called osculation frequencies (even if they also depend on the profile). Also for this reason, an expert user should perform a rigorous check of the EDC continuity, and fully automatic procedures for the analysis are difficult to implement in practice.

If the EDC shows a mode higher than the fundamental, it is then the result of the superposition of different propagation modes that could not be distinguished (i.e., apparent or effective dispersion curve). For these conditions, the spectrum is not only dominated by a single energy maximum for each frequency, but more than one local maximum can be found for a specific wavenumber (i.e., same frequency propagating at different velocities). The misidentifying higher modes as the fundamental mode causes severe errors in the inverted V_S profile (Tokimatsu et al. 1992b, Zhang & Chan 2003). Several methods have been proposed in the literature to account for higher modes, but the procedures are still not standardized and are

not implemented in most commercial codes. However, the use of multiple source offsets for MASW tests and specific processing technique for AVA tests helps to manage mode segregation and mode misidentification. Moreover, if correctly identified, higher modes represent useful information. They only become EU when the acquisition, processing, or inversion techniques are not able to deal appropriately with them (Maraschini et al. 2010).

Electric or electronic noise in receivers and cables and the acquisition system are types of incoherent noise (i.e., EU) both for MASW and AVA tests. This noise may be generated by power lines and other external sources and by imperfections in the recording system.

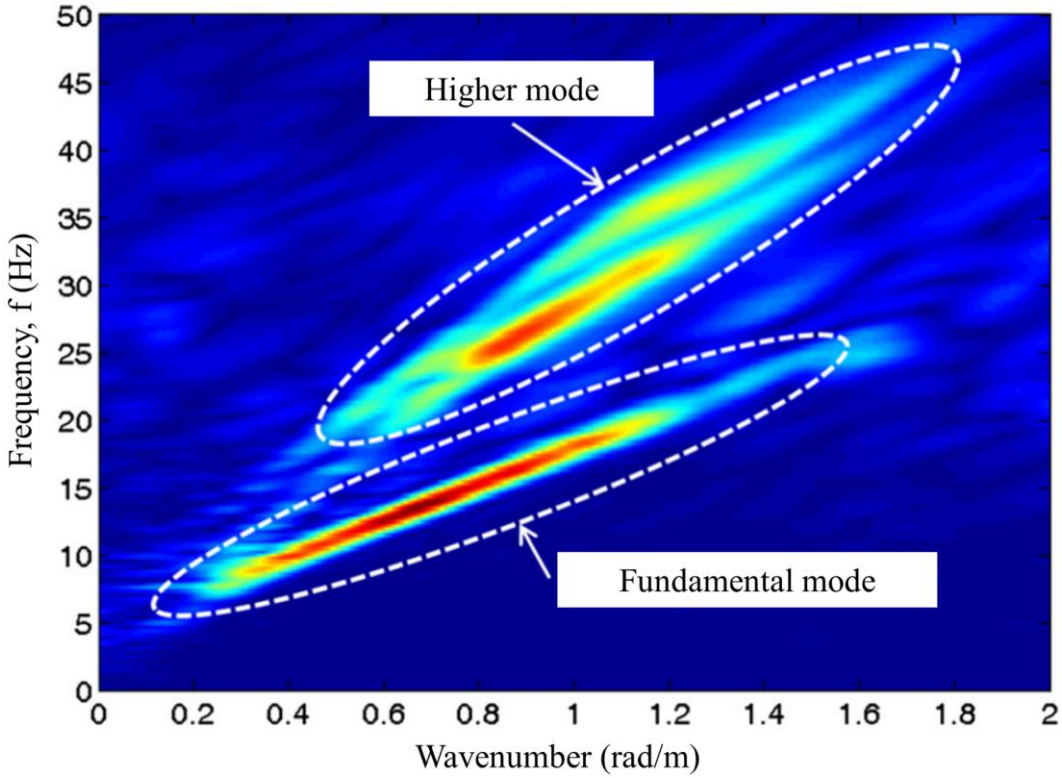

Figure 4.35. Example of an f-k spectrum with clear evidence of a higher mode identification (after Foti et al. (2018)).

Various studies in the literature attempted to quantify the EUs and AVs associated with the EDC. For SASW methods, Marosi & Hiltunen (2004), showed experimental values of the Coefficient Of Variation (COV) for V_R typically around 1.5%. They also found that samples were normally distributed for frequencies in the range 20–150 Hz. O'Neill (2004) analyzed numerical simulations and experimental results. He found that the COVs for Rayleigh wave phase velocities increase nonlinearly for decreasing frequencies (i.e., from 1% to around 30%) and proposed a Lorentzian distribution for the low-frequency range. The author also showed a strong dependence of the test repeatability on the length of the acquisition array.

This topic was then extensively discussed by Lai et al. (2005). The objective of their study was to determine how the uncertainty of the experimental data is mapped into the uncertainty of S-wave interval profiles. They showed that the EDC could

be subdivided in a low-frequency zone with higher uncertainties and a high-frequency zone with lower uncertainties, as expected. This is the result of the natural loss of resolution of the Rayleigh waves with depth and the experimental challenges for low-frequency waves generation. They also confirmed the findings in Marosi & Hiltunen (2004) showing a normal distribution of the R-wave velocity, as illustrated in Figure 4.36a. Further confirmation was obtained using a chi-square test application (Figure 4.36b).

More recently, Olafsdottir et al. (2018) corroborated the previous studies about the normal distribution of the R-wave velocity for an example dataset in South Iceland (Figure 4.36c-d) using the probabilistic theories illustrated by Shapiro & Wilk (1965) and Ross (2014).

For each study, however, precise identification of the contribution of EU and AV within the total standard deviation (or COV) is not straightforward. The influence of both EUs and AVs uncontrollably converges into the measured EDC.

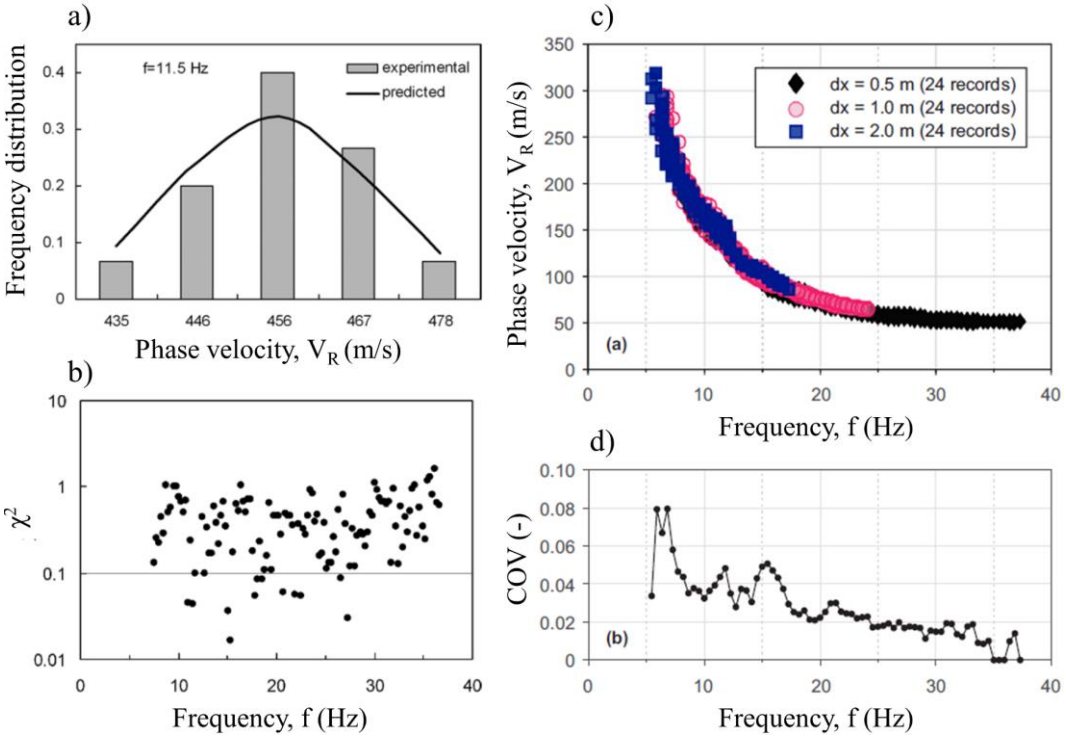

Figure 4.36. Epistemic uncertainties and aleatory variabilities converged in the EDC for active-source tests. a) Normal histogram of V_R for a fixed frequency (after Lai et al. (2005)), b) application of the chi-square test for the Normal assumption (after Lai et al. (2005)), c) example dataset of different measured EDCs in South Iceland (after Olafsdottir et al. (2018)), and d) calculated COV (after Olafsdottir et al. (2018)).

Inversion

The inversion process is the "last chapter of our story" (Socco & Strobbia 2004). In this stage, the model parameter identification problem is solved by using the EDC as a target. Indeed, this step allows obtaining the resulted interval V_S

velocity profile from the assumption of linear elastic and isotropic medium adopting a proper definition of the misfit function that is minimized in the inversion.

In geophysics, the term inversion means the *"estimation of the parameters of a postulated earth model from a set of observations"* (Lines & Treitel 1984). The requirements for the inversion are derived directly from the properties of the final result that can be summarized in the following statement: "*the result should be a unique subsoil model with adequate reliability and resolution down to the depth of interest and should be presented with the associated uncertainties"* (Socco & Strobbia 2004).

All inverse problems are ill-posed (Foti et al. 2014), which is perhaps their most relevant feature if compared with the well-posedness of the corresponding forward problems (Engl et al. 1996, Kirsch 2011). According to Hadamard (1923), a mathematical problem is defined as well-posed if it satisfies the following three conditions:

- For all admissible data, a solution exists (existence);
- For all admissible data, the solution is unique (uniqueness);
- The solution depends continuously on the data (stability).

If any of these three conditions fail to hold, Hadamard called the problem ill-posed. In inverse problems like in surface wave testing, the two conditions that are most often violated are uniqueness and stability.

A straightforward example of the inverse problem is a one-sided equation

$$? = 9$$

that can show an infinite number of left-hand side combinations that equally satisfy the mathematical problem (6+3, 12-3, 27/3, 3^2, 81^0.5). Another example drawn from structural engineering is that of a loaded, elastic beam. Although for a given loading configuration a unique deflected shape of the beam can be predicted (forward problem), the same deflected shape may be obtained from different loading patterns. Hence, the problem of determining the load configuration corresponding to a deflected shape (inverse problem) is ill-posed because the solution is not unique.

For surface wave inverse problems, non-uniqueness implies that a given EDC may correspond to more than one shear wave interval velocity profile of the soil deposit. Therefore, a single best-fitting profile is not generally an adequate representation of the solution because it does not provide an assessment of the uncertainties due to input data and inversion procedure. From a mathematical point of view, non-uniqueness of the solution of an inverse problem is caused by a lack of sufficient information to constrain the solution. Indeed, any a-priori information from other independent tests (e.g., seismic refraction and reflection, horizontal to vertical spectral ratio method, and/or electric tomography) or geological surveys with borehole data helps to constrain the inverse problem (Brown et al. 2002, Foti & Strobbia 2002, Socco et al. 2009, Cox & Teague 2016, Teague et al. 2017, Foti

& Passeri 2018). The constraint of the inversion can be obtained by reducing the variability of a specific parameter in the inversion or by performing a joint inversion (Comina et al. 2002, Foti et al. 2003, Comina et al. 2004, Arai & Tokimatsu 2005, Parolai et al. 2005, Piatti et al. 2013a, Piatti et al. 2013b). The joint inversion of independent geophysical and/or geotechnical measurements generally combines synergies of each test and provides more realistic estimations of the V_S profile.

Besides the ill-posedness of the inversion process, this operation is affected by other challenges. The inversion is a nonlinear problem, as the relationship between the data space (i.e., V_R-f) and the model space (i.e., V_S-z) is strongly nonlinear. Then, surface wave inverse problems are mixed-determined, as the model solution for deeper layers is dependent on the model solution for shallower layers (Socco & Strobbia 2004).

For the previous characteristics (i.e., ill-posedness, nonlinearity and mixed-determination) of the inversion process, it is strongly recommended that the solution is provided in conjunction with clear identification and quantification of the resulted EUs and AVs. These can be represented as an estimated bound on the best solution (Lai et al. 2005) or preferably as a set of equivalent solutions (Socco et al. 2010, Comina et al. 2011).

In the processing section, the initial information that can be inferred from the EDC were discussed. In particular, a rough initial V_S model can be defined for starting surface wave inversion (Figure 4.29) from the pseudo-depth and assuming approximately $V_S = 1.1V_R$. An example of this procedure is also given in Foti et al. (2018) and in Figure 4.37.

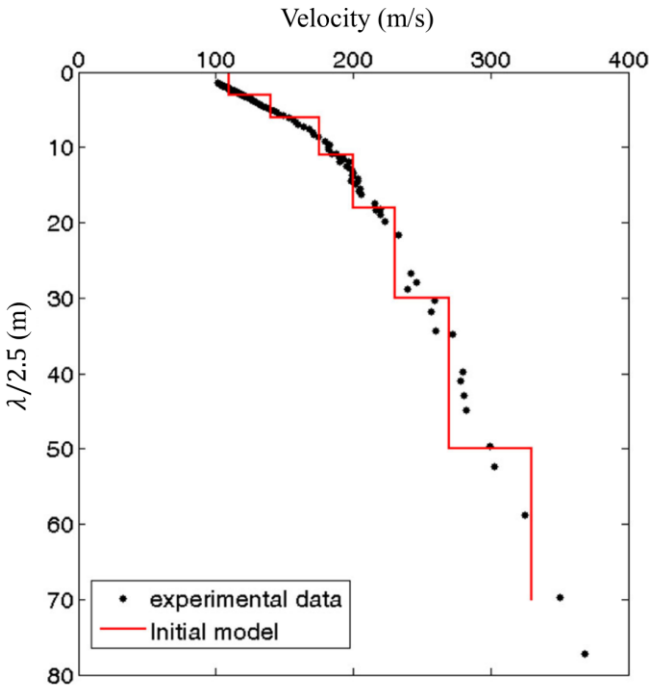

Figure 4.37. Approximated method to evaluate an initial model for the inversion process (after Foti et al. (2018)).

The inversion approach for surface wave testing can be summarized in four steps:

1) Assumption of a system of linear elastic layers stacked over a half-space. Each layer has a specific thickness H, a density ρ, a stiffness G (i.e., an interval velocity V_S) and a Poisson's ratio ν (or, alternatively, an interval velocity V_P);
2) Calculation of the Theoretical Dispersion Curve (TDC) associated with the system in 1) (i.e., forward problem);
3) Comparison of the TDC to the EDC acquired in the field and processed (i.e., definition of a misfit function);
4) Revision of the system parameters until a satisfactory fit is achieved (i.e., backward problem).

The first point regards the parametrization choice and leads to the scheme of interval velocity for V_S, as the central assumption is the horizontal and parallel (i.e., 1D) layers (Cox & Teague 2016). The analyst attempts to recover four model parameters for each layer (H, ρ, G, and ν) indirectly from data parameters in the EDC (V_R and f) (i.e., lack of constrains) (Foti & Strobbia 2002). Evidences in the literature demonstrated that G and H have the most influence on the TDC (Nazarian 1984). For this reason, the density and the Poisson's ratio (i.e., V_P) are usually assumed a-priori. As an alternative, also the Poisson's ratio can be varied during the inversion, limited to reasonable bounds and allowing a further degree of freedom in the problem. This last strategy, adopted in the present dissertation, has the great advantage to prevent the occurrence of physically unrealistic V_P-V_S pairs and to verify the in situ saturation conditions. In this context, it is important to know the transition depth between unsaturated and saturated soil. Indeed, for the saturated conditions, the behavior of the porous medium is controlled by the condition of absence of relative motion between phase solid and fluid phase (i.e., undrained conditions, low frequency formulation) (Biot 1956a, Biot 1956b, Miura et al. 2001). The consequences of an incorrect choice of the Poisson's ratio can be very relevant, as shown for example by Foti & Strobbia (2002) and Brown et al. (2002). In particular, Foti & Strobbia (2002) concluded that the position of the water-table is a crucial information to be accounted for during the inversion.

Moreover, the choice of the layering parameterization (i.e., number of layers) has a significant impact on the ability to recover the "true" layered model and represents the fifth model parameter (Cox & Teague 2016). The analyst should avoid an over-parametrization that leads to an unreliable final model (i.e., over-determined inversion due to the lack of constraints). On the contrary, the number of layers should be sufficient to reproduce the variation with depth, especially for the shallower portions of the deposit. An interesting alternative to the stack of discrete layers (i.e., interval velocities) is given by Rix & Lai (2007). The authors proposed to use a vertically heterogeneous model with continuously variable parameters with depth. This approach presents considerable engineering interest for the characterization of homogeneous coarse-grained materials where the V_S varies with confining stress (Santamarina et al. 2005).

The forward problem can be solved, under the previous assumptions, with a transfer matrix method (Thomson 1950, Haskell 1953, Knopoff 1964, Dunkin

1965, Press et al. 1992). Alternatively, other approaches like the dynamic stiffness matrix (Kausel & Roesset 1981, Kausel & Peek 1982) can be used. Moreover, multimodal inversion can also be performed. In these cases, the forward problem is solved not only for the fundamental mode but also higher modes are accounted for in the calculations (Maraschini & Foti 2010). In this case, the final solution is more robust and also the investigation depth can be increased (Passeri et al. 2018a). However, these types of inversions usually require particular expertise and efficient algorithms, especially in the case of stochastic analyses and the definition of a robust misfit function (Maraschini et al. 2010).

For each solution of the forward problem, the goodness-of-fit (i.e., TDC-EDC) of the chosen model is evaluated by a misfit function. Various misfit functions that calculate an overall/average misfit between the TDC and the EDC are presented in the literature. The most used was proposed by Wathelet et al. (2004) and written here as modified by Socco & Boiero (2008) and used in this dissertation

$$M = \left(\sum_{i=1}^{k} \frac{\left(V_{R,i} - \overline{V_{R,i}} \right)^2}{\sigma_{V_{R,i}}^2} \right) \sim \chi^2 \qquad \text{(Eq. 4.22)}$$

where k is the number of points in the EDC, $V_{R,i}$ is the R-wave velocity of the TDC corresponding to the experimental point at frequency i, $\overline{V_{R,i}}$ is the R-wave velocity of the EDC corresponding to the experimental point at frequency i, and $\sigma_{V_{R,i}}^2$ is the variance of the R-wave velocity at frequency i (as presented also in Figure 4.28a). This misfit function is similar to a RMS error, where the difference at each data point is normalized by the standard deviation. Misfit values less than one indicate that on average the theoretical dispersion curve is within one standard deviation of the experimental dispersion data across the entire frequency bandwidth. Furthermore, it can be demonstrated that M follows a chi-square distribution defined as the sum of the square of standard normal random variables.

The points 2) and 3) are usually repeated until a stable response is obtained (i.e., backward problem). Many optimization methods are usually adopted in this step and are classified as local search methods (LSM) and global search methods (GSM).

Local search methods use linearized and non-linearized least square algorithms. The search starts with an initial model (Figure 4.37) and iteratively changes it trying to reduce the misfit while only considering the immediate previous model. In this case, generally, only one single, "best" (sometimes calling it best is something oxymoronic) is retained after the inversion. Moreover, these methods are by far the most common in commercial software, even if they can be stuck in local minima (i.e., the fundamental importance of the starting model). Figure 4.38 shows an example of increasing degrees of complexity that may be encountered in solving nonlinear inverse problems, from a single, well-defined global minimum (Figure 4.38a) to a "flat bottom" with an uncountable, finite range of solutions (Figure 4.38d) (Foti et al. 2014).

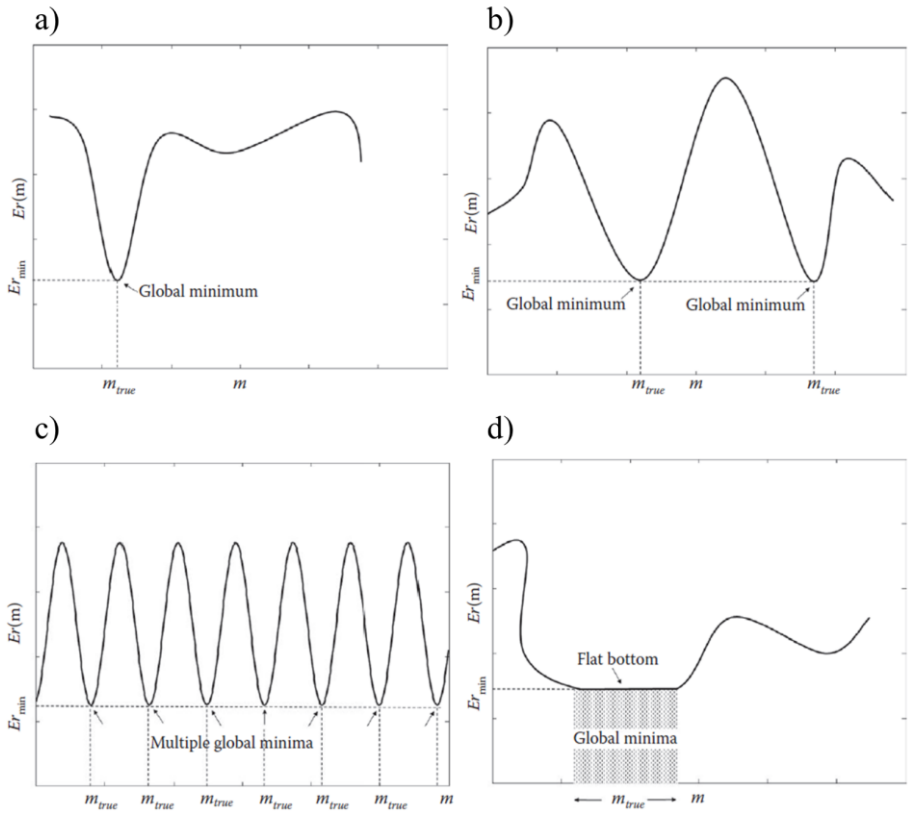

Figure 4.38. Prediction error as a function of a model parameter in the solution of a least-squares nonlinear inverse problem. (a) Well-defined single minimum corresponding to a unique solution. (b) Two well-separated minima with lack of uniqueness in the solution. (c) Infinite well-separated countable minima with severe lack of uniqueness in the solution due to the periodicity of the prediction error function. (d) "Flat bottom" having an uncountable finite range of solutions with severe lack of uniqueness due to ill-conditioning of the prediction error function (after Foti et al. (2014)).

Global search methods can be based on Monte Carlo algorithms (random search or improved Monte Carlo) or directed random search methods (e.g., generic algorithm, simulated annealing, and neighborhood algorithm). This class of methods generally avoids problems of local minima, and a suite of "equally good" models is retained by the stochastic method. Indeed, the resulted "best solution" (i.e., lowest misfit) obtained by the misfit function cannot be assumed as unique, leading to the well-known geophysical equivalence (Foti et al. 2009). This equivalence generates a statistical sample of V_S profiles selected to be equally corresponding to the experimental evidence, managing both EUs and AVs in the entire process. This sample represents a "picture" of the possible solutions of the surface wave test and should be used in ground response analyses performing multiple calculations (Socco et al. 2010, Comina et al. 2011).

In this dissertation, the equivalent profiles are obtained by applying a one-tail statistical test to the function of the ratio between the best misfit ($M_{min} = M_1$) and the misfit of the n-realization (M_n) of the improved Monte Carlo algorithm (Socco & Boiero 2008, Foti et al. 2009, Comina et al. 2011). Indeed, it is possible to demonstrate that this ratio follows a Fisher distribution

$$\frac{M_{min}}{M_n} = \frac{M_1}{M_n} \sim \frac{\chi^2_{min}}{\chi^2_n} = \frac{\chi^2_1}{\chi^2_n} > F_{\alpha}(\alpha, \kappa, \kappa) \qquad \text{(Eq. 4.23)}$$

where $M_{min} = M_1$ is the lowest misfit found with the Monte Carlo algorithm, M_n is the misfit of the n-generated-model, α is the level of confidence of the statistical test, and κ are the degrees of freedom of the statistical test. The chosen level of confidence α is 0,01 (Foti et al. 2009, Comina et al. 2011) and degrees of freedom equal to k (number of points of the experimental dispersion curve). Figure 4.39 shows an example of a Fisher distribution Probability Density Function (PDF) and the acceptance area defining the statistically equivalent sample of Vs profiles.

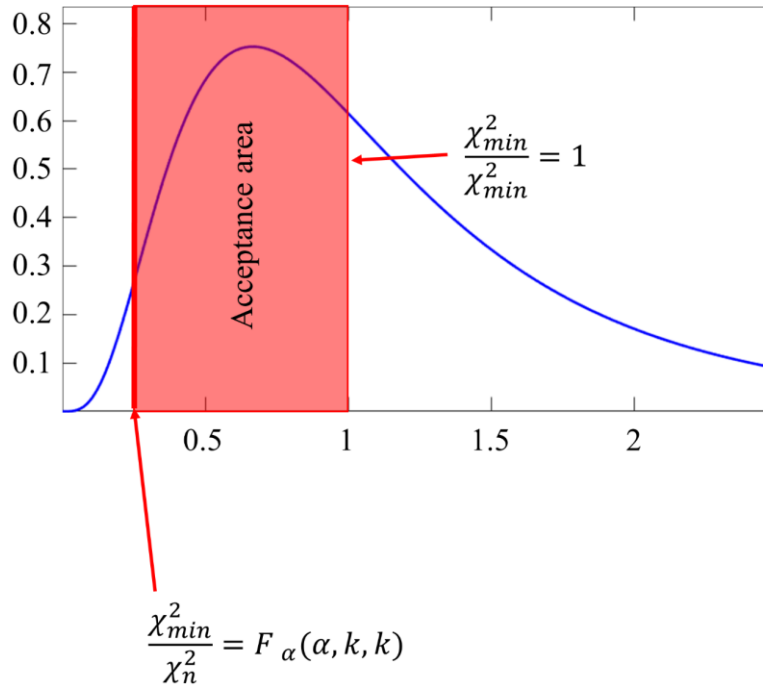

Figure 4.39. Probability density function of the Fisher distribution and example of the application of the one-tail statistical test to obtain the statistical sample of Vs profiles.

An example of the geophysical equivalence obtained after the application of the statistical test is provided for the case study of Accumoli, San Francesco square (WGS84 latitude 42.694° N, longitude 13.249° E). This site is part of the PSWD (Polito Shear Wave velocities Database) that will be presented in the next Chapter. Accumoli was investigated for the microzonation of central Italy and was severely struck by the seismic sequence that started on August 2016 and continued until October of the same year (Martino et al. 2017, Sextos et al. 2017, Stewart et al. 2017). At the end of the seismic sequence, Accumoli was almost entirely destroyed, as illustrated in the high-quality drone picture taken by the Geomatics team of the Politecnico di Torino (Figure 4.40).

Figure 4.40. High-quality drone picture of Accumoli (16-12-2016).

The site is located on a steep hill, and it is mainly composed of shallow (around 6 m depth) fractured sandstones with a pseudo-vertical stratification. The shallower layers show silty sand (0.5-3 m depth) followed by dense sand (3-6 m depth) layers as presented in Figure 4.41.

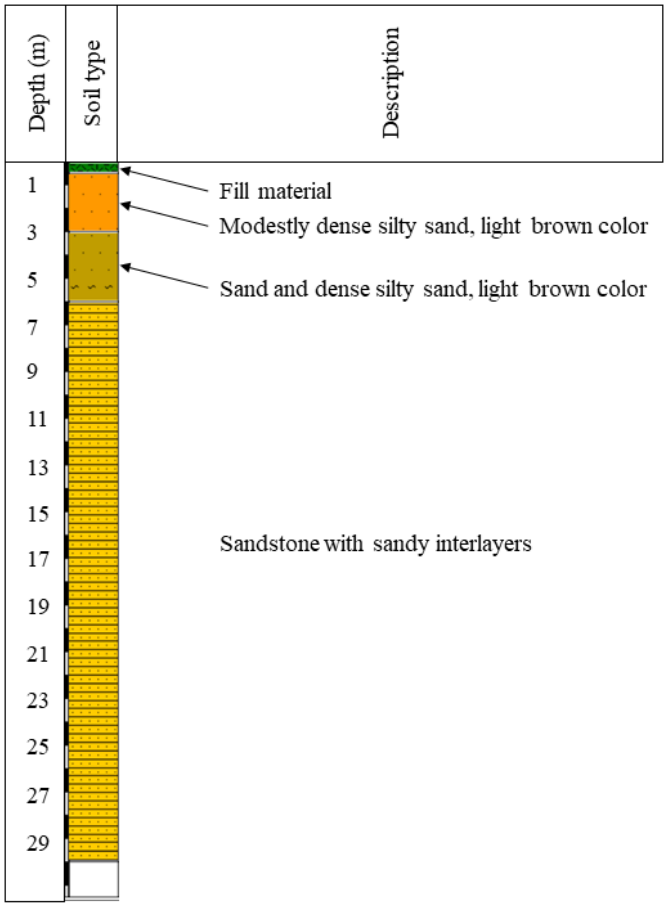

Figure 4.41. Borehole information of the site of Accumoli, San Francesco Square.

The geophysical survey was conducted on September 2016 and consisted of a MASW array of 24 geophones (SENSOR-SM-6/U-B, 4.5 Hz) with a 2 m spacing (i.e., 46 m) (Figure 4.40). The used equipment was a Geometrics 24 channel Geode Seismograph and an 8 kg sledgehammer impinging on the pavement. The space limitations and limited safety conditions did not allow the use of a larger setup.

Different shots from both the directions were repeated and stacked during the processing of the acquired data. An example of a good-quality f-k spectrum processed is given in Figure 4.32. The processing did not show any influence of higher modes. The EDC was obtained along with the V_R standard deviation for each frequency. These standard deviations can be assumed as a global estimation of the EUs and AVs identified and quantified at the site.

The inversion process followed a systematic and smart two-step approach that will be presented in the next Chapter. In general, this method is based on an improved Monte Carlo algorithm with a TDC scaling (Socco & Boiero 2008). In the first round, an initial statistical sample of the possible solutions is investigated using 200000 theoretical profiles for each inversion. The inversions are performed varying all parameters, except for the material density. These guidance inversions allow a rigorous assessment of the initial best model parameters (i.e., H, G, and ν). Then, an ad-hoc geostatistical model is used in combination with the lowest misfit solution obtained after the first stage. In this second round, the possible space of solutions is further investigated by an improved Monte Carlo inversion with 200000 samples and a variable number of layers (i.e., the fifth parameter often neglected in the inversion, Cox and Teague 2016). The results of the inversion are showed in Figure 4.42a as interval velocity profiles (in red the minimum misfit profile). Figure 4.42b shows the corresponding harmonic average shear wave velocity profiles (in red the minimum misfit). Figure 4.42b suggests that the geophysical equivalence should be evaluated on the harmonic average shear wave velocity profiles (Comina et al. 2011). Indeed, the results variability in Figure 4.42a is affected by the assumption of constant velocity within the layer (i.e., engineering schematization). Figure 4.42 suggests that the problem's statistics should be computed on the harmonic average profiles, as the interval velocity mean and standard deviation has no physical relevance (Passeri et al. 2019). On the contrary, the $V_{S,Z}$ (or, alternatively, the cumulated travel time) overcomes the choice of the layering giving a result that is more consistent with the physics of the wave propagation process. Moreover, the $V_{S,Z}$ shows similarities with the EDC, especially for the mixed-determination of the solution. Indeed, as V_R at a wavelength depends on the V_R of shorter wavelength, also the $V_{S,Z}$ at a specific depth depends on the $V_{S,Z}$ above (i.e., due to the cumulated travel-time).

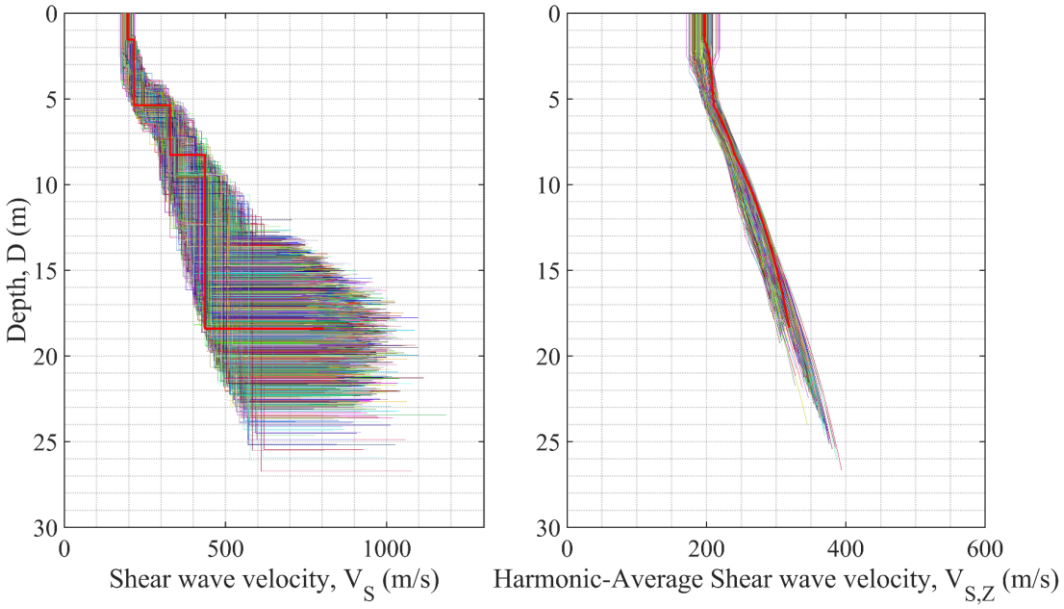

Figure 4.42. Results of the inversion for the site of Accumoli, San Francesco square. a) Statistical sample of the interval velocity shear wave profiles, and b) statistical sample of the harmonic average shear wave velocity profiles.

The TDC-EDC comparison in Figure 4.43 guarantees the geophysical equivalence (in red the minimum misfit and in black the EDC with the associated standard deviation). In this case, the statistical test selected 12512 profiles of 400000 with a misfit ranging from $M_1 = 0.0343$ and $M_{12512} = 0.0776$.

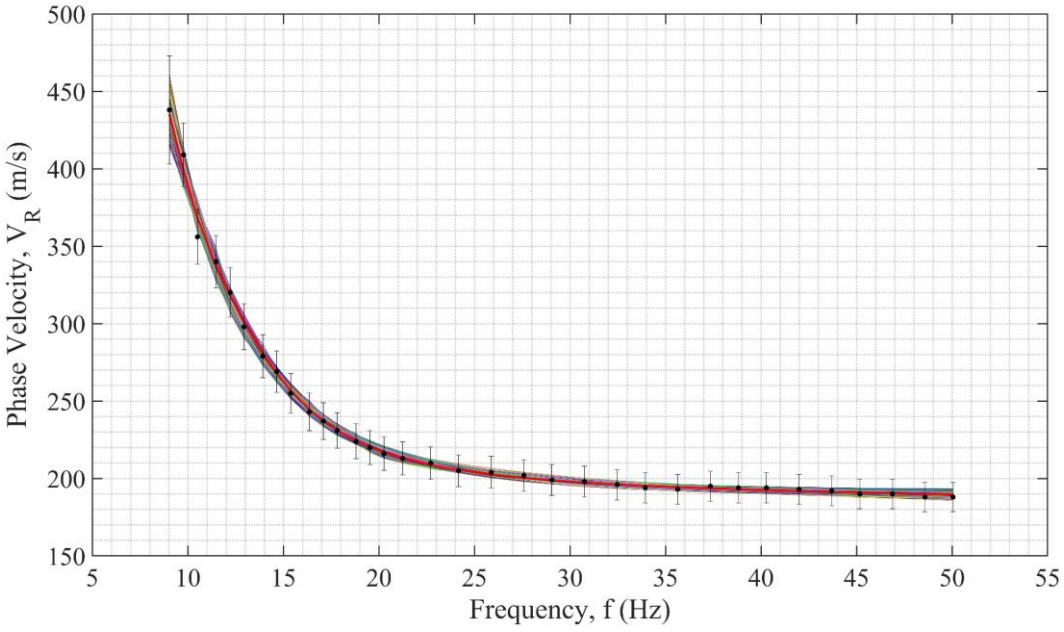

Figure 4.43. Results of the inversion for the site of Accumoli, San Francesco square (PSWD). Comparison between the experimental dispersion curve (in black with its standard deviation) and 12512 theoretical dispersion curves selected by the statistical test over 400000 initial models.

4.2.2.3 Horizontal to Vertical Spectral Ratio

The Horizontal to Vertical Spectral Ratio (HVSR or H/V) requires passive measurements with a single 3-component receiver placed on the ground (or, better, slightly buried for a better coupling). In particular, this method alone does not allow an accurate estimation of the shear wave velocity profile with depth. However, it can provide useful constraint about the position of strong impedance contrasts (i.e., deep interface characterization) to be used in the inversion process of surface wave tests (i.e., independent geophysical information). Moreover, a combined inversion of both EDC and the H/V curve can be performed to obtain more robust results (Arai & Tokimatsu 2005, Parolai et al. 2005).

The HVSR method was initially proposed by Nakamura (1989) as an estimate of the 1D Experimental Transfer Function (ETF) also described in Chapter 3. In particular, he observed that the ratio between the Fourier spectra of the horizontal and vertical components of the recorded motion followed a curve (called H/V or ellipticity curve). A clear peak in the H/V curve has been shown to act as a measure of the sites fundamental resonant frequency f_0. Nakamura stated, *"The spectrum ratio of the horizontal components and vertical component of microtremor bears resemblance to transfer function for horizontal motion of surface layers."* The work by Nakamura (1989) and Herak (2008) suggested that the S_H waves microtremors produced the observed experimental peaks in the curve. However, other studies demonstrated that R-waves (and secondly, Love waves) are the most influent waves that produced the H/V peak (Lermo & Chávez-García 1994, Fäh et al. 2001, Arai & Tokimatsu 2004, Malischewsky & Scherbaum 2004, Van Der Baan 2009, Tuan et al. 2011). More recent studies found that the total wavefield is responsible for the H/V peak (Bonnefoy-Claudet et al. 2006, Sánchez-Sesma et al. 2011, Lunedei & Albarello 2015).

The acquisition stage of the HVSR method consists of placing the 3-component receiver and record ambient vibrations. The recording time should be based on anticipated resonant frequency (lower frequencies require longer recording times). Generally, 30 minutes are sufficient (SESAME Team 2004).

In the processing stage, the analyst breaks recording into time steady-state windows and transform them into the frequency domain using a Discrete Fourier Transform (DFT). Each component (i.e., vertical, N-S, and E-W) is usually smoothed before the calculation of the ratio (the Konno & Ohmachi (1998) approach is the most common). Then, N-S and E-W (i.e., horizontal) components can be combined in various ways as

- Geometric mean $H = \sqrt{NS(f) * EW(f)}$;
- Total energy $H = \sqrt{NS(f)^2 + EW(f)^2}$;
- Squared average $H = \sqrt{\frac{NS(f)^2 + EW(f)^2}{2}}$;
- Directional energy $H = \sqrt{[NS(f)\cos(\theta)]^2 + [EW(f)\sin(\theta)]^2}$.

After the processing of each time window, the noise can be removed in the time or frequency domain, and the experimental H/V curve is obtained. An example of an experimental H/V curve with an identified peak is given in Figure 4.44 for the Fonte del Campo site (PSWD). However, the test can give flat responses in some cases. Different reasons can explain the absence of the peak in the ellipticity curve:

- The site can show no significant impedance contrast at (e.g., gradual normally dispersive site) or can be a rock outcrop with no significant amplifications (i.e., very stiff site);
- Anthropogenic noise can mask the site resonant frequency;
- The sensor is inadequately coupled with the ground;
- The sensor was not left to record for a sufficient amount of time to develop a stable estimate;
- The impedance contrast is representative of frequencies below limitations of the equipment (for this reason the use of 4.5 Hz geophones is discouraged);
- Testing was performed in a low energy environment; therefore, low-frequency energy was not present to excite the site's resonant frequency.

The assessment of the acceptability of the H/V curve can be done referring to the work of the SESAME project (SESAME Team 2004). The authors developed HVSR guidelines including clarity criteria for the identification of a good peak.

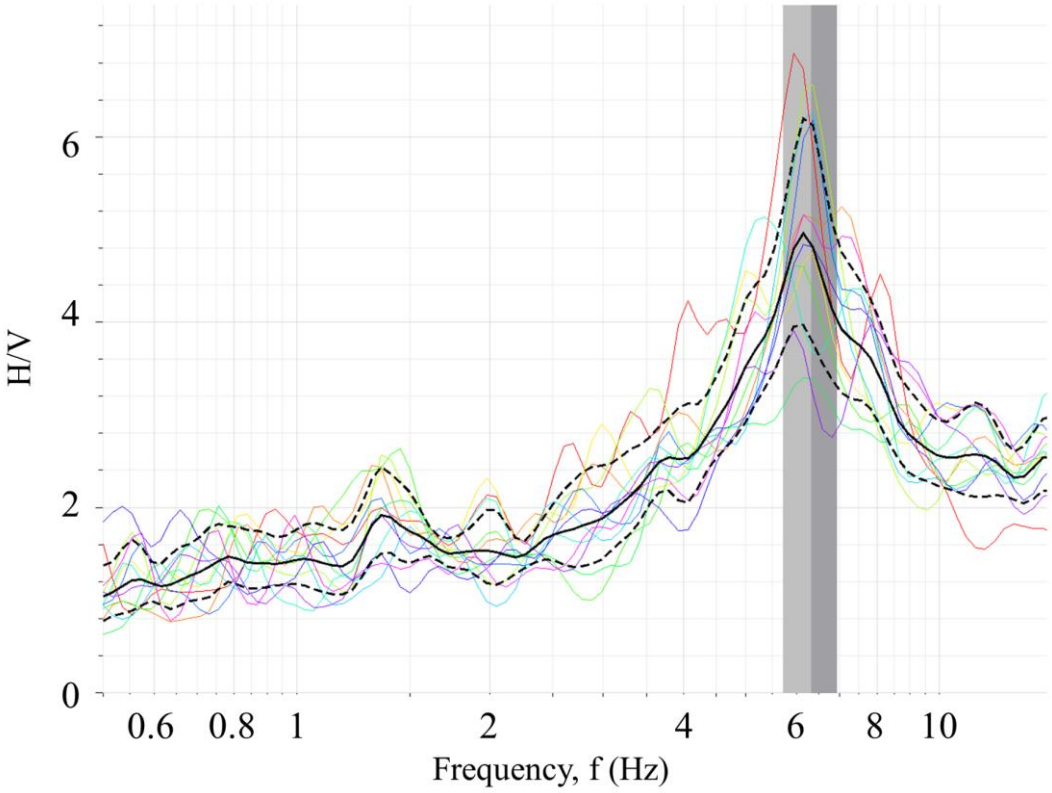

Figure 4.44. Example of an H/V curve obtained at the site of Fonte del Campo (after Passeri et al. (2018a)).

Once verified, the ellipticity curve can be used as geophysical information about the investigated site (Bergamo et al. 2011). As already discussed, the fundamental resonant frequency of a soil deposit can be approximated by the Eq. 4.5 (Kramer 1996). Hence, an experimental estimation of f_0 represents a useful independent information to be combined with other results of the geotechnical and geophysical survey (particularly useful for the inversion of surface wave tests). It is important to notice that also this experimental evidence is strictly related to the harmonic average shear wave velocity profile.

If the H/V curve is the only information at the site, the peak can provide insight into the sites general characteristics. It can also be used to assess the 3D nature of a site/area qualitatively. The ellipticity curve can help in identifying potential velocity reversals (Castellaro & Mulargia 2009). Recently, Vantassel et al. (2018) mapped the spatial variability (i.e., AV) of frequency peaks at CentrePort, Wellington. They showed rapid changes in fundamental site period, identifying a non-1D subsurface due to the bedrock depth oscillations. In this case study, complex H/V data can be used to warn the user of complex subsurface conditions. However, the estimation of a 1D V_S profile from the only H/V curve should be avoided (i.e., HVSR should not be used as a standalone method for performing dynamic site characterization) (Fäh et al. 2003, Molnar et al. 2017).

The ellipticity curve can also be used for a combined inversion with the EDC from a MASW test. An example of this approach was performed for a site included in the PSWD and located in the town of San Severino Marche. The geophysical survey was part of a project between the Politecnico di Torino and the Nagoya University for the safeguard of the historical Italian building heritage. Indeed, the Smeducci's tower rises at the investigated site. The Smeducci's tower (40 m high) was built in the 13th century and represents a symbol for the town and the entire Marche region. As for Accumoli, San Severino Marche is part of the area struck by the 2016 seismic events (other than the 1997 earthquake) and included in the massive microzonation program sponsored by the Italian Civil Protection. For these reasons, a team of experts was engaged in monitoring the dynamic behavior of the tower.

During the last decades, the tower was subjected to various retrofitting operations due to its worrying leaning (Figure 4.45). Also, much geotechnical information is available for the site from previous surveys (i.e., borehole logs, inclinometers, piezometers, SPT tests). These surveys investigated the local geology that is mainly composed of quite stiff materials and shallow bedrock. In particular, the geological 2D section in Figure 4.46 shows a first layer (1-4 m thick) of anthropic materials used to level the area. A second layer is detected, and it is composed by eluvial-colluvial deposits with a thickness ranging from 3 to 4 m. Then, a layer of fractured rock is shown with a thickness varying from 10 to 14 m, laying above a consistent rock halfspace. Hence, the local geology represents a significant challenge for the geophysical investigations, as a likely 2D response is expected. Moreover, the presence of many anthropic underground structures (e.g., the tower was retrofitted with a micro-piles umbrella) is a further complication for the in situ acquisitions.

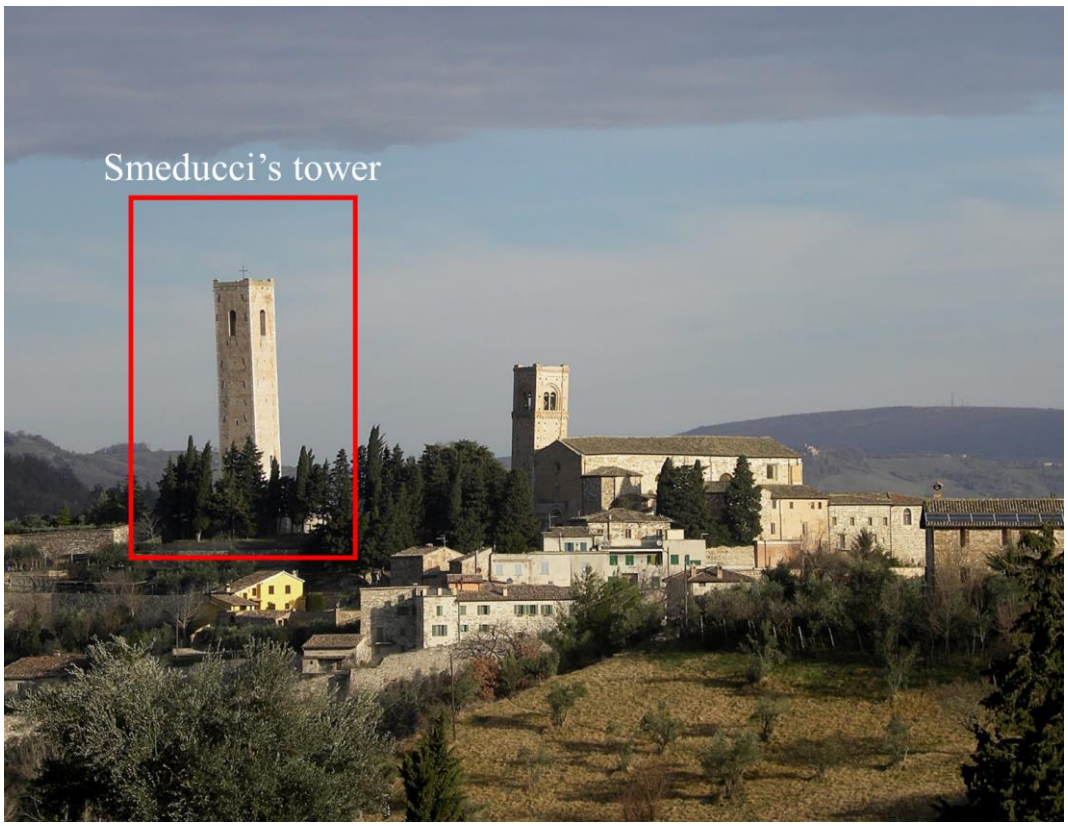

Figure 4.45. Smeducci's tower, San Severino Marche (Italy).

The geophysical survey of the tower (WGS84 latitude 43.226° N, longitude 13.167° E) consisted of two MASW arrays and three HVSR tests (Figure 4.46).

The first MASW array (i.e., MASW-1) was located along the S-W scarp, whereas the MASW-2 was located diagonally in the Smeducci's square. The MASW-1 was composed by 36 vertical geophones (SENSOR-SM-6/U-B, 4.5 Hz) spaced by 1 m (35 m array length). The MASW-2 was composed by 31 same vertical geophones spaced by 1.5 m (45 m array length). The acquisition setup consisted of a 24-channel Seismograph Geode and an 8 kg sledgehammer vertically impinging on the pavement or a metal plate. Multiple shots at different locations were performed, aiming at increasing the SNR and obtaining a reliable statistical sample for the evaluation of the V_R standard deviations.

Figure 4.46 also shows two HVSR measurements. These tests were performed with a single, 3-component, 2 Hz, geophone buried in the ground (Figure 4.27a). The same Seismograph used for the MASW tests was also adopted for the HVRS measurements. Each test refers to a 24 minutes' acquisition in a quite (i.e., no traffic or anthropic activities) environment.

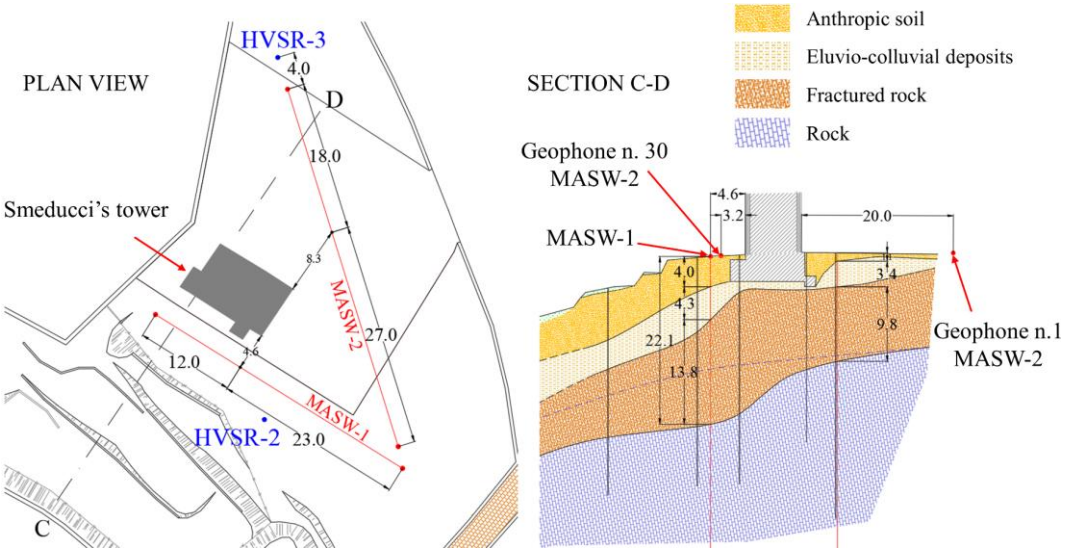

Figure 4.46. Plan view and a 2D geological section of the Smeducci's tower area with the location of the two MASW tests and two HVSR measurements.

The MASW processing was performed with an f-k transform that provided two different EDCs for each test location. The local geology investigated from MASW-2 (Figure 4.46) can be approximated as 1D (as also confirmed by the comparisons between forward and reverse multiple shots). Also for this reason, only the MASW-2 results were used for the following combined inversions.

The HVSR data were processed in GEOPSY with window lengths from 10 to 300 s. An anti-trigger algorithm and a high pass (2 Hz) filter were also used in the signals processing. After the processing, the SESAME criteria were applied to the H/V obtained curves. In particular, the HVSR-1 and HVSR-3 were discarded after the verification.

First, the only MASW-2 EDC was inverted by using the same approach seen for Accumoli (16798 accepted models) and presented in the next Chapter. The processed data were also inverted adopting the Neighborhood Algorithm implemented in GEOPSY (Sambridge 1999, Wathelet et al. 2004). This first stage of inversions was designed for a preliminary investigation of the space of the possible solutions. The results are in agreement, despite the different GSM adopted. Indeed, Figure 4.47 shows the comparison between the interval velocity profiles with the lowest misfit obtained with the different methods.

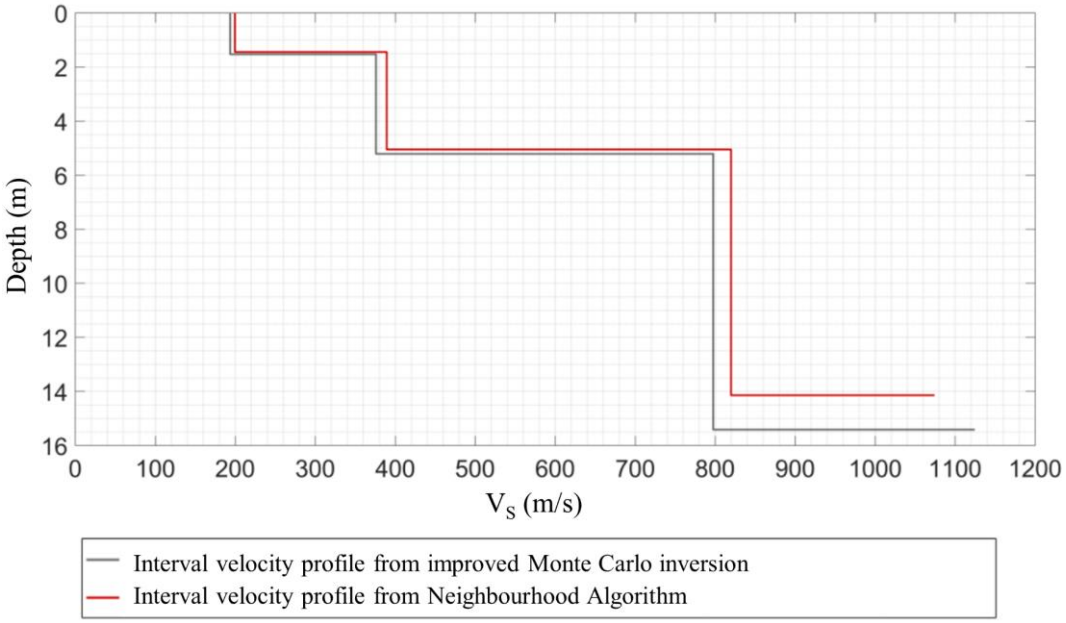

Figure 4.47. Comparison between lowest misfit interval velocity V_S profiles obtained with the improved Monte Carlo algorithm and the Neighbourhood Algorithm implemented in GEOPSY.

Thereafter, the combined EDC-H/V inversions were performed in GEOPSY. The input parameters were the EDC from MASW-2 test and the ellipticity curve from the HVSR-2 test. Then, 500000 models were generated from the software, assuming a maximum iteration equal to 1000. Figure 4.48a-b show the results of the lowest misfit solution. In particular, Figure 4.48a shows the excellent comparison between the lowest misfit TDC (in red) and the EDC (in black). Figure 4.48b shows the comparison between the ellipticity curve of the lowest misfit model (in red) and the experimental H/V curve (in black). Figure 4.48c shows the comparison between the interval V_S velocity profiles obtained by the inversion of the single MASW test (improved Monte Carlo approach) and the combined EDC-H/V inversion. From this last Figure, it is clear that the combined inversion allowed the investigation of a deeper portion of the site. In this case, the HVSR method showed a better resolution with depth and localized a further impedance contrast at depths around 35 m. This result is in agreement with the loss of resolution of the surface wave tests. In this case study, the $\lambda_{max} \cong 80$ m and the test conditions did not allow investigating the depth around the deeper interface.

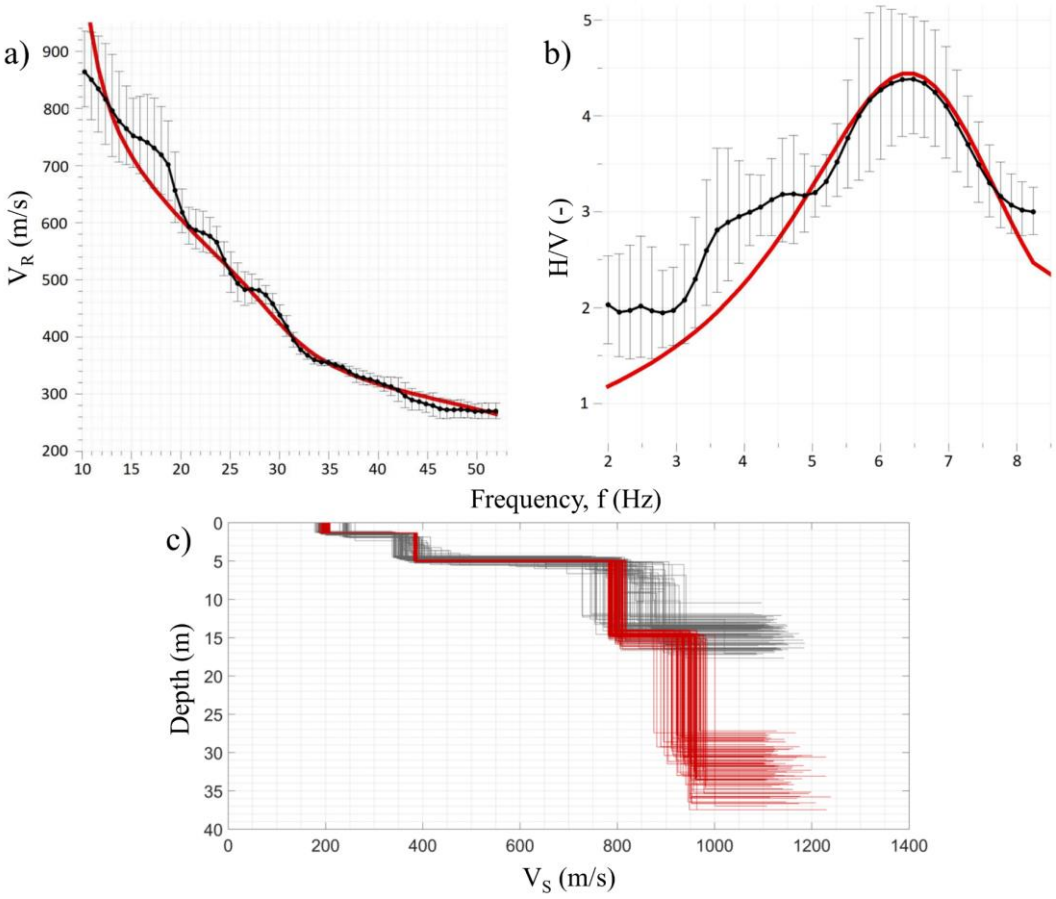

Figure 4.48. Results of the geophysical characterization of the Smeducci's Tower, San Severino Marche (Italy). a) Comparison between comparison between the lowest misfit TDC (in red) and the EDC (in black), and b) comparison between the ellipticity curve of the lowest misfit model (in red) and the experimental H/V curve (in black). c) Comparison between the interval Vs velocity profiles obtained by the inversion of the single MASW test and the combined EDC-H/V inversion.

4.2.3 Summary

The next Table 4.3 summarizes the sources of EUs and AVs identifiable for the seismic tests described in the previous sections from a purely theoretical point of view. This Table aims at giving a rigorous scheme to the analyst who performs seismic tests for near-surface characterization.

The most critical observation regards the balance (i.e., quantification) between the identified EUs and AVs and the dependence on the specific test and the characteristics of the investigated site. For these reasons, a practical and precise identification and quantification of the involved global uncertainties is often not feasible.

The identification and quantification of the EUs are dependent on the type of test, and every single source is listed in Table 4.3. In this regard, it is necessary to consider also the different resolution with the depth of each seismic test. The obtainable resolution of surface wave tests decreases as the depth increases while

invasive tests guarantee a good (for the DH) or excellent (for CH and PS suspension logging) detail even at considerable depths.

In the other hand, for AVs, each geophysical test has a spatial extension and investigates a different volume of the deposit, which should be compared with the extension of the area under analysis (Figure 4.49) (Comina et al. 2011). The most localized measurements can be obtained by using the PS suspension logging. Then, DH and CH tests that investigate a deposit's volume depending on the test configuration and distance source-receiver (i.e., the waves' path). Finally, the non-invasive tests investigate a much larger volume and produce an average response for the particular deposit (i.e., more appropriate when only the estimation of $V_{S,30}$ is required) (Comina et al. 2011, Stewart et al. 2014a). For these reasons, the quantification of the AV requires a systematic analysis of the site (i.e., geologic complexity) and test (i.e., spatial resolution) contributions of variability.

The previous observations confirm that a neat separation between EUs and AVs is practically very complex. These issues are then propagated into the adopted management method that should singularly treat both the epistemic and the aleatory contribute. However, indistinct management is usually carried out, as presented for the geostatistical model described in Chapter 6, both for surface wave and DH tests.

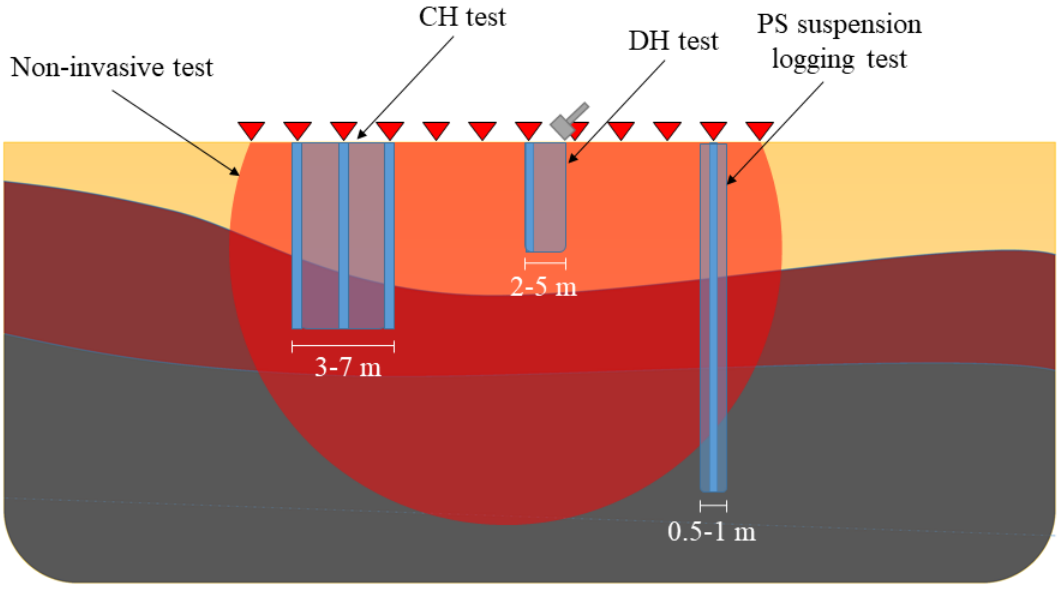

Figure 4.49. Different investigated volumes obtained by means of invasive (i.e., CH, DH, and PS suspension logging) and non-invasive (i.e., seismic refraction, and surface wave) tests to be accounted for in the identification and quantification of AVs.

Numerous inter-method (i.e., invasive vs. non-invasive) and intra-method (i.e., within the same class of tests) comparisons reported in the literature showed that the agreement between the results is good if the tests are scrupulously conducted and interpreted (Boore & Brown 1998, Brown et al. 2002, Moss 2008, Comina et al. 2011, Foti et al. 2011b, Kim et al. 2013b, Piatti et al. 2013a, Cox et al. 2014, Garofalo et al. 2016a, Garofalo et al. 2016b). These comparisons are usually based on independent analysis of the results and called "blind tests".

The first pioneer example is proposed by Boore & Brown (1998). They attested a substantial underestimation of V_S for the shallower layers, and a substantial overestimation for the deeper layers obtained with the surface wave methods. At that time, the results of the DH tests were indisputable and were considered as the true target. They stated that a possible explanation for the difference could be the different investigated volume.

Brown et al. (2002) expressed more confidence in the surface wave testing methods showing ten examples of inter-method comparisons. In one case, the site presented no lateral variations, and the SASW array was very close to the invasive tests. Likewise, the comparisons of the SASW profile against DH and PS suspension logging results were very satisfying. For a second example, there were more substantial differences in the inter-method comparison, especially close to the surface. However, the authors calculated the TDC associated with the DH profile with very different results. This evidence confirmed that the inter-method differences were probably due to the considerable lateral variability at the site. For all the remaining sites, Brown et al. (2002) generally found lower values of the velocity close to the surface by the SASW (i.e., around 15%). Furthermore, it should be noted that the DH tests were interpreted with the known stratigraphy, while for the SASW this information was not available. Also, the authors confirmed that the usual difference might be related to lateral variations and different investigated volumes (Boore & Brown 1998).

A systematic comparison of the uncertainties has recently been carried out in the InterPACIFIC project (Garofalo et al. 2016a, Garofalo et al. 2016b), in which three sites were characterized using repeated realizations of invasive and surface wave tests. The sites were selected to be representative of different stratigraphic situations. A rock outcrop characterizes the site of Cadarache. The Grenoble site consists of alluvial coarser relatively rigid materials with a deep seismic substrate. Finally, the Mirandola site has relatively deformable deposits above one stiff substrate placed at around 100 m depth. For each site, DH, CH, SDMT, and PS suspension logging were repeated.

Furthermore, a surface seismic dataset was distributed to different groups of analysts who interpreted it using different approaches. The results obtained in the study show comparable levels of uncertainty between invasive and surface wave tests. However, the lower resolution guaranteed by the surface wave tests is reflected in greater uncertainties in the identification of stratigraphic layers and consequently in the estimation of interval velocity, especially at significant depths.

The inter-method comparison, however, is often performed by the interval velocity V_S profile. As already discussed, this schematization of the subsurface represents only a simplification need for the GRAs. A better understanding of the inter-method differences can be achieved by looking at the harmonic average shear wave velocities. Many authors already suggested this type of comparison but only applied to $V_{S,30}$ (Bergamo et al. 2011). Figure 4.50 compares the results of invasive tests (CH, DH or PS suspension logging) with the results of the analysis of the propagation of surface waves in five different studies. Generally, the comparison is good enough for all soil classes.

In Figure 4.50, the data from the study by Comina et al. (2011) also report an estimated uncertainty associated with non-uniqueness of the solution quantified as the standard deviation of the set of profiles that equivalently honor the available experimental data. The impact of the non-uniqueness of the solution appears modest for the estimate of $V_{S,30}$ at eight sites. Similarly, Garofalo et al. (2014b) estimated the uncertainty also associated with invasive test and surface wave results during the InterPACIFIC project (Figure 4.50). Note that, for the InterPACIFIC project, more uncertainties are reported, compared to the results from Comina et al. (2011). This is mainly due to the different number of analysts that contributed to the blind test. On the other hand, the uncertainties from Comina et al. (2011) are associated with a single analyst.

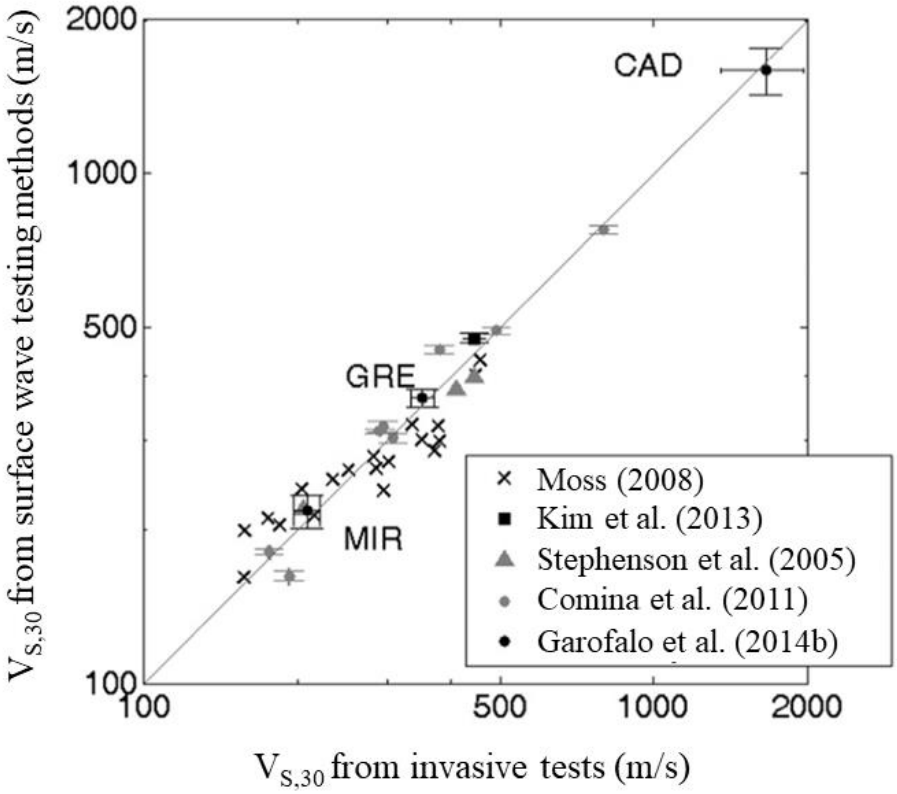

Figure 4.50. Comparison of $V_{S,30}$ obtained performing invasive or surface wave tests in five studies in the literature (after Garofalo et al. 2014b).

Table 4.2. Summary table for the identification and quantification of EUs and AVs in seismic tests.

Test	EPISTEMIC UNCERTAINTIES	ALEATORY VARIABILITIES
DOWN-HOLE SEISMIC TESTING	- Gross errors in the source, receivers, and DAQ system (inappropriate instruments) - Inadequate preparation of the borehole (i.e., casing, grouting) (for borehole-based) - Impenetrable stiff materials (for direct-push) - Picking (FA, PT, CO) (mainly for pseudo- and true-interval) - Potential near-surface refractions - Triggering/timing (particularly for pseudo-interval method) - Decreasing resolution with depth and low-energy sources (low SNR) (maximum 60-70 m) - Insufficient coupling of the shear beam and/or metal plate with the soil - Straight ray path assumption (true- and pseudo-interval and slope-based) - Inverse problem non-uniqueness (raytracing velocity analysis) - Preliminary choice of layer discretization (slope-based interpretation method) **Second-order importance:** - Borehole/cone vertical deviation - Tube waves generation (especially in water-filled boreholes and P-waves)	None (restricted and localized measurements).
CROSS-HOLE SEISMIC TESTING	- Gross errors in the source, receivers, and DAQ system (inappropriate instruments) - Inadequate preparation of the borehole (i.e., casing, grouting) (for borehole-based) - Picking (trigger, P-, and S-wave) - Potential refractions and generation of head waves (hidden layer) - Interpretative 1D model inadequateness (vertical homogeneity of the deposit) - Triggering/timing (in the case of 2-holes setup) - Decreasing resolution with the distance between the boreholes and low-energy sources (low SNR) - Insufficient coupling of the source lowered into the borehole with the surrounding soil - Borehole/cone vertical deviation	None (restricted and localized measurements).
PS-SL	- Picking strategies - Possible detection of tube waves (particularly pronounced with heavy casing and thick grout) - Poor signal quality - Very restricted investigated volume - Triggering/timing - Insufficient coupling of the source lowered into the borehole with the surrounding soil	None (restricted and localized measurements).

SEISMIC REFRACTION	- Gross errors in the source, receivers, and DAQ system (inappropriate instruments, particularly in the case of S-wave refraction test) - Triggering/timing - Inadequate if performed on pavements, asphalt or concrete (or in the presence of shallow thin stiff layers as desiccated crusts) - Picking strategies - Insufficient coupling of the shear beam and/or metal plate with the soil - Normally dispersive medium (i.e., the velocity has to increase with depth, no velocity inversions) assumption - Multi-layered models with thin interbedded materials (hidden layer and refraction equivalence) - Inverse problem non-uniqueness (tomography and multiple shots interpretation)	Dependent on the spatial length of the array and the interpretation strategy. Tomography and Generalized Raypath Method allow for the reconstruction of 2D models.
SURFACE WAVE TESTING (MASW AND AVA)	**ACQUISITION** - Gross errors in the source, receivers, and DAQ system (inappropriate instruments) - Insufficient coupling of the geophones with the ground or the pavement - Inadequate geometric initial design of the array or recording parameters (see Table 4.2), and/or insufficient number/locations of shots (for MASW) - Inadequate energy or narrow frequencies band produced by the source (for MASW) - Insufficient ambient vibrations level (for AVA) - Inadequate geometric initial design of the array or of recording parameters (for AVA) **PROCESSING** - Absence of a critical read of the EDC (maximum and minimum resolvable depths and the initial range of possible solutions, possible velocity inversions, relationship with the $V_{S,Z}$) - Higher modes misinterpretation - Incoherent noise (e.g., electric or electronic noise) - Near-field effects, body waves, air blast, incoherent noise (e.g., anthropic activities) (for MASW) and non-planar Rayleigh wavefront - Nondirectional energies (f-k methods), irregular arrays and modes mixing (SPAC methods) (for AVA) **INVERSION** - Ill-posedness of the non-unique solution - Nonlinearity and mixed-determination of the problem - Investigation of a limited space of solutions varying the five problem's parameters (especially for LSM) - Unacceptable differences between EDC and TDC evaluated by the misfit function - Inadequacy of the inversion model made by stacked horizontal layers (i.e., the presence of lateral variations) - Wrong use of a-priori information (e.g., borehole logs and saturation depth)	Dependent on the spatial length of the array (for active). Sites with strong lateral/spatial variations should be avoided. Passive tests measure ambient vibrations that provide a global average of the site response. The use of multiple arrays can help in the identification of lateral variations by comparing the results. Spatial windowing for long arrays can be used to obtain approximate 2D models.
HVSR	- Gross errors in the receiver (especially the natural frequency of the sensor) and DAQ system (inappropriate instruments) - Insufficient coupling of the geophone with the ground - Short acquisition windows - Noisy environments (i.e., incoherent noise) - No evidence of a clear peak (normally dispersive or outcrop sites, very low-frequency resonance for soft sites, insufficient ambient vibrations level) - Use of the test as a standalone method for performing dynamic site characterization (i.e., estimation of the V_S profile)	These tests measure ambient vibrations that provide a global average of the site response regardless for lateral variations. Multiple tests can help in the identification of lateral variations.

4.3 Management of EUs and AVs

The management (i.e., treatment) of the identified and quantified epistemic uncertainties and aleatory variabilities still represents an open topic for the scientific and technical community. This section starts with a pioneering example of the management of EUs and AVs. Then, two primary methods that are commonly adopted by scientists and professionals are described in details. In the subsequent parts, an extensive literature overview will be presented, critically illustrating applications and results of the management of EUs and AVs of V_S profiles.

The Electric Power Research Institute (EPRI) historically provides guidelines for the design of nuclear power plants in the US. These guidelines deal with methods for estimating strong design ground motions. The motivation is given by the need for a systematic, physically based, and empirically calibrated method that could be used to estimate ground motions for the design of nuclear power plants and other critical facilities.

In 1993, EPRI published the technical report called *"Guidelines for Determining Design Basis Ground Motions"*. This report aimed at developing a guideline for conducting a complete site investigation. In Chapter 6-Vol. 1, the report presents soils amplification factors for the 5% damped response spectra to accommodate the effects of soils on a generic basis. A set of five generic soil categories ranging from 6 to 165 m depth were presented as well as the V_S profiles used for EQL-GRAs, after a comparison with NL-GRA results. The stochastic analyses likely show the first example of management of uncertainties (i.e., even if they were not explicitly classified) in V_S profiles. In particular, a generic median soil profile was selected and chosen to be consistent with the generally stiff soils present under nuclear power plants located in the Eastern and Central United States. This generic interval V_S profile (Figure 4.51) intended to capture the behavior of soils ranging from gravels and sands to low plasticity sandy clays for five site categories.

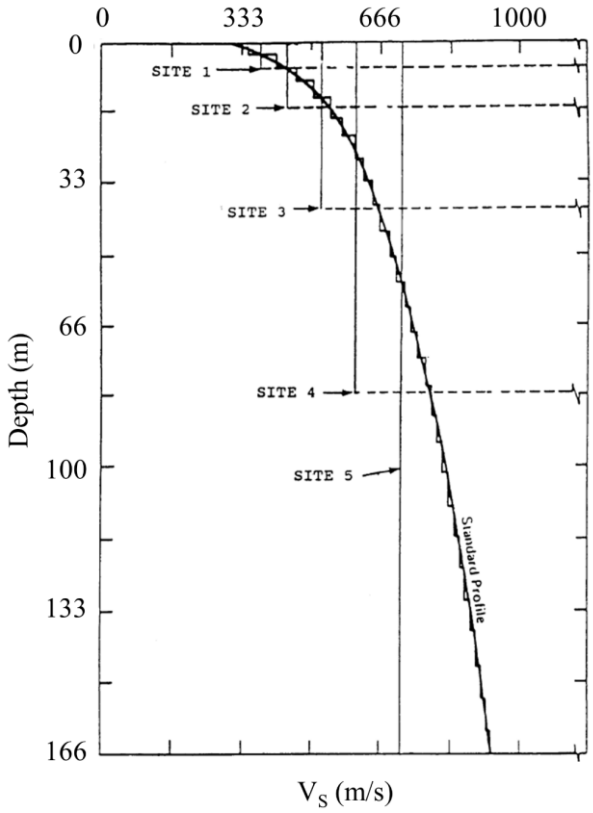

Figure 4.51. Standard soil profile appropriate for the Central and Eastern United States sited and site categories indicated by their respective soil column depth (after EPRI (1993)).

In order to accommodate for the variation in V_S interval velocity profiles, EPRI (1993) proposed a randomization model to account for uncertainties and variabilities. The uncertainty model applied separately to interval velocities and depths and was based on a probabilistic analysis of over 350 profiles taken from sites predominately in the conterminous United States. The statistics then represented both western and eastern sites of a broad range of possible site conditions. An example of randomized interval S-wave velocity profiles is given in Figure 4.52 along with the median profile (dashed line). The bedrock (i.e., halfspace) median velocity was initially assumed as 2000 m/s and the associated logarithmic standard deviation $\sigma_{\ln(V_S)} = 0.3$. The bedrock (i.e., halfspace) depth was separately randomized and was constrained to the ranges in depth to which category applied. Although this model was very simplified, it likely represents the first example of a geostatistical randomization model applied to interval V_S profiles.

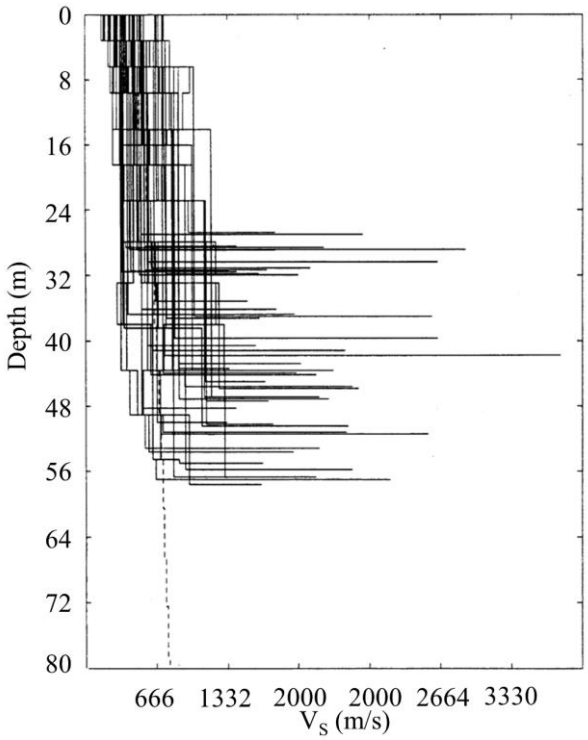

Figure 4.52. Random shear wave interval velocity profiles (separate randomization of interval velocity and depth) (after EPRI (1993)).

A subsequent report (EPRI 2013) presented the identification of uncertainties as epistemic uncertainties and aleatory uncertainties (i.e., variabilities). For the V_S profiles, EPRI (2013) suggested adopting multiple profiles or base cases to account for the epistemic uncertainty. Typically, three base cases are suggested. On the contrary, randomization about the base cases should be implemented to account for the variability in V_S over the scale of the footprint of a structure, which is treated as an aleatory uncertainty.

An interesting background on the IQM of uncertainties is initially provided and reported here to recall a few central concepts also discussed in Chapter 2. EPRI (2013) stated, in B2.1:

"There are two different types of uncertainty in the development of site-specific amplification functions. The first type of uncertainty is epistemic or lack of knowledge uncertainty. This represents the uncertainty in the development of the base-case models for site profile, dynamic properties, and seismological parameters. For well-characterized sites with abundant high-quality data this uncertainty would be reduced, possibly eliminating the need to vary some of the site parameters such as the site profile. This epistemic uncertainty would increase with decreasing confidence in the available data and information. This uncertainty is evaluated through the development of alternative base-case models. The approach applied for the development of alternative base-case models (epistemic uncertainty) is discussed in more detail in the following sections.

Secondly, at any given site, at the spatial dimensions of typical nuclear facilities (100-200 m) there is expected to be some variability in important site response

parameters such as shear wave velocities, nonlinear dynamic material properties at any depth across the footprint of the facility, and the overall thickness of soil/soft rock above firm rock site conditions. It is important to attempt to capture this uncertainty in the final estimates. This is treated as an aleatory (randomness) type of variability. Current practice represents this variability by developing a candidate shear wave velocity profile, depth and overall thickness of soil/soft rock and associated nonlinear dynamic material properties (shear modulus reduction and damping curves). This is referred to as a "base case" model. Subsequently, potential variations in shear wave velocity and layer thickness are represented by correlated random perturbations to the base-case values. This is frequently referred to as a randomization process. A sufficient number of realizations are used to develop stable statistical estimates (log median and log standard deviation) of the amplification functions".

It is essential to remark two points of the previous definitions. First, the identification and quantification of epistemic uncertainties is test- and site-dependent. Previous sections showed for V_S profiles (and in the previous Chapter for the other parameters/approaches in GRAs) that each type of seismic test is associated with a specific type and amount of EUs and AVs (Stewart et al. 2014a). Moreover, also the site conditions contribute to the final evaluation of the EUs involved in the process. Indeed, the IQM method should be rigorously applied for the specific characteristics of the site under analysis.

Secondly, EPRI (2013) explicitly considers the dimension of the structure (i.e., in this case, the nuclear power plant) to be designed (see the introduction of Chapter 3). The quantification of the aleatory variabilities in site response studies should account for the scale of the problem. The adopted models and their parameters should be designed and evaluated for the specific application. The use of generic models and parameters obtained for a broad class of site conditions should be firmly avoided.

4.3.1 Alternative (upper-range and lower-range) models

The generation of alternative base-case models is the proposed method to manage (i.e., treat) EUs in V_S profiles. It is also known as upper- and lower-range method (Griffiths et al. 2016b, Teague & Cox 2016, Teague et al. 2018, Passeri et al. 2019). The specific methodology to develop the alternative cases depends on the amount and type of information available at a given site. Conceptually in this context, for poorly characterized sites, multiple cases should be developed with broad ranges of epistemic uncertainty applied in the development of the parameters of the alternative cases. For sites that have more complete site characterization information available, smaller epistemic uncertainty factors can be employed in the development of alternative cases, as discussed in the previous section. Hence, the quantified uncertainty depends on the amount of information available along with how well the information is correlated with shear wave velocity. The section of the EPRI guidelines is here entirely reported and commented for completeness.

The first case regards conditions where geophysical information such as very limited V_S data exist and:
"[…] the estimate for uncertainty in shear wave velocity is to be taken as:

$$\sigma_{\ln(V_S)} = 0.35$$

This value is similar to a Coefficient of Variation (COV) of 0.25, which is consistent with Toro (1997) for observed spatial variability over a structural footprint of several hundred meters. The profile epistemic uncertainty factor of 0.35 is to be applied throughout the profile and is based on the estimates of epistemic uncertainty in $V_{S,30}$ developed for stiff profiles. The logarithmic factor assumes shear wave velocities are lognormally distributed and was originally developed to characterize the epistemic uncertainty in measured $V_{S,30}$ at ground motion recording sites where measurements were taken within 300 m from the actual site. The uncertainty accommodates spatial variability over maximum distances of 300 m, and is adopted here as a reasonable and realistic uncertainty assessment reflecting a combination of: (1) few velocity measurements over varying depth ranges, and (2) the spatial variability associated with observed velocities. The application of the uncertainty estimate over the entire profile that is based largely on $V_{S,30}$ implicitly assumes perfect correlation that is independent of depth. While velocities are undoubtedly correlated with depth beyond 30 m, which forms the basis for the use of $V_{S,30}$ as an indicator of relative site amplification over a wide frequency range, clearly the correlation is neither perfect nor remains high over unlimited depths. More direct support for the assumption of a $\sigma_{\ln(V_S)}$ of 0.35 comes from the measured range in ($V_{S,30}$) conditional on proxy inferences. For the four currently employed ($V_{S,30}$) proxies: surficial geology Geomatrix site category, topographic slope, and terrain, the overall within class or category uncertainty is about 0.35.
This uncertainty reflects the variability of measured ($V_{S,30}$) about the predicted value and is relatively constant across proxies. The proxy uncertainty of about 0.35 is a direct measure of the epistemic uncertainty of the predicted value or estimate and supports the adoption of 0.35 to quantify the velocity uncertainty for cases with few or absent direct measurements. For the application to site characterization the $\sigma_{\ln(V_S)}$ of 0.35 has been extended to the entire profile."

The second situation described in EPRI (2013) regards sites where velocity estimations are particularly sparse (e.g., based on inference from geotechnical/geologic information rather than geophysical measurements). Indeed, EPRI considers methods for the estimation of the interval V_S profile based on geotechnical/geologic inference rather than geophysical tests. This dissertation and Stewart et al. (2014a) firmly discouraged the determination of the small strain stiffness using other tests and/or geological assumptions. This observation is dramatically crucial for critical facilities such as nuclear power plants. In these cases, EPRI (2013) writes:

"[…] a conservative estimate of the uncertainty associated with the template velocity is to be taken as:

$$\sigma_{\ln(V_S)} = 0.5$$

The third case described in EPRI (2013) regards sites where multiple, detailed V_S profiles are available and:

"[…] the level of uncertainty may be significantly reduced, depending on the number, depth ranges, and vintage (quality) of the surveys. For sites with an intermediate level of information available, such as a single shear wave velocity profile of high-quality or shear wave velocities inferred from measured compressional-wave velocities $\sigma_{\ln(V_S)}$ may be reduced by a factor of two over the better constrained portions of the profile. A specific factor of two is taken to provide consistency across the sites."

The last case described in EPRI (2013) regards well-characterized sites with multiple measurements and:

"[…] the epistemic uncertainty may be further reduced. In all cases of reduced σ the range in base-case profiles reflecting epistemic uncertainty in shear wave velocity must represent a realistic expression of the existing information at the site as well as possible ranges in velocities for the materials considered. For all sites considered, the shear wave velocities developed for the upper- and lower-range base-cases must reflect realistic values for the respective geologic conditions at the site. The bases for these conclusions should be discussed in the report."

The sections above deserve few comments and observations. First, there is a typo when calculating the Coefficient Of Variation (i.e., the ratio of the mean and the standard deviation, COV) from the $\sigma_{\ln(V_S)} = 0.35$. Indeed, the corresponding relationship between the coefficient of variation and the logarithmic standard deviation is

$$COV = \sqrt{e^{\sigma_{\ln}^2} - 1} \qquad \text{(Eq. 4.24)}$$

If we introduce $\sigma_{\ln(V_S)} = 0.35$, the corresponding $COV = 0.36$ and not 0.25. (i.e., the logarithmic standard deviation and the coefficient of variation are very close for small values, as illustrated in Figure 4.53). This typo is misleading because the reader cannot understand which is the correct instruction (i.e., $\sigma_{\ln(V_S)} = 0.35$ or $\sigma_{\ln(V_S)} = 0.25$)

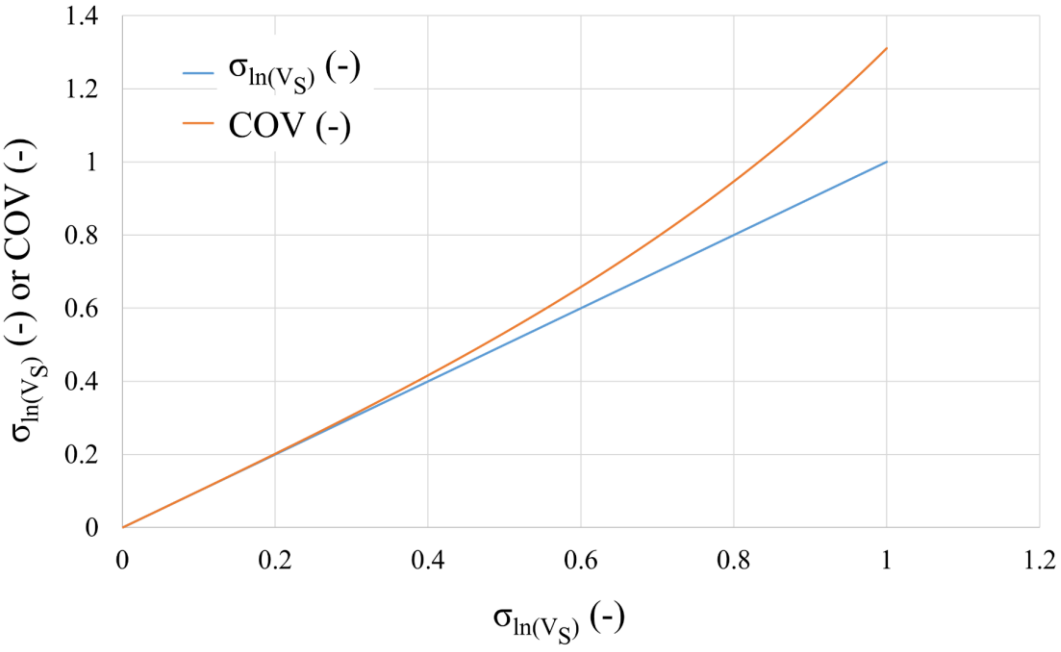

Figure 4.53. Mathematical relationship between the logarithmic standard deviation and the coefficient of variation.

The second observation regards contamination between the epistemic uncertainties and the aleatory variabilities in the report. EPRI 2013 states that the value of $\sigma_{\ln(V_S)} = 0.35$ is compatible with the observations made by Toro (1997) about the spatial variabilities for a footprint of several hundred meters. Then, they say that the uncertainties accommodate spatial variability over a maximum distance of 300 m, as applied for ground motion recording sites where measurements were taken within 300 meters. This comparison, however, appears misleading. The epistemic uncertainty does not reflect a spatial variability (i.e., AV) as it represents a different nature of uncertainties that can be reduced. Contrarily, the aleatory variabilities cannot be reduced with further and better quality investigation methods.

A further observation concerns the proposed velocity correlation combined with a lognormal distribution of the interval velocities. The application of the V_S shift (+/-) throughout the entire profile is mathematically explained as a perfect correlation (i.e., equal to one) between interval velocities of different layers. From a geophysical point of view, the management of epistemic uncertainties (i.e., measurements and/or model errors, see Table 4.3) cannot be implemented adopting a perfect correlation. In the previous sections, we discussed the test- and site-specific nature of epistemic uncertainties. In light of the previous discussions, the assumption of a perfect correlation is an unacceptable simplification of the problem. On the other hand, the assumption of the lognormal distribution is reasonable and will also be adopted in the next sections of this dissertation.

4.3.2 Geostatistical randomization models

In EPRI (2013), the management of the V_S aleatory variabilities that are expected across a specific site (i.e., mainly depending on the scale of the problem) consists of a randomization process. The aleatory variability about each base-case set of V_S profiles should be treated by randomizing (a sufficient number of realizations to produce stable estimates) S-wave interval velocities, layer thicknesses, and depth to reference rock (or reference half-space) through a particular class of stochastic models, termed geostatistical models[2].

In particular, in Section B-4.1, EPRI (2013) described the use of a particular geostatistical model:

"The velocity randomization procedure makes use of random field models (Toro, 1995) to generate V_S profiles. These models assume that the shear wave velocity at any depth is lognormally distributed and correlated between adjacent layers. The layer thickness model also replicates the overall observed decrease in velocity fluctuations as depth increases. This realistic trend is accommodated through increasing layer thicknesses with increasing depth. The statistical parameters required for generation of the velocity profiles are the standard deviation of the natural log of the shear wave velocity ($\sigma_{ln(V_S)}(z)$) and the interlayer correlation (ρ). For the footprint correlation model, the empirical $\sigma_{ln(V_S)}(z)$ is about 0.25 and decreases with depth to about 0.15 below about 15 m. To prevent unrealistic velocity realizations, a bound of $\pm 2\sigma_{ln(V_S)}(z)$ should be imposed throughout the profile. In addition, randomly generated velocity should be limited to 2.83 km/s. All generated velocity profiles should be compared to available site-specific data as a check to ensure that unrealistic velocity profiles are removed (and replaced) from the set of velocity profiles used to develop site response amplification functions. This process should be documented as part of the site response analysis."

The velocity randomization procedure described by EPRI (2013) refers to the geostatistical model developed by Toro (1995). In addition, in this case, the interval V_S velocity is assumed as lognormally distributed, whereas a specific correlation

[2] The theory of stochastic processes concerns the study of systems that evolve over time (but also more generally in space) according to probabilistic laws. Such systems or models describe complex phenomena of the real world that have the possibility of being random. Such phenomena are more frequent than we can believe and we meet all those times when the quantities we are interested in are not predictable with certainty. However, how these phenomena show a variability of possible outcomes that can be somehow explained or described, and then we can introduce the probabilistic model of the phenomenon. The term geostatistics refers to a branch of the more general spatial statistics that has had its first applications in the mining field and which owes its development mainly to the French scientist Matheron. This discipline was born with the aim of providing an estimator that allowed, starting from some sampled points, to reconstruct the complete spatial distribution of the concentration of precious metals within the studied field. This estimator had to take into account the double structured-random aspect that came out from the analysis of the data. Even though there was a specific erratic spatial variability in the metal concentrations, it was observed that by comparing samples performed in close points the precious metal contents were on average much more similar to when the samples compared were more distant. In light of this, the idea was simple enough: to find a way to use this continuity structure in making estimates in non-sampled points. These concepts can be also applied to the V_S profiles. In this case, however, the model accounts for a single (1D) spatial variable (i.e., the depth).

model (i.e., no perfect correlation) is introduced in the model. The model also consists of a statistical model (i.e., Poissonian) for the layer thicknesses that reproduces the typical increase of the thickness with depth. However, the model still implements the independent randomization of interval velocity and layer thicknesses.

Indeed, the fundamental assumption of the model still regards the randomization of the interval S-wave velocity profile. In previous sections, we have already discussed the intrinsic limitations that are included in this schematic representation of the soil deposit. This dissertation will propose to modify this assumption and proceed to a new randomization "philosophy". This new approach will be more consistent with the real physics of the problem. The main characteristic of the proposed model overcomes the interval velocity randomization, decomposing the problem into the primary random variables: length and time.

The Toro model (1995)

In 1995, Toro developed the first (and unique) geostatistical model applied to V_S interval velocity profiles for the management of AVs. This model (hereafter called TM95) is partially described in Kottke & Rathje (2009), Rathje et al. (2010) and Li & Asimaki (2010) and represents a fundamental pioneering work. The original presentation of the TM95 is published in consulting reports that are not readily available using proprietary datasets that are now dated (Stewart et al. 2014a).

The main aim of the work by Toro (1995) was the definition of a probabilistic model for the variation of V_S in soils and rocks, with the explicit purpose of calculating median amplification functions together with the uncertainties. In general, the model can also be used in the case of availability of measured profiles, but not in sufficient numbers for the definition of a specific model. Otherwise, it can be used in the case of total absence of repeated measures at the site, using the proposed sub-soil categories. Differently from work done for EPRI (1993) (Figure 4.52), for the TM95 many more V_S profiles were added to the database, allowing to regress a more refined model. Also, given the high number of profiles, the model parameters for different categories were calculated using two different classification methods (i.e., GeoMatrix and USGS, Figure 4.54).

Third Letter*	
Designation	Description
A	Rock. Instrument is founded on rock material (Vs > 600 m/s) or a very thin veneer (less than 5m) of soil overlying rock material.
B	Shallow (Stiff) Soil. Instrument is founded in/on a soil profile up to 20m thick overlying rock material, typically in a narrow canyon, near a valley edge, or on a hillside.
C	Deep Narrow Soil. Instrument is founded in/on a soil profile at least 20m thick overlying rock material in a narrow canyon or valley no more than several kilometers wide.
D	Deep Broad Soil. Instrument is founded in/on a soil profile at least 20m thick overlaying rock material in a broad canyon or valley.
E	Soft Deep Soil. Instrument is founded in/on a deep soil profile that exhibits low average shear wave velocity (Vs < 150 m/s).

Designation	Average Shear-Wave Velocity (30 m)*
A	greater than 750 m/s
B	360 to 750 m/s
C	180 to 360 m/s
D	less than 180 m/s

Figure 4.54. Soil classification schemes adopted by Toro (1995) (after Toro (1995)).

Toro (1995) used the PEA (Pacific Earthquake Analysis) database, which contained 745 V_S profiles. After a selection procedure, only those that were measured in situ (i.e., 557) were used for the development of the TM95. These profiles are the result of an interpretation (no raw velocities), and that came from geotechnical investigation surveys after 1974 (i.e., when in situ test quality standards changed in the US). Then, 92 profiles were grouped into 11 classes, according to the distance (i.e., from a hundred meters to a few kilometers). Seven of these classes also presented precise information on the location of the profiles in order to evaluate the correlation of the horizontal structures of V_S profiles. In addition to the distance clusters, V_S profiles were cataloged with GeoMatrix (Chiou et al. 2008) or with USGS (i.e., $V_{S,30}$-based). Of the 557, 541 have the USGS classification, while only 164 the GeoMatrix. Also, the categories are combined as A+B (rock or firm soil) and C+D (soft soil). An example of the interval velocity profiles used for the category USGS A+B is given in Figure 4.55. In particular, Figure 4.55a shows the entire dataset included in this class, whereas Figure 4.55b-c show the intra-class mean and logarithmic standard deviations of the interval velocity profiles.

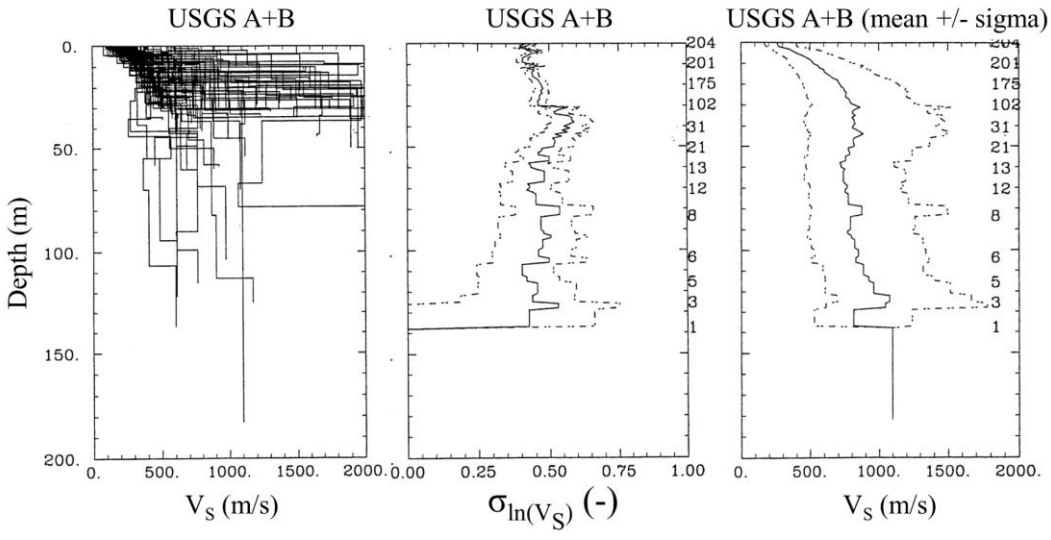

Figure 4.55. Interval velocity profiles included in the category USGS A+B. a) Interval velocity profiles, b) logarithmic standard deviation of the interval velocity profiles, and c) mean +/- 1 sigma profiles (after Toro (1995)).

Toro (1995) proposed a list of the sites included in the database with information about the site name, latitude and longitude, classification, and profile depth. From a precise inspection of these tables, few observations can be done.

First, the database does not show the method adopted for the estimation of the interval V_S profile. The author calls "on field" measurements. However, there are sites where also empirical correlations with other geotechnical tests (i.e., CPTs) were likely used.

Second, the database presents a substantial spatial variability between the sites (e.g., from California to Italy) and only 92 of 557 sites were grouped by distance in 11 classes (even if only seven classes show a precise location of the profile). Hence, the quantification of the AVs includes information ranging between very different geological environments. Moreover, the subsequent classification combines a spatial variability related to an uncontrollable spatial scale.

Third, the author classifies the profiles based on GeoMatrix or USGS systems. However, there is not clear evidence that the quantified AVs in the V_S profiles depends on these classification schemes (i.e., the average stiffness of the deposit). Furthermore, the database shows profiles with very limited depths. The USGS classification appears for some very superficial profiles (e.g., a 15.30 m depth in class C). Indeed, some profiles do not reach 30 m, but for which there is a USGS classification (e.g., one of 4 m depth).

The definition of the V_S profiles database allowed Toro (1995) assuming that:

- The distribution of the S-wave interval velocity is lognormal for each depth;
- The logarithmic standard deviation is constant with depth;
- If a profile presents an interval velocity of a layer higher than the average, then also the layer immediately below shows an interval velocity higher than the average.

The TM95 is then composed of three parts (Figure 4.56), which respect the observations above:

1) A layering model that describes the thickness of each layer (or the position of the interfaces, in an equivalent way), or rather the density of interfaces in one meter, which is a function of depth (Figure 4.56a);
2) The velocity model that describes the median interval velocity of each layer at its mid-depth (intra-layer) (Figure 4.56b);
3) The correlation model of the interval velocities of a layer with respect to the other layers as the depth varies (inter-layer) (Figure 4.56c).

The bedrock (i.e., half-space) is presented separately from the soil part. The depth of the bedrock is assumed uniformly distributed between a specified range, while its velocity is managed with its mean and standard deviation (always following a logarithmic distribution).

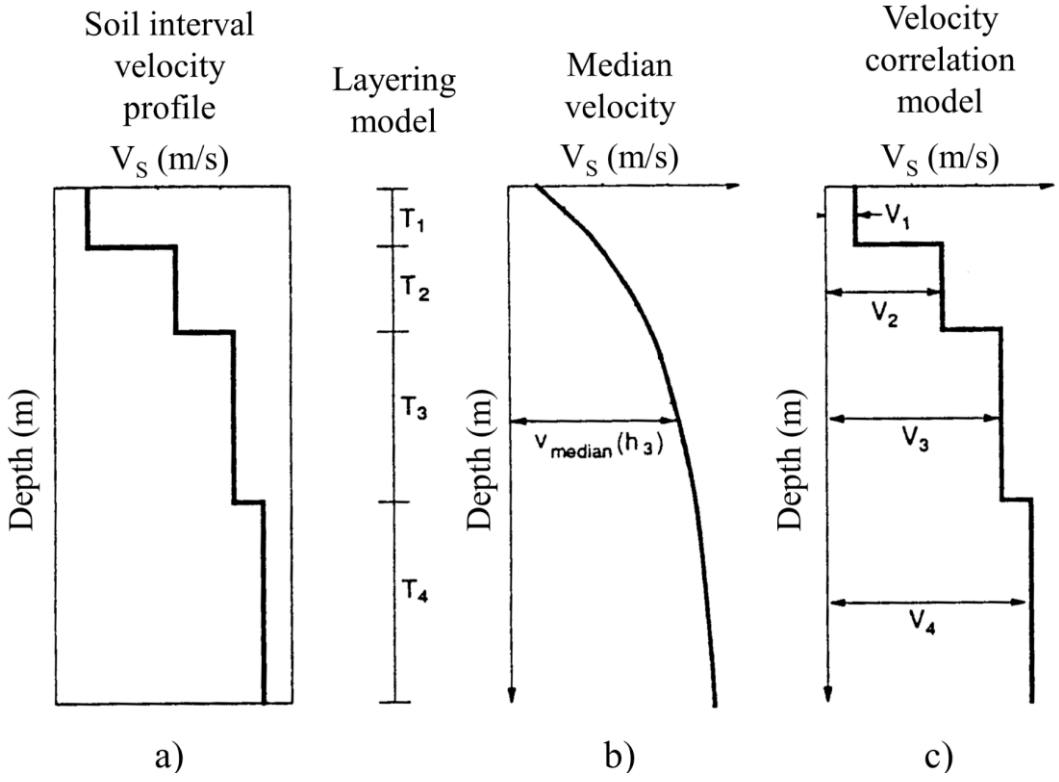

Figure 4.56. Essential three parts of the TM95. a) A layering model that describes the thickness of each layer (or the position of the interfaces, in an equivalent way), or rather the density of interfaces in one meter, which is a function of depth, b) the velocity model that describes the velocity of each layer at its mid-depth (intra-layer), and c) the correlation model of the velocities of a layer with respect to the other layers as the depth varies (inter-layer).

Layering model

The first ingredient of the TM95 for the management of AVs in V_S profiles is the layering model (Kottke & Rathje 2009) (Figure 4.56a). The initial idea comes

from the observation and the analysis of the collected data. Generally, interval velocity profiles have thinner layers at the surface, whereas they have a greater thickness at considerable depth. The choice among the various probabilistic distributions able to reproduce this natural/aleatory phenomenon fell on a Poissonian counting process with a depth-dependent rate (i.e., a non-homogeneous Poissonian counter process).

An aleatory process $N(t), t > 0$ is called a counter process if $N(t)$ represents the total number of events that occurred within the instant t. A typical example of a counter process is the number of people who have entered a particular store at time t, and then $N(t), t > 0$ is a counter process in which an event corresponds when a person arrives at the store. If we say that an event occurs when a child is born, then $N(t), t > 0$ is a counter process where $N(t)$ is the total number of child who were born until the instant t. From the definition, a counter process $N(t)$ should satisfy the following conditions:

- $N(t) > 0$;
- $N(t)$ is an integer value;
- If $s < t$ then $N\ (s) <\ N\ (t)$;
- For $s < t,\ N\ (t)\ - N\ (s)$ is equal to the number of events that have occurred in the interval $(s;\ t]$.

The realization of a counter process is a non-decreasing monotone function constant at times with jumps of unit width in correspondence with the arrival times $t_1, t_2, \ldots t_n$.

A counter process has independent (i.e., is called "Markovian") increments if the number of events occurs in disjoint time intervals are independent. This means for example that the number of valid events occurring within the instant 10 (i.e., $N(10)$) must be independent of the number of events found between the instants 10 and 15, that is $N\ (15)\ - N\ (10)$.

A counter process has stationary (i.e., is called "homogeneous") increments if the number of events found in any time interval depends only on the duration interval. In other words, if the number of events in the interval $(t_1 + s,\ t_2 + s)$, that is $N\ (t_2 + s) -\ N\ (t_1 + s)$, has the same distribution of the number of events found in the interval $(t_1,\ t_2), N\ (t_2) -\ N\ (t_1)$ for each $t_1 < t_2$ and $s >\ 0$.

One of the most important counter processes in time is the homogeneous Poisson process that can be defined as follows, for $N(t), t > 0$ and constant time-rate (or intensity) λ:

- $N(0) = 0$;
- The process has independent increments;
- The number of events in any duration interval t is a distribution of Poisson with average λt for every $s; t > 0$, that is

$$P[N(t+s) - N(s) = n] = \frac{e^{-\lambda t(\lambda t)^n}}{n!}\ for\ n = 0,1,2\ldots \qquad \text{(Eq. 4.25)}$$

Note that from the third condition follows that a homogeneous Poisson process has stationary increments and that $E\,[N(t)] = \lambda t$, which explains why it is called time-rate of the process. Indeed, a Poisson model is defined homogeneous (i.e., stationary) if it has constant time-rate, while not homogeneous (i.e., non-stationary) when the time-rate of the process is a dependent variable.

The definitions proposed were extended from the variable time to the variable space, adopting a non-homogeneous formulation. In the TM95, the Poisson model is applied to the distribution of the layer interfaces with depth. The average thickness of the layers is dependent on the depth (i.e., the count of interfaces with depth follows $\lambda(z)$, and the process in non-stationary). However, the thickness of the layer i remains probabilistically independent of the thickness of the $i-1$ (for the definition of a Poissonian process, it is still Markovian).

Generally, the distribution within each window for the thickness of the layers h is exponential, for which the relative Probability Density Function (PDF) is written as:

$$f(h) = \lambda e^{-\lambda h} \text{ for } h > 0 \qquad \text{(Eq. 4.26)}$$

whereas the Cumulative Density Function (CDF) can be written as:

$$F(h) = 1 - e^{-\lambda h} \text{ for } h > 0 \qquad \text{(Eq. 4.27)}$$

From the equations above, it is possible to generate random distributions of thicknesses h with a constant spatial-rate λ (e.g., in case of the homogeneous process):

$$h = \frac{\ln[1 - \mathrm{F(h)}]}{-\lambda} \text{ for } 0 < F(h) < 1 \qquad \text{(Eq. 4.28)}$$

However, Toro (1995) implemented a non-homogeneous Poisson model. He chose a modified power-law to characterize the dependence of the layer boundaries on the depth:

$$f(h,z) = e^{-\lambda(z)h} \text{ for } h > 0 \qquad \text{(Eq. 4.29)}$$

$$\lambda(z) = c_3(z + c_1)^{-c_2} \qquad \text{(Eq. 4.30)}$$

$$\lambda(z) = 1.98(z + 10.89)^{-0.89} \qquad \text{(Eq. 4.31)}$$

$$f(h,z) = e^{-[1.98(z+10.89)^{-0.89}]h} \text{ for } h > 0 \qquad \text{(Eq. 4.32)}$$

The parameters c_1, c_2, and c_3 are obtained from the database. Toro (1995) showed that the experimental data is quite in agreement with the model predictions. He plotted (Figure 4.57) the experimental transition rate as the number of interfaces 10 m above and 10 m below a certain depth, divided by the number of profiles (e.g.,

at 50 m it is calculated as the number of boundaries between 40 and 60 m divided by the number of database profiles that reach a depth greater than 50 m).

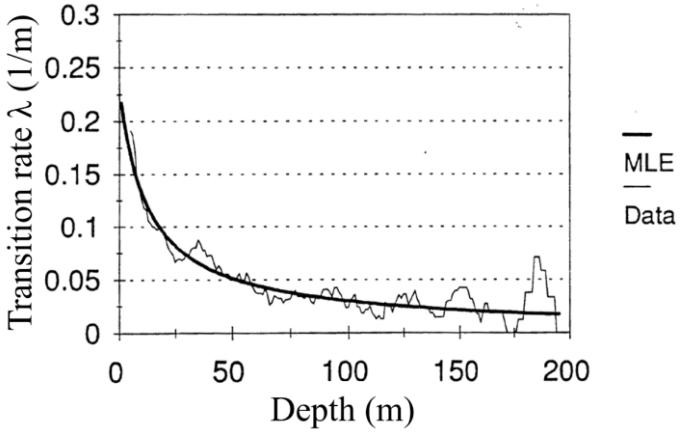

Figure 4.57. Comparison of the experimental transition rate obtained from the database and the theoretical transition rate obtained with the modified power law and the model parameters proposed (after Toro (1995)).

Velocity model (intra-layer and inter/layer)

The initial assumption of the TM95 regards the independence between the random variable "thickness" and the random variable "interval velocity". Indeed, once the model for the layer thicknesses was validated, Toro (1995) suggested separate management of the interval V_S velocities (i.e., intra-layer and inter-layer, Figure 4.56b-c).

In particular, the intra-layer model describes how the median velocities of each layer are distributed with respect to the median profile at depth z (i.e., equal to the depth of the layer's midpoint). Then, the interval velocity is assumed as lognormally distributed around the median, and the uncertainties are computed as a logarithmic standard deviation.

The inter-layer model represents the stochastic process that should reproduce the correlation of the interval velocity between consequent layers (i.e., the relationship between the random variable normalized as a function of depth). Two approaches were usually adopted prior to the introduction of the Toro model. The first allowed scaling and multiplying the velocity at each depth by a random factor or adding a quantity to the average velocity for each depth (McGuire et al. 1988, Toro et al. 1992, EPRI 2013). The second assumed, on the contrary, independence (i.e., that the velocity of a layer has no dependence on the layer above) (Constantine et al. 1991, Field and Jacob 1993). The TM95, instead, is in the middle of these two approaches, with a first-order autoregressive model.

Therefore, within the velocity model, one should take into account the discrete statistical distribution of the interval velocities of the individual layer (intra-layer) and the relationship between the velocity of a layer and that of the one above (inter-layer). These models are entirely independent in the TM95.

The intra-layer velocity model is based on a standard-normal discrete random variable S_i calculated as

$$S_i = \frac{\ln(\mathrm{V_i}) - \ln[\,\mathrm{V_{median}(i)}]}{\sigma_{\ln(\mathrm{V(i)})}} \qquad \text{(Eq. 4.33)}$$

where V_i is the interval velocity of the layer i referred to the depth of its midpoint, V_{median} is the velocity of the median profile at the same depth, and $\sigma_{\ln(\mathrm{V(i)})}$ is the logarithmic standard deviation at the same depth. Toro (1995) showed that S_i is approximable from a normal Gaussian distribution, which is equivalent to saying that V_i is approximable with a log-normal distribution, at a fixed depth z. In particular, Li & Asimaki (2010) used the theories described in Benjamin & Cornell (2014) to confirm the normal distribution, through the 10% Kolmogorov-Smirnof boundaries shown in Figure 4.58.

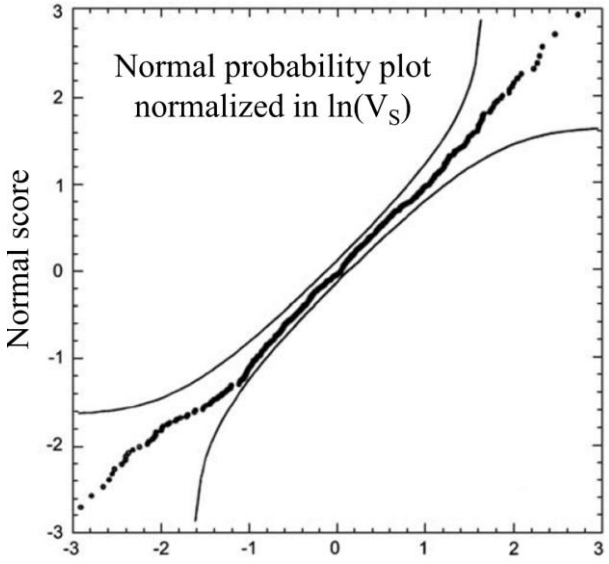

Figure 4.58. Lognormal probability plot evaluated using the ensemble of data from the EPRI shear wave velocity database. Smooth curves correspond to the 10% Kolmogorov-Smirnov bounds of the probability distribution. A lognormal distribution (after Li and Assimaki (2010)).

The inter-layer velocity model is based on a first-order autoregressive model. An autoregressive (AR) correlation is a mathematical model that predicts the value of a given physical quantity (generally a function of time) and place it in relation to the previous values. This means that the prediction of a given phenomenon over time (in our case, in space) is somehow influenced by what happened earlier (in our case, above). The model presented by Toro to evaluate layers' correlation is even more simplified because he used a first-order autoregressive correlation. This means that, unlike higher orders (2, 3, ... n), the prediction of the value of an event over time (i.e., space) is only a function of the previous (i.e., above) value. The first-order autoregressive model is used to correlate the interval velocity of one layer with the one above. As seen for the non-homogeneous Poisson model, the first-order autoregressive model is also a Markovian stochastic process. Indeed, it can be seen that the value at a certain depth is only a function of the previous one.

A particular case regards the first value, for $i = 1$

$$S_1 = \varepsilon_1$$

Then, for $i = 2,3 \dots n$

$$S_i = \rho S_{i-1} + \sqrt{1-\rho^2}\varepsilon_i$$

where S_i is the standard-normal discrete random variable described above for the layer i, ρ is the correlation coefficient (i.e., the coefficient of auto-correlation) referred to the depth of the S_i midpoint, S_{i-1} is the standard-normal discrete random variable for the layer $i-1$, and ε_i is a random variable with zero mean and unit standard deviation. The equation above means that the S_i of the layer i (corresponding to a depth equal to the depth of the layer midpoint) is a normal random variable with mean equal to ρS_{i-1} and standard deviation equal to $\sqrt{1-\rho^2}$.

For example, if we assume a coefficient of the auto-correlation ρ constant with depth, it is possible to write for the first layer (i.e., $i = 1$)

$$S_1 = \frac{\ln(\mathrm{V_1}) - \ln[\,\mathrm{V_{median}}(1)]}{\sigma_{\ln(\mathrm{V}(1))}} = \mathrm{normrnd}(0,1)$$

$$\xrightarrow{yields} \ln(\mathrm{V_1}) = \ln[\mathrm{V_{median}}(1)] + \sigma_{\ln(\mathrm{V}(1))}\mathrm{normrnd}(0,1)$$

where the normrnd can be easily implemented in MATLAB for extraction of a random value following a normal distribution with mean zero and unit standard deviation.

Then, for the following layer (i.e., $i = 2$)

$$S_2 = \frac{\ln(\mathrm{V_2}) - \ln[\,\mathrm{V_{median}}(2)]}{\sigma_{\ln(\mathrm{V}(2))}} = \rho S_1 + \sqrt{1-\rho^2}\varepsilon_2$$

$$= \mathrm{normrnd}(\rho S_{n-1}) + \sqrt{1-\rho^2}\varepsilon_2$$

$$= \mathrm{normrnd}(\mathrm{normrnd}(\rho S_{n-1}), \sqrt{1-\rho^2})$$

$$\xrightarrow{yields} \ln(\mathrm{V_2}) = \ln[\,\mathrm{V_{median}}(2)] + \sigma_{\ln(V(2))}\mathrm{normrnd}(\rho\mathrm{normrnd}(0,1)), \sqrt{1-\rho^2})$$

The same can be written for the last layer of the soil column (i.e., $i = n$)

$$S_n = \frac{\ln(\mathrm{V_n}) - \ln[\,\mathrm{V_{median}}(\mathrm{n})]}{\sigma_{\ln(\mathrm{V}(\mathrm{n}))}} = \rho S_{n-1} + \sqrt{1-\rho^2}\varepsilon_n$$

$$\ln(\mathrm{V_n}) = \ln[\mathrm{V_{median}}(\mathrm{n})] + S_n\sigma_{\ln(\mathrm{V}(\mathrm{n}))}$$

$$\xrightarrow{yields} \ln(\mathrm{V_n}) = \ln[\mathrm{V_{median}}(\mathrm{n})] + \sigma_{\ln(\mathrm{V}(\mathrm{n}))}\left\{\mathrm{normrnd}(\rho S_{n-1}), \sqrt{1-\rho^2}\right\}$$

Toro (1995) proposed a variable correlation coefficient with depth. In particular, he found that the correlation is higher for considerable depths and thin layers. The final formulation is, therefore, a function of depth z and distance between the mid-points t (i.e., different from the layers thickness h) as:

$$\rho(z,t) = \big(1 - \rho_z(z)\big)\rho_t(t) + \rho_z(z) \qquad \text{(Eq. 4.34)}$$

where

$$\rho_z(z) = \begin{cases} \rho_{200}\left[\dfrac{z + z_0}{200 + z_0}\right]^b \text{ for } z < 200\ m \\ \rho_{200} \text{ for } z > 200\ m \end{cases} \qquad \text{(Eq. 4.35)}$$

$$\rho_t(t) = \rho_0 e^{\left[-\frac{t}{\Delta}\right]} \qquad \text{(Eq. 4.36)}$$

The following Figure 4.59a reports the values of the various parameters of the model calculated by Toro (1995) and an example of USGS category A+B (Figure 4.59b). An observation that can be made about the obtained values of ρ_{200} that are close to the unit, which would represent a perfect correlation for the layers at depths greater than 200 m. However, the assumption of full correlation is not entirely supported by data, since the underlying data at large depths was scarce. As already mentioned, in fact, the correlation increases with depth, but not so much as to be equal to unity.

a)

	Category							
Parameter	Geomatrix A+B	Geomatrix C+D	USGS A+B	USGS C+D	USGS A	USGS B	USGS C	USGS D
sigma	0.46	0.38	0.35	0.36	0.36	0.27	0.31	0.37
rho0	0.96	0.99	0.95	0.99	0.95	0.97	0.99	0.00
Delta	13.1	8.0	4.2	3.9	3.4	3.8	3.9	5.0
rho200	0.96	1.00	1.00	1.00	0.42	1.00	0.98	0.50
h0	0.0	0.0	0.0	0.0	0.0	0.0	0.0	0.0
b	0.095	0.160	0.138	0.293	0.063	0.293	0.344	0.744
No. Profiles	45	109	204	253	35	169	226	27
No. Layers	243	692	280	1487	129	750	1349	136

b)

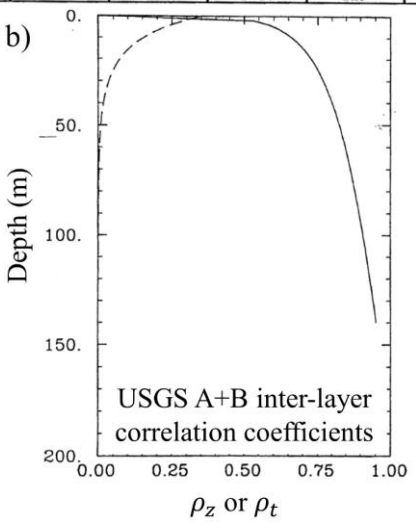

Figure 4.59. Results for the inter-layer correlation model proposed in the TM95. a) Table with the parameters classified for each category, and b)

example of the correlation factors with depth for USGS A+B (after Toro (1995)).

4.3.3 Literature overview

This section illustrates the main examples proposed in the literature where EUs and/or AVs in shear wave velocity models were identified, quantified, and managed. This part completes the discussion in Chapter 3 and Table 3.2, where the shear wave velocity models were addressed in depth.

Section 3.3.1 and Table 3.2 reported examples of IQM of EUs and AVs for studies that do not discuss in depth the geophysical aspect of the problem. In those studies, the V_S profile was only an experimental information to be used in GRAs (i.e., from the numerical modeler point of view). The examples listed in Table 3.2 with the V_S blackened box represent a fundamental basis for the reader who wants to introduce himself to this challenging topic. However, the present Chapter allows the reader to understand better geophysical concepts that were not clarified before, and that can now push the discussion to a further level. Thus, this section aims at summarizing further literature between geotechnics and geophysics and that should be added to that list in Table 3.2.

The first two pioneer examples are reported by Boore & Brown (1998) and Brown et al. (2002). As discussed, these works also showed an inter-method (i.e., invasive/surface wave) comparison for V_S profiles. The authors performed these comparisons also by looking at the different amplifications obtained by a simplified approach (i.e., simplified surface-to-bedrock TTFs). Although they did not perform a complete GRA, they focused the attention on the differences in the small-strain amplifications. Indeed, these differences are entirely depending on the assumed interval velocity profile and directly compare the different dynamic responses. The results obtained by Boore & Brown (1998) (six sites) are reported in Figure 4.60a, whereas the results obtained by Brown et al. (2002) (three sites) are in Figure 4.60b. In both cases, the vertical axis reports the ratio between the TTF of the surface wave test profiles and the invasive test profile. These plots showed a systematic overestimation of the motion obtained from the surface wave models, particularly for high frequencies. It is interesting to remark that these ratios put the invasive test as a target “true” result for the comparison (i.e., the denominator in the ratio). Nowadays, it is accepted that also invasive tests are subjected to a nonnegligible amount of EUs and AVs, as discussed in the previous sections.

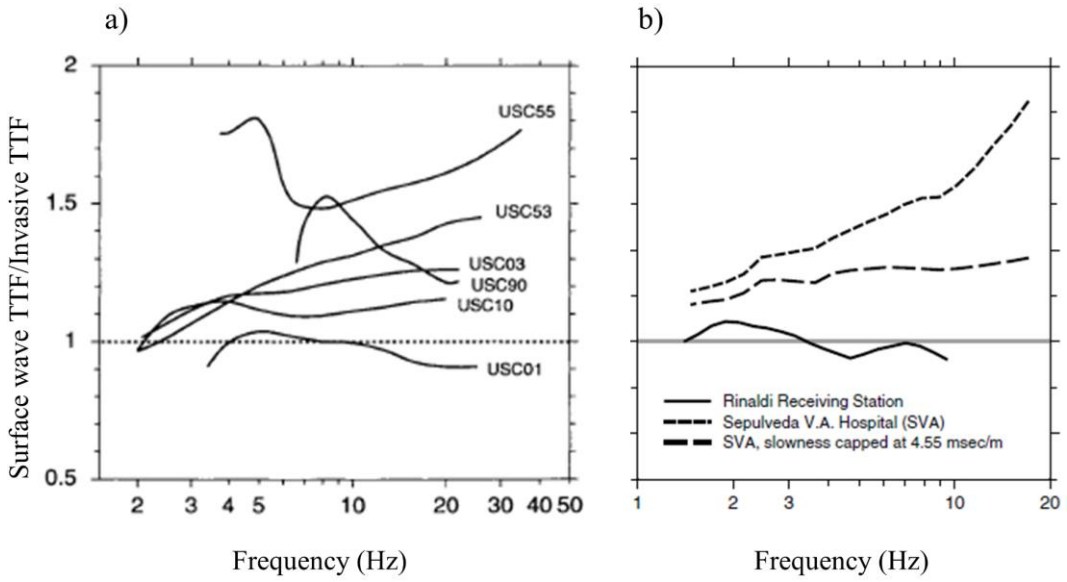

Figure 4.60. Inter-method comparison of the theoretical transfer function ratios (i.e., surface wave over invasive) proposed by a) Boore and Brown (1998) for six sites and b) Brown et al. (2002) for three sites (after Boore and Brown (1998) and Brown et al. (2002)).

Foti et al. (2009) suggested that the influence of EUs and AVs in surface wave testing methods (in particular the solution non-uniqueness) could be evaluated on the results of complete GRAs (i.e., not only in the small-strain range with TTFs). This idea is supported by the fact that Rayleigh waves propagate in the same way for a given class of equivalent profiles, then the dynamic response of the deposit should be similarly equivalent.

The authors adopted the improved Monte Carlo approach proposed in Socco & Boiero (2008) (i.e., the scale property and the one-tail statistical test) for the solution of the inverse problem. At the end of each inversion, this procedure confirms the equivalence of the obtained profiles and provides a framework of all equivalently "good" models.

Then, the authors showed on a synthetic dispersion curve (i.e., a real one perturbed with a Gaussian noise) that the propagation of uncertainties after EL or EQL GRAs is negligible. Six equivalent profiles were found, and each of them could have been selected with the same probability from a deterministic inversion. Comparisons are made on EL analyses with a single input motion, which is then scaled to three different PGAs for EQL analyses. Finally, a set of seven spectrocompatible input motions is selected for the site. The previous result is confirmed, showing that the geophysical equivalence after the inversion corresponds to an equivalence of the dynamic response of the profiles.

Two case studies are also described in Foti et al. (2009): Torre Pellice and La Salle. Also, in this case, spectrocompatible inputs were selected for EQL analyses. Figure 4.61a shows the equivalent interval velocity profiles for Torre Pellice, whereas Figure 4.61b shows the satisfactory EDC-TTC curves match. Figure 4.61c shows the excellent comparison regarding TTFs (i.e., small-strain dynamic behavior) and 4.61d shows the results as surface response spectra.

However, the results of Foti et al. (2009) were in contrast with evidence in Boaga et al. (2011), Roy et al. (2013), and Jakka et al. (2014).

For Boaga et al. (2011), Foti et al. (2009) limited the study to a specific type of V_S profile (i.e., very shallow bedrock and high impedance contrast). Thus, the authors generated five V_S synthetic interval velocity profiles with different characteristics from the deepest bedrock (minor impedance contrast) to the shallowest bedrock (significant impedance contrast). Their results showed a vast range of dynamic responses from profiles associated with the same EDC. However, Socco et al. (2012) highlighted two main concerns for Boaga et al. (2011) work. The first regarded the method used to estimate the solution non-uniqueness and the empirical formulation adopted for the standard deviations of the Rayleigh phase velocity. The second concern regarded the procedure used to apply the input motions in the GRAs.

Similarly to Boaga et al. (2011), Roy et al. (2013) and Jakka et al. (2014) proposed results in disagreement with Foti et al. (2009). However, the analyses by Jakka et al. (2014) were based on a very controversial inversion method. They used a neighborhood algorithm, which requires the acceptable misfit values as input for the inversion. They introduced a limit obtained from the experimental range +/- one standard deviation for each of the two investigated sites. In practice, they processed the various shots, found the EDCs, and calculated the +/- one standard deviation curves. These curves coincided with the empirical ones postulated by Boaga et al. (2011) and primarily opposed by Socco et al. (2012) at low frequencies. Once this process was completed, they calculated the misfit values relative to the two limit curves and proceeded to the inversion. In this way, for example, a TDC similar to these two limits could have been accepted. It is then inevitable that the variability propagated on GRA results is enormous, both as amplification factors (i.e., TTFs) and response spectra. These significant differences are due to the profiles selected for the subsequent EQL analyses that did not reflect the fundamental information contained in the EDC. In other words, the selected profiles did not trace an experimental site signature. Further discussions about this paper are detailed in Comina & Foti (2015) and Jakka et al. (2015), whereas Pettiti et al. (2015) provided comments on Roy et al. (2013).

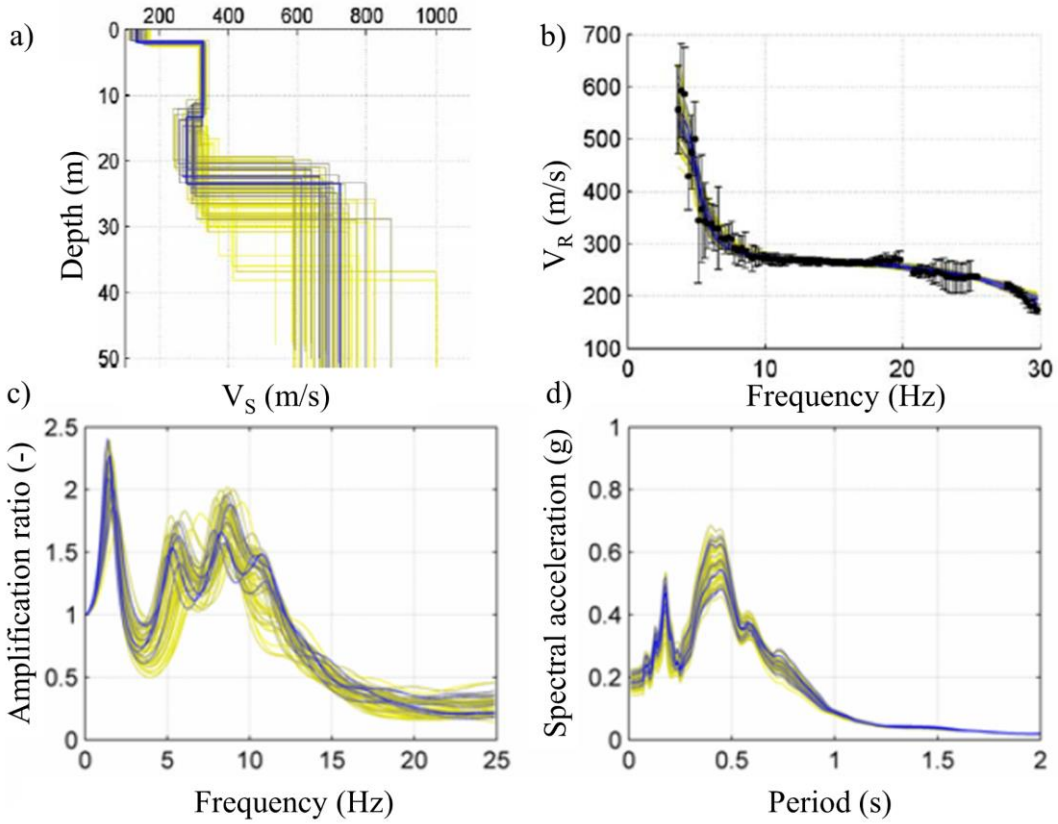

Figure 4.61. a) Equivalent interval velocity profiles for Torre Pellice, b) EDC-TTC comparison, c) comparison regarding TTF (i.e., small-strain dynamic behavior), and d) results as EQL surface response spectra (after Foti et al. (2009)).

Teague & Cox (2016) show a further example of IQM of EUs and AVs in V_S profiles propagated on GRAs. They studied the site 4 of the InterPACIFIC project. The dispersion curve of this site was semi-synthetic and corresponded to an unknown true profile for the participants to the blind test.

Also, there was also an H/V curve representing the particular site under investigation. This paper took into consideration EL and EQL analyses on different V_S profiles obtained with different approaches. In particular, the authors used 350 profiles obtained by an inversion of the EDC with seven different layering ratios (Cox & Teague 2016) (i.e., 50*7) (Figure 4.62). Generally, low layering ratios lead to a large number of thinner layers, while high layering ratios lead to less and thicker layers. All the TDCs seemed to fit the site signature EDC very well, as shown in Figure 4.62. However, the misfit values (in the brackets) gave an initial idea of the best layering model (i.e., best initial parametrization).

The authors also analyzed the profiles obtained from alternative (upper-range and lower-range) models. They applied a +/- 20% shift to the interval velocity models. This operation is partially in contrast with the EPRI (2013) guidelines and the lognormal distribution of the V_S profiles. However, the scaling operation (i.e., perfect inter-layer correlation) was applied to generate the upper- and lower-range

profiles. The TDCs of these profiles already showed a systematic inconsistency with the site signature EDC and are presented in green in Figure 4.62.

In addition to these 352 profiles, other 50+50 profiles were generated with the Toro model. The first 50 were obtained with site-specific parameters, while the second 50 profiles were obtained taking the standard parameters suggested by Toro for the specific USGS class. They calculated the TDC for each of the profiles generated with the Toro model, in order to compare them to the site signature represented by the EDC (Figure 4.63). The results of these profiles gave a preliminary idea according to the obtained misfit. In light of the experimental data, these results would have never been accepted.

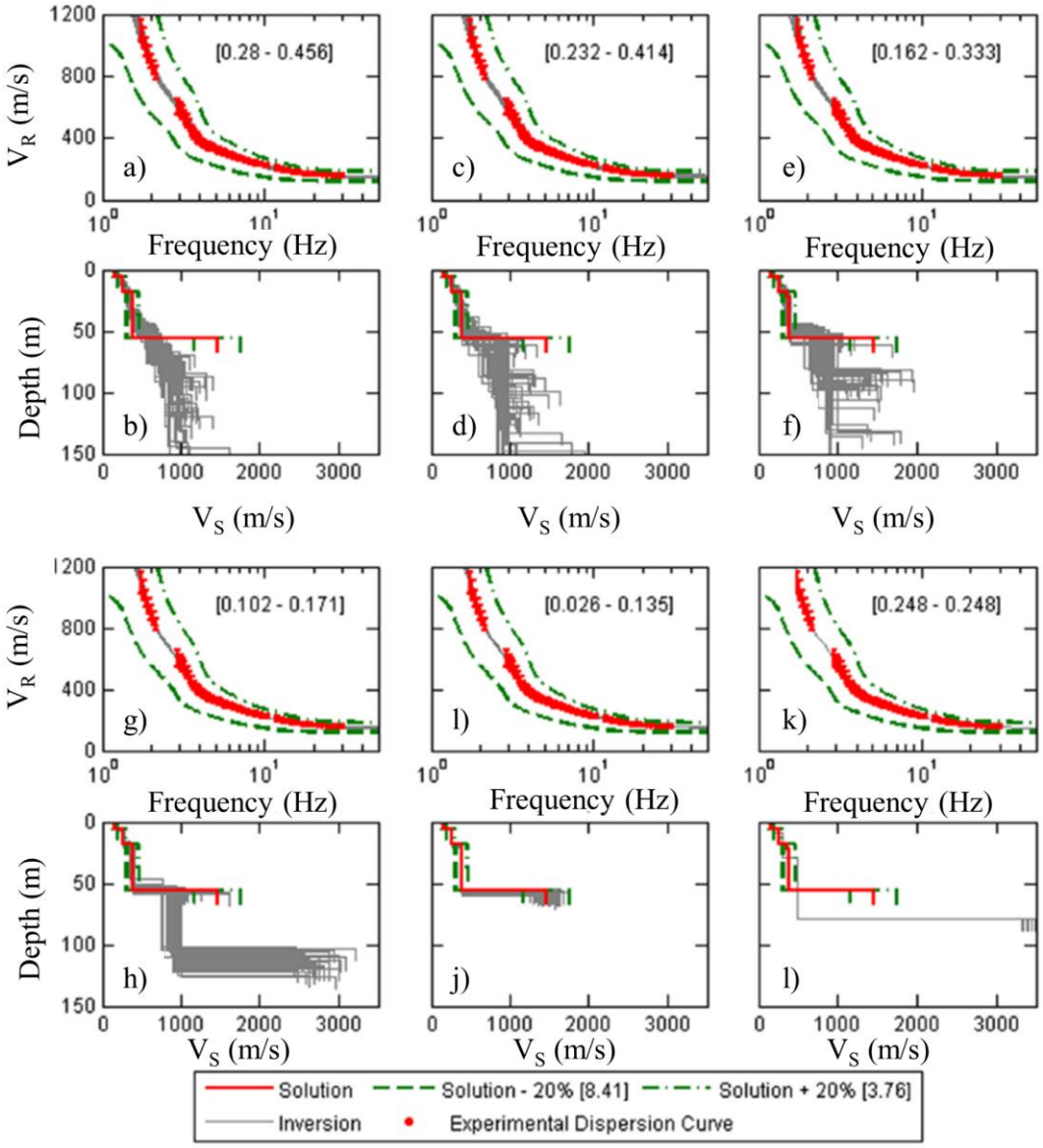

Figure 4.62. Fifty theoretical dispersion curves and 50 corresponding Vs profiles, respectively, obtained from surface wave inversions based on different layering ratios (from a) to l)). The numbers in brackets represent dispersion misfit values. Also shown are the theoretical dispersion curves and the Vs profiles corresponding to +/- 20% (after Teague and Cox (2016)).

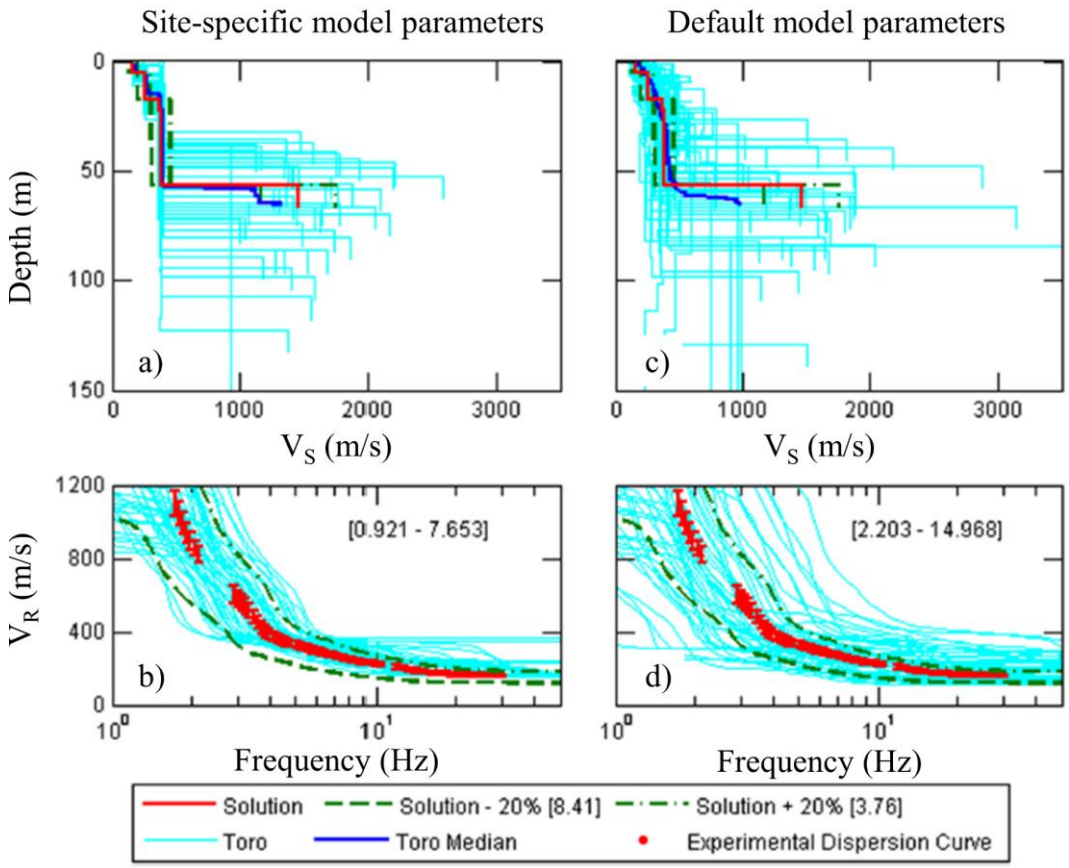

Figure 4.63. Fifty V_S profiles generated using the Toro model and their corresponding theoretical dispersion curve with a) and b) site-specific parameters and c), and d) default/recommended parameters (after Teague and Cox (2016)).

After a further comparison of the TTFs of the 452 profiles with the H/V curve, Teague & Cox (2016) proceeded to select eight input motions that were scaled to 0.05 g and 0.3 g to conduct EQL GRAs. At this point, they compared the medians of the eight inputs for each profile with the results of EQL GRAs coming from the true profile that was finally unveiled. They then proceeded to a new median to find the unique response spectrum for each of the 11 sets of profiles (i.e., seven from the inversion, two +/- 20%, and two from the Toro model) and compared them with the result of the true profile for 0.3 g. The results obtained from the high-intensity input motions are reported in Figure 4.64.

This work concludes that the profiles that come out of the inversions, although they may be visually different, provide accurate and representative results, in accordance with Foti et al. (2009). Both the +/- 20% and the Toro statistical profiles do not present adherence to the site signature EDC, which leads to inaccurate results of the corresponding GRAs. In general, the analyst should pay attention to the signatures of the deposit, whether they are a dispersion, ellipticity curves, and/or empirical transfer functions (even if H/V curves and ETF provide approximately the same information). Indeed, the H/V curves and the ETFs can be used as a fundamental independent a-priori information for the inversion process.

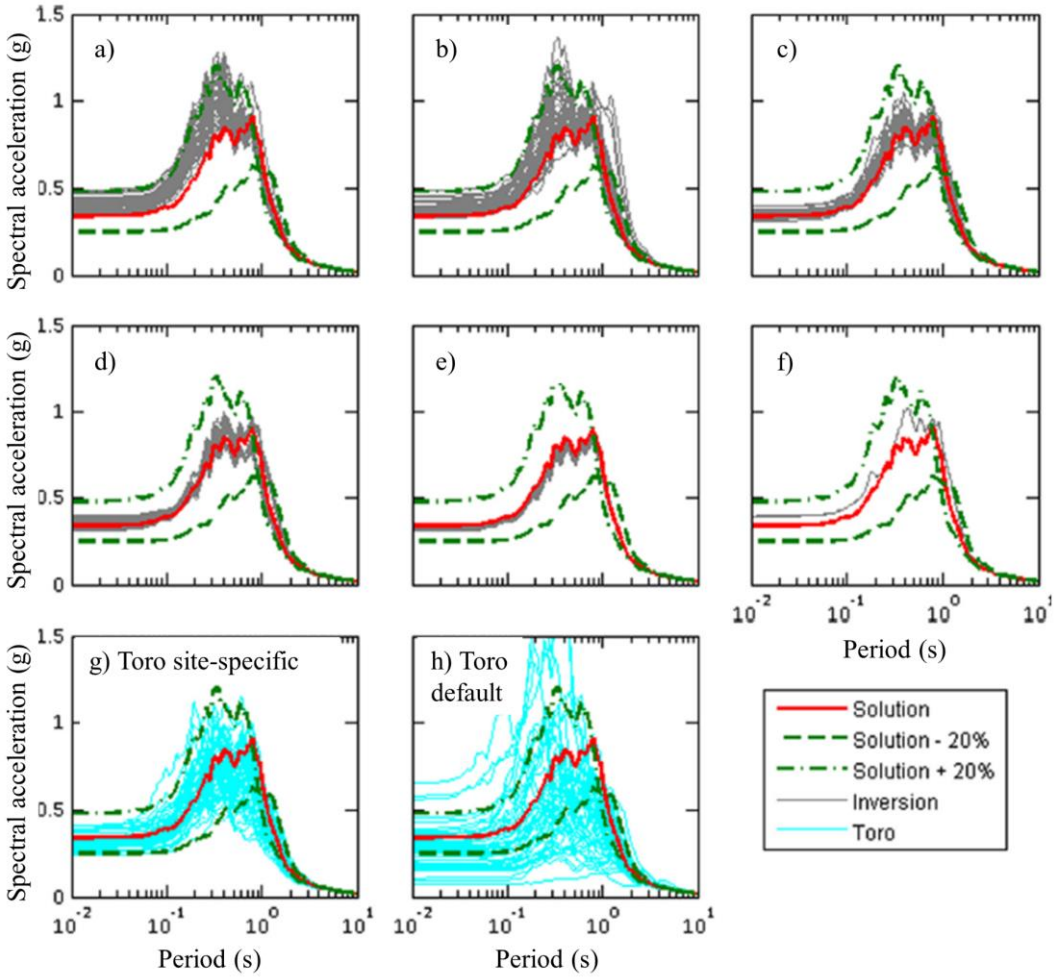

Figure 4.64. Median response spectra obtained from high-intensity EQL GRAs using a suite of 8 input motions scaled to a PGA of 0.3 g and V_S from inversion with different layering ratios (from a) to f)) and those from the Toro model with g) site-specific parameters, and h) default parameters. The response spectra for the solution +/- 20% are shown in all sub-plots for comparison (after Teague and Cox (2016)).

Two companion papers by Griffiths et al. (2016a) and Griffiths et al. (2016b) investigated in depth the influence of EUs and AVs in V_S profiles on GRAs. The authors described the results of the University of Texas at Austin team during the InterPACIFIC project. Differently from Teague and Cox (2016), in this case, two real sites (i.e., Mirandola and Grenoble) of the blind test were studied.

The first paper is preparatory to the second contribute. It is mainly descriptive of the activities and preliminary analyses that were conducted for Mirandola and Grenoble during the InterPACIFIC project (Garofalo et al. 2016a). Primarily, the authors generated three classes of V_S profiles (i.e., profiles from the inversion, statistical profiles, and randomized profiles). In Mirandola, Griffiths et al. (2016a) inverted both Rayleigh and Love EDCs, finding 1000 profiles that matched the EDC very well and were very similar to the V_S profile obtained with an independent CH test. Then, they randomly selected 50 of these V_S interval velocity profiles to proceed with the GRAs.

The second class of profiles is obtained as an alternative (upper-range and lower-range) models and calculating other statistical profiles. They generated six profiles: two +/- 20%, the ones corresponding to the 5th and 95th percentile, the median of the 50 inverted profiles discussed above and the one with the lowest misfit. This class of profiles was created to manage the epistemic uncertainties (even if the +/- 20% do not respect the lognormal distribution, as also discussed for Teague and Cox (2016)).

The last 50 profiles are obtained from the randomization method proposed by Toro with site-specific parameters to manage the aleatory variabilities.

Griffiths et al. (2016a) calculated the TDCs for each of the 106 profiles and compared them to the EDC (Figure 4.65). The results from the +/- 20% and Toro are almost entirely out of the experimental uncertainty, as demonstrated by Teague and Cox (2016). Indeed, these profiles do not trace the dispersion signature of the deposit.

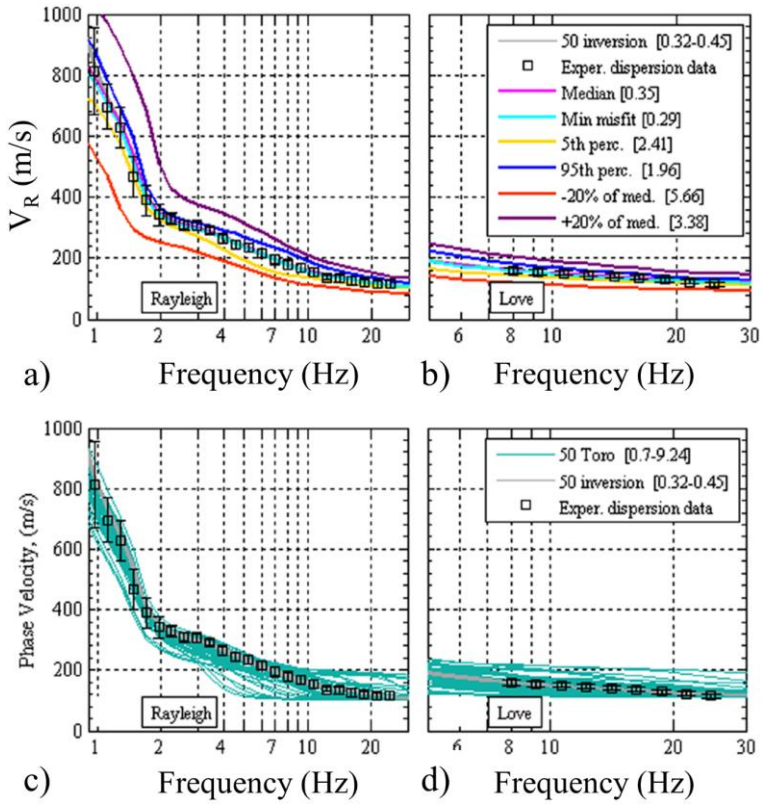

Figure 4.65. Profiles generated for the GRAs at Mirandola. Experimental dispersion data for Mirandola and the theoretical dispersion curves from the 50 inversions V_S profiles, the minimum misfit, the 5th and 95th percentile and the +/- 20% for a) Rayleigh wave and b) Love wave data (within square brackets the misfit values). Experimental dispersion data for Mirandola and the theoretical dispersion curves from the 50 inversions V_S profiles, and the 50 Toro-generated profiles for c) Rayleigh wave and d) Love wave data (within square brackets the misfit values) (after Griffiths et al. (2016a)).

In Griffiths et al. (2016b), the authors continued the work of the previous paper, adding the EL and EQL GRAs. They used a suite of eight input motions scaled to 0.5 g. In this case, there was not a true response to be used as a reference, as in

Teague and Cox (2016), and then they used the median response obtained from the 50 inversion profiles as a target. Griffiths et al. (2016b) calculated the response spectra and TTFs from EL analyses and initially found an enormous variability from the profiles of the Toro generation. Also, EQL analyses were performed, and results are presented in Figure 4.66 for Mirandola.

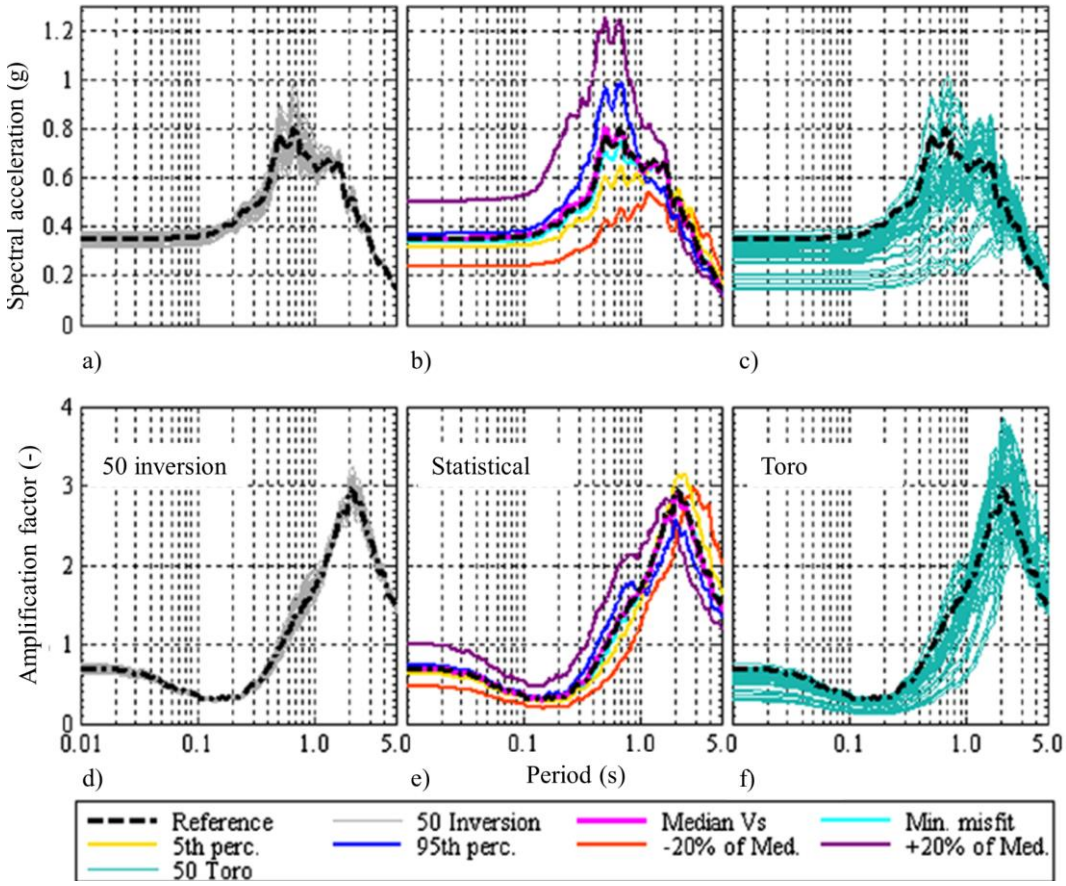

Figure 4.66. a-c) Equivalent linear response spectra and d-f) amplification factors for each Vs profile at Mirandola (after Griffiths et al. (2016b)).

Griffiths et al. (2016a) and Griffiths et al. (2016b) concluded that the results of GRAs obtained from the inverted profiles have undoubtedly lower variability than the other classes of profiles (i.e., statistical and Toro-generated). Statistically generated profiles are always outliers both for the small-strain and nonlinear response. The profiles obtained from the Toro model provided quite conflicting and variable results. Further results in Griffiths et al. (2016b) showed that, if a rejection criterion is applied to the Toro model generation, results that are more consistent can be obtained. However, this modification of the model does not solve the more significant problems seen in Figure 4.66 and represents only a partial solution.

The last example proposed in this literature review is a compendium of many aspects discussed in this Chapter. In particular, the authors used a combination of EDCs, H/V curves, and ETF as site signatures to be traced by the adopted velocity models.

Teague et al. (2018) investigated the measured vs. predicted ground response at the Garner Valley Downhole Array considering shear wave velocity uncertainty

from invasive and surface wave tests. The site under analysis was a DH-array with three sensors and measurements that cover more than 7000 events with a magnitude up to 7.2 and distances up to 720 km. At this site, the three main site signatures (i.e., EDC, H/V curve, and ETF) were available.

The ETF was calculated between the surface and the within the rock. Only seismic events that produced a linear viscoelastic behavior of the deposit were processed. Indeed, 42 events were used, and the ETFs were calculated using the method proposed by Tau and Rathje (2017). The results were calculated with respect to the three single accelerometers and both components for each of the recordings.

The authors collected interval velocity V_S profiles from a DH, a PS logging and two SASW tests (Figure 4.67a). The corresponding TTFs were compared for the profiles that reached the bedrock with the average ETF (Figure 4.67b). Results showed a wide discrepancy in the resonant frequencies, assessing the limited representativeness of the invasive results.

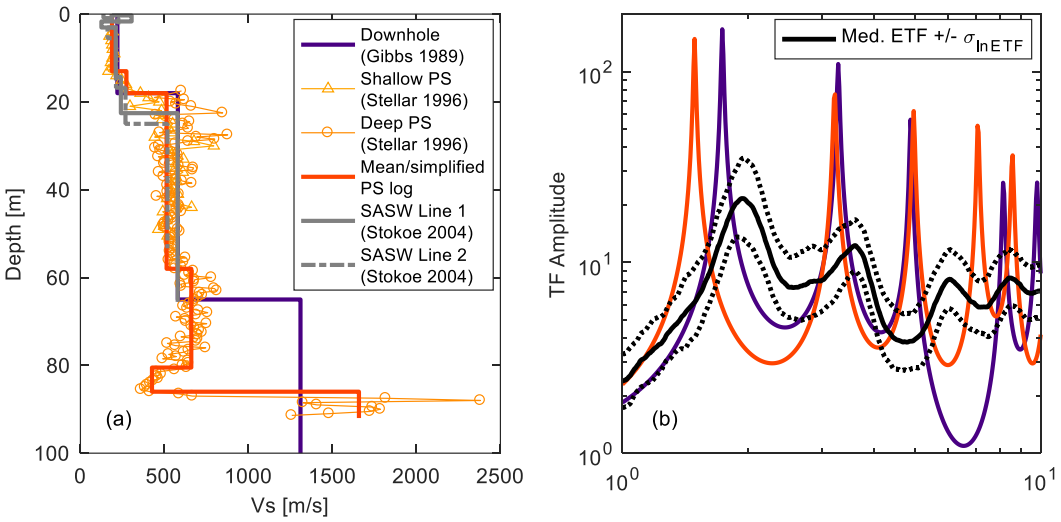

Figure 4.67. a) V_S profiles previously developed at the GVDA site using downhole testing (Gibbs 1989), shallow and deep PS suspension logging (Stellar 1996), and SASW testing (Stokoe et al. 2004b). b) Theoretical linear viscoelastic shear wave transfer functions (TTFs) between a depth of 150 m and the ground surface were computed for the previously developed V_S profiles that extended into rock (i.e., seismic downhole and simplified PS logging). Also shown in b) is the median ETF +/- σ_{lnETF} (after Teague et al. (2018)).

The primary idea of the paper was that if only measurements from invasive tests are available at the site, the spatial dispersion (i.e., AVs) of the profiles is unknown since most of the time the collection of a suitable statistical sample is prevented. Similarly, the management of EUs is not straightforward, given that each method has its peculiarities, as primarily discussed in this Chapter. Moreover, the previous examples showed a total failure of the conventional methods for the management of AVs and EUs. For these reasons, the authors decided to only randomize the invasive profiles with the Toro model and parameters suggested by

Stewart et al. (2014a). The results were provided as randomization of 100 profiles for each baseline in Figure 4.68a (DH-based) and Figure 4.68b (PS logging-based). As previously seen, the medians of the randomized suites (in dashed yellow) are very similar to the baseline choices, but there is a glaring discrepancy of many profiles, due to problems inherent to the Toro model.

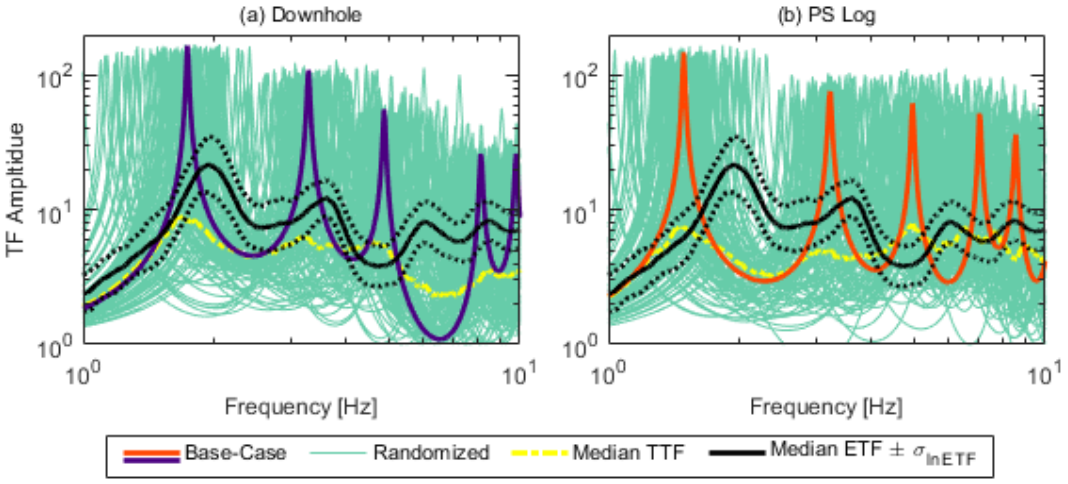

Figure 4.68. Theoretical linear viscoelastic shear wave transfer functions (TTFs) between a depth of 150 m and the ground surface for Vs profiles developed via randomization about the a) downhole Vs profile and b) PS suspension log Vs profile (after Teague et al. (2018)).

In addition to previously performed invasive and surface wave tests, the authors conducted a MASW test at the site. Furthermore, AVA measurements with a circle configuration were acquired, in order to obtain more information at different frequencies. The authors proceeded to evaluate also the H/V curves, in accordance with the SESAME criteria. The results showed a clear peak around 2 Hz (i.e., close to the peak of the ETF), with a definite tendency to increase with the opening of the measuring circle.

Three EDCs were obtained for each of the three accelerometers (i.e., North, South, and Central) in order to evaluate the spatial variability. For the experimental uncertainties, COVs of the Rayleigh phase velocity were also evaluated. The inversion of the EDCs was performed investigating the parameters of space with different layering ratios. An initial check concerning the results obtained with the HVSR tests was performed, rejecting all the realizations from the inversion that did not represent the H/V data.

The authors kept 33 profiles for each layering ratio (i.e., 6) and location (i.e., 3). This means 99 profiles for each layering ratio, which number is comparable with the 100 profiles obtained from the Toro model and the invasive test baselines.

In this way, the three locations together account for AVs at the site, while the EUs are taken into account with the different layering ratios.

Figure 4.69 shows the results of the TTFs calculated for each interval velocity profile from the inversion compared to the results of the HVSR method (i.e., ETF). The outcome is very satisfying, especially for the first resonance peaks that are very

well reproduced. This is in contrast with Figure 4.68, where the profiles obtained from the Toro model were inadequate to trace this further site signature.

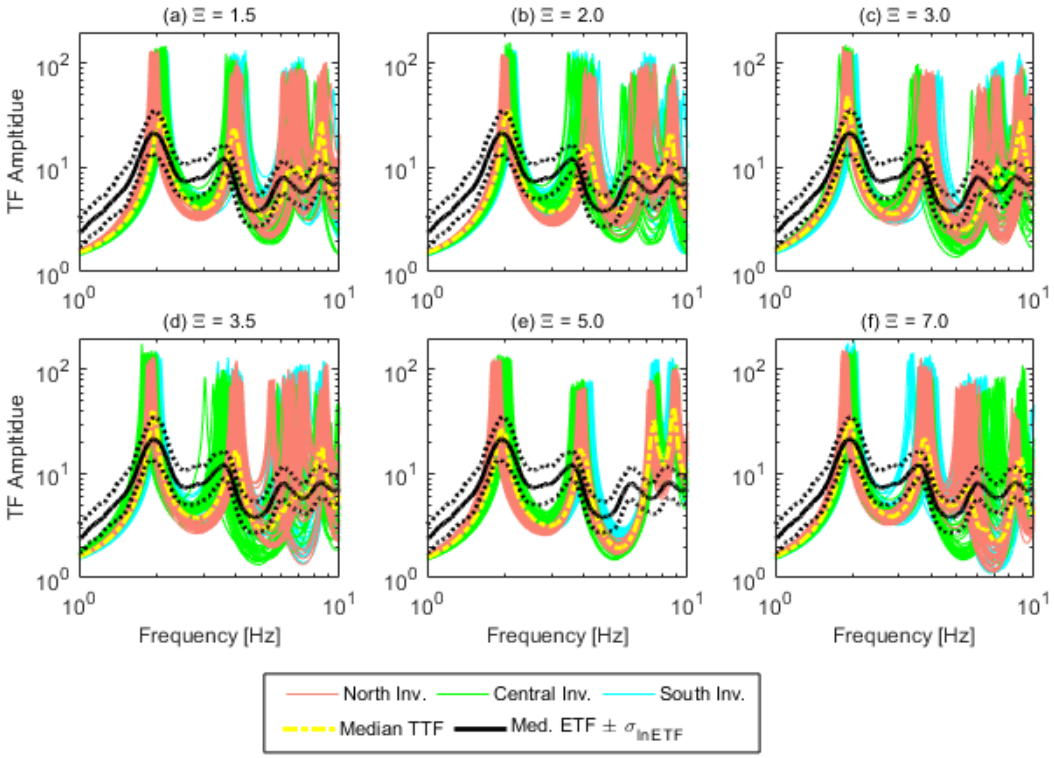

Figure 4.69. Theoretical linear viscoelastic shear wave transfer functions (TTFs) between the ground surface and a depth of 150 m computed using the inversion Vs for the 99 ground models from the North, Central, and South accelerometer locations developed using layering ratios of a) 1.5, b) 2.0, c) 3.0, d) 3.5, e) 5.0, and f) 7.0. The median transfer function, computed using 99 TTFs (33 from each accelerometer location), is indicated for each layering ratio. Also shown is the median ETF +/- σ_{lnETF} (after Teague et al. (2018)).

At the end of the study, Teague et al. (2018) proposed two methods to improve the Toro model. The first assumes a site-specific set of model parameters (as already seen in previous examples), while the second provides an "appendix" to the model that eventually rejects profiles in apparent disagreement with the site signatures.

The attempt made with the evaluation of site-specific parameters still showed inadequate results. This confirms that this approach is not a clear way to improve the results of the Toro model, as the architecture of the model itself seems biased.

The second attempt showed better results (Figure 4.70). The rejection criterion acts as a filter for meaningless profiles and reduces the obtained inconsistency with independent site signatures. However, this solution is only palliative, as a real modification of the model is not implemented.

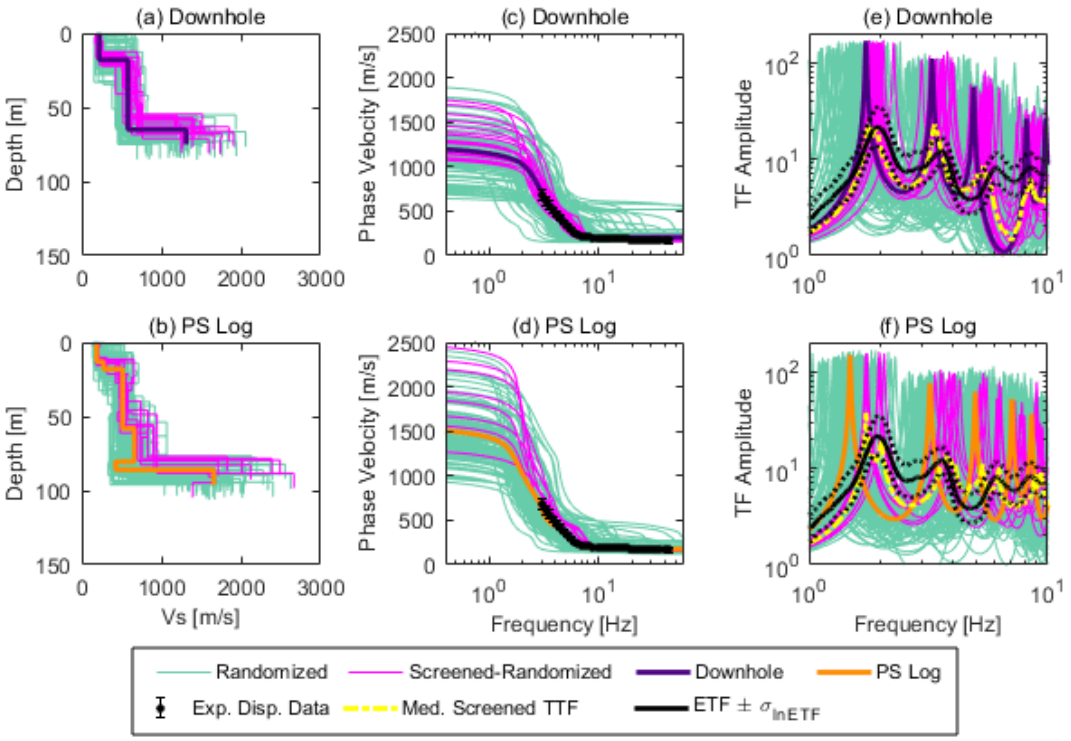

Figure 4.70. a, b) V_S profiles, c, d) theoretical fundamental mode Rayleigh wave dispersion curves, and e, f) TTFs associated with the randomized and screened-randomized V_S profiles. Randomized and screened-randomized profiles were developed using the downhole a, c, e) and PS log b, d, f) V_S profiles as base cases. Shown in c) and d) is the mean experimental dispersion data. Shown in e) and f) are the median ETF and its associated standard deviation.

Finally, following the initial suggestion by Stewart et al. (2014), also Teague and Cox (2016), Griffiths et al. (2016b), and Teague et al. (2018) remark the need for a new geostatistical model for the management EUs and AVs in V_S profiles. Indeed, the Toro model presents many inconsistencies for its specific formulation and randomizing "philosophy". This topic will be central in the next Chapters, with the presentation of an innovative geostatistical model for V_S profiles.

Chapter 5
Polito Shear Wave velocity Database (PSWD)

The present and following Chapters will focus on the shear wave velocity models obtained with surface wave testing methods. In particular, this Chapter is dedicated to the development of a specific database: the Polito Shear Wave velocity Database (PSWD). This database is the essential ingredient for the new geostatistical model presented in the next Chapter for surface wave methods. The collection of extensive and high-quality experimental measurements represents the core of the model. In addition, the PSWD allowed the regression of a useful formulation for the estimation of the experimental uncertainties associated with the experimental data. This formulation represents the first "side product" presented in the dissertation that combines uncertainties and variabilities in the experimental data. Note that the lack of further data in the PSWD represents the reason why a test-specific calibration cannot be performed so far for other seismic tests (e.g., Down-Hole tests, see Section 6.3).

The lack of a rigorous and complete database was indeed one of the most critical aspects of the Toro model (i.e., TM95) (Toro 1995) discussed in 4.3.2. Stewart et al. (2014a) openly suggested the compilation of a shared shear wave velocities database as a critical step towards the management of Epistemic Uncertainties (EUs) and Aleatory Variabilities (AVs) in Ground Response Analyses (GRAs).

Sadiq et al. (2018) and Ahdi et al. (2018) presented a database (heretofore referred to as the USVD database, for its name the United States Velocity community Database) for V_S profiles that is being developed, following similar examples presented over the last few years (Kayen et al. 2004, Stewart et al. 2014b, Ahdi et al. 2017). The USVD is an online map-based interface with downloadable V_S profiles and metadata information. Up to the date of the publication of this dissertation, the database implementation contains only data from California. In order for a site to be included in the USVD, the minimum requirements are geodetic coordinates, elevation values, and the shear wave velocity profile. The files are organized to store coordinates, velocity profiles, dispersion curve data (for surface wave methods), geotechnical data, and HVSR spectral ratios.

Velocity data in the USVD include the geophysical methods used to obtain the interval velocities profile, the type of recorded data, the maximum depth of the modeled profile and the calculated $V_{S,30}$. In the case of surface wave testing methods, the dispersion curve data can be queried as phase velocity with respect to wavelength or frequency. Also, geotechnical data include the penetration resistance of the soils in the profile, and survey logs with cone penetration and laboratory index test results (if available).

Ciancimino et al. (2018) and Aimar (2018) used a database of 272 real V_S profiles mainly from the Italian Strong Motion Database, the Swiss Strong Motion Network of the Swiss National Network (SED), and the European Interreg III project or Seismic hazard and alpine valley response analysis (SISMOVALP). In this case, they aimed at validating the simplified approaches included in Eurocode 8, NTC 2018 (i.e., Italian regulations), and SNZ (i.e., New Zealand regulations) for the soil class amplification factors. Figure 5.1 shows the selected models classified according to the last seismic regulations. Aimar (2018) extended the database with randomization adopting a modified Toro model by creating artificial profiles. In this context, the management of different measures of V_S represented the most crucial challenge. Indeed, different analysts and experimental methods were used in the database, leading to large experimental inhomogeneities.

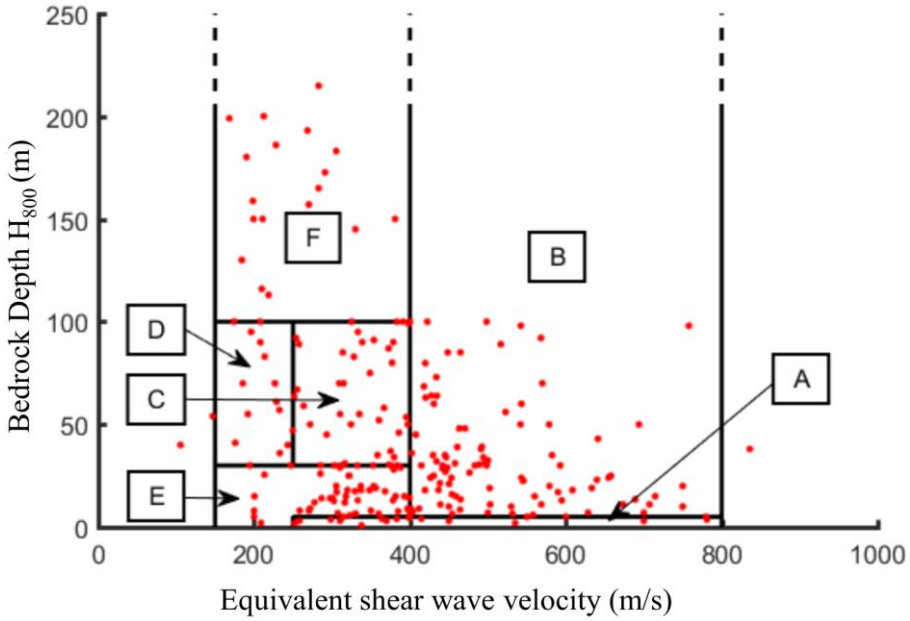

Figure 5.1. Shear wave velocity profiles classified according to the soil classes described in Eurocode 8 and used for the work by Aimar (2018).

5.1 Description of the database

The Polito Shear Wave velocity Database compiles a considerable number of geophysical tests that were performed by the Politecnico di Torino during the last 20 years. The primary attention is devoted to surface wave tests, as the geostatistical model will be developed for this type of tests. However, the database structure is flexible and allows storing additional information useful for the characterization of the site, including additional invasive and non-invasive tests. When enlarged, the PSWD will represent a fundamental basis for the calibration of the geostatistical model presented in Chapter 6 also for other seismic tests.

The first layer of the PSWD is implemented in a Microsoft Excel® spreadsheet to assist the user in the data compilation. This first layer is used to introduce information about the site, the geophysical tests, the geotechnical investigations, and every useful document. These data are stored in a mainsheet (converted into Table A1 in the Appendix) that is then linked to a single specific worksheet for each

site. These worksheets contain the results of the investigation and automatically plot the data for a first quality check.

The second layer of the PSWD is implemented in MATLAB®. A script reads the Excel file and converts the information into a structured file for allowing operations to be performed on the data. The code generates figures for a visual check of the data.

Up to the date of this dissertation (November 2018), 92 Italian sites have been included in the PSWD for their surface wave tests. The tests at the sites were selected to guarantee a high-quality standard. Thirty-nine of these sites also have an additional independent measurement from invasive tests, which allows an inter-method comparison. The surface wave tests for seventy-sites captured only the fundamental mode in the Experimental Dispersion Curve (EDC). Forty-nine of the sites have an experimental evaluation of the V_R standard deviation.

On the other hand, for 21 sites higher modes are apparently influent and are captured in the dispersion curves. Three of them have an experimental evaluation of the V_R standard deviation.

The minimum required data for each site are (see also Table A1):

- Location (latitude and longitude, WGS84);
- Geometry of the acquisition array (e.g., line, circle, triangle, L-shape);
- Array length and geophones spacing (for linear arrays) or maximum aperture (for 2D geometries);
- Type of sources (i.e., active or passive);
- Equipment;
- Experimental Dispersion Curve (EDC) characteristics (i.e., maximum and minimum wavelength, presence of higher modes, experimental estimation of V_R standard deviation);
- Single deterministic interval velocity V_S profile from previous inversions (i.e., maximum depth, V_S of the halfspace, type of adopted inversion).

Additional (i.e., optional) data for each site include:

- HVSR data (i.e., peak frequency and standard deviation);
- Estimation of the line of saturation from P-wave refraction tests;
- Geological and/or geotechnical information (e.g., borehole logs, laboratory test results);
- Invasive test interval velocity profiles (V_P and V_S).

References for the sites included in the PSWD are listed in the last column of Table A1 for further details.

The EDCs, the deterministic V_S interval velocity profiles, and the calculated $V_{S,Z}$ profiles are presented in the Appendix. Note that Figures A1-92 (left) show the EDC along with the standard deviation of the phase velocity for 52 sites (i.e., 49+3), as proposed by Lai et al. (2005) and discussed in O'Neill (2004).

Figures A1-92 (right) show the interval and harmonic average V_S profiles from surface wave methods as proposed in previous works (i.e., single-deterministic best fitting profiles). The interval and harmonic average V_S profiles from invasive tests are also shown (the available 39 sites). In the following Chapters, each EDC will be reinterpreted with a rigorous and systematic approach, leading to a statistical sample of equivalent solutions (Foti et al. 2009, Comina et al. 2011) (as presented in 4.2.2.2 for the Accumoli site).

The geographic position of the sites in the PSWD is shown in Figure 5.2 (each point has a specific color that will be consistently used during the entire dissertation). The highest density of sites is in the central (i.e., Abruzzo and Marche regions), Northeast (i.e., Friuli region), and Northwest (i.e., Piedmont region) Italian areas. Also, a large number of tests were performed in the Eastern part of Sicily.

Figure 5.3 shows the experimental wavelengths associated with the EDCs presented in Figures A1-A92. Note that the corresponding ID shown in the first column of Table A1 replaced the names of the sites. The common wavelengths go from 2-3 m to 50-60 m. However, a good number of experimental measurements covers a band from 1 m to 100 m. The user of the geostatistical model presented in the next Chapter should account for these ranges of applicability.

Figure 5.4 gives an initial idea of the characteristics of the sites included in the PSWD. This Figure shows the $V_{S,30}$ values computed from the single, deterministic interval velocity profiles from previous inversions (i.e., 'o'), or from additional invasive tests (if available, '+' for DH tests, '*' for CH tests, 'x' for PS, and '◊' for SDTM). The red lines divide the soil class categories as described in NEHRP or EC-8 (i.e., note that the NEHRP classification has a further class between 800 m/s and 1500 m/s). Many sites are classified as class C (for NEHRP, but class B for EC-8). The rest are mainly included in class D (for NEHRP, but class C for EC-8). Only two sites are classified in the last category (i.e., E for EC-8; CAT and Pisa, sites 11 and 50, respectively). It is interesting to note that, sometimes, the surface methods and invasive tests assign different classes to the same site (e.g., CAT, Roccafluvione, and Pontremoli-1 Maggio). This happens for sites with conditions close to the classification borders, for which the simplified approach for the site response analysis usually fails. In these cases, the influence of EUs and AVs on the test results can lead to an erroneous estimation of the surface motion.

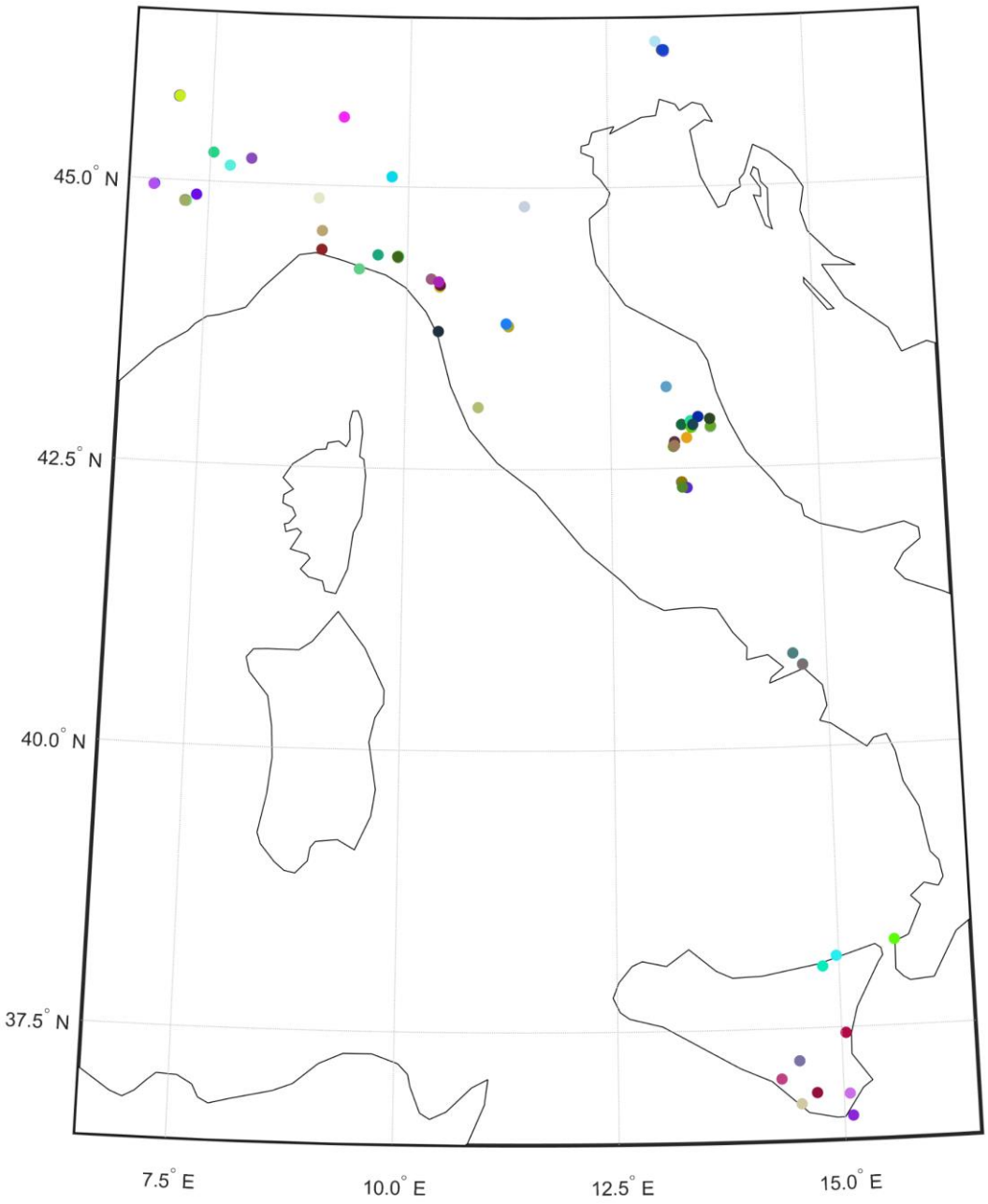

Figure 5.2. Spatial distribution of the sites investigated and included in the PSWD.

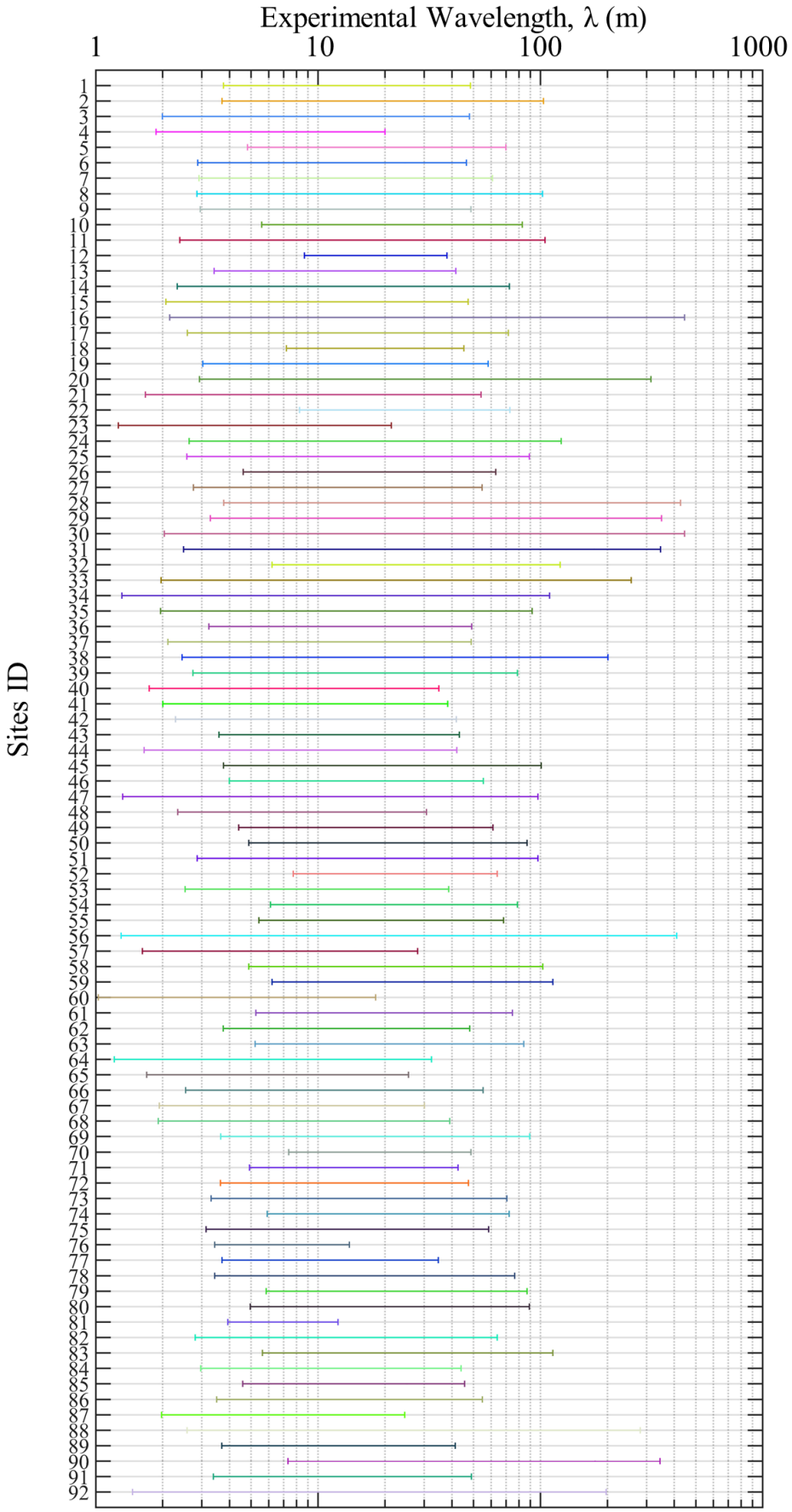

Figure 5.3. Experimental wavelengths associated with each EDC of sites included in the PSWD.

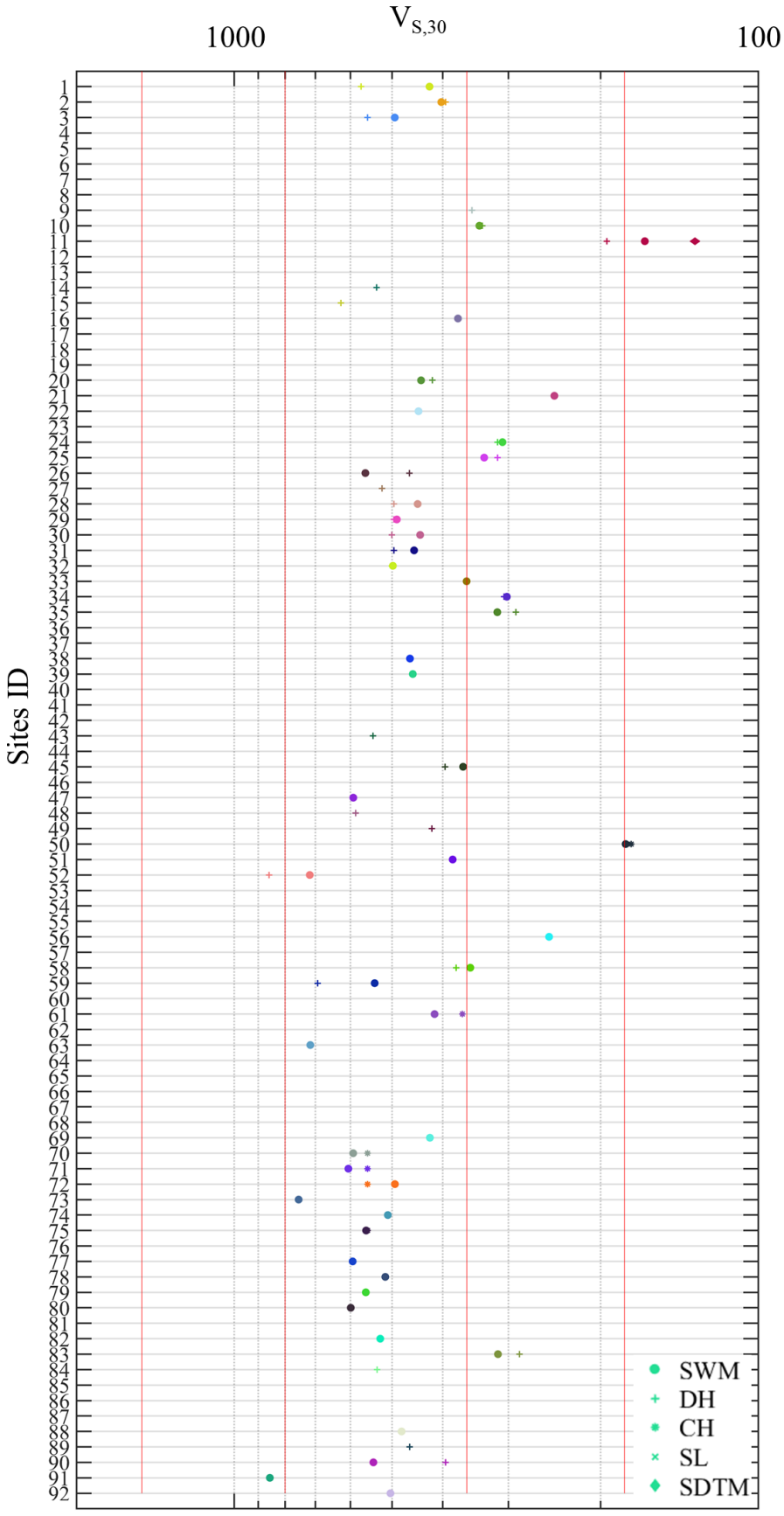

Figure 5.4. Classification of the sites included in the PSWD following the NEHRP or EC-8 provisions.

5.2 EDC uncertainties and variabilities

The epistemic uncertainties and aleatory variabilities associated with the acquisition and processing steps (see 4.2.2.2) are modeled via the standard deviation (i.e., σ_{V_R}) and/or the Coefficient Of Variation (i.e., COV_{V_R}) of the Rayleigh wave velocity at each frequency (Lai et al. 2005, Foti et al. 2014). Note that a precise distinction between EUs and AVs is practically unfeasible in this context. The uncertainties and variabilities in the EDC are usually propagated indistinctly to the management step. As already discussed in 5.1, 52 sites in the PSWD have an experimental estimation of the σ_{V_R} (Table A1). In the present section, only the σ_{V_R} associated with the fundamental mode in the EDC are addressed. This parameter is crucial for the application of the one-tail statistical test to the misfit function proposed by Wathelet et al. (2004) and the definition of the sample of equivalent profiles for each site (see Section 4.2.2.2 and Eq. 4.22-4.23).

A mathematical formulation was needed to estimate σ_{V_R} (or, equivalently, COV_{V_R}) for the 22 profiles in the database for which an experimental assessment was not available (i.e., 71-49). Several possible functional forms for σ_{V_R} or COV_{V_R} were investigated depending on frequency, wavelength, V_R, and combinations of them. In addition, different mathematical formulations and fitting algorithms were compared. The COV_{V_R} was found to be mainly dependent on the frequency f.

An initial estimation of $COV_{V_R}(f)$ was obtained by calculating the moving average and standard deviation of the experimental results (only fundamental modes). This operation suggested a $COV_{V_R} \cong 0.05$ at high frequencies that increases up to 0.15-0.2 at low frequencies. These values are in accordance with other examples in the literature (Marosi & Hiltunen 2004, O'Neill 2004, Lai et al. 2005, Foti et al. 2009, Comina et al. 2011, Wood & Cox 2012, Cox et al. 2014, Garofalo et al. 2016a, Garofalo et al. 2016b, Olafsdottir et al. 2018, Teague et al. 2018).

Two different functional forms were selected for the regression analysis:

- $COV_{V_R}(f) = af^b + c$ (i.e., power law);
- $COV_{V_R}(f) = ae^{bf} + ce^{df}$ (i.e., double exponential power law).

The fitting of the experimental COV_{V_R} was performed using the bisquare or the LAR (i.e., Least Absolute Residuals) robust regression algorithms for each functional form (Dumouchel & O'Brien 1992, Huber 2011). The bisquare method minimizes a weighted sum of squares, in which the weight given to each data point depends on how far the point is from the fitted line. Points near the line get full weight. Points farther from the line get reduced weight. Points that are farther from the line than would be expected by random chance get zero weight. The LAR method finds a curve that minimizes the absolute difference of the residuals, rather

than the squared differences. Therefore, extreme values have a minor influence on the fit.

Results are compared in Figure 5.5. First, Figure 5.5a shows the entire set of experimental COV_{V_R} values for the 52 sites, along with the calculated moving average. Then, Figure 5.5b shows the 4 different methods adopted for the fitting and the goodness-of-fit reported as Adjusted R-Square values. The final choice of the best model was conducted looking at the minimum Adjusted R-Square parameter and the behavior at low frequencies. Indeed, the power law led to an unrealistic vertical asymptote for low frequencies and was discarded. Hence, the double exponential power law obtained using the LAR robust method was selected as the best predictive model. In this case, there is a finite value at $f = 0\,Hz$ ($COV_{V_R} = 0.3 = a + c$) and the equation describes a slight increase of COV_{V_R} for high frequencies (Figure 5.5c). This shape of the curve is then in agreement with the observations made in 4.2.2.2. The loss of resolution for surface wave methods is associated both with too low (i.e., due to the lack of penetration at large depths) or too high (i.e., due to the spatial aliasing) frequencies. The minimum $COV_{V_R} \cong 0.03$ is shown for frequencies between 15 Hz and 35 Hz, where almost any array setup (Casella & Berger 2002) usually provides reliable results.

The values of the parameters are

$$a = 0.2822$$
$$b = -0.1819$$
$$c = 0.0226$$
$$d = 0.0077$$

An additional set of parameters is provided to obtain a conservative estimate, in case of low confidence in the experimental data (dashed red line in Figure 5.5c). This solution is obtained as the 10th percentile (i.e., 10% of the experimental values are above the fitting line). In this case, the suggested parameters are

$$a^* = 0.34$$
$$b^* = -0.1$$
$$c^* = 0.06$$
$$d^* = 0$$

Note that the fitting is valid up to 75 Hz. For higher frequencies, not enough experimental data were available for robust regression and the formulation should be adopted with caution. However, this range of frequencies is of little importance for near-surface characterization purposes.

Also, the suggested relationship regards only the uncertainties for the fundamental mode of the EDC. Further analyses are needed for an estimation of the standard deviations associated with higher mode EDCs.

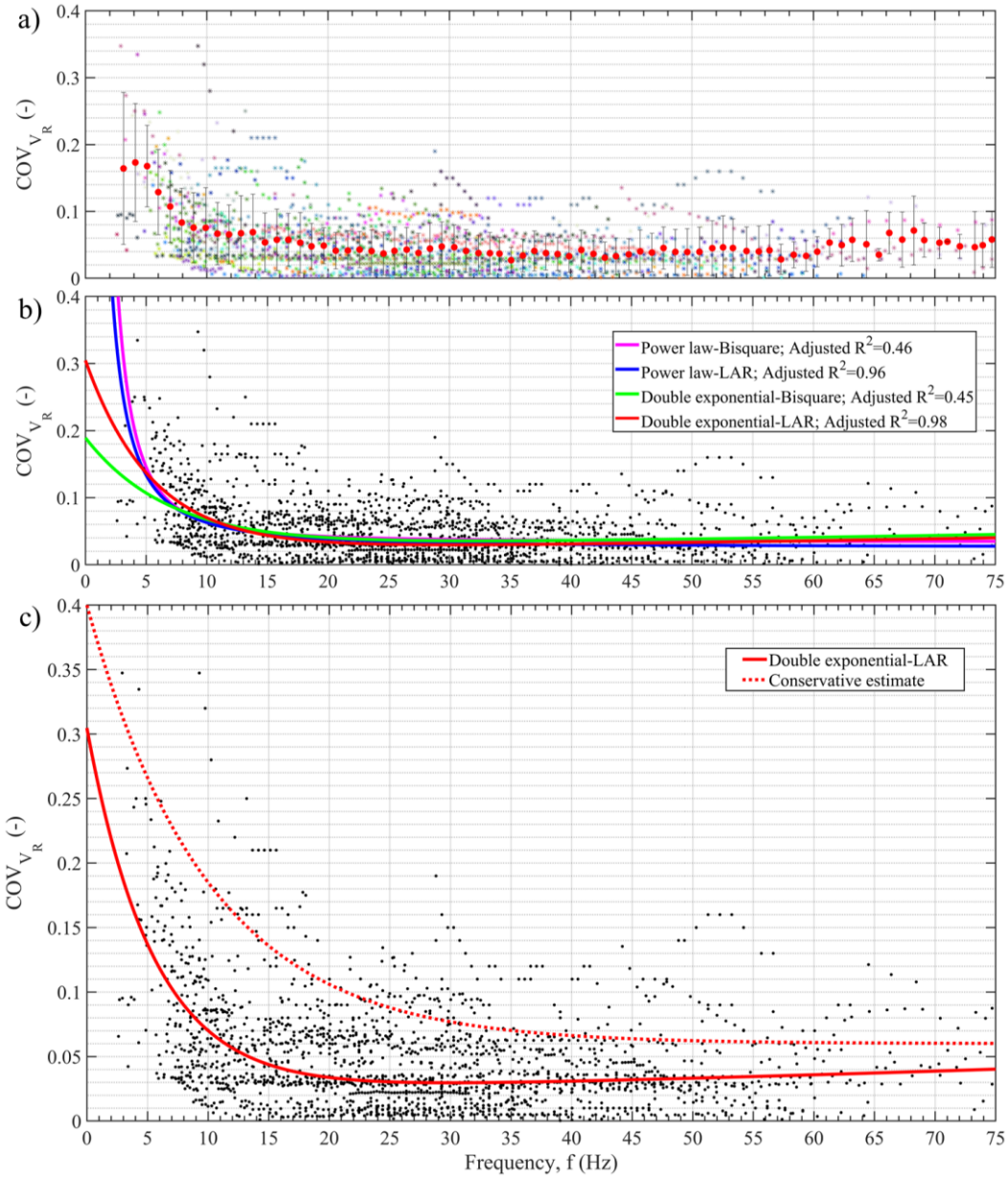

Figure 5.5. Fitting models for the coefficient of variation of the Rayleigh wave velocity, a) entire set of experimental values along with the calculated moving average, b) results of the 4 different approaches used for the fitting and Adjusted R-Square values, and c) selected best model and suggested precautionary choice.

Chapter 6
Randomization models

This Chapter primary presents a new geostatistical model for the independent management of Epistemic Uncertainties (EUs) and Aleatory Variabilities (AVs) in V_S profiles obtained via surface wave tests. This geostatistical model is used to develop a randomization process that generates shear wave velocity profiles consistent with the results of the inversions. Indeed, the primary goal is to reproduce the statistical sample of profiles in the most frequent case of a single available deterministic solution. The management of EUs and AVs follows the identification and quantification steps, then it can be indistinctly applied to both types of uncertainties. However, the model's parameters based on the Polito Shear Wave velocity Database (PSWD) will simultaneously represent both EUs and AVs, as a practical distinction for surface wave tests is prevented.

The model is also applied to the solution of the inverse Rayleigh problem for sites in the PSWD in 6.1. Indeed, various features of the geostatistical model will be anticipated in 6.1.2 for the "free-layering" model. The latter aims at introducing a variable number of layers in search of the best solution performed with the Monte Carlo approach. This randomization model is applied in 6.1.3 for the round-2 of inversions and is a companion of the geostatistical randomization model.

Section 6.2 is entirely dedicated to the geostatistical model calibrated for surface wave methods. This methodology aims at moving from a single-deterministic solution of the problem to a sample of statistical profiles consistent with the characteristics of the test and the site. The generation avoids time-consuming inversions that require specific expertise to obtain a statistically valid sample of equivalent profiles. Each component of this model will be discussed in detail and summarized in Section 6.2.2.

Section 6.3 illustrates the preliminary results of the geostatistical model applied to Down-Hole (DH) tests.

6.1 Solving the Rayleigh inverse problem

The primary goal of this section regards the development of a statistical sample of equivalent (in terms of misfit) V_S profiles (Foti et al. 2009, Comina et al. 2011) for each of the 71 sites in the PSWD where surface wave tests were performed. The equivalent V_S profiles complement the deterministic solution extracted from previous works and reported in Figures A1-92.

The inversion of the experimental dispersion curves in the PSWD followed a two-step process. First, the inversions were performed with a fixed number of layers equal to the number of layers adopted in the original deterministic solutions. This "standard" inversion (i.e., round-1) is reported in 6.1.1 and aimed at producing an initial (i.e., preliminary) ensamble of equivalent solutions for the inverse problem.

Note that the space of the solutions is not entirely investigated with a fixed number of layers. Indeed, a complete statistical sample of equivalent solutions can be obtained only if also this last degree of freedom is taken into account in the inversion process (Cox & Teague 2016).

Second, an inferential analysis was conducted on the results of the round-1 of inversions (Ang & Tang 1984, Casella & Berger 2002, Benjamin & Cornell 2014) and presented in 6.1.2. The inferential analysis allowed for developing a randomization model (hereafter-called free-layering model) for the inversions of round-2. This second round added a degree of freedom to the search of the solutions, as also the number of layers was considered as random variable. After this second round of inversions, each site is associated with a statistical set of best solutions that are the fundamental ingredients for the development of the actual geostatistical model presented in 6.2 for surface wave tests.

Note that the inferential process presented in 6.1.2 for the free-layering model gave essential results also for the development of the geostatistical model in 6.2 for surface wave tests. Ideally, the free-layering model represents a forward analysis randomization model, whereas the geostatistical model is the associated back-analysis randomization model (see Figure 6.1). Although the goal of these two randomization models is different (the first introduces a variable number of layers in search of the best solution, whereas the second moves from a single-deterministic solution of the problem to a sample of statistical profiles), they share the same mathematical architecture. Note that the term "forward-analysis" in this context has not the usual meaning used in geophysics (i.e., a solution of the direct wave propagation problem from a set of known parameters of the theoretical model).

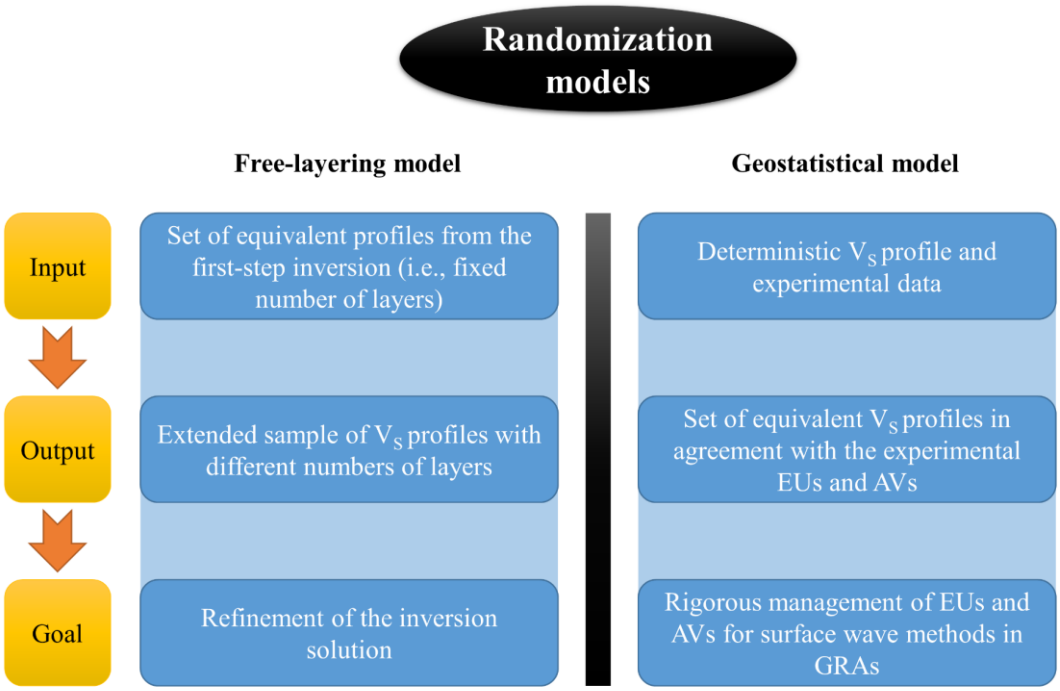

Figure 6.1. Input parameters, output parameters and the primary goal of the free-layering and geostatistical randomization models.

6.1.1 Round-1: inversion with a constant number of layers

The round-1 of inversions was performed with an improved Monte Carlo global search method (Socco & Boiero 2008) with 200000 samples varying the V_S, the layers thicknesses and the Poisson ratios. The forward geophysical problem was solved considering a stack of elastic, horizontal and homogeneous layers using the Haskell-Thomson approach (Thomson 1950, Haskell 1953). The Monte Carlo algorithm generated the samples with a fixed number of layers equal to the number of layers of the target deterministic solution. The analysis of the 200000 possible solutions used the misfit function proposed by Wathelet et al. (2004) for the n-realized (and scaled) profile (see also Equations 4.22-4.23 and Section 4.2.2.2-inversion)

$$M_n = \left(\sum_{i=1}^{k} \frac{\left(V_{R,i} - \overline{V_{R,i}}\right)^2}{\sigma_{V_{R,i}}^2} \right)_n \qquad \text{(Eq. 6.1)}$$

where k is the number of points in the EDC, $V_{R,i}$ is the R-wave velocity of the TDC corresponding to the experimental point at frequency i, $\overline{V_{R,i}}$ is the R-wave velocity of the EDC corresponding to the experimental point at frequency i, and $\sigma_{V_{R,i}}^2$ is the variance of the R-wave velocity at frequency i (as presented also in Figure 4.28a). It can be demonstrated that M_n follows a chi-square distribution with k degrees of freedom. This distribution corresponds to the distribution of the sum of the square of standard Gaussian random variables (Oldenburg & Li 2005, Socco & Boiero 2008). Indeed, $V_{R,i}$ follows a normal (i.e., Gaussian) distribution (Lai et al. 2005) and

$$\left(\frac{\left(V_{R,i} - \overline{V_{R,i}}\right)}{\sigma_{V_R}} \right)^2 = \left(S_{V_{R,i}}\right)^2 \sim \chi^2 \qquad \text{(Eq. 6.2)}$$

The objective of this process is to select a statistical sample of profiles that have a misfit (M_n) lower than a certain threshold value. The threshold value is selected by applying a statistical test to the function of the ratio between the best misfit and the n-realization (Oldenburg & Li 2005, Socco & Boiero 2008) that follows a Fisher distribution, so then

$$\frac{M_{min}}{M_n} \sim \frac{\chi_{min}^2}{\chi_n^2} > F_{\alpha}(\alpha, \mathrm{k}, \mathrm{k}) \qquad \text{(Eq. 6.3)}$$

The chosen level of confidence in this dissertation α is 0.01 (Foti et al. 2009, Comina et al. 2011) and degrees of freedom are equal to k (i.e., number of experimental points of the EDC). The profiles that pass the statistical test are included in the solution of the geophysical problem, representing a set of "equally good" solutions.

For each site, after the inversion, the statistical sample that passed the test was processed, and the following parameters were calculated and stored:

- M_{min} and number of accepted profiles;
- Harmonic shear wave velocity profiles ($V_{S,Z}(z)$) and cumulated travel time profiles ($tt_{S,Z}(z)$);
- Theoretical transfer functions (TTFs).

The TTFs are calculated with the same ancillary values of parameters (i.e., soil and halfspace unit weight and damping) for each V_S profile. As an example, the results of the Acquasanta Terme site are reported in the following. The round-1 of inversions produced a statistical sample of 629 equivalent profiles with $M_{min} = 0.0756$ (see also Table A2). Figure 6.2 shows the entire sample of Theoretical Dispersion Curves (TDCs) along with the EDC. The minimum misfit solution is in red. The agreement between the experimental and theoretical site signatures is mostly acceptable. Figure 6.3a shows the set of 629 equivalent interval V_S profiles that passed the statistical test.

Note that the maximum depth is automatically defined according to the maximum experimental wavelength (Foti et al. 2018). The interval velocity profiles finish with the velocity of the halfspace that has no thickness. The addition of thickness to the halfspace does not change the dynamic behavior of the measured profile, even if the EDC gives information more in-depth. Hence, the interval velocity profiles are presented up to the last interface above the maximum depth of investigation.

Note also that in the entire dissertation the term "halfspace" is not a synonym of "bedrock". The halfspace is the last identified interface where the V_S ends, independently of the velocity value. This is on purpose not consistent with the usual concept of bedrock (i.e., V_S > 600-800 m/s) for GRAs (Baturay & Stewart 2003, Stewart et al. 2014a, Passeri et al. 2018a). This distinction is essential because the geostatistical model has to be as flexible as possible and will not depend on any "artificial" classification method (as for the Toro model).

Figure 6.3b shows the harmonic average profiles that passed the statistical test. The minimum misfit solution is in red. The DH profile is in dashed black. Figure 6.3a and b confirm the significance of the $V_{S,Z}$ profile already discussed in Chapter 4. Indeed, the comparison of the 629 solutions is more suitable in Figure 6.3b, where the layers' schematization is abandoned, and the analyst can better compare the dynamic behavior (i.e., linked to the resonant frequency) of the obtained solutions. This observation is valid also for the inter-method (i.e., invasive vs. non-invasive) comparison. The user can assume good inter-method agreement from Figure 6.3a. However, Figure 6.3b highlights the expected differences, especially for shallow layers, that are the most influent in a GRA (Brown et al. 2002, Bazzurro & Cornell 2004a, Kwok et al. 2008, Rathje et al. 2010, Stewart et al. 2014a, Zalachoris & Rathje 2015). The typical loss of resolution of the DH test for shallow depths (see Section 4.2.1.1) leads to a consistent shift of the $V_{S,Z}$ profile and disagreement along the entire profile depth.

Figure 6.4 completes the comparison within the ensemble of solutions that passed the statistical test. This Figure shows the TTF as a further site signature (Baise et al. 2011, Teague et al. 2018) associated with the geophysical equivalence problem.

The TTFs show consistent similarities throughout a broad frequency band. However, the inter-method comparison is again problematic, especially for high frequencies (i.e., shallow depths). This is inherently due to the differences in the $V_{S,Z}$ profiles seen in Figure 6.4b.

Finally, as for the relationship between the halfspace velocity and depth, Figure 6.5 shows the example for Acquasanta Terme. A clear correlation exists between the two random variables. This correlation is due to the EDC that forces results with higher depths (i.e., longer wavelengths and lower frequencies) to reach also a higher shear wave velocity. This observation will be a pillar for the development of the new geostatistical model, which has to reproduce also this experimental evidence.

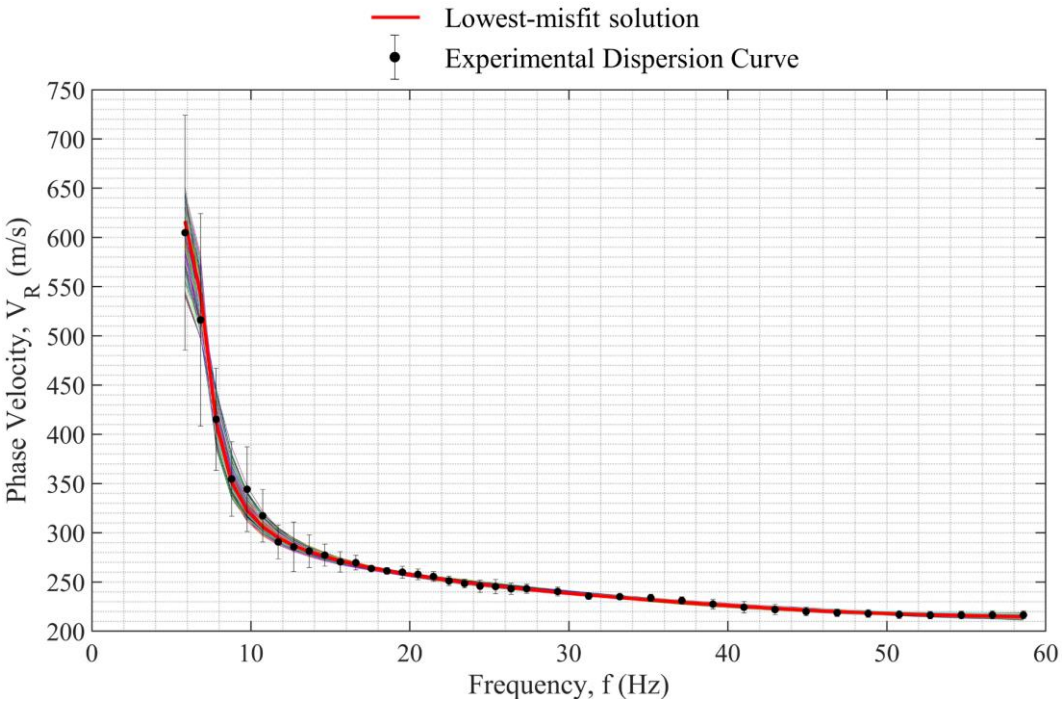

Figure 6.2. Set of equivalent TDCs obtained for the site of Acquasanta Terme (in red the minimum misfit) along with the EDC.

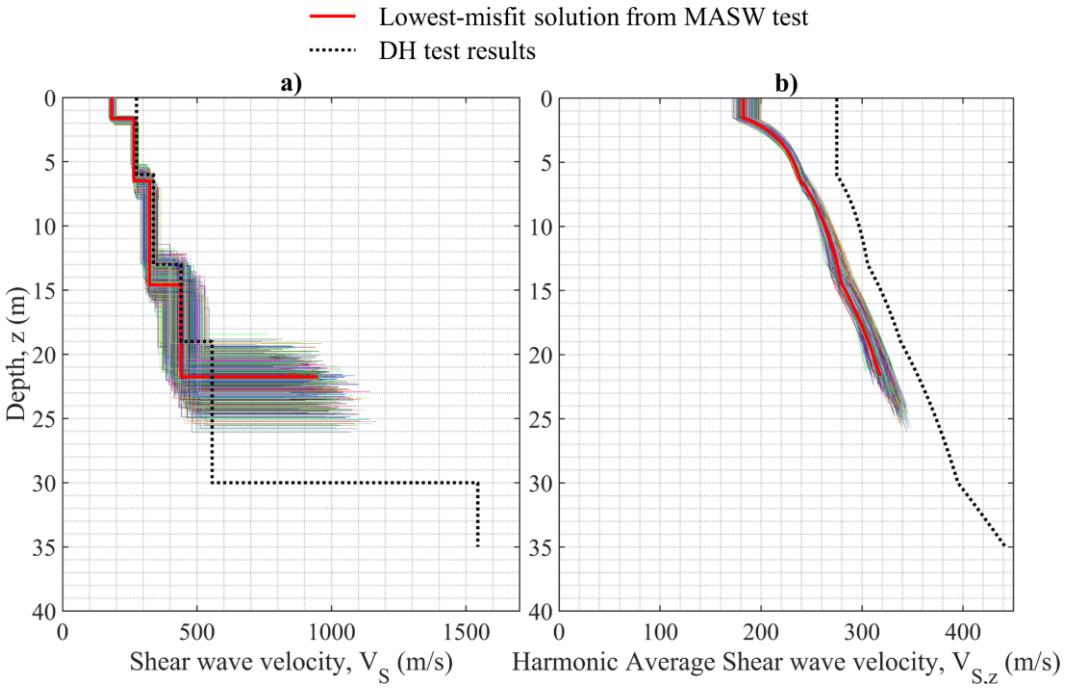

Figure 6.3. a) Set of equivalent interval velocity profiles and b) set of equivalent harmonic average shear wave velocity profiles obtained for the site of Acquasanta Terme (in red the minimum misfit and in dashed black the results from the DH test).

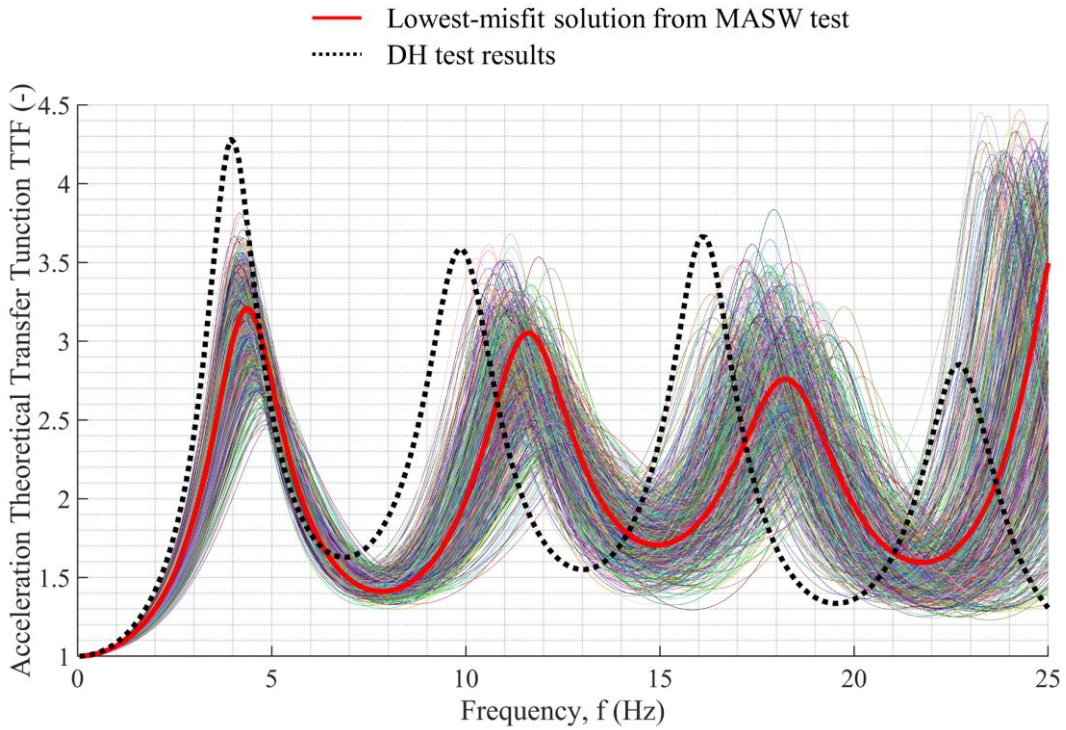

Figure 6.4. a) Set of equivalent interval velocity profiles and b) set of equivalent harmonic average shear wave velocity profiles obtained for the site of Acquasanta Terme (in red the minimum misfit and in dashed black the results from the DH test).

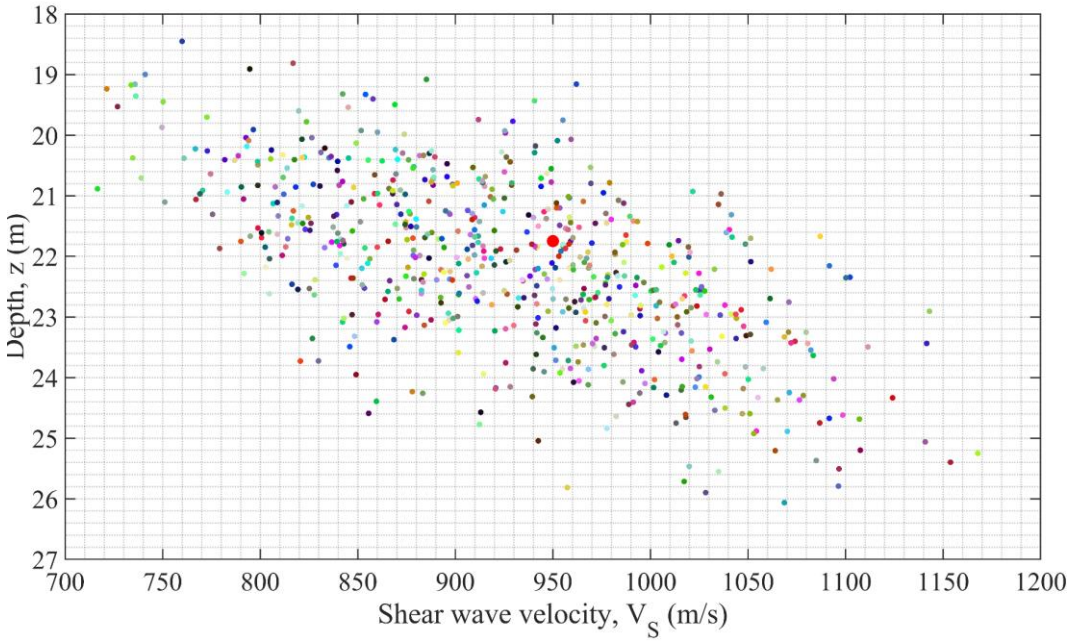

Figure 6.5. Correlation between the shear wave velocity and the depth of the halfspace for Acquasanta Terme.

The results presented for Acquasanta Terme are typical for the whole dataset. Table A2 summarizes the results of the round-1 of inversions in terms of minimum misfit and number of accepted profiles.

$V_{R,\lambda}$-$V_{S,Z}$ relationship

The recent literature suggested the use of transformation laws from the wavelength of the EDC to the depth of the corresponding $V_{S,Z}$ (i.e., $V_{R,\lambda}$-$V_{S,Z}$ or merely λ-z relationship). Section 4.2.2.2 discussed the concept of pseudo-depth (Eq. 4.19) for a first assessment of the V_S interval profile and/or a check of the results after the inversion. This rule of thumb is based on the Rayleigh waves particle motion against depth. Indeed, most R-wave vertical particle motion occurs over a depth approximately equal to one wavelength. Thus, the velocity of propagation is most influenced by the material within one wavelength from the free surface (Foti et al. 2014).

In Section 4.1 we also discussed that the harmonic average shear wave velocity could be seen as an integration of velocity over a specified thickness. The harmonic average shear wave velocity represents the simplest, physical, description of a traveling wave as it is calculated as a distance (i.e., a thickness) over time (i.e., the travel time). Brown et al. (2000), Martin & Diehl (2004), and Albarello & Gargani (2010) suggested the use of the V_R corresponding to a specific wavelength to estimate the $V_{S,30}$. However, the $V_{S,30}$ is only a single point of the $V_{S,Z}$ function that can be better exploited in light of these observations. Plotting the V_R vs. λ and the $V_{S,Z}$ vs. z profiles of the equivalent solutions, a remarkable similarity can be observed, as suggested in Socco et al. (2017).

The transformation between the wavelength λ and depth z is based on a λ-z (i.e., wavelength-depth) linear law that also depends on the Poisson's ratio (Socco & Comina 2017). This linear function is defined by searching on the $V_{S,Z}$ curve, for each point of the EDC, the couple λ-z where V_R=$V_{S,Z}$. Figure 6.6 shows an example of the procedure for the determination of the λ-z law for Acquasanta Terme after the inversions of round-1 . Note that this operation is conducted on the $V_{S,Z}$ average profile (solid red line in Figure 6.6). In this case, the halfspace has a thickness, and the profile is then extended by calculating the mean halfspace depth and the mean halfspace velocity. The investigation depth is assumed equal to $\lambda_{max}/2.5$.

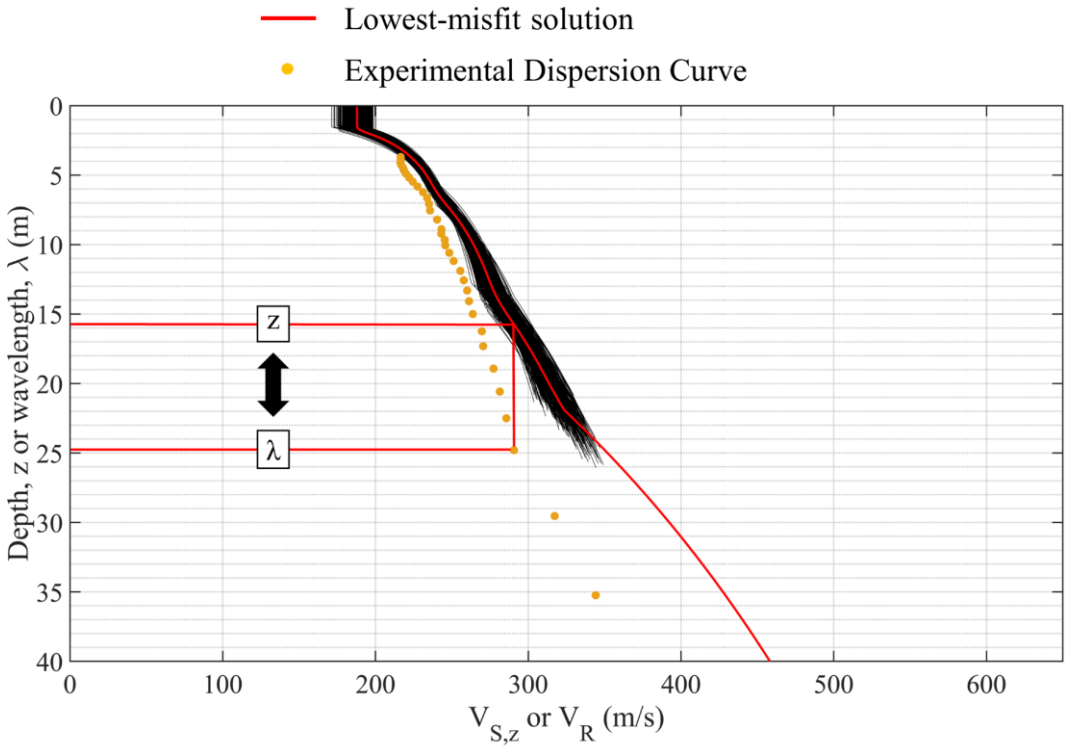

Figure 6.6. Determination of the wavelength-depth (i.e., λ-z) relationship for Acquasanta Terme.

The plot of each λ-z couple calculated for each of the 71 sites after the round-1 of inversions is shown in Figure 6.7. The data scatter is fitted with a simple linear equation in solid red

$$\lambda(z) = az + b \qquad \text{(Eq. 6.4)}$$

whereas the dashed red lined show the 68% confidence bounds of the fitting results. For example, for $z = 30\,m$, $\lambda(z) \cong 42\,m$. This gives a robust estimation of the $V_{S,30}$ in agreement with Brown et al. (2000), Martin & Diehl (2004), and Foti et al. (2018).

The λ-z can replace the use of the pseudo-depth proposed in Equation 4.19 and largely adopted for the analysis of surface wave methods. Indeed, this new transformation is experimentally verified and links two variables (i.e., V_R and $V_{S,Z}$) in a way that is physically consistent.

Note that this λ-z (i.e., a and b) is still based on the results of the round-1 inversion that are not completely refined. The results after the round-2 inversion are given in Section 6.1.3 but the results are very similar to those obtained for the round-1 inversions.

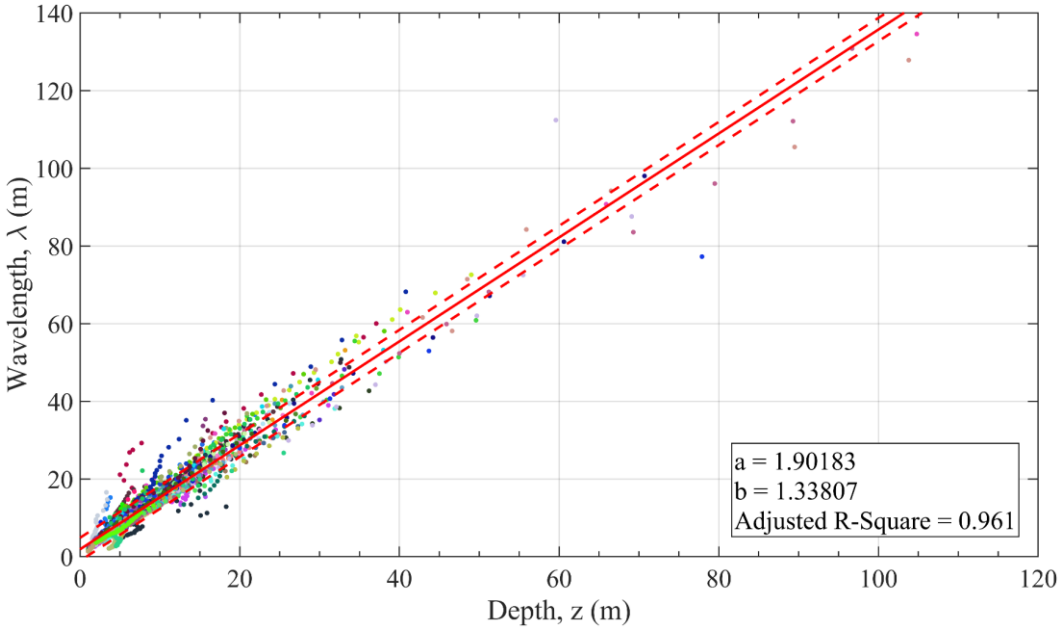

Figure 6.7. Determination of the wavelength-depth (i.e., λ-z) relationship after the first round of inversions.

The results of the application of the obtained λ-z relationship (i.e., $V_{R,\lambda}$-$V_{S,Z}$ relationship) are given for some sites as an example in Figure 6.8 (i.e., Accumoli, GMN, Tarcento-10, and Tarcento-2). This Figure shows the $V_{S,Z}$ profiles after the first round of inversions (in black) and the modified (i.e., shifted) curve with the experimental uncertainties (i.e., σ_{V_R}). The correspondence is excellent. This approach could give the chance for a direct interpretation of the experimental data. However, this application should be studied in depth with further analyses.

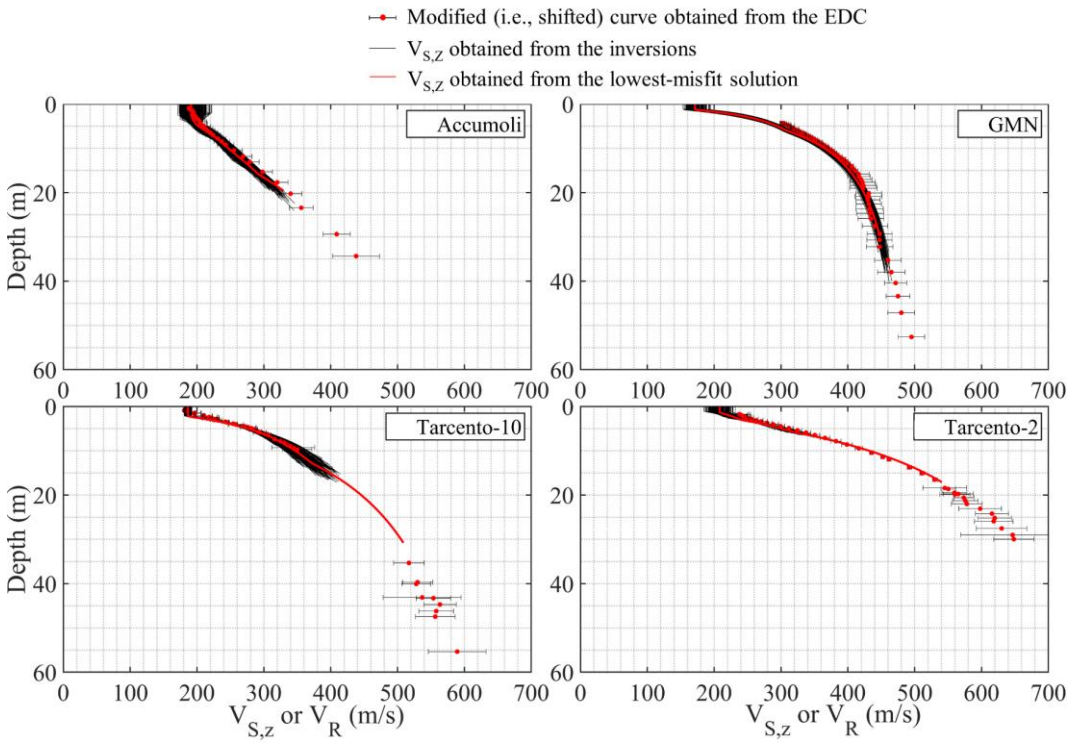

Figure 6.8. Application of the obtained *λ-z* transformation to Accumoli, GMN, Tarcento-10, and Tarcento-2.

6.1.2 Inferential process

The results of the first round inversions were analysed using a statistical inference method. The inferential analysis allowed developing the main characteristics of the geostatistical model presented in 6.2 for surface wave tests, but it is initially used for the free-layering model in 6.1.3. The following observations are indeed valid for both randomization models (see Figure 6.1).

The inferential procedure had to answer four main questions regarding:

1. The V_S statistical distribution for the layers;
2. The statistical distribution of the thickness of the layers with depth;
3. The correlation structure of the velocity between consecutive layers;
4. The distribution of the halfspace velocity and depth and the correlation between the halfspace velocity and halfspace depth.

The first three points regard the model above the halfspace (hereafter-called "column"), whereas the last point regards the halfspace model. It is essential to understand that these two models (column and halfspace) are initially independent and are eventually merged in the final part of the method with a physically based approach.

6.1.2.1 Statistical distribution of V_S

The first question can be answered by looking at the distributions of the results for Acquasanta Terme at each depth, as an example. Figure 6.9-6.14 have the same layout for different parameters. On the left-hand side (panel a), the investigated parameter is presented for a specific depth shown by a red horizontal line. Then, the panel b) illustrates the histograms (upper) and the Q-Q plots (lower) assuming a normal (i.e., Gaussian) distribution.

Similarly, the panel c) illustrates the histograms (upper) and the Q-Q plots (lower) assuming a lognormal distribution (Rasmussen 2004). A quantile-quantile plot (also called a Q-Q plot) visually assesses whether the sample data comes from a specified distribution. Practically, the sample data values are ordered from smallest to largest, then plotted against the expected value for the specified distribution at each quantile in the sample data. The quantile values of the input sample appear along the y-axis, and the theoretical values of the specified distribution at the same quantiles appear along the x-axis. If the resulting plot is linear, then the sample data likely comes from the specified distribution.

Figure 6.9 shows the analysis performed on the interval velocity profiles for Acquasanta Terme at a depth equal to 3 m. The Figure apparently confirms the assumption of the lognormal distribution of the V_S proposed by Toro (1995), Li & Asimaki (2010), and Kottke & Rathje (2009).

On the other hand, Figure 6.10 negates the assumption of the lognormal distribution. Figure 6.10 corresponds to the interval velocity profiles at a depth equal to 6 m, which is close to the depth of an interface. It is clear from both the histograms and the Q-Q plots that the interval velocity profiles cannot be modeled as lognormally distributed close to the depths of the interfaces. At these depths, the functions present a discontinuity, and the lognormal distribution cannot be applied due to the non-uniqueness of the interfaces position. The bimodal distribution is due to the presence of the velocity uncertainties of two layers at the same time. This observation represents the additional proof that the evaluation of V_S should always be carried out by considering the real physical quantities (i.e., lengths and times) separately. Interval velocities should be used only for 1D GRAs as "final result", but the data processing and the randomization models should be based on the separate random variables of length (i.e., thickness) and time (i.e., travel time or interval velocity) separately and modeled by continuous functions.

The evidence of the superiority of modeling interval velocities is confirmed by Figure 6.11-6.14, where the same analysis is presented for the harmonic average and cumulated travel time profiles. Both random variables show an excellent approximation by the normal and lognormal distributions at various depths. However, the lognormal distribution is preferred when modeling non-negative quantities such as velocities. Indeed, the lognormal model avoids unexpected results and better represents this class of physical quantities. Note that the lognormal assumption for the cumulated travel times inherently involves the lognormal assumption for the harmonic average profile. This topic was already discussed in 4.1 in Equation 4.2 and 4.4. Hence, the evidence of lognormally

distributed $V_{S,Z}$ follows the assumption of cumulated travel times lognormally distributed:

$$V_{S,z}(z) = \frac{z}{tt_{S,z}(z)} \quad \text{(Eq. 6.5)}$$

$$\log\left(V_{S,z}(z)\right) = \log(z) - \log\left(tt_{S,z}(z)\right) \quad \text{(Eq. 6.6)}$$

We can now conclude that the free-layering model and the geostatistical model have to separately randomize times and spaces (i.e., thicknesses, in the next section).

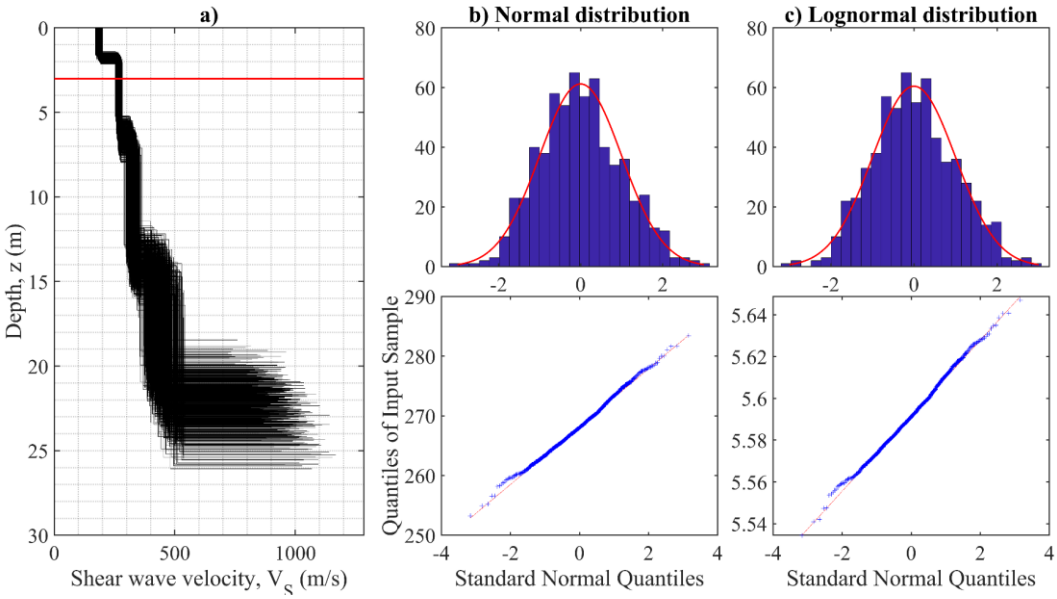

Figure 6.9. Inferential method applied to the interval velocity profiles at a depth equal to 3 m for Acquasanta Terme. a) Set of equivalent profiles obtained after the first round of inversions (i.e., fixed number of layers), b) normal distribution panel as a histogram and Q-Q plot, c) lognormal distribution panel as a histogram and Q-Q plot.

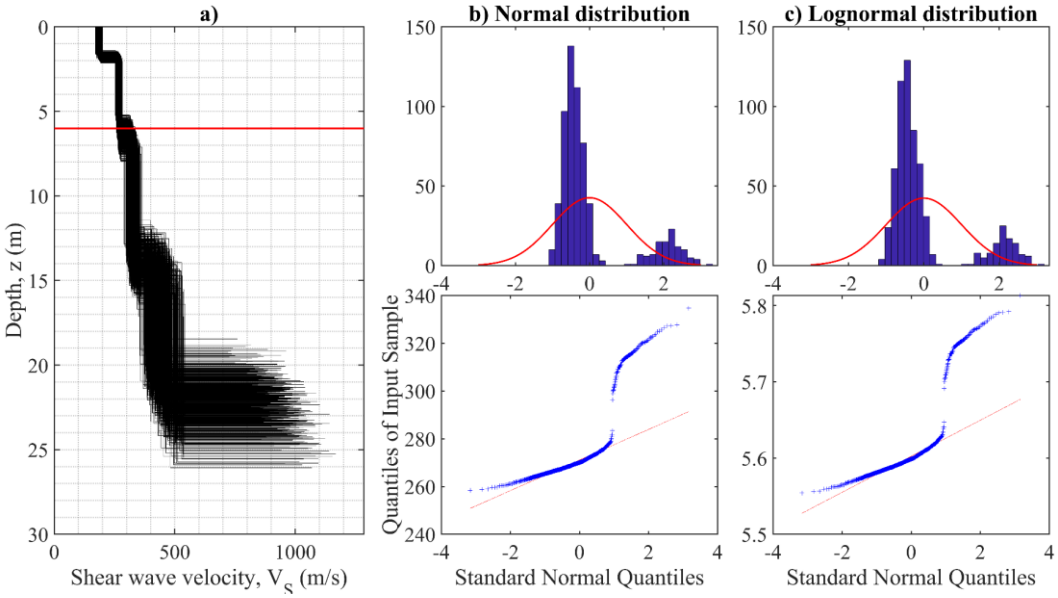

Figure 6.10. Inferential method applied to the interval velocity profiles at a depth equal to 6 m for Acquasanta Terme. a) Set of equivalent profiles obtained after the first round of inversions (i.e., fixed number of layers), b) normal distribution panel as a histogram and Q-Q plot, c) lognormal distribution panel as a histogram and Q-Q plot.

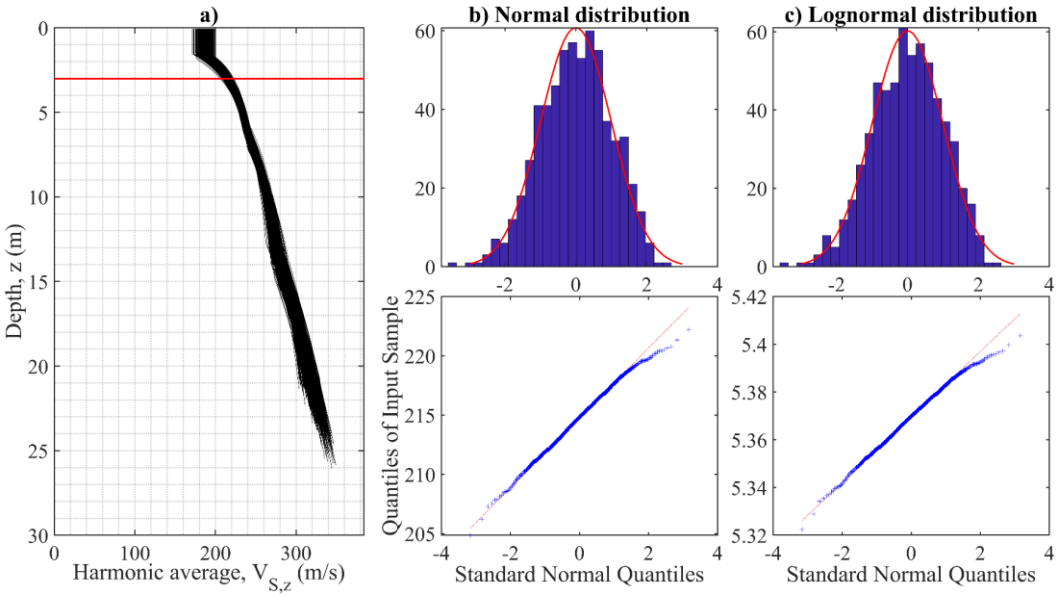

Figure 6.11. Inferential method applied to the harmonic average velocity profiles at a depth equal to 3 m for Acquasanta Terme. a) Set of equivalent profiles obtained after the first round of inversions (i.e., fixed number of layers), b) normal distribution panel as a histogram and Q-Q plot, c) lognormal distribution panel as a histogram and Q-Q plot.

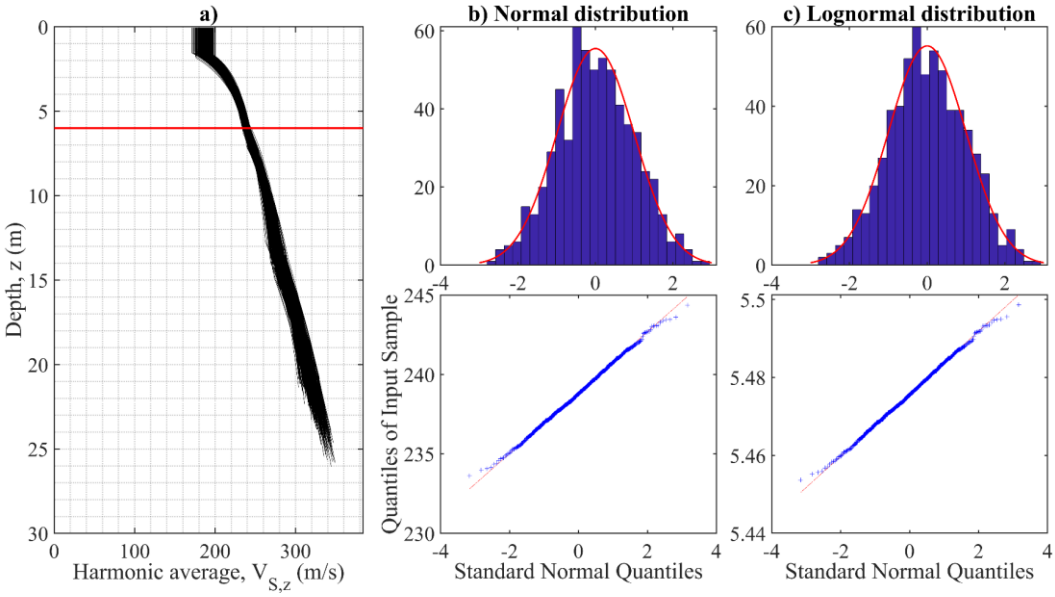

Figure 6.12. Inferential method applied to the harmonic average velocity profiles at a depth equal to 6 m for Acquasanta Terme. a) Set of equivalent profiles obtained after the first round of inversions (i.e., fixed number of layers), b) normal distribution panel as a histogram and Q-Q plot, c) lognormal distribution panel as a histogram and Q-Q plot.

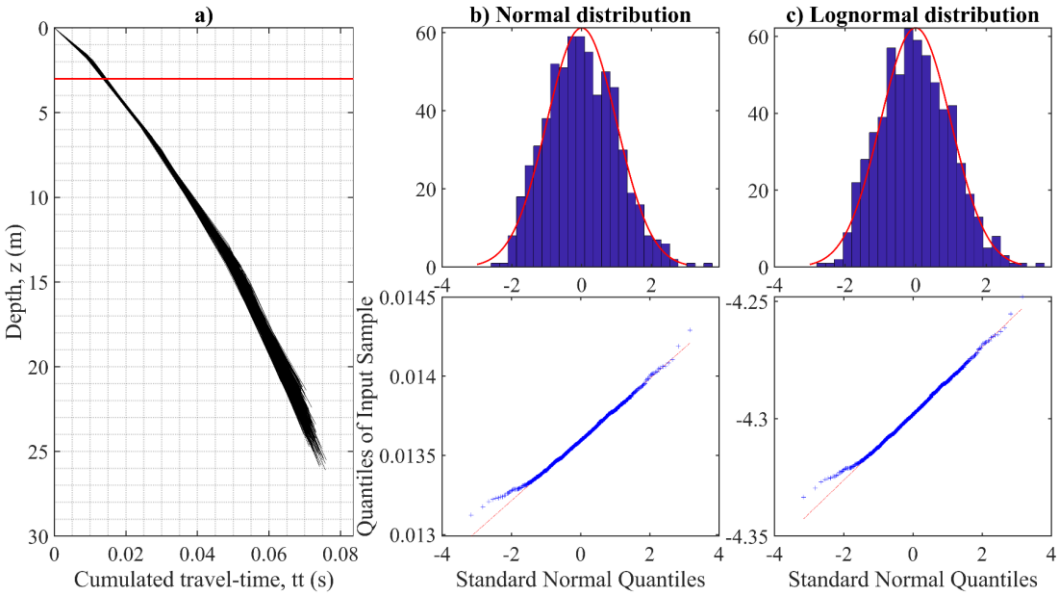

Figure 6.13. Inferential method applied to the cumulated travel time profiles at a depth equal to 3 m for Acquasanta Terme. a) Set of equivalent profiles obtained after the first round of inversions (i.e., fixed number of layers), b) normal distribution panel as a histogram and Q-Q plot, c) lognormal distribution panel as a histogram and Q-Q plot.

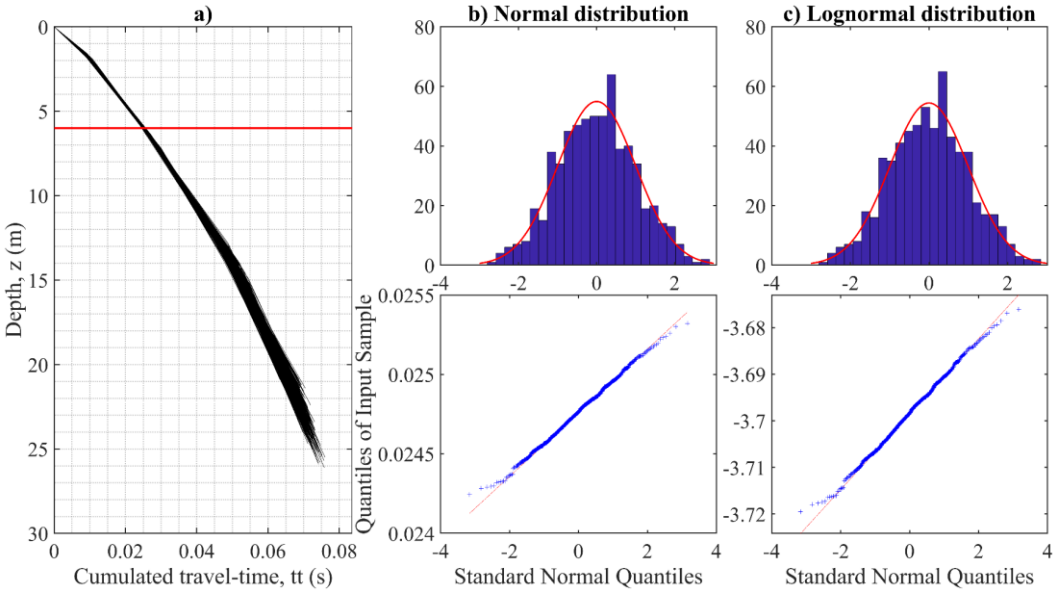

Figure 6.14. Inferential method applied to the cumulated travel time profiles at a depth equal to 6 m for Acquasanta Terme. a) Set of equivalent profiles obtained after the first round of inversions (i.e., fixed number of layers), b) normal distribution panel as a histogram and Q-Q plot, c) lognormal distribution panel as a histogram and Q-Q plot.

6.1.2.2 Statistical distribution of the thickness of the layers

The model chosen for the spatial random variable (i.e., the interfaces position with depth) is the non-homogenous Poisson model described by Toro (1995).

The non-homogeneous Poisson process is a Markovian and non-stationary process. It can be used for the distribution of layer thicknesses with a depth-dependent rate ($\lambda\,(z)$) assumed as a modified power-law model with parameters c_1, c_2 and c_3. These parameters can be site specific (i.e., obtained from a regression based on experimental data) or generic, as proposed in Toro (1995). The model is described by the typical Poisson exponential formulation in Equation 4.29

$$f(h,z) = e^{-\lambda(z)h} \text{ for } h > 0 \qquad \text{(Eq. 4.29)}$$

Two specific improvements are introduced to the basic formulation of the non-homogeneous Poisson's model to make the model specific for the purpose:

- Initial bounding of generated lambda in order to limit the model generation;
- Second acceptance or refusal criterion of generated layering distributions according to the depth resolution of the surface wave tests.

These additional conditions were developed to potentially mitigate the limitations of the Toro model reported by Griffiths et al. (2016b), Teague & Cox (2016), Teague et al. (2018) (see Section 4.3.3).

Initial bounding of generated lambda

The bounding of the generated $\lambda(z)$ is similar to the hypothesis usually adopted for the limitation of the samples generated by the lognormal distribution (e.g., +/- two standard deviations) (Li & Asimaki 2010, Rodriguez-Marek et al. 2014). In those cases, the realizations of the lognormal distribution that were out of a user-defined threshold were rejected. The same operation can be done for the $\lambda(z)$ generated by the non-homogeneous Poisson's model.

Experimental results for Acquasanta Terme in Figure 6.15 show that the $\lambda(z)$ after the round-1 of inversions are limited to an acceptance area (the example is valid for the entire dataset). The user of the randomization models (i.e., both the free-layering and the geostatistical model) can define an upper and lower multiplication factor to enlarge or squeeze the "admitted zone" by scaling the maximum and minimum fitted boundaries presented in Figure 6.15. This rejection criterion avoids the generation of unrealistic values of $\lambda(z)$ that lead to non-representative distributions of thicknesses.

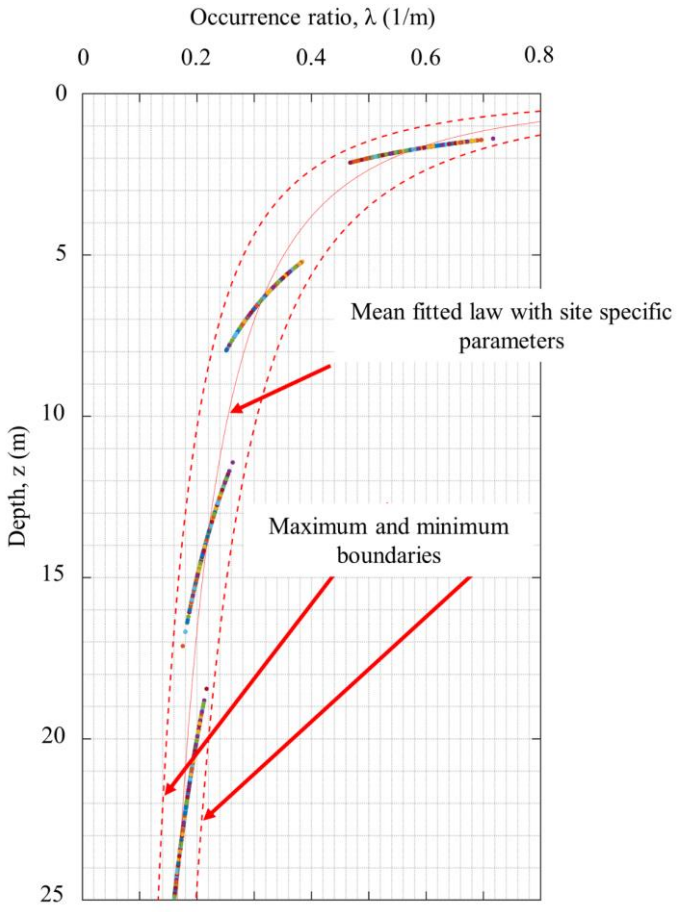

Figure 6.15. Rate of inter-layer boundaries (lambda) in the Vs profiles obtained in the round 2 inversion results for the Acquasanta Terme site. The mean and maximum and minimum boundaries of the depth-dependent layer occurrence ratio are also shown.

Acceptance or refusal criterion of generated layering distributions

The acceptance criterion of generated layering distributions is based on the observations made in 6.1.1. The λ-z transformation (i.e., $V_{R,\lambda}$-$V_{S,Z}$ relationship) is used for determining the maximum resolution with depth and, consequently, the minimum acceptable thickness that the randomization models can generate. This is strictly related to the surface wave methods.

As already discussed, the Toro model (1995) (i.e., TM95) did not account for any specific characteristic of the adopted geophysical method. One of the most challenging problem in TM95 was the generation of unacceptable thickness distributions. For example, for a surface wave test, the generation of a thin, deep layer is not consistent with the observations made in Section 4.2.2.2. The site signature (i.e., the EDC) loses resolution with depth, with an increasing dimension of "dark zones". These dark zones are associated with two consecutive values of V_R at different wavelengths (λ) that are now transformed into depths (z) (Figure 6.16). The idea is that the randomization models should limit the minimum thickness of the generated layer with depth, forcing the randomization models to generate layers that are in line with the experimental data.

Figure 6.16 exemplifies this operation for the case of Acquasanta Terme. The non-homogenous Poisson model is forced to avoid thicknesses smaller than the distance between two experimental points after the application of the λ-z transformation. Indeed, the randomization models does not have experimental information (i.e., enough resolution) to identify a thin layer at that depth.

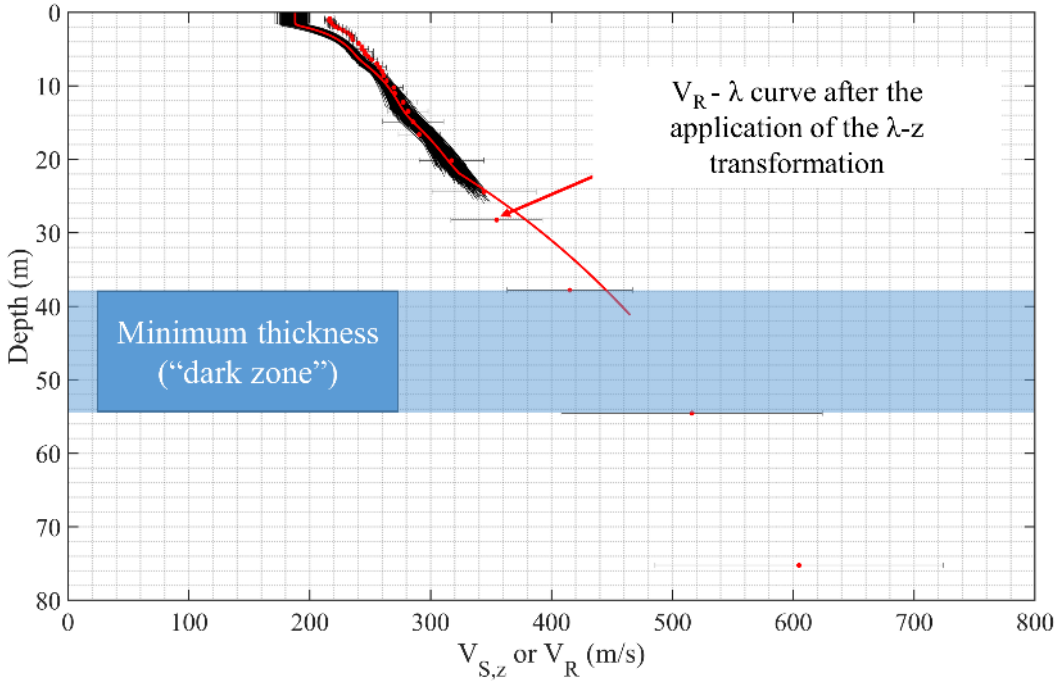

Figure 6.16. Example of application of the shift to the EDC (i.e., from wavelength to depth) and identification of the "dark zones" where the experimental information loses of resolution with depth (Acquasanta Terme).

The distance between two experimental points of the shifted EDC (see Section 6.1.1) is assumed as the minimum thickness at a depth equal to the midpoint depth and interpolated as shown for Acquasanta Terme (Figure 6.17). The red line in Figure 6.17 represents the experimental threshold that should be iteratively respected by the non-homogeneous Poisson's model. The same Figure shows the acceptable area.

Also, the minimum thickness of the first layer can be imposed on the models in a closed form. The randomization models allow the user choosing $\lambda_{min}/3$ or $\lambda_{min}/2$, as suggested by Foti et al. (2018).

This rejection criterion is different from the one presented by Teague et al. (2018). In that case, the authors adopted a rejecting criterion based on the calculation of the TTFs of the generated profiles concerning the TTF of the base-case profile. That operation is again a palliative solution to the inadequacies of the TM95, as it excluded the generated interval profiles a-posteriori. In the present case, the experimental information included in the EDC is fully exploited to a-priori generate compatible V_S profiles by separating lengths and times.

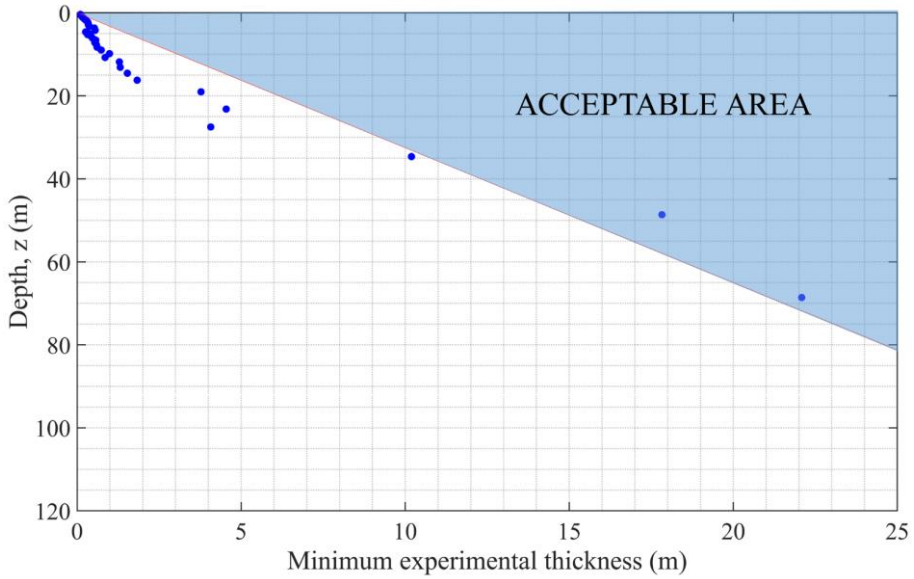

Figure 6.17. Regression of the minimum generable thickness imposed on the randomization model for Acquasanta Terme.

6.1.2.3 Inter-layer correlation

The randomization models (i.e., both the free-layering and the geostatistical model) use a first-order auto-regressive model (AR1), as proposed by Toro (1995) for the column. However, the correlation factor is computed on the cumulated travel times, differently from the TM95 who presented the correlation based on the interval velocities. This difference is essential and represents the innovation of the present work.

For each generated layering distribution, the free-layering randomization model calculates the logarithmic mean ($\overline{tt_{S,z}}$), the logarithmic standard deviation

($\sigma_{\ln(tt_{S,z})}$), and the correlation coefficient (ρ) between the random variables $tt_{S,z}$. When applied to the PSWD, these calculations are based on the results of the sample of round-1 inversions. This operation is prevented for the geostatistical model that does not use the results of the previous inversion, but will be properly calibrated, as discussed in 6.2 for surface wave tests. Then, the travel time is randomized with a user-defined limitation in terms of standard deviations (Li & Asimaki 2010, Rodriguez-Marek et al. 2014) and finally, the interval velocity profile of the column is composed.

6.1.2.4 Halfspace velocity and halfspace depth

The velocity of the halfspace can be studied as a semi-independent random variable with respect to the velocity of the layers above (the meaning for "semi-independent" will be clarified at the end of this section). It can be modeled without separating length and time random variables, as it has not a spatial dimension (i.e., no thickness). Figure 6.18 confirms that the lognormal distribution can also be used for the halfspace shear wave velocity.

The distribution of the halfspace depths is reported in Figure 6.19. The panel c) shows a good approximation by the lognormal distribution also for this random variable.

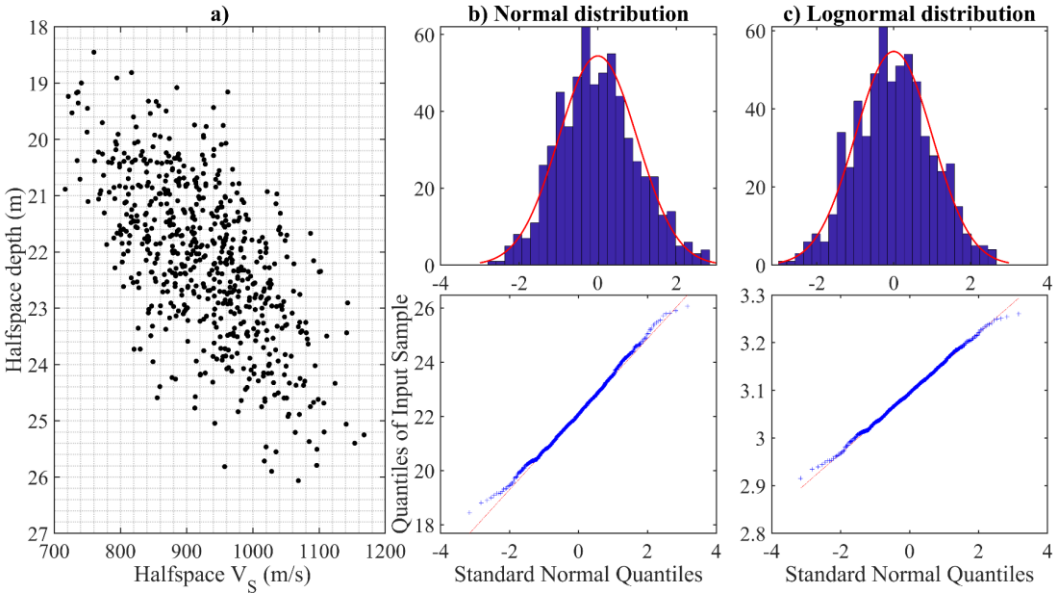

Figure 6.18. Inferential method applied to the halfspace velocities for Acquasanta Terme. a) Halfspace V_S-halfspace depth relationship after the first round of inversions (i.e., fixed number of layers), b) normal distribution panel as a histogram and Q-Q plot, c) lognormal distribution panel as a histogram and Q-Q plot.

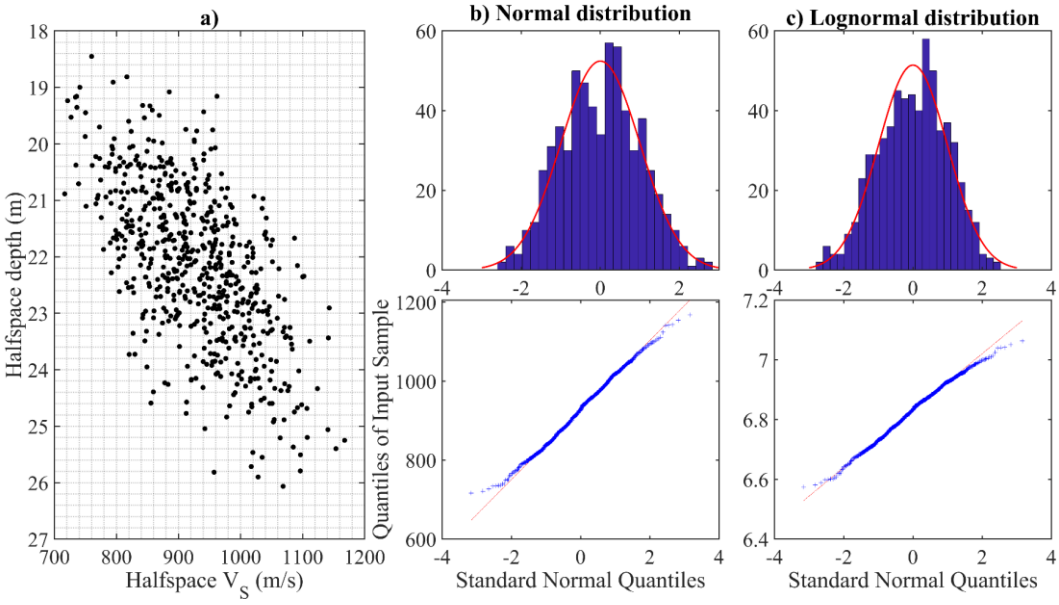

Figure 6.19. Inferential method applied to the halfspace depths for Acquasanta Terme. a) Halfspace Vs-halfspace depth relationship after the first round of inversions (i.e., fixed number of layers), b) normal distribution panel as a histogram and Q-Q plot, c) lognormal distribution panel as a histogram and Q-Q plot.

Figure 6.5, 6.18a, and 6.19a suggested the presence of a correlation structure between the halfspace velocity and depth. As expected, if the halfspace depth increases, the V_S should increase to be consistent with the experimental dispersion curve. This correlation can be seen in Figure 6.20. This Figure shows the correlation matrix between the two random variables and the value of Pearson's correlation coefficient (ρ^h) for Acquasanta Terme (Pearson 1895, Kendall 1946).

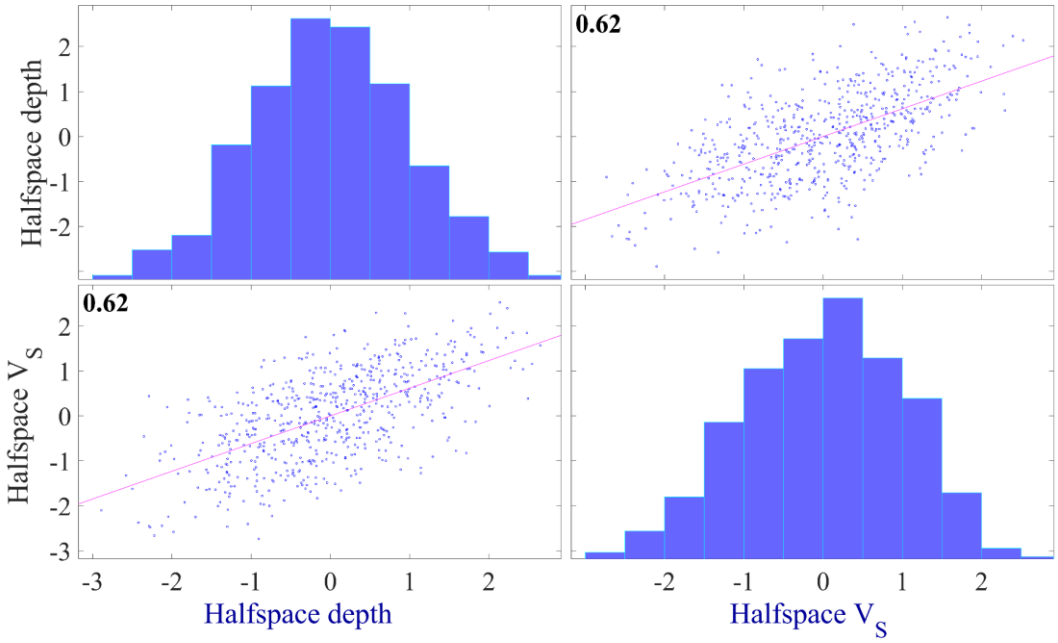

Figure 6.20. Correlation matrix plot for Acquasanta Terme and evaluation of the Pearson's linear correlation coefficient.

We can refer to the standard normal random variable halfspace depth

$$Sd_i^h = \frac{\left(\ln\left(\mathrm{d_i^h}\right) - \ln\left(\overline{\mathrm{d^h}}\right)\right)}{\sigma_{\ln(\mathrm{d^h})}} \qquad \text{(Eq. 6.7)}$$

and the standard normal random variable halfspace velocity

$$SV_i^h = \frac{\left(\ln\left(\mathrm{V_i^h}\right) - \ln\left(\overline{\mathrm{V^h}}\right)\right)}{\sigma_{\ln(\mathrm{V^h})}} \qquad \text{(Eq. 6.8)}$$

A simple first-order auto-regressive model can be used and

$$SV_i^h = \rho^h Sd_i^h + \epsilon_i\sqrt{1-(\rho^h)^2} \qquad \text{(Eq. 6.9)}$$

where $\rho^h Sd_i^h$ is the corresponding realization of a standard normal distribution for the halfspace depth, and ϵ_i is a separately (and randomly) sampled standard normal variate for the halfspace velocity having zero mean and unit standard deviation. So we can obtain SV_i^h as a realization of a random normal variable with mean $\rho^h Sd_i^h$ and standard deviation equal to $\sqrt{1-(\rho^h)^2}$, which is transformed in the natural value as

$$V_i^h\left(d_i^h\right) = \exp\left(SV_i^h\sigma_{\ln(\mathrm{V^h})} + \ln\left(\overline{\mathrm{V^h}}\right)\right) \qquad \text{(Eq. 6.10)}$$

At the beginning of this section, we defined the velocity of the halfspace as a semi-independent random variable with respect to the velocity of the layers above. This definition demonstrates that the randomized V_i^h depends on the randomized d_i^h. However, the merging of the halfspace characteristics into the column (i.e., the layers above the halfspace) represents a crucial step. Hence, the randomized d_i^h should be associated with a consistent layering of the column. Indeed, the halfspace depth is the link between the halfspace and the column.

An example can better explain this new feature of the randomization models. We can assume randomization of 10 profiles with a halfspace average depth of 100 m. The layering randomization is concluded and generated 10 different layering distributions that showed an interface at 95 m, 96 m, 97 m, 98 m, 99 m, 101 m, 102 m, 103 m, 104 m, 105 m. The halfspace randomization is concluded and generated a sequence of d_i^h= 102 m, 97 m, 101 m, 104 m, 96 m, 95 m, 105 m, 98 m, 99 m, and 103 m. If a blind implementation of the model is adopted, the same sequence of the d_i^h is assigned to the 10 column layering distributions. The new randomization models search for a consistent combination and assign the halfspace depths equal to the interface depths. This operation guarantees a further consistency of the randomization, as the layering is not distorted by the inclusion of the halfspace depth. Once the best combination is determined, the models generate the

halfspace velocity V_i^h that will be consistent with the halfspace depth and, consequently, the column's layering distribution.

6.1.3 Round-2: inversion with a variable number of layers

The improved Monte Carlo global search method (Socco and Boiero, 2008) was also used for the second round of inversions similarly to the round-1. In this case, however, also the layers number was considered as a random variable (Cox & Teague 2016).

The free-layering is used in this round-2 inversion. The model follows the characteristics described in Section 6.1.2 and was used in conjunction with the solutions of the first round inversions. In particular, this randomization model was developed following the observations proposed in Section 6.1.2, aiming at generating a new set of 200000 V_S interval velocity profiles. The results of the first round of inversions were used as reference base-case for the randomization. Hence, the values for the model parameters $\overline{tt_{S,z}}$, $\sigma_{\ln(\mathrm{tt_{S,z}})}$, ρ, $\overline{d^h}$, $\sigma_{\ln(\mathrm{d^h})}$, $\overline{V^h}$, $\sigma_{\ln(\mathrm{V^h})}$, and ρ^h are automatically estimated by the free-layering model reading the solution of the previous round of inversion. The free-layering model respected the global characteristics of the first set of equivalent profiles (i.e., harmonic average shear wave velocity and halfspace parameters), but generating layering distributions with a different number of interfaces (i.e., layers).

Figure 6.21 shows the schematic flow for the round-2 of inversions illustrating the concepts discussed in the previous sections.

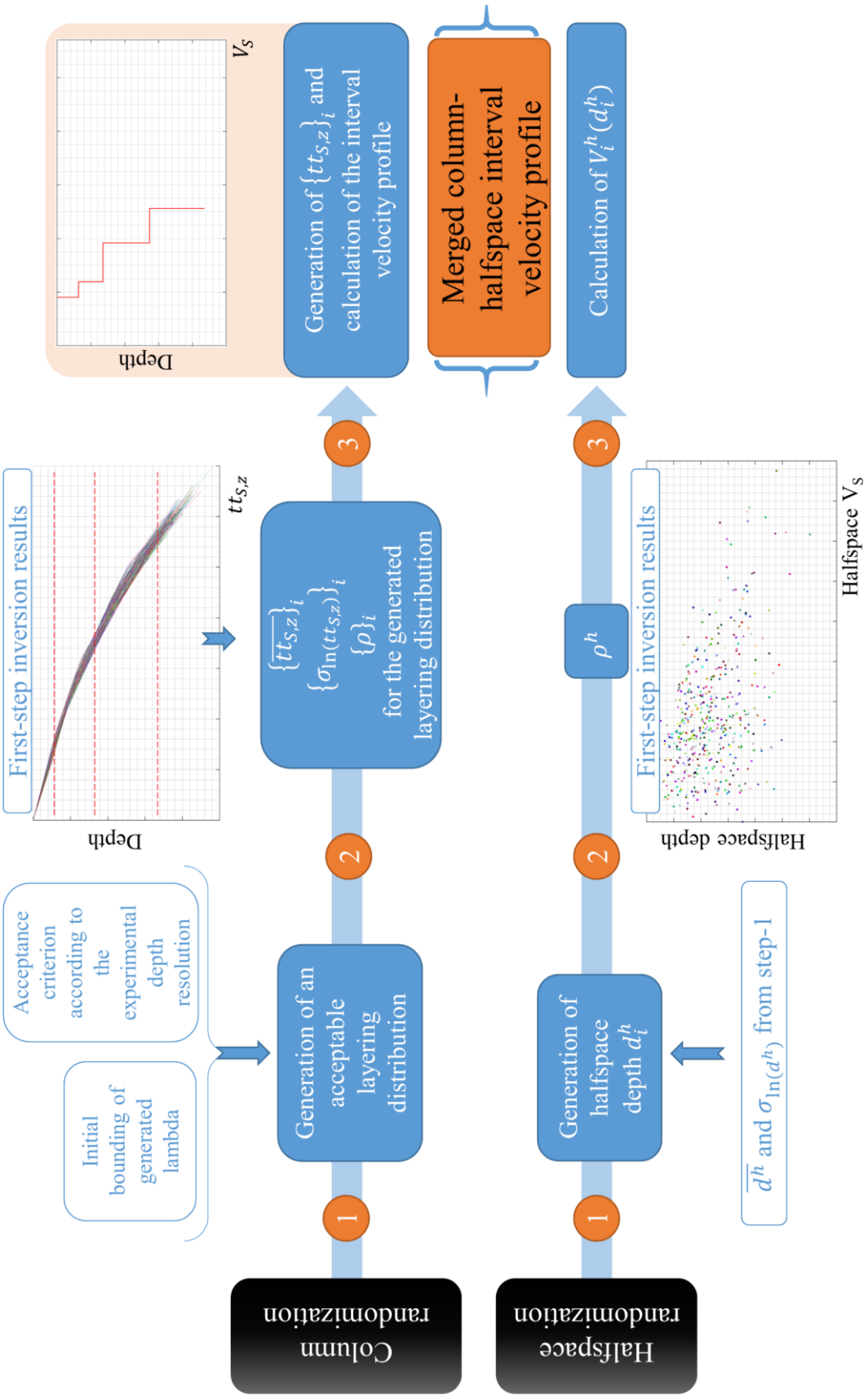

Figure 6.21. Schematic flow of the second round of inversions.

This new population of 200000 profiles was considered for a combined misfit analysis, and the statistical test was applied to the entire set of 400000 possible solutions.

Table A2 also summarizes the results of the second round of inversions and the misfit analysis on the "merged" sample of profiles. Forty-five (of seventy-one) sites show a reduction of the misfit after the addition of the free-layering condition (highlighted in green). Moreover, the second round of inversions of the remaining profiles led to a misfit almost similar to the one obtained after the first round of inversions, except for three sites that showed a considerable increase (highlighted in orange).

The last column in Table A2 quantifies the improvement of the solution calculating the ratio of the minimum misfit after the second round of inversions and the minimum misfit of the first round of inversions. Surprisingly, the average value of these misfit ratios is equal to one. This observation has different interpretations.

First, the second round inversions provides an essential reduction of the minimum misfit in case of inadequate layering adopted in the first round of inversions. The addition of the last degree of freedom to the inversion systematically avoids gross errors.

Second, if the layering adopted in the first round of inversions is adequate, the solution obtained after the second round of inversions is almost identical. Many times, the obtained misfit increases due to the lower number of samples investigated during the second round of inversions. Indeed, the second round of inversions generates 200000 profiles covering situations with a different number of layers. For example, if the first round of inversions generated 200000 profiles with 5 layers, the second-round generated 100000 profiles with 5 layers, 25000 with 6 and 4 layers, 12500 with 2, 3, 7, or 8 layers. If the global minimum is obtainable with 5 layers, the second round of inversions has fewer profiles with that number of interfaces.

Third, in case of particular layering distributions of the base-case (i.e., three sites with a misfit ratio higher than 1.5 in orange), the free-layering model is not capable of reproducing an adequate number of profiles with the same number of interfaces. This is due to the limitations of the non-homogeneous Poisson's model that cannot be solved with the modifications discussed in Section 6.1.2.2.

Each site is now associated with a statistical "picture" of best solutions. These pictures will be the fundamental ingredients for the development of the actual geostatistical model presented in Section 6.2 for surface wave tests. The Figures A93-163 show the results of the second round of inversions.

Figure 6.22 shows the updated λ-z linear trasformation law obtained with the refined sample of solutions. The a and b parameters of the linear regression slightly changed, as the goodness of fit (i.e., the adjusted R-Square). This small change demonstrates that the robustness of the linear transformation, and that the second round of inversions overall provided a better sample of equivalent results. This updated transformation law will be adopted for the layering generation of the geostatistical model presented in Section 6.2 for surface wave tests.

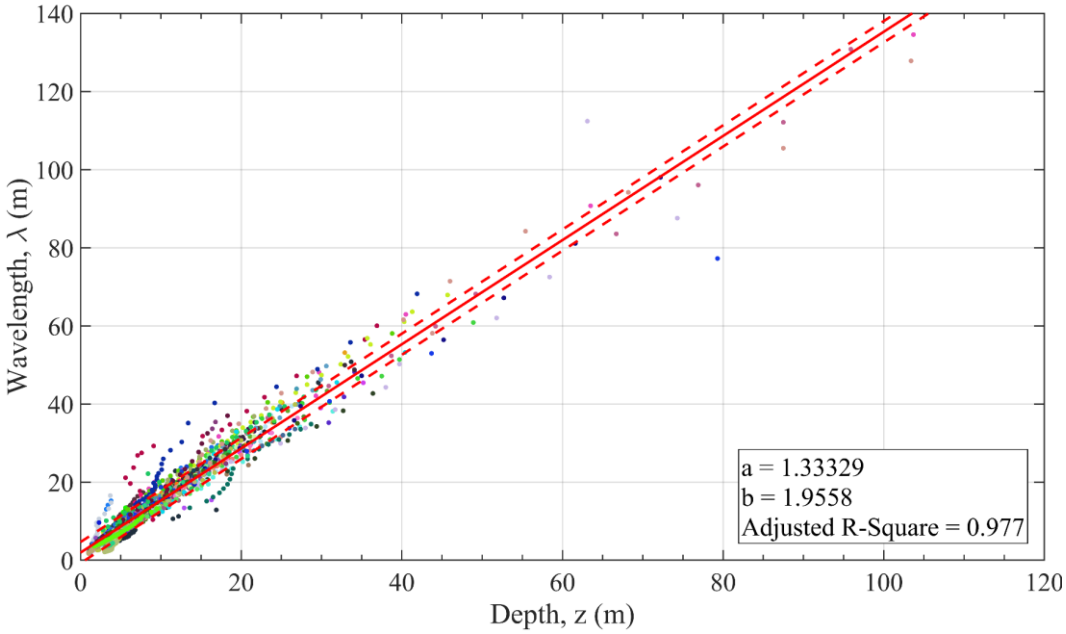

Figure 6.22. Determination of the wavelength-depth (i.e., λ-z) relationship after the second round of inversions.

6.2 The geostatistical model applied to surface wave testing methods

This Section deals with the presentation of the geostatistical model for the randomization of V_S profiles obtained via surface wave testing methods. The primary goal of the model is to solve the usual limitations of the single-deterministic approaches for the solution of the inverse problem. In addition, it can be used independently for EUs and AVs that are identified and quantified in the first steps of the IQM method. Indeed, the model is included in the final management step that is independent of the type of uncertainty. However, the model's parameters suggested from the PSWD include a simultaneous management of EUs and AVs, as a distinction in this case is practically unfeasible.

The essential characteristics of the proposed geostatistical model are:

- Calibration with a high-quality database of experimental measurements;
- Separation of the random variables relating to space and time;
- Site- and test-specific features:
    - Based on a rigorous identification and quantification of the EUs and AVs involved in the study;
    - Independent modeling (i.e., management, treatment) of the EUs and AVs specific and physically-based of the performed geophysical test;
- Flexibility and user-friendliness.

The geostatistical model presented here for surface wave testing methods is based on the Polito Shear Wave velocity Database (PSWD). The PSWD was built up following a rigorous selection procedure of surface wave tests performed over the last 20 years by the Politecnico di Torino, as illustrated in Section 5.1. A systematic inversion of measured dispersion curves was conducted for each site, thus guaranteeing the quality of the resulting velocity profiles. The PSWD represents the fundamental ingredient for the development of the geostatistical model. The processing of the PSWD serves to constrain the experimental parameters to be used in the geostatistical randomization model. These empirically-based parameters are the main topic of the next sections.

The separation of the random variables space and time is central to the model proposed in this dissertation. The model does not randomize interval velocities (i.e., the shear wave velocities associated with a stack of a finite number of horizontal layers), but instead assumes a neat separation between the fundamental physical quantities time (i.e., travel time) and space (layer thickness). The inadequacies of the interval velocity scheme for the randomization were extensively demonstrated in Section 6.1.2.1 and will be discussed again in the following sections. The interval velocity is just an engineering schematization of the problem to be used a-posteriori in the Ground Response Analysis (GRA). Moreover, the use of the harmonic average (i.e., the cumulated travel times) allows for a better reproduction of the geophysical results. Indeed, it separately accounts for sources of EUs and AVs discussed in Section 4.2 and avoids introducing parasite (i.e., multiple) uncertainties. This double-counting of uncertainties is typical if the model randomizes the interval velocity and the depth of interfaces (i.e., layer thicknesses), as proposed by Toro (1995).

The use and development of a new geostatistical model should be site- and test-specific. From the user point of view, a rigorous identification and quantification of EUs and AVs at the site should always be performed. This initial analysis is essential to the generation of V_S profiles compatible with the real scenario of the site. The user should investigate the case study accounting for the adopted test and the spatial scale of the problem and use site-specific model parameters (Li & Asimaki 2010, Rodriguez-Marek et al. 2014, Teague & Cox 2016, Teague et al. 2018). Similarly, the geostatistical model should be specific for a geophysical test (or class of similar methods). This allows reproducing realistic characteristics of the test regarding both EUs and AVs, although the model is independent of the type of uncertainty.

Last but not least, the geostatistical model has to be flexible in case of further improvements (e.g., an extension of applicability to other geophysical tests, see Section 6.3). The "core" of the model remains fixed, whereas additional dedicated parts can be introduced to specify the problem. Also, the geostatistical model should be offered on a shared and accessible platform and/or included in the most popular software for GRAs.

6.2.1 Model calibration

Section 6.1.3 described the equivalent solutions for each site. Indeed, after the second round of inversions, a homogeneous set of solutions for each site was obtained. The high quality is a result of the data in the PSWD and the application of a rigorous inversion method (i.e., the double-round process described in Section 6.1).

These V_S profiles were then processed to constrain the empirically-based parameters of the geostatistical model. As discussed previously, the main difference between the geostatistical model and the free-layering randomization model presented in Section 6.1 is that the geostatistical model is constrained directly from the V_S profiles obtained from the inversions. On the other hand, the randomization model calculates the necessary parameters from the solutions of the first step of inversions.

It is important to remark that the parameters that will be provided in the following sections are only indicative of site-specific values. These parameter values can be used in case of insufficient information and/or data from the site under analysis. Indeed, a site-specific calibration of the model parameters should always be preferred. The following indications can be used as a comparison for experimental validation.

Each statistical sample (i.e., site) was analyzed separating the column and the halfspace. The model parameters of the column are the travel-times logarithmic standard deviation (i.e., $\sigma_{\ln(\mathrm{tt_{S,z}})}$) and the travel-times inter-layer correlation coefficient (i.e., ρ) for the adopted autoregressive model.

The first model parameter of the halfspace is the correlation coefficient for the halfspace depth/velocity (i.e., ρ^h). In addition, the halfspace depth (i.e., d^h and $\sigma_{\ln(\mathrm{d^h})}$) and halfspace velocity (i.e., V^h and $\sigma_{\ln(\mathrm{V^h})}$) will be studied in conjunction with other variables of the problem.

Note that these last characteristics represent an innovation compared to the Toro model (1995). Indeed, the geostatistical model shows new perspectives for the merging of the column and the halfspace. Also, 6.1.2.4 described the automatic method for the "smart" merger of these two semi-independent random variables.

6.2.1.1 Travel-times logarithmic standard deviation

Figure 6.23 shows the $\sigma_{\ln(\mathrm{tt_{S,z}})}(z)$ calculated for each site up to the depth with a minimum sample size of fifty equivalent profiles. Specifically, for each site in the PSWD, the logarithmic standard deviation $\sigma_{\ln(\mathrm{tt_{S,z}})}$ is presented as a function of the depth z. The calculation stops at a depth where the statistical sample has less than 50 profiles.

Results show a typical range of values between 0.006 and 0.03. Also, the values can be approximated as constant with depth. Local peaks represent the influence of the position of the interfaces. However, the consistent global behavior is maintained and can be modeled as depth-independent. Note that a constant logarithmic standard

deviation is equivalent to a constant Coefficient Of Variation (i.e., $COV_{tt_{S,z}}$), as presented in Figure 4.53. This means that the Gaussian standard deviation $\sigma_{(tt_{S,z})}$ increases with depth, as the cumulated travel time increases. This observation is in line with the gradual loss of resolution of the surface wave tests with depth discussed in Section 4.2.2.2.

The same calculations were performed for the interval velocity profiles, as a comparison. In this case, the logarithmic standard deviation of the shear wave velocity (i.e., $\sigma_{\ln(V_S)}$) is presented in Figure 6.24a, as illustrated also in Toro (1995) (Figure 4.55). The resulted values range from 0.02 to 0.2 and are in accordance with other evidence in the literature mainly discussed in Chapter 4 and presented in Figure 6.24b (Rodriguez-Marek et al. 2014, Stewart et al. 2014a, Griffiths et al. 2016b, Teague & Cox 2016, Passeri et al. 2019).

As expected, the influence of the interfaces is predominant and different peaks are shown at various depths (note that the horizontal axis is in logarithmic scale). These peaks correspond to the depth of the interfaces, where a lognormal distribution cannot describe the interval velocity profile (Figure 6.10). This is further proof that the interval shear wave velocity can be modeled as lognormally distributed only within a layer, whereas the entire column does not respect this distribution.

Note that the values in Figure 6.24b by Griffiths et al. 2016 and Teague and Cox 2016 are obtained after the processing of a set of equivalent profiles. Also these authors show unrealistic peaks in the calculated $\sigma_{\ln(V_S)}$. On the other hand, the values illustrated by Rodriguez-Marek et al. 2014 and Passeri et al. (2019) a come from the analysis of a set of experimental measures. Finally, Stewart et al. 2014 suggests their parameters to overcome the large values proposed by Toro (1995).

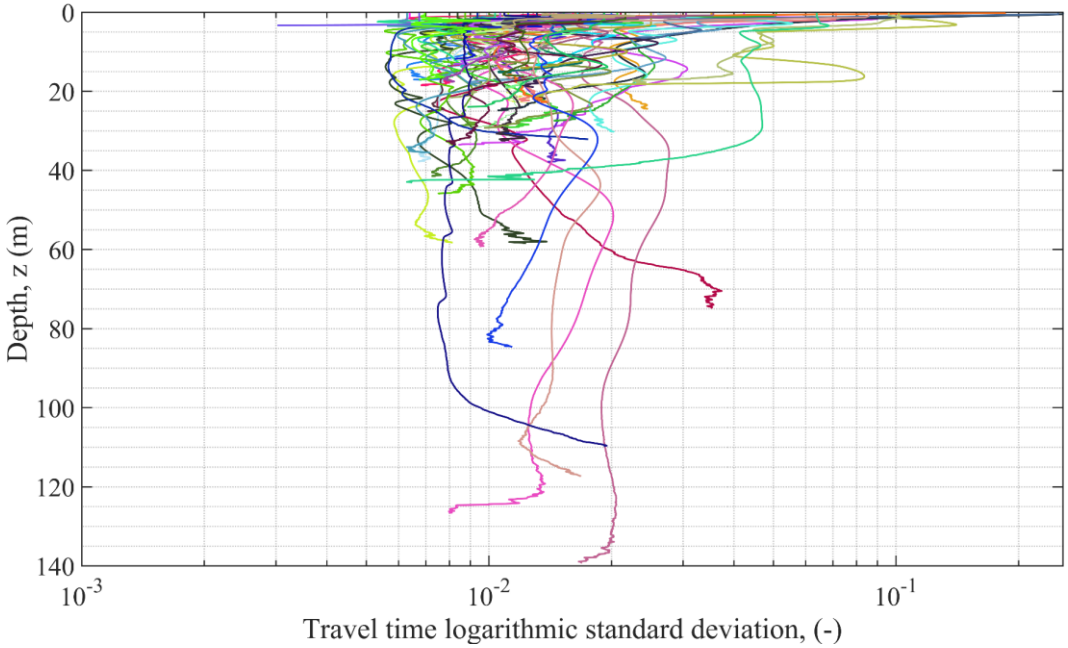

Figure 6.23. Logarithmic standard deviation calculated for the cumulated travel time for each site in the PSWD.

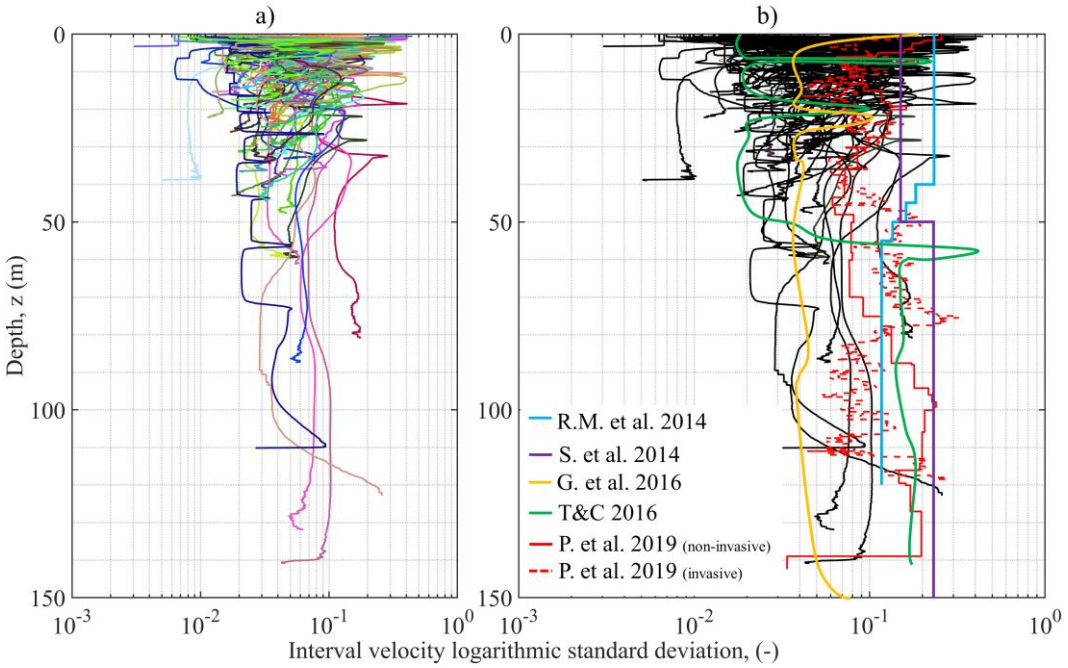

Figure 6.24. a) Logarithmic standard deviation calculated for the interval shear wave velocity profile for each site in the PSWD and b) same as a) including other results in the literature. Specifically, R.M. et al. 2014 (Rodriguez-Marek et al. 2014), G. et al. 2016 (Griffiths et al. 2016), T&C 2016 (Teague and Cox 2016), S. et al. 2014 (Stewart et al. 2014), P. et al. 2018 (Passeri et al. 2019).

6.2.1.2 Travel-times inter-layer correlation coefficient

The adopted model for the inter-layer correlation of the travel time variable is a first-order auto-regressive model (AR1), as discussed in Section 6.1.2.3 for the free-layering model. This section presents the regression of the model parameters. It is useful to rewrite the equation of the inter-layer correlation coefficient presented in Section 4.3.2 as:

$$\rho(z,t) = \big(1 - \rho_z(z)\big)\rho_t(t) + \rho_z(z) \qquad \text{(Eq. 4.34)}$$

where

$$\rho_z(z) = \begin{cases} \rho_{200}\left[\dfrac{z + z_0}{200 + z_0}\right]^b & \text{for } z < 200\ m \\ \rho_{200} & \text{for } z > 200\ m \end{cases} \qquad \text{(Eq. 4.35)}$$

$$\rho_t(t) = \rho_0 e^{\left[-\frac{t}{\Delta}\right]} \qquad \text{(Eq. 4.36)}$$

Figure 6.25 explains the geometrical meaning of the variables z (i.e., mid-point depth) and t (i.e., the distance between mid-points).

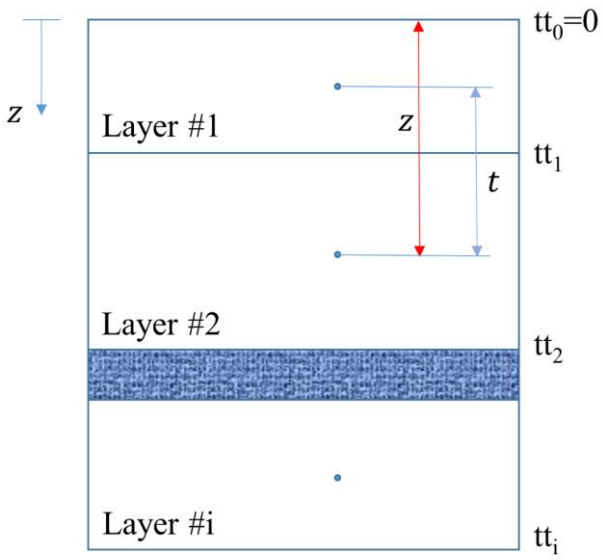

Figure 6.25. Geometrical variables included in the formulation for the proposed first-order auto-regressive model.

The value of z_0 was fixed to be equal to zero, as also proposed by Toro (1995). Hence, the model parameters to be estimated are ρ_{200}, b, ρ_0, and Δ with the following limitations:

$$-1 < \rho_{200} < 1$$
$$-1 < \rho_0 < 1$$

The regression was performed for each site (i.e., each statistical sample of equivalent profiles) using a Nonlinear Least Square approach and a Least Absolute Residual (i.e., LAR) robust method. This last choice was due to the large residuals expected during the regression.

The nonlinear fitting algorithm was strongly dependent on the starting parameters. For this reason, a multiple regression was designed with a Monte Carlo approach. For each site, the search was conducted randomizing 1000 quadruplets of starting values in the regression. In the end, the result of the regression with the best adjusted R-Square (i.e., goodness of fit) value was selected for the specific site.

Figure 6.26 shows the regression obtained for the Accumoli site as an example. The scattered blue dots represent the experimental inter-layer correlation coefficients (ρ) computed for each equivalent profile in the sample (i.e., 12512). The inter-layer correlation coefficients are calculated between each couple of interfaces of the profile. Figure 6.26a shows the $t - \rho$ space along with the best fitting surface. The same for Figure 6.26b and the $z - \rho$ space. Figure 6.26c shows the 3D space with the scattered experimental values and the best fitting surface for Accumoli. In this case, the best fitting values are $\rho_{200} = 0.7376$; $b = 0.3474$; $\rho_0 = 0.9250$; $\Delta = 4.2833$.

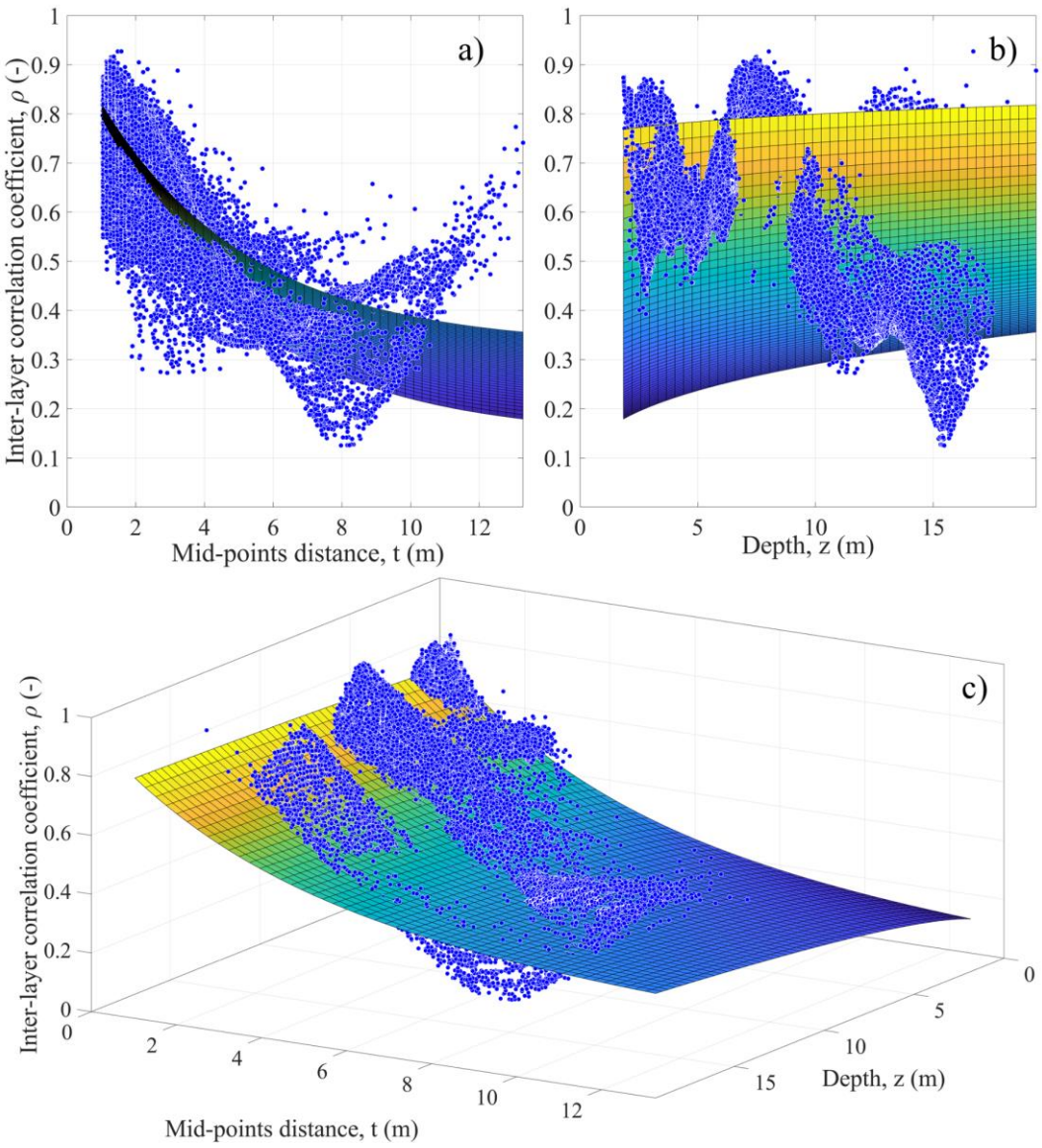

Figure 6.26. Results of the nonlinear regression of the experimental inter-layer travel-time correlation coefficients: a) $t - \rho$ space, b) $z - \rho$ space, and c) 3D space with the best fitting solution obtained for Accumoli.

The regression was performed for the entire database. The following results are provided as mean values for each model parameter (i.e., after an inter-sites average). These values can be compared with the values shown in Figure 4.59a. The results are in accordance with the ones proposed by Toro (1995). However, the present work gives the same model parameters for different soil classes, differently from Toro (1995). A cluster analysis was performed before the regression, but the results gave no indications for a possible grouping of the solutions based on the soil class. For this reason, the parameters below can be considered generally valid.

$$\rho_{200} = 0.7660$$
$$b = 0.2355$$
$$\rho_0 = 0.6364$$
$$\Delta = 5.8532$$

6.2.1.3 Correlation coefficient for the halfspace depth/velocity

The correlation between the halfspace depth (d^h) and halfspace velocity (V^h) was discussed and demonstrated in Section 6.1.2.4 (e.g., Figure 6.20 for Acquasanta Terme). The geostatistical model adopts the same first-order auto-regressive model illustrated for the free-layering randomization model.

Figure 6.27 shows the standard normal random variables for halfspace depth and velocity for all sites and all equivalent profiles (i.e., 1722118 samples). These random variables were calculated in logarithmic values to respect their lognormal distribution. The different color scale represents the points' density. The correlation coefficient was calculated between these two assembled (i.e., inter-site) random variables that are still clearly correlated. The value obtained is

$$\rho^h = 0.508$$

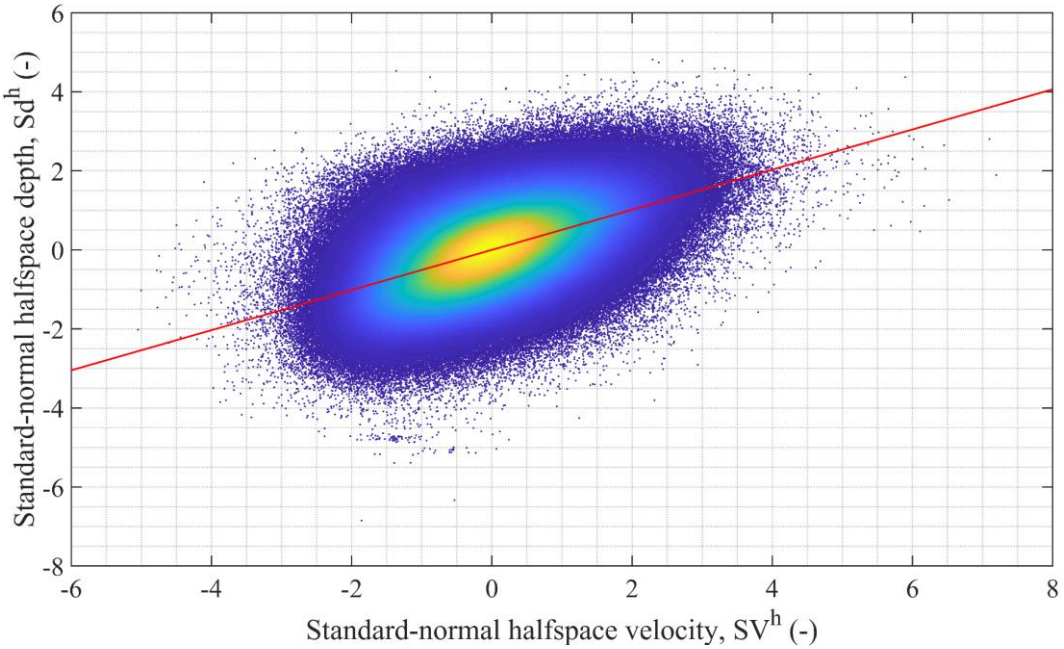

Figure 6.27. Standard-normal plot for the estimation of the correlation coefficient between the halfspace depth and halfspace velocity.

6.2.1.4 Halfspace depth and halfspace velocity

The present section illustrates the analysis conducted on the random variables halfspace depth (d^h) and halfspace velocity (V^h). This section of the dissertation provides also simple relationships for the estimation of the logarithmic standard deviations of these two random variables (i.e., $\sigma_{\ln(d^h)}$ and $\sigma_{\ln(V^h)}$).

The dependence of $\sigma_{\ln(d^h)}$ on various variables of the problem was initially investigated. At the end of the analysis of sensitivity, the coefficient of variation of the maximum experimental wavelength (i.e., $COV_{\lambda_{max}}$) was identified as the controlling parameter. This variable is normally distributed (Lai et al. 2005) and can be easily computed from the Experimental Dispersion Curve (EDC) as

$$COV_{\lambda_{max}} = \frac{\sigma_{\lambda_{max}}}{\overline{\lambda_{max}}}$$

where $\sigma_{\lambda_{max}}$ is the standard deviation of the experimental point associated with the maximum wavelength, and $\overline{\lambda_{max}}$ is the mean maximum experimental wavelength. These two quantities can be calculated from the EDC. Indeed, σ_λ is equal to the corresponding $\frac{\sigma_{V_R}}{f}$ as $\lambda = \frac{V_R}{f}$ and the frequency is assumed as a deterministic variable, and $\overline{\lambda_{max}} = \max\left(\frac{\overline{V_R}}{f}\right)$. In practice, the user can calculate the EDC as $\overline{V_R} - \bar{\lambda}$ (see Figure 4.28b-c) and find these two parameters $\sigma_{\lambda_{max}}$ and $\overline{\lambda_{max}}$.

The $COV_{\lambda_{max}}$ represents the experimental confidence resulted for the maximum obtained wavelength. We largely discussed in Chapter 4 the relationship between the wavelength and the maximum obtainable depth of the V_S profile (e.g., pseudo-depth). This topic was then expanded with the wavelength-depth transformations in Section 6.1.1. In practice, this first variable quantifies the experimental accuracy regarding the test resolution with depth.

The logarithmic standard deviation of the halfspace depth is also dependent on the ratio between the mean halfspace depth ($\overline{d^h}$) and the mean maximum experimental wavelength $\overline{\lambda_{max}}$ termed

$$\eta = \frac{\overline{d^h}}{\overline{\lambda_{max}}}$$

This second parameter describes how much the modeled halfspace depth is close to the maximum experimental wavelength. Foti et al. (2018) and Table 4.2 suggested values ranging between 1/2 and 1/3. However, each specific surface wave test has its peculiarities, and the chosen η is also depending on other external conditions of the problem.

Figure 6.28 shows the results of the regression (i.e., $COV_{\lambda_{max}} - \sigma_{\ln(\mathrm{d^h})}$ plan, $\eta - \sigma_{\ln(\mathrm{d^h})}$ plan, and 3D space). A simple linear interpolation was conducted, and the experimental values (same colors in the entire dissertation for each site) are presented along with the plane fitting function

$$\sigma_{\ln(\mathrm{d^h})} = \zeta_1 + \zeta_2\eta + \zeta_3 COV_{\lambda_{max}} \qquad \text{(Eq. 6.11)}$$

where

$$\zeta_1 = 0.0633$$
$$\zeta_2 = 0.0432$$
$$\zeta_3 = 0.0423$$

Figure 6.28 shows that the uncertainty in the detection of the halfspace depth ($\sigma_{\ln(\mathrm{d^h})}$) increases both with the uncertainty associated with the maximum

wavelength ($COV_{\lambda_{max}}$) and the vicinity to the maximum experimental wavelength ($\overline{\lambda_{max}}$). This results were expected in light of the specific characteristics of the surface wave methods. The reader can imagine the $COV_{\lambda_{max}}$ as a visual resolution of the halfspace position as a lens diopters. A higher number of lens diopters means a "more problematic" patient. Similarly, the η variable represents the viewing distance. A patient with a serious visual deficiency that want to push his skills to long distances is inevitably affected by large errors.

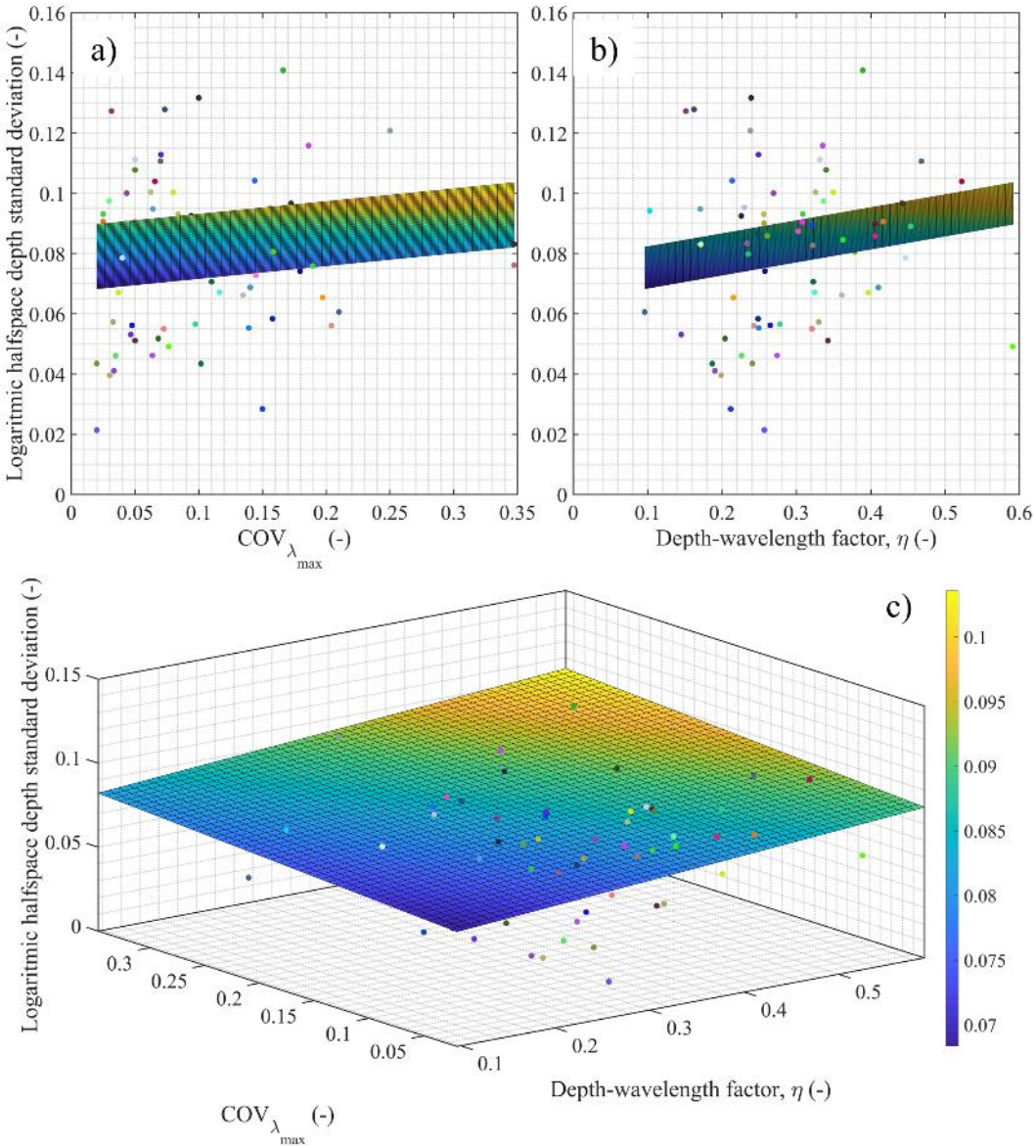

Figure 6.28. Results of the analysis of sensitivity performed for the logarithmic standard deviation of the halfspace depth. a) $COV_{\lambda_{max}} - \sigma_{\ln(d^h)}$ space, b) $\eta - \sigma_{\ln(d^h)}$, and c) 3D space with the interpolated experimental values.

The evaluation of the logarithmic standard deviation of the halfspace velocity followed the same procedure seen for the halfspace depth. In this case, the first most controlling parameter was found as the coefficient of variation of the phase velocity

associated with the longest wavelength (i.e., most of the times the highest phase velocity)

$$COV_{V_R|\lambda_{max}} = \frac{\sigma_{V_R|\lambda_{max}}}{\overline{V_{V_R|\lambda_{max}}}}$$

This variable shows the accuracy associated with the velocity of the deepest part of the investigated soil volume. It is equivalent to $COV_{\lambda_{max}}$ as $\sigma_{V_R|\lambda_{max}} = \sigma_{\lambda_{max}} f$ and $\overline{V_{V_R|\lambda_{max}}} = \overline{\lambda_{max}} f$, then

$$COV_{V_R|\lambda_{max}} = COV_{\lambda_{max}}$$

The two variables are equivalent as long as the frequency is treated as a determinist variable. However, the following observations are conducted for $COV_{V_R|\lambda_{max}}$ for clarity reasons. Indeed, it is easy to understand the dependency of $\sigma_{\ln(V^h)}$ by working with a coefficient of variation determined as a velocity.

The second controlling variable for the estimation of the logarithmic standard deviation of the halfspace velocity is η, as seen for $\sigma_{\ln(d^h)}$.

Figure 6.29 shows the results of the linear regression (i.e., $COV_{V_R|\lambda_{max}} - \sigma_{\ln(V^h)}$ plan, $\eta - \sigma_{\ln(V^h)}$ plan, and 3D space). The regression is well represented by a plane, i.e., a double first-order polinomial function as:

$$\sigma_{\ln(V^h)} = \nu_1 + \nu_2\eta + \nu_3 COV_{V_R|\lambda_{max}} \qquad \text{(Eq. 6.12)}$$

where

$$\nu_1 = 0.0017$$
$$\nu_2 = 0.2015$$
$$\nu_3 = 0.0872$$

The same observations for Figure 6.28 are valid also for Figure 6.29. As expected, the logarithmic standard deviation (i.e., accuracy) of the halfspace velocity increases with both $COV_{V_R|\lambda_{max}}$ and η.

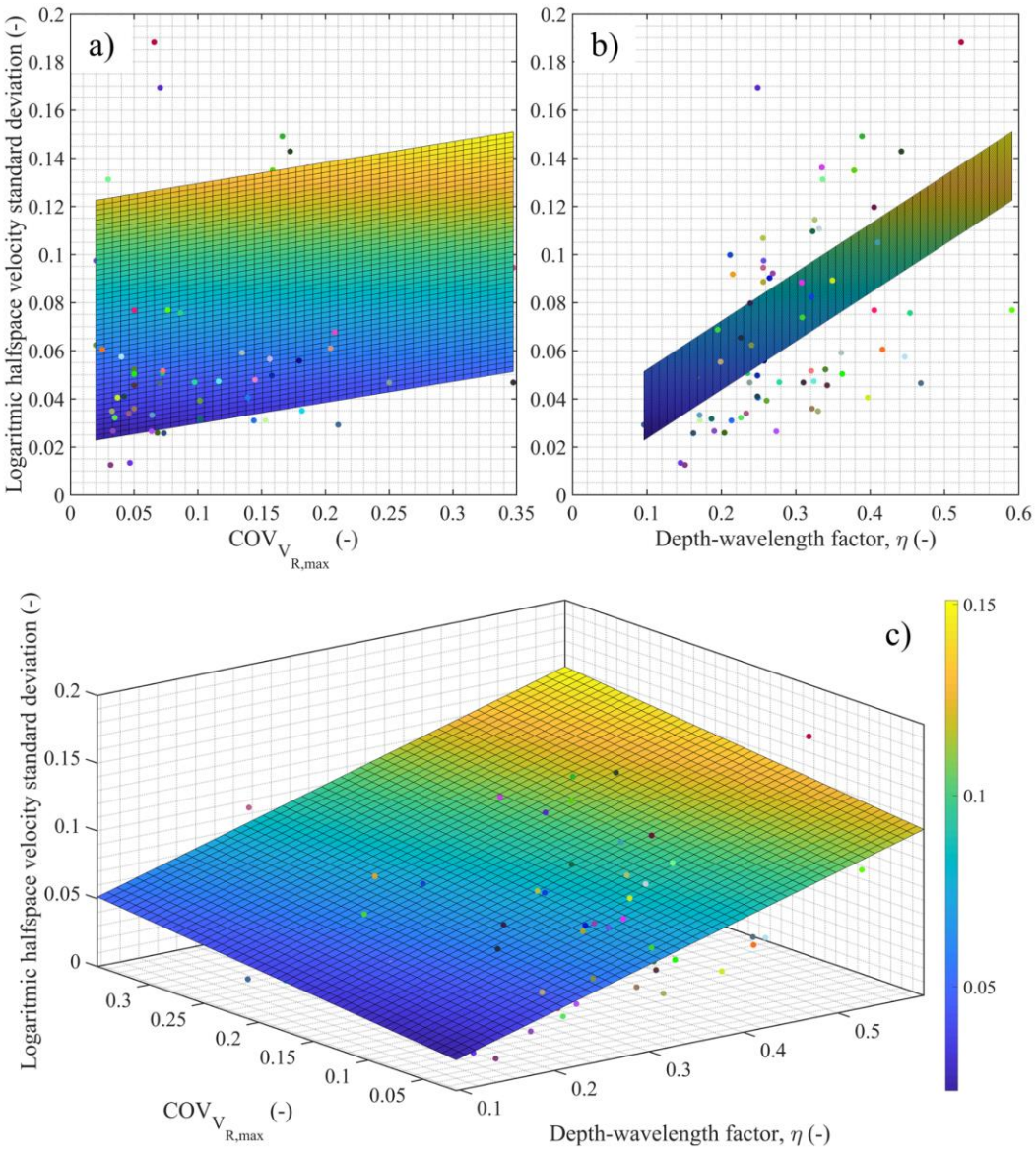

Figure 6.29. Results of the analysis of sensitivity performed for the logarithmic standard deviation of the halfspace velocity. a) $COV_{V_{R,max}} - \sigma_{\ln(V^h)}$ space, b) $\eta - \sigma_{\ln(V^h)}$, and c) 3D space with the interpolated experimental values.

6.2.2 Summary and example application

This last section summarizes the main characteristics of the geostatistical model proposed for surface wave testing methods. The summary provides a practical point of view of the model through an example of the application at the Accumoli site. This validation exercise evaluates the model's capabilities in reproducing the known solution in Figure A93. In this section, it is clear that the model is capable to generate a statistical sample of V_S profiles starting from the single-deterministic solution that is usually adopted in the analyses. Once more, the model is independent of the type and amount of uncertainties that are defined in the identification and quantification step. However, the model's parameters provided are based on a joint analysis of EUs and AVs in surface wave testing methods.

First, the input data for the randomization model are:

1. Experimental dispersion curve as frequency (f), Rayleigh waves phase velocity (V_R), and Rayleigh waves phase velocity standard deviation (σ_{V_R});
2. Single (i.e., deterministic) interval velocity V_S profile (i.e., base-case profile);
3. Poisson's ratio (ν) profile associated with the base-case profile.

Figure 6.30 shows the visual output of the model implemented in MATLAB® for the input parameters. Figure 6.30a presents the base-case V_S profile in terms of interval and harmonic average profiles (i.e., the solution with the lowest misfit in Figure A93). Figure 6.30a also includes the EDC proposed as $V_R - \lambda$ as seen in Figure 4.28b. The λ-z linear trasformation presented in 6.1.1 is applied to the EDC, and Figure 6.30a shows the transformed EDC that is in very good agreement with the $V_{S,Z}$ profile. Note that this comparison can be used for a first assessment of the goodness of the obtained solution. A transformed EDC that is not consistent with the $V_{S,Z}$ curve can be a sign of a biased inversion process.

Figure 6.30b shows the Poisson's ratio interval profile associated with the base-case velocity profile. This aspect deserves some observations.

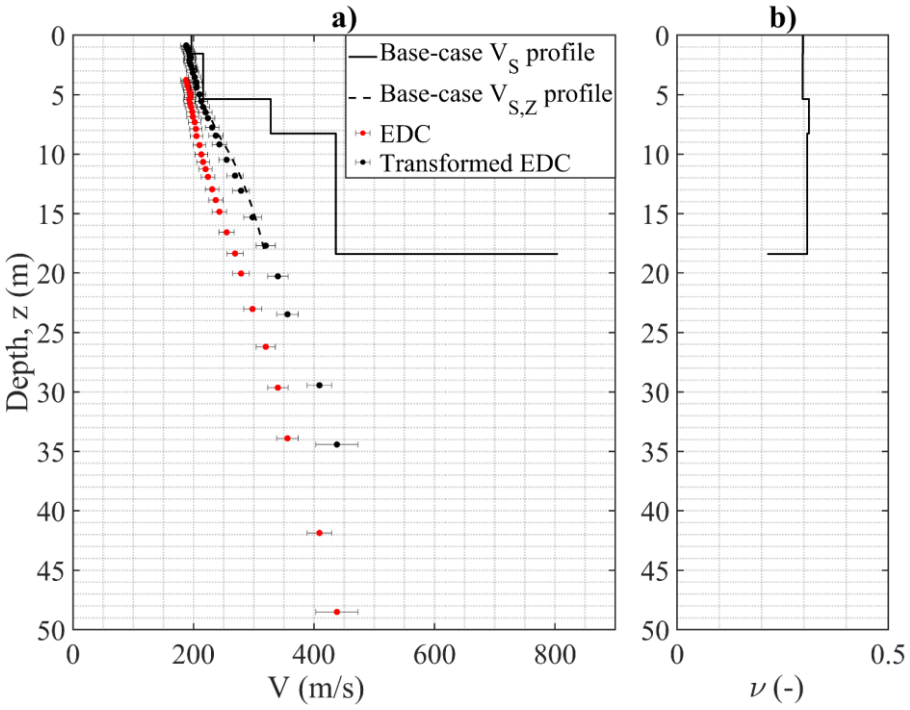

Figure 6.30. Input parameters for the geostatistical model, a) velocity profiles and experimental dispersion curve and b) Poisson's ratio profile associated with the base-case velocity profile (Accumoli).

The Poisson's ratio (ν) is a fundamental parameter for the solution of the surface wave propagation problem. It controls the V_P/V_S and V_R/V_S ratios and the global elastic response of the material (see 4.1.2 and Figure 4.9). The Poisson's ratio is then essential in the inversion process for the calculation of the forward

geophysical problem (i.e., the Theoretical Dispersion Curve, TDC) as discussed in 4.2.2.2 (Thomson 1950, Haskell 1953). Indeed, the TDC depends not only on the V_S profile but also on the ν (or, alternatively, the V_P profile). For these reasons, the geostatistical model should account also for the randomization of ν (or equivalently V_P). This is mandatory to "close the loop" and avoids the generation of unrealistic (or impossible) scenarios. Moreover, a rigorous global (i.e., V_S, V_P, and ν) randomization guarantees a better agreement with the EDC.

The observations above should lead to a question: *"is the EDC a site signature?"*. The answer is *"partially"* and depends on the applications. The EDC represents the site signature not only for the propagation of the shear waves. The inclusion of a further variable that completes the modeling of the elastic response leads to contamination in the definitions. If we are dealing with GRAs, the 1D approach works under the fundamental hypothesis of only shear waves traveling into the model. Then, the EDC cannot be considered a rigorous site signature in case of 1D models, as it inherently includes the presence of compressional waves.

For these reasons, the evaluation of the adherence (i.e., goodness) of the randomized V_S profiles with the site signature should be performed by looking at the Theoretical Transfer Functions (TTFs). The TTF depends only on the V_S profile (i.e., the unit weighs and the damping values can be fixed along the entire profile to have a rigorous comparison). The evaluation performed on the EDC (Griffiths et al. 2016a, Griffiths et al. 2016b, Teague & Cox 2016, Teague et al. 2018) is something forced because of the presence of a further depending variable. However, an assessment based on the respect of the EDC is always suggested (Foti et al. 2009). At the same time, the reader should have clarified that differences in the TDC-EDC can be due not only on an inadequate randomization model but also on a wrong choice of the ν (or equivalently V_P) profile.

The geostatistical model uses the Poisson's ratio profile of the base-case (Figure 6.30b) to calculate the interval velocity V_P profile. The V_P profile is a physically-based parameter that can be decomposed in the time and space variables (i.e., $V_{P,Z}$) for the randomization. On the other hand, the interval Poisson's ratio profile does not allow the calculation of a continuous (i.e., cumulated) equivalent curve. For these reasons, the geostatistical model is equipped with a further specific part that controls the generation of realistic V_S-V_P-ν. This operation is conducted following the flow shown in Figure 6.31.

First, the time variable $tt_{P,Z}$ is calculated from the $V_{P,Z}$ function of the base-case profile (i.e., no randomization). Then, the model assembles the V_P interval velocity for each generated layering distribution. The check is performed by calculating the Poisson's ratio associated with the V_S independently randomized and the V_P interval velocity (i.e., not randomized). This Poisson's ratio is an interval value, and it is compared to a user-defined acceptance area. This last operation is essential for many applications of surface wave methods. We discussed in Section 4.2.2.2 that the consequences of an incorrect choice of the Poisson's ratio can be very relevant (Brown et al. 2002, Foti & Strobbia 2002). In particular, Foti & Strobbia (2002) concluded that the position of the water-table is a crucial

information to be accounted for during the inversion. This a-priori information should be respected in the randomization of the profiles. The user can define physical boundaries for the generated Poisson's ratios in order to preserve the assumptions on the saturated conditions. If the calculated Poisson's ratio is within the acceptance limits, the V_P is not modified. Contrarily, if the calculated Poisson's ratio exceeds the acceptance limits, the ν_{lim} is used and the V_P is recalculated adopting this value.

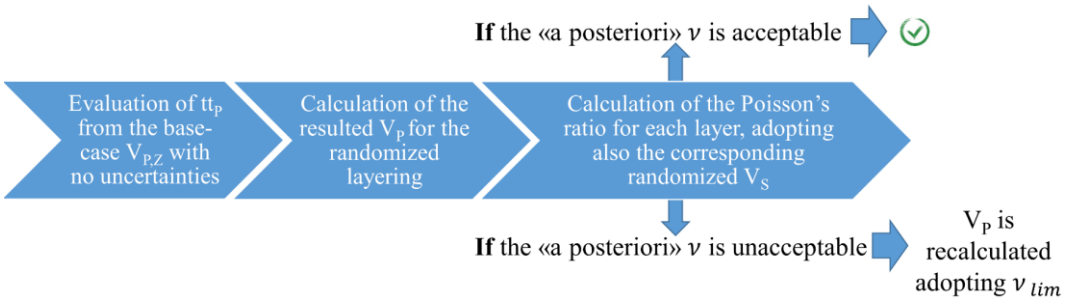

Figure 6.31. Schematic flow for the generation of consistent values of compressional wave velocities and Poisson's ratios.

At this point, all the essential characteristics of the model were discussed and are listed below:

1. Unlimited number of generated profiles;
2. Layering randomization (i.e., space variable) of the *column*:
    a. Automatic regression of the non-homogeneous Poisson model parameters from the base-case V_S profile;
    b. Application of user-defined restriction boundaries for the non-homogeneous Poisson model layering randomization;
    c. Application of thickness-limiting boundaries for the non-homogeneous Poisson model layering randomization based on the experimental resolution with depth;

3. Time randomization of the *column*:
    a. Application of user-defined restriction boundaries for the randomization of cumulated travel times $tt_{S,z}$ in terms of number of logarithmic standard deviations away from the logarithmic mean value;
    b. A-posteriori control conducted on the generated elastic parameters (i.e., V_P/V_S and Poisson's ratio);

4. *Halfspace*:
    a. Halfspace depth/velocity independent randomization;
    b. Halfspace depth/velocity correlation structure and "smart" merger of the column layering with the halfspace depth;

5. User-defined or regression-based selection of:

a. $\sigma_{\ln(\mathrm{tt_{S,z}})}$
b. ρ
c. ρ^h
d. $\sigma_{\ln(\mathrm{d^h})}$
e. $\sigma_{\ln(\mathrm{V^h})}$

The geostatistical model implemented in the actual version has no upper boundaries for the number of generated profiles. This is due to the continuous refinement operations of the code structure that is not time- or memory-consuming.

The geostatistical model is designed to be as independent as possible. The user has the initial control of the randomization, but each operation is conducted in automatic (if possible). One example is the regression of the model parameters for the non-homogeneous Poisson's model (i.e., c_1, c_2 and c_3) presented in Figure 6.32a,

At the same time, the model automatically limits the layering generations as discussed in 6.1.2.2 (see Figure 6.15) according to the user's choice. This operation is conducted with an iterative process, and the result is illustrated in Figure 6.32a for the Accumoli's example. Each point in Figure 6.32a represents a generated value of occurrence rate within the user-defined boundaries. The different curves (i.e., exponential law) are associated with a different number of layers generated by the model.

The layering generation is then limited according to the test resolution with depth and the observations made in 6.1.2.2 (see Figure 6.17). Figure 6.32b shows the generated points that respect the prescribed minimum thickness that is automatically calculated by a regression of the experimental data. Also, the user can select the minimum thickness of the first layer as 1/2 or 1/3 of the minimum experimental wavelength (in this case equal to 1.25 m).

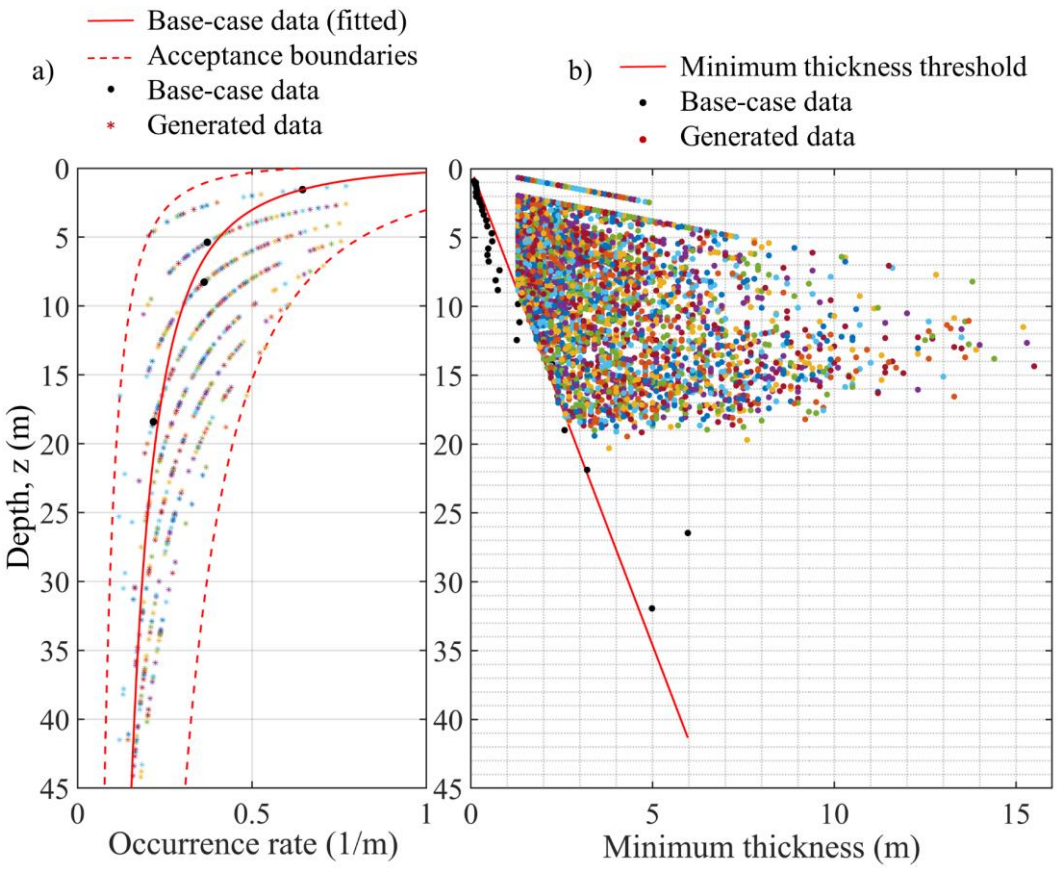

Figure 6.32. Layering generation for the example of Accumoli, a) occurrence rate of the base-case profile fitted and generated for the randomized profiles and b) minimum thickness limitation according to the experimental resolution with depth.

Once the layering distributions have been generated, the time randomization of the column is performed. The chosen parameters for this example are $\sigma_{\ln(\mathrm{tt}_{S,z})} = 0.01$, the inter-layer correlation coefficient ρ defined in 6.2.1.2 (i.e., $\rho_{200} = 0.7660$, $b = 0.2355$, $\rho_0 = 0.6364$, and $\Delta = 5.8532$), and time-boundaries set to +/- 2 logarithmic standard deviations. Figure 6.33 shows the results of the randomization for Accumoli in terms of cumulated travel-times, harmonic average profiles, and Poisson's ratios (i.e., entire column randomization). Figure 6.33a-b confirms the accordance of the randomized profiles with the physical fundamental quantities of the problem. In particular, Figure 6.33b demonstrates that the $V_{S,Z}$ and $V_{P,Z}$ values calculated at the bottom of each generated layer are included in a restricted area. Figure 6.33c shows that the generated Poisson's ratios at the midpoint of each randomized layer are within the user-defined acceptance area.

Figures 6.33d-e propose an a-posteriori check of the generated profiles. In particular, Figure 6.33d shows a 3D histogram plot obtained for the random variable $V_{S,Z,}$ whereas Figure 6.33e for the random variable ν. Both Figures demonstrate that the obtained distributions can be still seen as lognormal and do not show unusual shapes.

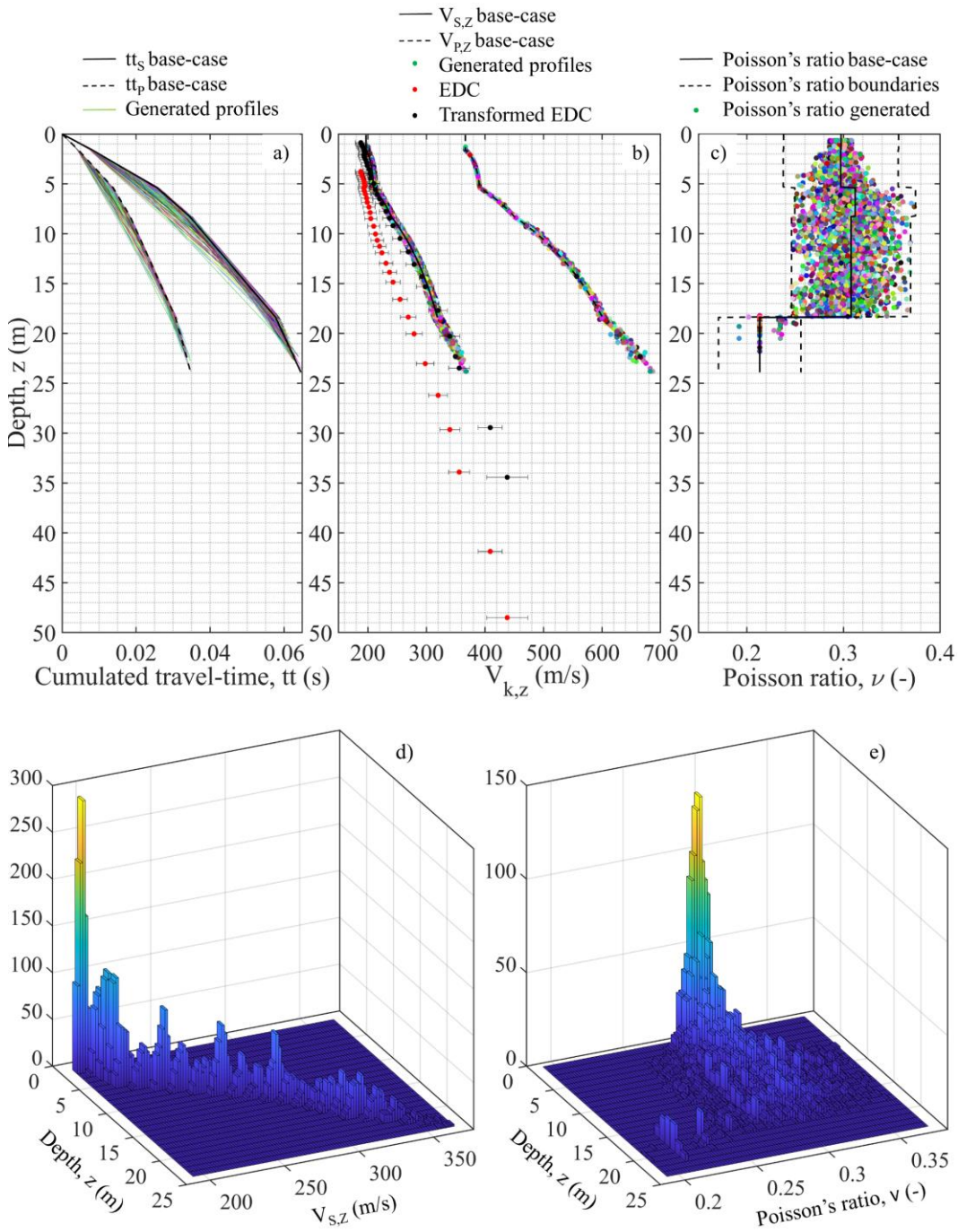

Figure 6.33. Results of the randomization for Accumoli. a) Randomized cumulated travel-times (for P- and S-waves), b) randomized harmonic average profiles (for P- and S-waves), c) generated Poisson's ratios, d) 3D histogram for the random variable Vs,z, and e) 3D histogram for the random variable Poisson's ratio.

Figure 6.33b shows the benefit of the independent randomization of the space and time. In the case of randomization of the interval velocity (i.e., Toro model), this agreement cannot be guaranteed. For example, Figure 6.34 shows the randomization of the Accumoli base-case with $\sigma_{\ln(tt_{S,z})} = 0$. This means that only the layering is randomized and the uncertainty in the velocity is discarded both with

the Toro (1995) model and the new geostatistical model. The resulted randomization should respect this assumption by modeling only the spatial variable.

The randomization obtained with the Toro model is entirely unrealistic, as the model can generate layers with a velocity only equal to the velocity of the three layers of the base-case (i.e., 197 m/s, 216 m/s, 328 m/s, and 436 m/s). This is due to the use of the interval velocity profile, instead of the continuous harmonic average profile. Consequently, the $V_{S,Z}$ profiles are out of the base-case profile, leading to altered dynamic behaviors, as shown by Griffiths et al. (2016b), Teague & Cox (2016), and Teague et al. (2018). Contrarily, the proposed geostatistical model gives results in excellent agreement with the base-case. In this case, only the uncertainty in the layering is introduced and modeled with different layering distributions. However, the variables separation allows avoiding the presence of the parasite uncertainties that perturb the Toro's solution.

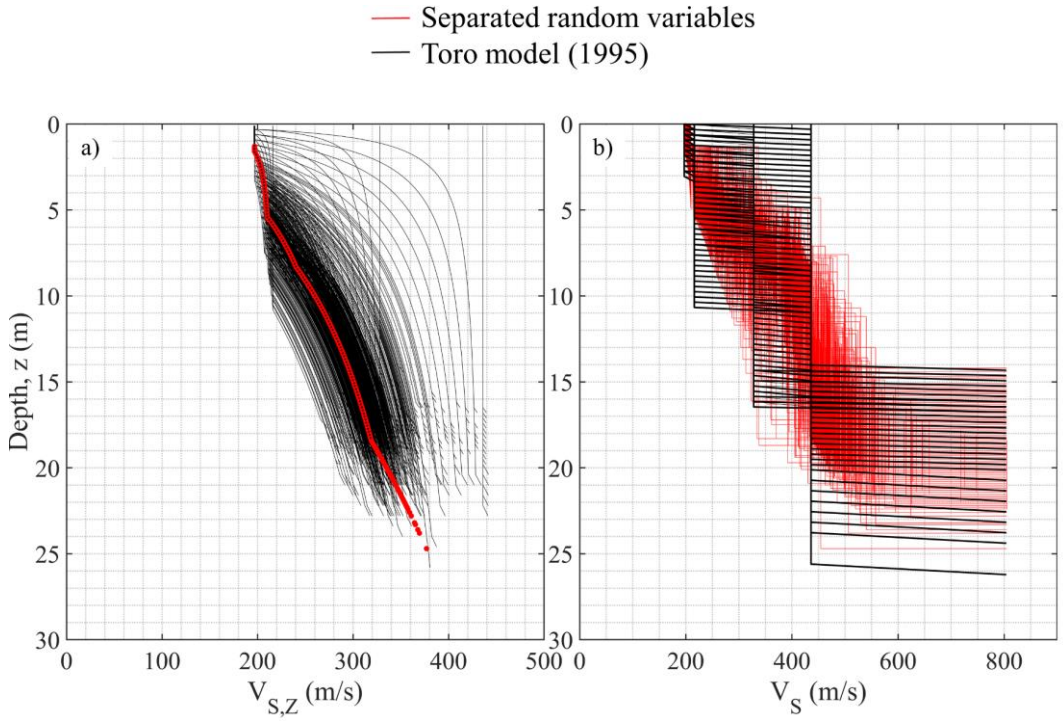

Figure 6.34. Example of randomization and comparison between the Toro (1995) model and the new geostatistical model proposed in the present Chapter. The comparison is conducted by introducing the uncertainty only in the spatial variable.

Figure 6.35 illustrates the randomization of the base-case profile. The randomization is performed by adopting the equations presented in 6.2.1.4 for $\sigma_{\ln(d^h)}$ and $\sigma_{\ln(V^h)}$. In addition, the correlation coefficient for the halfspace depth/velocity is assumed as $\rho^h = 0.508$.

Figure 6.35a shows the interval velocity profiles after the assembly of the layering (i.e., space) and time variables. Also, the velocity of the halfspace is merged into the interval velocity V_S and V_P profile as the last interface. Figure 6.35b shows the semi-independent randomization obtained exclusively for the halfspace

regarding velocity and depth (the colors illustrate the points' density, as for Figure 6.27). As already discussed, these values are merged into the column preserving the layering (see Section 6.1.2.4).

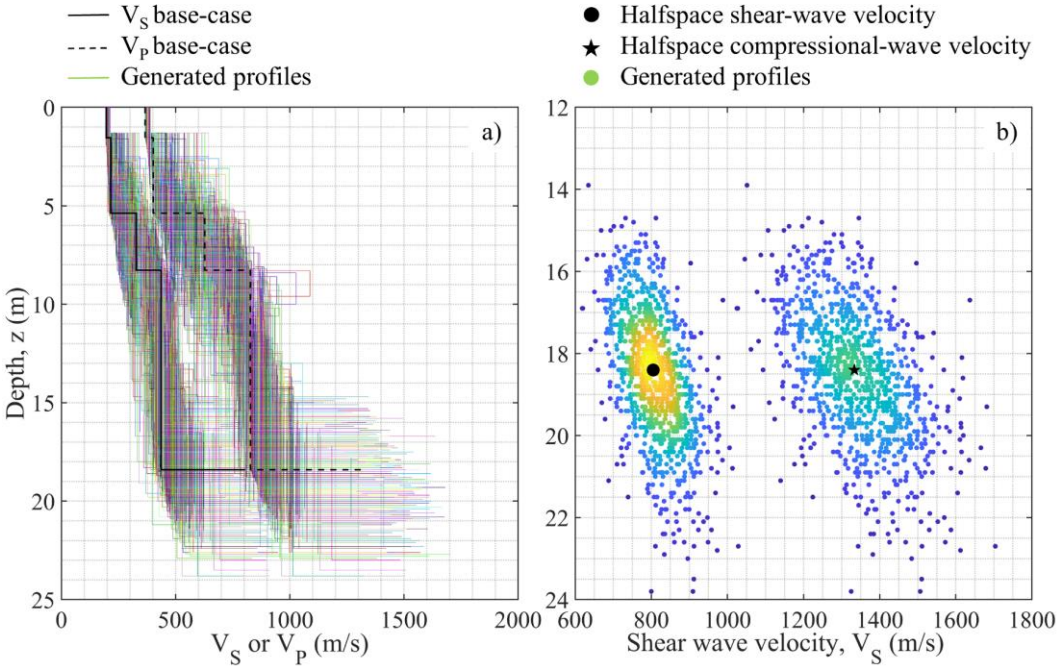

Figure 6.35. Complete Accumoli profile randomization.

The verification of the goodness of randomization is illustrated in Figure 6.36 in terms of theoretical dispersion curves (Figure 6.36a) and theoretical transfer functions (Figure 6.36b). As discussed above, the comparison shown in Figure 6.36a is not entirely adequate, as the TDC also depends on the Poisson's ratio (or equivalently V_P). In any case, the generated profiles are associated with consistent TDCs with respect with the TDC of the base-case profile. Figure 6.36a shows a large improvement if compared with the solutions obtained by the Toro model in Teague & Cox (2016), Griffiths et al. (2016a), and Teague et al. (2018). Only small differences are identifiable at high frequencies due to the generation of thicker, shallower layers that should have higher velocity to be consistent with the $V_{S,Z}$ profile.

Figure 6.36b shows the excellent agreement between the TTFs of the generated profiles and the TTF of the base-case profile. In this regard, the geostatistical model respects the site signature in terms of both amplitudes and resonant frequencies. Figure 6.36b also shows (i.e., gray background) the envelope of the TTFs calculated from the equivalent profiles in Figure A93. It is clear that the geostatistical model reproduces well the variabilities obtained after the inversion process.

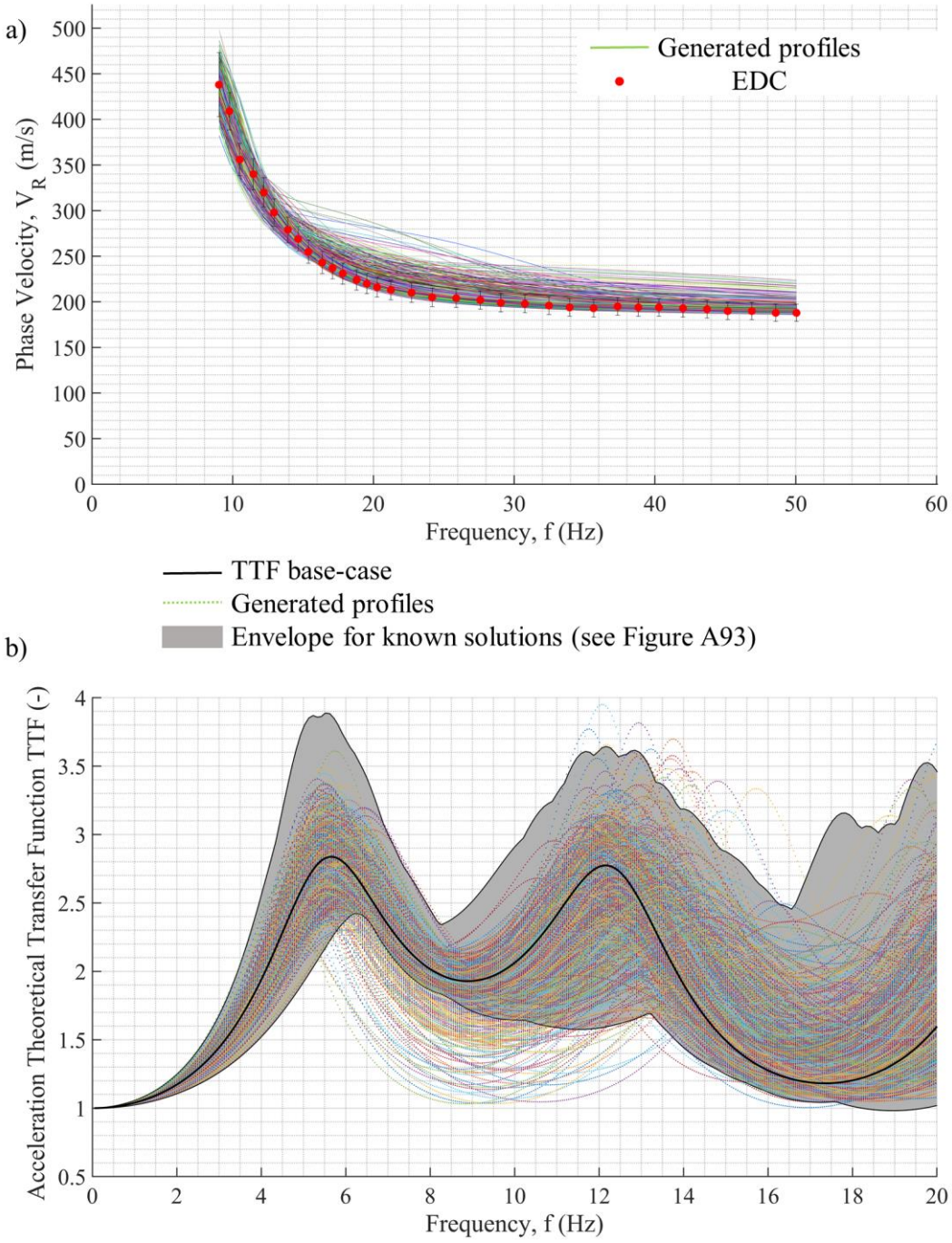

Figure 6.36. Validation of the randomization performed for the site of Accumoli, a) comparison as theoretical dispersion curves, and b) comparison as theoretical transfer functions.

6.3 Prototype application to Down-Hole testing methods

The present Section includes the extension of the geostatistical model to Down-Hole tests. This application represents a step-forward and demonstrates the flexibility of the proposed model discussed throughout the dissertation. However, the lack of a dedicated database prevents the calibration of the geostatistical model for these types of tests. As for the application to surface wave methods, also in this case the model can manage indistinctly EUs or AVs, generating an experimentally-

consistent sample of equivalent statistical profiles. However, these types of tests show a predominant contribution of the EUs in the quantification step. For this reason, the possible model calibration could address only for this contribution.

The proposed geostatistical model discussed in Section 6.2 can be applied for DH tests with only minor changes. From a theoretical point of view, the separation of the random variables characterizing space and time is most appropriate for this type of geophysical tests. Indeed, for DH tests the raw experimental results of the test are already obtained as times and lengths. The basic idea is then even more straightforward, as in this type of geophysical tests the analyst experimentally measures exactly spaces and times separately. Three observations should be discussed moving from the surface wave testing methods forward to DH tests. The following paragraphs try to answer the central questions of this evolution.

The first regards the application of the thickness-limiting boundaries for the non-homogeneous Poisson model. For surface wave testing methods, the layering randomization was based on the experimental resolution of the test with depth. The resolution with depth was obtained by analyzing the distances between experimental "transformed" wavelengths. The distance between two experimental points was assumed as the minimum thickness at a depth equal to the midpoint. For the DH test, the user can assume a minimum thickness dependent on the frequency of spatial measures with the depth of the experimental test (e.g., one acquisition every meter, then a minimum thickness of 2 m).

The second observation regards the user-defined parameters of the model both for the statistical distributions of shear wave velocity (i.e., space and time) and for the correlation model. For the geostatistical model in Section 6.2, the parameters were based on the results for the PSWD database; then even a non-expert user could have used the proposed database formulations. For DH applications, the user has to assume each parameter based on his/her knowledge of the test conditions and/or other a-priori information. The correlation parameters can be used from the Toro's (actually for interval velocities) or the ones obtained for the SWM (for travel times). This is due to the lack of enough information in the PSWD for this type of tests. The extension of the database will surely give the chance for a precise calibration of the model both for standard deviations and correlation coefficients.

The third observation deals with the bedrock depth-bedrock velocity correlation structure. This innovation was included in the geostatistical model because of the natural increase of velocity at low frequencies in the EDC. The same idea can be proposed for DH test applications, even if a more specific analysis is encouraged.

A preliminary application is proposed for the site of Acquasanta Terme that is included in the PSWD. The input parameters of the randomization are the deterministic V_S profile and the experimentally measured travel times with depth. Figure 6.37 shows the base-case solution and the experimental cumulated travel times of the DH test. Note that these travel times are automatically picked with a prototype method that is under development at the Politecnico di Torino. This algorithm is still under validation but is capable of estimating a standard deviation of the travel times for each depth. These standard deviations are used in this

application as an example; more research is needed in this regard for the estimation of experimental EUs and AVs associated with DH tests.

The randomization of the following 1000 profiles is performed with the following model parameters:

- $\overline{tt_{S,z}}$ equal to the mean value automatically picked and $\sigma_{\ln(tt_{S,z})} = 0.02$ (*assumed*, and time-limiting threshold after the randomization set at +/- $2\sigma_{\ln(tt_{S,z})}$);
- ρ as prescribed in Toro (1995) for the specific soil class;
- $\overline{d^h}$ equal to the mean value of the base-case profile and $\sigma_{\ln(d^h)} = 0.02$ (*assumed*);
- $\overline{V^h}$ equal to the mean value of the base-case profile and $\sigma_{\ln(V^h)} = 0.02$ (*assumed*);
- $\rho^h = 0.508$ as found for the surface wave testing methods;
- Thickness-limiting boundaries for the Non-Homogeneous Poisson model set at +/- 50% of the base-case (*assumed*).

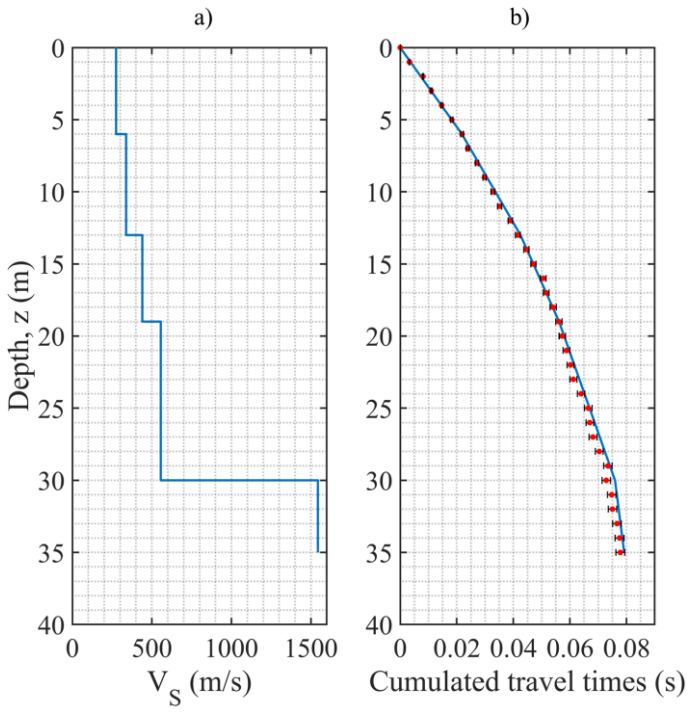

Figure 6.37. Base-case profile for the application of the geostatistical model to the DH test in Acquasanta Terme. a) Shear wave velocity base-case interval profile and b) cumulated travel times with experimental standard deviations compared to the cumulated travel times calculated from the base-case interval velocity profile.

Figure 6.38 shows the results of the randomization performed with the prototype geostatistical model applied to the solution of the DH test. The result presents an excellent agreement of the TTFs of the randomized profiles, with respect to the base-case. However, this prototype application needs further research

to be considered applicable in scientific and professional analyses. In particular, an in-depth and rigorous calibration with experimental results from DH tests in the PSWD is necessary to provide a range of suggested values for the model parameters.

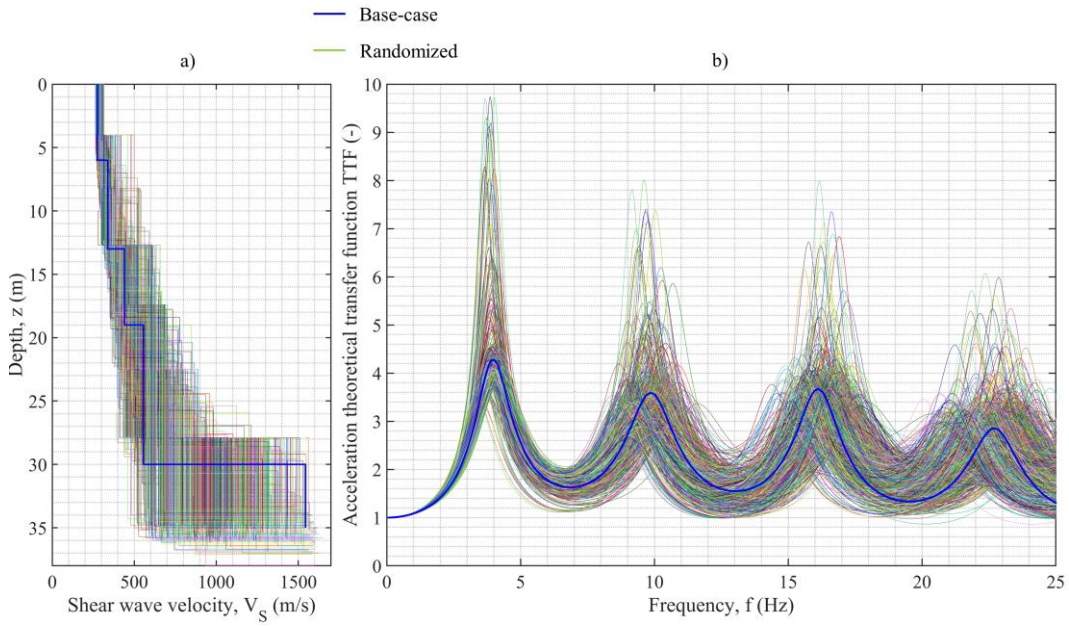

Figure 6.38. Randomization results obtained from the DH test performed in Acquasanta Terme. a) Interval velocity profiles reassembled and b) Theoretical Transfer Functions.

Chapter 7
Case study: Mirandola

This Chapter presents two validations of the geostatistical model described in Chapter 6 and is organized in three different parts. Section 7.1 briefly describes the blind test conducted at Mirandola during the InterPACIFIC project, for which multiple V_S profiles from surface wave and invasive methods are available. In Section 7.2, Ground Response Analyses (GRAs) are conducted at the site of Mirandola using the geostatistical model calibrated for surface wave methods for the generation of the statistical sample of equivalent profiles. The geostatistical model is applied to a deterministic base-case solution to simultaneously reproduce the Epistemic Uncertainties (EUs) and Aleatory Variabilities (AVs) empirically estimated by the different teams of the InterPACIFIC project. Also for this application, the identification and quantification of the two main contributes do not influence the results of the randomization. To isolate the effects of the V_S profile on the results of the GRA, all other parameters (see Section 3.1.2) are kept constant. The results of the geostatistical model are compared to the procedures prescribed by EPRI (2013) (see Section 4.3) both for the viscoelastic and nonlinear response. Section 7.2.3 compares the mean and standard deviations of the obtained responses in light of a hazard-consistent evaluation of the ground motion at the site (see Chapter 2). Finally, Section 7.3 shows the preliminary results of the geostatistical model applied to a Down-Hole (DH) test performed in Mirandola. In this case, the lack of a dedicated database prevented a rigorous calibration of the geostatistical model. However, the model is able to simultaneously reproduce the EUs and AVs, generating a sample of statistically equivalent profiles from a single deterministic base-case solution.

7.1 The InterPACIFIC project and Mirandola

The InterPACIFIC (Inter-comparison of methods for site PArameter and veloCIty proFIle Characterization) project aimed at evaluating the reliability, accuracy, and variability of different geophysical methods (i.e., surface waves and invasive) in estimating the V_S profiles (Garofalo et al. 2016a, b). Several teams of engineers, geophysicists and seismologists were invited to take part in the project. A list of the participants for the surface wave methods is provided in Table 7.1 along with the team's label and the country of origin. In addition, also invasive tests (i.e., Down-Hole, Cross-Hole, PS suspension logging, and Seismic Dilatometer) were performed during the project.

Three sites with different subsoil conditions were chosen to be part of the blind test: a soft-soil class (i.e., Mirandola), a stiff-soil class (i.e., Grenoble) and a hard-rock class (i.e., Cadarache) (Figure 7.1). This Chapter will deal only with the site of Mirandola. The stratigraphy is composed of alternating sequences of soft silty-clay layers and sandy horizons ($V_{S,30}$ between 180 and 360 m/s, Class D for NEHRP or Class C for the EC8 regulations) over approximately the top 100 m. Below these

successions, the geological substratum consists of marine and transitional deposits of lower-middle Pleistocene age.

Table 7.1. List of participants of the InterPACIFIC project for the surface wave methods (after Garofalo et al. 2016b).

ID	Label	Participants	Country
1	MU	Michael Asten, Monash University	Australia
2	CE	Diego Mercerat, CEREMA	France
3	IST1	Cécile Cornou, ISTerre	France
4	UT	Brady Cox, University of Texas	USA
5	INGV	Giuseppe Di Giulio, INGV	Italy
6	BFO	Thomas Forbriger, Black Forest Observatory	Germany
7	Geom	Koichi Hayashi, Geometrics	USA
8	IST2	Bertrand Guillier, ISTerre	France
9	KU	Shinichi Matsushima, Kyoto University	Japan
10	TT	Hiroaki Yamanaka, Tokyo Institute of Technology	Japan
11	GV	Antony Martin, Geovision	USA
12	SED	Valerio Poggi, Stefano Maranò, Jan Burjanek, Clotaire Michel, SED-ETHZ	Switzerland
13	PU	Matthias Ohrnberger, Potsdam University	Germany
14	PT	S. Foti and F. Garofalo, Politecnico di Torino	Italy

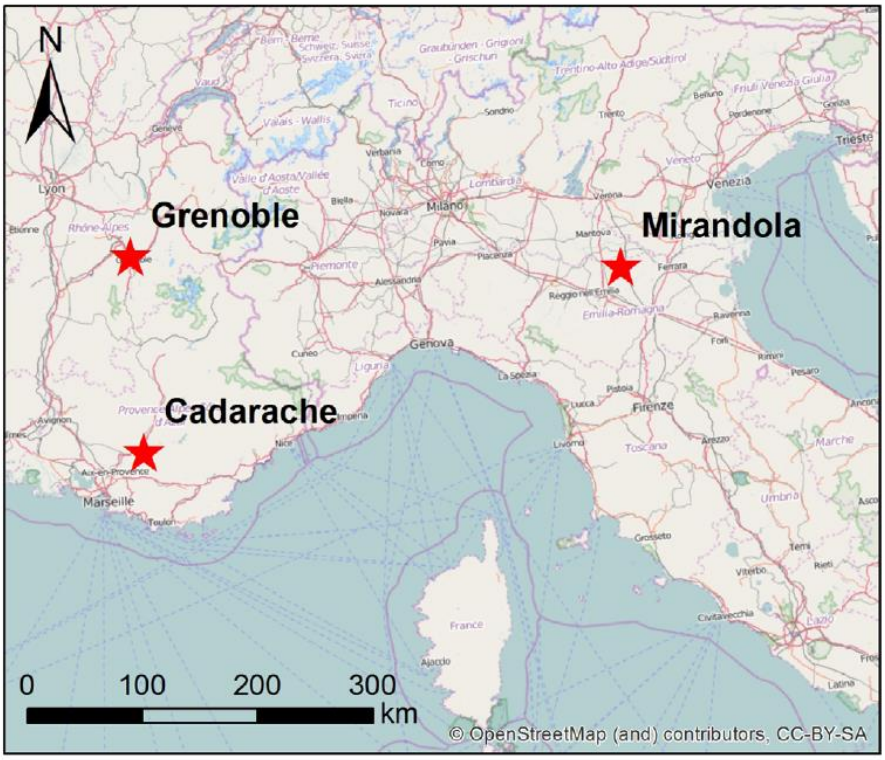

Figure 7.1. Location of the three sites analyzed during the InterPACIFIC project (after Garofalo et al. 2016b).

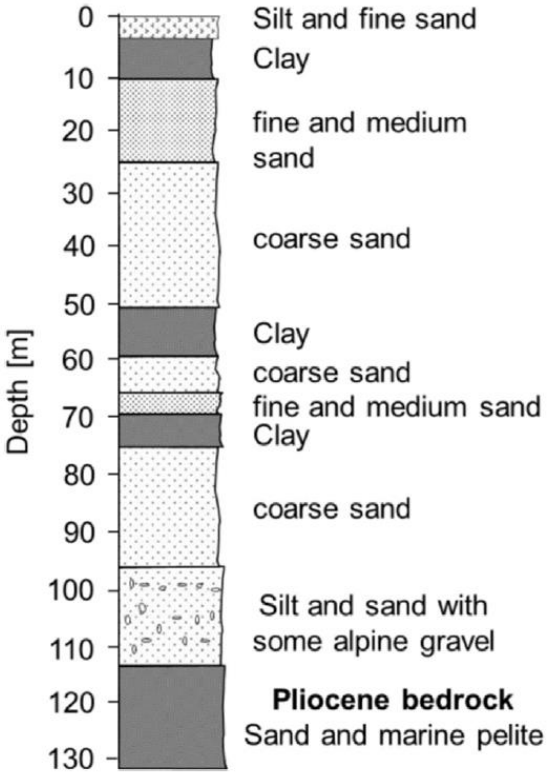

Figure 7.2. Stratigraphy of the Mirandola site (after Garofalo et al. 2016a).

For surface waves, the participants of the project analyzed a set of common data (i.e., common acquisition step) using their preferred strategies for the processing and inversion steps (see Section 4.2.2.2). Both active (i.e., from MASW tests) and passive (i.e., from AVA tests) surface wave data (see Section 4.2.2.2) were collected with arrays close to the boreholes, to obtain a significant comparison between the surface wave and the invasive methods (i.e., inter-method comparison). In order to ensure that each participant has performed a blind test, the same surface wave experimental datasets were provided to all teams with very little information about the sites.

Furthermore, several participants performed and interpreted invasive measurements of shear and compression wave velocities. At least two holes were available to perform invasive measurements. Several companies have repeated measurements in order to assess repeatability with different acquisition strategies and equipment.

Garofalo et al. (2016a, b) report the entire set of V_S profiles from both surface wave and invasive tests at Mirandola. The locations of the MASW and AVA's acquisitions, the boreholes, and the surface wave dataset characteristics are also reported in Figure 7.3. The reader can refer to these companion papers for more details regarding the sites and analysis results.

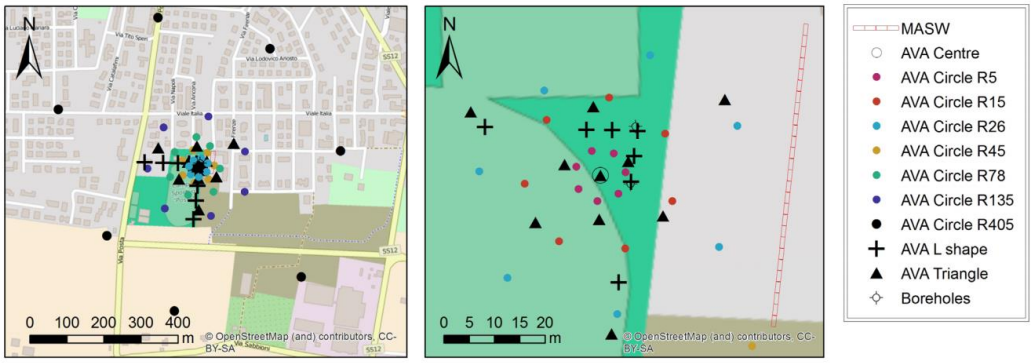

Fig. 2. Mirandola: maps of the arrays. (Left) whole area interested by the acquisition. (Right) close-up view of the area. The largest triangular array is not shown.

Table 4
Mirandola: datasets. T= time window, ΔT=time sampling.

label	Dataset	Num. channels	Time sampling	Space sampling
AV1	Active (vertical)	48	T=2 s, ΔT= 0.25 ms	Receiver spacing=1 m
AV2	Active (vertical)	48	T=2 s, ΔT= 0.25 ms	Receiver spacing=2 m
AH	Active (horizontal)	24	T=2 s, ΔT= 0.25 ms	Receiver spacing=2 m
PC1	Passive circular	15	T=01:00:00 ΔT= 5 ms	Radii=5 and 15 m
PC2	Passive circular	15	T=01:15:00 ΔT= 5 ms	Radii=15 and 45 m
PC3	Passive circular	15	T=01:13:00 ΔT= 5 ms	Radii=45 and 135 m
PC4	Passive circular	15	T=01:58:30 ΔT= 5 ms	Radii=135 and 405 m
PC5	Passive circular	15	T=01:20:00 ΔT= 5 ms	Radii=26 and 78 m
PT	Passive triangular	16	T=01:29:00 ΔT= 5 ms	Sides=12.5, 25, 50, 100, and 200 m
PT2	Passive large triangular	10	T=03:24:30 ΔT= 5 ms	Sides=4000, 2000, 1000 m
PL	Passive L-shape	13	T=00:59:30 ΔT= 5 ms	Distances=5, 10, 30, 60, 100, and 150 m

Figure 7.3. Locations and characteristics of the surface wave acquisitions performed at Mirandola (after Garofalo et al. 2016b) and position of the boreholes.

7.2 Surface wave testing methods

This section deals exclusively with surface wave methods. All teams at Mirandola processed the fundamental mode of the Rayleigh waves dispersion curve. Some teams have also analyzed higher or effective modes, while others included Love wave analysis (Table 7.2). Another popular choice was the combination of the recovered information from both active and passive seismic data, as also reported in Table 7.2 (see Section 4.2.2.2).

Table 7.2. Processing and inversion strategies adopted by each team at Mirandola (after Garofalo et al. 2016b).

ID	Team	dataset	Surface wave mode	Additional information	Dispersion analysis processing	Inversion algorithm	Software
1	MU	PC1, PC3, PT, PT2	RE	HVSR	SPAC_directFit	LLS_EYE	Mmspacfit
2	CE	PT	R0	HVSR	SPAC+FK	NA	Geopsy
3	IST1	PC1, PC2, PC3, PC4, PC5	R0 R1, L0	Ellipticity	FK	NA	Geopsy
4	UT	AV1, AV2, AH, PC1, PC2, PC3, PC4, PC5, PT, PL	R0, R1, L0		SPAC+FDBF	NA	Geopsy
5	INGV	AV1, AV2, AH, PC1, PC2, PC3, PC4, PC5, PT, PT2, PL	R0, L0, L1	HVSR	FK	NA	Geopsy
6	BFO	AV1, AV2, AH	R0, R1, R2		FB	LLS_EYE	Germlin (In-house)
7	Geom	AV2, PC1, PC5, PT2	RE	HVSR	PS	GA	Seisimager
8	IST2	PC1, PC2, PC3, PC4, PC5	R0	HVSR	FK	NA	Geopsy
9	KU	PC1, PC2, PC4, PC5, PT, PT2	R0		SPAC	EYE	In-house
10	TT	PT	R0		SPAC	SA-GA	In-house
11	GV	AV1, AV2, PC1, PC2, PC3, PC4, PC5	R0	Water table (refraction analysis)	SPAC+PS	NLS	Seisimager; WinSASW
12	SED	PC1, PC2, PC3, PC4	R0, R1, R3, R4, L0, L1	Ellipticity	3C+WD	NA	In-house; Dinver
13	PU		R0		SPAC	NA	Geopsy
14	PT	AV1, AV2, PC3, PC4	R0		FK+FDBF	MC	in-house

Label	Method	Data
FK	Frequency-wavenumber transform	active
PF	Slowness-frequency transformation method	active
PS	Phase-shift transform, a special case of PF transform	active
FDBF	Frequency domain beamformer	passive
HFK	High resolution frequency-wave-number transform	passive
SPAC	Spatial Autocorrelation Coefficient method	passive
MSPAC	Modified SPAC	passive
3C+WD	Three component high-resolution f-k analysis and wave field decomposition	passive
SPAC_directFit	SPAC spectra computed from smoothed coherency-frequency spectra	passive
FB	Fourier-Bessel expansion coefficients	active
Ellipticity	Ellipiticity of Rayleigh waves from the noise recordings	passive

Label	Algorithm
NA	Neighborhood Algorithm
MC	Monte Carlo method
GA	Genetic Algorithm
SA-GA	Simulated Annealing and genetic algorithm in an hybrid heuristic search method
NLS	Non-linearized least-squares algorithm
LLS_EYE	Linearized Least Square and trial and error procedure
EYE	Trial and error procedure

Only a subset of V_S profiles that clearly identified a marked impedance contrast at depth are considered for GRAs and extensively presented in Passeri et al. (2019). This selection criterion resulted in 12 profiles from surface wave tests.

The Experimental Dispersion Curves (EDCs) corresponding to the selected subset of test results are shown in Figure 7.4. The legend also shows the identification letters used in Passeri et al. (2019) (e.g., MU_V stands for MU, as reported in Garofalo et al. 2016a, b, and V for the profile V, as reported in Passeri et al. (2019)). Most analysts estimated the dispersion of Rayleigh waves within a frequency band of about 1-20 Hz. Dispersion estimates in terms of Coefficients of Variation (i.e., COVs) typically range between 5% and 10% (Garofalo et al. 2016b). The variability shows a rapid increase at higher and lower frequencies. For the high-frequency band, this observation is likely associated with lateral variability in the deep part of the deposit. In the low-frequency band, the resolvable frequency limits are due to the geometry of the array and the quality of the data. The experimental frequency band is wider for the teams who combined active and passive data, while it is slightly narrower for who relied solely on active or passive data.

Note that the EDC obtained by the University of Texas at Austin (i.e., UT, U) is highlighted in black dots and is shown along with the standard deviation of the phase velocity (i.e., σ_{V_R}, see Section 5.2) (Griffiths et al. 2016a). The solution of this team was chosen as base-case for the application of the geostatistical model described in Section 6.2.

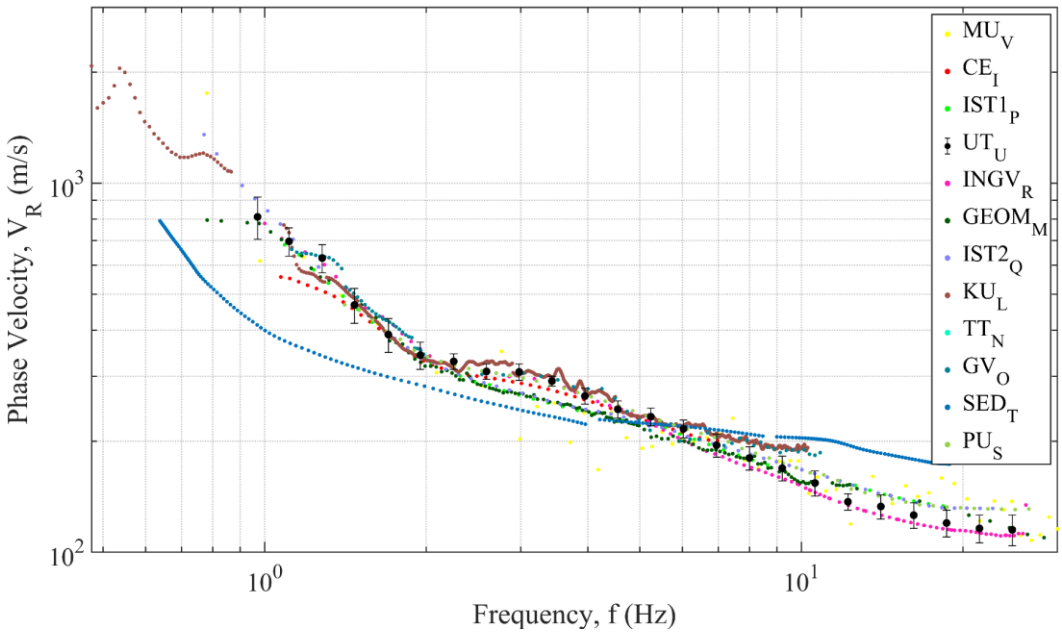

Figure 7.4. Experimental Dispersion Curves obtained by different teams at the site of Mirandola.

Figure 7.5 shows the selected V_S profiles from surface wave tests for GRAs as interval (Figure 7.5a) and harmonic average (Figure 7.5b) profiles (see 4.1). The base-case profile from UT is highlighted in thick black. None of the analysts of the surface wave tests identified the thin, low-velocity soil layer at about 75 m that is reported by the invasive profiles detailed in Garofalo et al. (2016a). However, the surface wave profiles do not present velocity spikes, as is the case for most of the invasive profiles. Moreover, the surface wave profiles are generally in intra-method (i.e., within the class of geophysical method, surface waves or invasive) agreement, as extensively discussed in Garofalo et al. (2016b).

Figure 7.5 also shows a V_S profile obtained by Laurenzano et al. (2017) in a work separate from the InterPACIFIC project. The V_S profile shown corresponds to the best match of the small-strain, linear viscoelastic Theoretical Transfer Function (TTF) with the small-strain Empirical Transfer Function (ETF) (Baise et al. 2011) (see the introduction to Chapter 3). Laurenzano et al. (2017) processed a 3-sensor (surface, 31 m depth, and 126 m depth) down-hole array data at Mirandola. The ETF (called the 'experimental interferometric function' by Laurenzano et al. 2017) was obtained by processing 25-recorded seismic events in the North-East part of Italy between June 2014 and October 2015, with magnitudes ranging between 2.1 and 3.7 and hypocentral depths ranging from 5.2 km and 57.2 km. The authors considered the V_S profile resulting from a CH test as a reference and they build up a set of compatible constant velocity layers models, with layer thickness determined from the stratigraphic profile and V_S values varying within arbitrary wide bounds. For each model, Laurenzano et al. (2017) then computed the TTF and compared it with the experimental one. Further details about the signal processing and specific procedures are discussed in Laurenzano et al. (2017). This V_S soil profile has the best match with the ETF site signature; hence, it will be referred to as 'TTF-best' and represents an essential independent reference.

The V_S profiles in Figure 7.5 indicate that there is generally a good agreement between the profiles obtained from surface wave tests and the TTF-best soil profile. However, the TTF-best profile by Laurenzano et al. (2017) shows a velocity inversion at shallow depths that is not identified by any surface wave test.

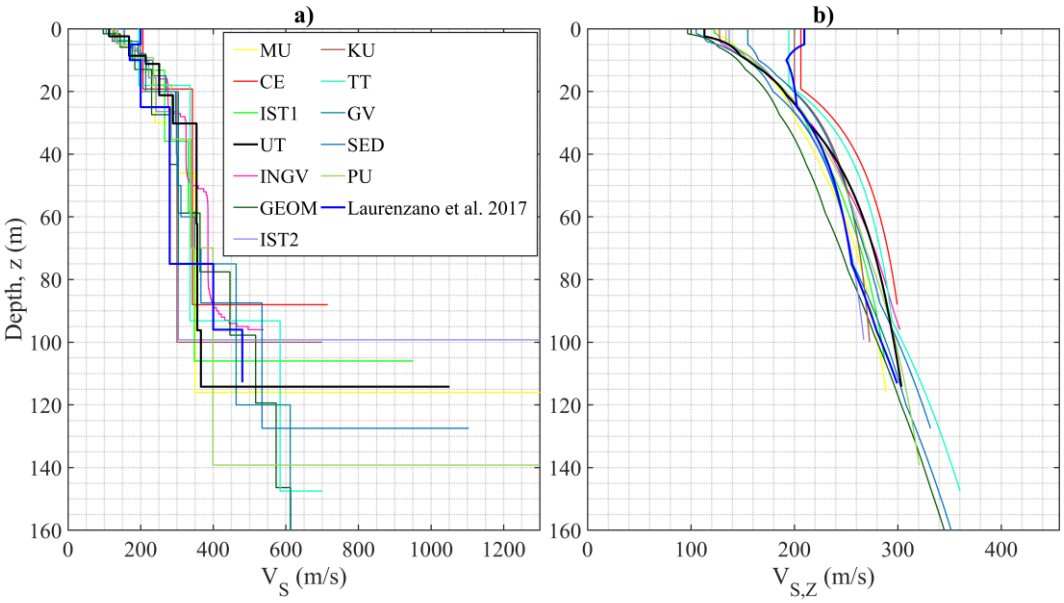

Figure 7.5. Profiles at Mirandola selected for the Ground Response Analyses, a) interval velocity profiles, and b) harmonic average profiles.

At this point, the reader should imagine possessing only the solution obtained by the UT (EDC and V_S profile), the base-case. So far, both in the scientific community and engineering practice for critical facilities, the management of EUs and AVs was conducted with the procedures explained in Section 4.3.

The first method prescribes to create profiles (i.e., upper/lower range profiles) shifted by a value of V_S logarithmic standard deviation (i.e., assuming an inter-layer perfect correlation, see Section 4.3.1). In this study, the minimum value of 0.25 prescribed by EPRI (2013) is applied to the UT's profile (Passeri et al. 2019). Figure 7.6a shows that the upper/lower range interval velocity profiles generally bracket the values for the surface wave V_S experimental profiles. However, Figure 7.6b illustrates the dramatic alteration of the harmonic average profiles obtained by the upper/lower range profiles. The essential change is clear, for example, by looking at the $V_{S,30}$ values. The base-case (i.e., UT's) profile has a $V_{S,30}$ = 213 m/s, the lower range profile has a $V_{S,30}$ = 166 m/s (i.e., even different soil class for NEHRP and EC8), and the upper range profile has a $V_{S,30}$ = 274 m/s.

Figure 7.6 also shows 1000 profiles obtained by the standard Toro model (TM95) around the UT's base-case profile. This method is prescribed by EPRI (2013) for the management of AVs in shear wave velocity profiles (see Section 4.3.2). In the present study, the logarithmic standard deviation of the base-case profile is assumed as suggested by Stewart et al. (2014a) (see Figure 6.24). The Poisson's model parameters are assumed equal to the ones suggested by Toro, as for the parameters of the inter-layer correlation model. The lognormal distribution

of the halfspace depth is included in the randomization with a logarithmic standard deviation equal to 0.1. Note that this value is in agreement with the statistical analyses performed in Passeri et al. (2019) for Mirandola. In this case, both the interval velocity and harmonic average profiles are entirely out of range, compared to the experimental results. Note that this is true even if the reduced $\sigma_{\ln(V_S)}$ proposed by Stewart et al. (2014a) is adopted (an almost doubled value is suggested in Toro (1995)). This is due to the randomization of the interval velocities and the unavoidable parasite uncertainties introduced by this type of randomization (Li & Asimaki 2010, Griffiths et al. 2016b, Teague & Cox 2016, Teague et al. 2018).

The last set of 1000 profiles presented in Figure 7.6 is obtained from the new geostatistical model around the UT's solution (in gray). These randomizations are based on the harmonic averaged velocity, $V_{S,Z}$, as discussed in Section 6. Also in this case, the model is adopted in the "blind" form (i.e., assuming suggested and non-site-specific model parameters, as described in Section 6.2.1). This choice is made to replicate the typical applications of the randomization models in engineering practice, where the user typically does not have the data of different and repeated measurements at the site. Moreover, this choice assures consistency with the parameters adopted for the Toro model for a rigorous comparison. The results of this second randomization excellently reproduce the EUs and AVs experimentally estimated at Mirandola, especially as harmonic average profiles (Figure 7.6b). The randomized profiles show $V_{S,Z}$ functions with a controlled deviation from the base-case.

Note that the term "controlled" is used to say that the user can increase or decrease the uncertainties. The variability of the obtained randomized profiles can be calibrated (see Section 6.2.1), but the geostatistical model always assures a fundamental consistency that does not exist for the TM95. This is in agreement with the observations presented throughout the dissertation. The geostatistical model is able to randomize the V_S profiles independently of the nature of the uncertainties. For these reasons, the identification and quantification steps show their crucial role before the management step in the IQM methodology. However, note that the analyses conducted with the parameters based on the PSWD simultaneously manage EUs and AVs.

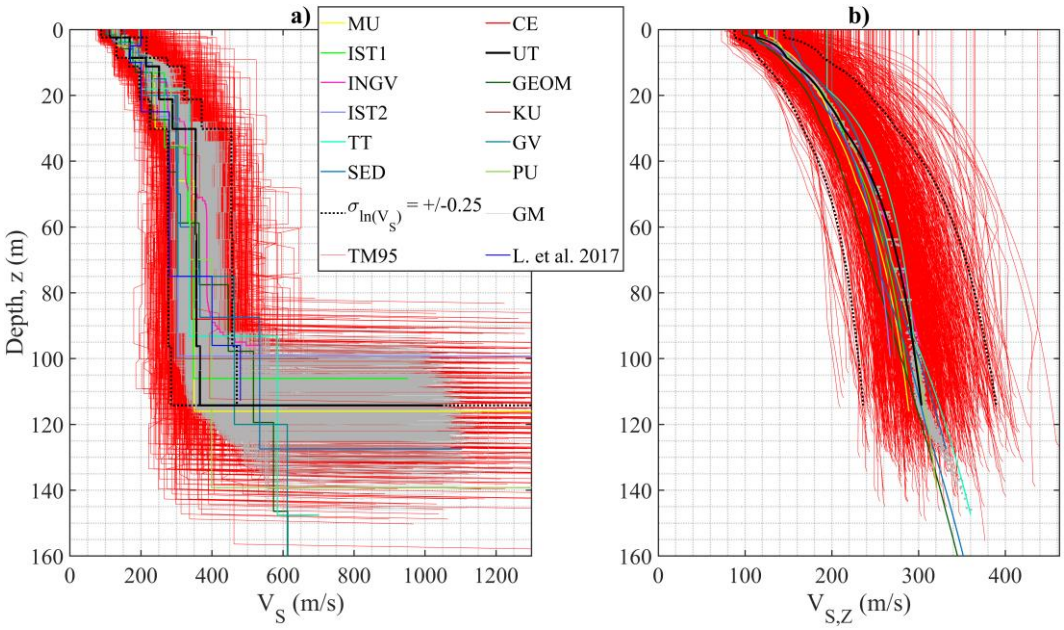

Figure 7.6. Profiles at Mirandola selected for the Ground Response Analyses including the upper/lower range profiles, the profiles generated by the Toro model, and the profiles generated by the new geostatistical model as a) interval velocity profiles, and b) harmonic average profiles.

Further confirmation of the problems with both the methods proposed in EPRI (2013) is given in Figure 7.7. This Figure shows the comparison of the Theoretical Dispersion Curves (TDCs) with the EDCs also shown in Figure 7.4. Note that the dispersion curves corresponding to the V_S profile randomized following the EPRI randomization do not match the EDC. This is a similar problem to the mismatch of the harmonic average velocity shown in Figure 7.6b, as expected. Indeed, the relationship between the $V_{S,Z}$, and the V_R was discussed and demonstrated in Section 6.1.1. These two functions differ for a simple linear transformation. For this reason, the inadequacy of using the upper/lower range profiles and the profiles from the TM95 randomization also results in problems matching the TDCs. At the same time, the TDC calculated from the profiles randomized with the new geostatistical model are in excellent agreement with the EDC (i.e., site signature) of the base-case (i.e., UT's).

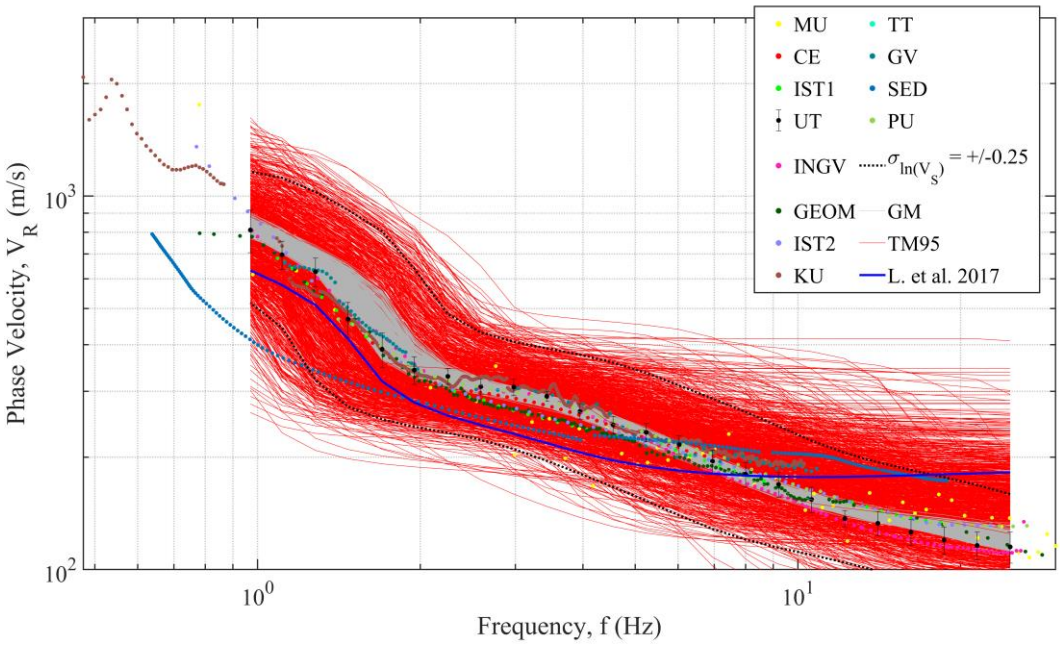

Figure 7.7. Experimental Dispersion Curves obtained by different teams at the site of Mirandola and Theoretical Dispersion Curves calculated from the set of profiles available for the subsequent Ground Response Analyses, included the solution obtained from the work by Laurenzano et al. (2017).

At this point of the study, five classes of profiles are available for the GRAs (Figure 7.6):

1. 12 experimental profiles from the different participants of the InterPACIFIC project obtained using the surface wave dataset;
2. 1 TTF-best profile obtained by Laurenzano et al. (2017) that primarily respects the experimental information of the ETF;
3. 2 upper/lower range profiles obtained from the EPRI (2013) provisions around the UT's solution for the management of the EUs;
4. 1000 profiles randomized around the UT's solution adopting the TM95 and standard (i.e., non-site-specific) model parameters (suggested by EPRI for the management of AVs);
5. 1000 profiles randomized around the UT's solution adopting the new geostatistical model and standard (i.e., non-site-specific) model parameters.

Frequency-domain GRAs are conducted using SHAKEVT (Lasley et al. 2014), which has been previously verified against DEEPSOIL (Hashash et al. 2015) and STRATA (Kottke & Rathje 2009). Both Linear visco-Elastic (LE) and EQuivalent Linear (EQL) analyses are conducted (see 3.1.2.4).

For the LE analyses, only the suggested Darendeli's small strain damping (D_{min}, 3.1.2.6) is used. Viscoelastic behavior is also assigned to the halfspace, with damping set at 0.5%. The density of each layer is estimated considering the stratigraphy.

The EQL analyses are performed using a shear strain ratio of 0.65. The modulus reduction and damping curves of Darendeli (2001) are used (see Section 3.1.2.2) using the soil information from the borehole logs in Mirandola. Additional details regarding the IMs are given in the following. The LE analyses are first used to evaluate the linear response of each V_S profile. This response is evaluated using the TTFs, as also illustrated in Figure 6.4 and Figures A93-163. EQL analyses are then performed, and results are given in terms of the 5% damped pseudo-Spectral Acceleration (SA) Response Spectra (RS) and Amplification Functions (AFs) (i.e., the ratio of the pseudo-spectral acceleration at the surface to the pseudo-spectral acceleration of the IM).

When performing GRAs and evaluating the effects of soil nonlinearity, it is essential to account for the effects of input ground motion characteristics, as discussed in 3.1.2.3. In order to represent ground motions with varying intensity, duration and frequency content, two suites of ground motions selected and scaled by Griffiths et al. (2016b) have been used. These include one suite for a target moment magnitude (M_W) earthquake of 6.0 and another for M_W = 7.5. The procedures used to obtain the input ground motions for an M_W = 7.5 earthquake are explained in detail below. Similar procedures were used for the M_W = 6.0 ground motions.

A target spectrum for the selection of input motions was determined from the ground motion prediction equation of Boore & Atkinson (2008), assuming an M_W = 7.5 earthquake, a Joyner-Boore distance of 15 km, and an average V_S in the top 30 m ($V_{S,30}$) of 760 m/s. The Pacific Earthquake Engineering Research Center strong-motion database was used to develop a library of 80 time histories recorded at sites with $V_{S,30}$ between 500 and 1,500 m/s, distances between 5 and 80 km, and M_W between 7.0 and 8.0. Using the library of 80 motions, the computer program SigmaSpectra (Kottke & Rathje 2008) was used to select and scale eight time histories that, on average, matched the shape of the target response spectrum (Griffiths et al. 2016b). To investigate how different input motion intensities affect the nonlinear response of the V_S profiles, these eight input time histories were each further scaled to Peak Ground Accelerations (PGAs) of 0.1 and 0.5 g. Similarly, eight additional input ground motions were fit to a target spectrum for an M_W = 6.0 event in order to investigate the impact of frequency content on the site response estimates. Only the eight M_W = 6.0 input motions scaled to 0.1 g, and the eight M_W = 7.5 input motions scaled to 0.5 g are used herein for EQL analyses.

In addition to the scaling operations described above, the input time histories have also been adjusted in order to account for the variable halfspace stiffness indicated by each of the V_S profiles (Passeri et al. 2018a). These modifications have been performed in order to permit a consistent comparison between the responses of profiles with different reference conditions. An adaptation of the method proposed by Boore (2013) (see also Boore and Brown 1998 and Boore 2003) has been used. The amplification/deamplification factor is estimated using the quarter wavelength method and is given by:

$$A(f(z)) = \sqrt{\frac{Z_S}{\overline{Z(f)}}} \qquad \text{(Eq. 7.1)}$$

where Z_S is the reference halfspace condition impedance (i.e., the product of density and shear wave velocity, see Equation 4.8) and $\overline{Z(f)}$ is an average of near-surface seismic impedances. In Boore (2003a) $\overline{Z(f)}$ is a function of frequency because it represents a time-weighted average from the surface to a depth equivalent to a quarter wavelength. For this study, it is possible to assume a constant velocity below the column-halfspace interface, hence $\overline{Z(f)} = Z_b$, where Z_b is the impedance at the halfspace of each V_S profile.

Moreover, Z_S represents the 'rock reference condition' of the Boore and Atkinson ground motion prediction equation used for the IMs selection (V_S=760 m/s). For simplicity, the densities of soil and rock are assumed equal. Since Z_b is assumed to be frequency-independent, the modification of the IMs is reduced to a constant factor

$$A = \sqrt{\frac{760\frac{m}{s}}{V^h}} \qquad \text{(Eq. 7.2)}$$

that is applied to modify the IM suites for each V_S profile. Interestingly, if a halfspace velocity of $V^h = 1500\frac{m}{s}$ is used in Equation 7.2, the simplified amplification/deamplification factor is approximately equal to the ratios of NEHRP site factors for class B and class A, which is equal to 0.8 (Seyhan & Stewart 2014).

7.2.1 Linear viscoelastic response

Linear, viscoelastic analyses were conducted for each V_S profile of the five classes. Figure 7.8 shows a comparison of the surface-to-halfspace ('outcrop' motion) TTFs. The Figure also includes the average HVSR (see Section 4.2.2.3) resonant frequency peak (f_0) measured around the site during the InterPACIFIC project (Prof. Brady R. Cox, personal communication and Mascandola et al. (2019)).

The amplitudes of the linear, viscoelastic TTF are likely too high because laboratory D_{min} values were used in the calculations. These lab-based D_{min} values only account for material damping. They do not account for other factors that contribute to apparent damping in situ, such as radiation damping and backscattering (Zalachoris and Rathje 2015). However, comparable TTF amplitude values among the 12 V_S surface wave profiles (i.e., Class-1) were obtained, except for profiles $IST2_Q$, PU_S, and MU_V, which have either stiffer halfspace or a more significant depth to halfspace than the other V_S profiles. Also, the TTF calculated from the profile suggested by Laurenzano et al. (2017) (i.e., Class-2) is in agreement with the surface wave profiles and, in particular, with the UT's solution (i.e., the base-case of the exercise).

Figure 7.8 also compares the fundamental elastic resonant frequencies obtained from the TTFs for the five classes of profiles. Observe that the f_0 values for all of the Class-1 V_S profiles are consistent with the resonant frequency obtained using HVSR (except for the V_S profiles $IST1_I$, $GEOM_M$, and $INGV_R$ that present slightly different values). As opposed to the TTF amplitudes, profiles $IST2_Q$, PU_S, and MU_V show a good agreement in terms of f_0. The same observation is valid for the first resonant frequency of the profile suggested by Laurenzano et al. (2017).

The previous observations are not valid for the profiles suggested by EPRI (2013) for the management of EUs and AVs (i.e., Class-3 and Class-4). The upper/lower range profiles exhibit f_0 values well outside the range of the measured V_S profiles. The scaling of the base-case profile produces a consequent inacceptable scaling of both TDCs (Figure 7.8. Comparison of the five classes of profiles as Theoretical Transfer Functions. The experimental resonant frequency obtained by the HVSR test is also indicated. Interestingly, the amplitudes of the TTFs are preserved, as the impedance contrasts are also linearly scaled.

The profiles obtained with the TM95 show scattered amplitude peaks concerning the base-case profile. This is further evidence that these profiles do not reproduce well the small strain (i.e., elastic) soil behavior and the site signature corresponding to the resonant frequency of the site (i.e., HVSR f_0). In this context, the V_S profiles are altered, and the viscoelastic response reflects the results of the randomization.

On the contrary, the profiles obtained randomizing the base-case UT's solution with the new geostatistical model (i.e., Class-5) show consistent results. The agreement is confirmed for both resonant frequencies and amplitude peaks. The parameter that mainly controls the obtained variability is $\sigma_{\ln(\mathrm{tt}_{S,z})}(z)$ (see 6.2.1.1) and could be increased by the user. However, the geostatistical model will always ensures a control of the randomized profiles, thanks to its characteristics, as discussed in Section 6.2.

The observations above are also valid for Figure 7.9, where the first resonant frequency of the TTF for each of the 1000 realizations is plotted. Note that these viscoelastic resonant frequencies are a fundamental signature of the profile, and should be in accordance with the independent experimental site signatures (i.e., HVSR peak and the resonant frequency of the ETF). Also, the asymmetric scatter of the results is due to the lognormal distribution that is behind the randomization process (i.e., logarithmic distribution seen on a linear scale).

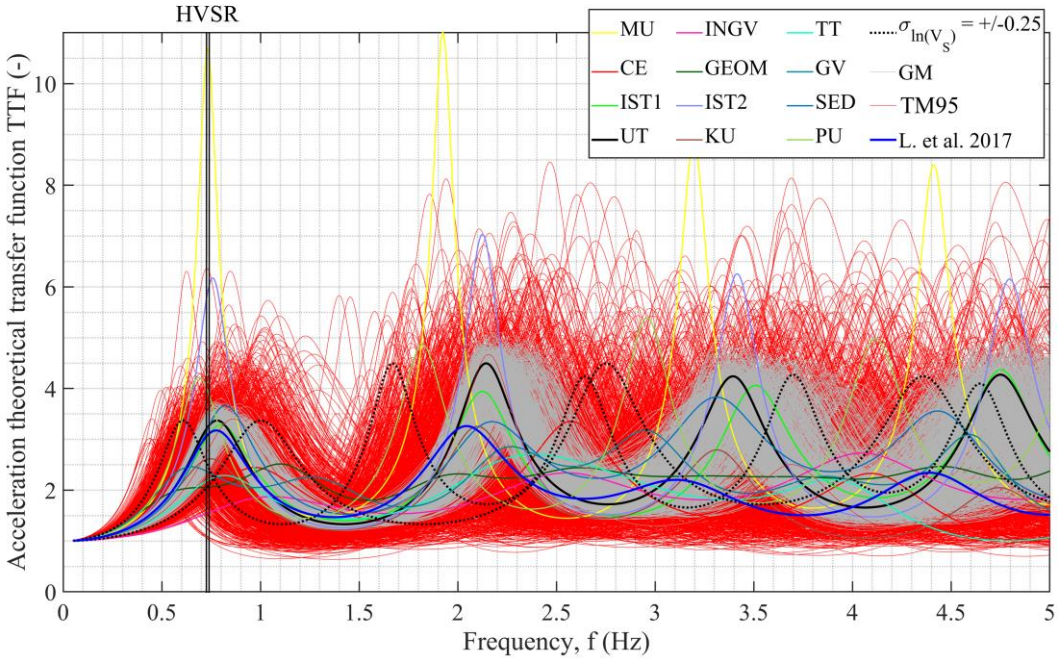

Figure 7.8. Comparison of the five classes of profiles as Theoretical Transfer Functions. The experimental resonant frequency obtained by the HVSR test is also indicated.

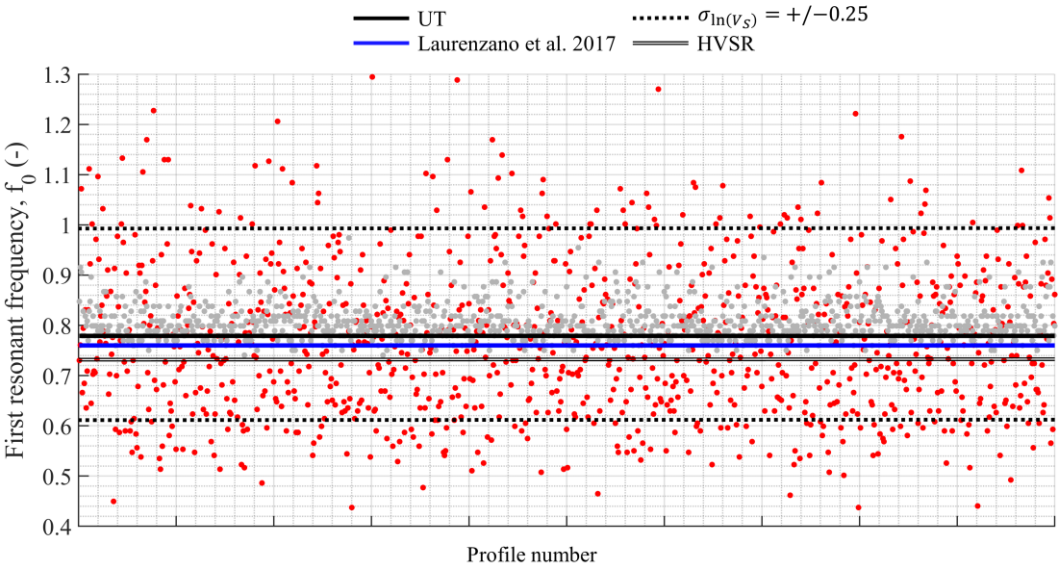

Figure 7.9. Comparison obtained for the first resonant frequencies of the theoretical transfer functions for each of the 1000 profiles of Class 4 and Class 5 profiles.

7.2.2 Equivalent linear analyses

The EQL-GRA results for the 0.1 g IMs suite are presented in Figure 7.10 for the five classes of profiles presented in Section 7.2. Acceleration Response Spectra at the ground surface (RS) are shown in Figure 7.10a. Figure 7.10b shows the same results in terms of Amplification Functions (AFs).

For the Class-1, profiles $IST2_Q$, PU_S, and MU_V showed unusual halfspace characteristics and TTF amplitude peaks; however, the EQL response is in line with the other surface wave profiles. The results obtained for the profile in Laurenzano et al. (2017) show lower responses compared to Class-1 profiles regarding both RS and AFs. This is due to the high strains induced in the soft layer identified at depths of 5 to 10 m. This low-velocity layer converged at high damping values that effectively place limits on the responses, as also demonstrated in Zalachoris & Rathje (2015) and Passeri et al. (2019).

The Class-3 and Class-4 profiles show evident inconsistencies with the GRA results of the measured profiles and the base-case UT's profile, as expected from the viscoelastic results. In particular, the peak frequencies of the upper/lower range profiles do not match with the peak frequencies of the base-case V_S profile. This is in accordance with other insights in the literature regarding the use of assumed upper/lower bound V_S profiles to account for epistemic uncertainty propagation in GRAs (Griffiths et al. 2016b, Teague & Cox 2016, Passeri et al. 2019) and with the results shown in Figure 7.8. In that Figure, these profiles showed inconsistency with the experimental site signatures (i.e., HVSR and ETF peaks), the surface wave V_S profiles and the UT's base-case profile. Also, note that the upper/lower range base-case profiles do not provide consistent bounds to the uncertainty for both RS and AFs. The range of spectral accelerations for these profiles is close to that of the measured profiles at short periods but is more significant at intermediate periods.

A similar inadequacy can be seen for the class-4 profiles (i.e., TM95-based). In this case, the variability of the results is even more significant, regarding both SA and AFs. However, this class of profiles seems to better reproduce the resonance periods (i.e., the "shape" of the spectrum), compared to the results of the base-case profile. This evidence is not confirmed looking at Figure 7.10b, where the variability of the calculated AFs is overwhelming. From both Figure 7.10a and Figure 7.10b, the reader can glimpse a higher density of lower responses (i.e., unconservative mean response, compared to the base-case).

On the contrary, the GRA results obtained from the Class-5 profiles have AFs and SAs that are compatible with the AFs of the 12 measured profiles (Class-1 profiles). The variability of the response around the base-case is controlled and limited to shapes (i.e., frequencies) consistent with the experimental data. This means that the dynamic behavior of the base-case profile is preserved, reproducing a level of EUs and AVs in line with the experimental information.

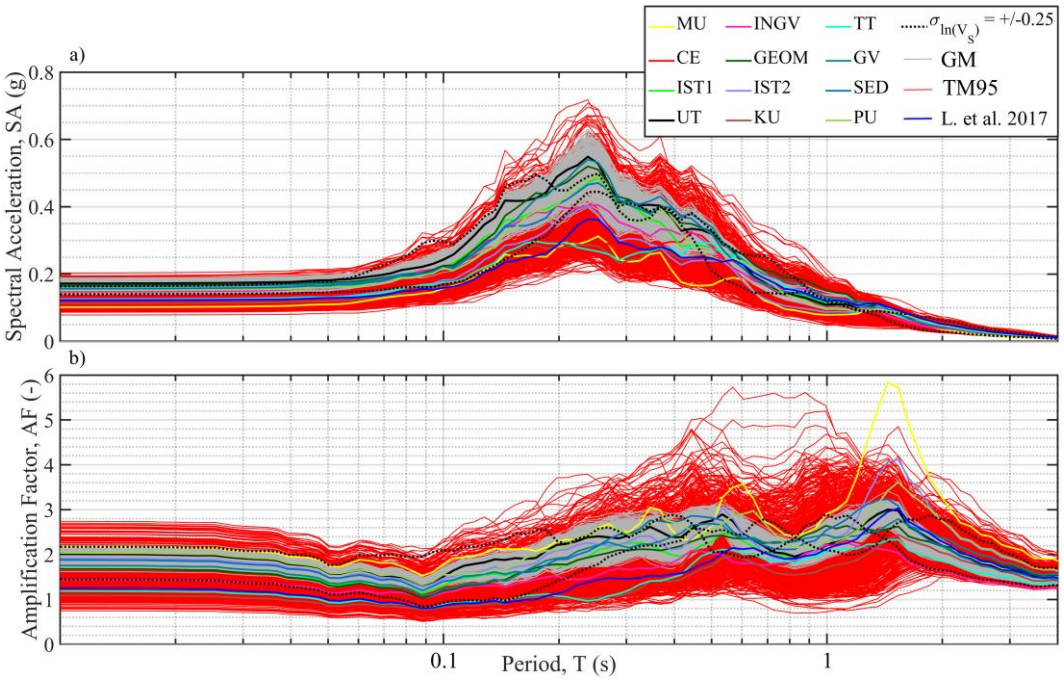

Figure 7.10. Results of the Equivalent Linear Analyses conducted for the five classes of profiles and the 0.1 g scaled input motions, a) Surface Response Spectra and b) Amplification Functions.

The EQL-GRA results for the higher intensity IMs suite are reported in Figure 7.11. The variabilities in the V_S profiles propagated to spectral accelerations and amplification functions are more substantial than for the low-intensity ground motion suite (Figure 7.10). Profiles $IST2_Q$, PU_S, and MU_V of the Class-1 still produce RS results in good agreement with the global response.

The response of the TTF-best profile still shows lower estimates, compared to the other classes of profiles. For this strong intensity IMs suite, the incompatibility of the upper/lower range base-case V_S profiles and the profiles obtained from the TM95 increased. The GRAs show anomalous results, both in terms of frequency content and amplitudes, plotting significantly outside of the experimental area for the entire range of periods both in terms of spectral accelerations (Figure 7.11a) and amplification functions (Figure 7.11b). Note that the scattering of the results increased due to the nonlinearity of the response (Griffiths et al. 2016b, Teague & Cox 2016, Passeri et al. 2019).

On the other hand, the compatibility of the results obtained by the Class-5 profiles is also confirmed for these high-strain responses. The new geostatistical model presented in Section 6.2 provides a reasonable reproduction of the EUs and AVs of the base-case profile.

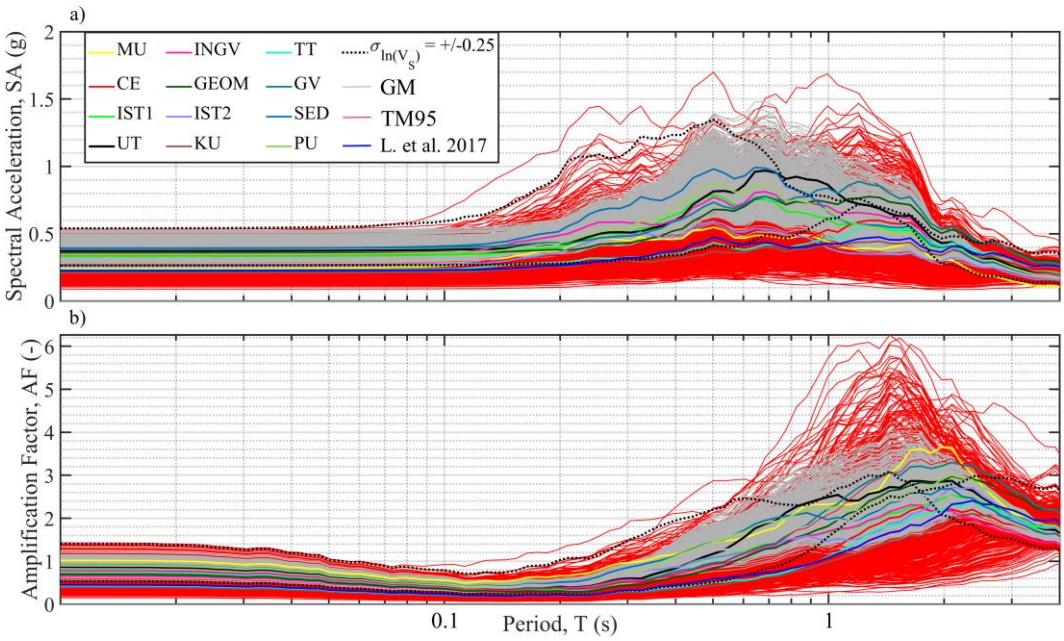

Figure 7.11. Results of the Equivalent Linear Analyses conducted for the five classes of profiles and the 0.5 g scaled input motions, a) Surface Response Spectra and b) Amplification Functions.

7.2.3 Discussion

This last section illustrates the results of the EQL analyses performed in Section 7.2.2 as mean (presented in natural scale, but calculated in logarithmic values) and logarithmic standard deviations of the surface RS and the AFs (i.e., both the assumed as lognormally distributed). We first discussed in Chapter 2 how these quantities are essential for performing hazard-consistent one-dimensional ground response analyses for ground motion predictions (Stewart et al. 2014a).

Figure 7.12 shows the results in terms of logarithmic mean RS at the surface. This Figure includes the results obtained with the base-case UT's profile, the two methods suggested by EPRI (2013), and the geostatistical model proposed in Section 6.2. The results from the upper/lower range profiles demonstrate the alteration of the dynamic response introduced with this method, particularly for the high-intensity IMs suite. Figure 7.12c reports an entirely aliased response spectrum, compared to the base-case (i.e., both for periods and amplitudes).

The results obtained from the profiles randomized with the TM95 show dangerous unconservative results, for both intensity inputs. This was apparent from Figure 7.10 and Figure 7.11, and it is here confirmed. The lower responses are due to the large number of soft profiles generated by TM95. These profiles lead to a high-strains concentration, especially for shallow depths that produces high-damping levels at convergence.

On the other hand, Figure 7.12a-c shows the mean response by the new geostatistical model is consistent with the mean response of the best-estimated profile. Figure 7.13 shows the same results as amplification functions, confirming the observations presented for the RS.

Figure 7.12b-d and 7.12b-d report the logarithmic standard deviations of the surface RS and AFs for the class-4 and class-5 profiles (i.e., 1000 profiles for each class), as also presented in Bazzurro & Cornell (2004a), Kwok et al. (2008), Stewart & Kwok (2008), Li & Asimaki (2010), Rathje et al. (2010), Papaspiliou et al. (2012a), Kaklamanos et al. (2013b), Rodriguez-Marek et al. (2014), Kaklamanos et al. (2015), Teague & Cox (2016). These Figures confirm the presence of parasite uncertainties introduced with the TM95. These uncertainties are not realistic, but only represent the product of a biased randomization model that is not empirically-based and adherent with the reality. As expected, both the $\sigma_{\ln(SA)}$ and $\sigma_{\ln(AF)}$ dramatically increase with the nonlinear response.

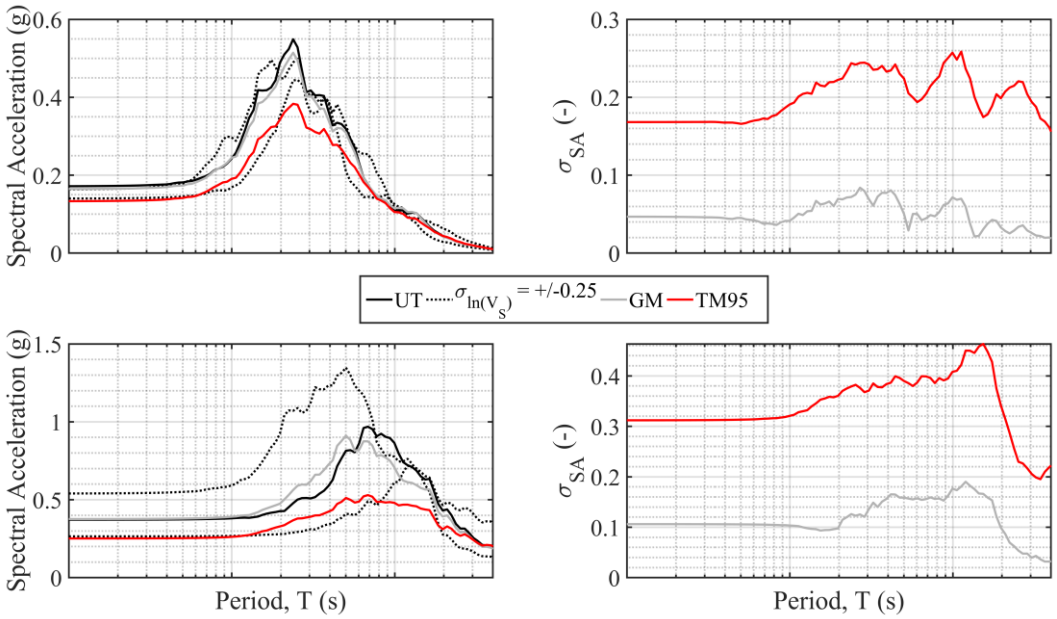

Figure 7.12. Mean response spectra and logarithmic standard deviations for a) and b) the low-intensity input motions suite and for c) and d) the high-intensity input motions suite.

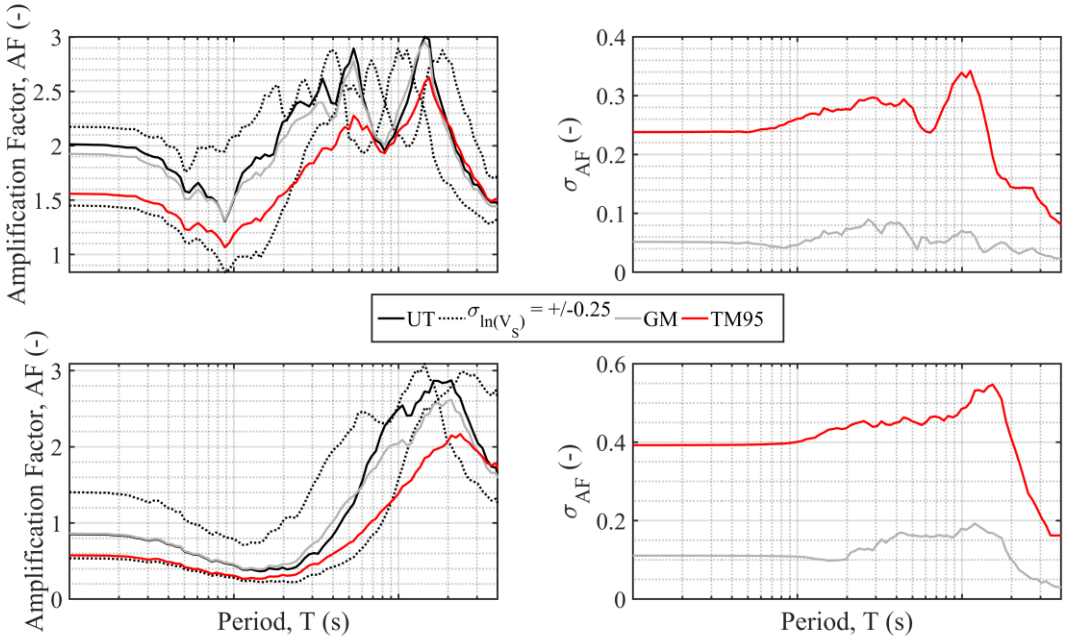

Figure 7.13. Mean amplification functions and logarithmic standard deviations for a) and b) the low-intensity input motions suite and for c) and d) the high-intensity input motions suite.

7.3 Down-Hole testing methods

This Section deals with the prototype version of the geostatistical model presented in Section 6.3 for Down-Hole tests. Two different companies performed DH tests at the site of Mirandola (i.e., Geovision and Solgeo). Each company performed the measurements with their own equipment. However, Geovision performed the measurements in two directions (East-West, EW, and North-South, NS). In addition, the University of Texas at Austin (UT) reinterpreted the experimental DH data acquired by Geovision and provided an alternative V_S estimate. This Section will then present four different solutions. Similarly to the analyses performed in Section 7.2, the NS profile obtained by the Geovision company was chosen as single deterministic base-case solution for the randomization. Note that the work by Garofalo et al. (2016b) included a third company who took part in the DH tests. This solution has been discarded in the present Section for the unrealistic biases shown in the results.

Figure 7.14 shows the V_S models from DH tests as interval (Figure 7.14a) and harmonic average (Figure 7.14b) profiles (see Section 4.1). The DH profiles are generally in an excellent intra-method agreement. All the DH tests identified the thin, low-velocity soil layer at about 75 m, differently from the profiles discussed in Section 7.2 for surface wave methods and reported here in green. Then, the solutions by Geovision and UT reached a V_S compatible with a bedrock formation (V_S over 600 m/s) at around 118 m. Figure 7.14 also proposes an inter-method comparison, especially in terms of harmonic average profiles. For example, Figure 7.14b shows higher velocities obtained by the DH tests for the shallower layers,

except for three solutions from the surface wave tests that generated a thick first layer. This was probably due to a low resolution at high frequencies for the surface wave tests. It is clear that the differences in the shallower layers influence also the $V_{S,Z}$ at larger depths. This is in agreement with evidences in the literature that identified the shallower layers like the ones that mostly control the ground response of the entire deposit.

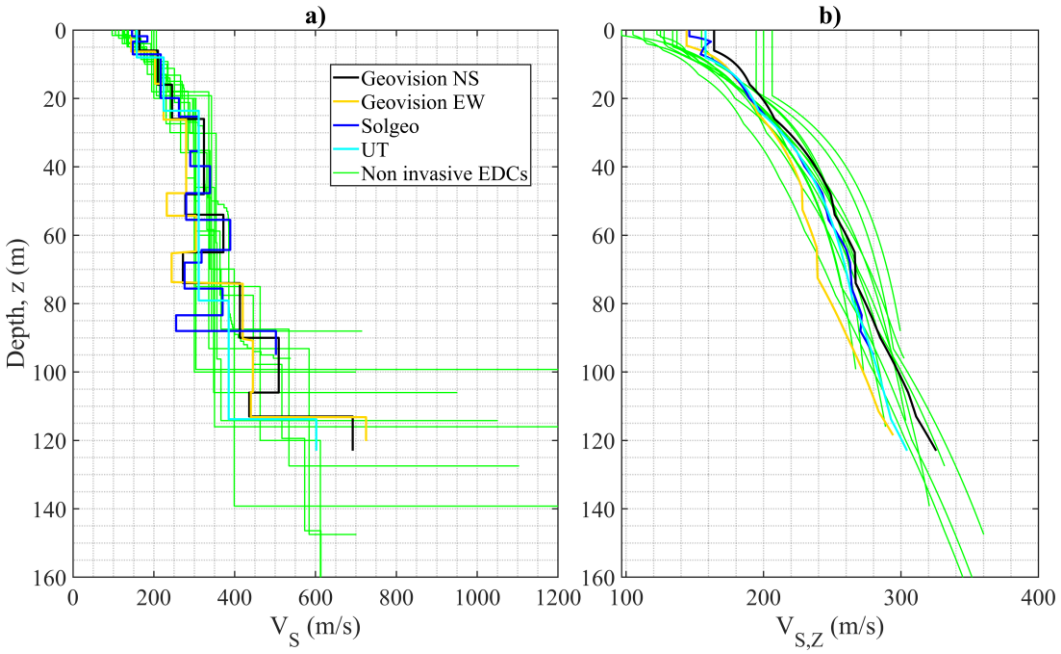

Figure 7.14. Selected DH profiles at Mirandola: a) interval velocity profiles, and b) harmonic average profiles. In green, the profiles obtained from surface wave methods are also shown (see Figure 7.5).

As discussed for the surface wave profiles, the reader should now imagine possessing only the single deterministic base-case solution (i.e., Geovision NS). The first standard procedure for the management of EUs prescribes to create profiles shifted by a defined value of V_S logarithmic standard deviation. Also in this Section, the minimum value of 0.25 prescribed by EPRI (2013) is applied to the base-case profile. Figure 7.15a shows the generated upper/lower range interval velocity profiles. Figure 7.15b illustrates the dramatic alteration of the harmonic average profiles obtained by these profiles, compared to the experimental results. This evidence is in total agreement with the results obtained for surface wave methods and demonstrates once more the inadequacy of this simplistic approach for the management of EUs.

Figure 7.15 also shows 1000 profiles obtained by the standard Toro model around the base-case profile for the management of AVs. Also for these analyses, the reduced logarithmic standard deviation of the base-case profile is assumed (see Figure 6.24). The Poisson's model parameters are taken equal to the ones suggested by Toro, as for the parameters of the inter-layer correlation model. The lognormal distribution of the halfspace depth is included in the randomization with a logarithmic standard deviation equal to 0.1. Also in this case, both the interval velocity and harmonic average profiles are entirely out of range. This is due to the

interval velocities randomization that introduces parasite uncertainties in the randomization.

The last set of 1000 profiles presented in Figure 7.15 (in gray) is obtained from the new geostatistical model around the DH base-case solution. Similarly to Section 6.3, the model is adopted in the prototype version with the same model's parameters used for Acquasanta Terme. This choice here assures a rigorous comparison with the 1000 profiles obtained with the TM95. The results of this second randomization follow the EUs and AVs experimentally estimated at Mirandola, especially as harmonic average profiles (Figure 7.15b). Results in Figure 7.15 can be seen as a first validation of the prototype model.

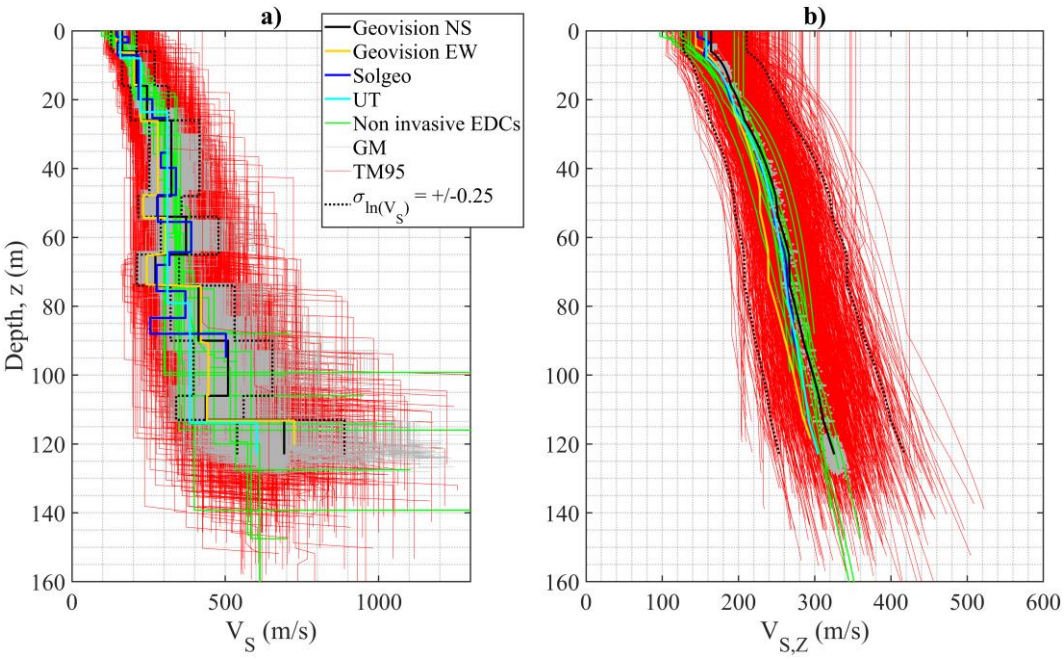

Figure 7.15. Down-Hole profiles at Mirandola including the upper/lower range profiles, the profiles generated by the Toro model, and the profiles generated by the prototype geostatistical model as a) interval velocity profiles, and b) harmonic average profiles. In green, also the solutions obtained from surface wave methods are proposed (see Figure 7.6).

A second validation of the geostatistical model applied to DH testing methods is given in Figure 7.16. This Figure shows the comparison of the TDCs calculated for the profiles in Figure 7.15. Figure 7.16 also presents the EDCs collected in the InterPACIFIC project and discussed in Section 7.2. The dispersion curves corresponding to the V_S profiles randomized following both the EPRI methodologies do not match the TDC of the base-case. On the contrary, the TDCs calculated from the profiles randomized with the new geostatistical model are in excellent agreement with the TDC of Geovision NS. Note that there is also a good comparison between the randomized TDCs and the EDCs obtained with surface wave tests. This is a further proof that the inter-method comparison was largely satisfactory for Mirandola. Also, the TDCs of the DH profiles shows a good intra-method agreement also from this different perspective.

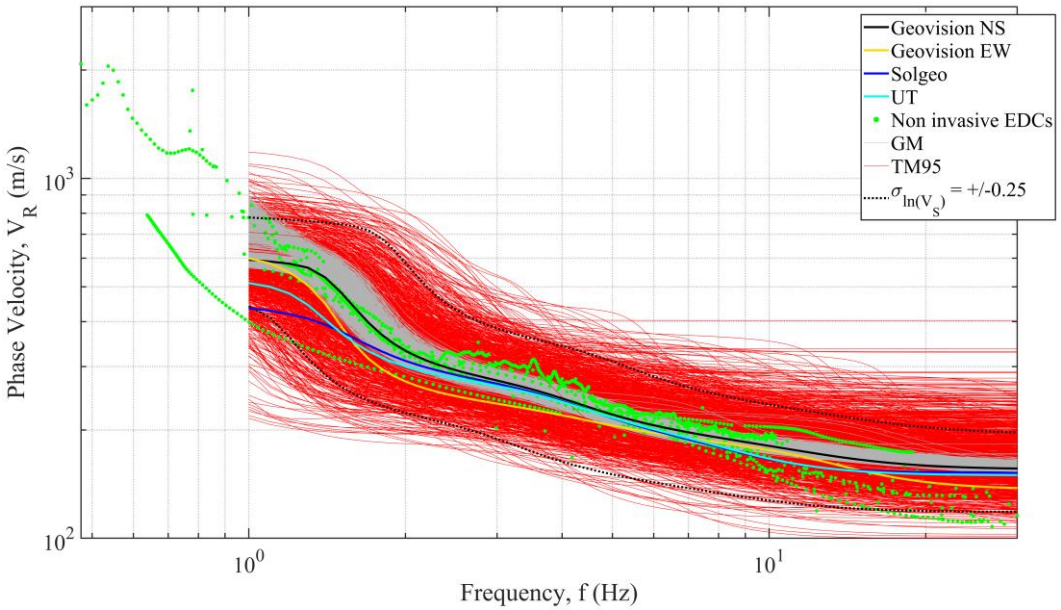

Figure 7.16. Theoretical Dispersion Curves associated with the DH profiles obtained by different teams at the site of Mirandola and calculated from the set of profiles from EPRI provisions and from the prototype geostatistical model.

The last validation of the prototype model for DH tests is given in Figure 7.17, where the TTFs are compared, similarly to Figure 7.8, also with the results of the HVSR test. First, the DH tests show a good agreement with this independent surface wave test in terms of first resonance peaks. The inter-method comparison is satisfactory also between the DH and the remaining solutions from surface wave methods in green. Note that these profiles have higher peaks that are due to the stronger impedance contrasts that are typical of the soil model used for the inversions.

Figure 7.17 also includes the results of the different methods for the management of uncertainties. Once more, the two methods suggested in the EPRI provisions seem to be highly inadequate for the purpose. On the contrary, the prototype model applied to the DH test presents results consistent with the base-case, the other DH tests and the solutions from the surface wave tests.

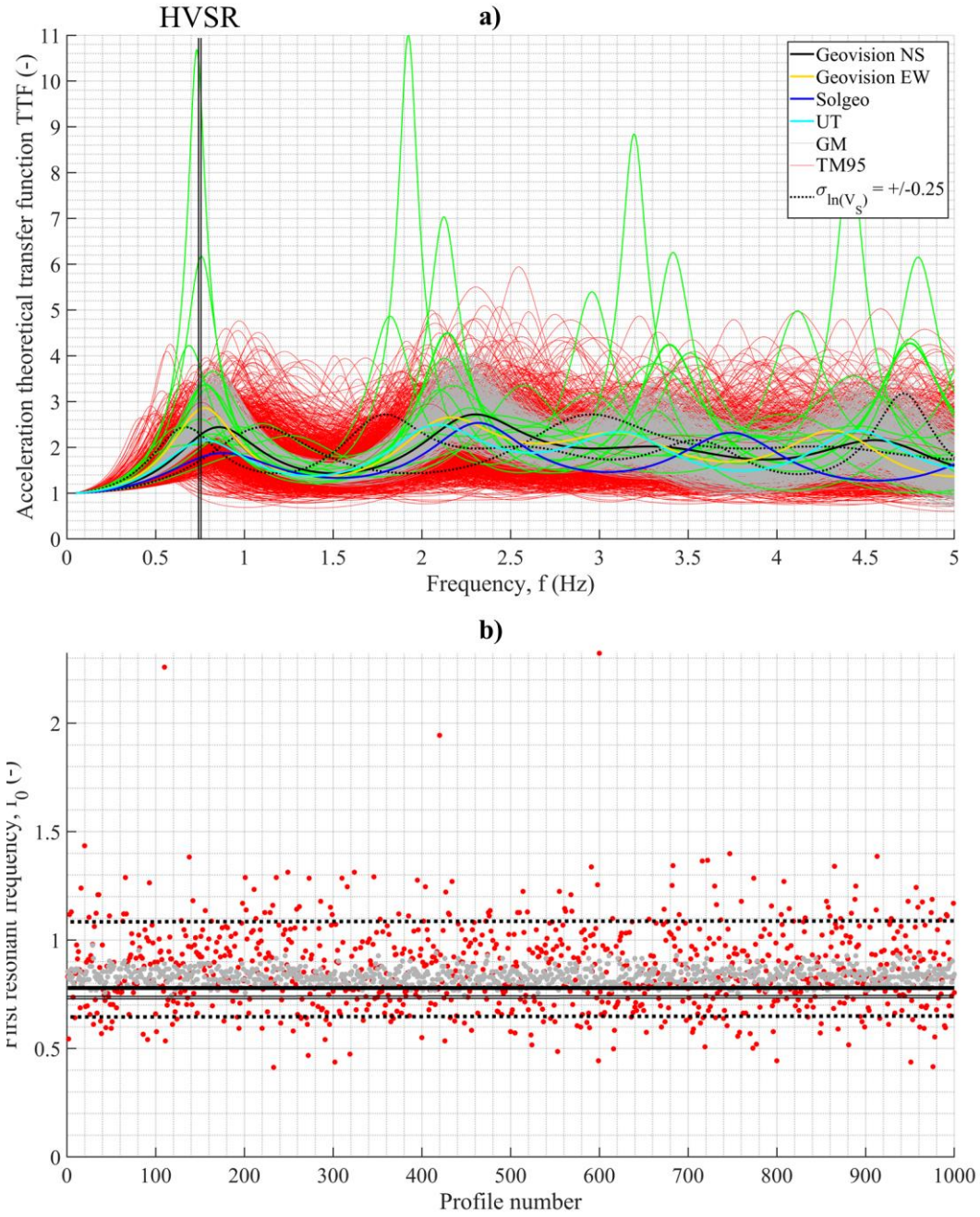

Figure 7.17. a) Comparison of the profiles as Theoretical Transfer Functions. The experimental resonant frequency obtained by the HVSR test is also indicated. b) Comparison obtained for the first resonant frequencies of the Theoretical Transfer Functions.

Chapter 8
Conclusions and Recommendations

This brief final Chapter includes three sections. The first summarizes the results and the main characteristics of the new proposed geostatistical model. Then, Section 8.2 discusses the observations regarding the three main "side products" presented in the dissertation; namely, a robust $V_{R,\lambda}$-$V_{S,Z}$ relationship, an estimated model for the standard deviation of the Rayleigh waves phase velocity, and the development of an efficient inversion method with a variable number of layers. Section 8.3 presents an overview of future refinements, evolutions and further validations of the randomization model along with the possible developments of the side products.

8.1 New geostatistical model

This research principally focused on the development of a new geostatistical model for the independent management of epistemic uncertainties (EUs) and aleatory variabilities (AVs) in shear wave velocity (V_S) profiles obtained with surface wave methods. The primary goal of this model is then to generate a sample of experimentally-equivalent V_S profiles starting from the single deterministic solution that is usually proposed after the inversion process.

The new randomization model fits into the broad process of Identification, Quantification, and Management of EUs and AVs. This methodology represents a crucial part of hazard-consistent probabilistic analyses. Particularly, the Identification and Quantification represent the crucial steps for the subsequent independent management of EUs and AVs by means of the geostatistical model. The separation of the two main contributes should be performed upstream from the management step. For example, the model's parameters suggested for surface wave testing methods simultaneously reproduce the EUs and AVs. This is due to the practical issues in separating the uncertainties in the experimental dispersion curve.

The IQM method is here aimed at Ground Response Analyses (GRAs). These simulation methods include mainly six different sources of uncertainties and variabilities. The analyst should always account for these sources of uncertainty, which are exhaustively discussed in the dissertation. Notably, recent studies demonstrated that the V_S profile and the tests used for its estimation play a crucial role in contributing to global uncertainties in site response. The dissertation presents a full and comprehensive discussion of the specific EUs and AVs associated with each type of geophysical test.

The geostatistical model has to overcome the drawbacks of the methods usually adopted for scientific and technical applications. Indeed, various authors demonstrated the inadequacy of the methods proposed in EPRI (2013) for the management of EUs and AVs in V_S profiles. These methods are recalled and

described in the dissertation, along with various applications presented in the literature. The development of a modern method for the independent management of EUs and AVs in V_S profiles was then required (Stewart et al. 2014). In particular, the dissertation builds on the Toro (1995) randomization model aiming at solving the limits of this geostatistical model. The essential characteristics of the proposed geostatistical model are summarised in the following with a side-by-side comparison with the model proposed by Toro (1995). Note that the following observations are primary valid in case of surface wave tests. However, the flexibility of the model allows expanding its capabilities to other geophysical tests (e.g., Down-Hole, tests).

Calibration using a high-quality database

The new geostatistical model relies on the PSWD (Polito Shear Wave velocity Database). This collection of experimental measurements ensures high-quality standards. Indeed, the PSWD was compiled after a rigorous selection of the surface wave tests performed by the Politecnico di Torino in the past 20 years. Then, a systematic reinterpretation of the recorded data was performed for each site with a rigorous two-step inversion procedure. After the second round of inversions, a homogeneous set of solutions (i.e., the "picture" of the geophysical equivalence) for each site was available. These solutions were then used to calibrate the empirically-based parameters of the geostatistical model for surface wave methods. Each statistical sample (i.e., site) was analyzed separating the elastic halfspace from the material above. A set of model parameters is obtained in the dissertation for the analysed profiles; these parameters can be used as generic guidance for cases when there is insufficient information and/or data about the site under analysis. However, a site-specific calibration of the model parameters is always encouraged. The PSWD represents the fundamental ingredient for the development of the additional "side-products" discussed in Section 8.2. On the same hand, the lack of enough data in the database so far prevended a precise calibration of the model for other geophysical tests.

Physics-based separation of the primary random variables

The new geostatistical model is based on a separation of the random variables quantifying space and time. This point is likely the most relevant innovation introduced compared with existing geostatistical models (e.g., the Toro 1995 model). The geostatistical model drops the use interval velocities (i.e., the wave propagation velocity of a soil layer) and assumes instead a separation between the fundamental physical quantities of space and time. The dissertation widely presented the inadequacies of using interval velocities in a randomization scheme. The interval velocity can be seen as an engineering schematization of the problem to be a-posteriori used for numerical analyses. Instead, the harmonic average velocity is a more efficient parameter. The use of the harmonic average velocities allows a better reproduction of the results of geophysical tests. Indeed, it avoids introducing parasite uncertainties (i.e., uncertainties that are not due to the testing process, but that result from the selected randomization scheme). The double-counting of uncertainties results from models that randomize separately interval velocities and the depth of interfaces, as proposed in Toro (1995).

Site- and test-specific characteristics

A basic postulate of this dissertation is that the analyst should perform a rigorous identification and quantification of EUs and AVs specifically for the site under analysis. This recognition is essential for a randomization of V_S profiles compatible with the specific "boundary conditions" of the case study. The geostatistical model is only the last step of a complex methodology. For this reason, an adequate identification and quantification of the uncertainties is crucial for the following independent randomization process of EUs and AVs. The analyst should account for the adopted geophysical test and the spatial scale of the problem, using site-specific model parameters. At the same time, the geostatistical model for surface wave testing methods has specific and physically-based characteristics for this class of non-invasive tests. This allows reproducing realistic characteristics for both EUs and AVs. Both the site- and test-specific characteristics of the randomization model are an advancement with respect to the method proposed by Toro (1995). In that case, the randomization model proposed generic parameters clustered by soil classification schemes. Also, the architecture of the method did not address the specific peculiarities of the specific geophysical test. The extension of the geostatistical model to other geophysical tests then requires a special attention to the specific characteristics of the method. In particular, the model's parameters suggested for each seismic test should account for the possible separation of the two main contributes. This is in line with the observations made in the dissertation. For example, a precise distinction is unfeasible for surface wave testing methods, then the proposed model's parameters simultaneously reproduce EUs and AVs. On the contrary, a deeper analysis for DH tests can lead to a separate management of the uncertainties. In this case, the larger contribution comes from EUs that can be precisely evaluated in the regression of the model's parameters.

A validation of the proposed geostatistical model for surface wave testing methods is reported for two case studies. The first regards the application for a site included in the PSWD (Accumoli). In this case, the results are in agreement with the solutions obtained by the inversion process accounting for the geophysical equivalence. The comparison is performed for the Theoretical Transfer Functions (TTFs) that controls the dynamic small-strains behavior of the profile. A further validation is proposed for a site not included in the database: Mirandola (Italy). This site was primarily investigated during the InterPACIFIC project and represents an important benchmark for the new geostatistical model. The results obtained after the randomization of one base-case are excellent regarding both TTFs and EQuivalent Linear (EQL) analyses.

The dissertation also proposes the development and preliminary validation of the geostatistical randomization model applied to DH tests. As already discussed, a precise calibration is prevented by the lack of enough experimental data for this type of test. However, a first application of the model to two sites gave encouraging results. In particular, the model was used with a generic set of parameters for the sites of Acquasanta Terme and Mirandola. In both cases, the model shows consistent results both in terms of reliability and consistency with the experimental evidences.

The dissertation highlighted the inadequacies of the approaches usually adopted in stardard practice and prescribed by EPRI (2013). Both methods for the management of EUs and AVs led to unrealistic results that do not represent the real physics of the problem. These limitations can be solved by means of the new geostatistical model proposed.

8.2 Side products

The three main side products presented in the dissertation are the robust $V_{R,\lambda}$-$V_{S,Z}$ relationship, the regression of the predictive law for the estimation of the standard deviation of Rayleigh waves phase velocity, and the development of an efficient inversion method with a variable number of layers.

First, the relationship found between the wavelength λ and depth z is based on a simple linear law. This relationship could provide a robust estimation of the $V_{S,30}$ and the soil class just by looking at the Experimental Dispersion Curve (EDC). The $V_{R,\lambda}$-$V_{S,Z}$ relationship should replace the use of the pseudo-depth adopted for the analysis of surface wave methods, as it is experimentally verified and links two physically consistent variables. The dissertation proposes a $V_{R,\lambda}$-$V_{S,Z}$ relationship obtained with the refined sample of solutions after the second round of inversions. This relationship is also adopted for the layering generation of the geostatistical model.

The processing of the PSWD allowed regressing an equation that estimates the experimental Coefficient of Variation (COV_{V_R}) of the Rayleigh wave velocity, which allows the computation of the corresponding standard deviations. The solution shows a larger uncertainty for low frequencies and a slight increase of COV_{V_R} for high frequencies. This shape of the curve agrees with the main characteristics of surface wave testing methods. Indeed, the loss of resolution for surface wave methods is associated both with very low or very high frequencies. In the first case, it is due to the lack of penetration at large depths, whereas the spatial aliasing produces uncertainties at high frequencies. The set of best fitting values for the selected double-exponential law are provided in the dissertation. An additional set of parameters is provided to obtain a conservative estimate that is applicable for cases where there is low confidence in the experimental data. However as mentioned before, obtaining site specific data is preferable.

The second round of the inversions performed for the sites in the PSWD allowed the development of a procedure that added a degree of freedom to the search of the solutions. This model, referred to as the *free-layering* model, also considers the number of layers as random variables. Ideally, the free-layering model represents a forward analysis randomization model, whereas the geostatistical model discussed in Section 8.1 is the associated back-analysis randomization model. The free-layering model was used in conjunction with the solutions of the first round inversions. The free-layering model respected the global characteristics of the first set of equivalent profiles, but generating layering distributions with a different number of layers. Results show a general decrease of the misfit of the

solutions, demonstrating the larger space of investigated solutions by the Monte Carlo algorithm.

8.3 Recommendations for Future Research

The geostatistical model presented in the dissertation for surface wave methods should be validated by different users for real applications. Some details of the calibration need further research aiming at finding more adequate functional forms (e.g., inter-layer correlation). The presented validations give encouraging results. However, the innovations of the present research gain value only if independent users can easily adopt the geostatistical model for different case studies. For these reasons, the geostatistical model should be shared with academics and professionals and likely implemented in a GRA software for an automatic procedure.

In addition, the geostatistical model should be extended to different geophysical tests rather than only surface wave testing methods. An example for DH tests is already presented in the dissertation and needs ulterior research to be refined and calibrated by means of a dedicated part of the PSWD.

The $V_{R,\lambda}$-$V_{S,Z}$ relationship could give a chance for a direct inversion of the experimental data. However, this application should be studied in depth with further analyses. Further research should also investigate the influence of the Poisson's ratio on the obtained relationship. The suggested relationship for the EUs and AVs included in the EDC regards only the fundamental mode of the EDC. Further analyses are needed for an estimation of the standard deviations associated with higher modes in the EDCs. The free-layering inversion method gave interesting results in this dissertation. However, independent users should validate the capabilities of this proposed approach.

Last but not least; the PSWD could be expanded including more information about the investigated sites. Also, other geotechnical tests can be accounted other than in situ geophysical tests (e.g., CPTs, SPTs, dynamic and static laboratory tests). This can reduce the uncertainties in the interface depths. The implementation of an open-access (e.g., web Java-based) and digitalized database of high-quality data can be used and shared for scientific and professional purposes.

References

Aaqib, M., Hashash, A., and Pehlivan, M. 2018. Importance of Implied Strength Correction for 1D Site Response at Shallow Sites at a Moderate to Low Seismicity Region.

Abrahamson, N. A., and Bommer, J. J. 2005. Probability and uncertainty in seismic hazard analysis. *Earthquake spectra,* 21**:** 603-607.

Afshari, K., and Stewart, J. 2015a. Uncertainty of site amplification derived from ground response analysis.

Afshari, K., and Stewart, J. P. 2015b. Effectiveness of 1D ground response analyses at predicting site response at California vertical array sites.

Ahdi, S. K., Sadiq, S., Ilhan, O., Bozorgnia, Y., Hashash, A., Kwak, D. Y., Park, C. B., and Yong, A. 2018. Development of a United States Community Shear Wave Velocity Profile Database. *Geotechnical Earthquake Engineering and Soil Dynamics V GSP 291 330*.

Ahdi, S. K., Stewart, J. P., Ancheta, T. D., Kwak, D. Y., and Mitra, D. 2017. Development of VS Profile Database and Proxy-Based Models for VS30 Prediction in the Pacific Northwest Region of North America. *Bulletin of the Seismological Society of America,* 107**:** 1781-1801.

Aimar, M. 2018. *Stochastic analysis of seismic ground response for verification of standard simplified approaches.* Master of Science, Politecnico di Torino.

Aki, K., and Larner, K. L. 1970. Surface motion of a layered medium having an irregular interface due to incident plane SH waves. *Journal of geophysical research,* 75**:** 933-954.

Aki, K., and Richards, P. 1980. Quantitative seismology: Theory and methods. *San Francisco*.

Al Atik, L., Abrahamson, N., Bommer, J. J., Scherbaum, F., Cotton, F., and Kuehn, N. 2010. The variability of ground-motion prediction models and its components. *Seismological Research Letters,* 81**:** 794-801.

Albarello, D., and Gargani, G. 2010. Providing NEHRP soil classification from the direct interpretation of effective Rayleigh-wave dispersion curves. *Bulletin of the Seismological Society of America,* 100**:** 3284-3294.

Algermissen, S. T., Perkins, D., Thenhaus, P., Hanson, S., and Bender, B. 1982. Probabilistic estimates of maximum acceleration and velocity in rock in the contiguous United States. *US Geological Survey Open-File Report,* 82**:** 99.

Algermissen, S. T., and Perkins, D. M. 1976. A probabilistic estimate of maximum acceleration in rock in the contiguous United States. US Geological Survey.

Amir-Faryar, B., Aggour, M. S., and Mccuen, R. H. 2017. Universal model forms for predicting the shear modulus and material damping of soils. *Geomechanics and Geoengineering,* 12**:** 60-71.

Amorosi, A., Boldini, D., and Di Lernia, A. 2016. Seismic ground response at Lotung: Hysteretic elasto-plastic-based 3D analyses. *Soil Dynamics and Earthquake Engineering,* 85**:** 44-61.

Anderson, J. G., and Brune, J. N. 1999. Probabilistic seismic hazard analysis without the ergodic assumption. *Seismological Research Letters,* 70**:** 19-28.

Andrade, J. E., and Borja, R. I. 2006. Quantifying sensitivity of local site response models to statistical variations in soil properties. *Acta Geotechnica,* 1**:** 3-14.

Andrus, R., Zhang, J., Ellis, B., and Juang, C. 2003. Guide for estimating the dynamic properties of South Carolina soils for ground response analysis.

Andrus, R. D., Mohanan, N. P., Piratheepan, P., Ellis, B. S., and Holzer, T. L. Predicting shear-wave velocity from cone penetration resistance. Proceedings of the 4th International Conference on Earthquake Geotechnical Engineering, Thessaloniki, Greece, 2007.

Andrus, R. D., and Stokoe, K. H. 2000. Liquefaction resistance of soils from shear-wave velocity. *Journal of geotechnical and geoenvironmental engineering,* 126**:** 1015-1025.

Ang, A. H.-S., and Tang, W. H. 1984. *Probability concepts in engineering planning and design*.

Arai, H., and Tokimatsu, K. 2004. S-wave velocity profiling by inversion of microtremor H/V spectrum. *Bulletin of the Seismological Society of America,* 94**:** 53-63.

Arai, H., and Tokimatsu, K. 2005. S-wave velocity profiling by joint inversion of microtremor dispersion curve and horizontal-to-vertical (H/V) spectrum. *Bulletin of the Seismological Society of America,* 95**:** 1766-1778.

Aristizabal, C., Bard, P.-Y., Gómez, J., and Beauval, C. Integration of site effects into PSHA: a comparison between two fully probabilistic methods for the Euroseistest case. 16th European Conference on Earthquake Engineering, 2018.

Asimaki, D., and Li, W. 2012. Site-and ground motion-dependent nonlinear effects in seismological model predictions. *Soil Dynamics and Earthquake Engineering,* 32**:** 143-151.

Asimaki, D., Li, W., Steidl, J., and Schmedes, J. 2008. Quantifying nonlinearity susceptibility via site-response modeling uncertainty at three sites in the Los Angeles Basin. *Bulletin of the Seismological Society of America,* 98**:** 2364-2390.

Asimaki, D., and Steidl, J. 2007. Inverse analysis of weak and strong motion downhole array data from the Mw7. 0 Sanriku-Minami earthquake. *Soil Dynamics and Earthquake Engineering,* 27**:** 73-92.

Astm Standard Test Methods for Crosshole Seismic Testing-D4428/D4428M-14.

Astm Standard Test Methods for Downhole Seismic Testing-ASTM D7400-14.

Astm, D. 2011. 6432, Standard Guide for Using the Surface Ground Penetrating Radar Method for Subsurface Investigation. *Annual Book of ASTM Standards*.

Atkinson, G. M. 2006. Single-station sigma. *Bulletin of the Seismological Society of America,* 96**:** 446-455.

Bahrampouri, M., Rodriguez-Marek, A., and Bommer, J. J. 2018. Mapping the uncertainty in modulus reduction and damping curves onto the uncertainty of site amplification functions. *Soil Dynamics and Earthquake Engineering*.

Baise, L., Thompson, E., Kaklamanos, J., and Dorfmann, L. Complex site response: Does one-dimensional site response work. 4th IASPEI (International Association of Seismology and Physics of the Earth's Interior)/IAEE (International Association of Earthquake Engineering) International Symposium on the Effects of Surface Geology on Seismic Motion (ESG4), Santa Barbara, California, 2011. 23-26.

Baker, J. W., and Allin Cornell, C. 2006. Spectral shape, epsilon and record selection. *Earthquake Engineering & Structural Dynamics,* 35**:** 1077-1095.

Baker, J. W., and Cornell, C. A. 2008. Uncertainty propagation in probabilistic seismic loss estimation. *Structural Safety,* 30**:** 236-252.

Ballard, R. 1964. Determination of soil shear moduli at depths by in-situ vibratory techniques. ARMY ENGINEER WATERWAYS EXPERIMENT STATION VICKSBURG MISS.

Bard, P.-Y., and Bouchon, M. 1980a. The seismic response of sediment-filled valleys. Part 1. The case of incident SH waves. *Bulletin of the seismological society of America,* 70**:** 1263-1286.

Bard, P.-Y., and Bouchon, M. 1980b. The seismic response of sediment-filled valleys. Part 2. The case of incident P and SV waves. *Bulletin of the Seismological Society of America,* 70**:** 1921-1941.

Bard, P.-Y., Cadet, H., Endrun, B., Hobiger, M., Renalier, F., Theodulidis, N., Ohrnberger, M., Fäh, D., Sabetta, F., and Teves-Costa, P. 2010. From non-invasive site characterization to site amplification: recent advances in the use of ambient vibration measurements. *Earthquake Engineering in Europe.* Springer.

Baturay, M. B., and Stewart, J. P. 2003. Uncertainty and bias in ground-motion estimates from ground response analyses. *Bulletin of the Seismological Society of America,* 93**:** 2025-2042.

Baziw, E. J. 2002. Derivation of seismic cone interval velocities utilizing forward modeling and the downhill simplex method. *Canadian geotechnical journal,* 39**:** 1181-1192.

Bazzurro, P., and Cornell, C. A. 2004a. Ground-motion amplification in nonlinear soil sites with uncertain properties. *Bulletin of the Seismological Society of America,* 94**:** 2090-2109.

Bazzurro, P., and Cornell, C. A. 2004b. Nonlinear soil-site effects in probabilistic seismic-hazard analysis. *Bulletin of the Seismological Society of America,* 94**:** 2110-2123.

Benjamin, J. R., and Cornell, C. A. 2014. *Probability, statistics, and decision for civil engineers*, Courier Corporation.

Bergamo, P., Boiero, D., and Socco, L. V. 2012. Retrieving 2D structures from surface-wave data by means of space-varying spatial windowingSpatial windowing of surface-wave data. *Geophysics,* 77**:** EN39-EN51.

Bergamo, P., Comina, C., Foti, S., and Maraschini, M. 2011. Seismic characterization of shallow bedrock sites with multimodal Monte Carlo inversion of surface wave data. *Soil Dynamics and Earthquake Engineering,* 31**:** 530-534.

Bettig, B., Bard, P., Scherbaum, F., Riepl, J., Cotton, F., Cornou, C., and Hatzfeld, D. 2001. Analysis of dense array noise measurements using the modified spatial auto-correlation method (SPAC): application to the Grenoble area. *Bollettino di Geofisica Teorica ed Applicata,* 42**:** 281-304.

Biot, M. A. 1956a. Theory of propagation of elastic waves in a fluid-saturated porous solid. I. Low-frequency range. *The Journal of the acoustical Society of america,* 28**:** 168-178.

Biot, M. A. 1956b. Theory of propagation of elastic waves in a fluid-saturated porous solid. II. Higher frequency range. *the Journal of the Acoustical Society of America,* 28**:** 179-191.

Boaga, J., Vignoli, G., and Cassiani, G. 2011. Shear wave profiles from surface wave inversion: the impact of uncertainty on seismic site response analysis. *Journal of Geophysics and Engineering,* 8**:** 162.

Bommer, J., Scott, S., and Sarma, S. 2000. Hazard-consistent earthquake scenarios. *Soil Dynamics and Earthquake Engineering,* 19**:** 219-231.

Bommer, J. J. 2003. Uncertainty about the uncertainty in seismic hazard analysis. *Engineering Geology,* 70**:** 165-168.

Bommer, J. J., and Abrahamson, N. A. 2006. Why do modern probabilistic seismic-hazard analyses often lead to increased hazard estimates? *Bulletin of the Seismological Society of America,* 96**:** 1967-1977.

Bommer, J. J., Coppersmith, K. J., Coppersmith, R. T., Hanson, K. L., Mangongolo, A., Neveling, J., Rathje, E. M., Rodriguez-Marek, A., Scherbaum, F., and Shelembe, R. 2015. A SSHAC level 3 probabilistic seismic hazard analysis for a new-build nuclear site in South Africa. *Earthquake Spectra,* 31**:** 661-698.

Bonilla, L. F., Steidl, J. H., Gariel, J.-C., and Archuleta, R. J. 2002. Borehole response studies at the Garner Valley downhole array, southern California. *Bulletin of the Seismological Society of America,* 92**:** 3165-3179.

Bonnefoy-Claudet, S., Cotton, F., and Bard, P.-Y. 2006. The nature of noise wavefield and its applications for site effects studies: A literature review. *Earth-Science Reviews,* 79**:** 205-227.

Boore, D. M. 2003a. Simulation of ground motion using the stochastic method. *Seismic Motion, Lithospheric Structures, Earthquake and Volcanic Sources: The Keiiti Aki Volume.* Springer.

Boore, D. M. 2003b. Simulation of ground motion using the stochastic method. *Pure and applied geophysics,* 160**:** 635-676.

Boore, D. M. 2004. Can site response be predicted. *Journal of earthquake Engineering,* 8**:** 1-41.

Boore, D. M., and Atkinson, G. M. 2008. Ground-motion prediction equations for the average horizontal component of PGA, PGV, and 5%-damped PSA at spectral periods between 0.01 s and 10.0 s. *Earthquake Spectra,* 24**:** 99-138.

Boore, D. M., and Brown, L. T. 1998. Comparing shear-wave velocity profiles from inversion of surface-wave phase velocities with downhole measurements: systematic differences between the CXW method and downhole measurements at six USC strong-motion sites. *Seismological Research Letters,* 69**:** 222-229.

Borcherdt, R. On the observation, characterisation, and predictive GIS mapping of strong ground shaking for seismic zona tion. Proceedings, Pacific Conference on Earthquake Engineering, Auckland, New Zealand November, 1991. 20-24.

Borcherdt, R. D. 1994. Estimates of site-dependent response spectra for design (methodology and justification). *Earthquake spectra,* 10**:** 617-653.

Borcherdt, R. D. VS30–A site-characterization parameter for use in building Codes, simplified earthquake resistant design, GMPEs, and ShakeMaps. The 15th World Conference on Earthquake Engineering, 2012.

Brandenberg, S. J., Bellana, N., and Shantz, T. 2010. Shear wave velocity as function of standard penetration test resistance and vertical effective stress at California bridge sites. *Soil Dynamics and Earthquake Engineering,* 30**:** 1026-1035.

Brown, L., Diehl, J. G., and Nigbor, R. L. A simplified procedure to measure average shear-wave velocity to a depth of 30 meters (VS30). Proceedings of 12th world conference on earthquake engineering, 2000. 1-8.

Brown, L. T., Boore, D. M., and Stokoe, K. H. 2002. Comparison of shear-wave slowness profiles at 10 strong-motion sites from noninvasive SASW measurements and measurements made in boreholes. *Bulletin of the Seismological Society of America,* 92**:** 3116-3133.

Budnitz, R. J., Apostolakis, G., and Boore, D. M. 1997. Recommendations for probabilistic seismic hazard analysis: guidance on uncertainty and use of experts. Nuclear Regulatory Commission, Washington, DC (United States). Div. of Engineering Technology; Lawrence Livermore National Lab., CA (United States); Electric Power Research Inst., Palo Alto, CA (United States); USDOE, Washington, DC (United States).

Cabas, A., and Rodriguez-Marek, A. 2018. Toward Improving Damping Characterization for Site Response Analysis.

Callerio, A., Janicki, K., Milani, D., Priano, S., and Signori, M. Cross-hole tests at Zelazny most tailings pond, Poland-highlights and statistical interpretation of results. Near Surface Geoscience 2013-19th Eage European Meeting of Environmental and Engineering Geophysics, 2013.

Campanella, R. 1994. Field methods for dynamic geotechnical testing: An overview of capabilities and needs. *Dynamic Geotechnical Testing II.* ASTM International.

Capon, J. 1969. High-resolution frequency-wavenumber spectrum analysis. *Proceedings of the IEEE,* 57**:** 1408-1418.

Casella, G., and Berger, R. L. 2002. *Statistical inference*, Duxbury Pacific Grove, CA.

Castellaro, S., and Mulargia, F. 2009. The effect of velocity inversions on H/V. *Pure and Applied Geophysics,* 166**:** 567-592.

Chen, Y.-H., and Tsai, C.-C. P. 2002. A new method for estimation of the attenuation relationship with variance components. *Bulletin of the Seismological Society of America,* 92**:** 1984-1991.

Chiou, B., Darragh, R., Gregor, N., and Silva, W. 2008. NGA project strong-motion database. *Earthquake Spectra,* 24**:** 23-44.

Ciancimino, A., Foti, S., and Lanzo, G. 2018. Stochastic analysis of seismic ground response for site classification methods verification. *Soil Dynamics and Earthquake Engineering,* 111**:** 169-183.

Comina, C., and Foti, S. 2015. Discussion on "Implications of surface wave data measurement uncertainty on seismic ground response analysis" by Jakka et al. *Soil Dynamics and Earthquake Engineering,* 74**:** 89-91.

Comina, C., Foti, S., Boiero, D., and Socco, L. 2011. Reliability of VS, 30 evaluation from surface-wave tests. *Journal of geotechnical and geoenvironmental engineering,* 137**:** 579-586.

Comina, C., Foti, S., Sambuelli, L., Socco, L. V., and Strobbia, C. Joint inversion of VES and surface wave data. Symposium on the Application of Geophysics to Engineering and Environmental Problems 2002, 2002. Society of Exploration Geophysicists, HRR6-HRR6.

Comina, C., Foti, S., Socco, L., and Strobbia, C. Geophisycal characterization for seepage potential assessment along the embankments of the Po river. ISC'2, 2004. -, 451-458.

Cornell, C. A. 1968. Engineering seismic risk analysis. *Bulletin of the Seismological Society of America,* 58**:** 1583-1606.

Cox, B., Stolte, A., Stokoe Ii, K. H., and Wotherspoon, L. 2018. A Direct Push Crosshole (DPCH) Test Method for the In-Situ Evaluation of High-Resolution P- and S-wave Velocities. *Geotechnical Test Journal*.

Cox, B., Wood, C., and Teague, D. Synthesis of the UTexas1 surface wave dataset blind-analysis study: Inter-analyst dispersion and shear wave velocity uncertainty. Geo-Congress 2014: Geo-characterization and Modeling for Sustainability, 2014. 850-859.

Cox, B. R. 2006. *Development of a direct test method for dynamically assessing the liquefaction resistance of soils in situ.*

Cox, B. R., and Beekman, A. N. 2010. Intramethod Variability in ReMi Dispersion Measurements and V s Estimates at Shallow Bedrock Sites. *Journal of Geotechnical and Geoenvironmental Engineering,* 137**:** 354-362.

Cox, B. R., and Teague, D. P. 2016. Layering ratios: a systematic approach to the inversion of surface wave data in the absence of a priori information. *Geophysical Journal International,* 207**:** 422-438.

Cramer, C. H. 2003. Site-specific seismic-hazard analysis that is completely probabilistic. *Bulletin of the Seismological Society of America,* 93**:** 1841-1846.

Cramer, C. H. 2006. Quantifying the uncertainty in site amplification modeling and its effects on site-specific seismic-hazard estimation in the upper Mississippi embayment and adjacent areas. *Bulletin of the Seismological Society of America,* 96**:** 2008-2020.

Cramer, C. H., Gomberg, J. S., Schweig, E. S., Waldron, B. A., and Tucker, K. 2004. The Memphis, Shelby County, Tennessee, Seismic Hazard Maps. *US Geological Survey Open-File Report,* 1294.

Darendeli, M. B. 2001. Development of a new family of normalized modulus reduction and material damping curves.

De Almeida, A. a. D., Assumpção, M., Bommer, J. J., Drouet, S., Riccomini, C., and Prates, C. L. 2018. Probabilistic seismic hazard analysis for a nuclear power plant site in southeast Brazil. *Journal of Seismology***:** 1-23.

Der Kiureghian, A., and Ditlevsen, O. 2009. Aleatory or epistemic? Does it matter? *Structural Safety,* 31**:** 105-112.

Dobry, R., Borcherdt, R., Crouse, C., Idriss, I., Joyner, W., Martin, G. R., Power, M., Rinne, E., and Seed, R. 2000. New site coefficients and site classification system used in recent building seismic code provisions. *Earthquake spectra,* 16**:** 41-67.

Dobry, R., and Vucetic, M. 1987. Dynamic properties and seismic response of soft clay deposits.

Dumouchel, W., and O'brien, F. Integrating a robust option into a multiple regression computing environment. Computing and graphics in statistics, 1992. Springer-Verlag New York, Inc., 41-48.

Dunkin, J. W. 1965. Computation of modal solutions in layered, elastic media at high frequencies. *Bulletin of the Seismological Society of America,* 55**:** 335-358.

Ec8 2005. Eurocode 8: Design of structures for earthquake resistance-part 1: general rules, seismic actions and rules for buildings. *Brussels: European Committee for Standardization*.

Engl, H. W., Hanke, M., and Neubauer, A. 1996. *Regularization of inverse problems*, Springer Science & Business Media.

Epri 1993. Guidelines for Determining Design Basis Ground Motions. 1: Method and Guidelines for Estimating Earthquake Ground Motion in Eastern North America.

Epri 2013. Seismic Evaluation Guidance: Screening, Prioritization and Implementation Details (SPID) for the Resolution of Fukushima Near-Term Task Force Recommendation 2.1: Seismic *EPRI, Report 1025287, Palo Alto, CA, 2012*.

Faccioli, E. 1979. Engineering seismic risk analysis of the Friuli Region.

Faccioli, E., Paolucci, R., and Vanini, M. 2015. Evaluation of probabilistic site-specific seismic-hazard methods and associated uncertainties, with applications in the Po Plain, northern Italy. *Bulletin of the Seismological Society of America,* 105**:** 2787-2807.

Faccioli, E., Vanini, M., and Frassine, L. Complex site effects in earthquake ground motion, including topography. 12th European Conference on Earthquake Engineering, 2002a.

Faccioli, E., Vanini, M., and Frassine, L. Complex" site effects in earthquake ground motion, including topography. 12th European Conference on Earthquake Engineering, 2002b.

Fäh, D., Kind, F., and Giardini, D. 2001. A theoretical investigation of average H/V ratios. *Geophysical Journal International,* 145**:** 535-549.

Fäh, D., Kind, F., and Giardini, D. 2003. Inversion of local S-wave velocity structures from average H/V ratios, and their use for the estimation of site-effects. *Journal of Seismology,* 7**:** 449-467.

Falcone, G., Boldini, D., and Amorosi, A. 2018. Site response analysis of an urban area: A multi-dimensional and non-linear approach. *Soil Dynamics and Earthquake Engineering,* 109**:** 33-45.

Field, E. H., and Jacob, K. H. 1993. Monte-Carlo simulation of the theoretical site response variability at Turkey Flat, California, given the uncertainty in the geotechnically derived input parameters. *Earthquake Spectra,* 9**:** 669-701.

Foti, S. 2000. *Multistation methods for geotechnical characterization using surface waves.* Politecnico di Torino.

Foti, S. 2002. Numerical and experimental comparison between two-station and multistation methods for spectral analysis of surface waves. *Rivista Italiana di Geotecnica,* 36**:** 11-22.

Foti, S. 2003. Small-strain stiffness and damping ratio of Pisa clay from surface wave tests. *Geotechnique,* 53**:** 455-461.

Foti, S., Comina, C., Boiero, D., and Socco, L. 2009. Non-uniqueness in surface-wave inversion and consequences on seismic site response analyses. *Soil Dynamics and Earthquake Engineering,* 29**:** 982-993.

Foti, S., Hollender, F., Garofalo, F., Albarello, D., Asten, M., Bard, P.-Y., Comina, C., Cornou, C., Cox, B., and Di Giulio, G. 2018. Guidelines for the good practice of surface wave analysis: a product of the InterPACIFIC project. *Bulletin of Earthquake Engineering,* 16**:** 2367-2420.

Foti, S., Lai, C. G., and Lancellotta, R. 2002. Porosity of fluid-saturated porous media from measured seismic wave velocities. *Géotechnique,* 52**:** 359-373.

Foti, S., Lai, C. G., Rix, G. J., and Strobbia, C. 2014. *Surface wave methods for near-surface site characterization*, CRC Press.

Foti, S., Parolai, S., Albarello, D., and Picozzi, M. 2011a. Application of surface-wave methods for seismic site characterization. *Surveys in geophysics,* 32**:** 777-825.

Foti, S., Parolai, S., Bergamo, P., Di Giulio, G., Maraschini, M., Milana, G., Picozzi, M., and Puglia, R. 2011b. Surface wave surveys for seismic site characterization of accelerometric stations in ITACA. *Bulletin of Earthquake Engineering,* 9**:** 1797-1820.

Foti, S., and Passeri, F. 2016. Reliability of soil porosity estimation from seismic wave velocities. *ISC5-International Conference on Geotechnical and Geophysical Soil Characterisation, Gold Coast, Australia,* 1**:** 425-430.

Foti, S., and Passeri, F. 2018. Reliability and Accuracy of Seismic Tests in Geotechnical Site Characterization. *Geotechnics for Natural and Engineered Sustainable Technologies.* Springer.

Foti, S., Sambuelli, L., Socco, V. L., and Strobbia, C. 2003. Experiments of joint acquisition of seismic refraction and surface wave data. *Near surface geophysics,* 1**:** 119-129.

Foti, S., and Strobbia, C. Some notes on model parameters for surface wave data inversion. Symposium on the Application of Geophysics to Engineering and Environmental Problems 2002, 2002. Society of Exploration Geophysicists, SEI6-SEI6.

Frankel, A. 1995. Mapping seismic hazard in the central and eastern United States. *Seismological Research Letters,* 66**:** 8-21.

Frankel, A. D., Petersen, M. D., Mueller, C. S., Haller, K. M., Wheeler, R. L., Leyendecker, E., Wesson, R. L., Harmsen, S. C., Cramer, C. H., and Perkins, D. M. 2002. Documentation for the 2002 update of the national seismic hazard maps. *US Geological Survey Open-File Report,* 420**:** 39.

Gabriels, P., Snieder, R., and Nolet, G. 1987. In situ measurements of shear-wave velocity in sediments with higher-mode Rayleigh waves. *Geophysical prospecting,* 35**:** 187-196.

Gao, L., Xia, J., Pan, Y., and Xu, Y. 2016. Reason and condition for mode kissing in MASW method. *Pure and Applied Geophysics,* 173**:** 1627-1638.

Garofalo, F., Foti, S., Hollender, F., Bard, P., Cornou, C., Cox, B., Dechamp, A., Ohrnberger, M., Perron, V., and Sicilia, D. 2016a. InterPACIFIC project: Comparison of invasive and non-invasive methods for seismic site characterization. Part II: Inter-comparison between surface-wave and borehole methods. *Soil Dynamics and Earthquake Engineering,* 82**:** 241-254.

Garofalo, F., Foti, S., Hollender, F., Bard, P., Cornou, C., Cox, B., Ohrnberger, M., Sicilia, D., Asten, M., and Di Giulio, G. 2016b. InterPACIFIC project: Comparison of invasive and non-invasive methods for seismic site characterization. Part I: Intra-comparison of surface wave methods. *Soil Dynamics and Earthquake Engineering,* 82**:** 222-240.

Gibbs, J. F. 1989. Near-surface P-and S-wave velocities from bore hie measurements near Lake Hemet, California. *US Geological Survey Open-File Report,* 89**:** 630.

Goulet, C. A., and Stewart, J. P. 2009. Pitfalls of deterministic application of nonlinear site factors in probabilistic assessment of ground motions. *Earthquake Spectra,* 25**:** 541-555.

Goulet, C. A., Stewart, J. P., Bazzurro, P., and Field, E. Integration of site-specific ground response analysis results into probabilistic seismic hazard analyses. Proceedings, 4th International Conference on Earthquake Geotechnical Engineering, 2007.

Griffiths, S. C., Cox, B. R., Rathje, E. M., and Teague, D. P. 2016a. Mapping dispersion misfit and uncertainty in V s profiles to variability in site response estimates. *Journal of Geotechnical and Geoenvironmental Engineering,* 142**:** 04016062.

Griffiths, S. C., Cox, B. R., Rathje, E. M., and Teague, D. P. 2016b. Surface-wave dispersion approach for evaluating statistical models that account for shear-wave velocity uncertainty. *Journal of Geotechnical and Geoenvironmental Engineering,* 142**:** 04016061.

Grünthal, G., Stromeyer, D., Bosse, C., Cotton, F., and Bindi, D. 2018. The probabilistic seismic hazard assessment of Germany—version 2016, considering the range of epistemic uncertainties and aleatory variability. *Bulletin of Earthquake Engineering***:** 1-57.

Hadamard, J. 1923. Lectures on Cauchy's Problem in Linear Partial Differential Equations, Yale Univ. *Press. New Haven*.

Hardin, B. O., and Drnevich, V. P. 1972a. Shear modulus and damping in soils: design equations and curves. *Journal of Soil Mechanics & Foundations Div,* 98.

Hardin, B. O., and Drnevich, V. P. 1972b. Shear modulus and damping in soils: measurement and parameter effects. *Journal of Soil Mechanics & Foundations Div,* 98.

Hartzell, S., Bonilla, L., and Williams, R. A. 2004. Prediction of nonlinear soil effects. *Bulletin of the Seismological Society of America,* 94**:** 1609-1629.

Hashash, Y., Musgrove, M., Harmon, J., Groholski, D., Phillips, C., and Park, D. 2015. DEEPSOIL 6.1, User manual. *Board of Trustees of University of Illinois at Urbana-Champaign, Urbana*.

Hashash, Y., Phillips, C., and Groholski, D. R. 2010. Recent advances in non-linear site response analysis.

Hashash, Y. M., and Park, D. 2002. Viscous damping formulation and high frequency motion propagation in non-linear site response analysis. *Soil Dynamics and Earthquake Engineering,* 22**:** 611-624.

Haskell, N. A. 1953. The dispersion of surface waves on multilayered media. *Bulletin of the seismological Society of America,* 43**:** 17-34.

Hegazy, Y. A., and Mayne, P. W. 2006. A global statistical correlation between shear wave velocity and cone penetration data. *Site and Geomaterial Characterization.*

Herak, M. 2008. ModelHVSR—A Matlab® tool to model horizontal-to-vertical spectral ratio of ambient noise. *Computers & Geosciences,* 34**:** 1514-1526.

Hibbett, Karlsson, and Sorensen 1998. *ABAQUS/standard: User's Manual*, Hibbitt, Karlsson & Sorensen.

Hollender, F., Maufroy, E., Bard, P.-Y., and Ameri, G. 2018. Are we ready to perform fully site-specific seismic hazard studies in low-to-moderate seismicity areas? A synthesis of the CASHIMA program results. *Conference: 16th European Conference on Earthquake Engineering at ThessalonikiAt: Thessaloniki, Greece*.

Horike, M. 1985. Inversion of phase velocity of long-period microtremors to the S-wave-velocity structure down to the basement in urbanized areas. *Journal of Physics of the Earth,* 33**:** 59-96.

Huang, D., Wang, G., Wang, C., and Jin, F. 2018. A Modified Frequency-Dependent Equivalent Linear Method for Seismic Site Response Analyses and Model Validation using KiK-Net Borehole Arrays. *Journal of Earthquake Engineering***:** 1-18.

Huber, P. J. 2011. Robust statistics. *International Encyclopedia of Statistical Science.* Springer.

Idriss, I. 2004. Evolution of the state of practice. *Int. Workshop on the Uncertainties in Nonlinear Soil Properties and Their Impact on Modeling Dynamic Soil Response, Pacific Earthquake Engineering Research Center, Richmond, Calif.*

Ishibashi, I., and Zhang, X. 1993. Unified dynamic shear moduli and damping ratios of sand and clay. *Soils and Foundations,* 33**:** 182-191.

Iwasaki, T., Tatsuoka, F., and Takagi, Y. 1978. Shear moduli of sands under cyclic torsional shear loading. *Soils and Foundations,* 18**:** 39-56.

Jakka, R. S., Roy, N., and Wason, H. 2014. Implications of surface wave data measurement uncertainty on seismic ground response analysis. *Soil Dynamics and Earthquake Engineering,* 61**:** 239-245.

Jakka, R. S., Roy, N., and Wason, H. 2015. Reply on "Implications of surface wave data measurement uncertainty on seismic ground response analysis". *Soil Dynamics and Earthquake Engineering,* 74**:** 92-95.

Jamiolkowski, M. 2012. Role of geophysical testing in geotechnical site characterization. *Soils and Rocks,* 35.

Jamiolkowski, M., Ricceri, G., and Simonini, P. Safeguarding Venice from high tides: site characterization and geotechnical problems. Proceedings of the 17th International Conference on Soil Mechanics and Geotechnical Engineering, Alexandria, Egypt, 2009. Citeseer, 5-9.

Jones, A. L., Kramer, S. L., and Arduino, P. 2002. *Estimation of uncertainty in geotechnical properties for performance-based earthquake engineering*, Pacific Earthquake Engineering Research Center, College of Engineering, University of California.

Jones, R. 1958. In-situ measurement of the dynamic properties of soil by vibration methods. *Geotechnique,* 8**:** 1-21.

Joyner, W. B., and Chen, A. T. 1975. Calculation of nonlinear ground response in earthquakes. *Bulletin of the Seismological Society of America,* 65**:** 1315-1336.

Kaklamanos, J., Baise, L., and Dorfmann, L. Quantification of uncertainty in nonlinear soil models at a representative seismic array. 11th International Conference on Structural Safety and Reliability (ICOSSAR 2013), 2013a.

Kaklamanos, J., Baise, L. G., Thompson, E. M., and Dorfmann, L. 2015. Comparison of 1D linear, equivalent-linear, and nonlinear site response models at six KiK-net validation sites. *Soil Dynamics and Earthquake Engineering,* 69**:** 207-219.

Kaklamanos, J., Bradley, B. A., Thompson, E. M., and Baise, L. G. 2013b. Critical parameters affecting bias and variability in site-response analyses using KiK-net downhole array data. *Bulletin of the Seismological Society of America,* 103**:** 1733-1749.

Kaklamanos, J., Thompson, E. M., Baise, L. G., and Dorfmann, L. Identifying and Modeling Complex Site Response Behavior: Objectives, Preliminary Results, and Future Directions. Proceedings of the 2011 NSF Engineering Research and Innovation Conference, Atlanta, Georgia, Grant, 2011.

Kausel, E., and Asimaki, D. 2002. Seismic simulation of inelastic soils via frequency-dependent moduli and damping. *Journal of Engineering Mechanics,* 128**:** 34-47.

Kausel, E., and Peek, R. 1982. Dynamic loads in the interior of a layered stratum: an explicit solution. *Bulletin of the Seismological Society of America,* 72**:** 1459-1481.

Kausel, E., and Roesset, J. M. 1981. Stiffness matrices for layered soils. *Bulletin of the seismological Society of America,* 71**:** 1743-1761.

Kayen, R., Seed, R. B., Moss, R. E., Cetin, O. K., Tanaka, Y., and Tokimatsu, K. 2004. Global shear wave velocity database for probabilistic assessment of the initiation of seismic-soil liquefaction. *Civil and Environmental Engineering***:** 37.

Kendall, M. G. 1946. The advanced theory of statistics. *The advanced theory of statistics.*

Kim, B., Campbell, K., Hashash, Y., Kottke, A., Li, W., and Asimaki, D. 2013a. A predictive model for the relative differences between nonlinear and equivalent-linear site response analyses.

Kim, B., and Hashash, Y. M. 2013. Site response analysis using downhole array recordings during the March 2011 Tohoku-Oki earthquake and the effect of long-duration ground motions. *Earthquake Spectra,* 29**:** S37-S54.

Kim, B., Hashash, Y. M., Stewart, J. P., Rathje, E. M., Harmon, J. A., Musgrove, M. I., Campbell, K. W., and Silva, W. J. 2016. Relative Differences between Nonlinear and Equivalent-Linear 1-D Site Response Analyses. *Earthquake Spectra,* 32**:** 1845-1865.

Kim, D.-S., Bang, E.-S., and Kim, W.-C. 2004. Evaluation of various downhole data reduction methods for obtaining reliable V s profiles. *Geotechnical Testing Journal,* 27**:** 585-597.

Kim, D., Park, H., and Bang, E. 2013b. Round Robin test for comparative study of in-situ seismic tests. *Geotechnical and geophysical site characterization,* 4**:** 1427-1434.

Kirsch, A. 2011. *An introduction to the mathematical theory of inverse problems*, Springer Science & Business Media.

Knopoff, L. 1964. A matrix method for elastic wave problems. *Bulletin of the Seismological Society of America,* 54**:** 431-438.

Konno, K., and Ohmachi, T. 1998. Ground-motion characteristics estimated from spectral ratio between horizontal and vertical components of microtremor. *Bulletin of the Seismological Society of America,* 88**:** 228-241.

Kottke, A., and Rathje, E. 2009. Technical manual for Strata. PEER Report 2008/10, Pacific Earthquake Engineering Research Center, College of Engineering. *University of California, Berkeley*.

Kottke, A., and Rathje, E. M. 2008. A semi-automated procedure for selecting and scaling recorded earthquake motions for dynamic analysis. *Earthquake Spectra,* 24**:** 911-932.

Kramer, S. L. 1996. Geotechnical Earthquake Engineering Prentice Hall. *New York*.

Kramer, S. L., and Paulsen, S. B. Practical use of geotechnical site response models. Proc. Int. Workshop on Uncertainties in Nonlinear Soil Properties and their Impact on Modeling Dynamic Soil Response, 2004. Univ. of California Berkeley, 10.

Krinitzsky, E. L. 1995. Deterministic versus probabilistic seismic hazard analysis for critical structures. *Engineering geology,* 40**:** 1-7.

Kwok, A. O., Stewart, J. P., and Hashash, Y. M. 2008. Nonlinear ground-response analysis of Turkey flat shallow stiff-soil site to strong ground motion. *Bulletin of the Seismological Society of America,* 98**:** 331-343.

Kwok, A. O., Stewart, J. P., Hashash, Y. M., Matasovic, N., Pyke, R., Wang, Z., and Yang, Z. 2007. Use of exact solutions of wave propagation problems to guide implementation of nonlinear seismic ground response analysis procedures. *Journal of Geotechnical and Geoenvironmental Engineering,* 133**:** 1385-1398.

Lacoss, R. T., Kelly, E. J., and Toksöz, M. N. 1969. Estimation of seismic noise structure using arrays. *Geophysics,* 34**:** 21-38.

Lai, C. G., Foti, S., and Rix, G. J. 2005. Propagation of data uncertainty in surface wave inversion. *Journal of Environmental & Engineering Geophysics,* 10**:** 219-228.

Lai, C. G., and Wilmanski, K. 2007. *Surface waves in geomechanics: Direct and inverse modelling for soils and rocks*, Springer Science & Business Media.

Lanzo, G., Vucetic, M., and Doroudian, M. 1997. Reduction of shear modulus at small strains in simple shear. *Journal of Geotechnical and Geoenvironmental Engineering,* 123**:** 1035-1042.

Lasley, S., Green, R., and Rodriguez-Marek, A. Comparison of equivalent-linear site response analysis software. Proc., 10th US National Conf. on Earthquake Engineering, 2014.

Laurenzano, G., Priolo, E., Mucciarelli, M., Martelli, L., and Romanelli, M. 2017. Site response estimation at Mirandola by virtual reference station. *Bulletin of Earthquake Engineering,* 15**:** 2393-2409.

Lee, Y., and Anderson, J. G. 2000. Potential for improving ground-motion relations in southern California by incorporating various site parameters. *Bulletin of the Seismological Society of America,* 90**:** S170-S186.

Lermo, J., and Chávez-García, F. J. 1994. Are microtremors useful in site response evaluation? *Bulletin of the seismological society of America,* 84**:** 1350-1364.

Li, J., and Rosenblad, B. 2011. Experimental study of near-field effects in multichannel array-based surface wave velocity measurements. *Near Surface Geophysics,* 9**:** 357-366.

Li, W., and Asimaki, D. 2010. Site-and motion-dependent parametric uncertainty of site-response analyses in earthquake simulations. *Bulletin of the Seismological Society of America,* 100**:** 954-968.

Lin, P.-S., Chiou, B., Abrahamson, N., Walling, M., Lee, C.-T., and Cheng, C.-T. 2011. Repeatable source, site, and path effects on the standard deviation for empirical ground-motion prediction models. *Bulletin of the Seismological Society of America,* 101**:** 2281-2295.

Lines, L., and Treitel, S. 1984. Tutorial: A review of least-squares inversion and its application to geophysical problems. *Geophysical prospecting,* 32**:** 159-186.

Lippus, C. 2007. Fundamentals of Seismic Refraction Theory, Acquisition, and Interpretation. *Geometrics, Inc.*

Lopes, I., Santos, J. A., and Gomes, R. C. 2014. V S profile: measured versus empirical correlations—a Lower Tagus river valley example. *Bulletin of Engineering Geology and the Environment,* 73**:** 1127-1139.

Louie, J. N. 2001. Faster, better: shear-wave velocity to 100 meters depth from refraction microtremor arrays. *Bulletin of the Seismological Society of America,* 91**:** 347-364.

Lunedei, E., and Albarello, D. 2015. Horizontal-to-vertical spectral ratios from a full-wavefield model of ambient vibrations generated by a distribution of spatially correlated surface sources. *Geophysical Journal International,* 201**:** 1142-1155.

Luo, Y., Xia, J., Miller, R. D., Xu, Y., Liu, J., and Liu, Q. 2008. Rayleigh-wave dispersive energy imaging using a high-resolution linear Radon transform. *Pure and Applied Geophysics,* 165**:** 903-922.

Luzi, L., Bindi, D., Puglia, R., Pacor, F., and Oth, A. 2014. Single-station sigma for Italian strong-motion stations. *Bulletin of the Seismological Society of America,* 104**:** 467-483.

Makra, K., and Chávez-García, F. J. 2016. Site effects in 3D basins using 1D and 2D models: an evaluation of the differences based on simulations of the

seismic response of Euroseistest. *Bulletin of Earthquake Engineering,* 14**:** 1177-1194.

Makra, K., and Raptakis, D. 2016. UNCERTAINTIES ON VS PROFILES AND SITE RESPONSE AT A VERTICAL STRONG MOTION ARRAY. *Bulletin of the Geological Society of Greece,* 50**:** 1525-1534.

Malischewsky, P. G., and Scherbaum, F. 2004. Love's formula and H/V-ratio (ellipticity) of Rayleigh waves. *Wave motion,* 40**:** 57-67.

Maraschini, M., Ernst, F., Foti, S., and Socco, L. V. 2010. A new misfit function for multimodal inversion of surface waves. *Geophysics,* 75**:** G31-G43.

Maraschini, M., and Foti, S. 2010. A Monte Carlo multimodal inversion of surface waves. *Geophysical Journal International,* 182**:** 1557-1566.

Marchetti, S., Monaco, P., Totani, G., and Marchetti, D. 2008. In situ tests by seismic dilatometer (SDMT). *From research to practice in geotechnical engineering.*

Marosi, K. T., and Hiltunen, D. R. 2004. Characterization of SASW phase angle and phase velocity measurement uncertainty. *Geotechnical Testing Journal,* 27**:** 205-213.

Martin, A. J., and Diehl, J. G. Practical experience using a simplified procedure to measure average shear-wave velocity to a depth of 30 meters (VS30). 13th World Conf. on Earthquake Engineering, 2004. International Association for Earthquake Engineering Tokyo.

Martino, S., Cercato, M., Ciancimino, A., Della Seta, M., Di Martino, G., Esposito, C., Foti, S., Giannini, L., Hailemikael, S., Lenti, L., Martini, G., Paciello, A., Pallone, F., Passeri, F., Peloso, A., Rivellino, S., Scarascia Mugnozza, G., Socco, L. V., Troiani, F., Varone, F., and Verrubbi, V. 2017. Peculiarities of local seismic response modelling faced during the third level seismic microzonation studies in the municipality of accumoli (Rieti, italy). *Proceedings of GNDTS Conference, Trieste 14-16 November 2017*.

Mascandola, C., Massa, M., Barani, S., Albarello, D., Lovati, S., Martelli, L., and Poggi, V. 2019. Mapping the Seismic Bedrock of the Po Plain (Italy) through Ambient-Vibration Monitoring. *Bulletin of the Seismological Society of America*.

Mayne, P. W., and Rix, G. J. 1995. Correlations between shear wave velocity and cone tip resistance in natural clays. *Soils and foundations,* 35**:** 107-110.

Mcgann, C. R., Bradley, B. A., Taylor, M. L., Wotherspoon, L. M., and Cubrinovski, M. 2015. Development of an empirical correlation for predicting shear wave velocity of Christchurch soils from cone penetration test data. *Soil Dynamics and Earthquake Engineering,* 75**:** 66-75.

Mcguire, R. K. 1995. Probabilistic seismic hazard analysis and design earthquakes: closing the loop. *Bulletin of the Seismological Society of America,* 85**:** 1275-1284.

Mcguire, R. K. 2008. Probabilistic seismic hazard analysis: Early history. *Earthquake Engineering & Structural Dynamics,* 37**:** 329-338.

Mcmechan, G. A., and Yedlin, M. J. 1981. Analysis of dispersive waves by wave field transformation. *Geophysics,* 46**:** 869-874.

Melchers, R. E., and Beck, A. T. 2018. *Structural reliability analysis and prediction*, John Wiley & Sons.

Menq, F.-Y. 2003. *Dynamic properties of sandy and gravelly soils.*

Miura, K., Yoshida, N., and Kim, Y. 2001. Frequency dependent property of waves in saturated soil. *Soils and Foundations,* 41**:** 1-19.

Moehle, J. 2003. A Framework for Performance-Based Earthquake Engineering. ATC-15-9, Workshop on the Improvement of Building Structural Design and Construction Practices.

Molnar, S., Cassidy, J., Castellaro, S., Cornou, C., Crow, H., Hunter, J., Matsushima, S., Sànchez-Sesma, F., and Yong, A. Application of MHVSR for site characterization: State-of-the-art. Proc. of the 16th World Conf. on Earthquake Engineering, 2017.

Morikawa, N., Kanno, T., Narita, A., Fujiwara, H., Okumura, T., Fukushima, Y., and Guerpinar, A. 2008. Strong motion uncertainty determined from observed records by dense network in Japan. *Journal of Seismology,* 12**:** 529-546.

Moss, R. E. S. 2008. Quantifying measurement uncertainty of thirty-meter shear-wave velocity. *Bulletin of the Seismological Society of America,* 98**:** 1399-1411.

Nakamura, Y. 1989. A method for dynamic characteristics estimation of subsurface using microtremor on the ground surface. *Railway Technical Research Institute, Quarterly Reports,* 30.

Narazian, S., and Stokoe, K. 1983. Use of spectral analysis of surface waves for determination of moduli and thickness of pavement systems. *Transportation Research Record,* 954.

Nazarian, S. 1984. *In situ determination of elastic moduli of soil deposits and pavement systems by spectral-analysis-of-surface-waves method.* University of Texas at Austin.

Neducza, B. 2007. Stacking of surface waves. *Geophysics,* 72**:** V51-V58.

Nolet, G., and Panza, G. F. 1976. Array analysis of seismic surface waves: limits and possibilities. *Pure and Applied geophysics,* 114**:** 775-790.

Ntc 2018. Norme Tecniche per le Costruzioni *Consiglio Superiore dei Lavori Pubblici, Ministero per le Infrastrutture e dei Trasporti*.

O'neill, A. Shear velocity model appraisal in shallow surface wave inversion. Symposium on the Application of Geophysics to Engineering and Environmental Problems 2004, 2004. Society of Exploration Geophysicists, 1544-1555.

Okada, H. 2003. The microtremor survey method: Geophysical Monograph Series, no. 12. *Soc Explor Geophys Tulsa,* 135.

Olafsdottir, E. A., Bessason, B., and Erlingsson, S. 2018. Combination of dispersion curves from MASW measurements. *Soil Dynamics and Earthquake Engineering,* 113**:** 473-487.

Oldenburg, D. W., and Li, Y. 2005. Inversion for applied geophysics: A tutorial. *Investigations in geophysics,* 13**:** 89-150.

Olsen, K. 2000. Site amplification in the Los Angeles basin from three-dimensional modeling of ground motion. *Bulletin of the Seismological Society of America,* 90**:** S77-S94.

Pagliaroli, A., Moscatelli, M., Scasserra, G., Lanzo, G., and Raspa, G. 2015. Effects of uncertainties and soil heterogeneity on the seismic response of archaeological areas: a case study. *ITALIAN GEOTECHNICAL JOURNAL-RIVISTA ITALIANA DI GEOTECNICA,* 49**:** 79-97.

Papaspiliou, M., Kontoe, S., and Bommer, J. J. 2012a. An exploration of incorporating site response into PSHA-part II: Sensitivity of hazard estimates to site response approaches. *Soil Dynamics and Earthquake Engineering,* 42**:** 316-330.

Papaspiliou, M., Kontoe, S., and Bommer, J. J. 2012b. An exploration of incorporating site response into PSHA—Part I: Issues related to site response analysis methods. *Soil Dynamics and Earthquake Engineering,* 42**:** 302-315.

Park, C. B., Miller, R. D., and Xia, J. 1999. Multichannel analysis of surface waves. *Geophysics,* 64**:** 800-808.

Park, D., and Hashash, Y. M. 2004. Soil damping formulation in nonlinear time domain site response analysis. *Journal of Earthquake Engineering,* 8**:** 249-274.

Park, D., and Hashash, Y. M. 2005a. Evaluation of seismic site factors in the Mississippi Embayment. I. Estimation of dynamic properties. *Soil Dynamics and Earthquake Engineering,* 25**:** 133-144.

Park, D., and Hashash, Y. M. 2005b. Evaluation of seismic site factors in the Mississippi embayment. II. Probabilistic seismic hazard analysis with nonlinear site effects. *Soil Dynamics and Earthquake Engineering,* 25**:** 145-156.

Parolai, S., Picozzi, M., Richwalski, S., and Milkereit, C. 2005. Joint inversion of phase velocity dispersion and H/V ratio curves from seismic noise recordings using a genetic algorithm, considering higher modes. *Geophysical research letters,* 32.

Passeri, F., Bahrampouri, M., Rodriguez-Marek, A., and Foti, S. 2018a. Influence of the Uncertainty in Bedrock Characteristics on Seismic Hazard: A Case Study in Italy.

Passeri, F., Comina, C., Marangoni, V., Foti, S., and Amoroso, S. 2018b. Geophysical Monitoring of Blast-induced Liquefaction at the Mirabello (NE Italy) Test Site. *Journal of Environmental & Engineering Geophysics,* 23**:** 14.

Passeri, F., Foti, S., Cox, B., and Rodriguez-Marek, A. 2019. Influence of estimated epistemic uncertainties in shear wave velocity models on ground response analyses. *Earthquake Spectra,* 35**:** 26.

Patel, N. S. 1981. *Generation and attenuation of seismic waves in downhole testing.* University of Texas at Austin.

Pearson, K. 1895. Note on regression and inheritance in the case of two parents. *Proceedings of the Royal Society of London,* 58**:** 240-242.

Pehlivan, M., Rathje, E. M., and Gilbert, R. B. 2016. Factors influencing soil surface seismic hazard curves. *Soil Dynamics and Earthquake Engineering,* 83**:** 180-190.

Peterson, J. 1993. Observations and modeling of seismic background noise.

Pettiti, A., Foti, S., and Comina, C. 2015. Comment on “Effect of surface wave inversion non-uniqueness on 1D seismic ground response analysis” by Roy et al. *Natural Hazards,* 75**:** 975-981.

Phillips, C., and Hashash, Y. M. 2009. Damping formulation for nonlinear 1D site response analyses. *Soil Dynamics and Earthquake Engineering,* 29**:** 1143-1158.

Piatti, C., Foti, S., Socco, L. V., and Boiero, D. 2013a. Building 3D Shear-Wave Velocity Models Using Surface Waves Testing: The Tarcento Basin Case History. *Bulletin of the Seismological Society of America,* 103**:** 1038-1047.

Piatti, C., Socco, L., Boiero, D., and Foti, S. 2013b. Constrained 1D joint inversion of seismic surface waves and P-refraction traveltimes. *Geophysical Prospecting,* 61**:** 77-93.

Pitilakis, K., Raptakis, D., Lontzetidis, K., Tika-Vassilikou, T., and Jongmans, D. 1999. Geotechnical and geophysical description of EURO-SEISTEST, using field, laboratory tests and moderate strong motion recordings. *Journal of Earthquake Engineering,* 3**:** 381-409.

Pitilakis, K., Riga, E., and Anastasiadis, A. 2013. New code site classification, amplification factors and normalized response spectra based on a worldwide ground-motion database. *Bulletin of Earthquake Engineering,* 11**:** 925-966.

Poggiagliolmi, E., Berkhout, A., and Boone, M. 1982. Phase unwrapping, possibilities and limitations. *Geophysical Prospecting,* 30**:** 281-291.

Press, W. H., Teukolsky, S. A., Vetterling, W. T., and Flannery, B. P. 1992. Numerical recipes in FORTRAN (Cambridge. Cambridge Univ. Press.

Rasmussen, C. E. 2004. Gaussian processes in machine learning. *Advanced lectures on machine learning.* Springer.

Rathje, E., and Kottke, A. Relative differences between equivalent linear and nonlinear site response methods. 5th International conference on earthquake geotechnical engineering, Santiago, Chile, 2011.

Rathje, E., Pehlivan, M., Gilbert, R., and Rodriguez-Marek, A. 2015. Incorporating site response into seismic hazard assessments for critical facilities: A probabilistic approach. *Perspectives on Earthquake Geotechnical Engineering.* Springer.

Rathje, E. M., Kottke, A. R., and Trent, W. L. 2010. Influence of input motion and site property variabilities on seismic site response analysis. *Journal of geotechnical and geoenvironmental engineering,* 136**:** 607-619.

Rayleigh, J. W. S. 2015. The theory of sound. Vol. 1.

Redpath, B. B. 1973. Seismic refraction exploration for engineering site investigations. Army Engineer Waterways Experiment Station, Livermore, Calif.(USA). Explosive Excavation Research Lab.

Redpath, B. B. 2007. Downhole measurements of shear-and compression-wave velocities in boreholes C4993, C4996, C4997 and C4998 at the Waste Treatment Plant DOE Hanford Site. *PNNL-16559, Redpath Geophysics, Murphys, California*.

Régnier, J., Bonilla, L. F., Bard, P. Y., Bertrand, E., Hollender, F., Kawase, H., Sicilia, D., Arduino, P., Amorosi, A., Asimaki, D., Boldini, D., Chen, L., Chiaradonna, A., Demartin, F., Ebrille, M., Elgamal, A., Falcone, G., Foerster, E., Foti, S., Garini, E., Gazetas, G., Gélis, C., Ghofrani, A., Giannakou, A., Gingery, J. R., Glinsky, N., Harmon, J., Hashash, Y., Iai, S., Jeremić, B., Kramer, S., Kontoe, S., Kristek, J., Lanzo, G., Lernia, A. D., Lopez-Caballero, F., Marot, M., Mcallister, G., Mercerat, E. D., Moczo, P., Montoya-Noguera, S., Musgrove, M., Nieto-Ferro, A., Pagliaroli, A., Pisanò, F., Richterova, A., Sajana, S., Paola, M., D'avila, S., Shi, J., Silvestri, F., Taiebat, M., Tropeano, G., Verrucci, L., and Watanabe, K. 2016a. International benchmark on numerical simulations for 1D, nonlinear site response (PRENOLIN): Verification phase based on canonical cases. *Bulletin of the Seismological Society of America,* 106**:** 2112-2135.

Régnier, J., Bonilla, L. F., Bard, P. Y., Bertrand, E., Hollender, F., Kawase, H., Sicilia, D., Arduino, P., Amorosi, A., Asimaki, D., Boldini, D., Chen, L., Chiaradonna, A., Demartin, F., Elgamal, A., Falcone, G., Foerster, E., Foti, S., Garini, E., Gazetas, G., Gélis, C., Ghofrani, A., Giannakou, A., Gingery, J., Glinsky, N., Harmon, J., Hashash, Y., Iai, S., Kramer, S., Kontoe, S., Kristek, J., Lanzo, G., Lernia, A. D., Lopez-Caballero, F., Marot, M., Mcallister, G., Mercerat, E. D., Moczo, P., Montoya-Noguera, S.,

Musgrove, M., Nieto-Ferro, A., Pagliaroli, A., Passeri, F., Richterova, A., Maria, S. S., D'avila, P. S., Shi, J., Silvestri, F., Taiebat, M., Tropeano, G., Vandeputte, D., and Verrucci, L. 2018. PRENOLIN: International Benchmark on 1D Nonlinear Site-Response Analysis—Validation Phase Exercise. *Bulletin of the Seismological Society of America*.

Régnier, J., Cadet, H., and Bard, P. Y. 2016b. Empirical quantification of the impact of nonlinear soil behavior on site response. *Bulletin of the Seismological Society of America,* 106**:** 1710-1719.

Reynolds, J. M. 2011. *An introduction to applied and environmental geophysics*, John Wiley & Sons.

Richart, F., Hall, J., and Woods, R. 1970. Vibrations of soils and foundations. International Series in Theoretical and Applied Mechanics. Englewood Cliffs, NJ: Prentice-Hall.

Rix, G. J., and Lai, C. G. Model-based uncertainty in surface wave inversion. Symposium on the Application of Geophysics to Engineering and Environmental Problems 2007, 2007. Society of Exploration Geophysicists, 969-975.

Robertson, P. 2009. Interpretation of cone penetration tests—a unified approach. *Canadian geotechnical journal,* 46**:** 1337-1355.

Robertson, P. Interpretation of in-situ tests-some insights. Mitchell Lecture. Proceedings of the 4th International Conference on Geotechnical and Geophysical Site Characterization (ISC'4). Porto de Galinhas, Pernambuco, Brazil, 2012.

Roblee, C., and Chiou, B. A proposed Geoindex model for design selection of non-linear properties for site response analysis. International workshop on uncertainties in nonlinear soil properties and their impact on modeling dynamic soil response. PEER Headquarters, UC Berkeley, 2004. 18-19.

Roblee, C., Silva, W., Toro, G., and Abrahamson, N. Variability in site-specific seismic ground-motion design predictions. Uncertainty in the Geologic Environment: From theory to practice, 1996. ASCE, 1113-1133.

Rodriguez-Marek, A., Montalva, G. A., Cotton, F., and Bonilla, F. 2011. Analysis of single-station standard deviation using the KiK-net data. *Bulletin of the Seismological Society of America,* 101**:** 1242-1258.

Rodriguez-Marek, A., Cotton, F., Abrahamson, N. A., Akkar, S., Al Atik, L., Edwards, B., Montalva, G. A., and Dawood, H. M. 2013. A model for single-station standard deviation using data from various tectonic regions. *Bulletin of the seismological society of America,* 103**:** 3149-3163.

Rodriguez-Marek, A., Rathje, E., Bommer, J., Scherbaum, F., and Stafford, P. 2014. Application of single-station sigma and site-response characterization in a probabilistic seismic-hazard analysis for a new nuclear site. *Bulletin of the Seismological Society of America,* 104**:** 1601-1619.

Rollins, K. M., Evans, M. D., Diehl, N. B., and Iii, W. D. D. 1998. Shear modulus and damping relationships for gravels. *Journal of Geotechnical and Geoenvironmental Engineering,* 124**:** 396-405.

Romanowicz, B. 2002. Inversion of surface waves: a review. *International Geophysics Series,* 81**:** 149-174.

Ross, S. M. 2014. *Introduction to probability and statistics for engineers and scientists*, Academic Press.

Roy, N., Sankarjakka, R., and Wason, H. 2013. Effect of surface wave inversion non-uniqueness on 1D seismic ground response analysis. *Natural hazards,* 68**:** 1141-1153.

Sabra, A. I. 1981. *Theories of light: from Descartes to Newton*, CUP Archive.
Sadiq, S., Ilhan, O., Ahdi, S. K., Bozorgnia, Y., Hashash, Y. M., Kwak, D. Y., Park, D., Yong, A., and Stewart, J. 2018. A proposed seismic velocity profile database model. *GEESD V, Geotechnical Earthquake Engineering and Soil Dynamics conference, Austin, Texas, June 2018*.
Sambridge, M. 1999. Geophysical inversion with a neighbourhood algorithm—II. Appraising the ensemble. *Geophysical Journal International,* 138**:** 727-746.
Sánchez-Sesma, F. J., Rodríguez, M., Iturrarán-Viveros, U., Luzón, F., Campillo, M., Margerin, L., García-Jerez, A., Suarez, M., Santoyo, M. A., and Rodríguez-Castellanos, A. 2011. A theory for microtremor H/V spectral ratio: application for a layered medium. *Geophysical Journal International,* 186**:** 221-225.
Santamarina, J. C., Rinaldi, V. A., Fratta, D., Klein, K. A., Wang, Y.-H., Cho, G. C., and Cascante, G. 2005. A survey of elastic and electromagnetic properties of near-surface soils. *Near-surface geophysics,* 1**:** 71-87.
Schramm, K. A., Abbott, R. E., Asten, M., Bilek, S., Pancha, A., and Patton, H. J. 2012. Broadband Rayleigh-Wave Dispersion Curve and Shear-Wave Velocity Structure for Yucca Flat, Nevada. *Bulletin of the Seismological Society of America,* 102**:** 1361-1372.
Seed, H. B., Wong, R. T., Idriss, I., and Tokimatsu, K. 1986. Moduli and damping factors for dynamic analyses of cohesionless soils. *Journal of Geotechnical Engineering,* 112**:** 1016-1032.
Sesame Team. The SESAME project: an overview and main results. Proc. of 13th World Conf. on Earthquake Engineering, Vancouver, BC, Canada, August, 2004. 1-6.
Sextos, A., De Risi, R., Pagliaroli, A., Foti, S., Passeri, F., Ausilio, E., Cairo, R., Capatti, M. C., Chiarabando, F., Chiaradonna, A., Dashti, S., De Silva, F., Dezi, F., Durante, M. G., Lanzo, G., Sica, S., Simonelli, A. L., and Zimmaro, P. 2017. Local site effects and incremental damage of buildings during the 2016 Central Italy earthquake sequence. *Earthquake Spectra*.
Seyhan, E., and Stewart, J. P. 2014. Semi-empirical nonlinear site amplification from NGA-West2 data and simulations. *Earthquake Spectra,* 30**:** 1241-1256.
Shapiro, S. S., and Wilk, M. B. 1965. An analysis of variance test for normality (complete samples). *Biometrika,* 52**:** 591-611.
Shi, J., and Asimaki, D. 2017. From stiffness to strength: Formulation and validation of a hybrid hyperbolic nonlinear soil model for site-response analyses. *Bulletin of the Seismological Society of America,* 107**:** 1336-1355.
Silva, W., Abrahamson, N., Toro, G., and Costantino, C. 1997. Description and validation of the stochastic ground motion model. *Submitted to Brookhaven National Laboratory, Associated Universities, Inc. Upton, New York*.
Sismica, G. D. L. M. D. P. 2004. Redazione della mappa di pericolosità sismica prevista dall'Ordinanza PCM 3274 del 20 marzo 2003. *Rapporto Conclusivo per il Dipartimento della Protezione Civile, INGV, Milano-Roma,* 5.
Socco, L., and Strobbia, C. 2004. Surface-wave method for near-surface characterization: A tutorial. *Near Surface Geophysics,* 2**:** 165-185.
Socco, L. V., and Boiero, D. 2008. Improved Monte Carlo inversion of surface wave data. *Geophysical Prospecting,* 56**:** 357-371.

Socco, L. V., Boiero, D., Foti, S., and Wisén, R. 2009. Laterally constrained inversion of ground roll from seismic reflection records. *Geophysics,* 74**:** G35-G45.

Socco, L. V., and Comina, C. 2017. Time-average velocity estimation through surface-wave analysis: Part 2—P-wave velocity. *Geophysics,* 82**:** U61-U73.

Socco, L. V., Comina, C., and Khosro Anjom, F. 2017. Time-average velocity estimation through surface-wave analysis: Part 1—S-wave velocity. *Geophysics,* 82**:** U49-U59.

Socco, L. V., Foti, S., and Boiero, D. 2010. Surface-wave analysis for building near-surface velocity models—Established approaches and new perspectives. *Geophysics,* 75**:** 75A83-75A102.

Socco, L. V., Foti, S., Comina, C., and Boiero, D. 2012. Comment on 'Shear wave profiles from surface wave inversion: the impact of uncertainty on seismic site response analysis'. *Journal of Geophysics and Engineering,* 9**:** 241.

Stellar, R. 1996. New borehole geophysical results at GVDA. *NEES@ UCSB Internal Report*.

Stewart, J. P. 2008. *Benchmarking of nonlinear geotechnical ground response analysis procedures*, Pacific Earthquake Engineering Research Center.

Stewart, J. P., Afshari, K., and Hashash, Y. M. 2014a. Guidelines for performing hazard-consistent one-dimensional ground response analysis for ground motion prediction. *PEER Rep,* 16.

Stewart, J. P., and Baturay, M. B. 2001. Uncertainties and residuals in ground motion estimates at soil sites.

Stewart, J. P., Klimis, N., Savvaidis, A., Theodoulidis, N., Zargli, E., Athanasopoulos, G., Pelekis, P., Mylonakis, G., and Margaris, B. 2014b. Compilation of a local VS profile database and its application for inference of VS 30 from geologic-and terrain-based proxies. *Bulletin of the Seismological Society of America,* 104**:** 2827-2841.

Stewart, J. P., and Kwok, A. O. 2008. Nonlinear seismic ground response analysis: Code usage protocols and verification against vertical array data. *Geotechnical earthquake engineering and soil dynamics IV*.

Stewart, J. P., Lanzo, G., Ausilio, E., Cairo, R., Bozzoni, F., Capatti, M. C., Della Pasqua, F., Dezi, F., Di Sarno, L., Simonelli, A. L., Foti, S., Chiarabando, F., Dabove, P., Di Pietra, V., Maschio, P., Passeri, F., Sgobio, A., Teppati Losè, L., Franke, K. W., Reimschiissel, B., Galadini, F., Falcucci, E., Gori, S., Kayen, R., Kishida, T., Lingwall, B., Pagliaroli, A., Giallini, S., Gogoladze, Z., Vessia, G., Pizzi, A., Di Domenica, A., Pelekis, P., Santo, A., De Falco, M., Forte, G., Scasserra, G., Magistris, S. D., Castiglia, M., Fierro, T., Gautam, D., Mignelli, L., Staniscia, F., Sextos, A., De Risi, R., Sica, S., Mucciacciaro, M., Tommasi, P., Di Giulio, A., Tropeano, G., Durante, M. G., and Zimmaro, P. 2017. GEER REPORT: Engineering Reconnaissance Following the October 2016 Central Italy Earthquakes - Version 2.

Stokoe, K., Darendeli, M., Gilbert, R., Menq, F., and Choi, W. Development of a new family of normalized modulus reduction and material damping curves. International workshop on uncertainties in nonlinear soil properties and their impact on modeling dynamic soil response, PEER Headquarters, UC Berkeley, 2004a. 18-19.

Stokoe, K., Ii, M. Y., Lee, N., and Lopez, R. In situ seismic methods: recent advances in testing, understanding and applications. Proceedings of the 14th Conference Geotechniques, 1989.

Stokoe, K., Roberts, J., Hwang, S., Cox, B., Menq, F., and Van Ballegooy, S. 2014. *Effectiveness of inhibiting liquefaction triggering by shallow ground improvement methods: Initial field shaking trials with TRex at one site in Christchurch, New Zealand*, Taylor & Francis Group, London.

Stokoe, K. H. 1994. Characterization of geotechnical sites by SASW method, in Geophysical characterization of sites. *ISSMFE Technical Committee# 10*.

Stokoe, K. H., Jennie, C., Milton, T., Asli Kurtulus, M., and Menq, F.-Y. 2004b. SASW measurements at the NEES garner valley test site, California. *Data report. College of Engineering, University of Texas-Austin, Austin, TX Google Scholar*.

Stokoe, K. H., and Santamarina, J. C. Seismic-wave-based testing in geotechnical engineering. ISRM International Symposium, 2000. International Society for Rock Mechanics.

Stokoe, K. H., and Woods, R. D. 1972. In situ shear wave velocity by cross-hole method. *Journal of Soil Mechanics & Foundations Div,* 98.

Stolte, A., and Cox, B. 2019. Towards consideration of epistemic uncertainty in shear wave velocity measurements obtained via SCPT.

Strobbia, C., and Cassiani, G. 2011. Refraction microtremors: Data analysis and diagnostics of key hypotheses. *Geophysics,* 76**:** MA11-MA20.

Sun, J. I., Golesorkhi, R., and Seed, H. B. 1988. *Dynamic moduli and damping ratios for cohesive soils*, Earthquake Engineering Research Center, University of California Berkeley.

Sykora, D. W., and Koester, J. P. Correlations between dynamic shear resistance and standard penetration resistance in soils. Earthquake Engineering and Soil Dynamics II—Recent Advances in Ground-Motion Evaluation, 1988. ASCE, 389-404.

Taborda, R., López, J., Karaoglu, H., Urbanic, J., and Bielak, J. 2010. Speeding up finite element wave propagation for large-scale earthquake simulations. *Parallel Data Laboratory Tech. Rept. CMUPDL-10,* 109.

Teague, D., Cox, B., Bradley, B., and Wotherspoon, L. 2017. Development of deep shear wave velocity profiles with estimates of uncertainty in the complex inter-bedded geology of Christchurch, New Zealand. *Earthquake Spectra*.

Teague, D. P., and Cox, B. R. 2016. Site response implications associated with using non-unique vs profiles from surface wave inversion in comparison with other commonly used methods of accounting for vs uncertainty. *Soil Dynamics and Earthquake Engineering,* 91**:** 87-103.

Teague, D. P., Cox, B. R., and Rathje, E. M. 2018. Measured vs. predicted site response at the garner valley downhole array considering shear wave velocity uncertainty from borehole and surface wave methods. *Soil Dynamics and Earthquake Engineering,* 113**:** 339-355.

Thompson, E. M., Baise, L. G., Kayen, R. E., and Guzina, B. B. 2009. Impediments to predicting site response: Seismic property estimation and modeling simplifications. *Bulletin of the Seismological Society of America,* 99**:** 2927-2949.

Thompson, E. M., Baise, L. G., Tanaka, Y., and Kayen, R. E. 2012. A taxonomy of site response complexity. *Soil Dynamics and Earthquake Engineering,* 41**:** 32-43.

Thompson, E. M., and Wald, D. J. 2016. Uncertainty in VS 30-based site response. *Bulletin of the Seismological Society of America,* 106**:** 453-463.

Thomson, W. T. 1950. Transmission of elastic waves through a stratified solid medium. *Journal of applied Physics,* 21**:** 89-93.

Tokimatsu, K. 1997. Geotechnical site characterization using surface waves. *Earthquake geotechnical engineering*.

Tokimatsu, K., Shinzawa, K., and Kuwayama, S. 1992a. Use of short-period microtremors for V S profiling. *Journal of Geotechnical Engineering,* 118**:** 1544-1558.

Tokimatsu, K., Tamura, S., and Kojima, H. 1992b. Effects of multiple modes on Rayleigh wave dispersion characteristics. *Journal of geotechnical engineering,* 118**:** 1529-1543.

Toro, G. 1995. Probabilistic models of site velocity profiles for generic and site-specific ground-motion amplification studies. *Department of Nuclear Energy Brookhaven National Laboratory, Upton, New York*.

Toro, G., Silva, W., Mcguire, R., and Herrmann, R. 1992. Probabilistic seismic hazard mapping of the Mississippi Embayment. *Seismological Research Letters,* 63**:** 449-475.

Toro, G. R., Abrahamson, N. A., and Schneider, J. F. 1997. Model of strong ground motions from earthquakes in central and eastern North America: best estimates and uncertainties. *Seismological Research Letters,* 68**:** 41-57.

Tuan, T. T., Scherbaum, F., and Malischewsky, P. G. 2011. Summary. *Geophysical Journal International,* 184**:** 793-800.

Valle-Molina, C. 2006. *Measurements of Vp and Vs in dry, unsaturated and saturated sand specimens with piezoelectric transducers.*

Van Der Baan, M. 2009. The origin of SH-wave resonance frequencies in sedimentary layers. *Geophysical Journal International,* 178**:** 1587-1596.

Vantassel, J., Cox, B., Wotherspoon, L., and Stolte, A. 2018. Mapping Depth to Bedrock, Shear Stiffness, and Fundamental Site Period at CentrePort, Wellington, Using Surface-Wave Methods: Implications for Local Seismic Site Amplification. *Bulletin of the Seismological Society of America*.

Volpini, C., and Douglas, J. 2018. An accessible approach for the site response analysis of quasi-horizontal layered deposits. *Bulletin of Earthquake Engineering***:** 1-21.

Vucetic, M., and Dobry, R. 1991. Effect of soil plasticity on cyclic response. *Journal of geotechnical engineering,* 117**:** 89-107.

Wair, B. R., Dejong, J. T., and Shantz, T. 2012. *Guidelines for estimation of shear wave velocity profiles*, Pacific Earthquake Engineering Research Center.

Wathelet, M., Jongmans, D., and Ohrnberger, M. 2004. Surface-wave inversion using a direct search algorithm and its application to ambient vibration measurements. *Near surface geophysics,* 2**:** 211-221.

Wielandt, E. 1993. Propagation and structural interpretation of non-plane waves. *Geophysical Journal International,* 113**:** 45-53.

Wood, C., and Cox, B. 2012. A comparison of MASW dispersion uncertainty and bias for impact and harmonic sources. *GeoCongress 2012: State of the Art and Practice in Geotechnical Engineering.*

Wood, C., Mcgann, C., Cox, B., Green, R., Wotherspoon, L., and Bradley, B. 2017. A comparison of CPT-Vs correlations using a liquefaction case history database from the 2010-2011 Canterbury Earthquake Sequence.

Wotherspoon, L., Cox, B., Stokoe, K., Ashfield, D., and Phillips, R. Utilizing Direct-Push Crosshole Testing to Assess the Effectiveness of Soil Stiffening Caused by Installation of Stone Columns and Rammed Aggregate Piers. 6th International Conference on Earthquake Geotechnical Engineering 1-4 November 2015 Christchurch NZ, 2015.

Xia, J., Xu, Y., and Miller, R. D. 2007. Generating an image of dispersive energy by frequency decomposition and slant stacking. *Pure and Applied Geophysics,* 164**:** 941-956.

Yee, E., Stewart, J. P., and Tokimatsu, K. 2013. Elastic and large-strain nonlinear seismic site response from analysis of vertical array recordings. *Journal of Geotechnical and Geoenvironmental Engineering,* 139**:** 1789-1801.

Yniesta, S., Brandenberg, S., and Shafiee, A. 2017. ARCS: A one dimensional nonlinear soil model for ground response analysis. *Soil Dynamics and Earthquake Engineering,* 102**:** 75-85.

Yong, A., Martin, A., Stokoe, K., and Diehl, J. 2013. ARRA-funded V S30 measurements using multi-technique approach at strong-motion stations in California and central-eastern United States. US Geological Survey.

Yoon, S., and Rix, G. J. 2009. Near-field effects on array-based surface wave methods with active sources. *Journal of Geotechnical and Geoenvironmental Engineering,* 135**:** 399-406.

Zalachoris, G., and Rathje, E. M. 2015. Evaluation of one-dimensional site response techniques using borehole arrays. *Journal of Geotechnical and Geoenvironmental Engineering,* 141**:** 04015053.

Zhang, J., Andrus, R. D., and Juang, C. H. 2005. Normalized shear modulus and material damping ratio relationships. *Journal of Geotechnical and Geoenvironmental Engineering,* 131**:** 453-464.

Zhang, J., Andrus, R. D., and Juang, C. H. 2008. Model uncertainty in normalized shear modulus and damping relationships. *Journal of geotechnical and geoenvironmental engineering,* 134**:** 24-36.

Zhang, S. X., and Chan, L. S. 2003. Possible effects of misidentified mode number on Rayleigh wave inversion. *Journal of Applied Geophysics,* 53**:** 17-29.

Zywicki, D. J. 2007. The impact of seismic wavefield and source properties on ReMi estimates. *Innovative Applications of Geophysics in Civil Engineering.*

Appendix

Table A1. List of sites included in the PSWD.

ID	Site information		Surface wave testing methods												HVSR		Saturation depth (m) P-wave refraction test	Invasive tests				Reference
			Test setup							EDC characteristics				Single deterministic interval velocity V_S profile								
	Location (name)	Latitude (°)	Longitude (°)	Line	Length (m)	Spacing (m)	Circle	Triangle	L-shaped	Passive array aperture (m)	Source (A=active, P=passive)	Higher modes	Phase velocity st. dev.	Maximum wavelength (m)	Minimum wavelength (m)	Investigation depth (m)	V_S of the halfspace (m/s)	Inversion (MC=Monte Carlo, MC-multi=Monte Carlo multimodal, IFM=Iterative Forward	Peak frequency (Hz)	Standard deviation (Hz)		DH	CH	PS	SDTM	
1	Accumoli	42.694	13.249	■	46	2				-	A		■	48.5	3.8	30	742	MC	-	-	-	■				
2	Acquasanta Terme	42.771	13.414	■	34.5	1.5				-	A		■	103.2	3.7	40	1031	MC	-	-	-	■				Foti et al. (2011b)
3	AQA	42.376	13.339	■	34.5	1.5				-	A	■		48.0	2.0	40	1205	MC-multi	10	-	-	■				
4	Bovisio-L2	45.609	9.169	■	23.5	0.5				-	A		■	20	2	9	535	IFM	-	-	-					
5	Caselle Landi-1	45.091	9.795	■	46	2				-	A			70.0	4.8	18	335	IFM	-	-	3					Comina et al. (2004)
6	Caselle Landi-2	45.091	9.795	■	69	3				-	A			46.5	2.9	18	285	IFM	-	-	2.5					Strobbia and Foti (2006)
7	Caselle Landi-3	45.091	9.795	■	92	4				-	A			60.8	2.9	18	259	IFM	-	-	-					Comina et al. (2004)
8	Caselle Landi-5	45.087	9.790	■	69	3				-	A			102.2	2.9	18	370	IFM	-	-	2.5					Comina et al. (2004)
9	Castel di Lama-Campo	42.860	13.704	■	35	1				-	A		■	48.7	3.0	25	580	MC	-	-	-	■				
10	Castel di Lama-Strada	42.870	13.708	■	70	2				-	A		■	82.9	5.6	40	571	MC	-	-	-	■				

Table A1. (continues).

11	CAT	37.447	15.046		70.5	1.5			50	A+P		104.7	2.4	104	888	MC	1.49	-	-			Foti et al. (2011b)		
12	Cesana-1	44.954	6.811		46	2			-	A		38	9	15	675	IFM	-	-	-					
13	Cesana-2	44.953	6.809		46	2			-	A		42	3	13	531	IFM	-	-	-					
14	CG-Loc. Alle Monache	44.123	10.409		46	2			-	A		72.5	2.3	25	686	IFM	-	-	-					
15	CG-Zona industriale	44.115	10.406		46	2			-	A		47.3	2.1	20	831	MC-multi	-	-	-			Maraschini et al. (2010)		
16	CLG	37.212	14.521		47	1			22.5	A+P		444.3	2.2	32	862	MC-multi	-	-	11.6			Foti et al. (2011b)		
17	Firenze-Piazza Duomo	43.773	11.256		46	2			-	A		71.8	2.6	15	639	IFM	-	-	-					
18	Firenze-Uffizi	43.769	11.257		35	1.5			-	A		45.3	7.2	20	1040	IFM	-	-	-					
19	Firenze-Via di Novoli	43.793	11.226		46	2			-	A		58.3	3.1	16	419	IFM	-	-	-			Lai et al. (2005)		
20	Fonte del Campo	42.692	13.256		118	2			75	A+P		314.2	2.9	100	2747	MC-multi	6.1	0.1	10			Passeri et al. (2018a)		
21	GEA	37.056	14.315		70.5	1.5			-	A		54.1	1.7	30	389	MC-multi	-	-	3.3			Foti et al. (2011b)		
22	GMN	46.292	13.123		141	3			-	A		73	8	40	701	MC	-	-	-			Piatti et al. (2013b)		
23	GNV	44.432	8.932		23.5	0.5			-	A		21	1	10	1338	MC-multi	-	-	1			itaca.mi.ingv.it		
24	GRI-Campo Sportivo-EW	42.731	13.268		47	1			-	A		124.1	2.6	30	679	MC	-	-	2.5					
25	GRI-Campo Sportivo-NS	42.731	13.268		94	2			-	A		89.2	2.6	35	670	MC	-	-	4					

Table A1. (continues).

26	Grisciano Conoide	42.736	13.268		94	2			-	A			63.0	4.6	34	1038	MC	-	-	10			
27	Ilica	42.703	13.264		35	1			-	A			54.7	2.7	25	473	MC	-	-	4			Socco and Comina (2017)
28	La Salle A	45.740	7.070		70.5	1.5			75	A+P			427	4	100	1291	MC	-	-	-			
29	La Salle B	45.747	7.073		34.5	1.5			30	A+P			350.8	3.3	105	1405	MC	-	-	-			Socco et al. (2009)
30	La Salle C	45.746	7.078		34.5	1.5			75	A+P			444.3	2.0	120	1340	MC	-	-	-			Socco et al. (2009)
31	La Salle D	45.744	7.074		46	2			40	A+P			346.7	2.5	93	1464	MC	-	-	-			Socco et al. (2009)
32	La Salle E	45.743	7.078		70.5	1.5			75	A+P			122.9	6.2	91	1018	MC	-	-	-			Comina et al. (2011)
33	L'Aquila (Il Moro)	42.379	13.349		70.5	1.5			50	A+P			256.0	2.0	40	802	MC-multi	11	-	-			
34	L'Aquila (Pianola)	42.328	13.409		47	1			50	A+P			110	1	59	915	MC	-	-	-			Comina et al. (2011)
35	L'Aquila (Roio Piano)	42.330	13.353		70.5	1.5			50	A+P			92	2	74	618	MC	-	-	-			Comina et al. (2011)
36	Massa M.-Cantiere	43.050	10.888		34.5	1.5			-	A			49.1	3.2	24	1090	IFM	-	-	-			
37	Massa M.-Parcheggio	43.050	10.888		46	2			-	A			48.8	2.1	19	780	IFM	-	-	-			
38	Mathi-1&2	45.255	7.536		47	2			20	A+P			201	2	76	1122	IFM	-	-	-			Comina e Foti 2007
39	Mathi-3	45.255	7.536		23	1			-	A			78.8	2.7	39	786	IFM	-	-	-			Comina e Foti 2007

Table A1. (continues).

40	Mirabello-Last-July	44.836	11.449	■	47	1			-	A		■	35	2	19	233	IFM	-	-	-	■				Passeri et al. (2018b)
41	Mirabello-Post-May	44.836	11.449	■	47	1			-	A		■	38	2	19	250	IFM	-	-	-	■				
42	Mirabello-Pre-Feb	44.836	11.449	■	47	1			-	A		■	42	2	19	275	IFM	-	-	-	■				
43	Montemonaco	42.888	13.354	■	105	3			-	A		■	43	4	20	1066	MC	-	-	-	■				
44	NTE	36.910	15.069	■	18.4	0.8			-	A	■		42.0	1.6	20	869	MC-multi	-	-	2.8					Foti et al. (2011b)
45	Offida	42.934	13.698	■	70	2			-	A		■	100.8	3.8	47	1649	MC	-	-	-	■				
46	Palmiano-Castel San Pietro	42.920	13.463	■	23	1			-	A	■	■	55.4	4.0	25	935	MC	-	-	-					Foti et al. (2011b)
47	PCH	36.712	15.092	■	23	1			-	A	■		97.5	1.3	40	1225	MC-multi	-	-	1.9					
48	Piazza al Serchio	44.185	10.300	■	34.5	1.5			-	A			30.7	2.3	15	556	IFM	-	-	-	■				
49	Pieve Fosciana	44.135	10.411	■	69	3			-	A			61.1	4.4	24	645	IFM	-	-	-	■				
50	Pisa	43.723	10.397	■	57.5	2.5	■		40	A+P		■	87	5	50	284	MC	-	-	-		■			Comina et al. (2011)
51	PNR	44.876	7.344	■	47	1			-	A	■		97.5	2.9	55	621	MC-multi	0.92	-	8.5					Foti et al. (2011b)
52	Pontremoli-1 maggio	44.371	9.881	■	46	2			-	A		■	64	7.7	30	1262	MC	-	-	1	■				Comina et al. (2011)
53	Pontremoli-ASL 2	44.386	9.886	■	46	2			-	A			39	3	9	885	IFM	-	-	3	■				Foti et al. (2003)
54	Pontremoli-Bocciofila	44.374	9.881	■	46	2			-	A			79	6	19	1037	IFM	-	-	-	■				
55	Pontremoli-Giochi	44.378	9.875	■	46	2			-	A			68	5	15	868	IFM	-	-	-	■				

Table A1. (continues).

56	PTT0	38.134	14.975		23	1			-	A		409.6	1.3	65	861	MC-multi	3.8	-	2.8			Puglia et al. (2011)
57	RGS	36.925	14.703		11.5	0.5			-	A		28.1	1.7	20	1201	MC-multi	-	-	-			Foti et al. (2011b)
58	Roccafluvione	42.859	13.474		70	2			-	A		102.5	4.9	40	1162	MC	-	-	-			
59	Rotella	42.953	13.558		105	3			-	A		113.8	6.2	50	1033	MC	-	-	-			
60	RNS	44.595	8.936		23.5	0.5			-	A		18.1	1.0	10	795	MC-multi	-	-	4.6			Foti et al. (2011b)
61	Saluggia	45.216	8.020		69	3			-	A		75	5	40	684	MC	-	-	-			Comina et al. (2011)
62	San Severino Marche 1	43.226	13.176		35	1			-	A		48	19	22	1636	MC	-	-	-			
63	San Severino Marche 2	43.226	13.176		45	1.5			-	A		84	5	35	1125	MC	-	-	-			
64	Sarno-Connola	40.734	14.717		47	1			-	A		32	1	20	412	MC-multi	-	-	-			Coutinho and Mayne (2012)
65	Sarno-Santa Lucia	40.730	14.717		47	1			-	A		26	1.7	20	409	MC-multi	-	-	-			
66	Sarno-Tuostolo	40.831	14.603		47	1			-	A		55	2.5	20	449	MC-multi	-	-	-			
67	SCR	36.829	14.527		23	1			-	A		30	2	15	1184	MC-multi	-	-	-			Bergamo et al. (2011)
68	SEL	44.265	9.403		32.9	0.7			-	A		39	1.9	13	620	MC-multi	11.5	-	-			Foti et al. (2011b)
69	Settimo Torinese	45.148	7.751		70.5	1.5			-	A		90	3.7	45	724	MC	-	-	-			

Table A1. (continues).

70	Tarcento-1	46.215	13.205		47	1			-	A			49	7	35	941	MC	-	-	14													Piatti et al. (2013a)
71	Tarcento-2	46.215	13.211		47	1			60	A+P			43	5	30	846	MC	-	-	11													
72	Tarcento-3	46.217	13.215		47	1			60	A+P			47	4	33	755	MC	-	-	15													
73	Tarcento-4	46.216	13.224		47	1			-	A			71	3	39	1140	MC	-	-	6													
74	Tarcento-5	46.211	13.207		47	1			-	A			72	6	45	1221	MC	-	-	20													
75	Tarcento-6	46.213	13.211		47	1			-	A			59	3	40	948	MC	-	-	15													
76	Tarcento-7	46.213	13.216		47	1			-	A			14	3	12	322	MC	-	-	17													
77	Tarcento-8	46.214	13.219		47	1			-	A			35	4	30	888	MC	-	-	15													
78	Tarcento-10	46.211	13.216		47	1			60	A+P			77	3	50	651	MC	-	-	20													
79	Tarcento-11	46.212	13.219		47	1			60	A+P			87	6	40	856	MC	-	-	13													
80	Tarcento-12	46.209	13.220		47	1			-	A			89	5	45	1109	MC	-	-	12													
81	Tarcento-15	46.203	13.226		47	1			-	A			12	4	10	756	MC	-	-	6													
82	TOR	38.044	14.815		46	2			-	A			64.0	2.8	30	1308	MC-multi	5.62	-	3.6													Puglia et al. (2011)
83	Torre Pellice-Depuratore	44.817	7.220		46	2			80	A+P			114	6	61	741	MC	-	-	-													Socco and Comina (2017)
84	Torre Pellice-Giardini	44.821	7.220		46	2			60	A+P			44	3	14	820	MC	-	-	11.8													Socco and Comina (2017)
85	Torre Pellice-Parco Giochi	44.820	7.204		46	2			-	A			46	5	14	770	MC	-	-	-													Socco et al. (2009)

Table A1. (continues).

| | | |

Left. Each site is presented with its EDC (phase velocity vs. frequency) and +/- one standard deviation error bars (if available, for 52 sites, see Table A1).

Right. The interval (solid line) and harmonic (dashed line) shear wave velocity profile from previous inversions are presented with the same colors of the associated EDC. For 39 sites (see A1), also the interval (solid line) and harmonic (dashed line) shear wave velocity profile from the invasive test are shown in black (line for the DH, stars for CH, and diamonds for SDTM).

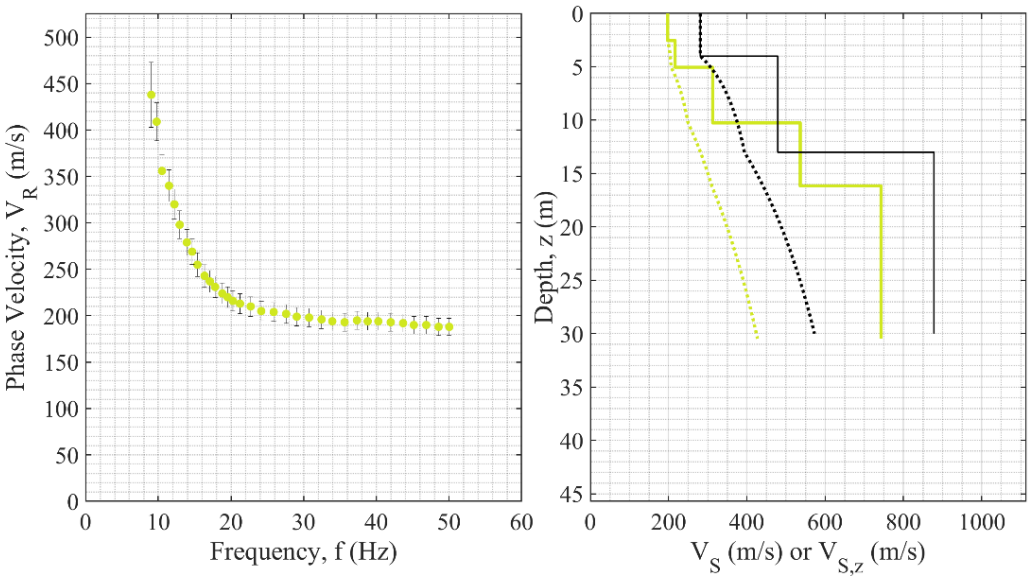

Figure A1. EDC (left), Vs and Vs,z (right) for Accumoli (ID 1).

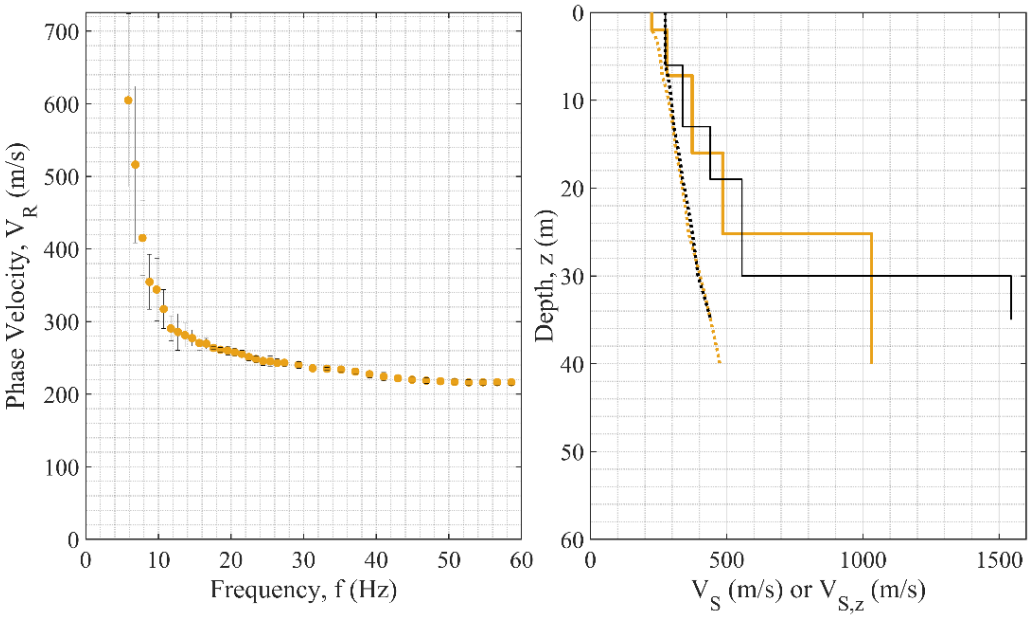

Figure A2. EDC (left), Vs and Vs,z (right) for Acquasanta Terme (ID 2).

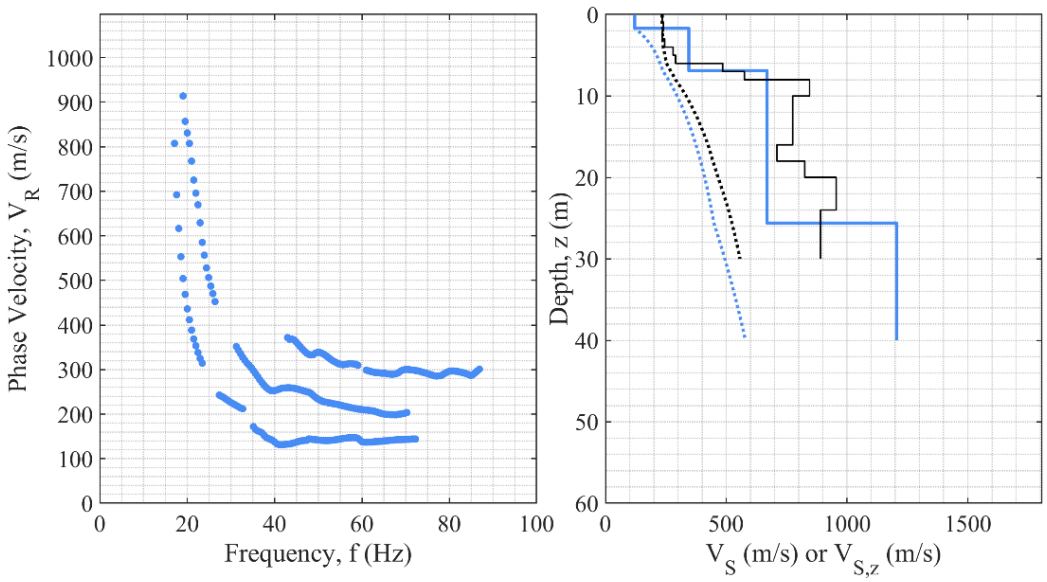

Figure A3. EDC (left), Vs and Vs,z (right) for AQA (ID 3).

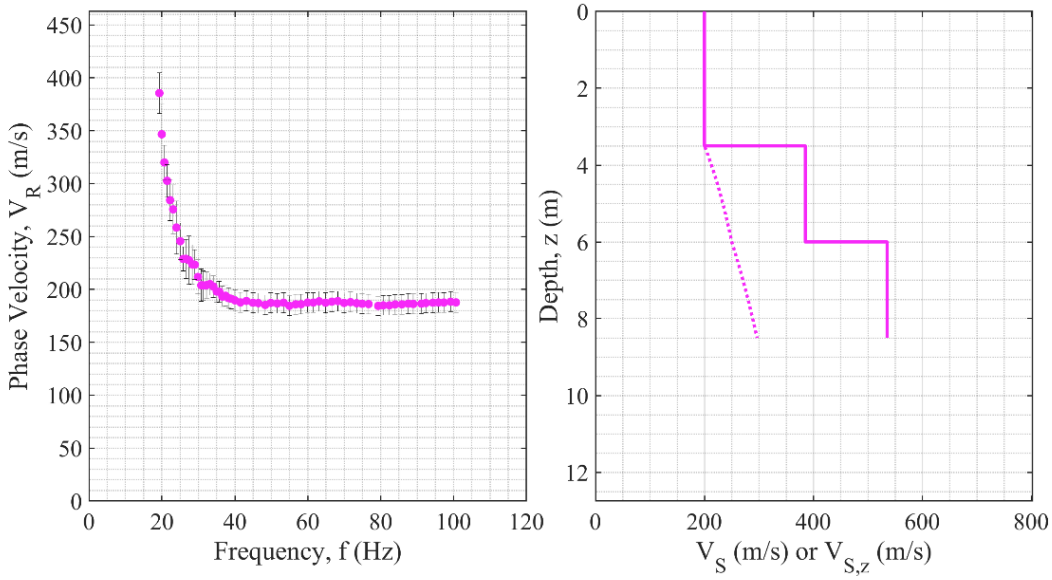

Figure A4. EDC (left), Vs and Vs,z (right) for Bovisio-L2 (ID 4).

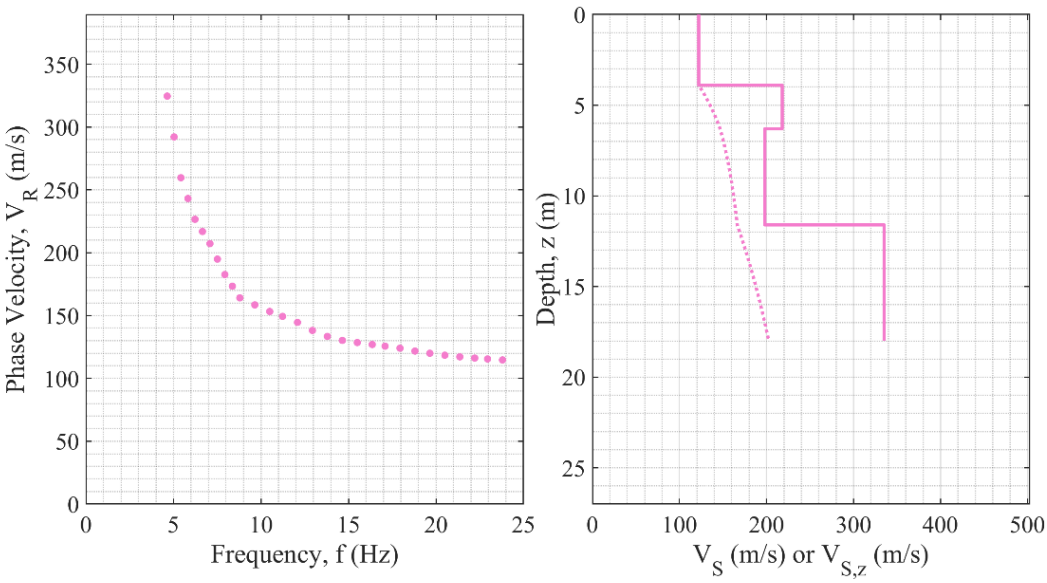

Figure A5. EDC (left), V_S and $V_{S,z}$ (right) for Caselle Landi-1 (ID 5).

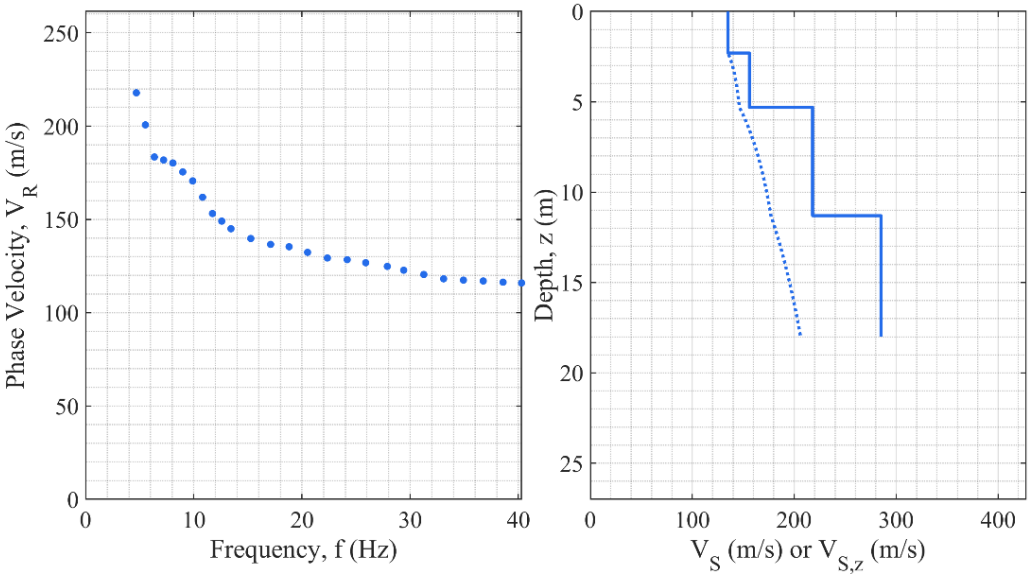

Figure A6. EDC (left), V_S and $V_{S,z}$ (right) for Caselle Landi-2 (ID 6).

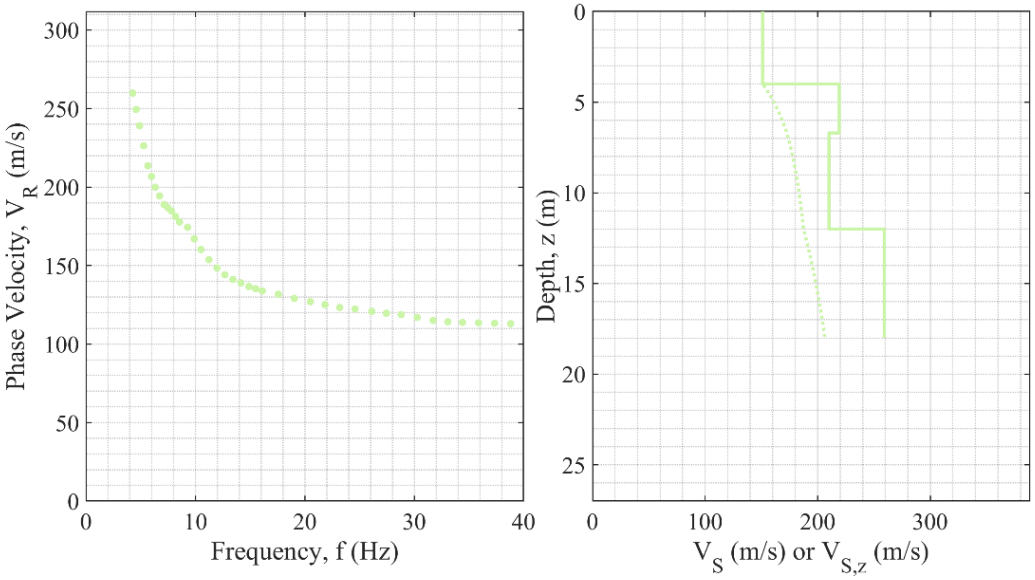

Figure A7. EDC (left), Vs and Vs,z (right) for Caselle Landi-3 (ID 7).

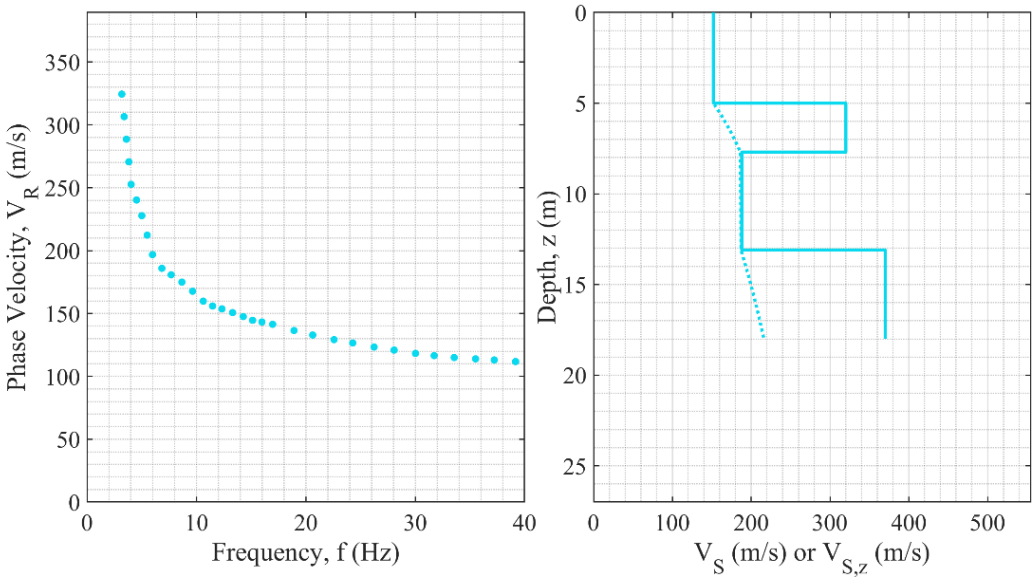

Figure A8. EDC (left), Vs and Vs,z (right) for Caselle Landi-5 (ID 8).

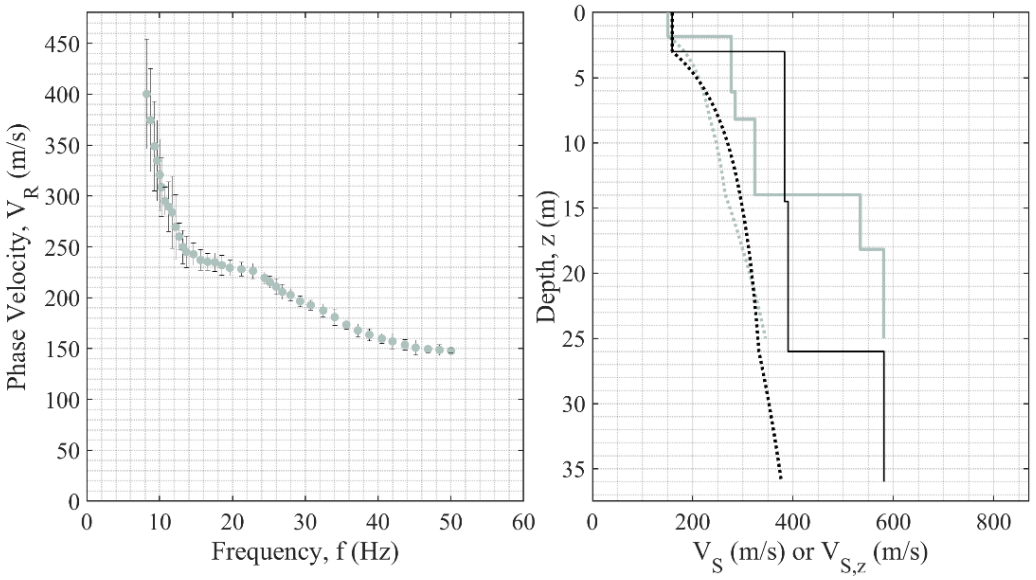

Figure A9. EDC (left), Vs and Vs,z (right) for Castel di Lama-Campo (ID 9).

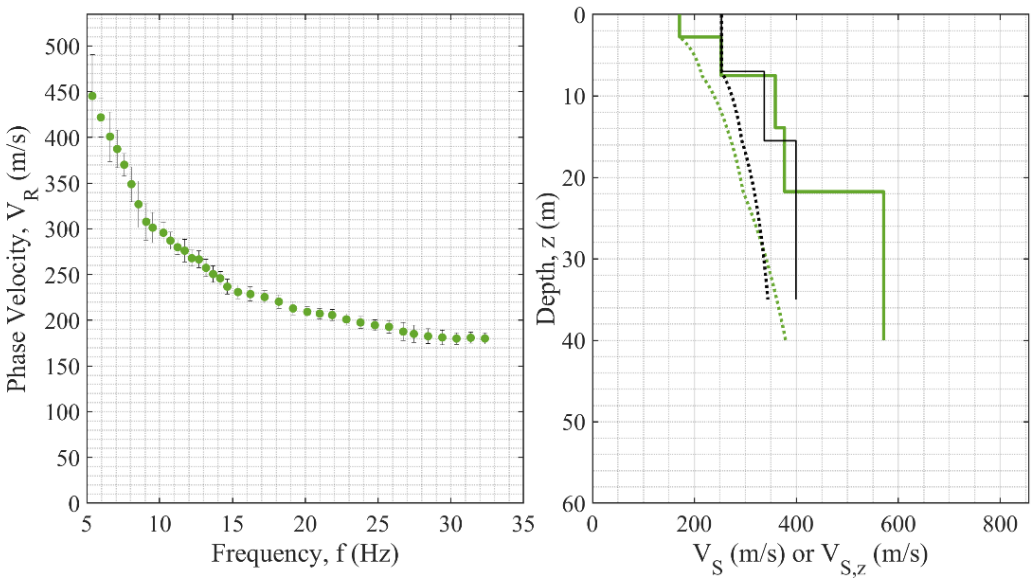

Figure A10. EDC (left), V_S and $V_{S,z}$ (right) for Castel di Lama-Strada (ID 10).

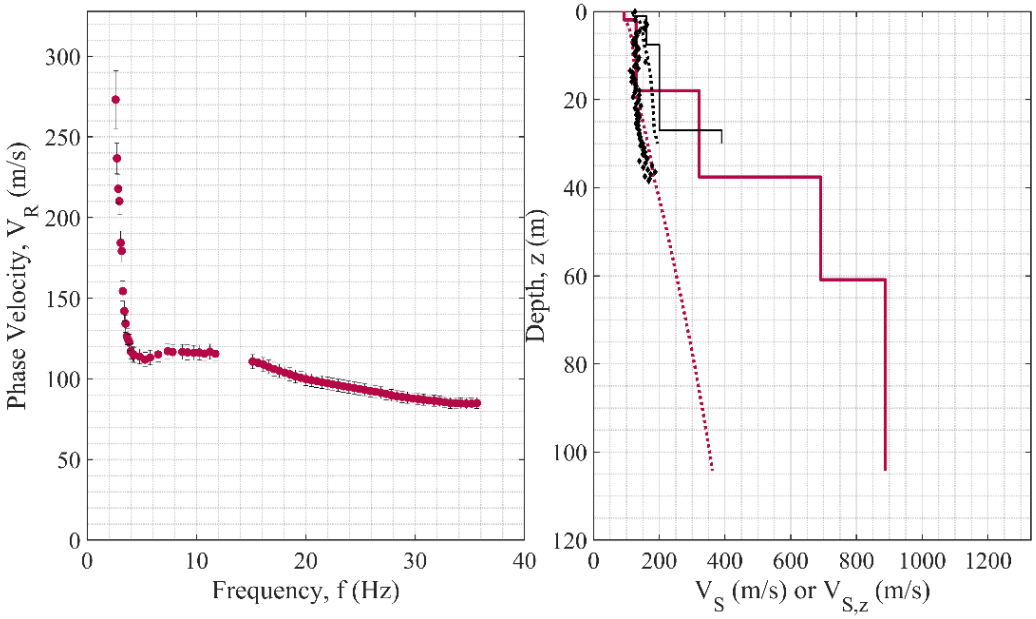

Figure A11. EDC (left), V_S and $V_{S,z}$ (right) for CAT (ID 11).

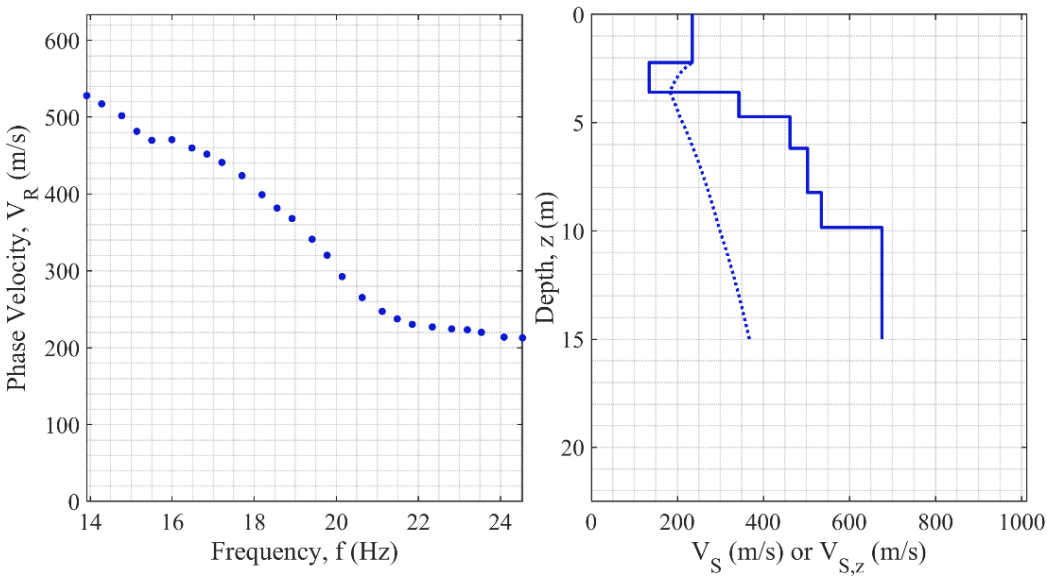

Figure A12. EDC (left), Vs and Vs,z (right) for Cesana-1 (ID 12).

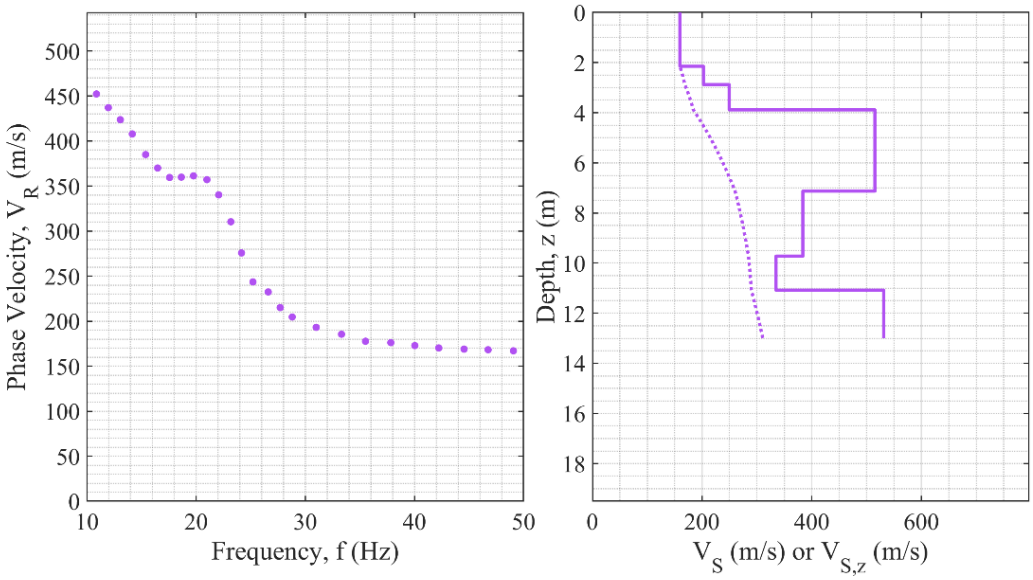

Figure A13. EDC (left), Vs and Vs,z (right) for Cesana-2 (ID 13).

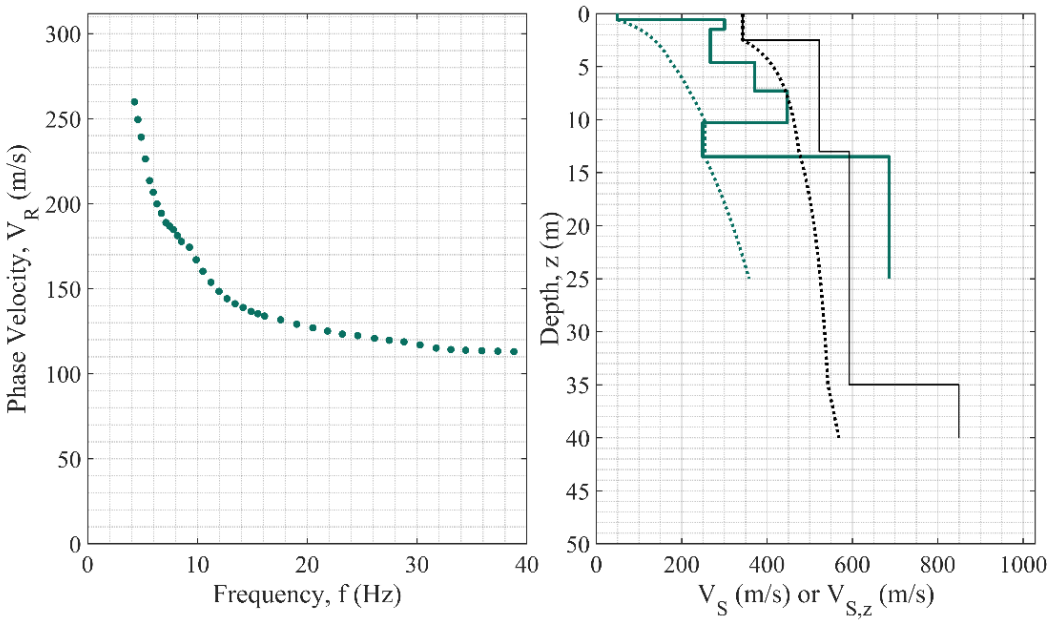

Figure A14. EDC (left), V_S and $V_{S,z}$ (right) for CG-Loc. Alle Monache (ID 14).

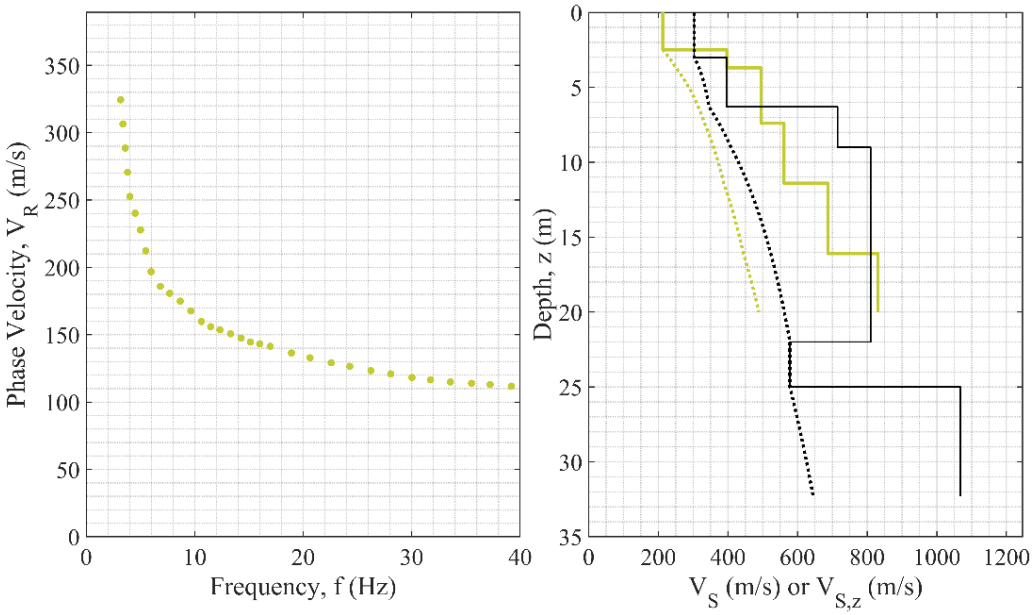

Figure A15. EDC (left), V_S and $V_{S,z}$ (right) for CG-Zona industriale (ID 15).

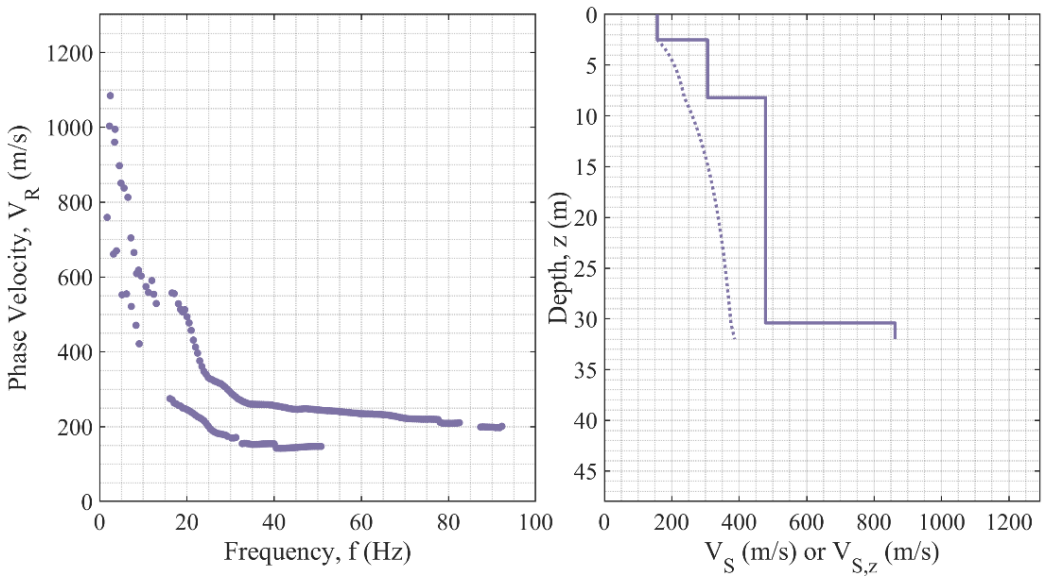

Figure A16. EDC (left), V_S and $V_{S,z}$ (right) for CLG (ID 16).

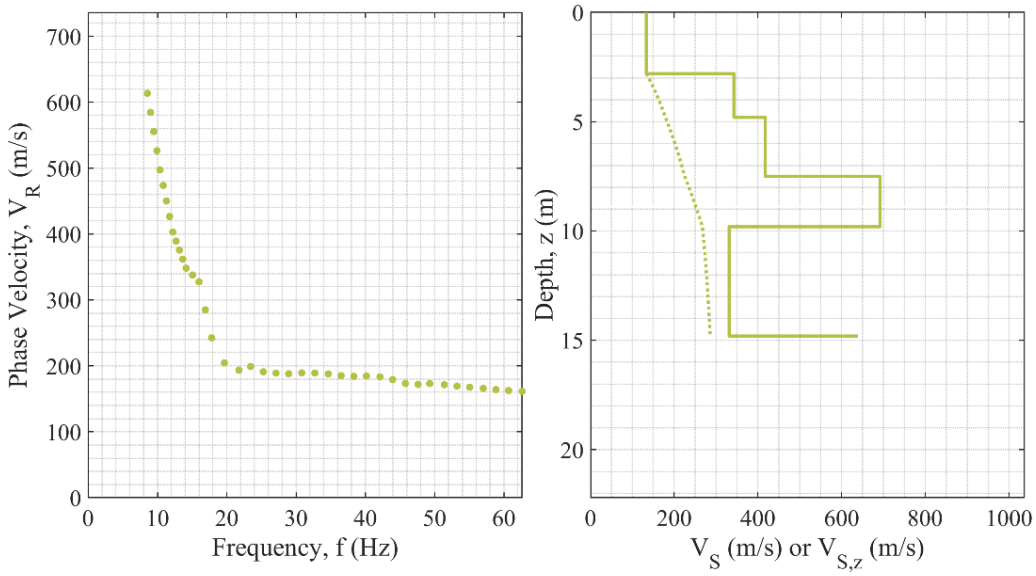

Figure A17. EDC (left), V_S and $V_{S,z}$ (right) for Firenze-Piazza Duomo (ID 17).

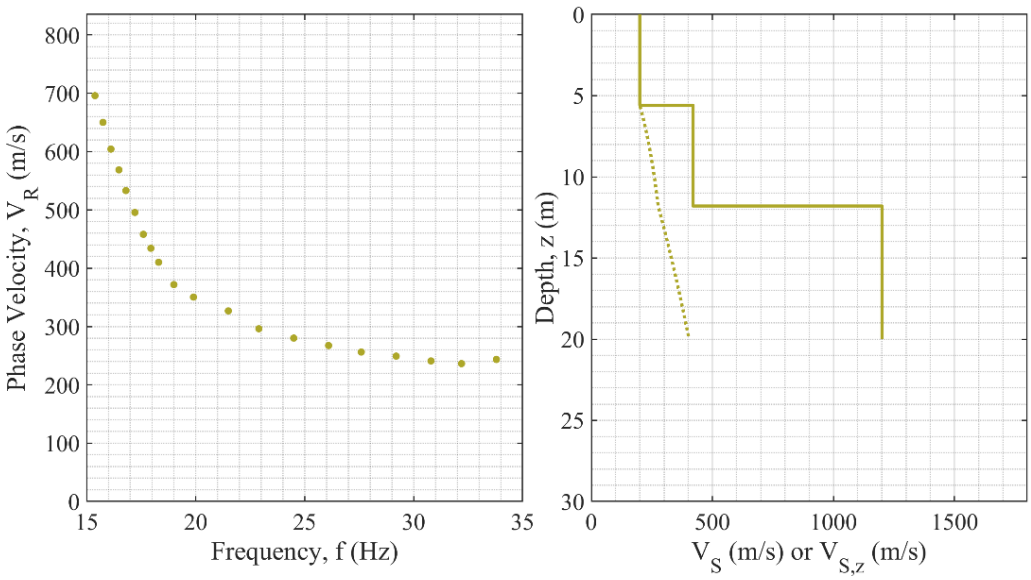

Figure A18. EDC (left), Vs and Vs,z (right) for Firenze-Uffizi (ID 18).

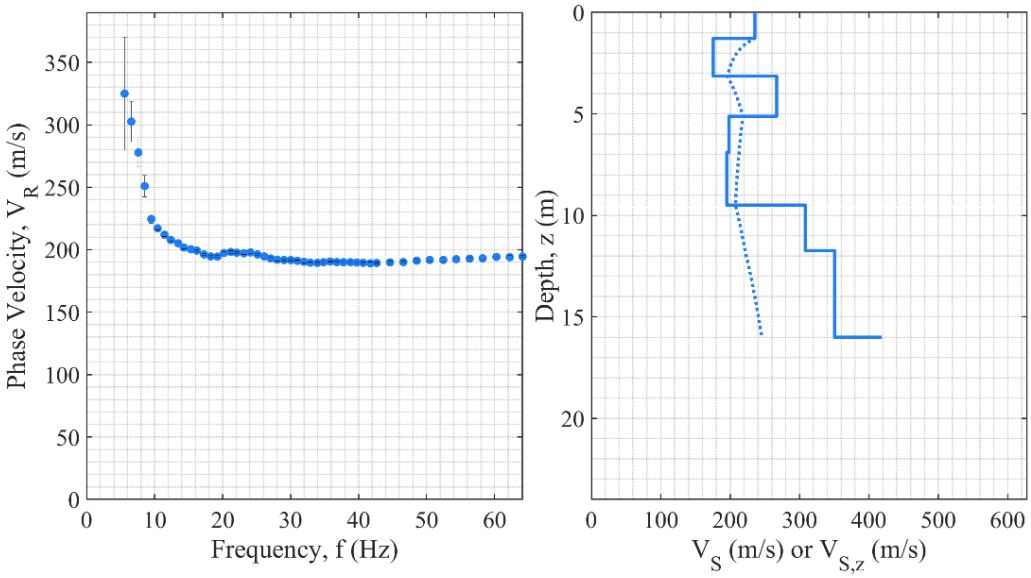

Figure A19. EDC (left), Vs and Vs,z (right) for Firenze-Via di Novoli (ID 19).

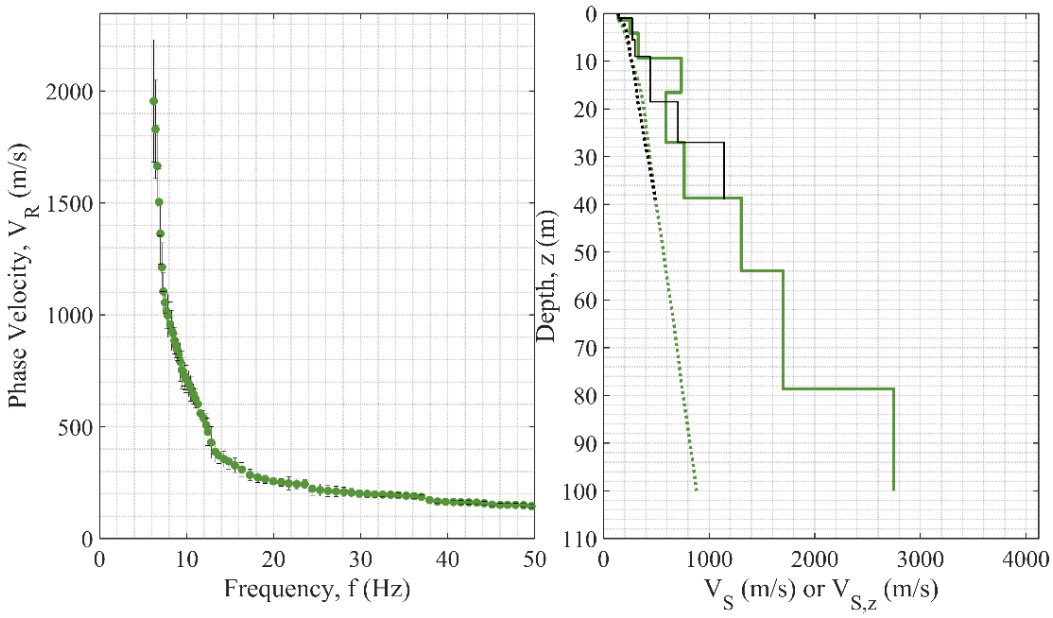

Figure A20. EDC (left), Vs and Vs,z (right) for Fonte del Campo (ID 20).

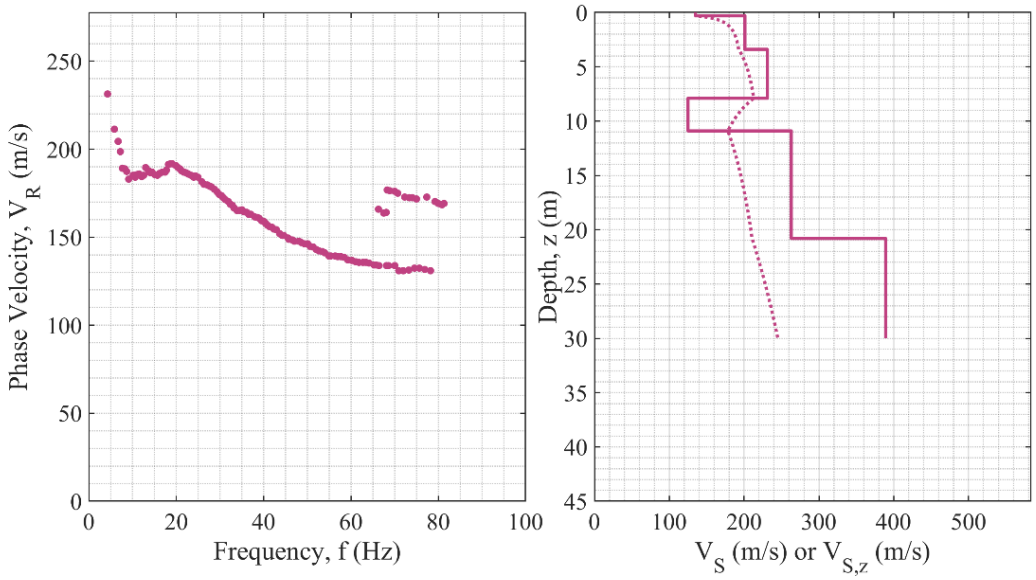

Figure A21. EDC (left), Vs and Vs,z (right) for GEA (ID 21).

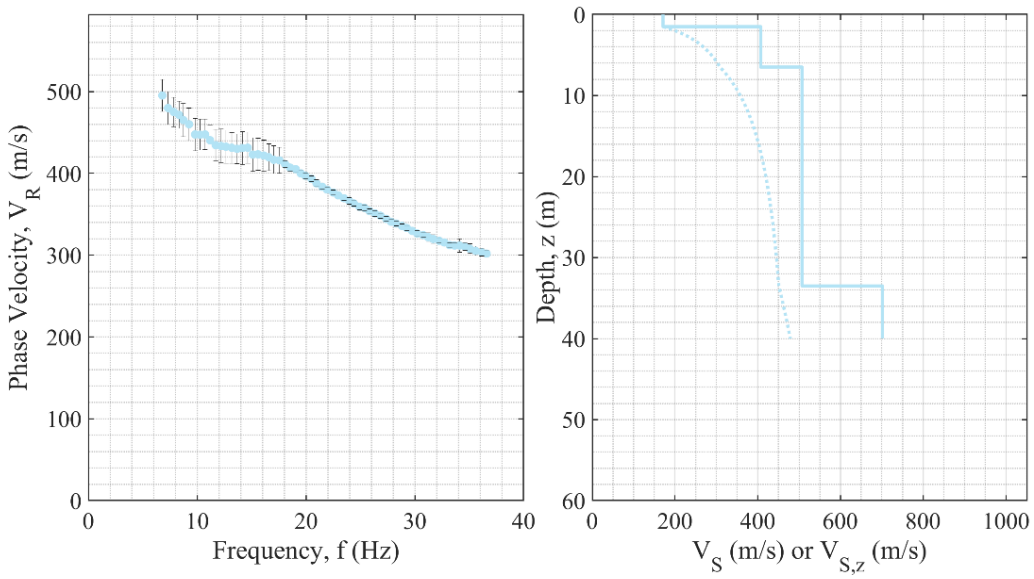

Figure A22. EDC (left), V_S and $V_{S,Z}$ (right) for GMN (ID 22).

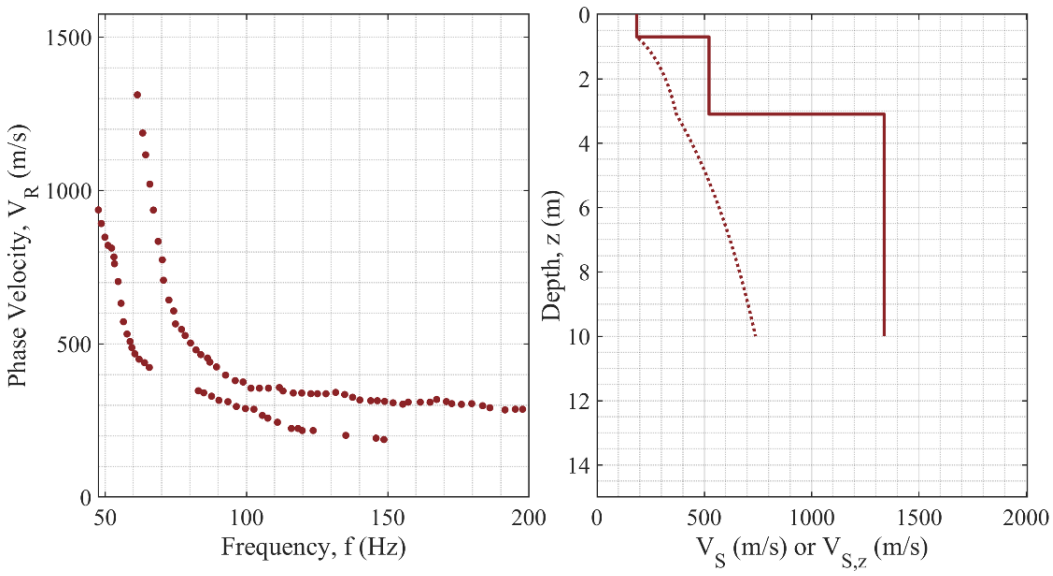

Figure A23. EDC (left), V_S and $V_{S,Z}$ (right) for GNV (ID 23).

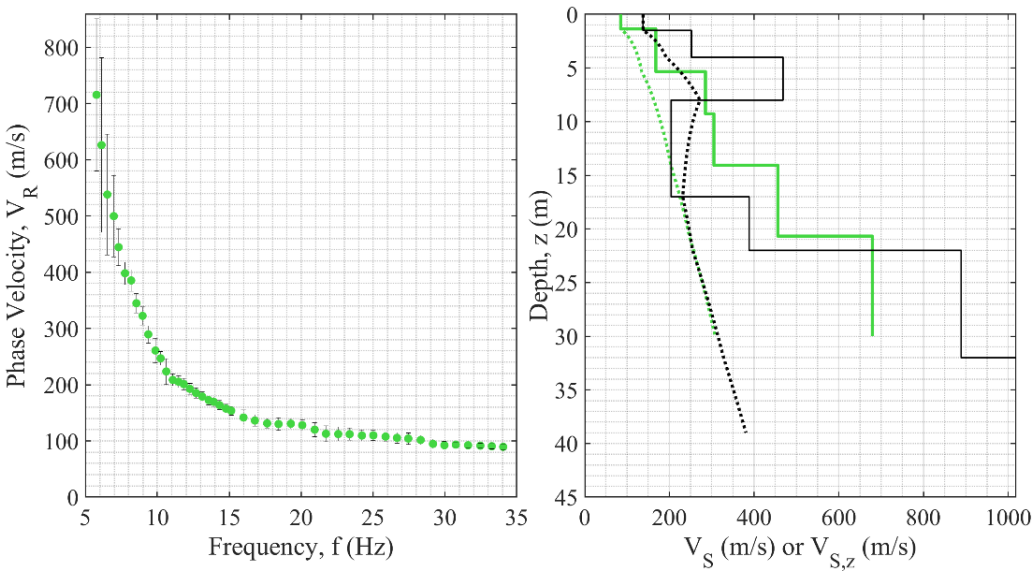

Figure A24. EDC (left), V_S and $V_{S,Z}$ (right) for GRI-Campo Sportivo-EW (ID 24).

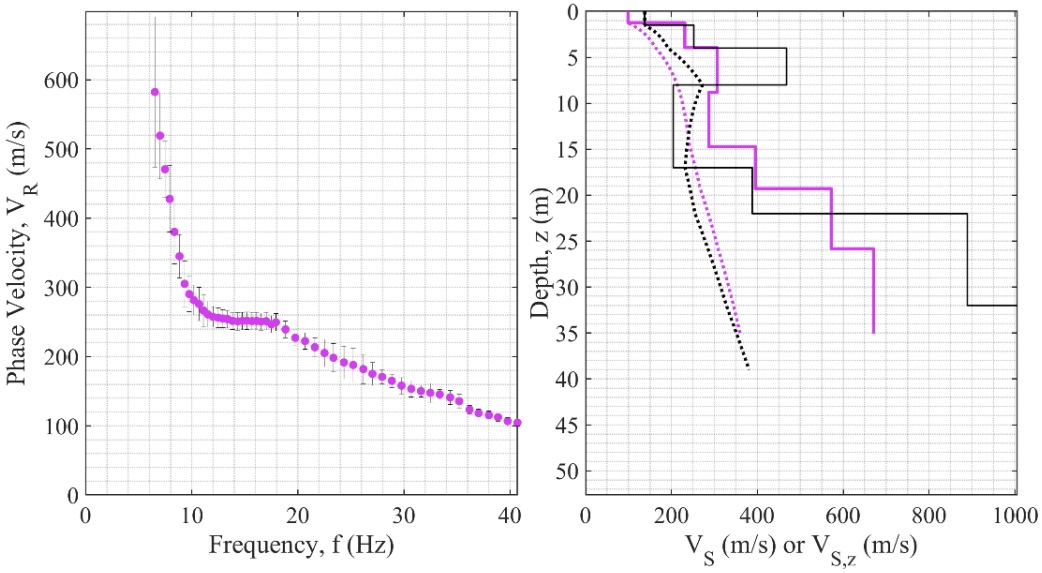

Figure A25. EDC (left), V_S and $V_{S,Z}$ (right) for GRI-Campo Sportivo-NS (ID 25).

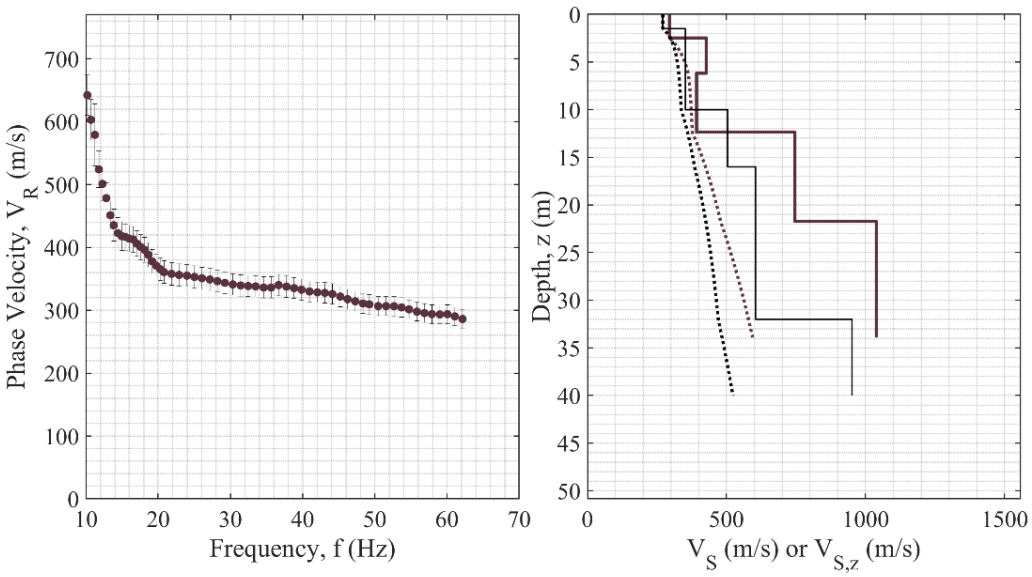

Figure A26. EDC (left), Vs and Vs,z (right) for Grisciano Conoide (ID 26).

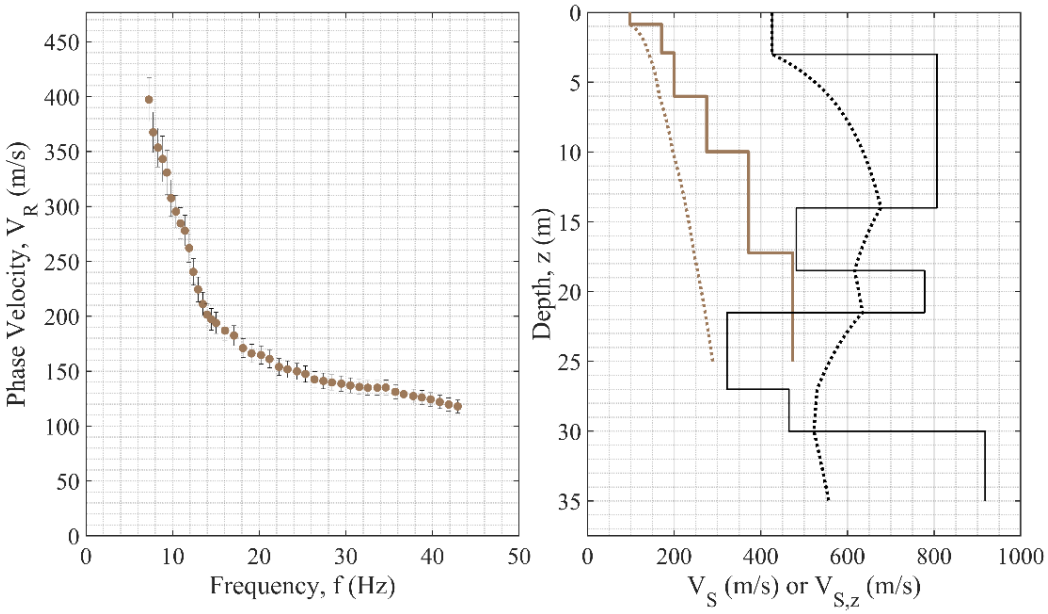

Figure A27. EDC (left), Vs and Vs,z (right) for Illica (ID 27).

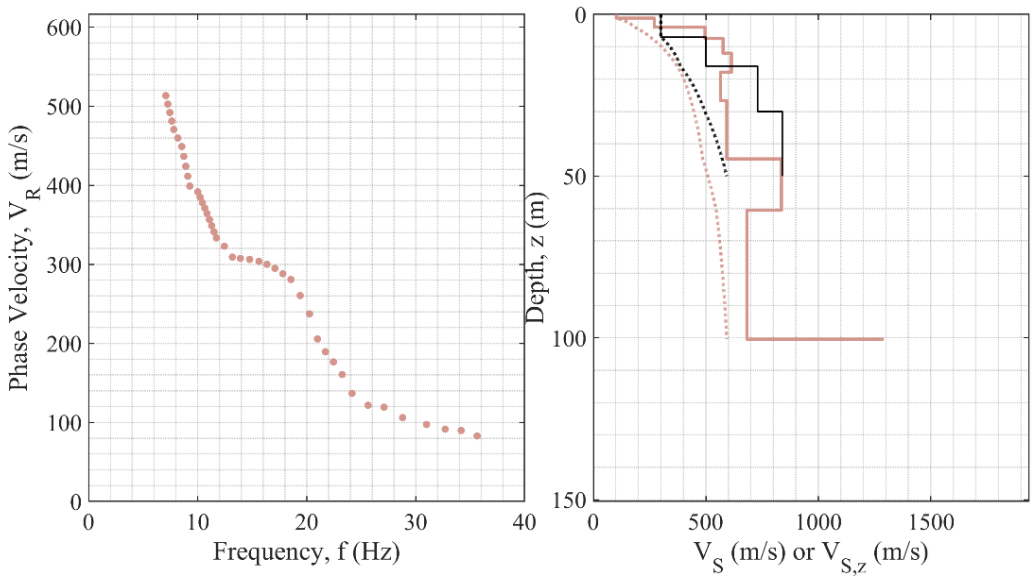

Figure A28. EDC (left), Vs and Vs,z (right) for La Salle A (ID 28).

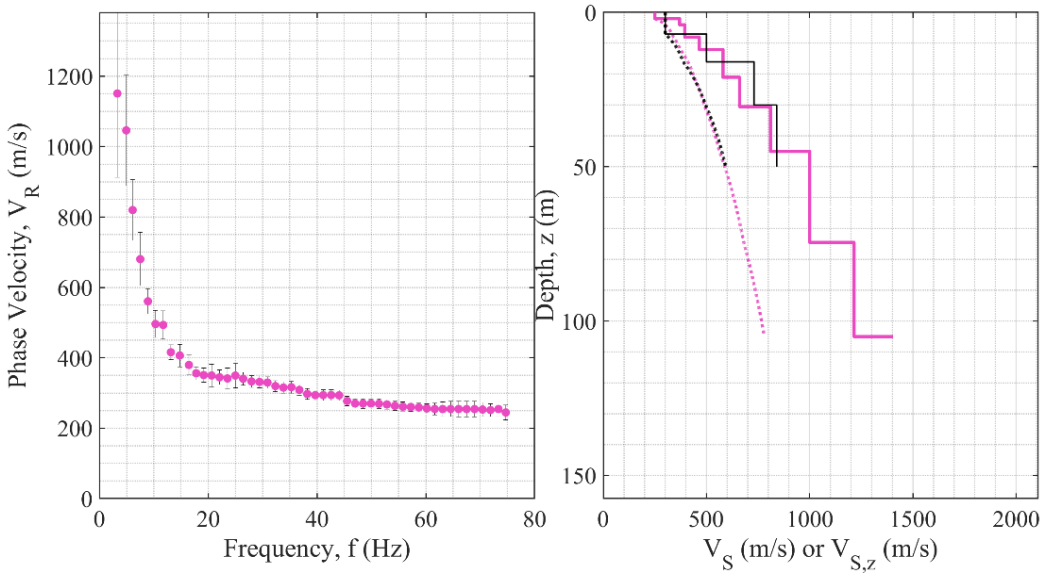

Figure A29. EDC (left), Vs and Vs,z (right) for La Salle B (ID 29).

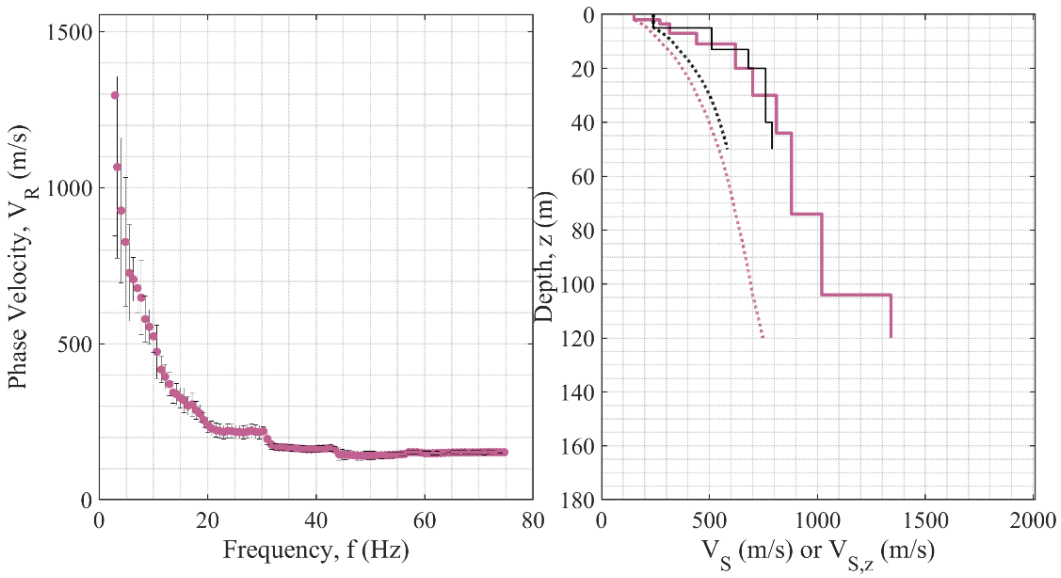

Figure A30. EDC (left), V_S and $V_{S,z}$ (right) for La Salle C (ID 30).

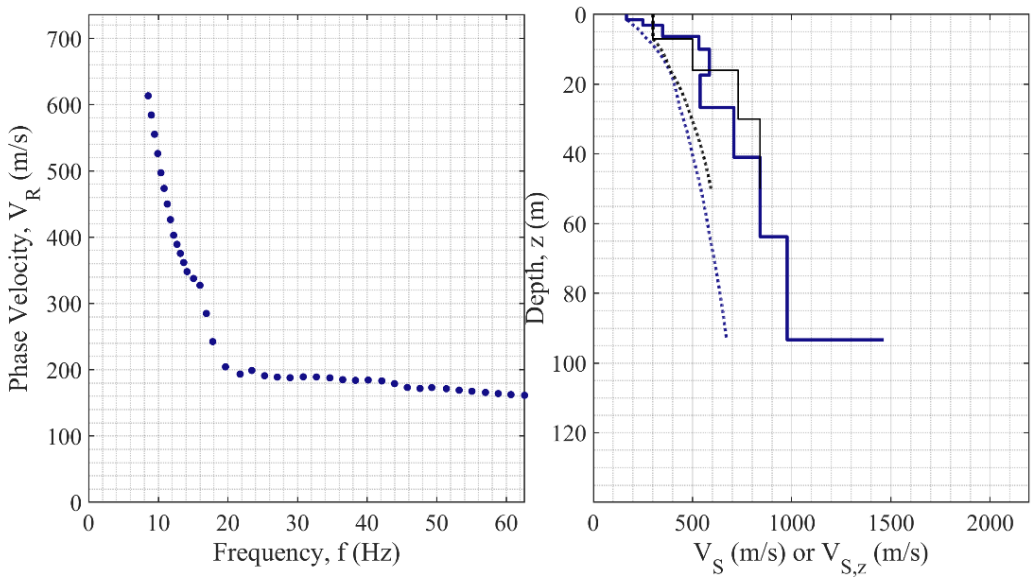

Figure A31. EDC (left), V_S and $V_{S,z}$ (right) for La Salle D (ID 31).

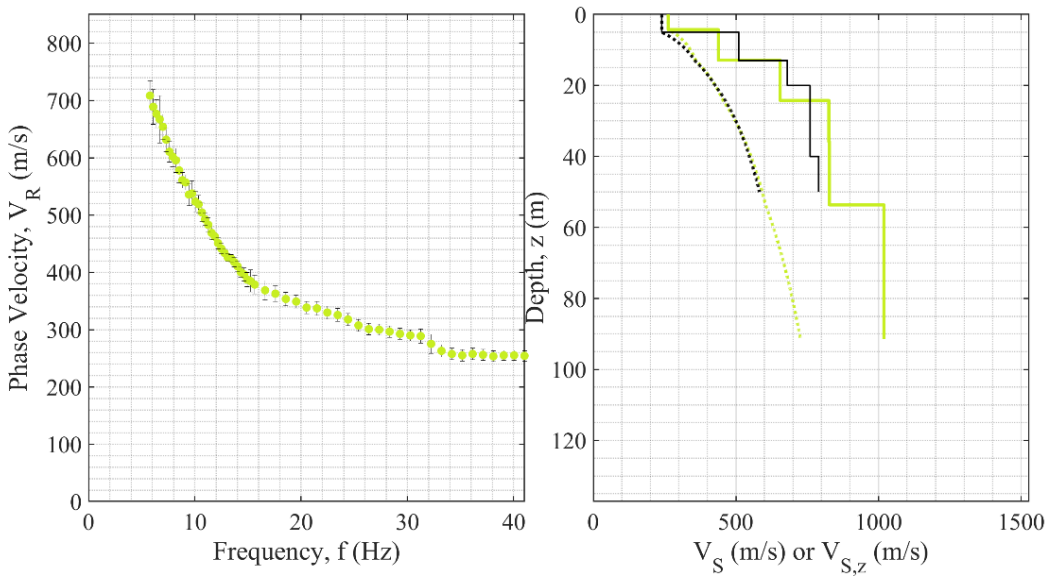

Figure A32. EDC (left), Vs and Vs,z (right) for La Salle E (ID 32).

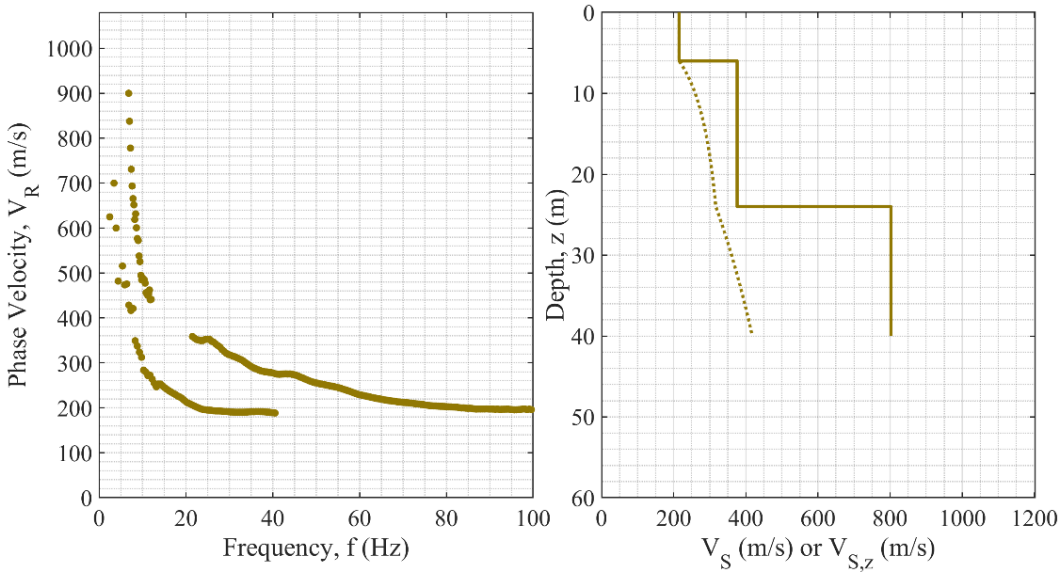

Figure A33. EDC (left), Vs and Vs,z (right) for L'Aquila (il Moro) (ID 33).

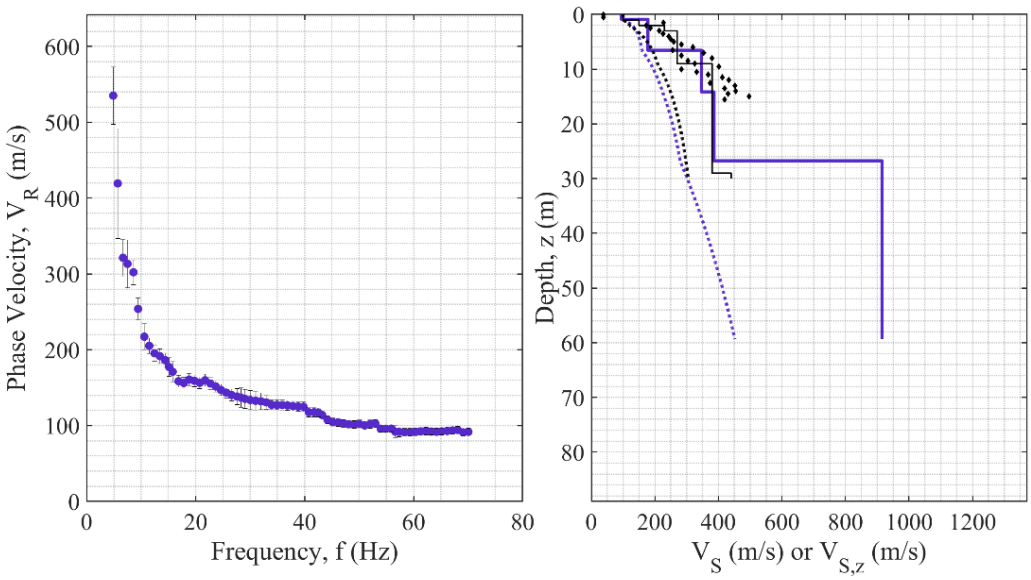

Figure A34. EDC (left), V_S and $V_{S,z}$ (right) for L'Aquila (Pianola) (ID 34).

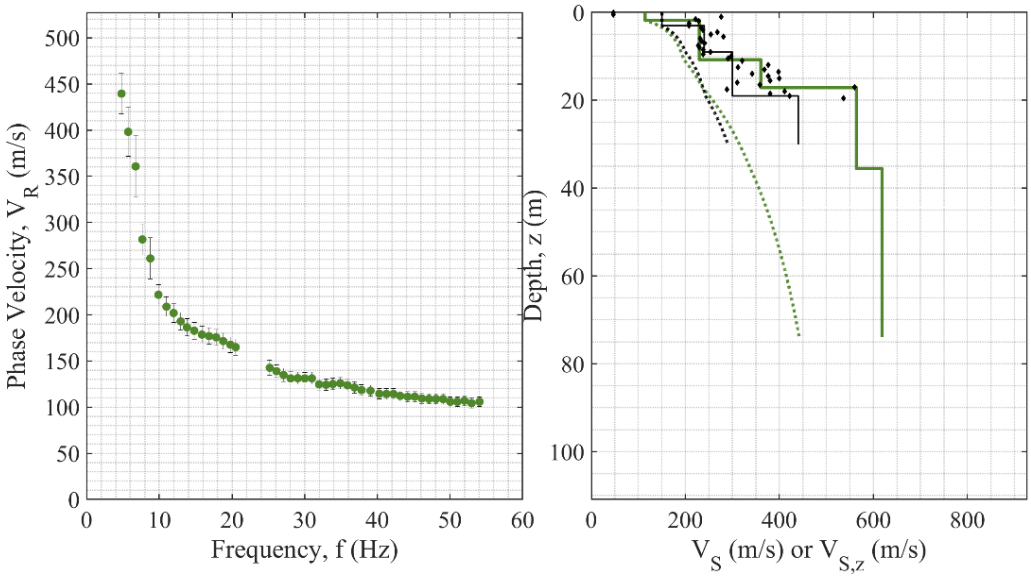

Figure A35. EDC (left), V_S and $V_{S,z}$ (right) for L'Aquila (Roio Piano) (ID 35).

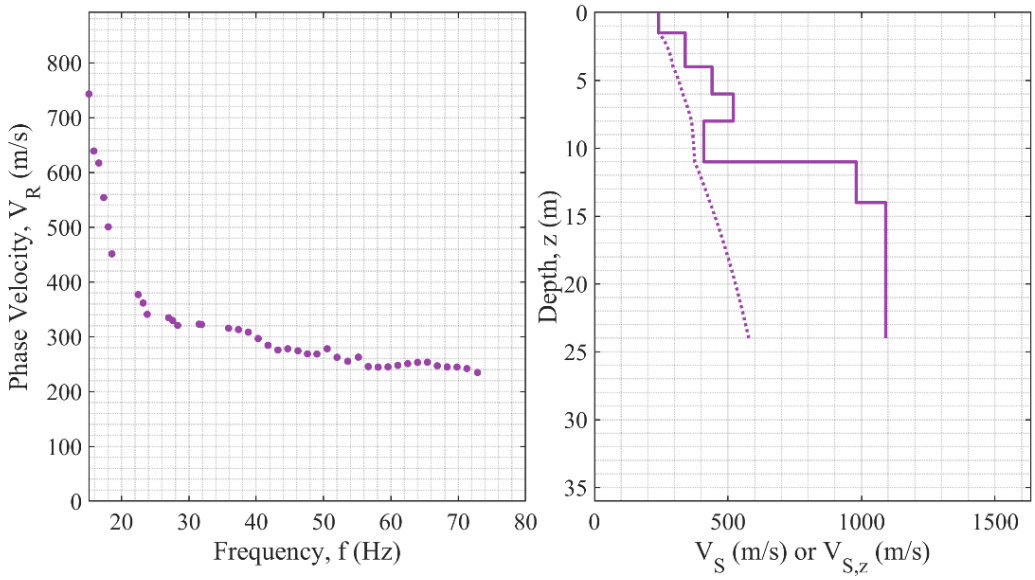

Figure A36. EDC (left), Vs and Vs,z (right) for Massa M.-Cantiere (ID 36).

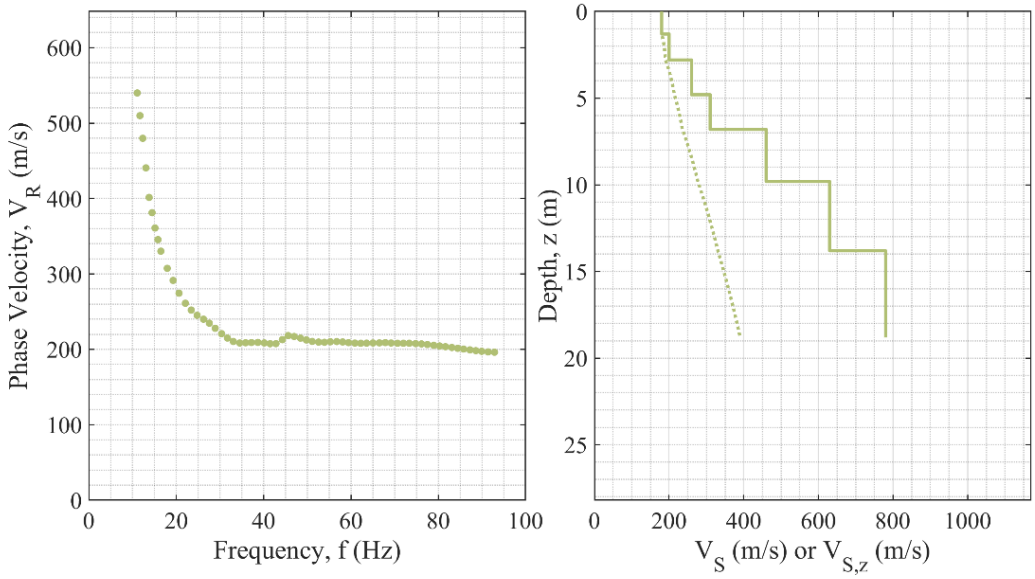

Figure A37. EDC (left), Vs and Vs,z (right) for Massa M.-Parcheggio (ID 37).

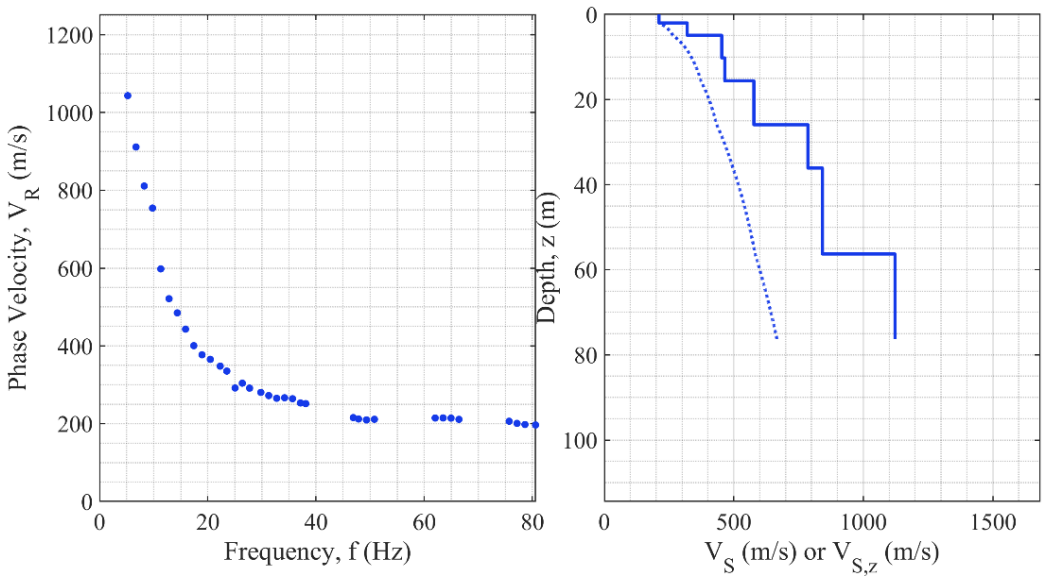

Figure A38. EDC (left), Vs and Vs,z (right) for Mathi-1&2 (ID 38).

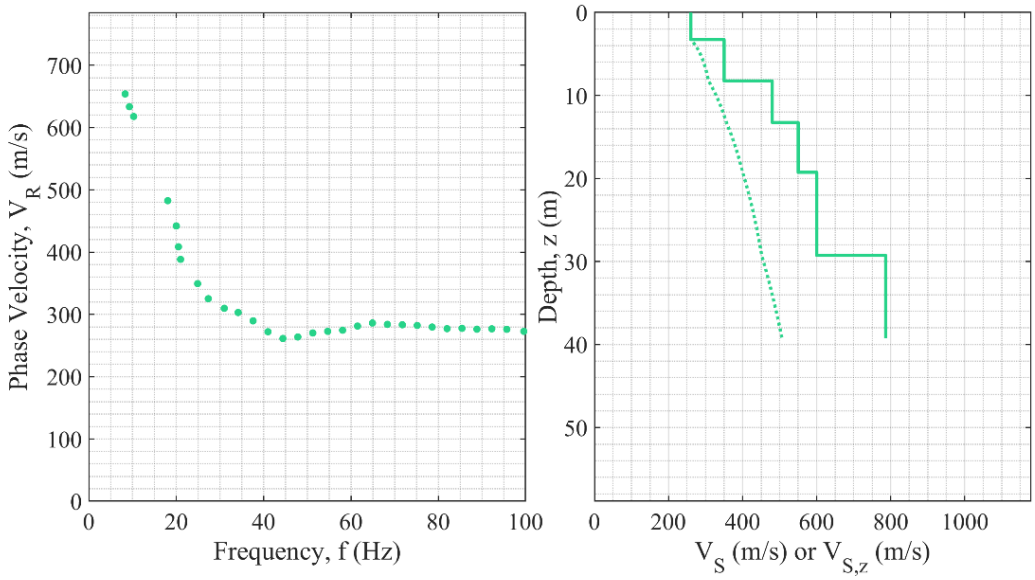

Figure A39. EDC (left), Vs and Vs,z (right) for Mathi-3 (ID 39).

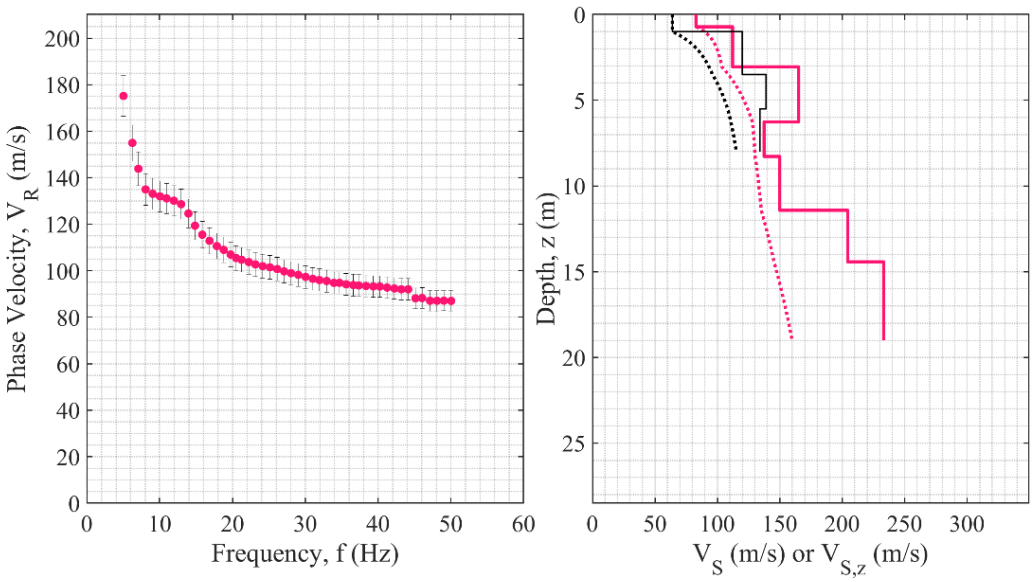

Figure A40. EDC (left), Vs and Vs,z (right) for Mirabello-Last-July (ID 40).

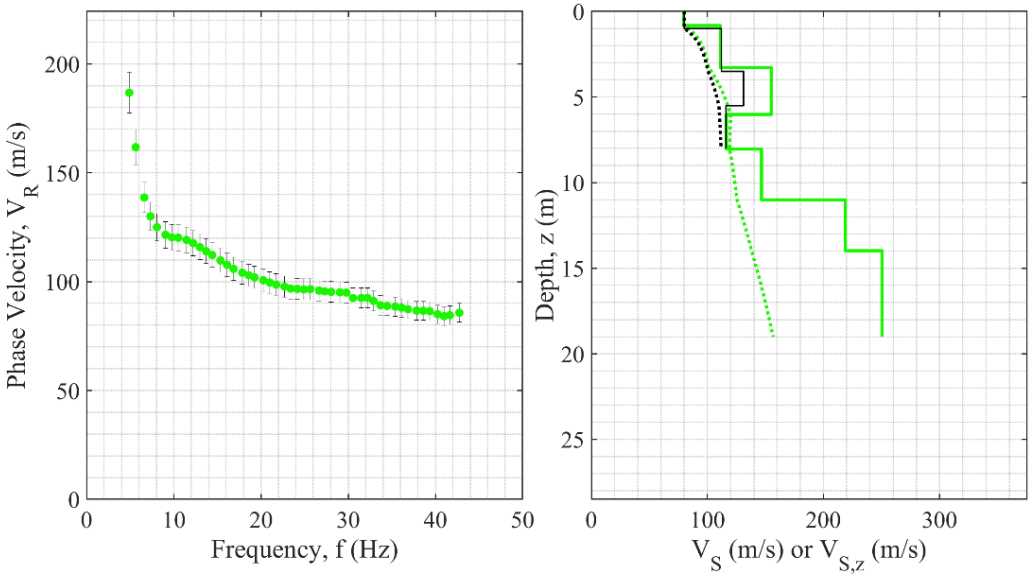

Figure A41. EDC (left), Vs and Vs,z (right) for Mirabello-Post-May (ID 41).

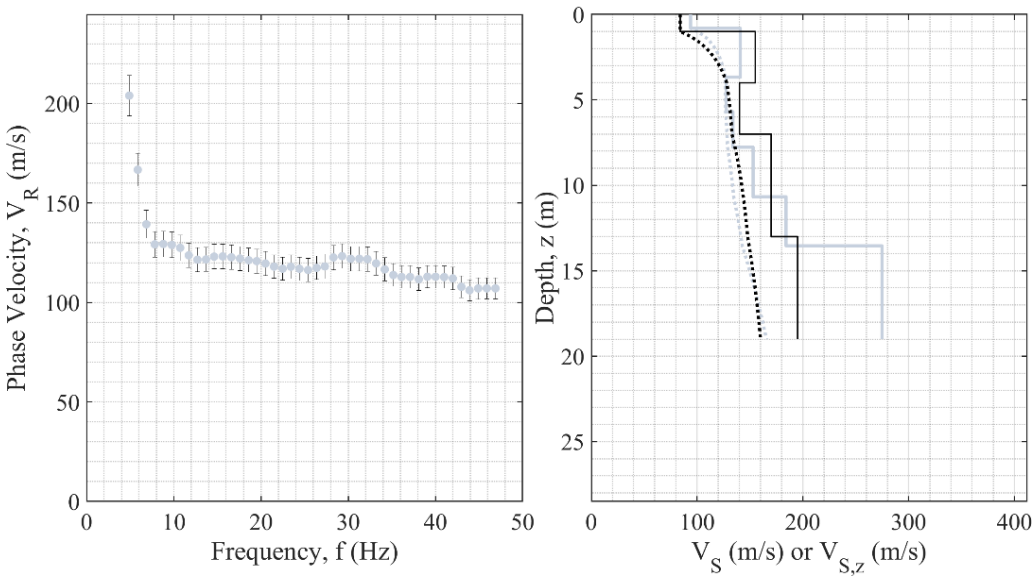

Figure A42. EDC (left), V_S and $V_{S,z}$ (right) for Mirabello-Pre-Feb (ID 42).

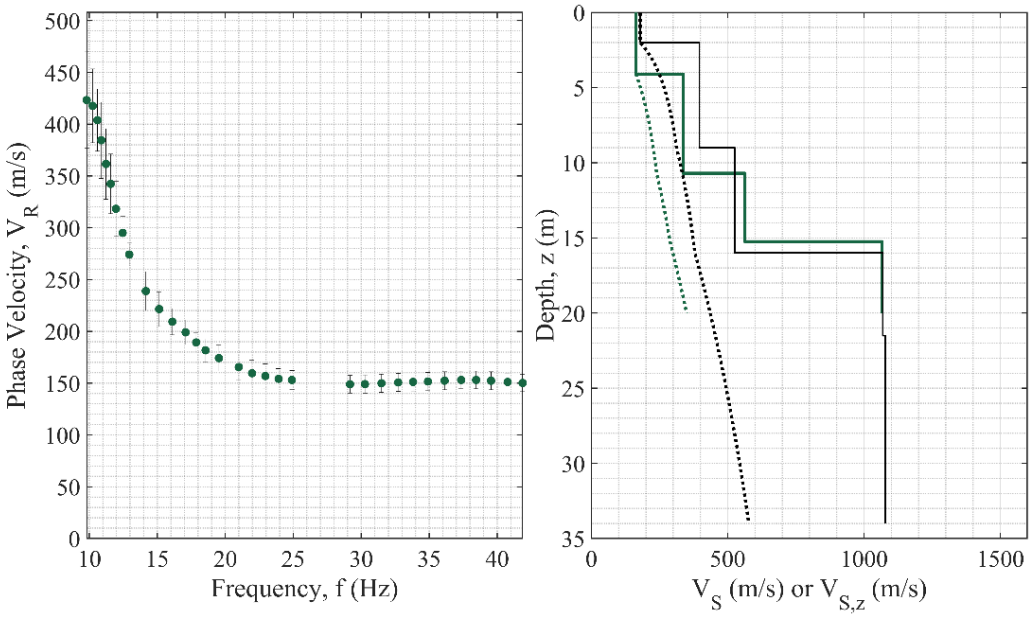

Figure A43. EDC (left), V_S and $V_{S,z}$ (right) for Montemonaco (ID 43).

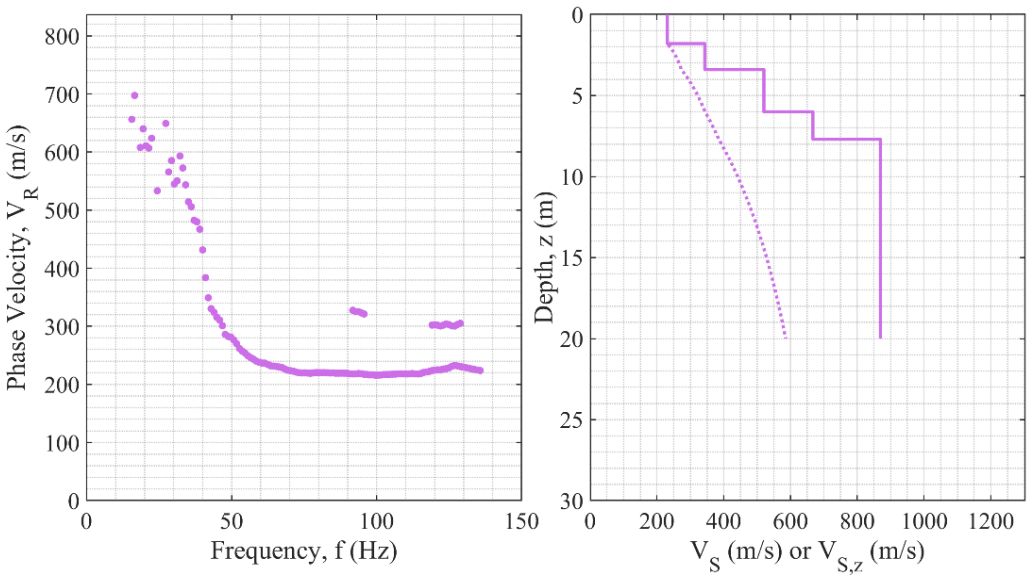

Figure A44. EDC (left), V_S and $V_{S,Z}$ (right) for NTE (ID 44).

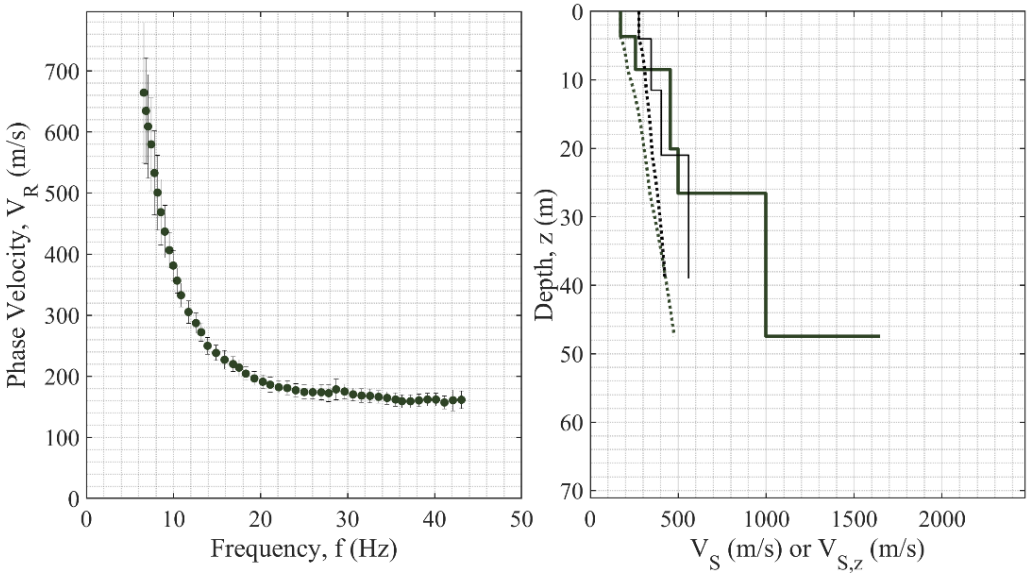

Figure A45. EDC (left), V_S and $V_{S,Z}$ (right) for Offida (ID 45).

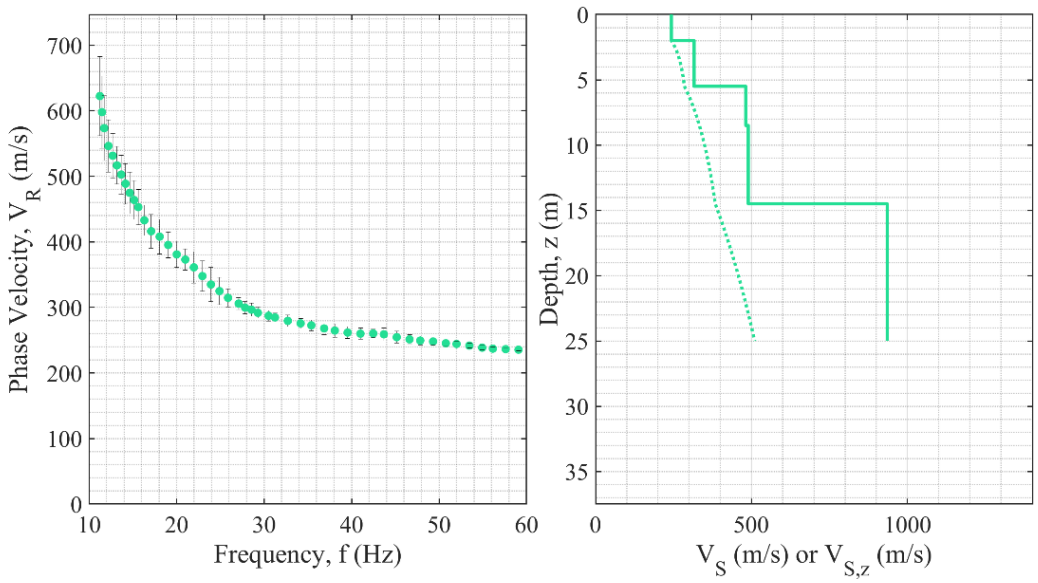

Figure A46. EDC (left), V_S and $V_{S,Z}$ (right) for Palmiano-Castel San Pietro (ID 46).

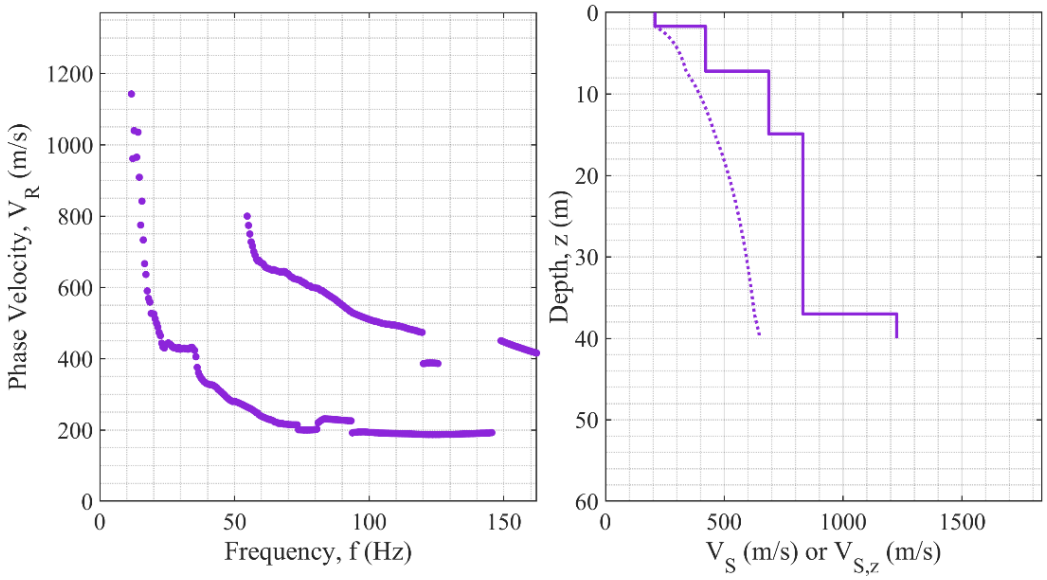

Figure A47. EDC (left), V_S and $V_{S,Z}$ (right) for PCH (ID 47).

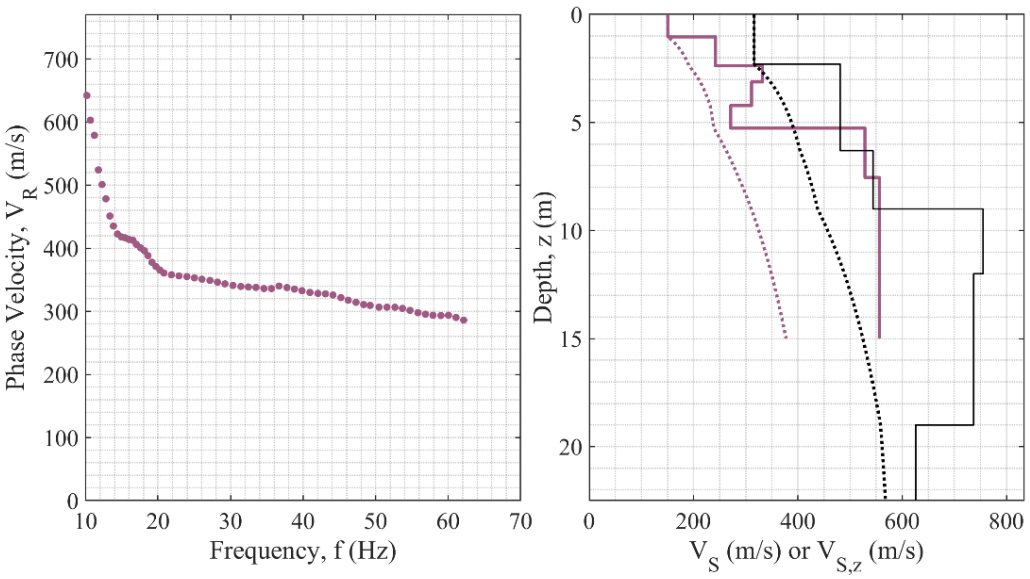

Figure A48. EDC (left), V_S and $V_{S,z}$ (right) for Piazza al Serchio (ID 48).

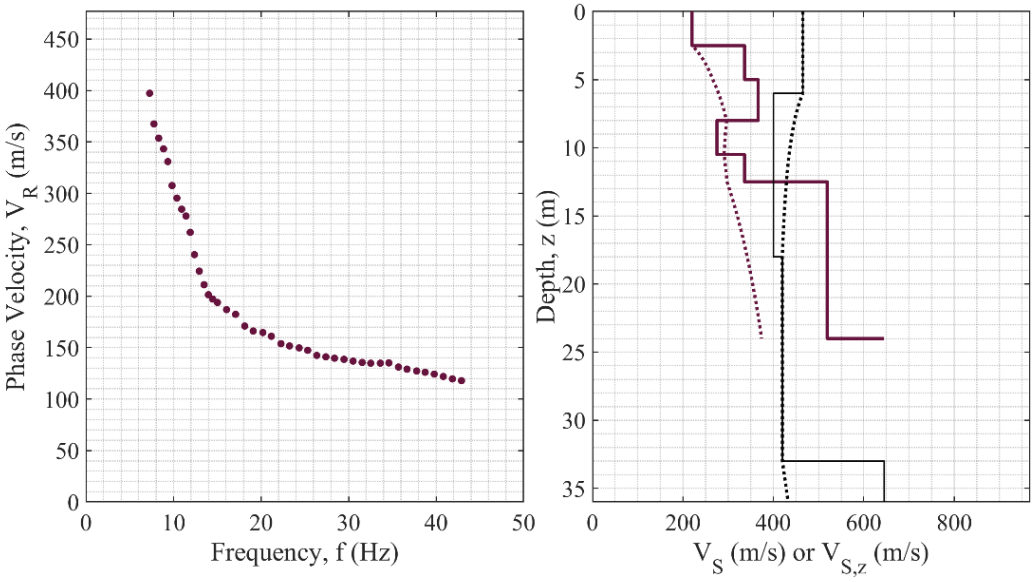

Figure A49. EDC (left), V_S and $V_{S,z}$ (right) for Pieve Fosciana (ID 49).

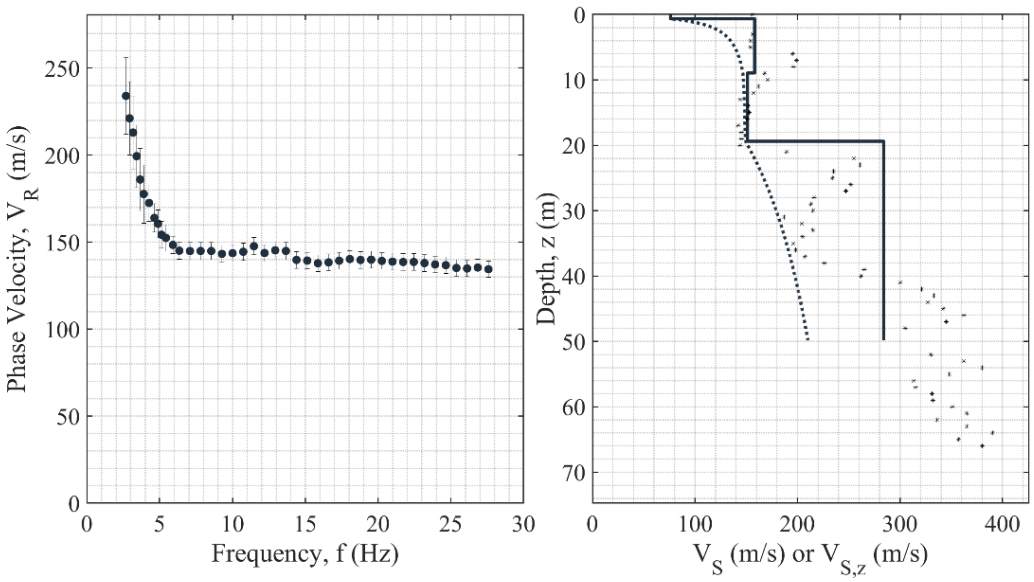

Figure A50. EDC (left), V_S and $V_{S,z}$ (right) for Pisa (ID 50).

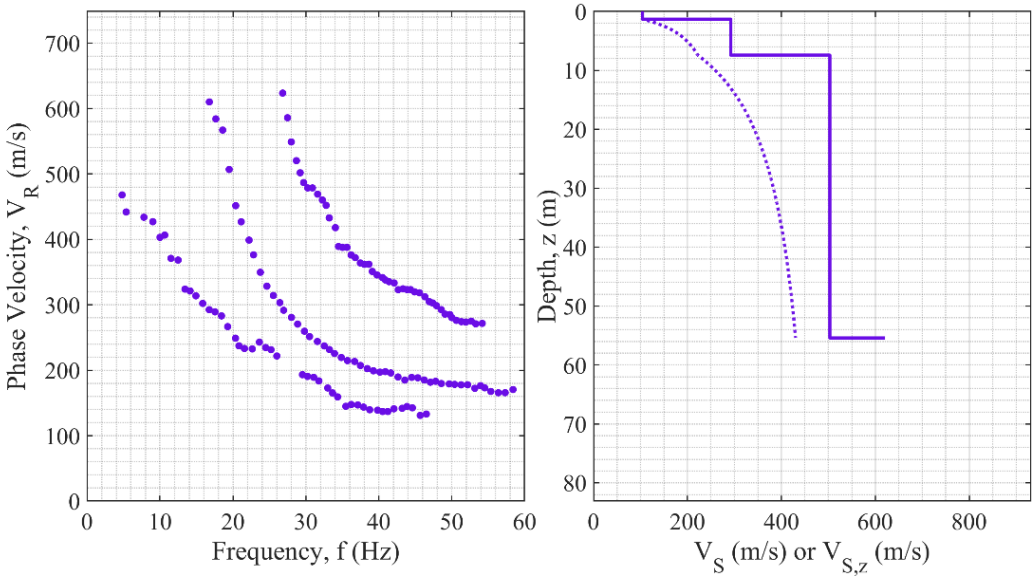

Figure A51. EDC (left), V_S and $V_{S,z}$ (right) for PNR (ID 51).

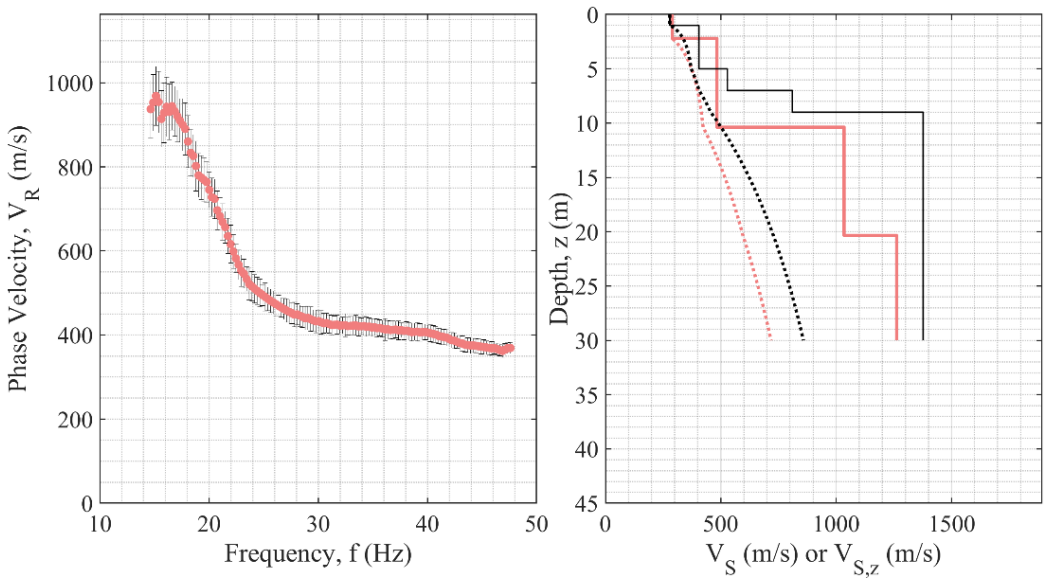

Figure A52. EDC (left), Vs and Vs,z (right) for Pontremoli-1 Maggio (ID 52).

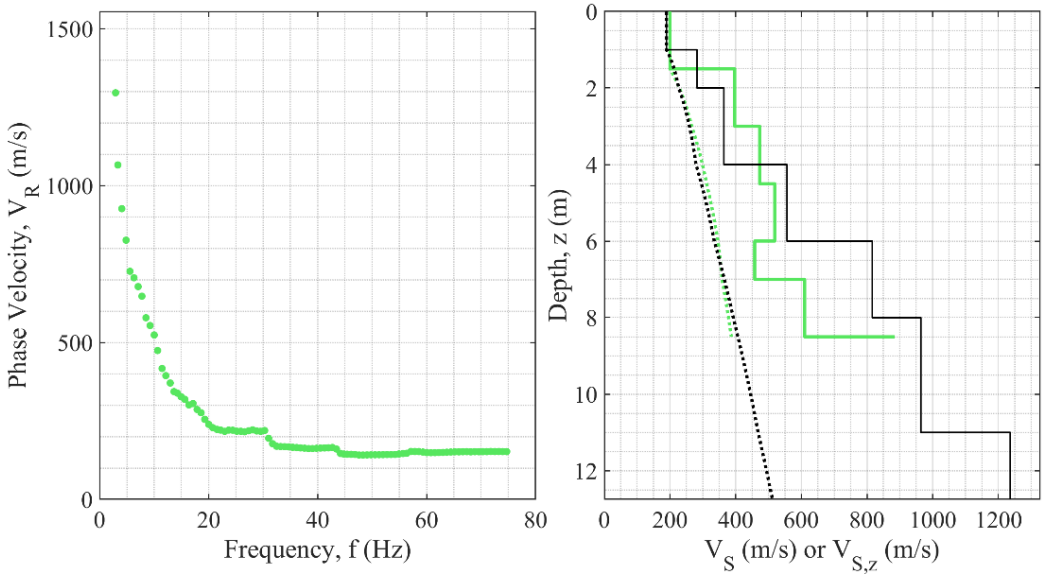

Figure A53. EDC (left), Vs and Vs,z (right) for Pontremoli-ASL 2 (ID 53).

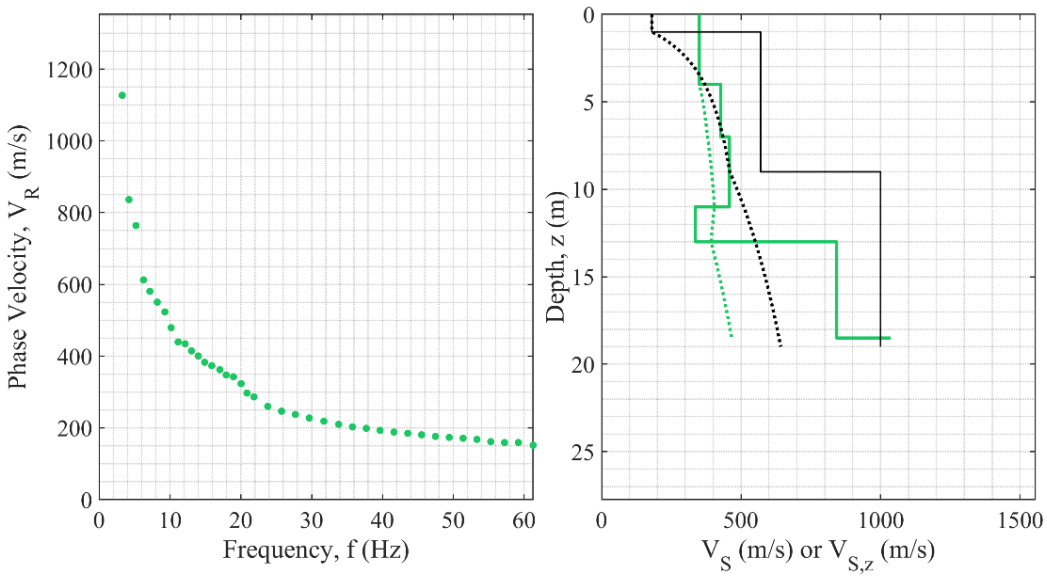

Figure A54. EDC (left), V_S and $V_{S,Z}$ (right) for Pontremoli-Bocciofila (ID 54).

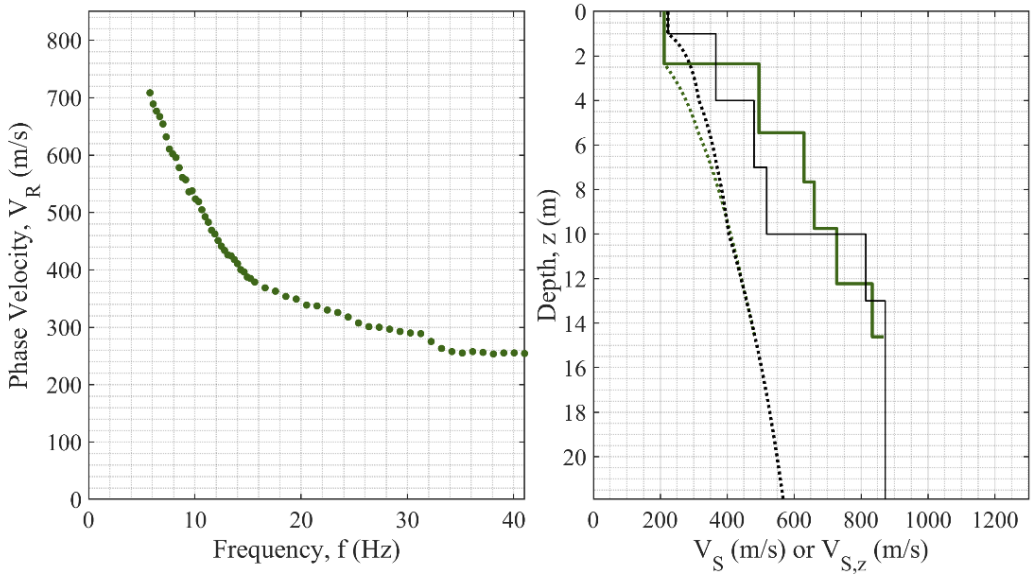

Figure A55. EDC (left), V_S and $V_{S,Z}$ (right) for Pontremoli-Giochi (ID 55).

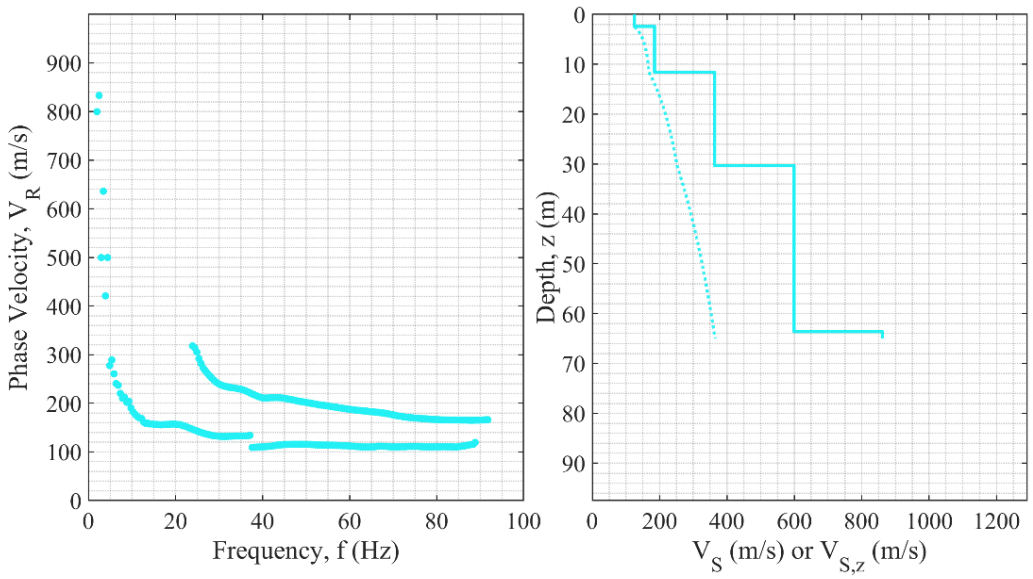

Figure A56. EDC (left), V_S and $V_{S,Z}$ (right) for PTT0 (ID 56).

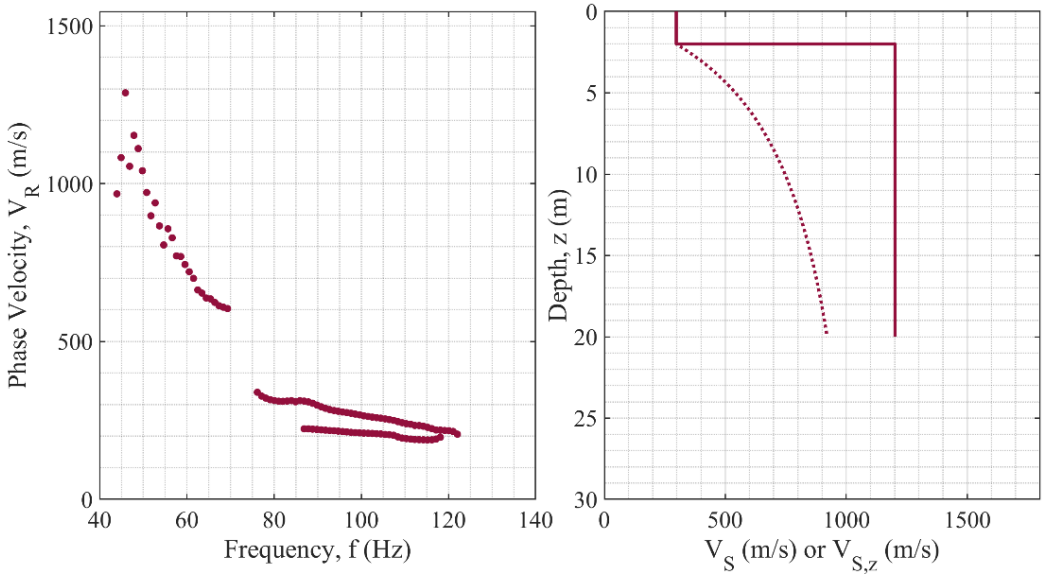

Figure A57. EDC (left), V_S and $V_{S,Z}$ (right) for RGS (ID 57).

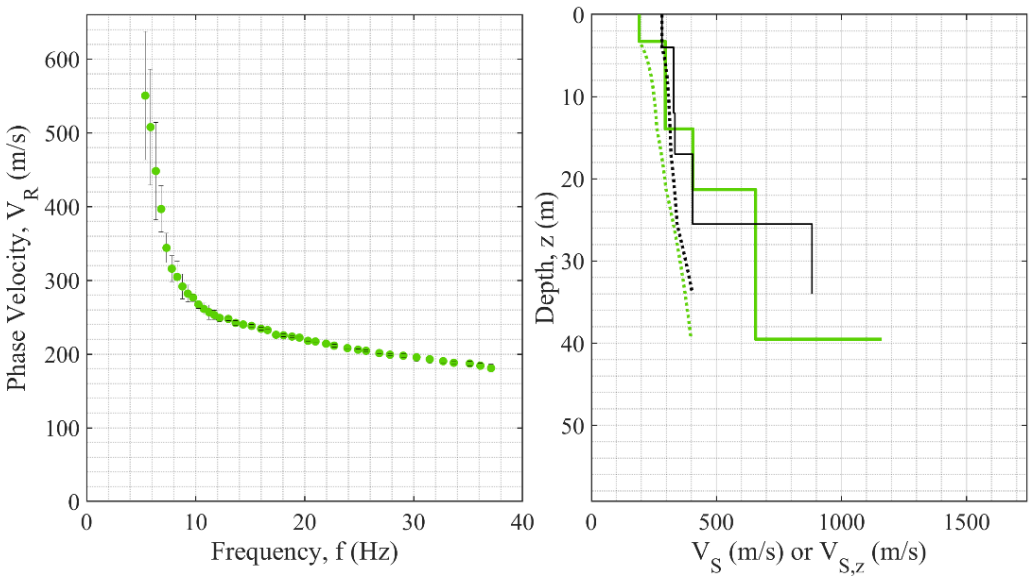

Figure A58. EDC (left), V_S and $V_{S,z}$ (right) for Roccafluvione (ID 58).

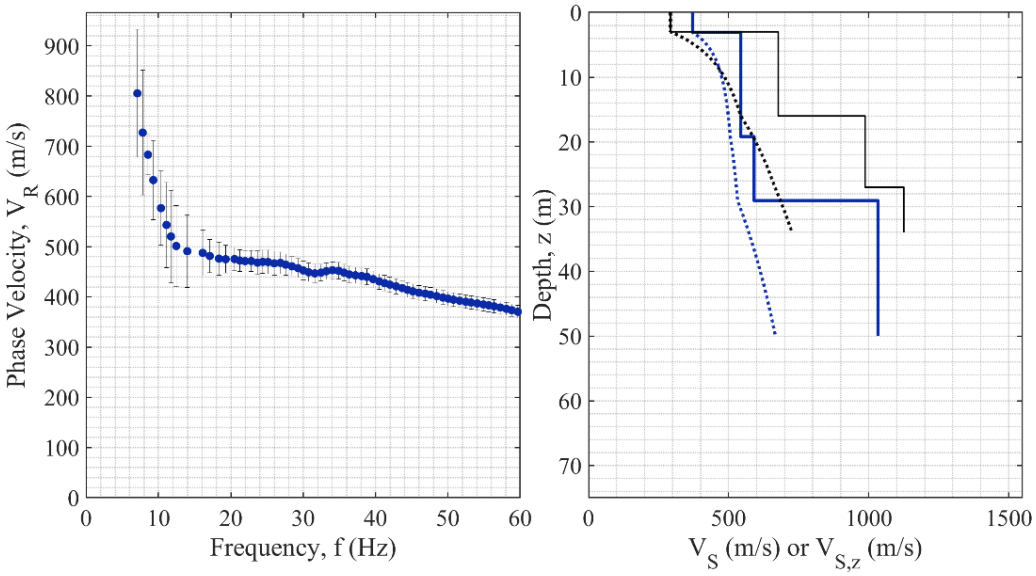

Figure A59. EDC (left), V_S and $V_{S,z}$ (right) for Rotella (ID 59).

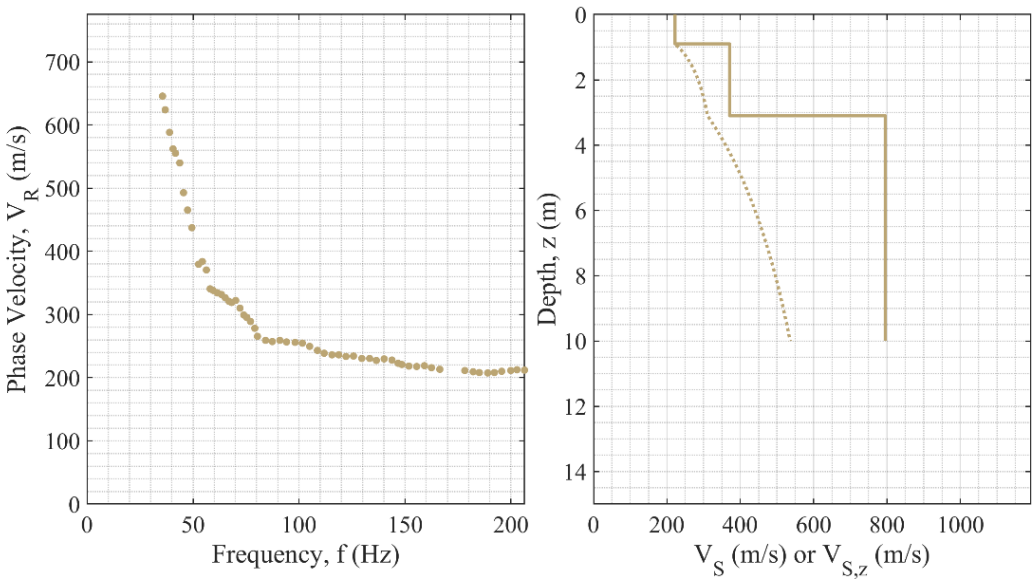

Figure A60. EDC (left), V_S and $V_{S,z}$ (right) for RNS (ID 60).

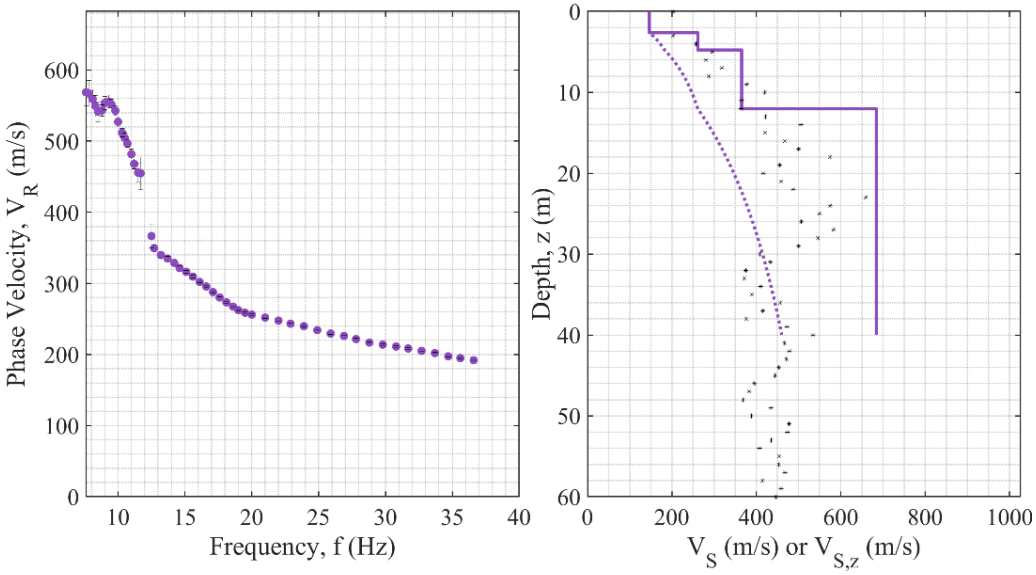

Figure A61. EDC (left), V_S and $V_{S,z}$ (right) for Saluggia (ID 61).

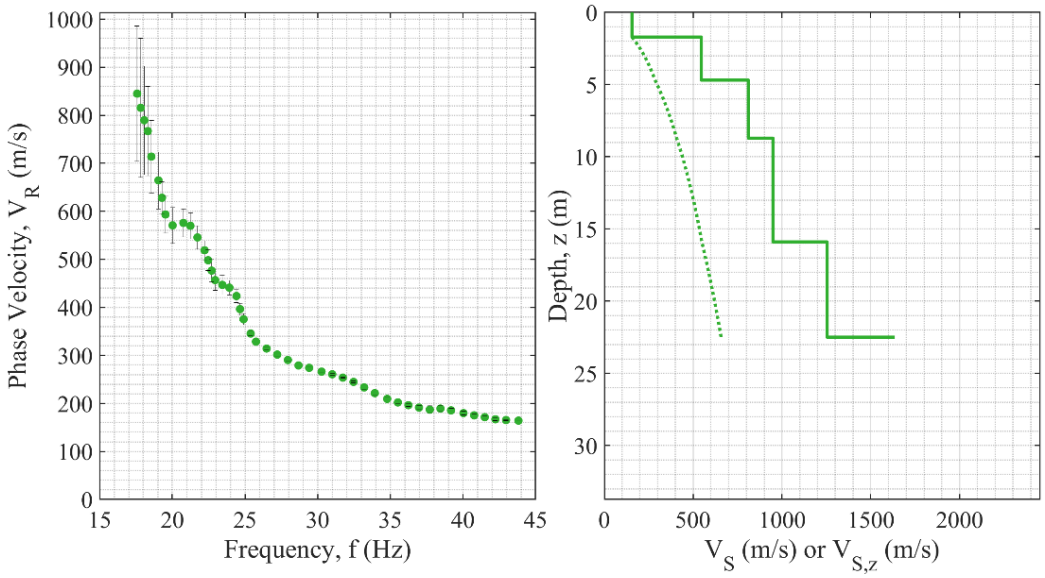

Figure A62. EDC (left), Vs and Vs,z (right) for San Severino Marche-1 (ID 62).

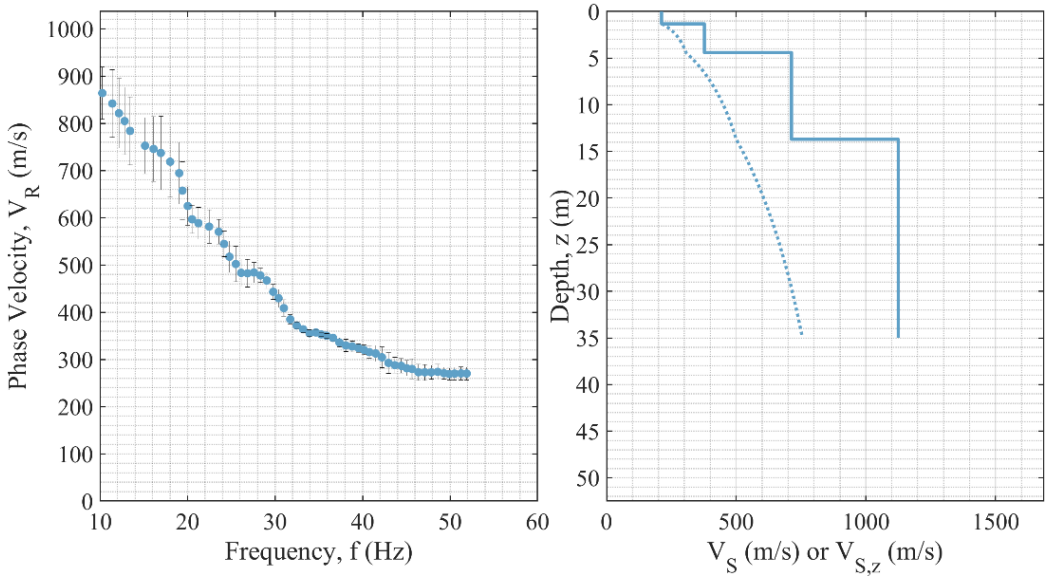

Figure A63. EDC (left), Vs and Vs,z (right) for San Severino Marche-2 (ID 63).

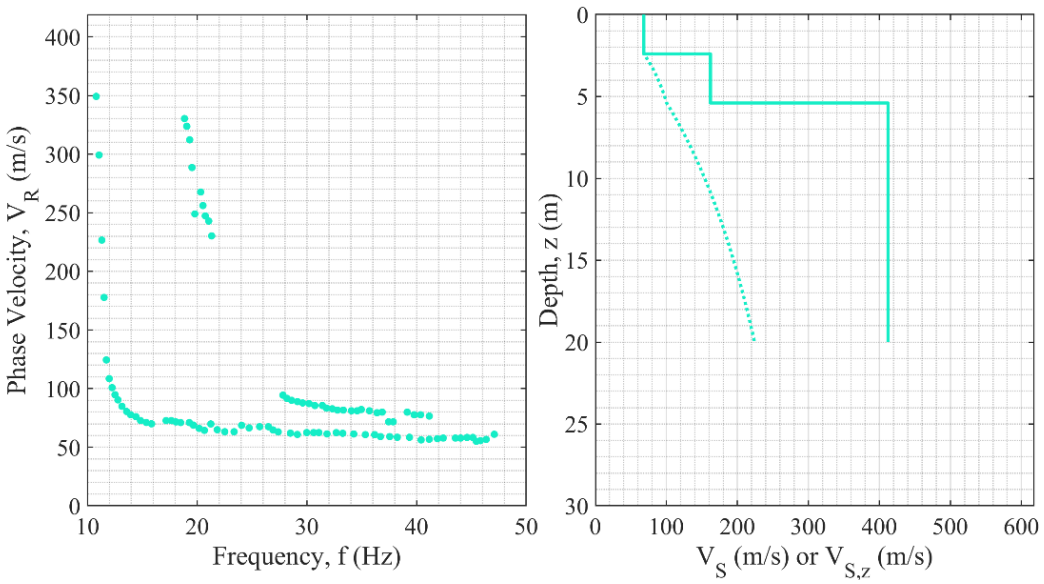

Figure A64. EDC (left), Vs and Vs,z (right) for Sarno-Connola (ID 64).

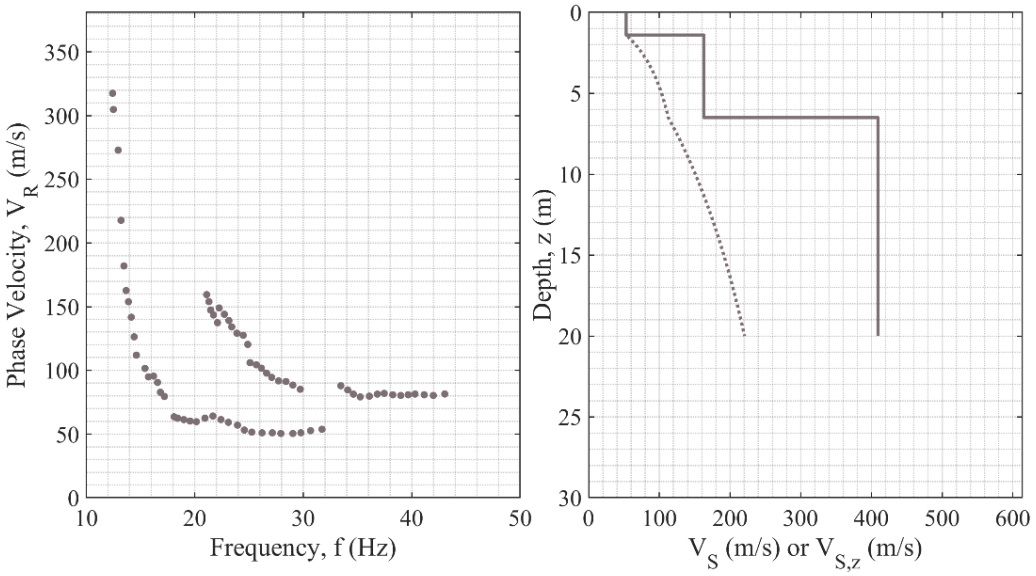

Figure A65. EDC (left), Vs and Vs,z (right) for Sarno-Santa Lucia (ID 65).

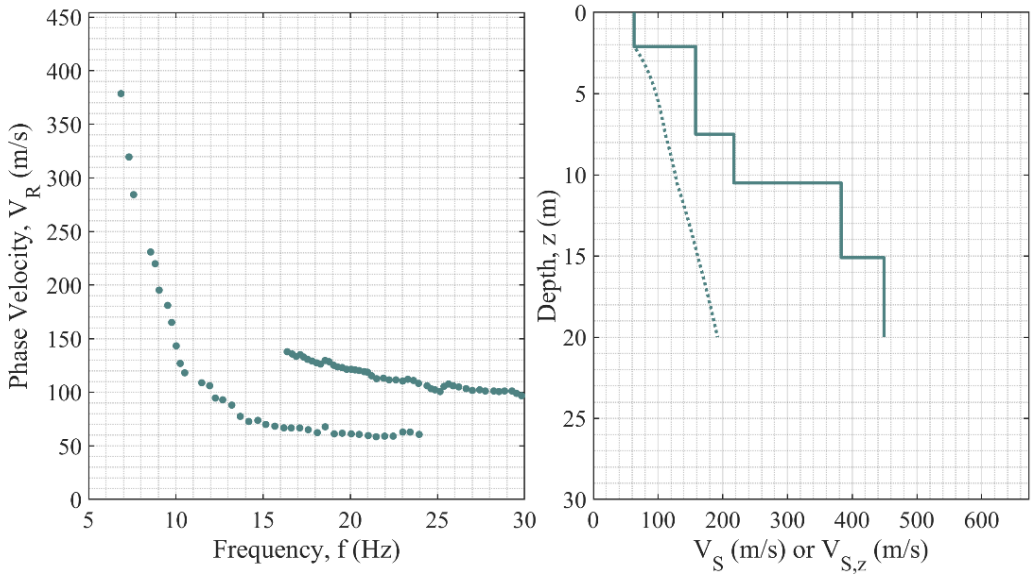

Figure A66. EDC (left), Vs and Vs,z (right) for Sarno-Tuostolo (ID 66).

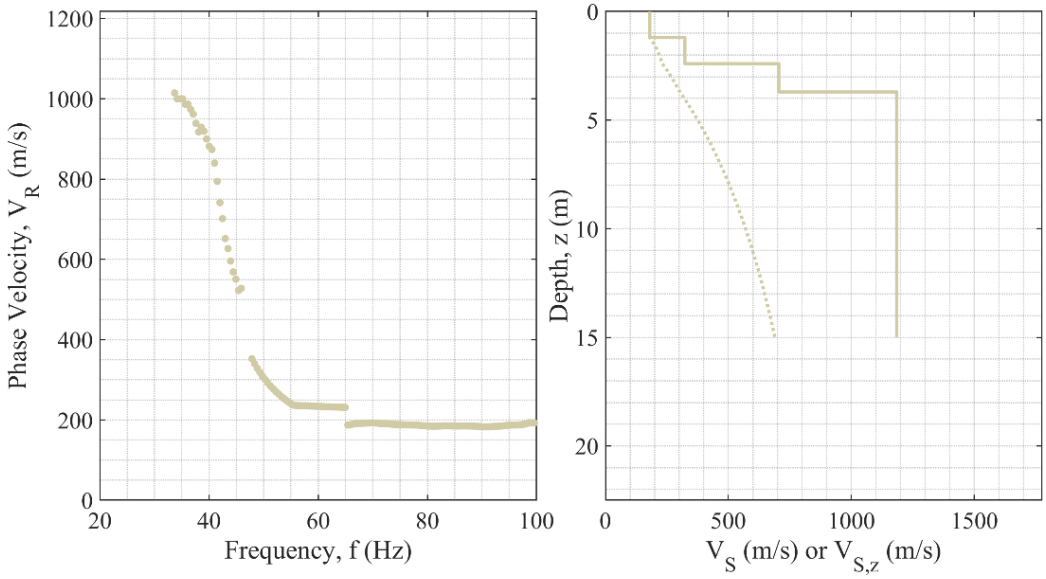

Figure A67. EDC (left), Vs and Vs,z (right) for SCR (ID 67).

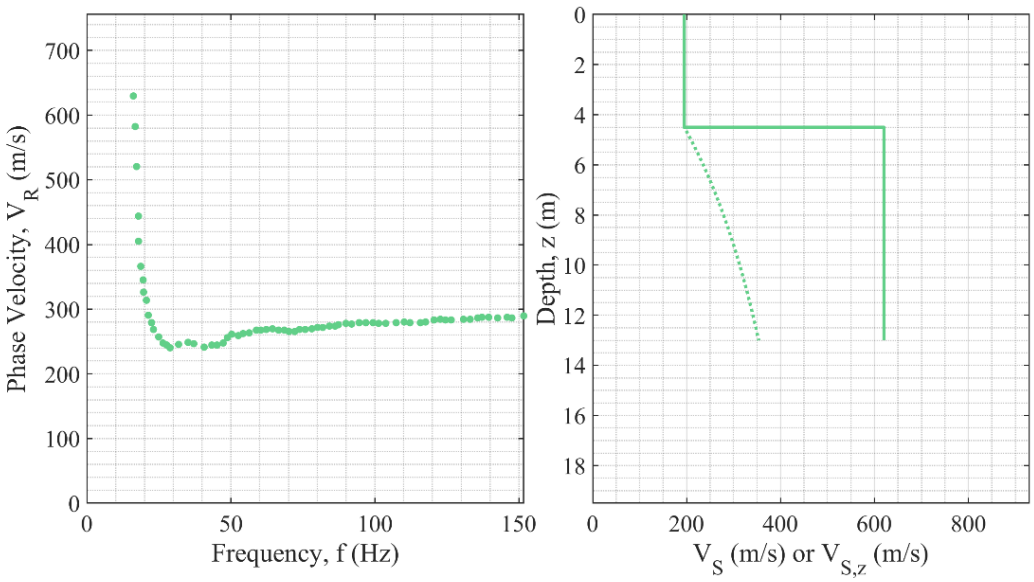

Figure A68. EDC (left), V_S and $V_{S,z}$ (right) for SEL (ID 68).

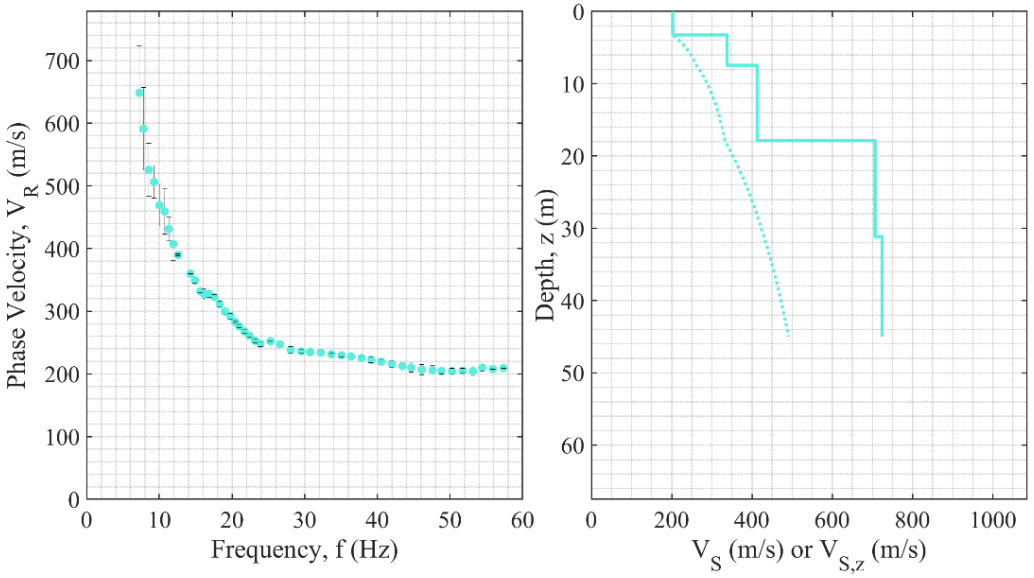

Figure A69. EDC (left), V_S and $V_{S,z}$ (right) for Settimo Torinese (ID 69).

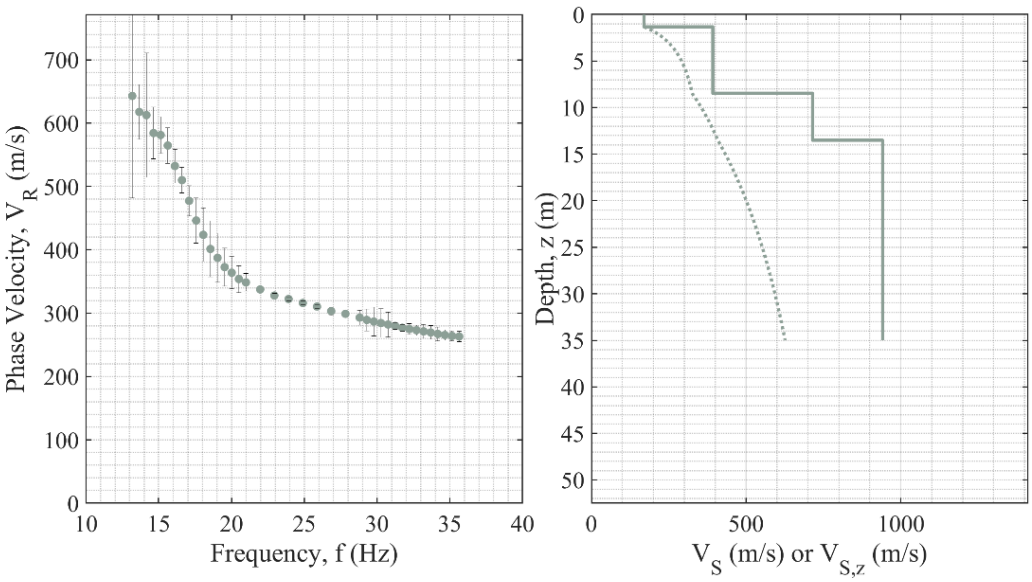

Figure A70. EDC (left), Vs and Vs,z (right) for Tarcento-1 (ID 70).

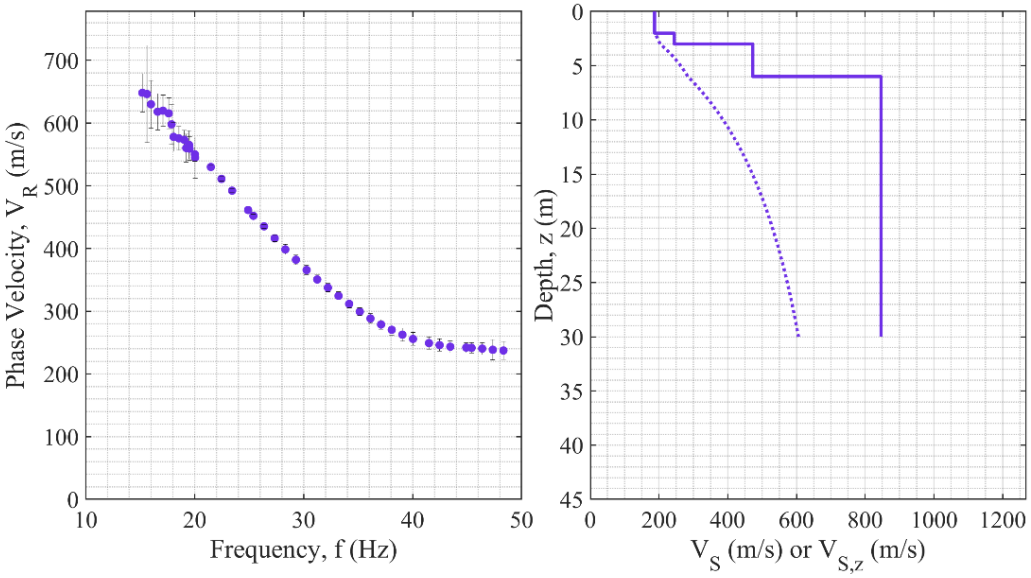

Figure A71. EDC (left), Vs and Vs,z (right) for Tarcento-2 (ID 71).

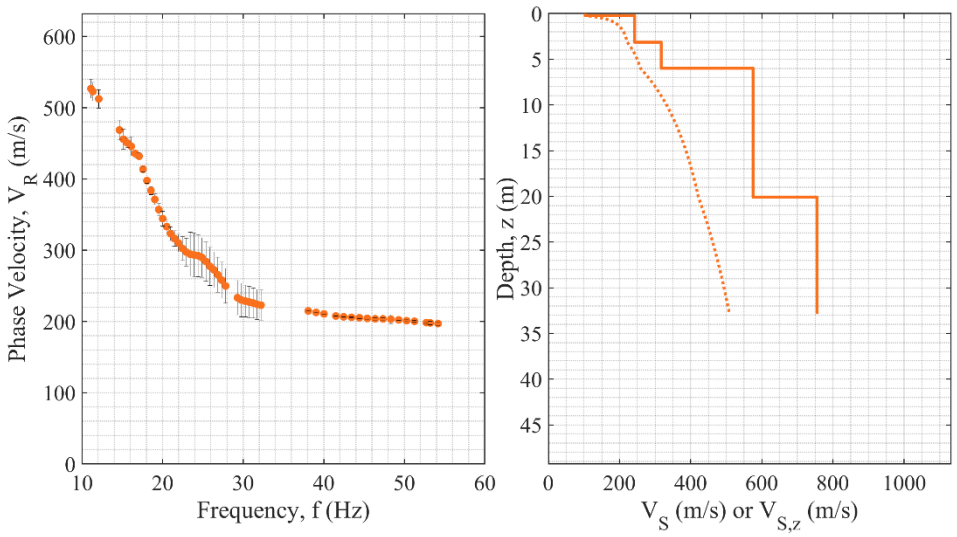

Figure A72. EDC (left), Vs and Vs,z (right) for Tarcento-3 (ID 72).

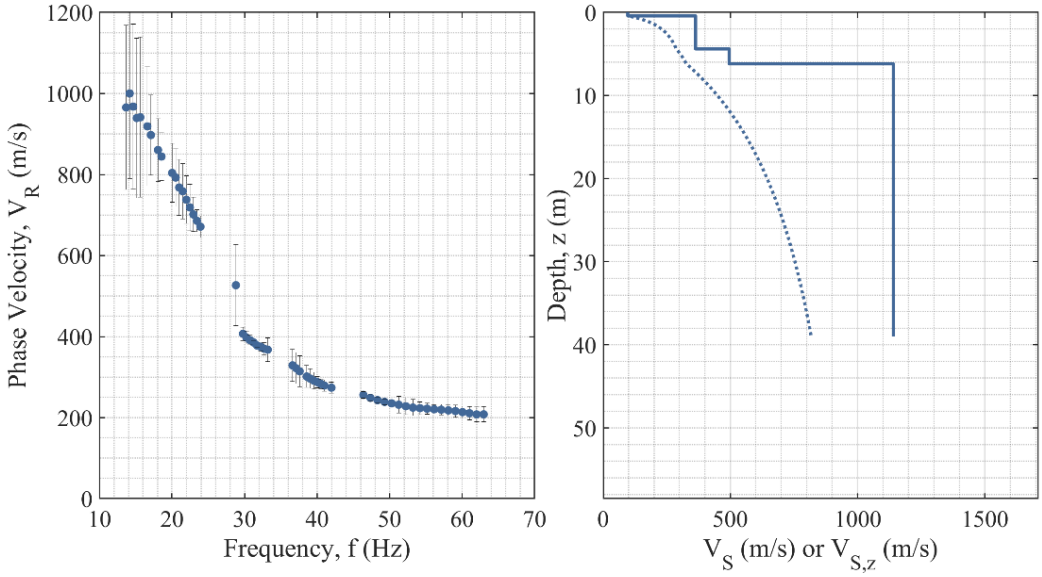

Figure A73. EDC (left), Vs and Vs,z (right) for Tarcento-4 (ID 73).

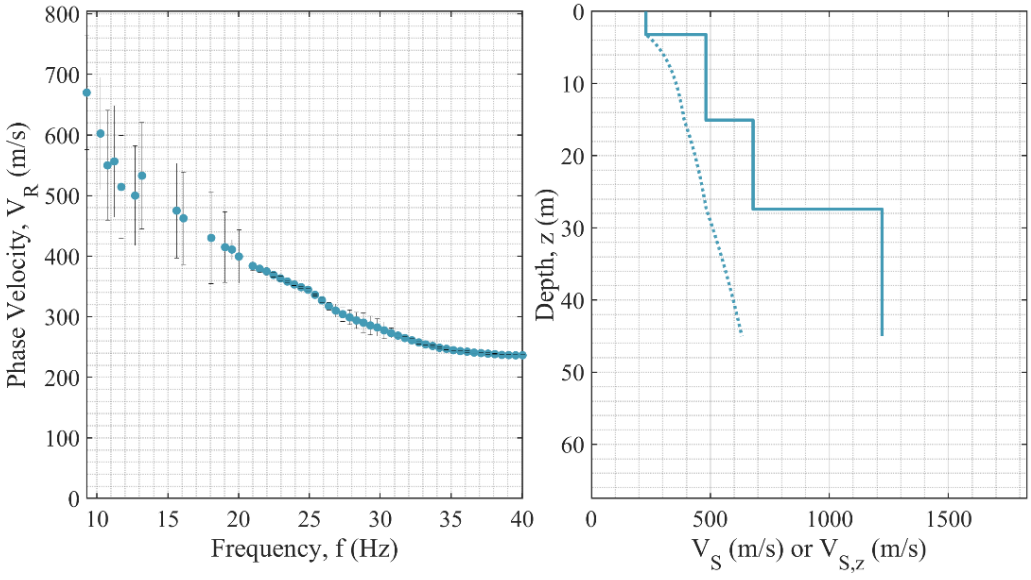

Figure A74. EDC (left), Vs and Vs,z (right) for Tarcento-5 (ID 74).

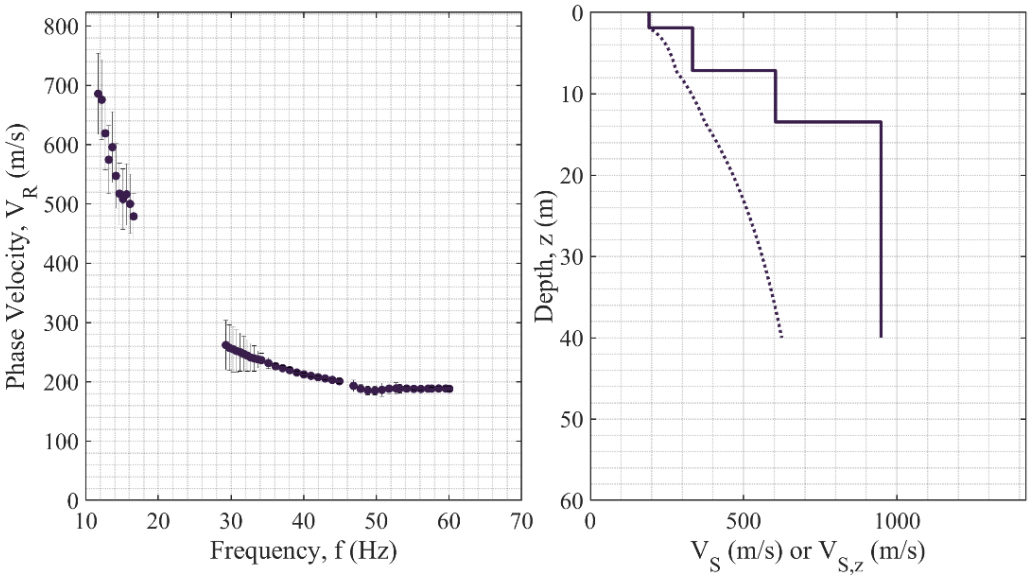

Figure A75. EDC (left), Vs and Vs,z (right) for Tarcento-6 (ID 75).

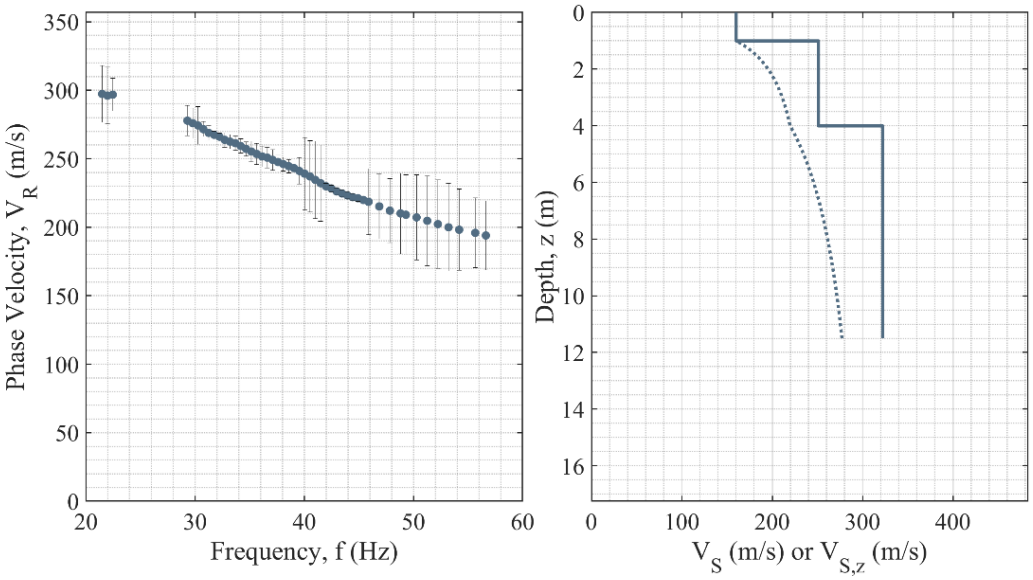

Figure A76. EDC (left), Vs and Vs,z (right) for Tarcento-7 (ID 76).

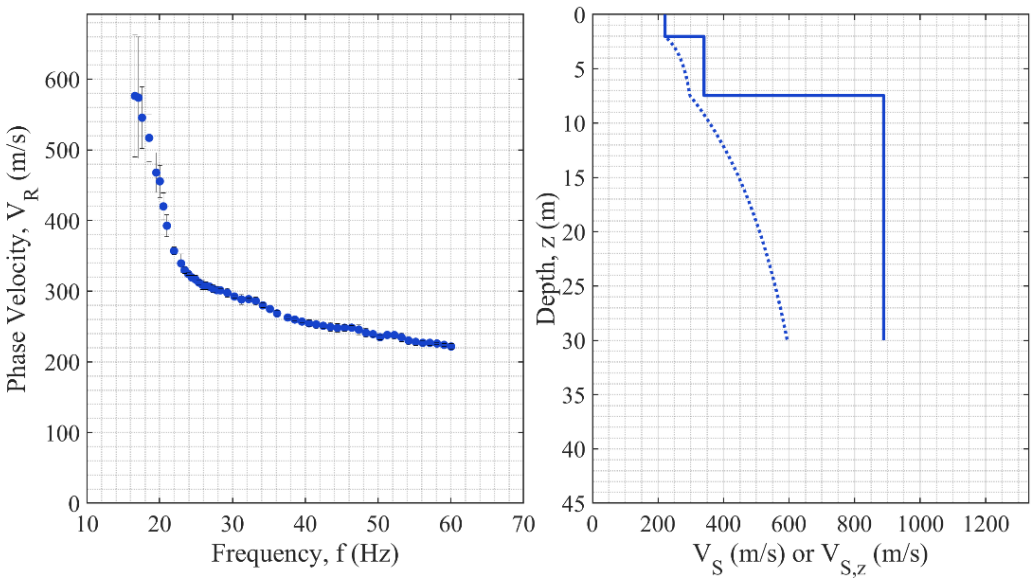

Figure A77. EDC (left), V_S and $V_{S,Z}$ (right) for Tarcento-8 (ID 77).

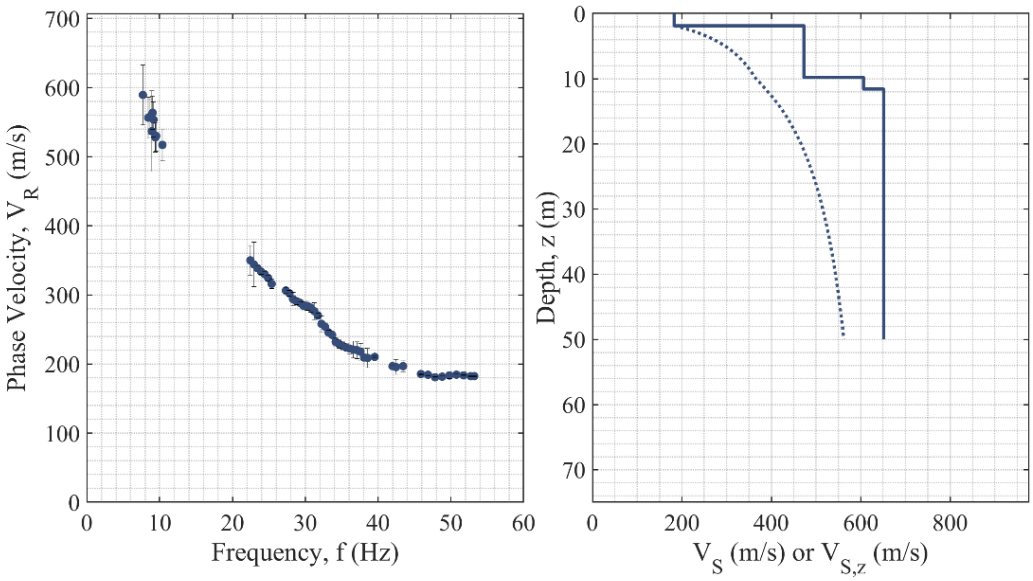

Figure A78. EDC (left), V_S and $V_{S,Z}$ (right) for Tarcento-10 (ID 78).

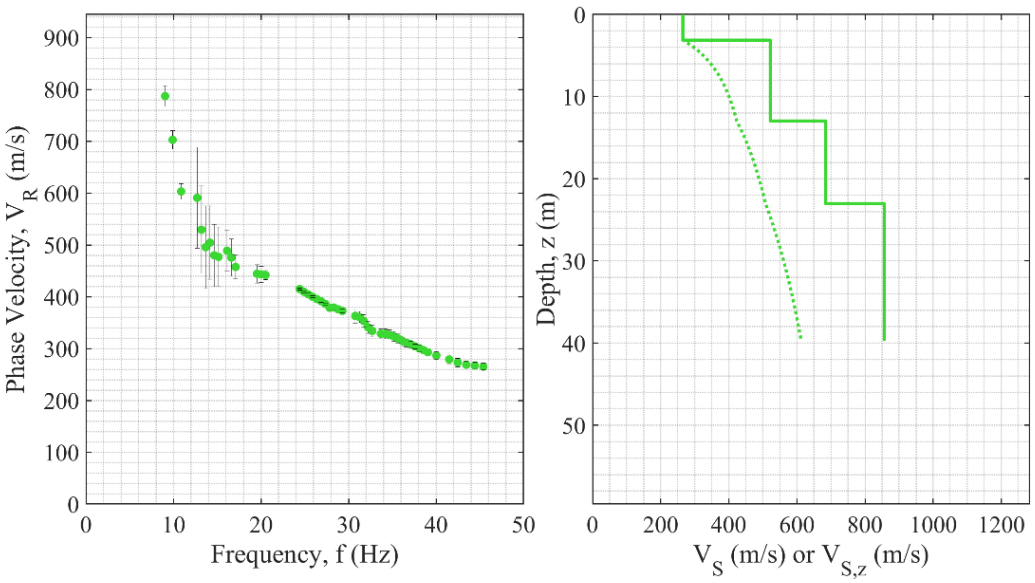

Figure A79. EDC (left), V_S and $V_{S,z}$ (right) for Tarcento-11 (ID 79).

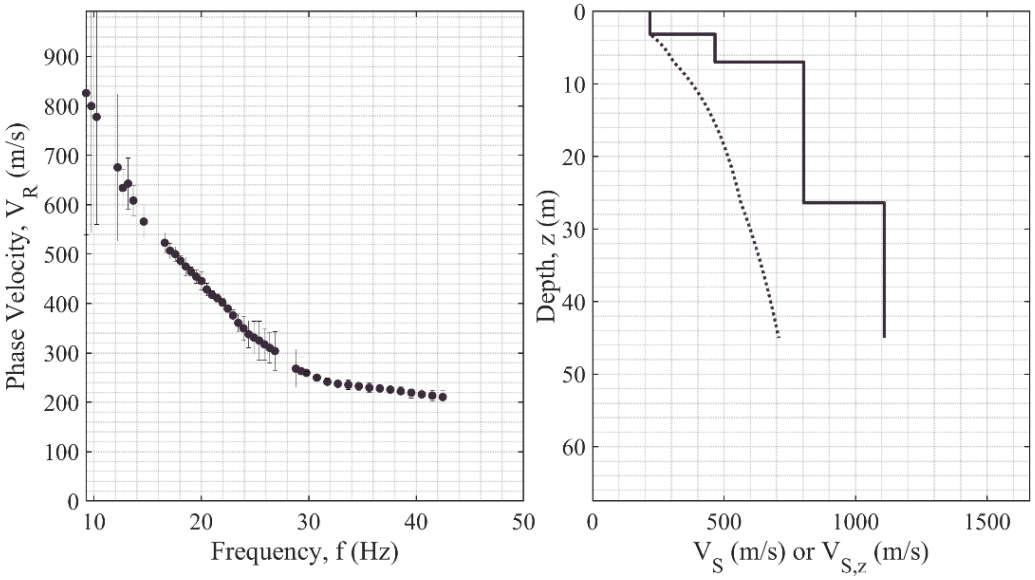

Figure A80. EDC (left), V_S and $V_{S,z}$ (right) for Tarcento-12 (ID 80).

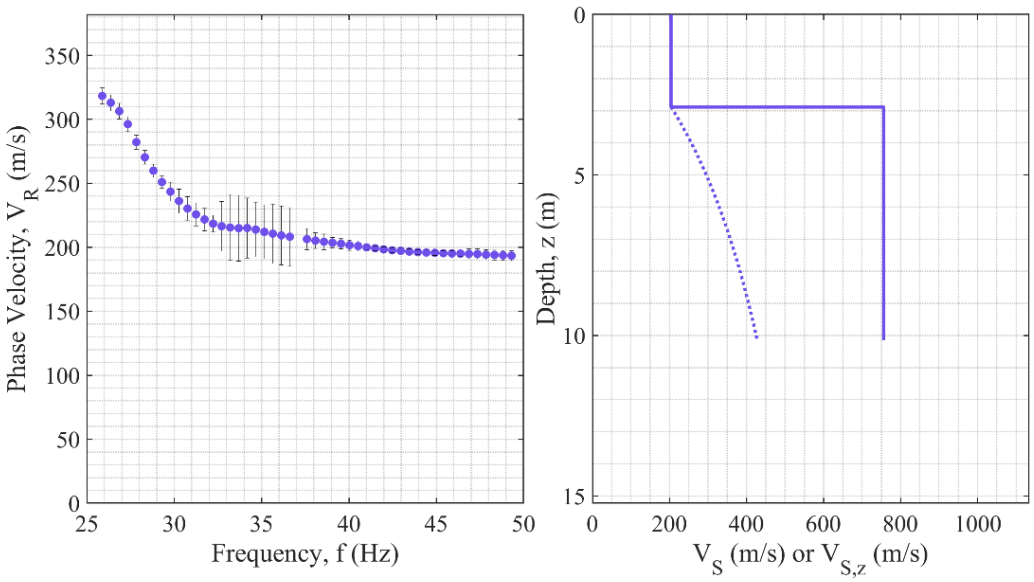

Figure A81. EDC (left), V_S and $V_{S,z}$ (right) for Tarcento-15 (ID 81).

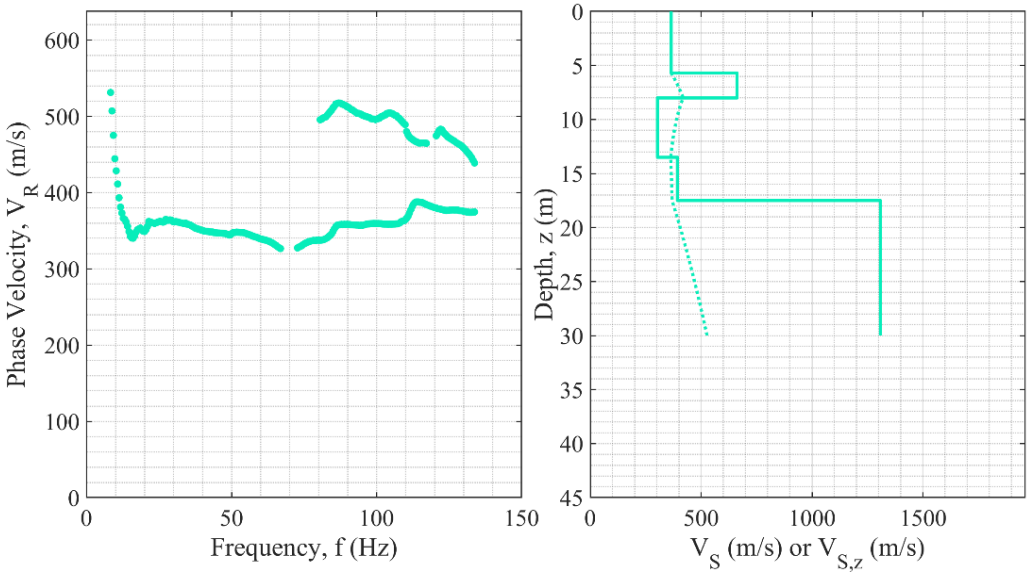

Figure A82. EDC (left), V_S and $V_{S,z}$ (right) for TOR (ID 82).

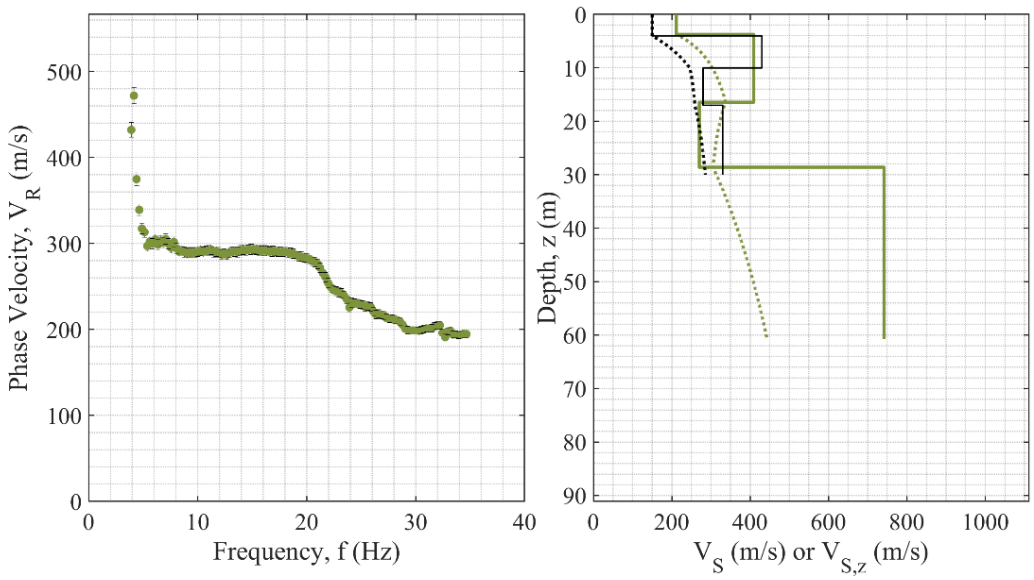

Figure A83. EDC (left), Vs and Vs,z (right) for Torre Pellice-Depuratore (ID 83).

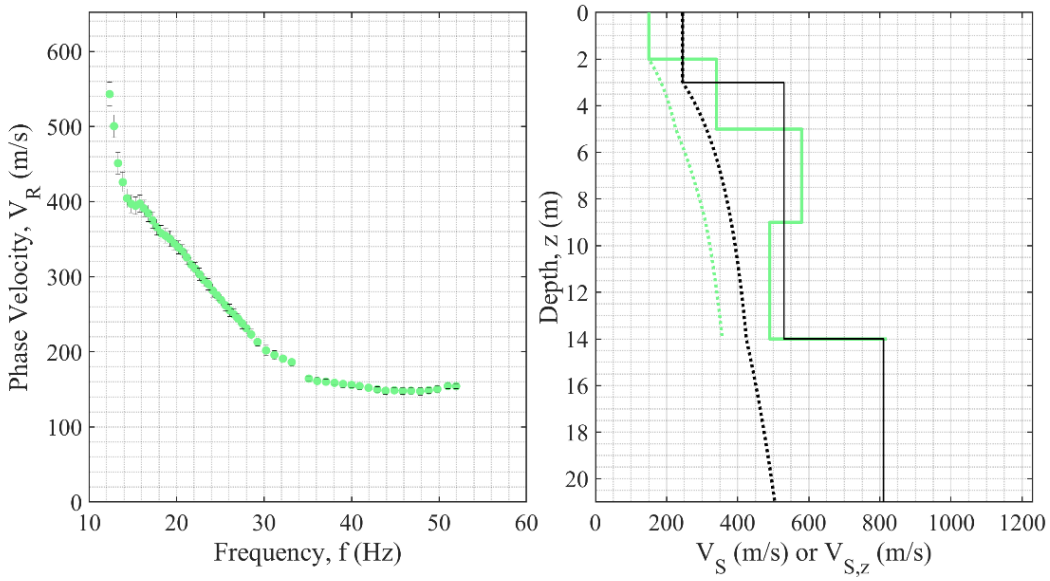

Figure A84. EDC (left), Vs and Vs,z (right) for Torre Pellice-Giardini (ID 84).

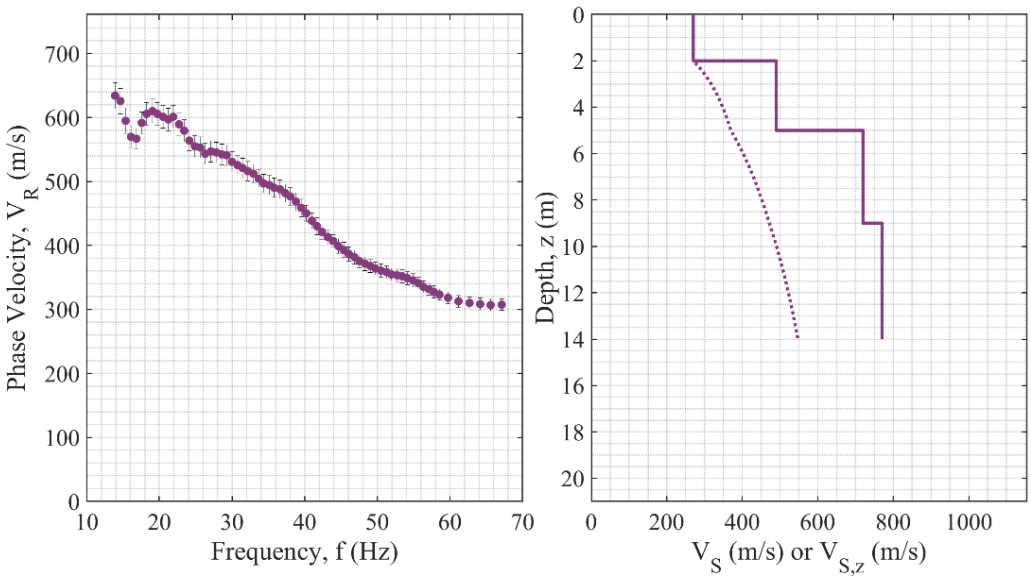

Figure A85. EDC (left), V_S and $V_{S,z}$ (right) for Torre Pellice-Giochi (ID 85).

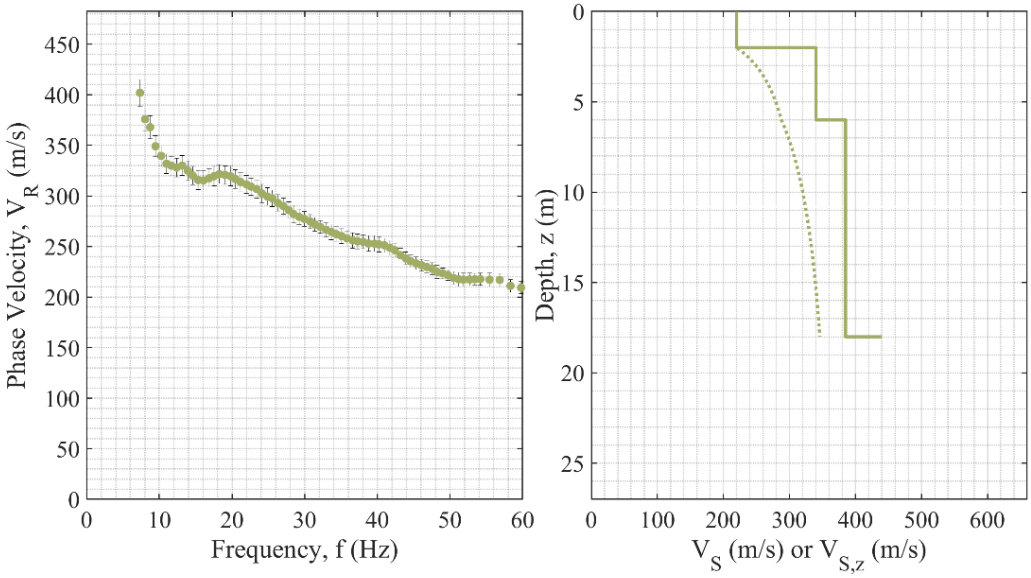

Figure A86. EDC (left), V_S and $V_{S,z}$ (right) for Torre Pellice-Torrente (ID 86).

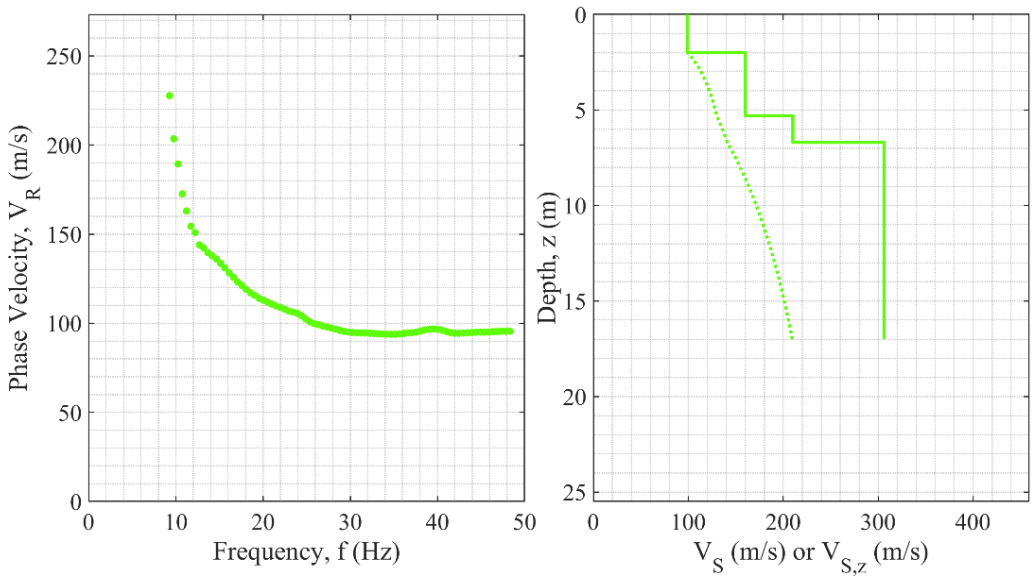

Figure A87. EDC (left), Vs and Vs,z (right) for TRF0 (ID 87).

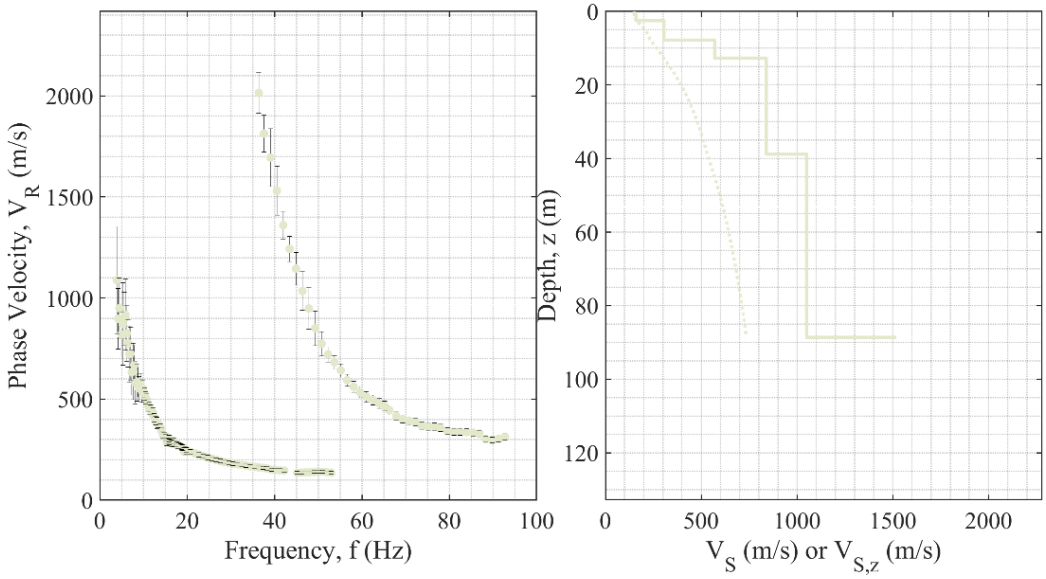

Figure A88. EDC (left), Vs and Vs,z (right) for TRT (ID 88).

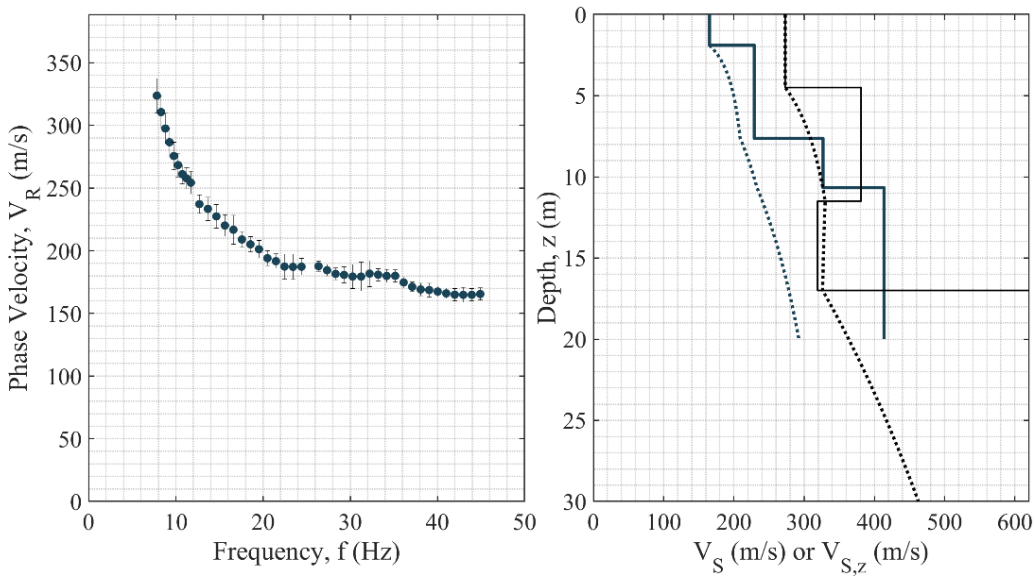

Figure A89. EDC (left), Vs and Vs,z (right) for Venarotta (ID 89).

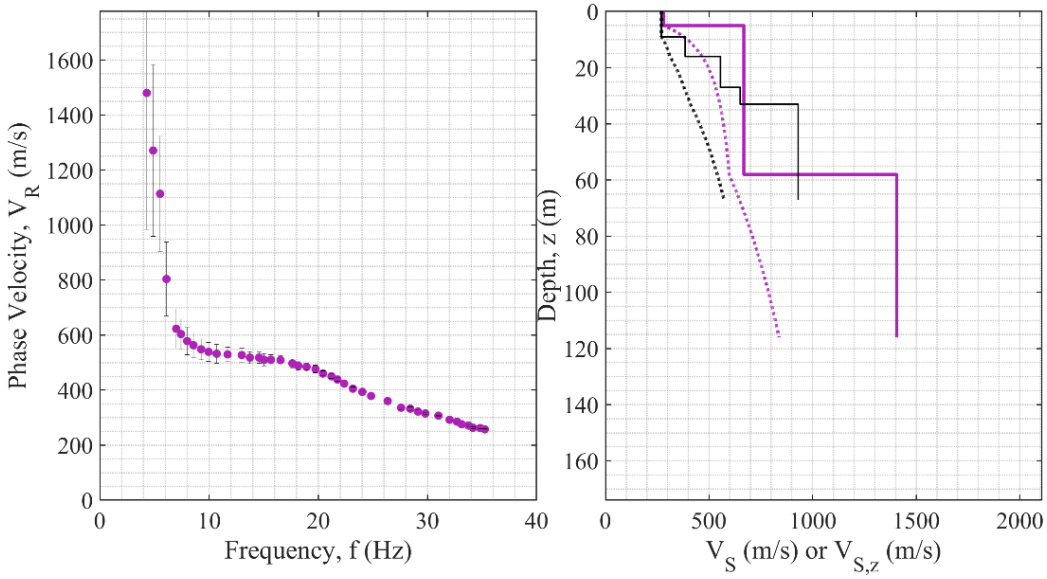

Figure A90. EDC (left), Vs and Vs,z (right) for Villa Collemandina (ID 90).

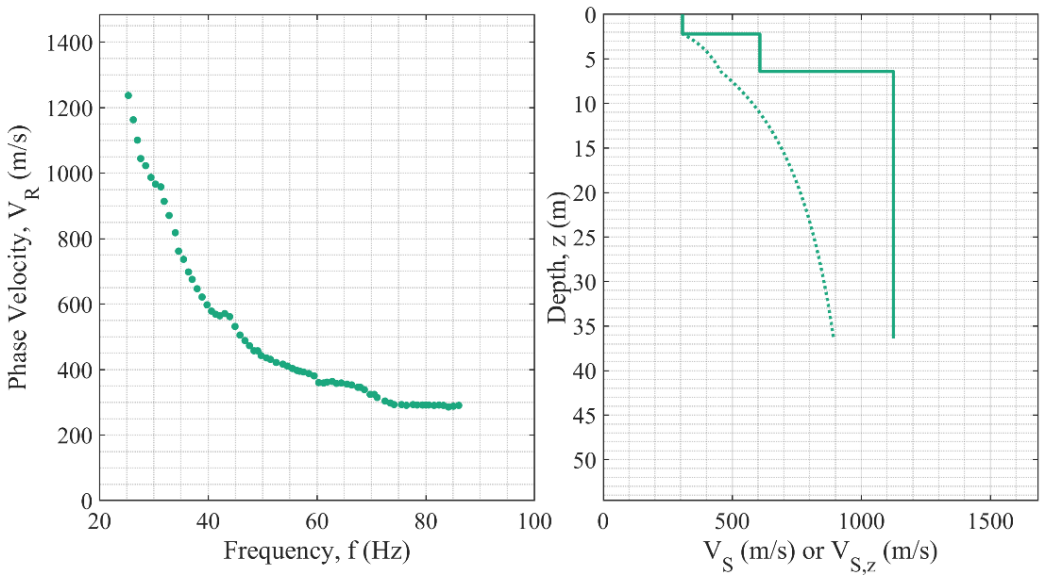

Figure A91. EDC (left), Vs and Vs,z (right) for VRL (ID 91).

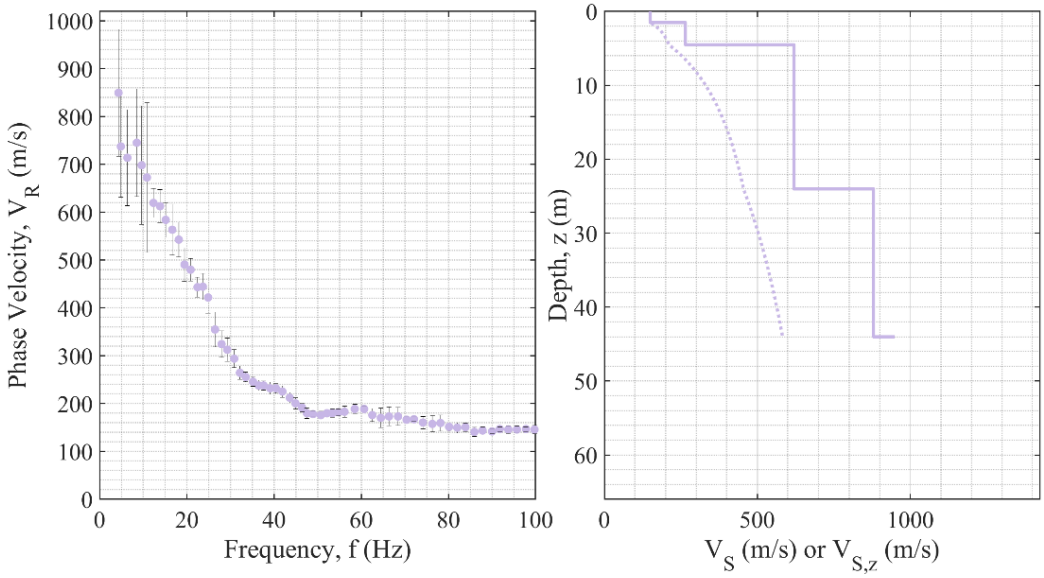

Figure A92. EDC (left), Vs and Vs,z (right) for Tarvisio (ID 92).

Table A2. Summary of the inversion results after the first-round, the second-round inversion and after the merging procedure.

		ROUND-1		ROUND-2		FINAL RESULTS		RATIO
ID	Site	M_{min}	# of profiles	M_{min}	# of profiles	M_{min}	# of profiles	
1	Accumoli	0.046	450	0.034	12384	0.034	12512	0.74
2	Acquasanta Terme	0.076	629	0.138	1454	0.076	677	1.83
4	Bovisio-L2	0.058	3901	0.052	20802	0.052	23339	0.9
5	Caselle Landi-1	0.091	3476	0.073	26687	0.073	28347	0.81
6	Caselle Landi-2	0.076	1148	0.063	70605	0.063	71150	0.83
7	Caselle Landi-3	0.167	1073	0.090	13946	0.090	13953	0.54
8	Caselle Landi-5	0.421	8196	0.265	32655	0.265	33640	0.63
9	Castel di Lama-Campo	0.075	618	0.076	32232	0.075	31742	1.01
10	Castel di Lama-Strada	0.082	2098	0.079	58319	0.079	60205	0.97
11	CAT	0.743	2826	0.758	14446	0.743	14895	1.02
12	Cesana-1	0.113	710	0.160	49897	0.113	27382	1.42
13	Cesana-2	0.188	1652	0.224	47446	0.188	25789	1.19
14	CG-Loc. Alle Monache	0.294	208	0.291	10229	0.291	10432	0.99
17	Firenze-Piazza Duomo	0.559	581	0.905	10543	0.559	1060	1.62
18	Firenze-Uffizi	0.163	6875	0.583	13334	0.163	6875	3.58
19	Firenze-Via di Novoli	1.578	2315	1.757	34964	1.578	27116	1.11
22	GMN	0.085	188	0.078	1320	0.078	1449	0.91
24	GRI-Campo Sportivo-EW	0.211	1549	0.178	4918	0.178	5491	0.84

25	GRI-Campo Sportivo-NS	0.529	687	0.404	205	0.404	310	0.76
26	Grisciano Conoide	0.096	111	0.064	23963	0.064	23976	0.66
27	Illica	0.106	859	0.100	55149	0.100	55792	0.94
28	La Salle A	0.985	53	0.860	3371	0.860	3395	0.87
29	La Salle B	0.083	1172	0.086	4906	0.083	5644	1.03
30	La Salle C	0.365	13475	0.389	18238	0.365	28697	1.06
31	La Salle D	0.159	110	0.163	68768	0.159	64313	1.03
32	La Salle E	0.141	151	0.134	17603	0.134	17709	0.95
34	LAquila (Pianola)	0.321	1438	0.246	23842	0.246	24067	0.77
35	LAquila (Roio Piano)	0.231	1036	0.135	58039	0.135	58060	0.59
36	Massa M.-Cantiere	0.755	1182	0.597	29313	0.597	29561	0.79
37	Massa M.-Parcheggio	0.232	217	0.313	380	0.232	320	1.35
38	Mathi-1&2	0.689	2379	0.655	102058	0.655	104051	0.95
39	Mathi-3	0.496	2775	0.731	41399	0.496	8068	1.47
40	Mirabello-Last-July	0.043	211	0.042	30936	0.042	31132	0.99
41	Mirabello-Post-May	0.033	69	0.032	9380	0.032	9433	0.96
42	Mirabello-Pre-Feb	0.148	5502	0.156	105356	0.148	102689	1.05
43	Montemonaco	0.081	4149	0.077	18365	0.077	21821	0.95
45	Offida	0.063	1242	0.061	63009	0.061	64036	0.96
46	Palmiano-Castel San Pietro	0.122	357	0.047	228	0.047	228	0.38
48	Piazza al Serchio	0.484	1447	0.384	32236	0.384	32671	0.79
49	Pieve Fosciana	0.335	3589	0.319	111149	0.319	114259	0.95

50	Pisa	0.148	5382	0.176	13851	0.148	8263	1.19
52	Pontremoli-1 maggio	0.075	771	0.097	4385	0.075	837	1.29
53	Pontremoli-ASL 2	0.179	110	0.201	8930	0.179	5767	1.12
54	Pontremoli-Bocciofila	0.411	721	0.442	72114	0.411	62463	1.07
55	Pontremoli-Giochi	0.243	828	0.226	25535	0.226	26184	0.93
58	Roccafluvione	0.306	331	0.225	2406	0.225	2495	0.74
59	Rotella	0.023	468	0.024	8166	0.023	7301	1.05
60	RNS	0.288	61	0.285	5560	0.285	5620	0.99
61	Saluggia	1.941	73	1.477	17441	1.477	17460	0.76
62	San Severino Marche-1	1.761	1932	1.242	22575	1.242	22789	0.71
63	San Severino Marche-2	0.385	2704	0.399	17535	0.385	16978	1.04
69	Settimo Torinese	1.800	143	2.187	110	1.800	183	1.22
70	Tarcento-1	0.097	361	0.072	1545	0.072	1639	0.74
71	Tarcento-2	0.179	198	0.135	3390	0.135	3423	0.75
72	Tarcento-3	1.971	111	2.010	1133	1.971	1145	1.02
73	Tarcento-4	0.210	124	0.219	26	0.210	142	1.04
74	Tarcento-5	0.508	216	0.501	8396	0.501	8601	0.99
75	Tarcento-6	0.172	477	0.168	6844	0.168	7277	0.97
76	Tarcento-7	0.032	115	0.030	14421	0.030	14521	0.95
77	Tarcento-8	1.119	392	1.060	14735	1.060	15034	0.95
78	Tarcento-10	2.553	378	2.454	55638	2.454	55974	0.96
79	Tarcento-11	0.476	124	0.233	256	0.233	256	0.49

80	Tarcento-12	0.057	211	0.060	1875	0.057	1774	1.05
81	Tarcento-15	0.268	2750	0.262	21885	0.262	24512	0.98
83	Torre Pellice-Depuratore	1.217	1221	1.233	1992	1.217	3036	1.01
84	Torre Pellice-Giardini	0.718	1484	0.810	27194	0.718	17228	1.13
85	Torre Pellice-Parco Giochi	0.399	328	0.351	40732	0.351	40911	0.88
86	Torre Pellice-Torrente	0.331	10236	0.275	29307	0.275	32848	0.83
87	TRF0	0.322	2843	0.274	39019	0.274	40058	0.85
89	Venarotta	0.267	8396	0.177	39693	0.177	41517	0.66
92	Tarvisio	0.830	841	0.594	39487	0.594	39596	0.72

Upper-Left. Interval velocity profiles obtained after the second-round inversion. In red the minimum misfit profile, in solid black the minimum misfit profile obtained from the first-round inversion. Note that if the second-round inversion did not obtain a solution with lower misfit, the minimum misfit profile remains solid black. In dashed black (if available) the DH test profile, in '*' black (if available) the CH test profile, in 'x' (if available) the suspension logging test profile, in '◊' (if available) the SDTM test profile.

Upper-Right. Harmonic average velocity profiles obtained after the second-round inversion. In red the minimum misfit profile, in solid black the minimum misfit profile obtained from the first-round inversion. Note that if the second-round inversion did not obtain a solution with lower misfit, the minimum misfit profile remains solid black. In dashed black (if available) the DH test profile, in '*' black (if available) the CH test profile, in 'x' (if available) the suspension logging test profile, in '◊' (if available) the SDTM test profile.

Lower-Left. EDCs obtained after the second-round inversion. In red the minimum misfit curve, in solid black the minimum misfit curve obtained from the first-round inversion. Note that if the second-round inversion did not obtain a solution with lower misfit, the minimum misfit EDC remains solid black.

Lower-Right. Theoretical transfer functions (TTFs) obtained after the second-round inversion. In red the minimum misfit function, in solid black the minimum misfit function obtained from the first-round inversion. Note that if the second-round inversion did not obtain a solution with lower misfit, the minimum misfit function remains solid black. In dashed black (if available) the DH test function, in '*' black (if available) the CH test function, in 'x' (if available) the suspension logging test function, in '◊' (if available) the SDTM test function.

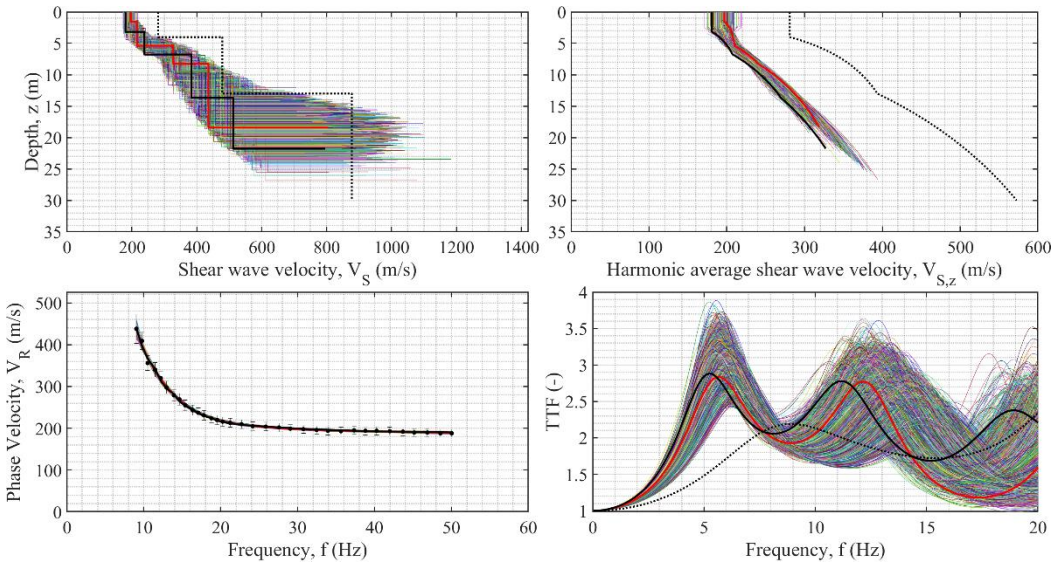

Figure A93. Final results of the inversions for Accumoli (ID 1).

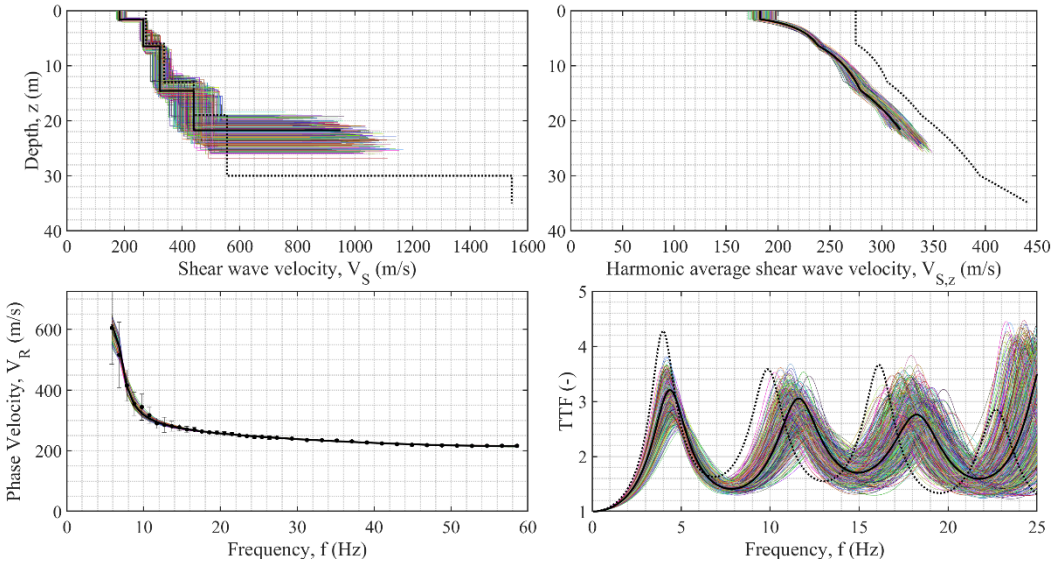

Figure A94. Final results of the inversions for Acquasanta Terme (ID 2).

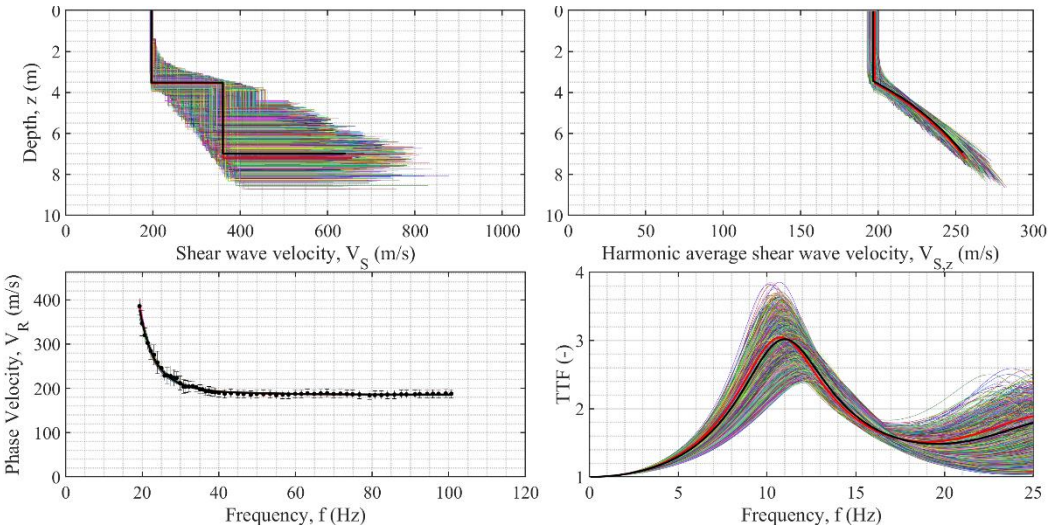

Figure A95. Final results of the inversions for Bovisio-L2 (ID 4).

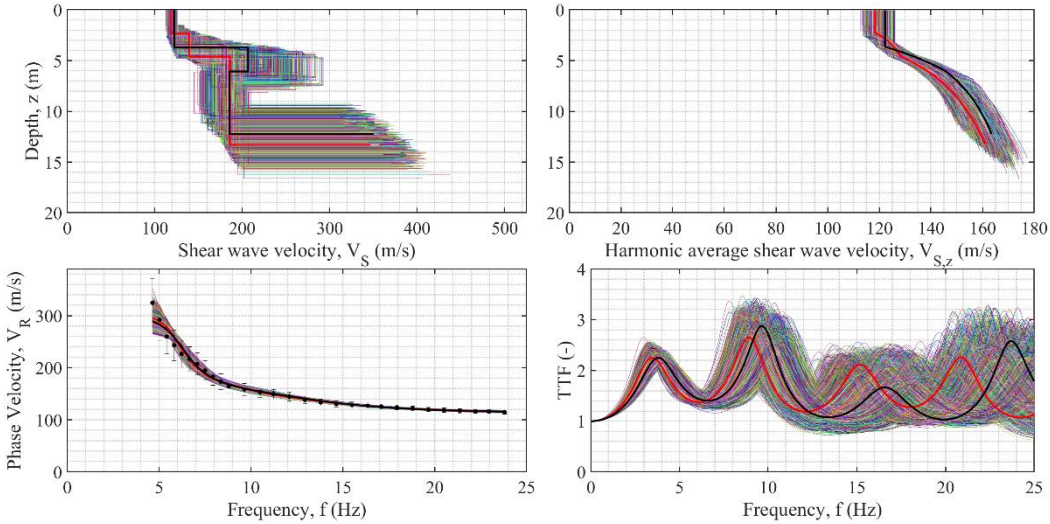

Figure A96. Final results of the inversions for Caselle Landi-1 (ID 5).

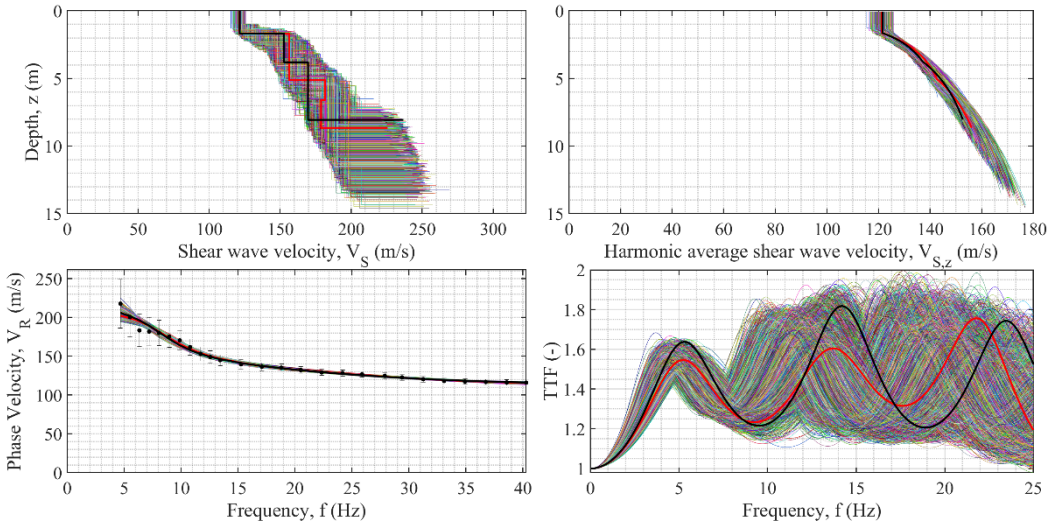

Figure A97. Final results of the inversions for Caselle Landi-2 (ID 6).

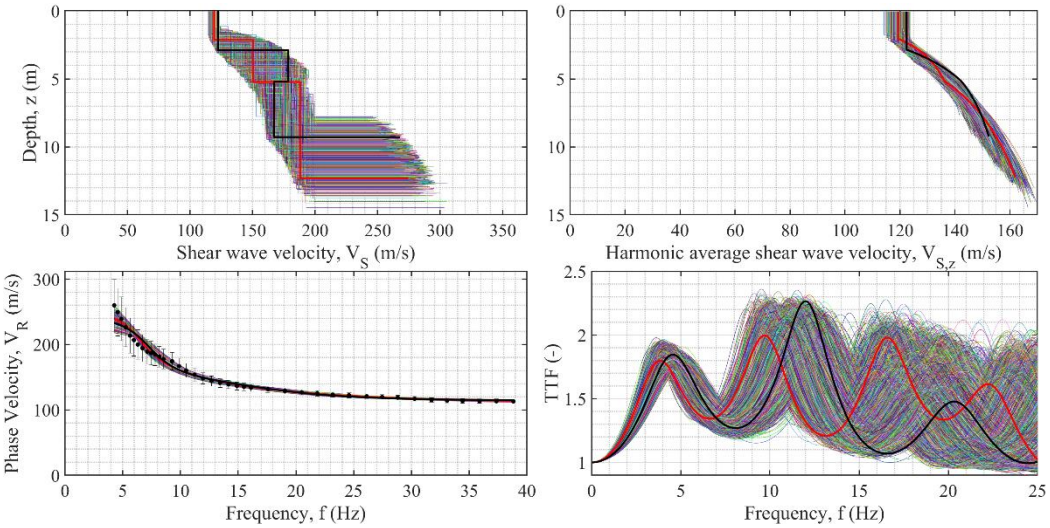

Figure A98. Final results of the inversions for Caselle Landi-3 (ID 7).

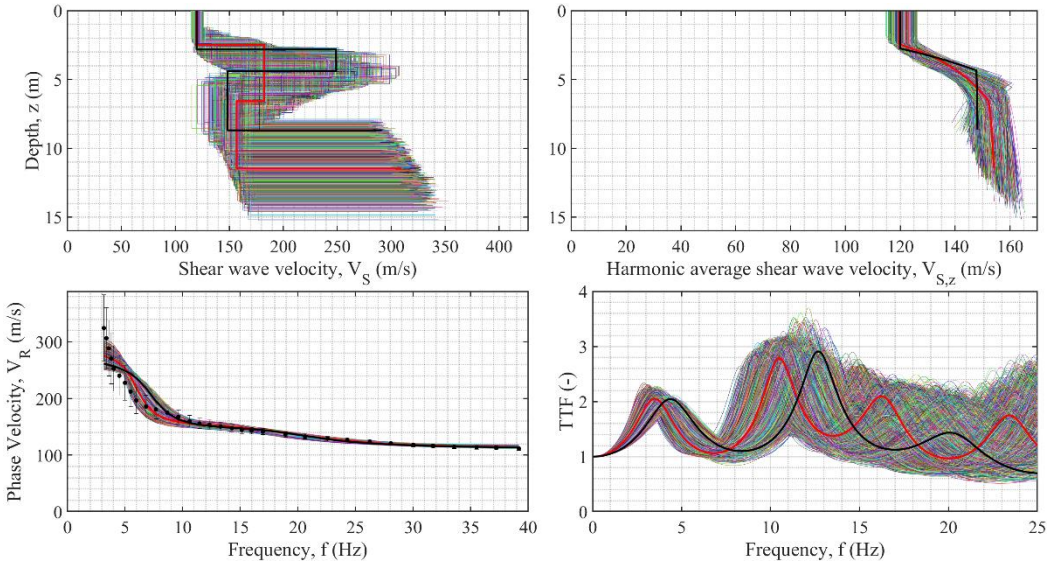

Figure A99. Final results of the inversions for Caselle Landi-5 (ID 8).

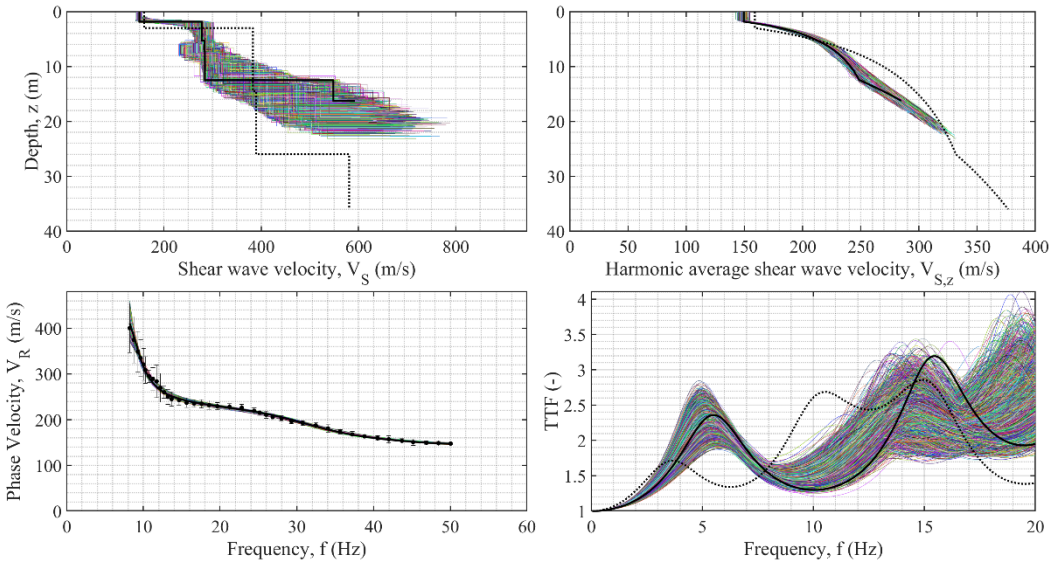

Figure A100. Final results of the inversions for Castel di Lama-Campo (ID 9).

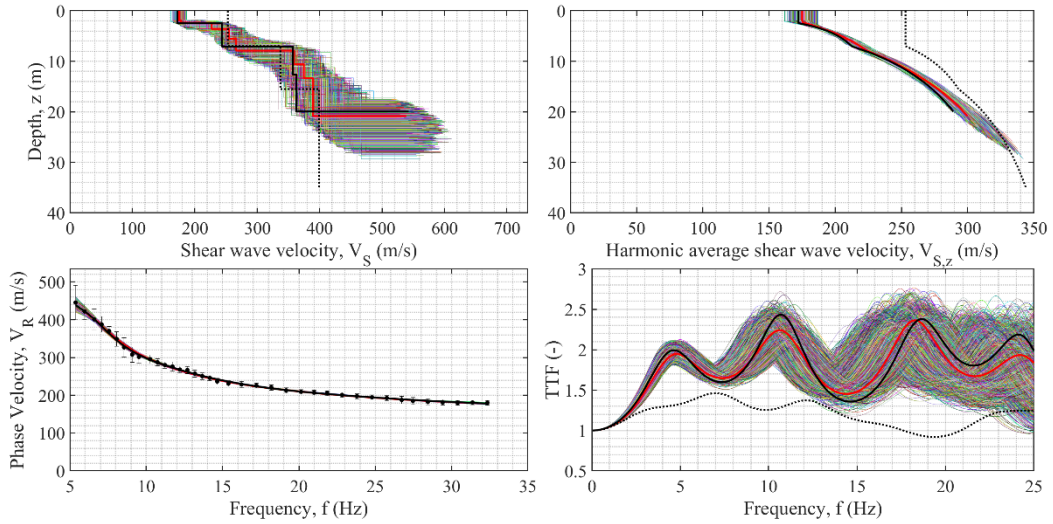

Figure A101. Final results of the inversions for Castel di Lama-Strada (ID 10).

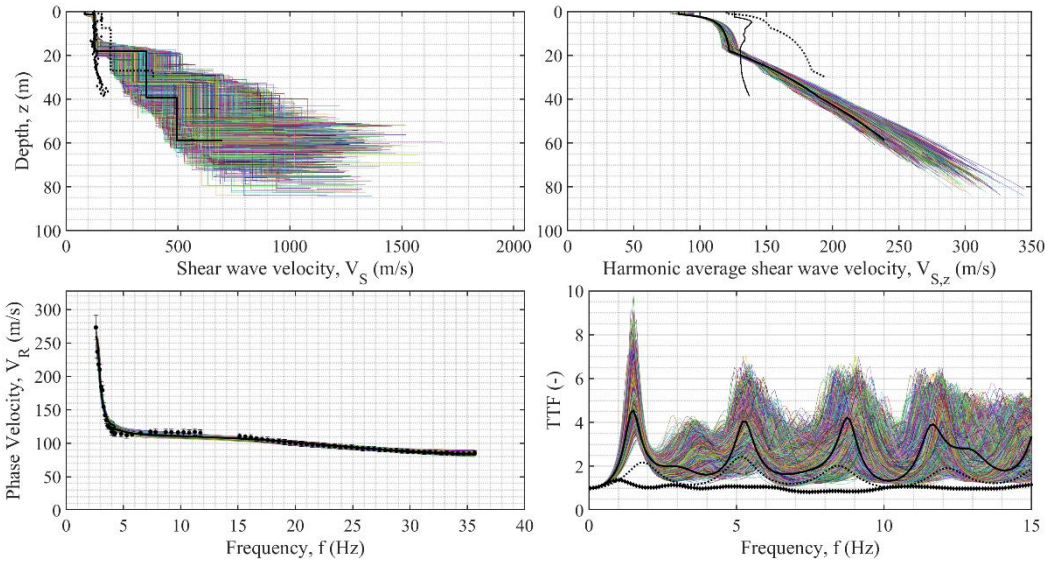

Figure A102. Final results of the inversions for CAT (ID 11).

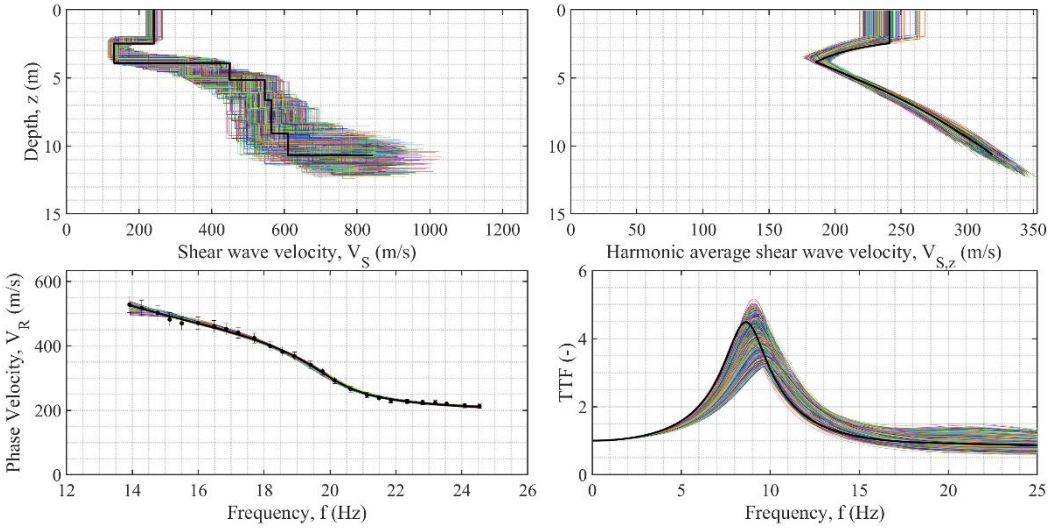

Figure A103. Final results of the inversions for Cesana-1 (ID 12).

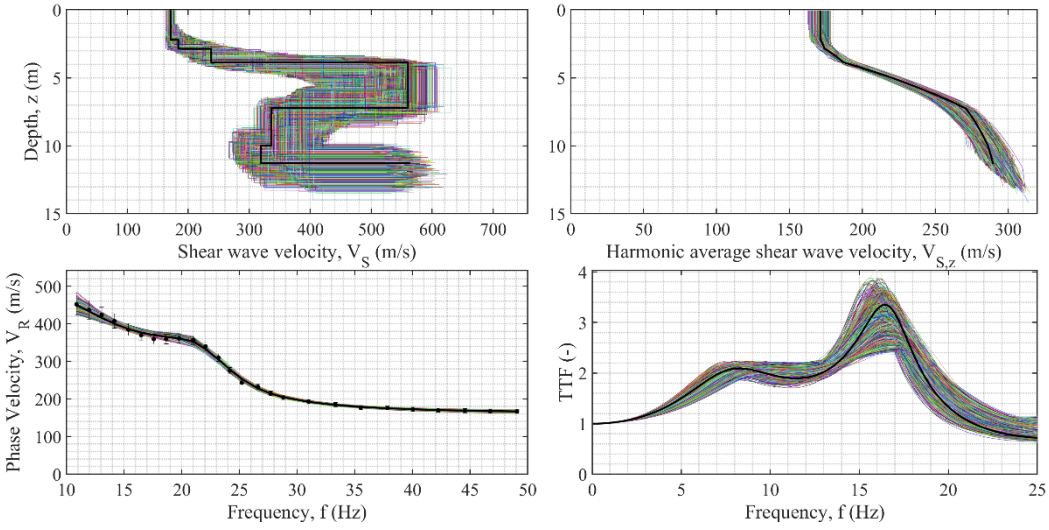

Figure A104. Final results of the inversions for Cesana-2 (ID 13).

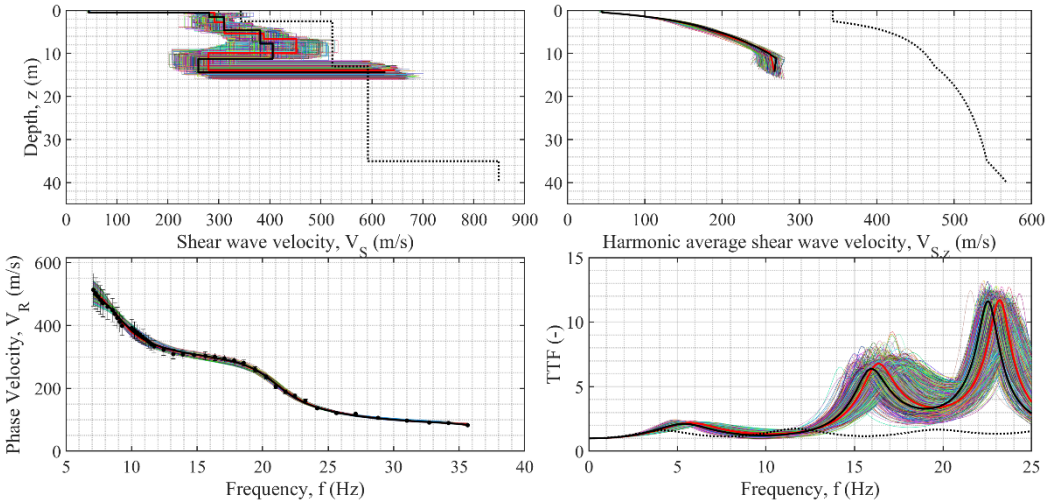

Figure A105. Final results of the inversions for CG-Loc. Alle Monache (ID 14).

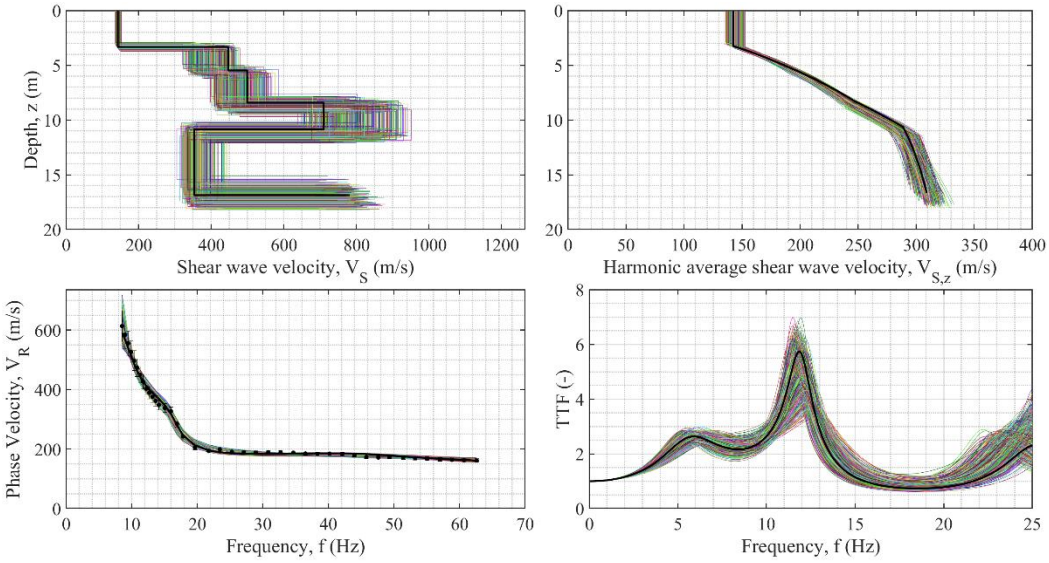

Figure A106. Final results of the inversions for Firenze-Piazza Duomo (ID 17).

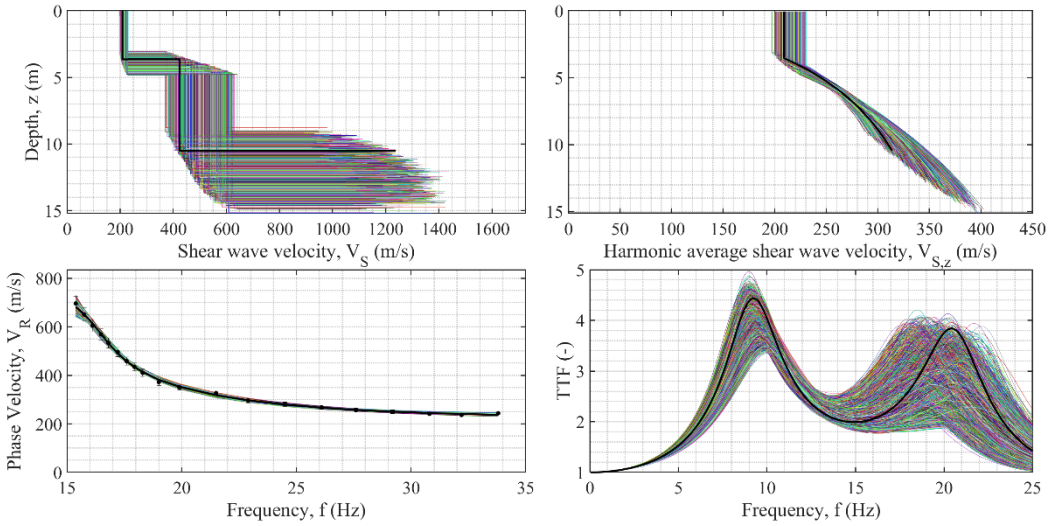

Figure A107. Final results of the inversions for Firenze-Uffizi (ID 18).

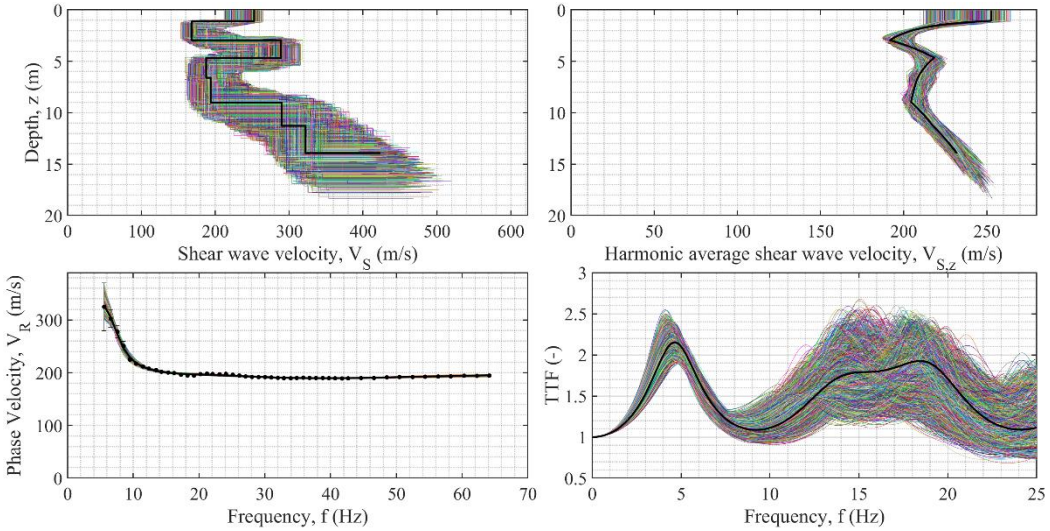

Figure A108. Final results of the inversions for Firenze-Via di Novoli (ID 19).

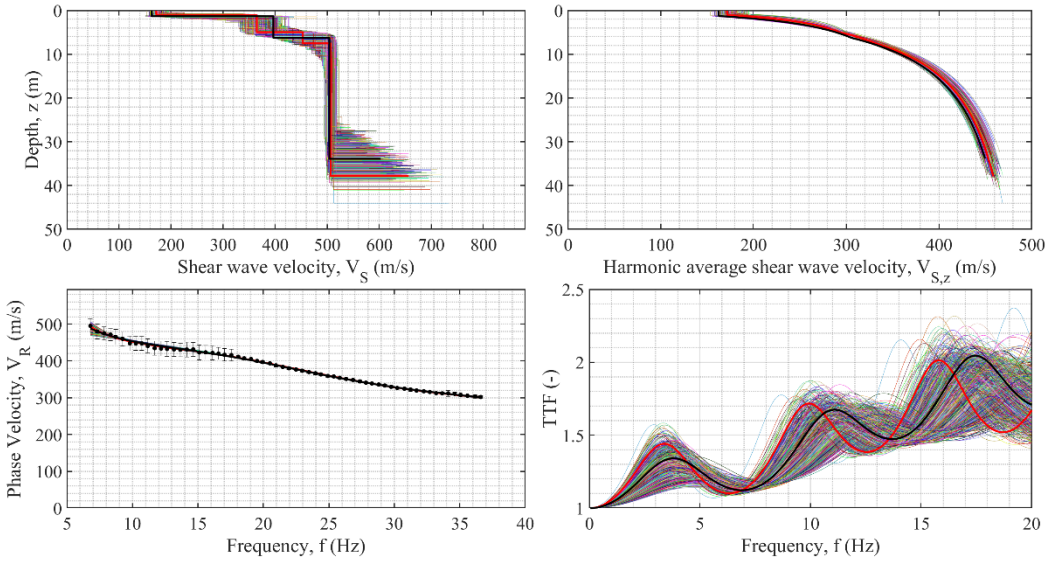

Figure A109. Final results of the inversions for GMN (ID 22).

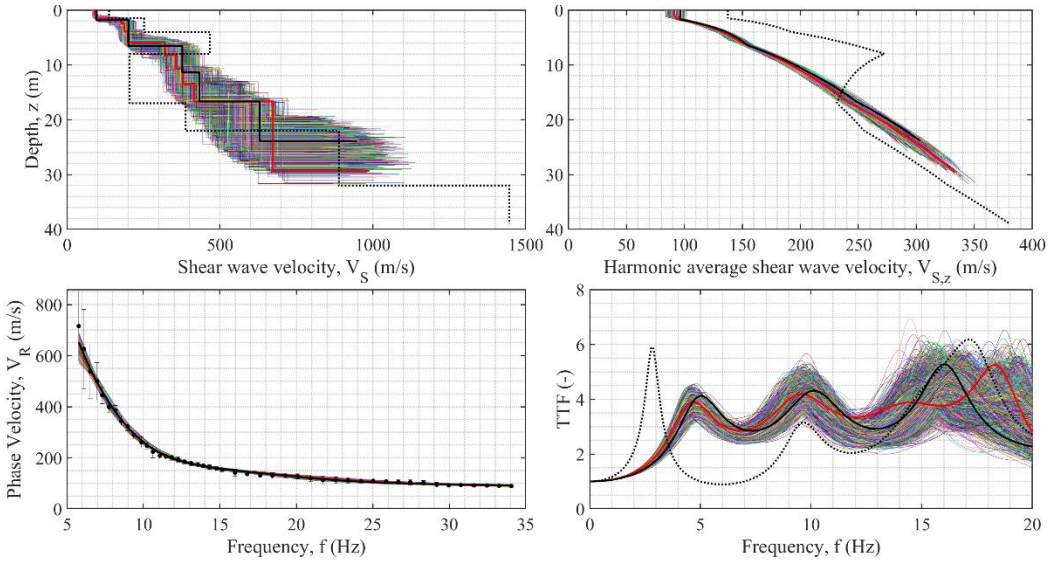

Figure A110. Final results of the inversions for GRI-Campo Sportivo-EW (ID 24).

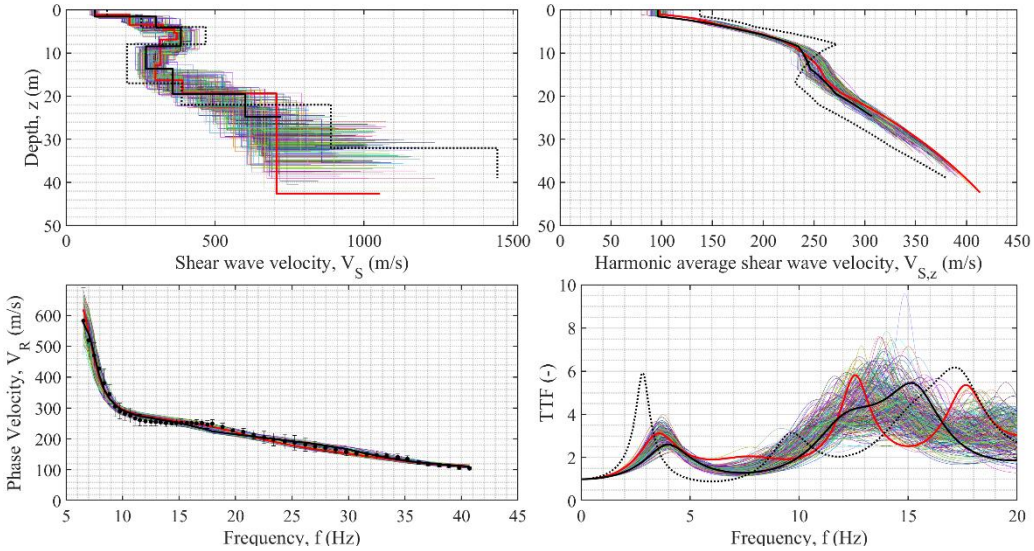

Figure A111. Final results of the inversions for GRI-Campo Sportivo-NS (ID 25).

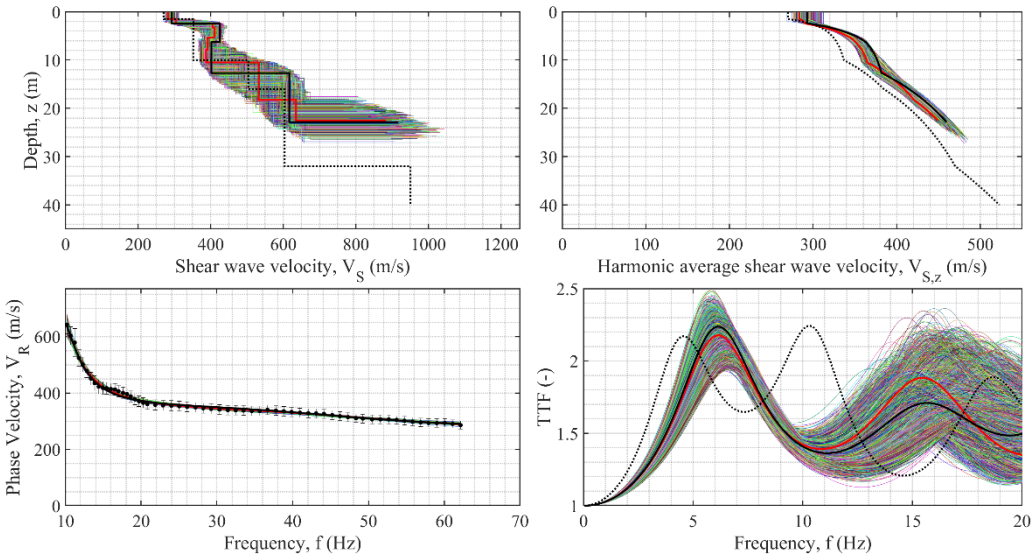

Figure A112. Final results of the inversions for Grisciano Conoide (ID 26).

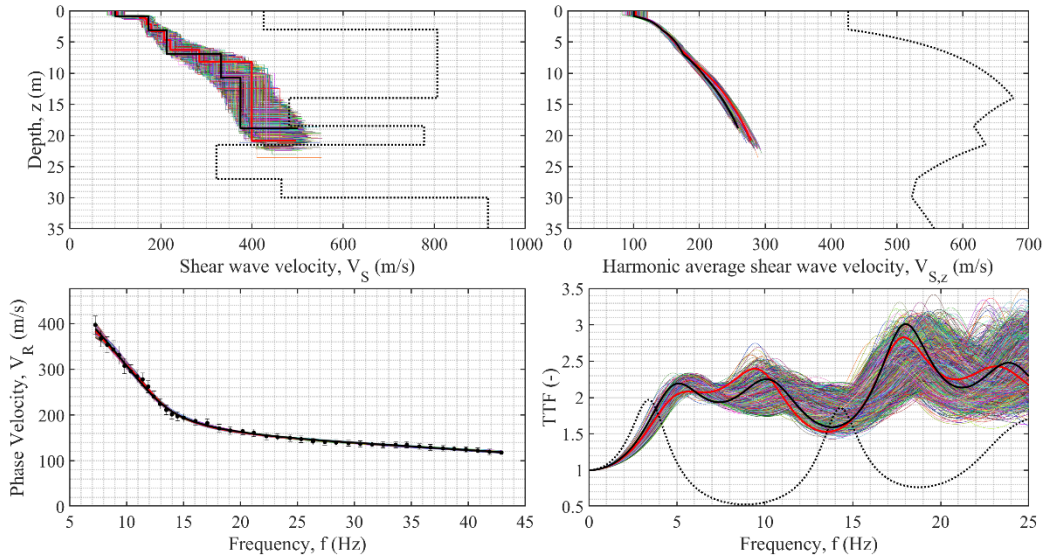

Figure A113. Final results of the inversions for Illica (ID 27).

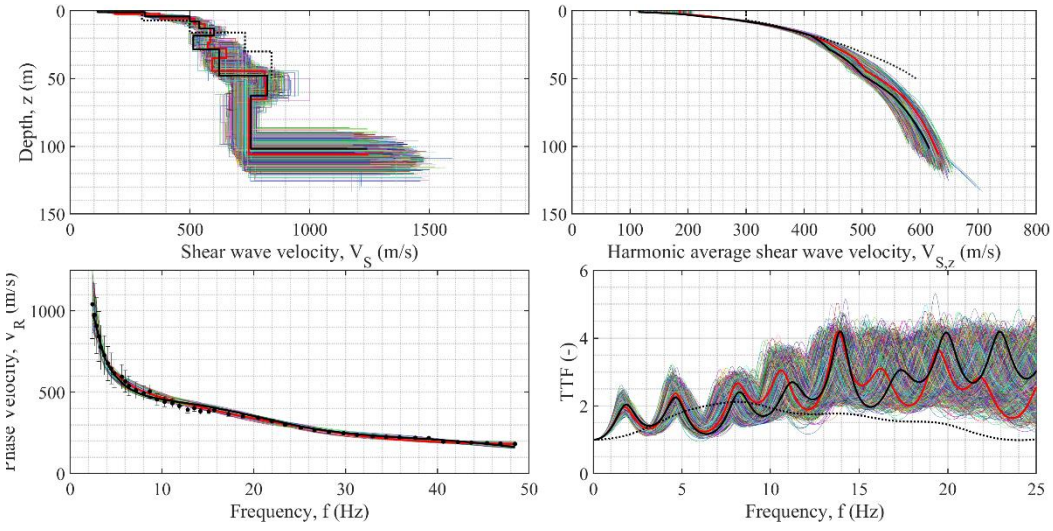

Figure A114. Final results of the inversions for La Salle A (ID 28).

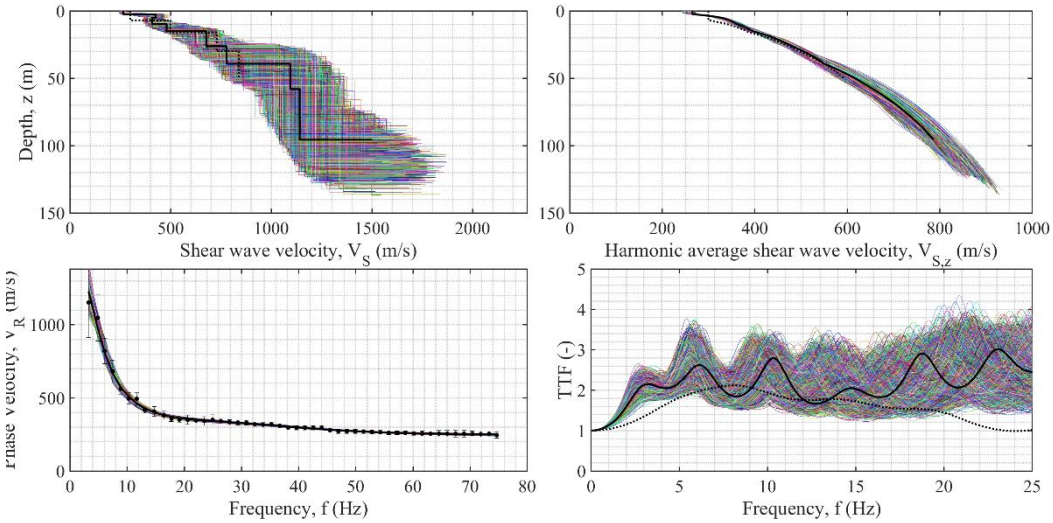

Figure A115. Final results of the inversions for La Salle B (ID 29).

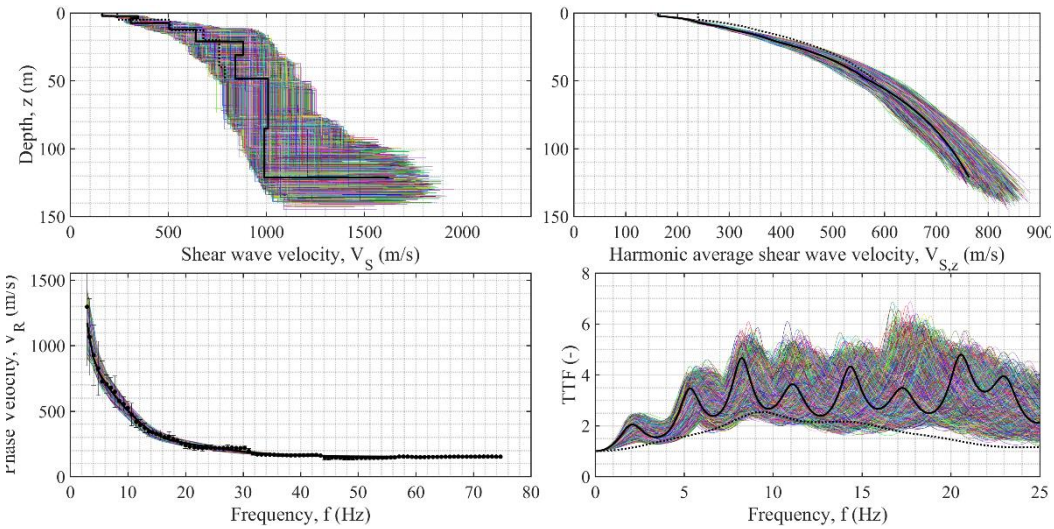

Figure A116. Final results of the inversions for La Salle C (ID 30).

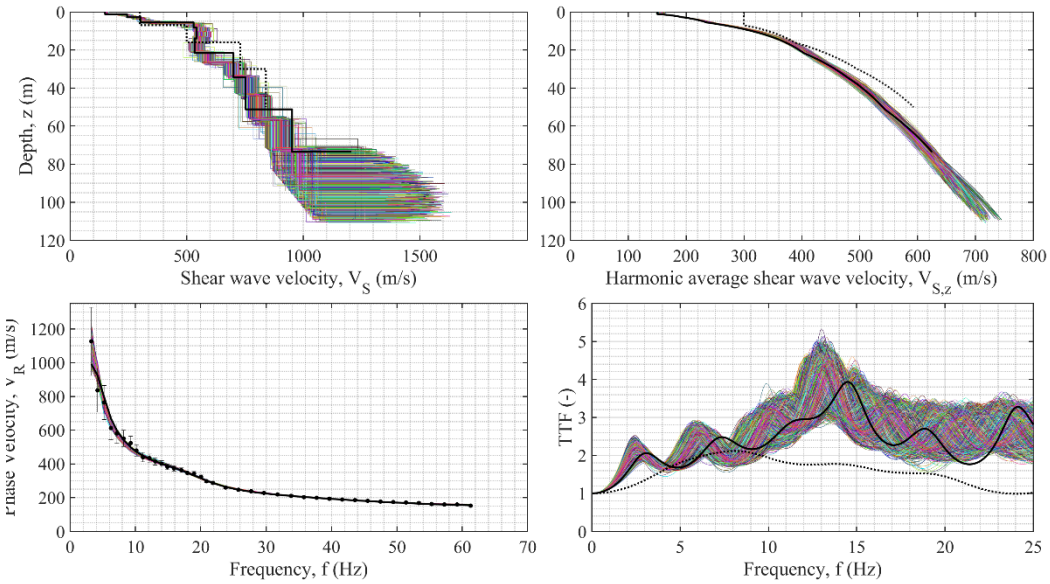

Figure A117. Final results of the inversions for La Salle D (ID 31).

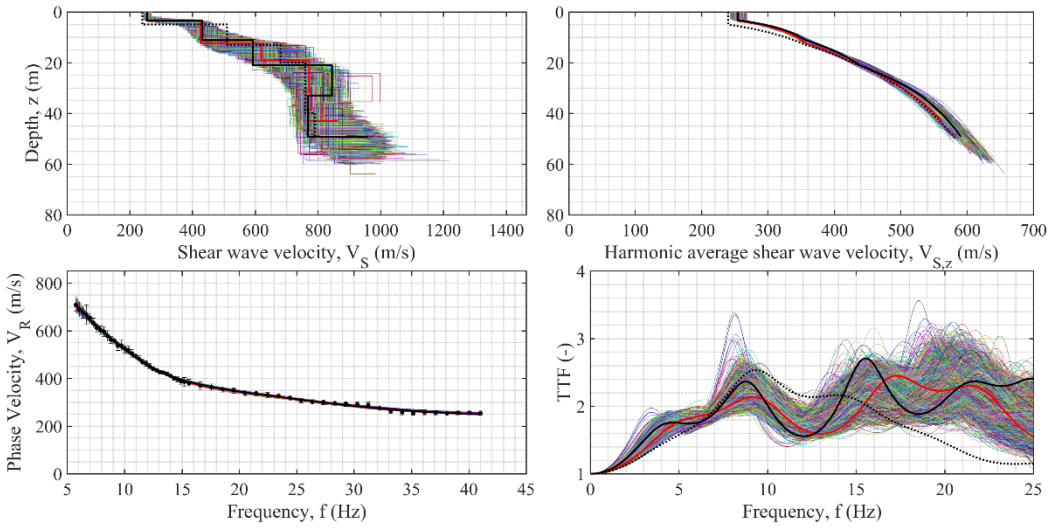

Figure A118. Final results of the inversions for La Salle E (ID 32).

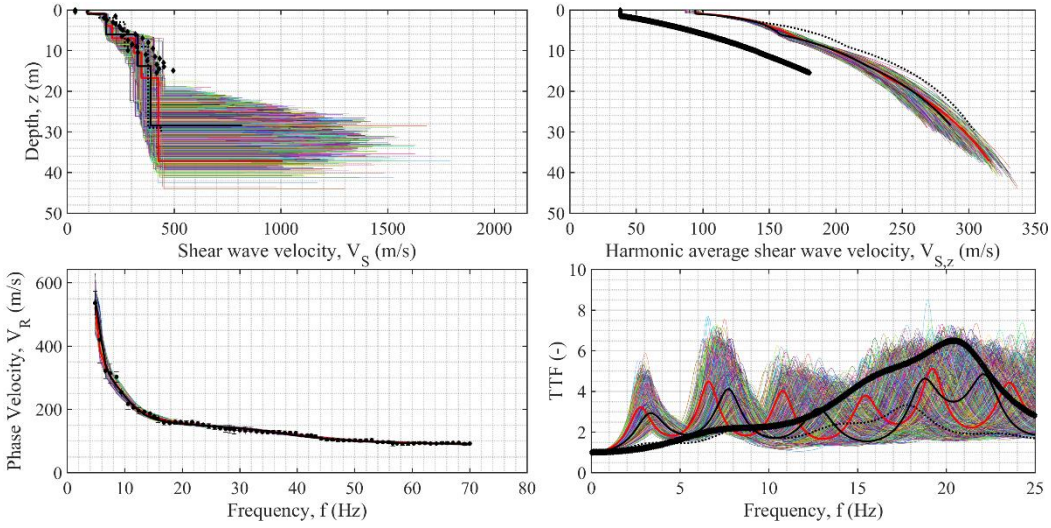

Figure A119. Final results of the inversions for L'Aquila (Pianola) (ID 34).

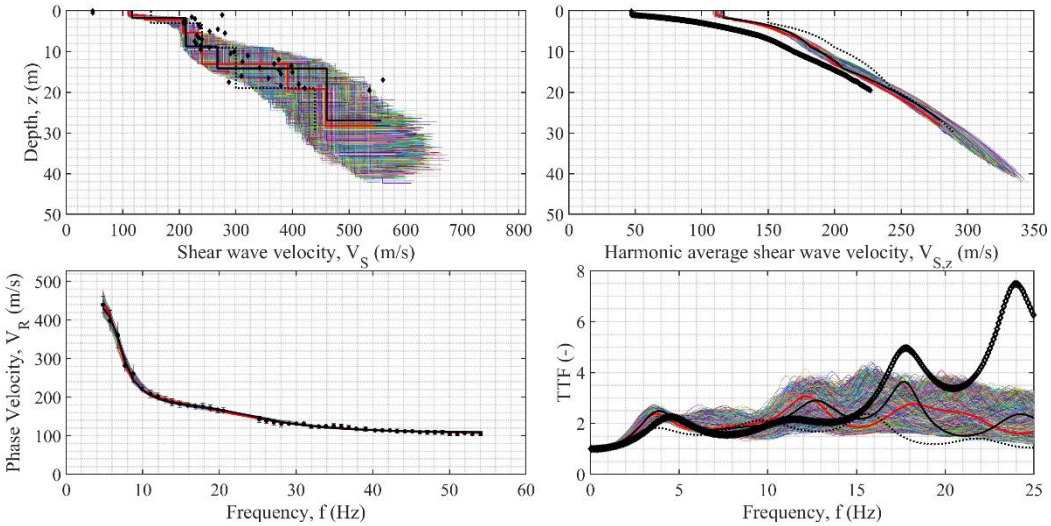

Figure A120. Final results of the inversions for L'Aquila (Roio Piano) (ID 35).

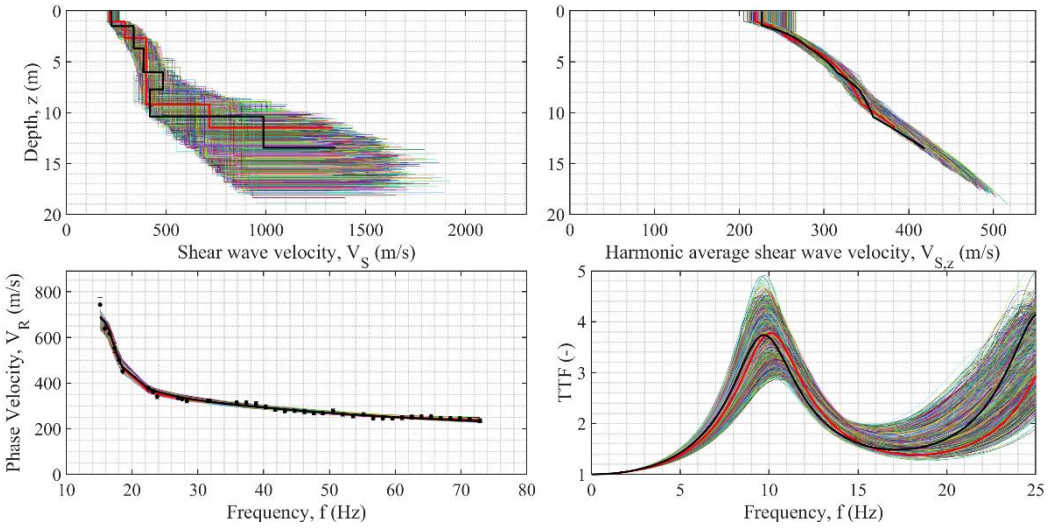

Figure A121. Final results of the inversions for Massa M.-Cantiere (ID 36).

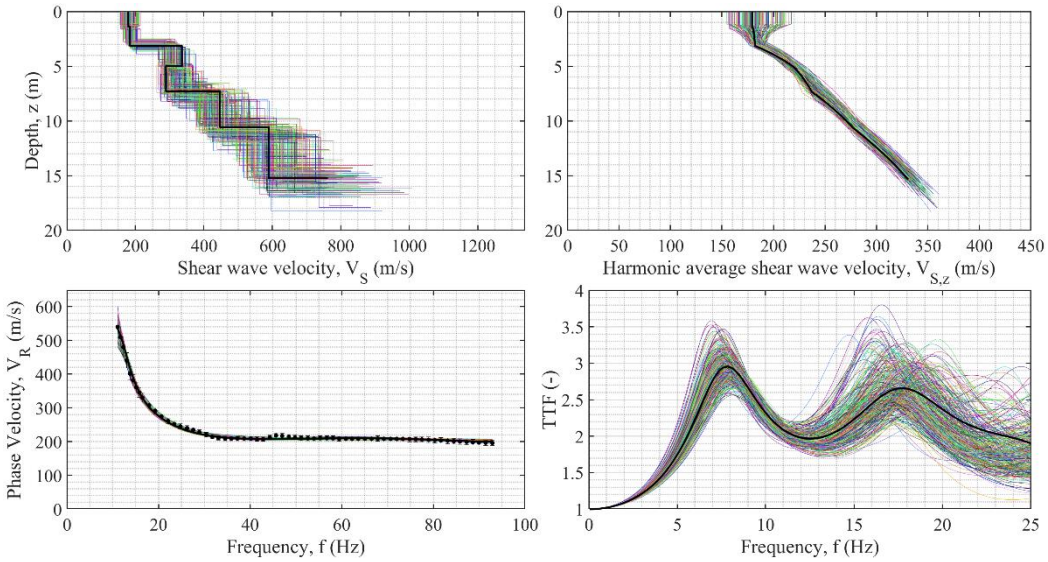

Figure A122. Final results of the inversions for Massa M.-Parcheggio (ID 37).

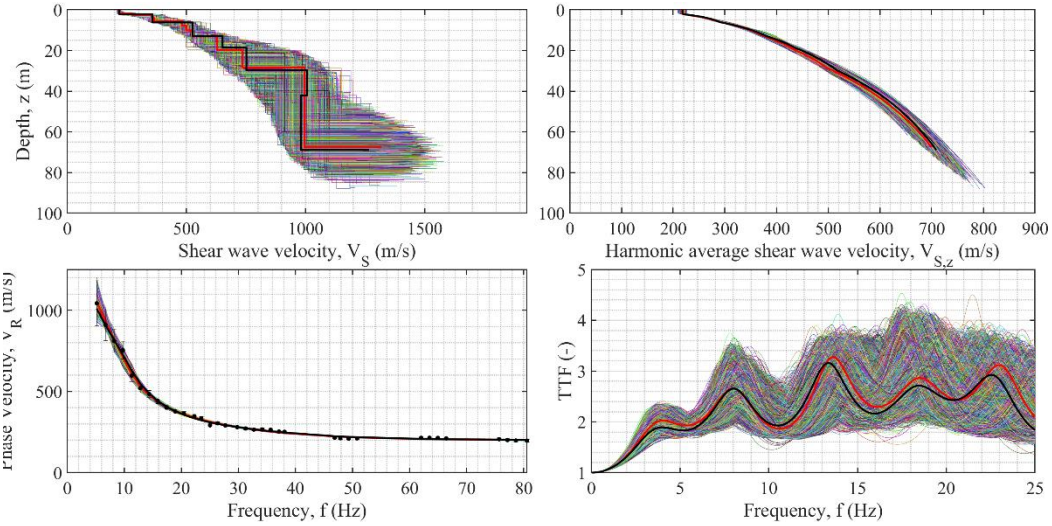

Figure A123. Final results of the inversions for Mathi-1&2 (ID 38).

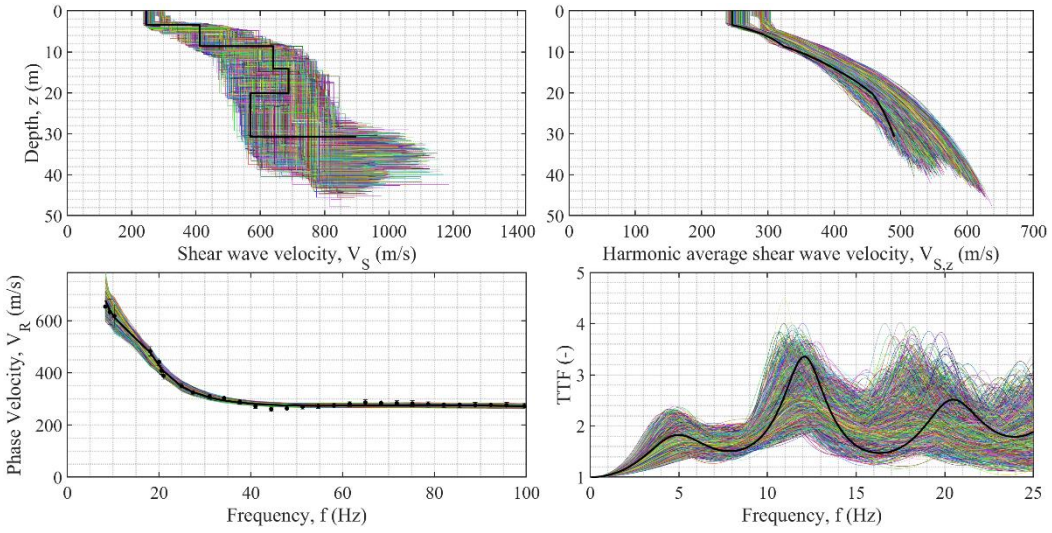

Figure A124. Final results of the inversions for Mathi-3 (ID 39).

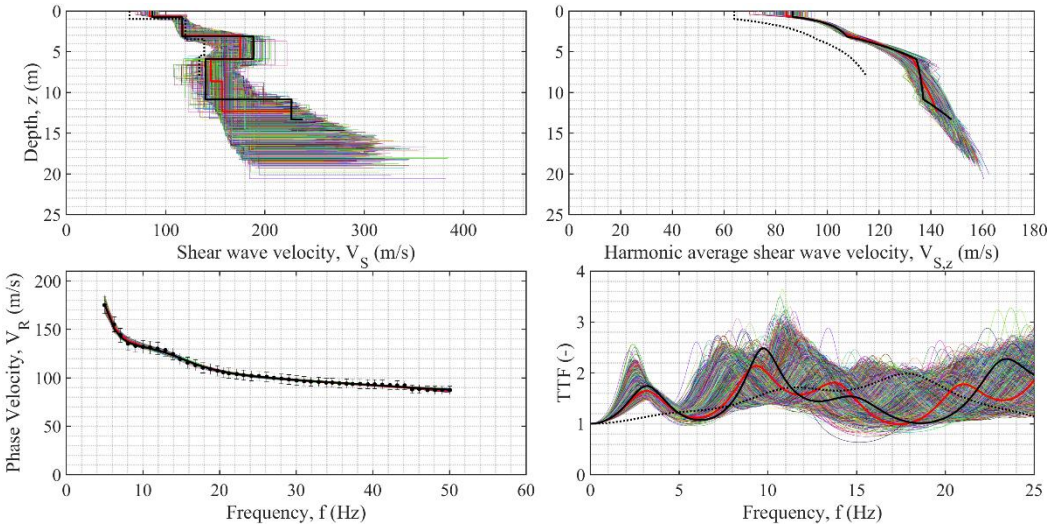

Figure A125. Final results of the inversions for Mirabello-Last-July (ID 40).

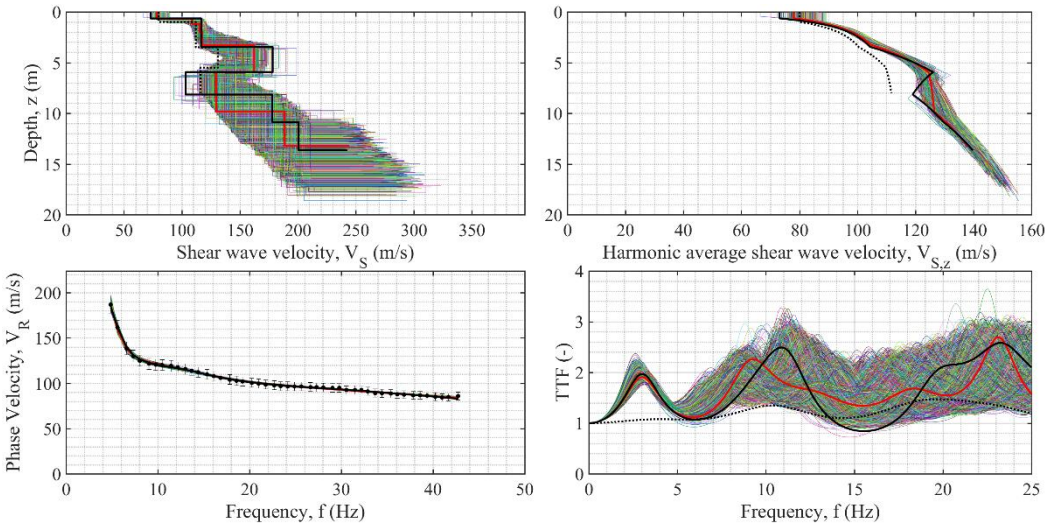

Figure A126. Final results of the inversions for Mirabello-Post-May (ID 41).

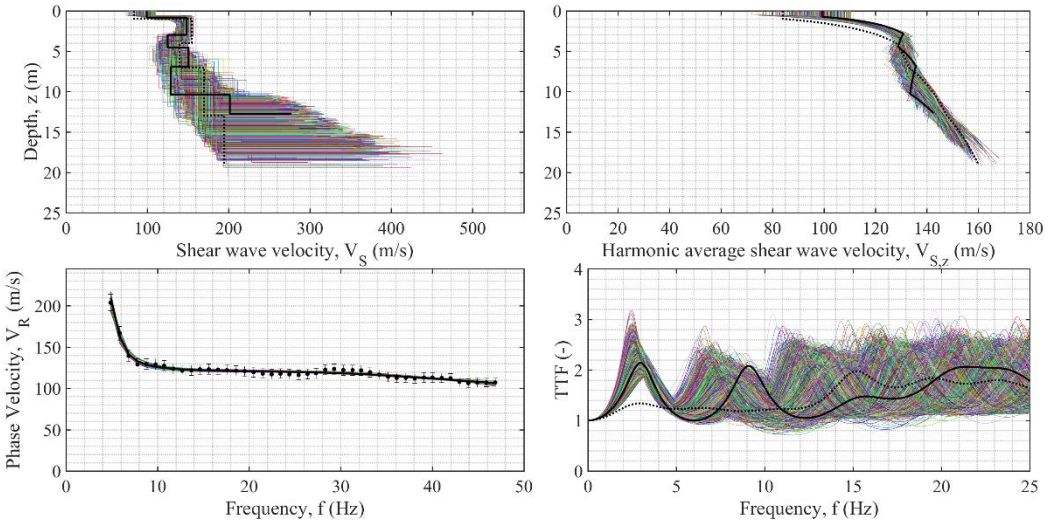

Figure A127. Final results of the inversions for Mirabello-Pre-Feb (ID 42).

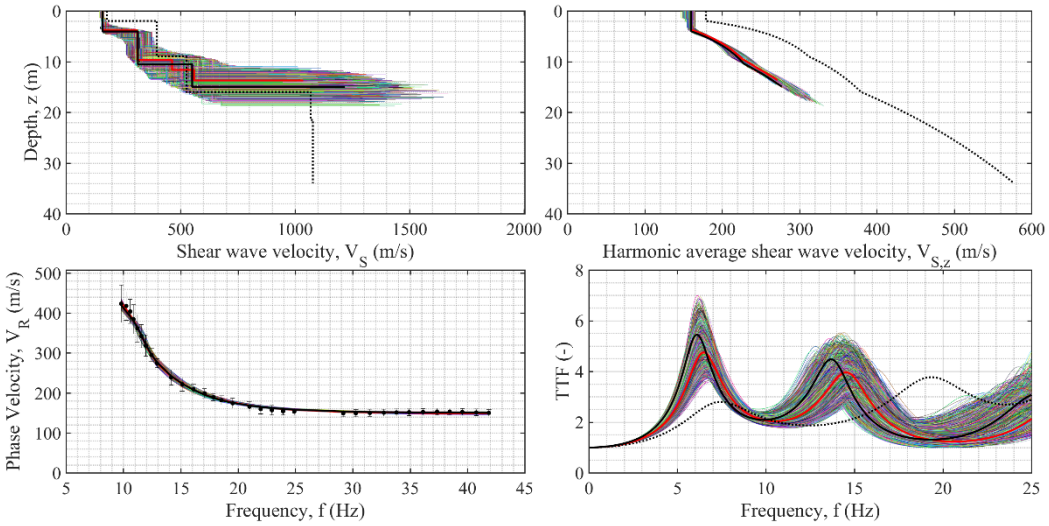

Figure A128. Final results of the inversions for Montemonaco (ID 43).

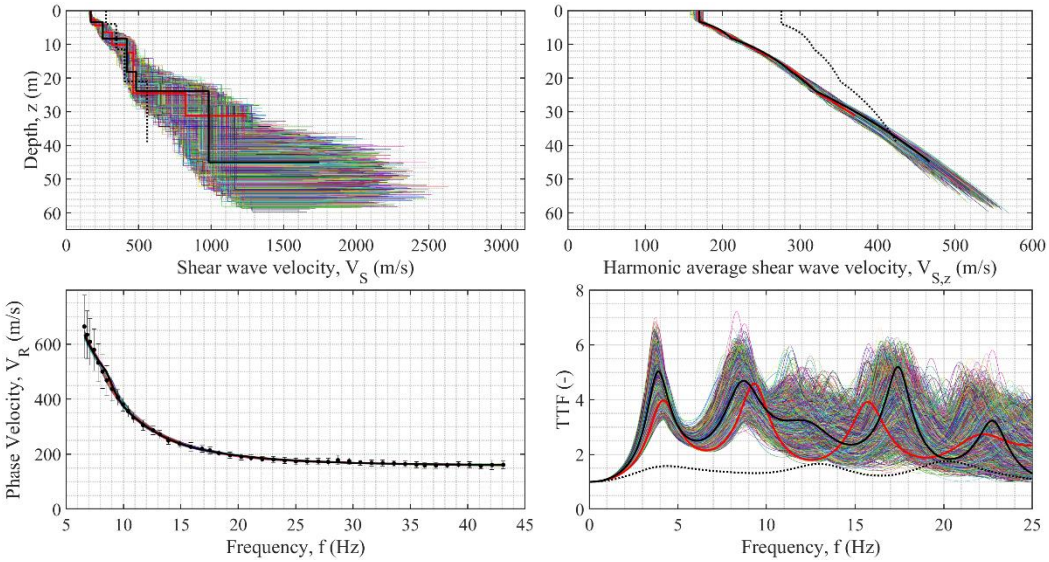

Figure A129. Final results of the inversions for Offida (ID 45).

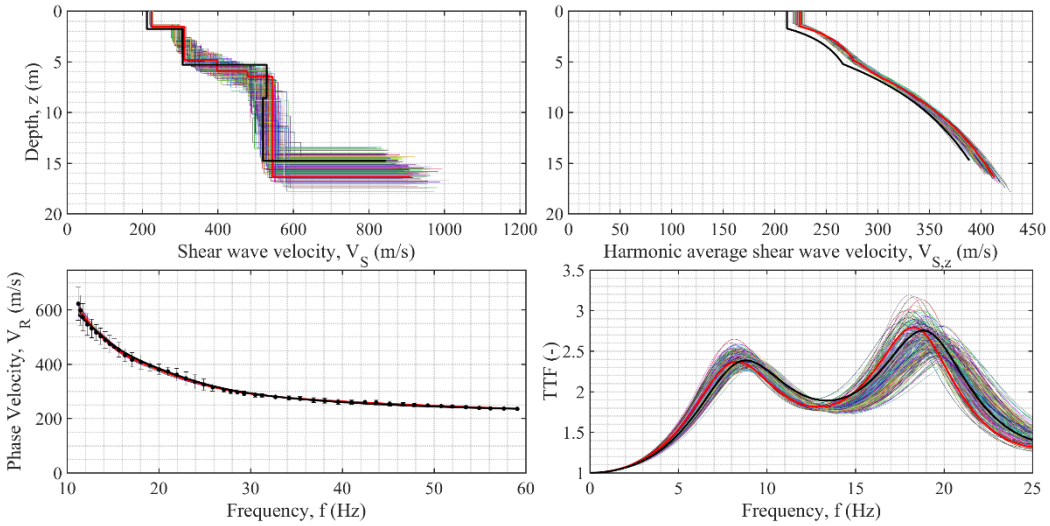

Figure A130. Final results of the inversions for Palmiano-Castel San Pietro (ID 46).

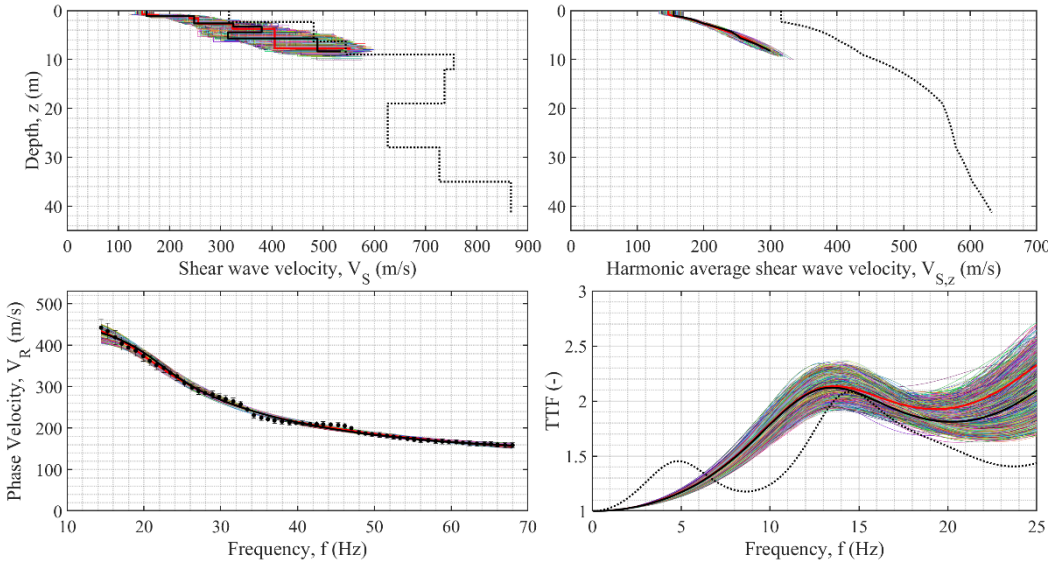

Figure A131. Final results of the inversions for Piazza al Serchio (ID 48).

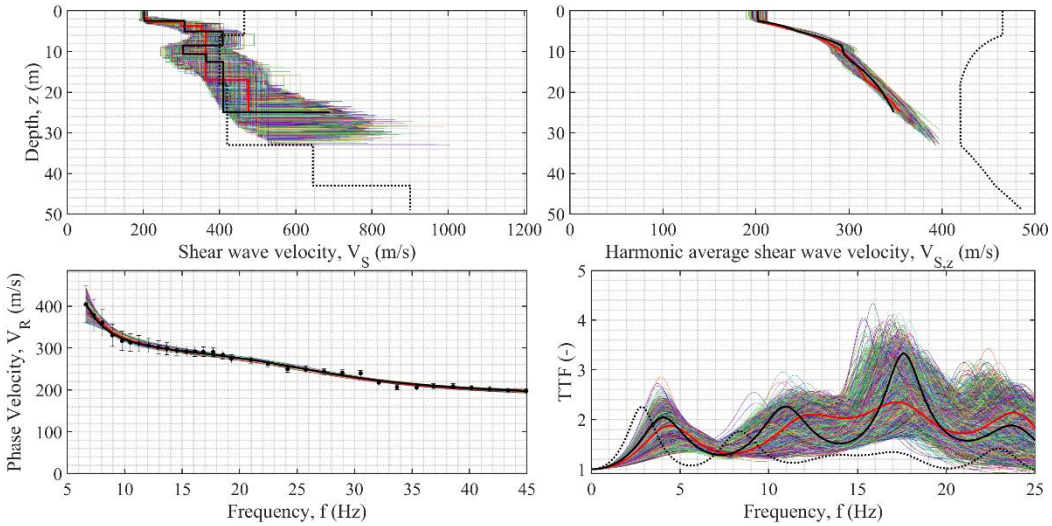

Figure A132. Final results of the inversions for Pieve Fosciana (ID 49).

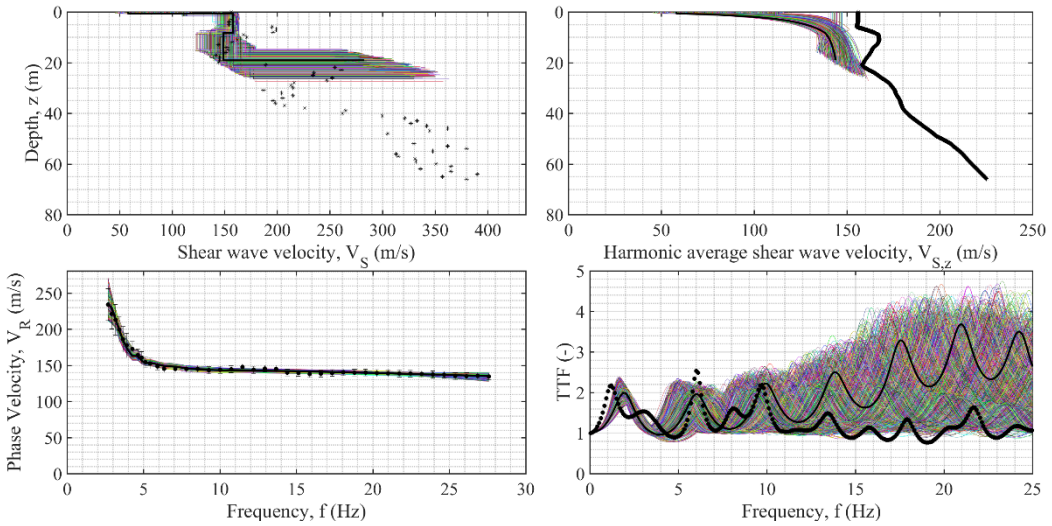

Figure A133. Final results of the inversions for Pisa (ID 50).

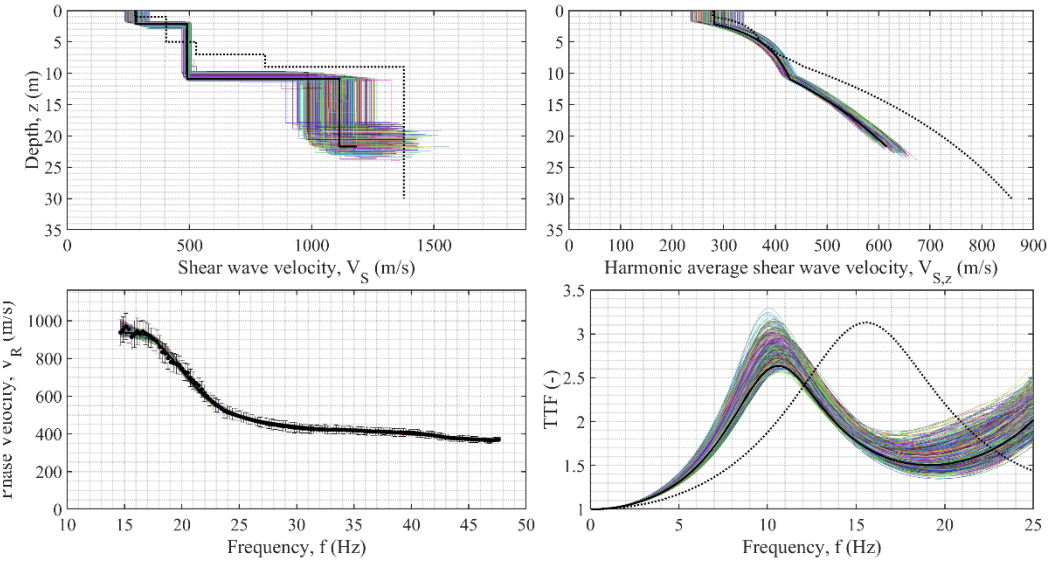

Figure A134. Final results of the inversions for Pontremoli-1 Maggio (ID 52).

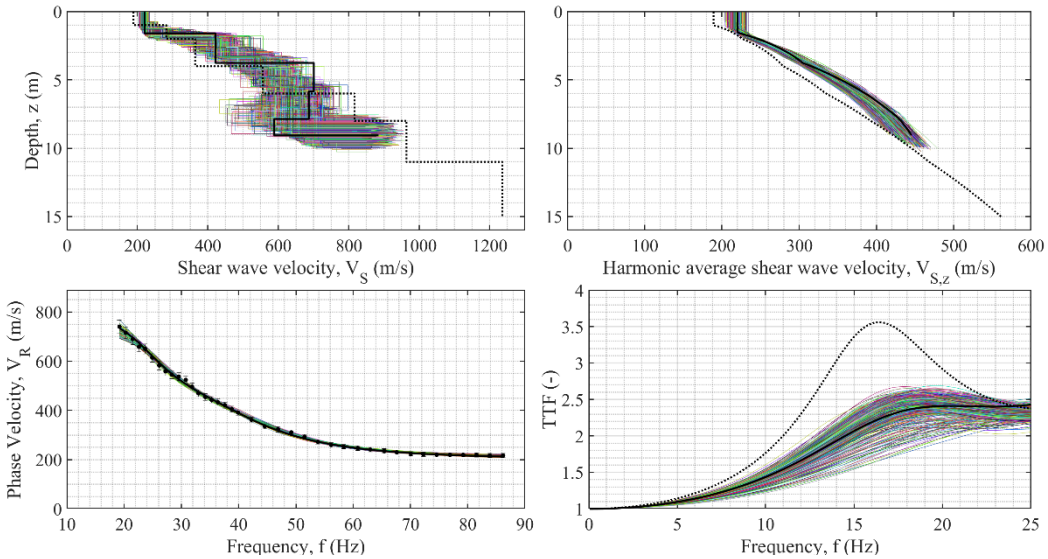

Figure A135. Final results of the inversions for Pontremoli-ASL 2 (ID 53).

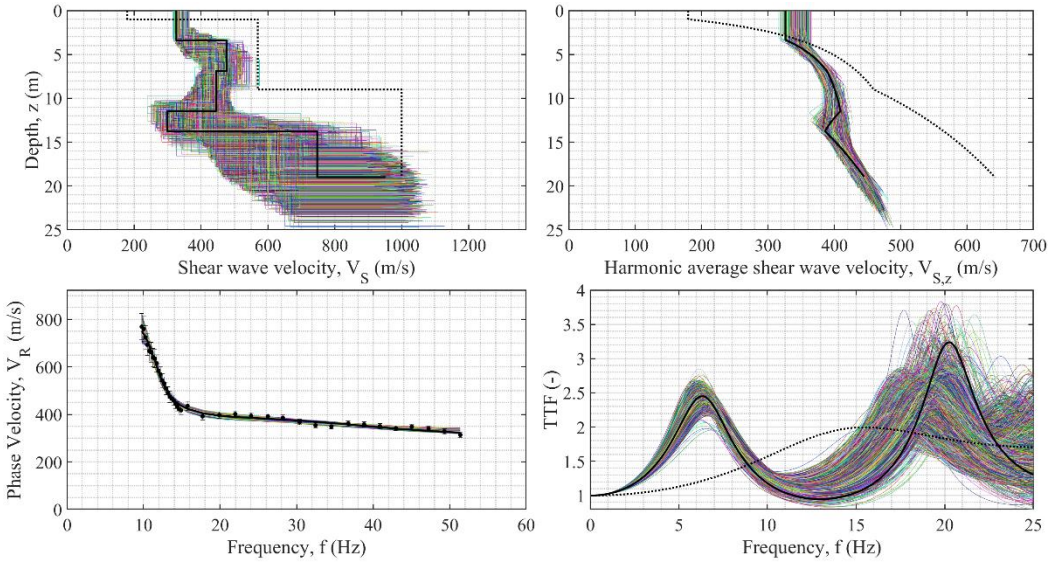

Figure A136. Final results of the inversions for Pontremoli-Bocciofila (ID 54).

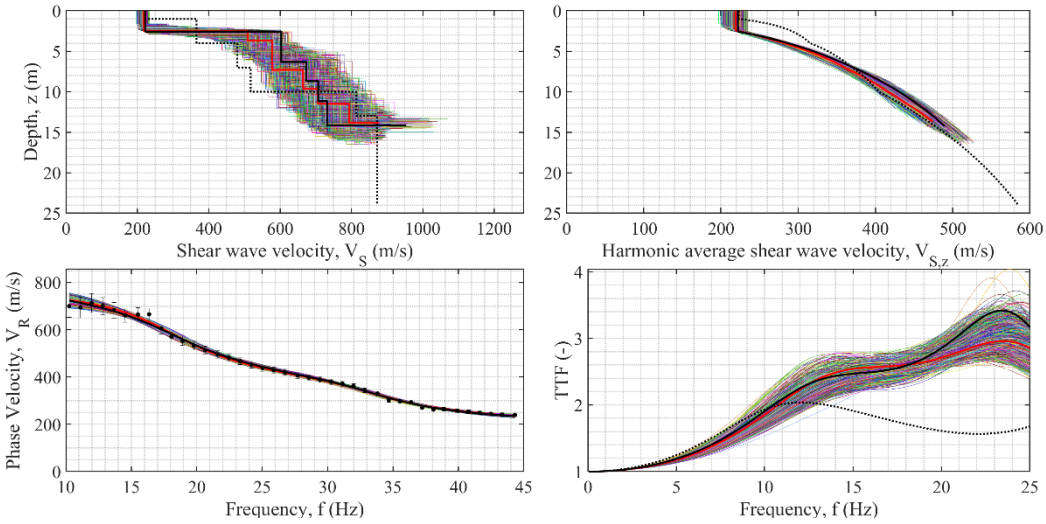

Figure A137. Final results of the inversions for Pontremoli-Giochi (ID 55).

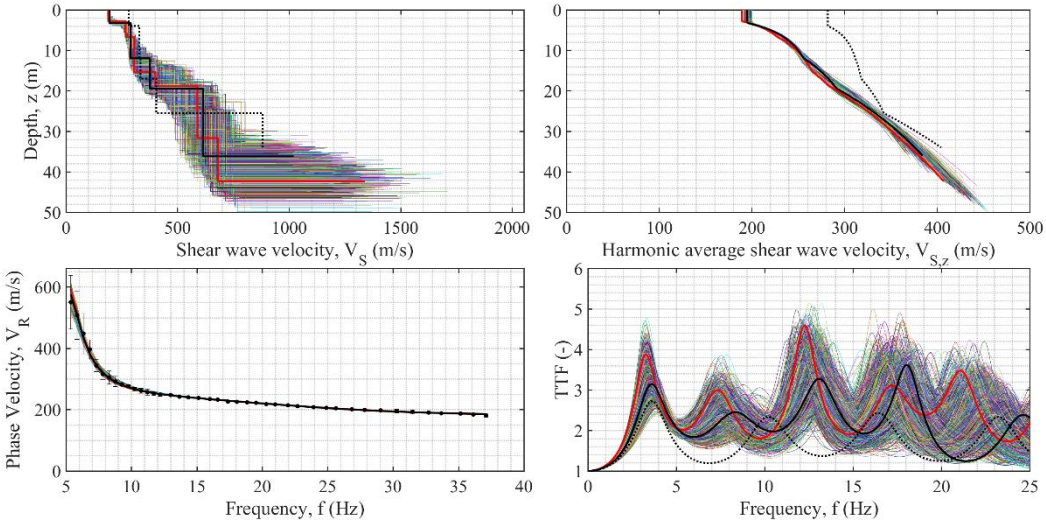

Figure A138. Final results of the inversions for Roccafluvione (ID 58).

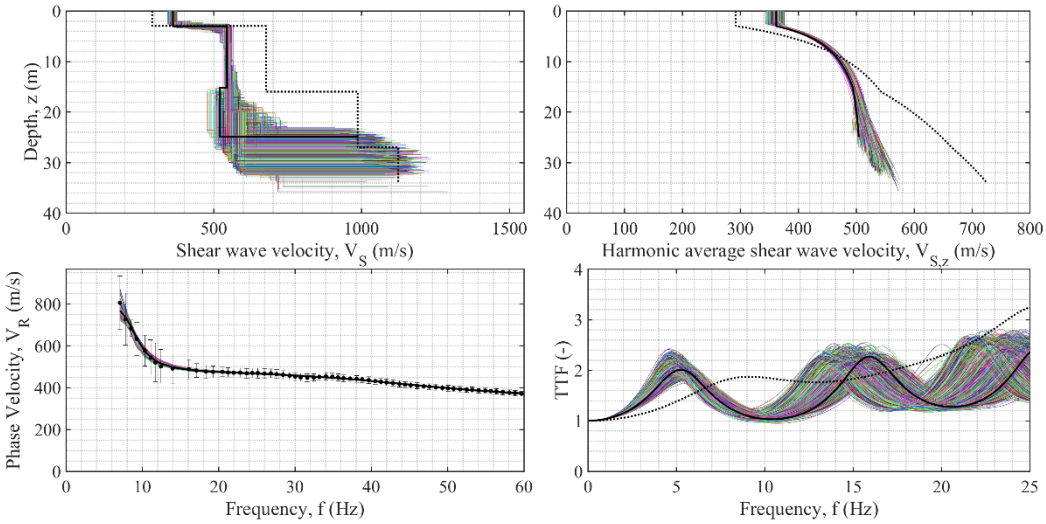

Figure A139. Final results of the inversions for Rotella (ID 59).

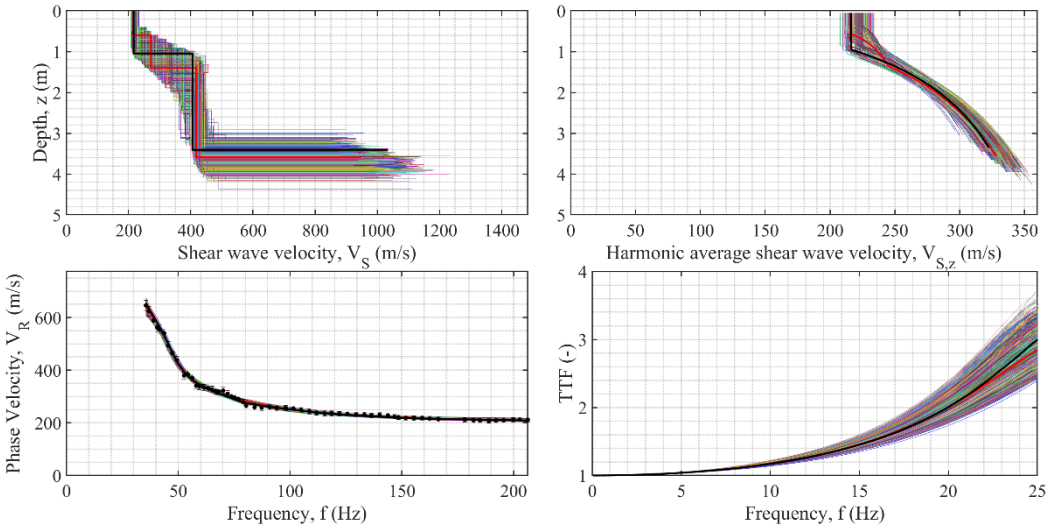

Figure A140. Final results of the inversions for RNS (ID 60).

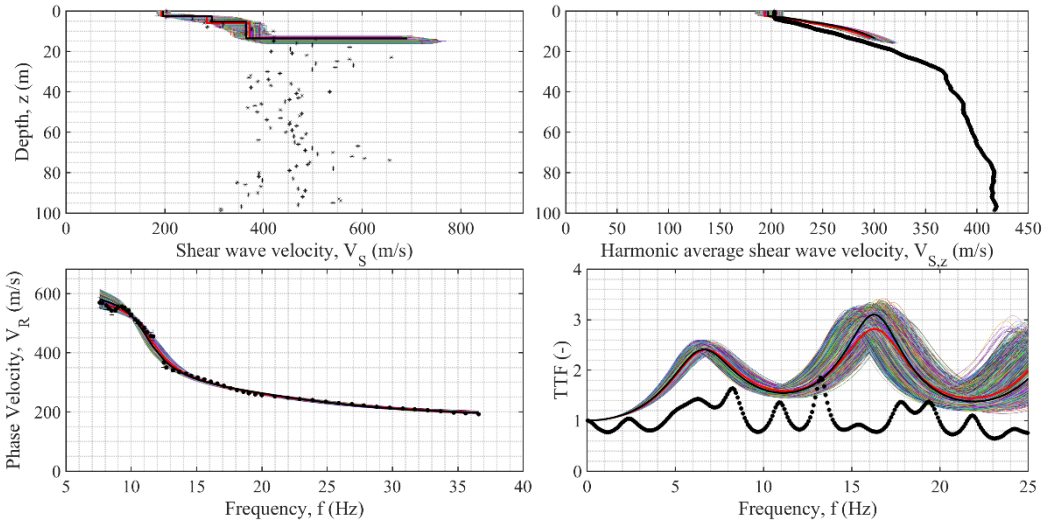

Figure A141. Final results of the inversions for Saluggia (ID 61).

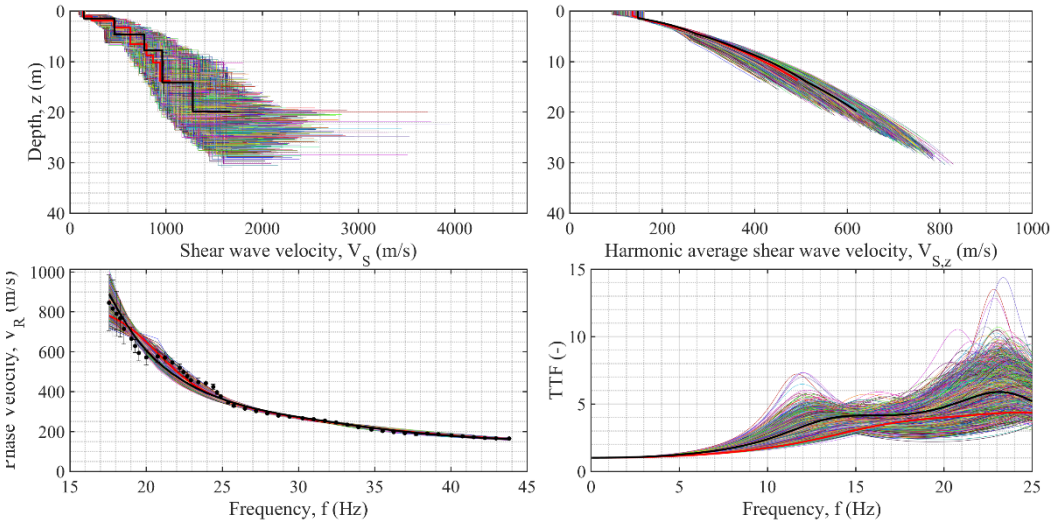

Figure A142. Final results of the inversions for San Severino Marche-1 (ID 62).

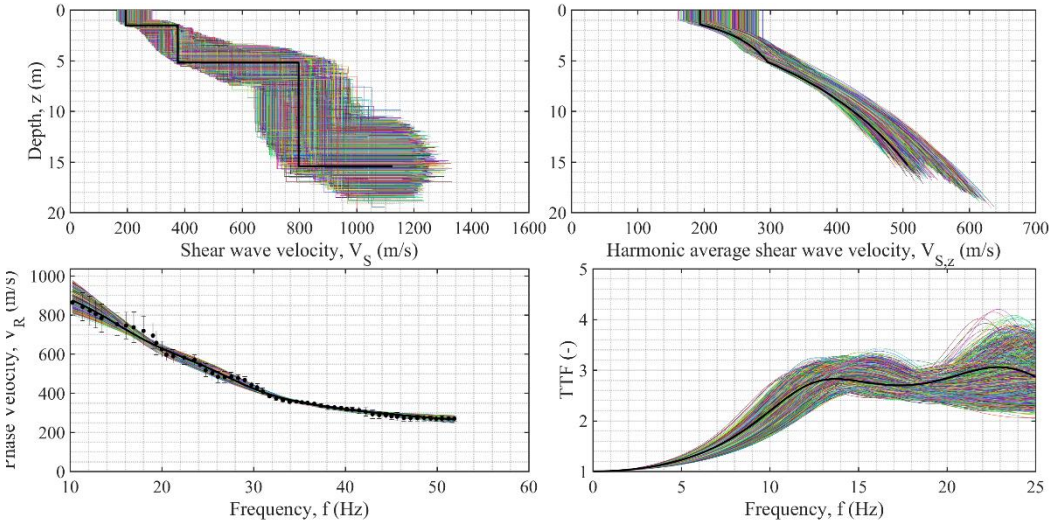

Figure A143. Final results of the inversions for San Severino Marche-2 (ID 63).

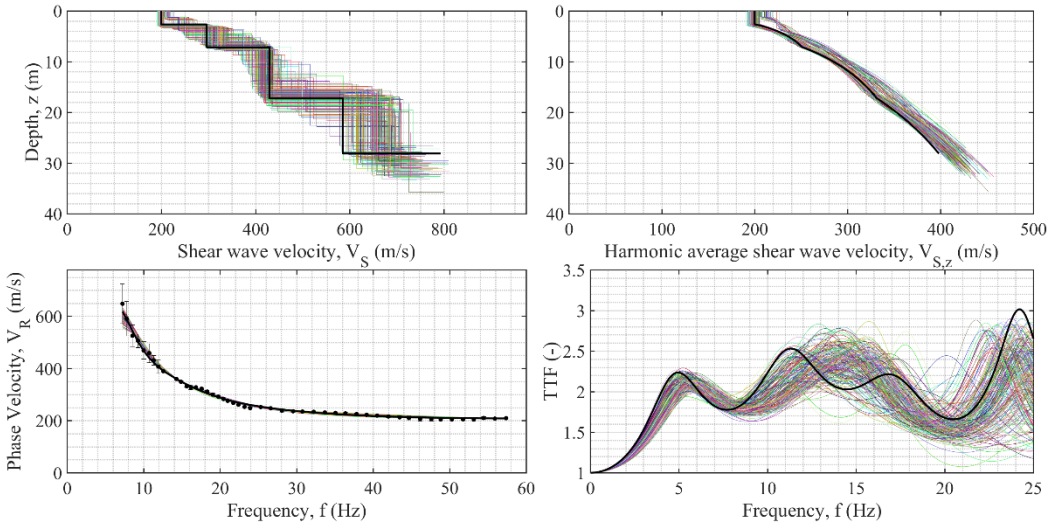

Figure A144. Final results of the inversions for Settimo Torinese (ID 69).

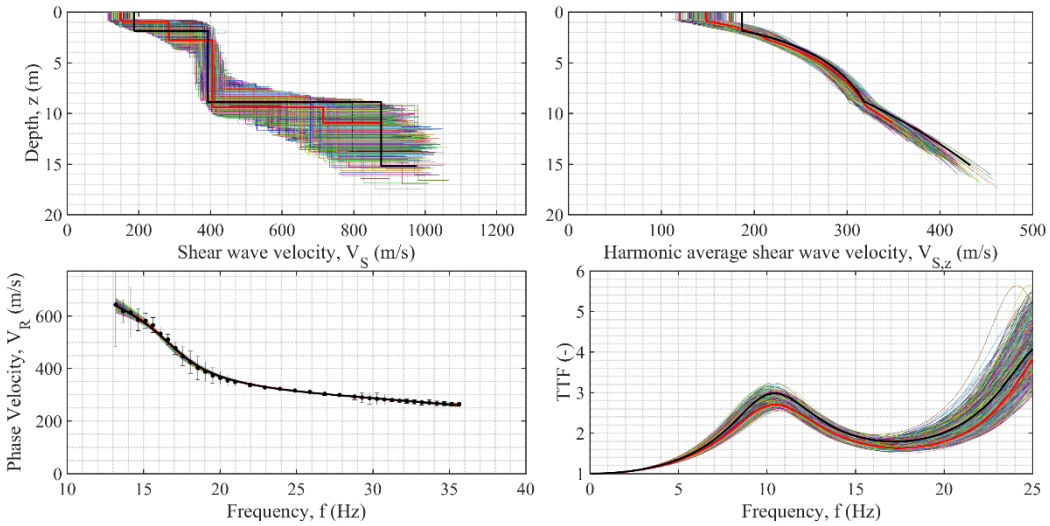

Figure A145. Final results of the inversions for Tarcento-1 (ID 70).

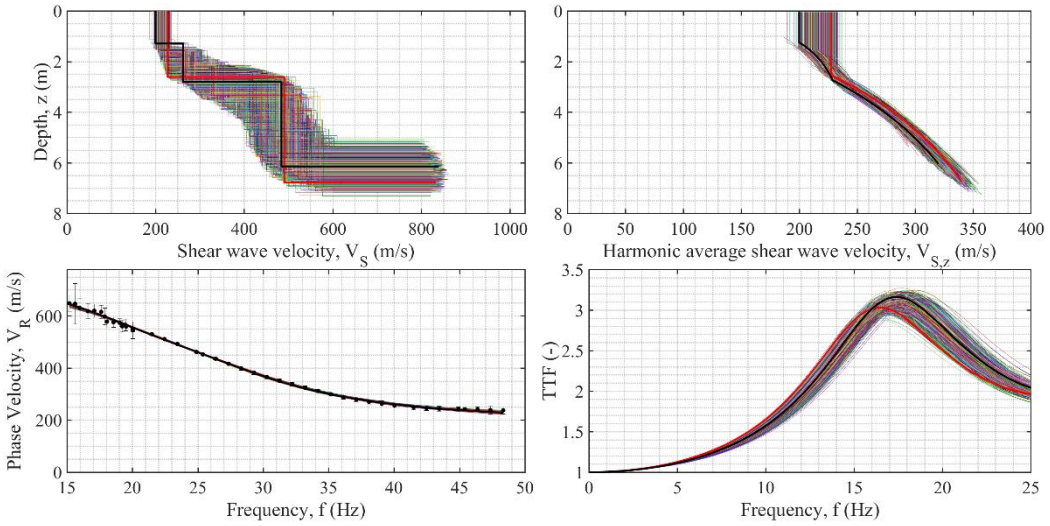

Figure A146. Final results of the inversions for Tarcento-2 (ID 71).

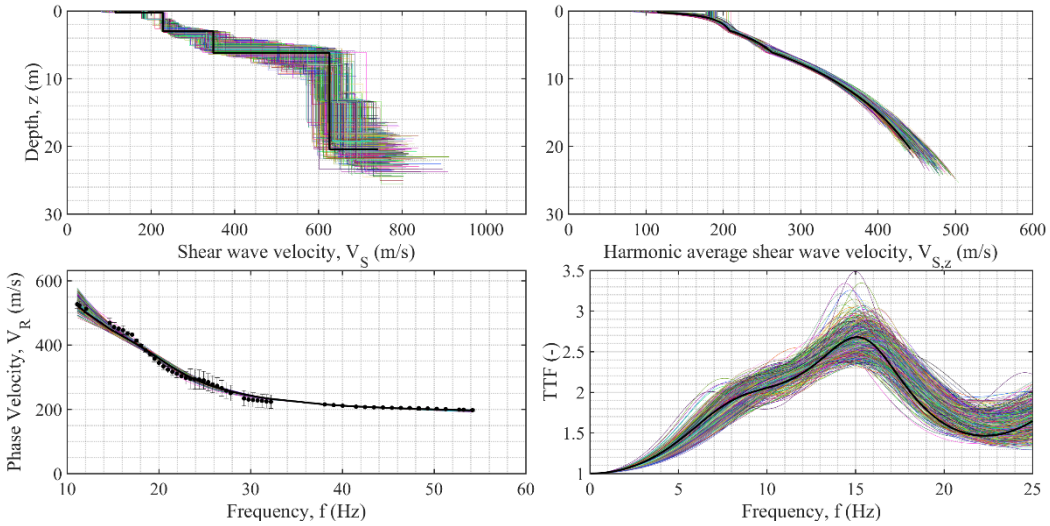

Figure A147. Final results of the inversions for Tarcento-3 (ID 72).

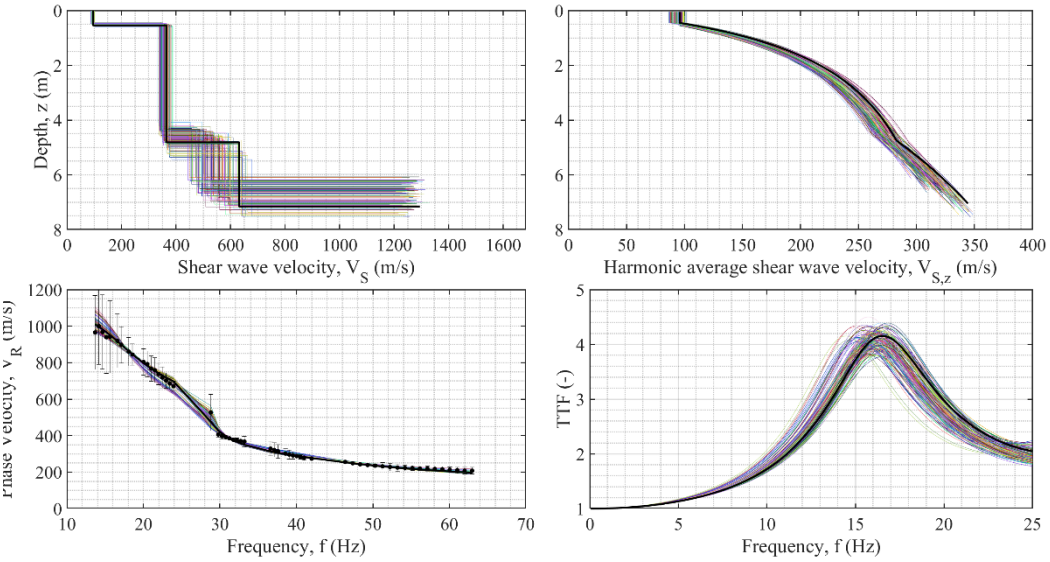

Figure A148. Final results of the inversions for Tarcento-4 (ID 73).

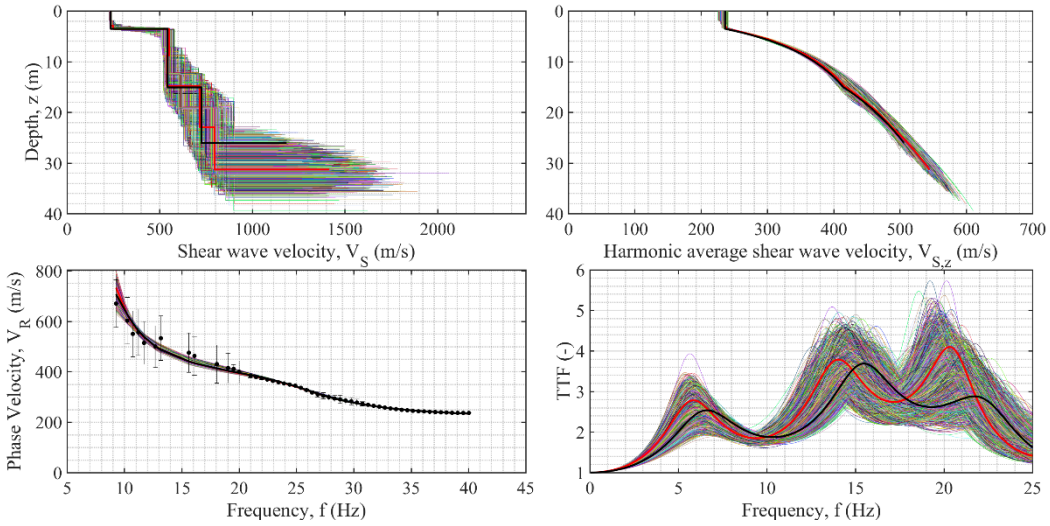

Figure A149. Final results of the inversions for Tarcento-5 (ID 74).

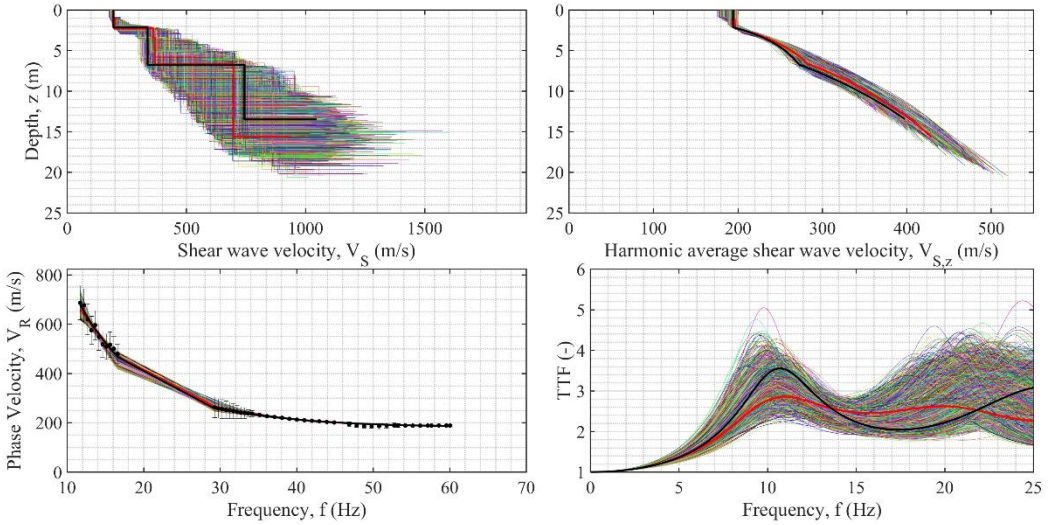

Figure A150. Final results of the inversions for Tarcento-6 (ID 75).

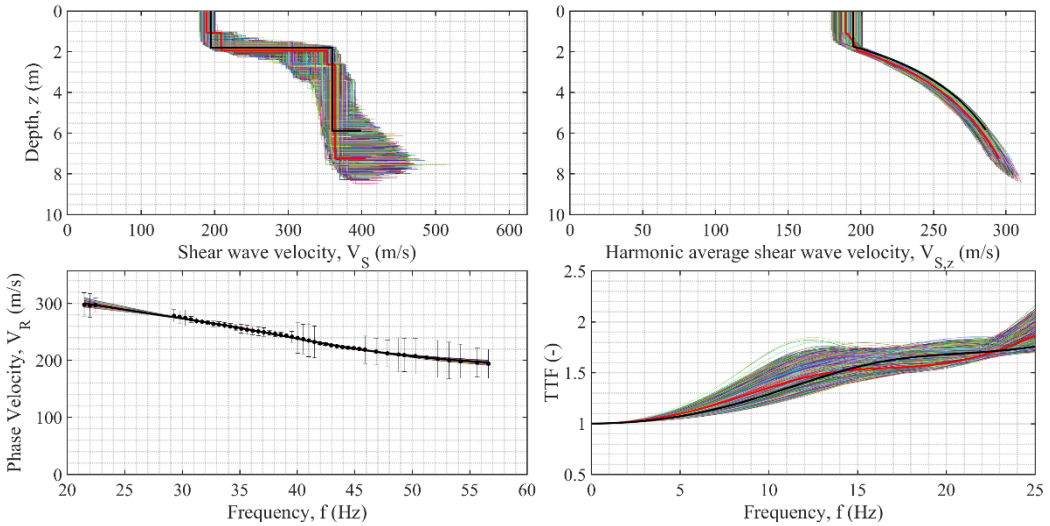

Figure A151. Final results of the inversions for Tarcento-7 (ID 76).

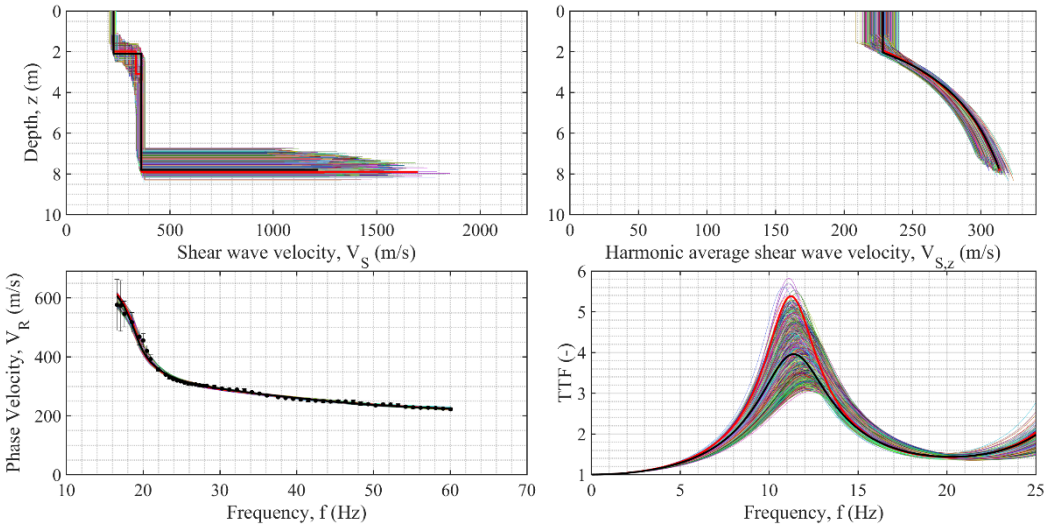

Figure A152. Final results of the inversions for Tarcento-8 (ID 77).

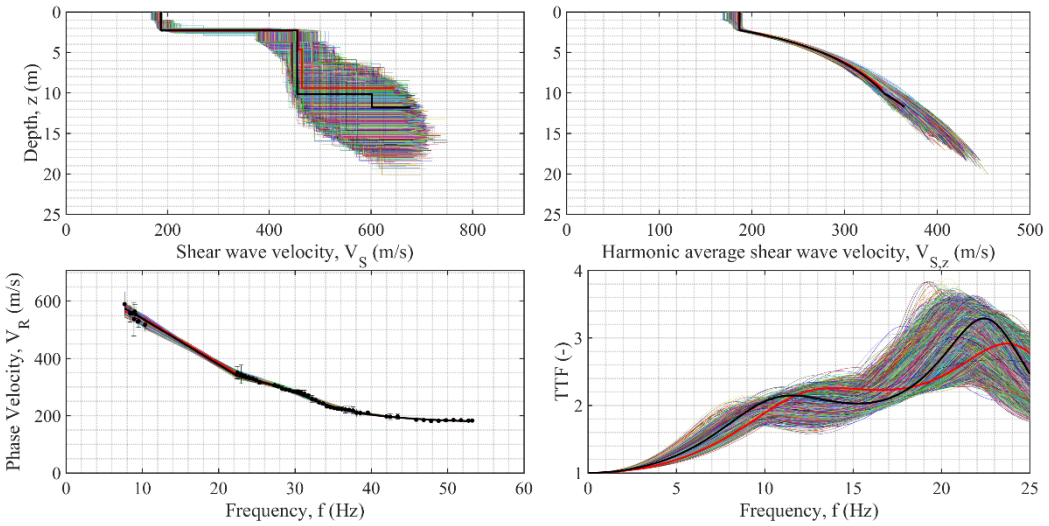

Figure A153. Final results of the inversions for Tarcento-10 (ID 78).

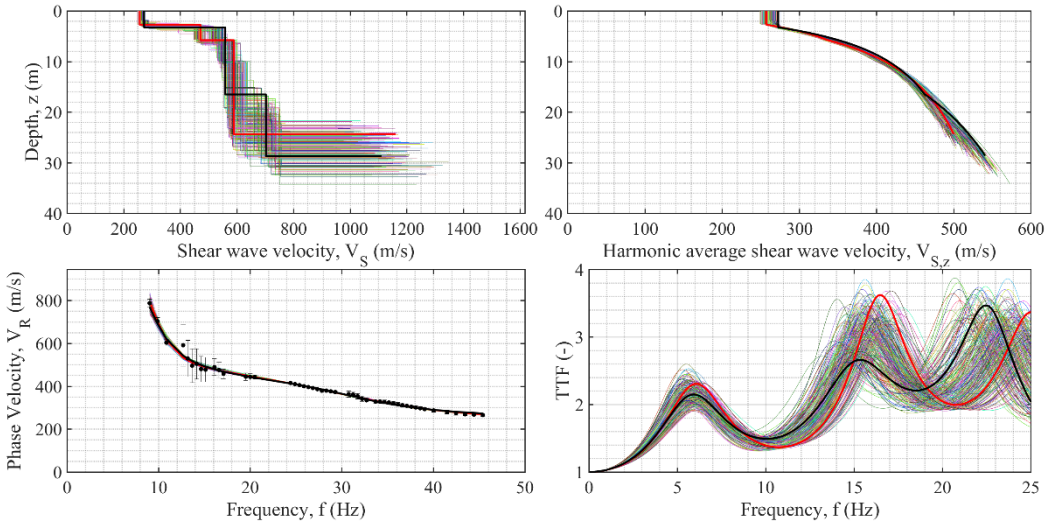

Figure A154. Final results of the inversions for Tarcento-11 (ID 79).

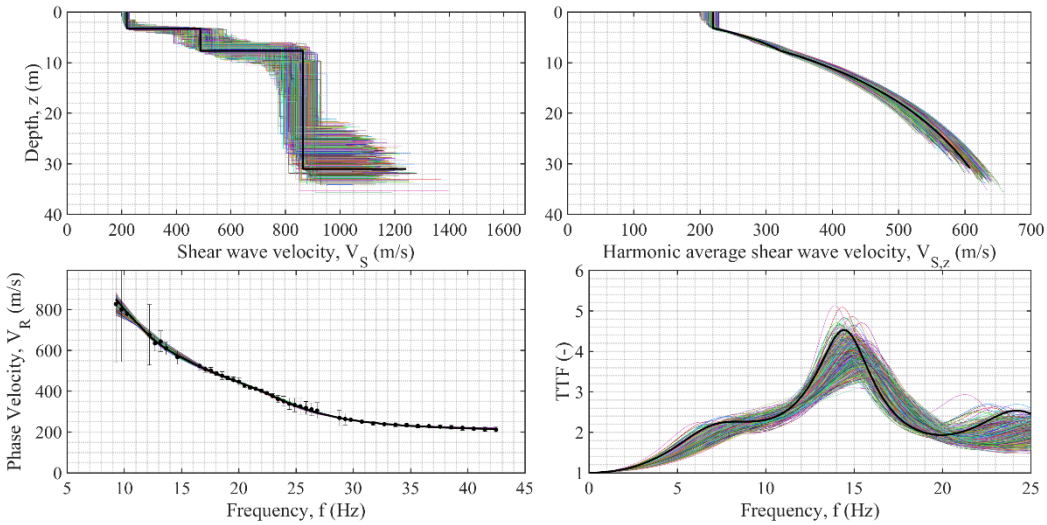

Figure A155. Final results of the inversions for Tarcento-12 (ID 80).

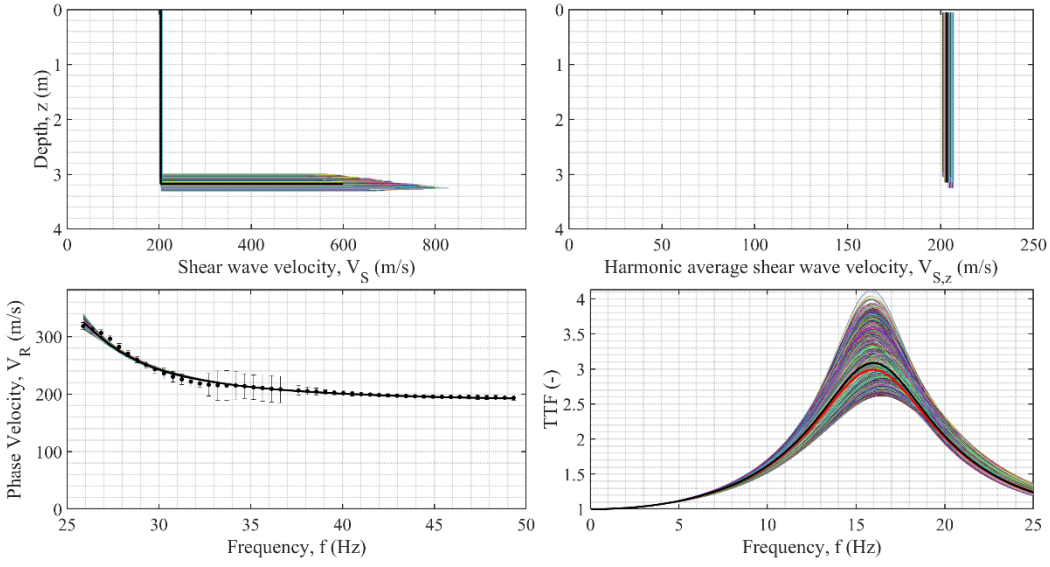

Figure A156. Final results of the inversions for Tarcento-15 (ID 81).

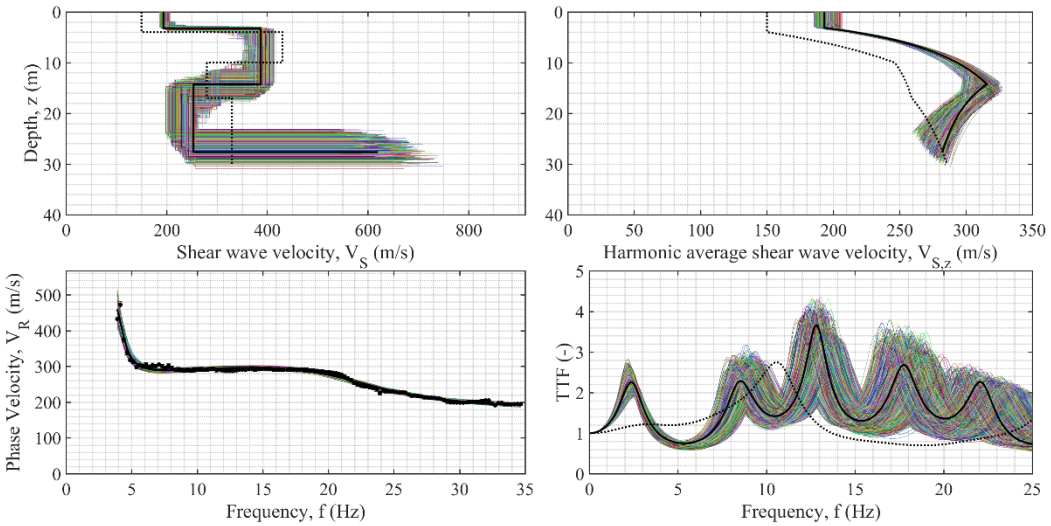

Figure A157. Final results of the inversions for Torre Pellice-Depuratore (ID 83).

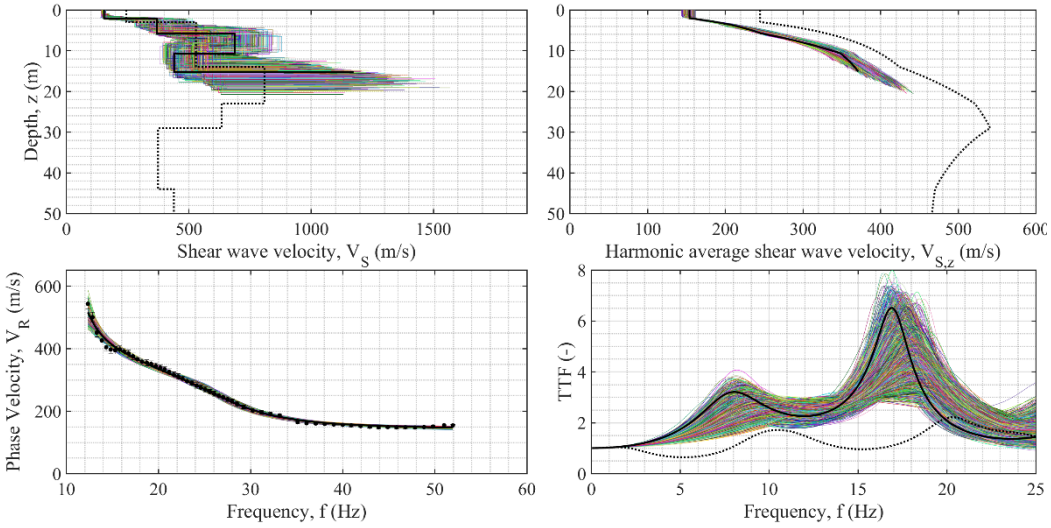

Figure 158. Final results of the inversions for Torre Pellice-Giardini (ID 84).

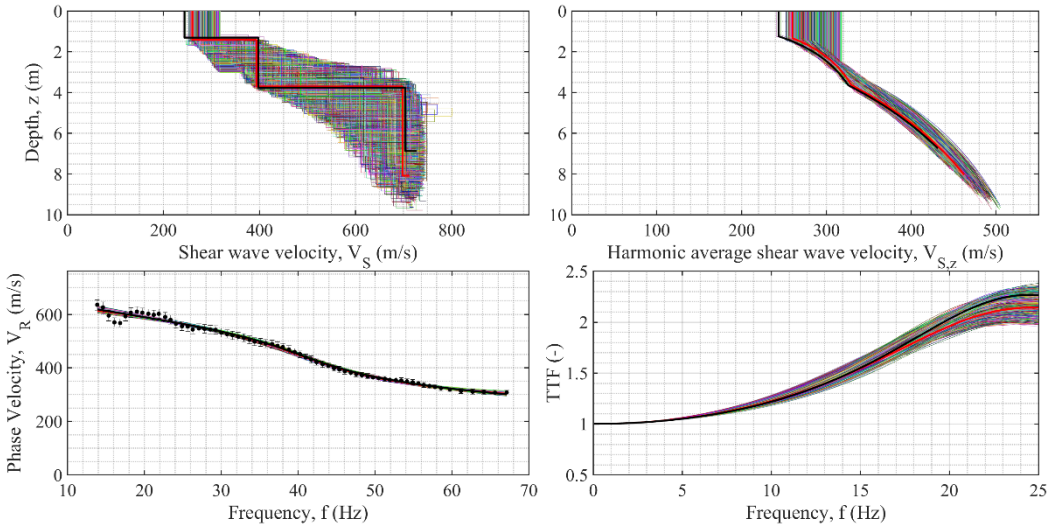

Figure A159. Final results of the inversions for Torre Pellice-Giochi (ID 85).

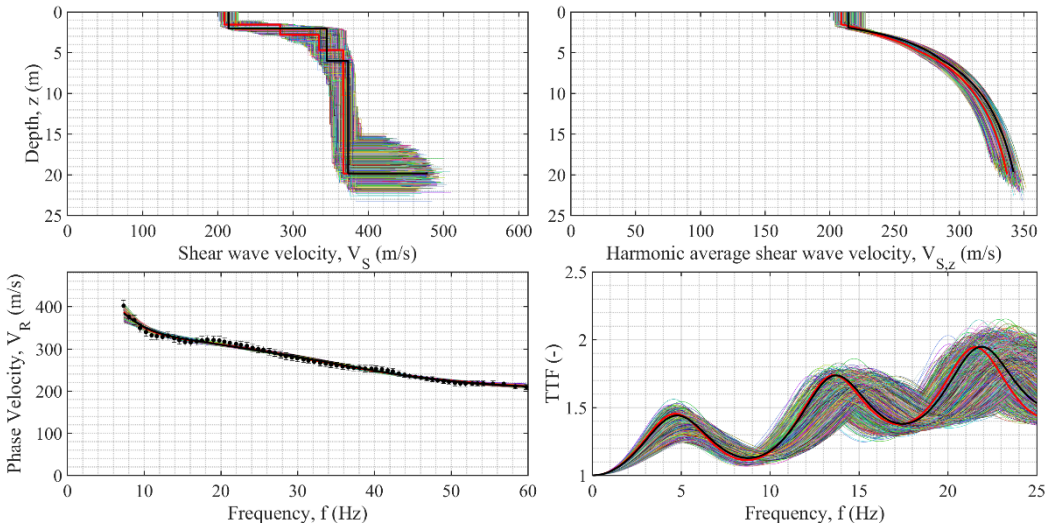

Figure A160. Final results of the inversions for Torre Pellice-Torrente (ID 86).

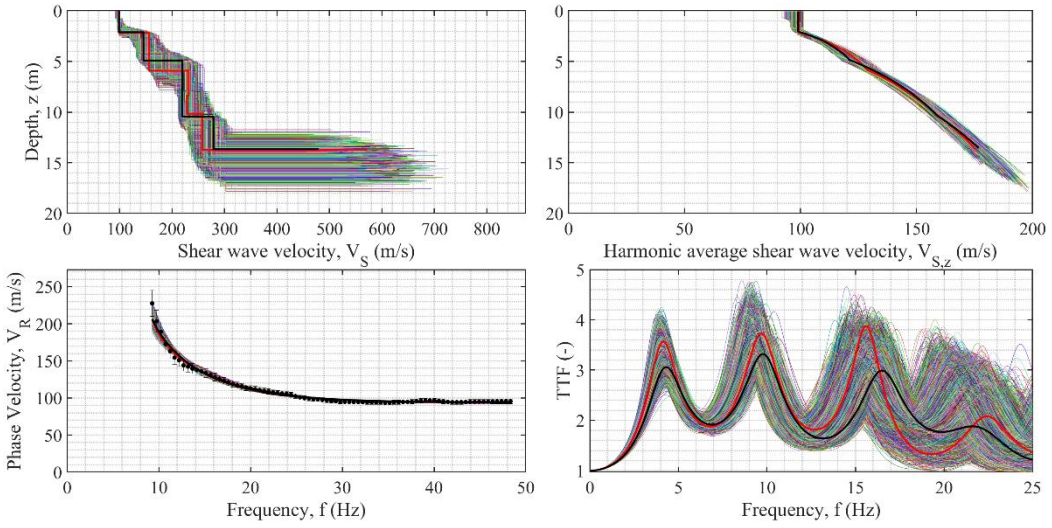

Figure A161. Final results of the inversions for TRF0 (ID 87).

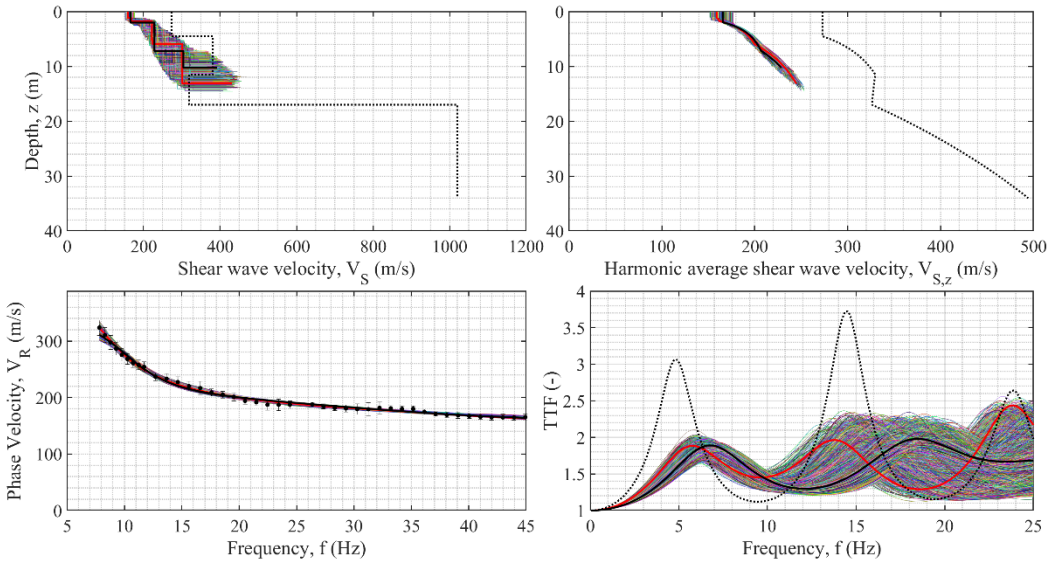

Figure A162. Final results of the inversions for Venarotta (ID 89).

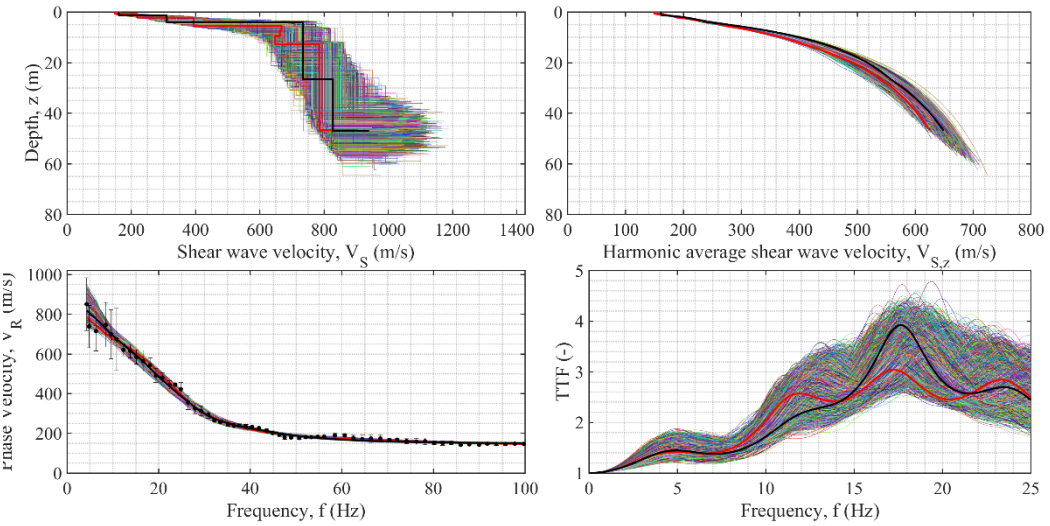

Figure A163. Final results of the inversions for Tarvisio (ID 92).